Proceedings

of

Symposium on Energy Engineering in the 21st Century (SEE2000)

Volume 1

Edited by

Ping Cheng
Mechanical Engineering Department
The Hong Kong University of Science and Technology
Clear Water Bay, Kowloon, Hong Kong

Begell House
New York, Wallingford (U.K.)

DISTRIBUTION STATEMENT A
Approved for Public Release
Distribution Unlimited

DTIC QUALITY INSPECTED 1

20000223 146

January 9-13, 2000 Hong Kong

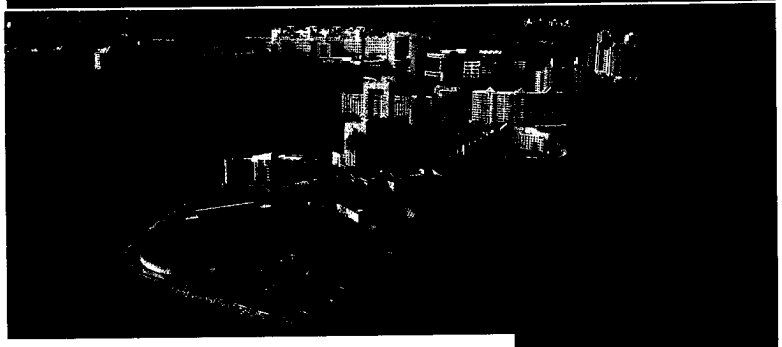

Proceedings of

Symposium on Energy Engineering in the 21st Century (SEE 2000)

Volume **One**

DISTRIBUTION STATEMENT A
Approved for Public Release
Distribution Unlimited

Begell House New York, Wallingford (U.K.)

Ping Cheng Editor

Library of Congress Cataloging-in-Publication Data

Catalog record is available from the Library of Congress.

This book represents information obtained from authentic and highly regarded sources. Reprinted material is quoted with permission, and sources are indicated. A wide variety of references are listed. Every reasonable effort has been made to give reliable data and information, but the authors and the publisher cannot assume responsibility for the validity of all materials or for the consequences of their use.

All rights reserved. This book, or any parts thereof, may not be reproduced in any form without written consent from the publisher.

Direct all inquiries to Begell House, Inc., 79 Madison Avenue, New York, NY 10016.

© 2000 by Begell House, Inc.

ISBN 1-56700-132-7 (hard cover edition)

Printed in Hong Kong 1 2 3 4 5 6 7 8 9 0

REPORT DOCUMENTATION PAGE

Form Approved
OMB No. 0704-0188

The public reporting burden for this collection of information is estimated to average 1 hour per response, including the time for reviewing instructions, searching existing data sources, gathering and maintaining the data needed, and completing and reviewing the collection of information. Send comments regarding this burden estimate or any other aspect of this collection of information, including suggestions for reducing the burden, to Department of Defense, Washington Headquarters Services, Directorate for Information Operations and Reports (0704-0188), 1215 Jefferson Davis Highway, Suite 1204, Arlington, VA 22202-4302. Respondents should be aware that notwithstanding any other provision of law, no person shall be subject to any penalty for failing to comply with a collection of information if it does not display a currently valid OMB control number.

PLEASE DO NOT RETURN YOUR FORM TO THE ABOVE ADDRESS.

1. REPORT DATE *(DD-MM-YYYY)*	2. REPORT TYPE	3. DATES COVERED *(From - To)*
14-02-2000	Conference Proceedings	9-13 Jan 00

4. TITLE AND SUBTITLE

Proceedings of Symposium on Energy Engineering in the 21st Century (SEE 2000) ~~(Four Volumes)~~ Vol. 1

5a. CONTRACT NUMBER
F6256299M9146

5b. GRANT NUMBER

5c. PROGRAM ELEMENT NUMBER

6. AUTHOR(S)

Conference Committee

5d. PROJECT NUMBER

5e. TASK NUMBER

5f. WORK UNIT NUMBER

7. PERFORMING ORGANIZATION NAME(S) AND ADDRESS(ES)

Hong Kong University of S&T
Clear Water Bay
Hong Kong
Hong Kong

8. PERFORMING ORGANIZATION REPORT NUMBER
N/A

9. SPONSORING/MONITORING AGENCY NAME(S) AND ADDRESS(ES)

AOARD
UNIT 45002
APO AP 96337-5002

10. SPONSOR/MONITOR'S ACRONYM(S)
AOARD

11. SPONSOR/MONITOR'S REPORT NUMBER(S)
CSP-991002

12. DISTRIBUTUION/AVAILABILITY STATEMENT

Approved for public release; distribution is unlimited.

13 SUPPLEMENTARY NOTES

14. ABSTRACT

Volume 1, Page 1 – 406 Includes:
Keynote Papers, Forced Convection, Natural Convection, and Boiling and Condensation
Volume 2, Page 407 – 903 Includes:
Two-Phase Flow, Porous Media, Heat Pipes and Thermosyphons, Conduction and Radiation, Microscale Heat Transfer, Heat Transfer Enhancement, Solar Energy & Nuclear Energy, Thermal Storage, Melting & Solidification
Volume 3, Page 904 – 1,345 Includes:
Drying & Food Processing, Heat Exchangers, Air-Conditioning and Refrigeration, Cryogenic Engineering, Energy and Environment, Combustion and Fire
Volume 4, Page 1,346 – 1,734 Includes: Cycle Analysis, Engine Combustion, Waste Treatment by Thermal Methods, Fuel Cells, Clean Combustion Technology, Coal Combustion

15. SUBJECT TERMS

Fire Surpression

16. SECURITY CLASSIFICATION OF:			17. LIMITATION OF ABSTRACT	18. NUMBE OF PAGES	19a. NAME OF RESPONSIBLE PERSON
a. REPORT	b. ABSTRACT	c. THIS PAGE			Terence J. Lyons, M.D.
U	U	U	UU	1,734	19b. TELEPHONE NUMBER *(Include area code)* +81-3-5410-4409

FORWARD

The signing of the Montreal Protocol in 1987 and the Kyoto Protocol in 1997 by various nations serves as a reminder once again of the intimate relationship between energy and environment, which will no doubt remain one of the major issues in the 21st Century. This is particularly so in Southeast Asia, where industrial growth has taken place at such a rapid pace during the last two decades. At the same time, research in energy engineering is accelerating in this part of the world. At the Hong Kong University of Science and Technology (HKUST), the Center for Energy and Thermal Systems (CETS) was recently established for the research and development of energy efficient and environmentally benign thermal systems. Thus, it is a privilege for CETS to be able to host the Symposium on Energy Engineering in the 21st Century (SEE2000) on the HKUST campus between 9-13 January 2000, the first international energy engineering conference ever held in Hong Kong.

The aim of this Symposium is to provide a forum for technical interchange in various aspects of energy engineering. The 226 papers (including 11 keynote papers) presented in the 25 technical sessions of the Symposium are published in this proceedings which contains 4 volumes, covering a variety of topics from heat and mass transfer, various energy and thermal systems, to clean combustion technology.

It has been a great pleasure for me to work with Symposium Co-Chairmen Professor Kefa Cen of the Zhejiang University and Professor Patrick Takahashi of the University of Hawaii in the planning of this Symposium. I would like to express my sincere thanks to keynote speakers for their efforts in writing up-to-date review papers, to members of the International Advisory Committee and the Organizing Committee for their enthusiasm in promoting the Symposium, and to members of the Local Committee for their hard work in reviewing the manuscripts. Special thanks are due to Dr. H. H. Qiu (the Symposium Secretariat) and Ms. Lotta Tse for their help in making conference arrangements, as well as to Ms. Ellie Ho, Ms. Ronnie Tse and other clerical staff for their help in the typing of the manuscripts and for the preparation of the proceedings. The generous financial support from the K. C. Wong Education Foundation, U.S. Air Force Asian Office of Aerospace Research and Development, U.S. Army Research Office - Far East, U.S. Office of Naval Research - Asia, and the International Technic HVAC Company are gratefully acknowledged.

Ping Cheng
Symposium Chair

Hong Kong
January 2000

SYMPOSIUM CHAIRMAN

Professor Ping Cheng
Department of Mechanical Engineering
Hong Kong University of Science and Technology
Clear Water Bay, Kowloon, Hong Kong
Fax: (852) 2358-1543 E-mail: mepcheng@ust.hk

SYMPOSIUM CO-CHAIRMEN

Professor Kefa Cen
Institute for Thermal Power Engineering
Zhejiang University
Hangzhou 310027, China
Fax: (86) 571-595-1616
E-mail: kfcen@sun.zju.edu.cn

Professor Patrick Takahashi
Hawaii Natural Energy Institute
University of Hawaii
Honolulu, Hawaii 96822, U.S.A.
Fax: (808) 956-2336
E-mail: ptakaha@uhccmvs.uhcc.hawaii.edu

SYMPOSIUM SECRETARIAT

Dr. H. H. Qiu
Department of Mechanical Engineering
Hong Kong University of Science and Technology
Clear Water Bay, Kowloon, Hong Kong
Fax: (852) 2358-1543 E-mail: meqiu@ust.hk

INTERNATIONAL ADVISORY COMMITTEE

Tien, C. L., (Honorary Chairman), University of California, Berkeley
Bull, S. R., National Renewable Energy Laboratory, Golden
Chen, X. J., Xian Jiaotong University, Xian
Chiu, H. H., Cheng Kung University, Tainan
Cotta, R. Federal University of Rio de Janeiro, Rio de Janeir
De Vahl Davis, G., University of New South Wales, Sydney
Fang, L. J., Industrial Technology Research Institute, Hsinchu
Fletcher, "Skip" L. S., Texas A & M University, College Station
Fujita, Y., Kyushu University, Fukuoka
Goldstein, R., University of Minnesota, Minneapolis
Gori, F., University of Rome, Rome
Hahne, E., University of Stuttgart, Stuttgart
Leontiev, A. I., Moscow State University, Moscow
Martynenko, O. G., Byelorussian Academy of Sciences, Minsk
Mayinger, F., Technical University of Munich, Munich
Mujumdar, A. S., McGill University, Montreal
Ro, S. T., Seoul National University, Seoul
Shi, S. X., Tianjin University, Tianjin
Sidemann, S., Israel Institute of Technology, Haifai
Tanasawa, I., Tokyo University of Agriculture & Technology, Tokyo
Viskanta, R., Purdue University, West Lafayette
Wang, B. X., Tsinghau University, Beijing
Yang, K. T., University of Notre Dame, Notre Dame

ORGANISING COMMITTEE

Auracher, H. L., Technical University of Berlin, Berlin
Cai, R. X., Institute of Engineering Thermophysics, Beijing
Chen, T. S., University of Missouri, Rolla
Faghri, A., University of Connecticut, Storrs
Fujii, T., Kobe University, Kobe
Fukusako, S., Hokkaido University, Sapporo
Groll, M., University of Stuttgart, Stuttgart
Guo, Z. Y., Tsinghua University, Beijing
Howell J., University of Texas, Austin
Inaba, H., Okayama University, Okayama
Kakac, S., University of Miami, Miami
Kashiwagi, T., Tokyo University of Agriculture & Technology, Tokyo
Kaviany, M., University of Michigan, Ann Arbor
Kennedy, L. A., The University of Illinois at Chicago, Chicago
Kim, Jong Hyun, EPRI, Palo Alto
Kurosaki, Y., University of Electro-Communications, Tokyo
Law, C. K., Princeton University, Princeton
Lee, J. S., Seoul National University, Seoul
Lloyd, A. C., Desert Research Institute, Reno
Lou, D. Y. S., University of Nebraska, Lincoln
Minkowycz, W. J., University of Illinois at Chicago, Chicago
Nelson, R. A., Los Alamos National Laboratory, Los Alamos
Ni, M. J., Zhejiang University, Hangzhou
Nishio, S., University of Tokyo, Tokyo
Peng, X. F., Tsinghua University, Beijing
Peterson, G. P., Texas A & M University, College Station
Radebaugh, R., National Institute of Standards and Technology, Boulder
Saitoh, T. S., Tohoku University, Sendai
Serizawa, A., Kyoto University, Kyoto
Shoji, M., University of Tokyo, Tokyo
Son, J. E., Korea Institute of Energy Research, Taejon
Straub, J., Technical University of Munich, Munich
Suzuki, K., Kyoto University, Kyoto
Tong, T. W., Colorado State University, Fort Collins
Wang, C. Y., Pennsylvania State University, College Park

LOCAL COMMITTEE

Hsu, C. T, HKUST
Chao, Y. H., HKUST
Chi, Y, Zhejiang University
Kot, S. C., HKUST
Lee, H. K., HKUST
Qiu, H. H., HKUST
Zhao, T. S., HKUST.

SPONSORS

American Society of Mechanical Engineers
Japanese Society of Mechanical Engineers
Chinese Society of Power Engineering
International Center of Heat and Mass Transfer
K. C. Wong Education Foundation
U.S. Air Force Asian Office of Aerospace Research and Development
U.S. Army Research Office-Far East
U.S. Office of Navy Research-Asia

SUMMARY OF TECHNICAL SESSIONS

Volume 1

A. Keynote Papers
B. Forced Convection
C. Natural Convection
D. Boiling and Condensation

Volume 2

E. Two-Phase Flow
F. Porous Media
G. Heat Pipes and Thermosyphons
H. Conduction and Radiation
I. Microscale Heat Transfer
J. Heat Transfer Enhancement
K. Solar Energy & Nuclear Energy
L. Thermal Storage
M. Melting and Solidification

Volume 3

N. Drying and Food Processing
O. Heat Exchangers
P. Air-Conditioning and Refrigeration
Q. Cryogenic Engineering
R. Energy and Environment
S. Combustion and Fire

Volume 4

T. Cycle Analysis
U. Engine Combustion
V. Waste Treatment by Thermal Methods
W. Fuel Cells
X. Clean Combustion Technology
Y. Coal Combustion

CONTENTS OF VOLUME 1

	Forward	**iii**
A.	**Keynote Papers**	**1**
A1.	Hybrid Thermoacoustic-Stirling Engines and Refrigerators *G. W. Swift*	2
A2.	Renewable Energy in the 21st Century *S. R. Bull*	18
A3.	Length Scales and Innovative Use of Nonequilibria in Combustion in Porous Media *M. Kaviany and A. A. M. Oliveira*	32
A4.	Prospects of Highly Efficient Power Generation Technologies Based on Natural Gas Utilization to Reduce CO_2 Emission *M. Hirata*	57
A5.	Effect of Fluid Properties on Pool Boiling, Bubble Dynamics and Thermal Patterns on the Wall *G. Hetsroni, A. Mosyak and R. Rozenblit*	72
A6.	Heat Transfer Aspect to Upgrade the Quality of Plastics *Y. Kurosaki, I. Satoh and T. Saito*	84
A7.	Thermal and Non-Thermal Regimes of Gliding Arc Discharges *O. Mutaf-Yardimci, A. V. Saveliev, A. A. Fridman and L. A. Kennedy*	96
A8.	Multicomponent Gas-Liquid Flows with Chemical Reactions and Phase Transitions in Tubular Reactors or Furnaces *R. Nigmatulin*	110
A9.	Novel Concept and Approaches of Heat Transfer Enhancement *Z. Y. Guo and S. Wang*	118
A10.	Boiling Heat Transfer in Normal and Quantum Liquid Helium *M. X. Francois, F. Jebali and M. C. Duluc*	127
A11.	Meeting California's Air-Quality Goals- The Role of New Technologies and Fuels *A. C. Lloyd*	138
B.	**Forced Convection**	**148**
B1.	A Novel Finite Difference Method for Flow Simulation and Visualization *K. Kuwahara*	149
B2.	Numerical Study on Three-Dimensional Flow and Heat Transfer Characteristics of Turbulent Flows over a Backward-Facing Step in a Rectangular Duct *H. Iwai, E. C. Neo and K. Suzuki*	161
B3.	Near-Wall Modeling of Turbulent Heat Transfer with Different Prandtl Numbers *C. Y. Zhao and R. M. So*	169
B4.	A Method for Viscous Incompressible Flows with a Simplified Collocated Grid System *J. H. Nie, Z. Y. Li, Q. W. Wang and W. Q. Tao*	177
B5.	Effect of Aspect Ratio on Mixed Convective Heat Transfer in a Horizontal Rectangular Duct *K. Ichimiya and K. Toriyama*	184
B6.	Numerical Prediction of Convective Heat Transfer and Secondary Flow Characteristics in a Curved Rectangular Duct with Concave Heating *T. T. Chandratilleke, Nursubyakto and A. Altraide*	191
B7.	Numerical Analysis on Laminar Flow and Heat Transfer in Staggered Elliptic Tube Banks *H. Yoshikawa, K. Yang and T. Ota*	199
B8.	Effects of Tip Clearance and Rotation on Three-Dimensional Flow Fields in Turbine Cascades *B. Han and R. J. Goldstein*	206

B9. Film Cooling from Two Rows of Holes with Opposite Orientation Angles Injectant Behaviors 212
J. Ahn, I. S. Jung and J. S. Lee

B10. Effusion Cooled Combustor Lines of Gas Turbines-An Assessment of the Contributions of Convective, Impingement, and Film Cooling 221
A. Schulz, S. Wittig and M. Martiny

B11. Experimental Study of the Flows within a Levitated Spot-Heated Drop 229
E. H. Trinh, S. K. Chung and S. S. Sadhal

B12. Cooling of Two Cylinders in a Row by a Slot Jet of Air 239
F. Gori and L. Bossi

B13. Heat Transfer Enhancement from Cylindrical Heaters to a Water Slot Jet 247
C. Bartoli, S. Fagguani and M. Lorenzini

B14. The Influence of Prandtl Number on Heat Transfer Effects Around a Sphere Placed in a Turbulent Boundary Layer 255
C. F. Li, G. Hetsroni and A. Mosyak

B15. Heat Transfer in the Wake Behind a Longitudinal Vortex Generator Immersed in Drag-Reducing Channel Flows 262
J. F. Eschenbacher, M. Joko, K. Nakabe and K. Suzuki

B16. Heat Transfer and Fluid Flow for a Thermal Plasma Jet Impinging Normally on a Flat Plate 270
X. Chen, P. Han, H. P. Li and X. H. Ye

B17. Study on Characteristics of Air Duct of Small Scale Refrigeration Installation with Air Forced Convection Cooling 279
W. Hu and H. Shao and X. C. Que

C. Natural Convection **287**

C1. Numerical Computation of Oscillatory Rayleigh-Benard Natural Convection of Gallium in a Rectangular Region with Aspect Ratios Equal to Five 288
M. Hatabaka, T. Tagawa and H. Ozoe

C2. Natural Convective Heat Transfer in a Composed thermal Diode 295
Y. J. Kim, I. J. Hwang and U. C. Jeong

C3. Natural Convection of Liquid Metal with and without Seebeck Effect 302
M. Kaneda, T. Tagawa, H. Ozoe, K. Kakimoto and Y. Inatomi

C4. Improvement of the Basic Correlation Equations and Transition Criteria of Natural Convection Heat Transfer 310
S. M. Yang

C5. Heat Transfer Enhancement of Horizontal Cylinder by Ultrasound 316
N. Zhu

C6. A Thermal Design Approach for Natural Air-Cooled Electronics Equipment Casings 321
M. Ishizuka

C7. Natural Convection of Cold Water in a Rectangle 328
E. V. Kalabin and P. T. Zubkov

D. Boiling and Condensation **334**

D1. Critical Heat Flux in Subcooled Pool Boiling 335
J. Li, S. Yokoya, M. Watanabe and M. Shoji

D2. Nucleation Site Interaction and Its Effects on Nucleate Boiling Heat Transfer 343
X. F. Peng, L. H. Chai and B. X. Wang

D3. Effects of Parallel Electrodes on Electro-Hydrodynamically (EHD) Enhanced Boiling Heat Transfer 349
J. Madadnia, V. Ramsden and T. H. Nguyen

D4. EHD Enhancement of Boiling Heat Transfer in Vertical Tube 355
E. An, R. Li, H. L. Yu, Z. H. Chen, X. Huang and X. L. Zhang

D5. Bubble Structure of High Heat Flux Boiling in Two-Dimensional Space 360
S. Nishio and H. Tanaka

D6. Experimental Studies for EHD Boiling Heat Transfer Enhancement Outside a Tube 367
X. Huang, R. Y. Li, H. L. Yu, E. An and Z. H. Chen
D7. Superheat Limit of Liquid Mixtures 373
C. Liu, D. L. Zeng and K. Q. Xing
D8. Experiment of Boiling Heat Transfer in a New Type of Horizontal Three-Dimensional Microfin Tube for R134A 379
J. Zhou, Q. H. Chen, M. D. Xin, G. Zhang and W. Z. Cui
D9. Experimental Study on Phase Distribution in Inclined Subcooled Boiling Annulus 384
T. H. Lee, M. O. Kim, H. K. Cho and G. C. Park
D10. Boiling Heat Transfer and Frictional Pressure Drop in Internally Rebbed Tubes at High Pressures 393
T. K. Chen, Y. H. Luo, J. X. Zheng and Q. C. Bi
D11. Transient Boiling Heat Transfer on Small Finned Surfaces 399
S. Kumagai, J. Fushimi and M. Izumi

Authors Index to Volumes 1-4 x

A. Keynote Papers

HYBRID THERMOACOUSTIC-STIRLING ENGINES AND REFRIGERATORS

G. W. Swift
Condensed Matter and Thermal Physics Group
Los Alamos National Laboratory
Los Alamos NM 87545 USA
Email: swift@lanl.gov; Fax: 505-665-7652

Keywords: Stirling engine, Stirling refrigerator, acoustics, thermoacoustics

ABSTRACT. The use of thermoacoustic principles to eliminate all moving parts from Stirling engines and refrigerators leads to devices with the inherently high efficiency of the Stirling cycle and the simplicity of no moving parts. We have demonstrated over 40% of the Carnot efficiency in such a device; higher efficiency appears to be possible. The gas dynamics resembles that of free-piston Stirling devices, but with gas inertia playing the role of piston masses. However, large time-averaged flows can be superimposed on the oscillating flows. Control of the time-averaged flows is essential to ensure that they do not reduce efficiency by convecting significant amounts of heat.

1. INTRODUCTION

The typical Stirling engine of a century ago had many moving parts: crankshafts, connecting rods, pistons. The mechanical parts dominated the thermal parts—in volume, weight, and visual impact—in these machines. Since then, engineers have sought to simplify such machines by elimination of moving parts. Eliminating connecting rods and crankshafts produced free-piston [1,2] Stirling engines and refrigerators, in which the moving pistons bounce against gas "springs" in resonance. The liquid-piston Stirling engine [3], in which liquid in two U tubes serves the function of the two pistons of the ordinary Stirling engine, also eliminates moving parts.

Ceperley [4,5] realized that the phasing between pressure and velocity in the heat exchangers of Stirling devices is the same as that in a traveling acoustic wave, so he proposed eliminating everything but the working gas itself, using acoustics to control the gas motion and gas pressure. Ceperley's work showed the need to consider sound-wave behavior in the working gas of Stirling devices, with variations in important variables such as pressure and velocity depending strongly and continuously on the coordinate x along the direction of gas motion, and with these x dependences due to inertial and compressive effects in the gas in addition to the effects of flow resistance.

We have recently built a hybrid thermoacoustic-Stirling engine [6,7] and a hybrid thermoacoustic-Stirling refrigerator [8], combining Ceperley's ideas with a modern thermoacoustic perspective [9]. This manuscript is only an introduction to such hybrids; details can be found in the references.

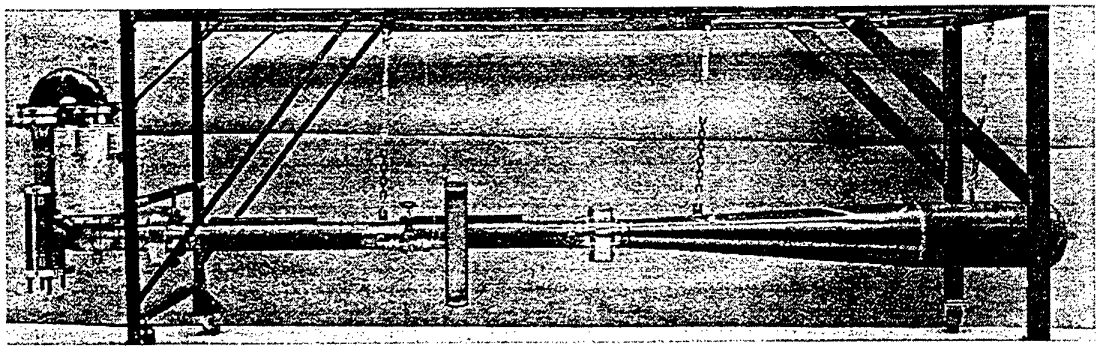

Fig. 1: A hybrid thermoacoustic-Stirling heat engine for research.

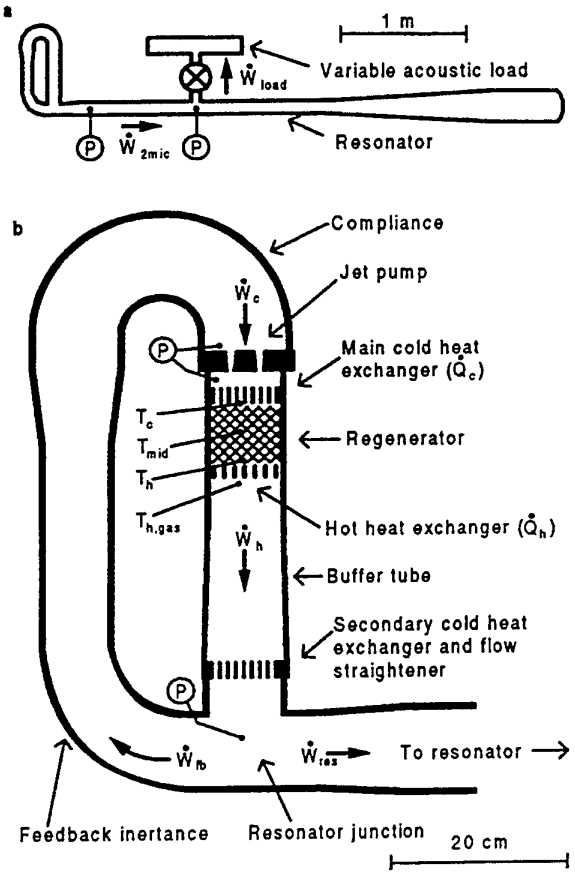

Fig. 2: The hybrid thermoacoustic-Stirling engine. (a) Overview, as in the photo. (b) The heart of the engine. The two heat exchangers labeled "cold" are held at ambient temperature by flowing water.

2. EXAMPLES

Example: Acoustic-Stirling heat engine. In the heat engine [6,7] shown in **Figs. 1** and **2**, heat was supplied to the engine electrically, and waste heat was removed by a water stream; the engine delivered up to 890 W of acoustic power to the resonator. Some of that acoustic power was dissipated in the resonator, but most was delivered to a variable acoustic load, the small vertical cylinder near the center of **Fig. 1**. This engine has delivered 710 W of acoustic power to the resonator with an efficiency equal to 42% of the Carnot efficiency. (Here, efficiency is acoustic power delivered to the resonator to the right of the junction, divided by electric power supplied to the engine's heater, and the temperatures used in the Carnot factor are those of the gas just below the hot heat exchanger and of the engine's cooling water.) Suppression of steady flow around the small torus containing the heat exchangers is crucial for this high efficiency, as we will discuss below. Thirty-bar helium filled the system, oscillating at 80 Hz. The resonator is essentially half-wavelength, with pressure oscillations 180° out of phase at the right end of the fat portion on the right and in the small torus containing the heat exchangers on the left. The highest velocity occurs in the center of the resonator, at the small end of the long cone.

The key idea in this and other Stirling engines is that the gas in the regenerator experiences thermal expansion when the pressure is high and thermal contraction when the pressure is low. Thus the gas in the regenerator does work every cycle, pumping acoustic power into the sound wave. The sound wave in turn provides two things: oscillating pressure, and oscillating motion that causes the gas in the regenerator to experience the oscillating temperature responsible for the thermal expansion and

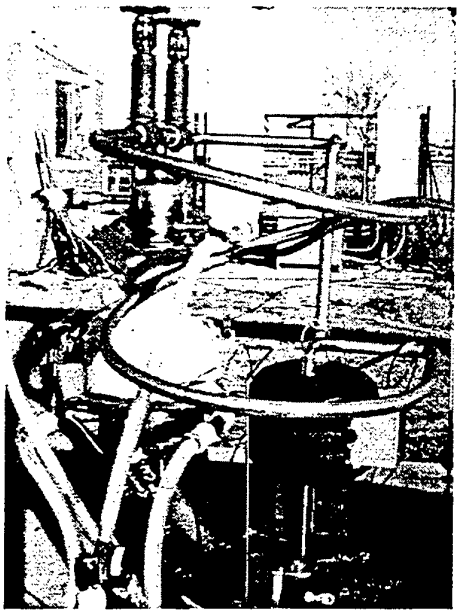

Fig. 3: The Cryenco 2-kW orifice pulse-tube refrigerator.

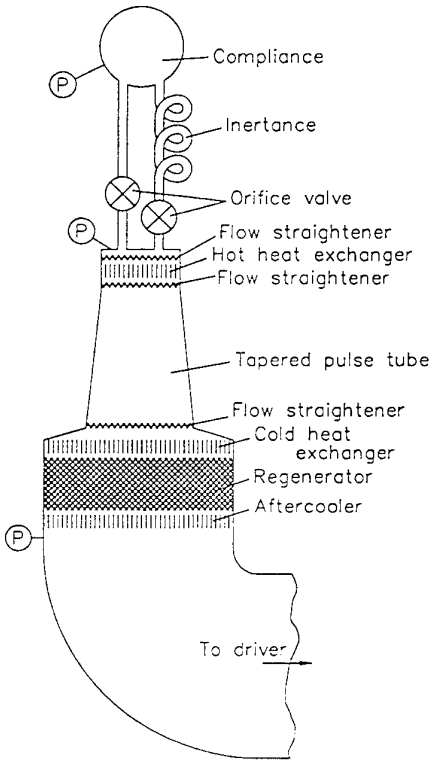

Fig. 4: Schematic of the Cryenco orifice pulse-tube refrigerator. "P" indicates the location of a pressure sensor. Ambient-temperature water flows through the "hot" heat exchanger and aftercooler. The regenerator diameter is approximately 20 cm.

contraction. These complex, coupled oscillations appear spontaneously whenever the temperature at the hot end of the regenerator is high enough. The velocity of the gas along the regenerator's temperature gradient is substantially in phase with the oscillating pressure, so good thermal contact between gas and regenerator is required to cause the thermal expansion and contraction steps to be in phase with the oscillating pressure. This thermal contact is achieved by making the channel size in the regenerator much smaller than the thermal penetration depth.

Example: Orifice pulse-tube refrigerator. The orifice pulse-tube refrigerator shown in **Figs. 3** and **4** was built by Cryenco for liquefaction of natural gas [10,11]. At about 3 bar, natural gas (methane) liquefies at 120 Kelvin; this refrigerator provided 2 kW of refrigeration at that temperature, with a COP as high as 23% of the Carnot COP. (Here, the coefficient of performance COP is the heat removed from the methane stream divided by the acoustic power incident on the aftercooler from below, and the temperatures used in the Carnot factor are those of the liquefied methane and of the cooling water.) The working gas was helium at a pressure of thirty atmospheres, driven at 40 Hz by a thermoacoustic engine through a resonator, not shown in the figures.

The key idea in this and other Stirling, pulse-tube, and hybrid refrigerators is that gas near the cold heat exchanger must be displaced into the open space away from the regenerator, adiabatically cooled, and displaced back through the cold heat exchanger where it can absorb heat from the load. The wave must provide oscillating pressure and oscillating displacement with this required phasing.

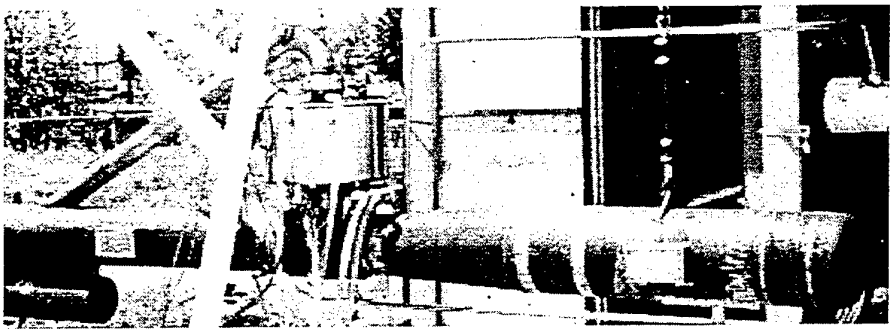

Fig. 5: A hybrid acoustic-Stirling refrigerator. A cylindrical stainless-steel vacuum jacket hides the regenerator and pulse tube, which are similar in size to those of the refrigerator in Fig. 3. The 10-cm-diam pipe recovers acoustic power from the top of the pulse tube.

Example: Acoustic-Stirling refrigerator. The refrigerator described in Ref. [8] illustrates many of the principles of hybrid thermoacoustic-Stirling refrigeration, but had unimpressive overall performance. The refrigerator shown in **Fig. 5** was recently built at Cryenco [10] according to these principles, and should have comparable cooling power and higher COP than the orifice pulse-tube refrigerator of **Fig. 3**, but measurements have not been completed as of the writing of this manuscript.

3. THE THERMOACOUSTIC PERSPECTIVE

Waves

In the thermoacoustic perspective [9], the momentum equation shows how oscillations in velocity are coupled to spatial gradients in oscillating pressure, and the continuity equation shows how oscillations in pressure are coupled to spatial gradients in oscillating velocity. Throughout, we assume monofrequency, steady, "small" oscillations—an approximation that we refer to simply as "the acoustic approximation." Ordinarily we think of sound waves as *small* coupled oscillations of pressure and velocity: Even a painfully loud sound, such as 120 dB re 20 μPa, is a "small" oscillation, because $|p_1| \sim 0.0002 p_m$. Fortunately, the thermoacoustic approach remains reasonably accurate even for the "large" oscillations encountered in hybrid thermoacoustic-Stirling engines and refrigerators, typically $|p_1| \sim 0.1 p_m$, with $|p_1| > 10^5$ Pa.

We assume that all time dependence is purely sinusoidal, at frequency f and angular frequency $\omega = 2\pi f$. Then variables such as pressure p *could* be written

$$p(x,t) = p_m + C(x)\cos\left[\omega t + \phi(x)\right]. \tag{1}$$

It is much more convenient to rewrite Eq. (1) as

$$p(x,t) = p_m + \mathrm{Re}\left[p_1(x)e^{i\omega t}\right], \tag{2}$$

where $p_1(x)$ is a complex function of x such that

$$|p_1(x)| = C(x) \qquad \text{and} \qquad \text{phase}[p_1(x)] = \phi(x). \tag{3}$$

This notation is preferred because a single symbol (with subscript 1) stands for both amplitude and phase, and because all the shortcuts of complex arithmetic can be used.

Hence, the thermoacoustic approach to Stirling engines and refrigerators writes the relevant variables as

$$\text{pressure } p = p_m + \mathrm{Re}\left[p_1(x)e^{i\omega t}\right], \tag{4}$$

$$\text{volume flow rate } U = \mathrm{Re}\left[U_1(x)e^{i\omega t}\right], \tag{5}$$

$$x \text{ component of velocity } u = \mathrm{Re}\left[u_1(x,y,z)e^{i\omega t}\right], \tag{6}$$

$$\text{temperature } T = T_m(x) + \mathrm{Re}\left[T_1(x,y,z)e^{i\omega t}\right], \tag{7}$$

$$\text{density } \rho = \text{similar to } T, \tag{8}$$

$$\text{viscosity } \mu = \mu(x), \tag{9}$$

$$\text{thermal conductivity } k, \text{ etc.} = \text{similar to } \mu. \tag{10}$$

We are most interested in p_1 and U_1, as described by the momentum and continuity equations. The acoustic approximation to the x-component of the momentum equation is

$$i\omega\rho_m u_1 = -\frac{dp_1}{dx} + \mu\left[\frac{\partial^2 u_1}{\partial y^2} + \frac{\partial^2 u_1}{\partial z^2}\right]. \tag{11}$$

Regarding Eq. (11) as a differential equation for $u_1(y,z)$, with boundary condition $u_1 = 0$ at the solid surface, obtaining that solution, and integrating it with respect to y and z over the cross-sectional area A of the channel, we obtain the volume flow rate U_1. Solving this result for dp_1 yields

$$dp_1 = -\frac{i\omega\rho_m\, dx/A}{1-f_\nu}U_1, \tag{12}$$

where f_ν is a geometry-dependent function shown in **Fig. 6**. In effect, we regard this approximation to the momentum equation as the origin of pressure gradient in thermoacoustics: The motion U_1 of the gas causes the pressure gradient. The function f_ν is known for many geometries: boundary-layer approximation [12], parallel plates [13], circular pores [13], rectangular channels [14], the spaces between pins oriented along the direction of acoustic oscillations and arranged in a triangular array [15], and (to some extent) in the important case of screen beds [16].

In the same way that the momentum equation leads to Eq. (12), the equations of state, heat transfer, and continuity lead to.

$$dU_1 = -\frac{i\omega A\, dx}{\gamma p_m}\left[1 + (\gamma-1)f_\kappa\right]p_1 + \frac{(f_\kappa - f_\nu)}{(1-f_\nu)(1-\sigma)}\frac{dT_m}{T_m}U_1, \tag{13}$$

where $\gamma = c_p/c_V$ is the specific-heat ratio and $\sigma = \mu c_p/k$ is the Prandtl number. We regard this approximation to the continuity equation as the origin of gradients in volume flow rate in thermoacoustics.

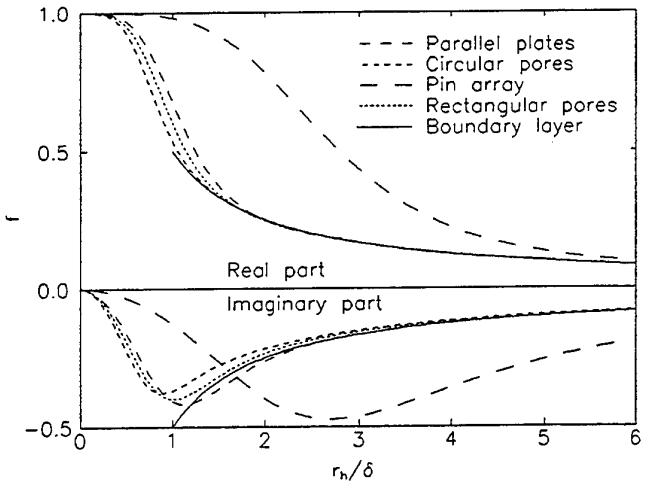

Fig. 6: Thermoacoustic spatial-average function f for several geometries. The hydraulic radius r_h is the ratio of cross-sectional area to perimeter, and the penetration depth δ is either the viscous penetration depth $\delta_\nu = \sqrt{2\mu/\omega\rho}$ or the thermal penetration depth $\delta_\kappa = \sqrt{2k/\omega\rho c_p}$. The rectangle has 6:1 aspect ratio, and the pin array has $r_o/r_i = 6$. The boundary-layer limit is approached at large r_h in all geometries.

Equations (12) and (13) are applicable to a wide variety of circumstances, and may be considered two of the principal tools of thermoacoustic analysis. To gain intuitive appreciation of these two equations, we can follow the outline indicated in **Fig. 7**. In the figure, a channel of length dx is considered in two ways: in terms of the momentum equation to obtain its inertance and viscous resistance, and in terms of the continuity equation to obtain its compliance, thermal-relaxation resistance, and thermally induced volume-flow-rate source. Combining these two points of view yields a complete impedance picture for thermoacoustics.

If we rewrite Eq. (12) in the form

$$dp_1 = -\left(i\omega l\, dx + r_\nu\, dx\right) U_1, \tag{14}$$

as shown schematically in the left part of **Fig. 7**, then the inertance, l, and the viscous resistance, r_ν, per unit length of channel can be written

$$l = \frac{\rho_m}{A}\frac{1-\mathrm{Re}\left[f_\nu\right]}{\left|1-f_\nu\right|^2} \qquad \text{and} \qquad r_\nu = \frac{\omega\rho_m}{A}\frac{\mathrm{Im}\left[-f_\nu\right]}{\left|1-f_\nu\right|^2}. \tag{15}$$

These expressions show how the pressure gradient in a duct arises from inertial and viscous effects. Similarly, Eq. (13) can be rewritten in the form

$$dU_1 = -\left(i\omega c\, dx + \frac{1}{r_\kappa}dx\right) p_1 + e\, dx\, U_1, \tag{16}$$

as shown schematically in the right part of **Fig. 7**. The compliance per unit length c and the thermal-relaxation conductance per unit length $1/r_\kappa$ are given by

$$c = \frac{A}{\gamma p_m}\left(1 + \left[\gamma - 1\right]\mathrm{Re}\left[f_\kappa\right]\right) \qquad \text{and} \qquad \frac{1}{r_\kappa} = \frac{\gamma-1}{\gamma}\frac{\omega A}{p_m}\frac{\mathrm{Im}\left[-f_\kappa\right]}{}. \tag{17}$$

These expressions show that a gradient in U_1 can be caused either by pressure or by flow along the temperature gradient. Consider the compliance first. If $f_\kappa = 0$, there is no thermal contact between gas and solid, so the density oscillations are adiabatic; in this case, $1/\gamma p_m$ is the correct compressibility, and

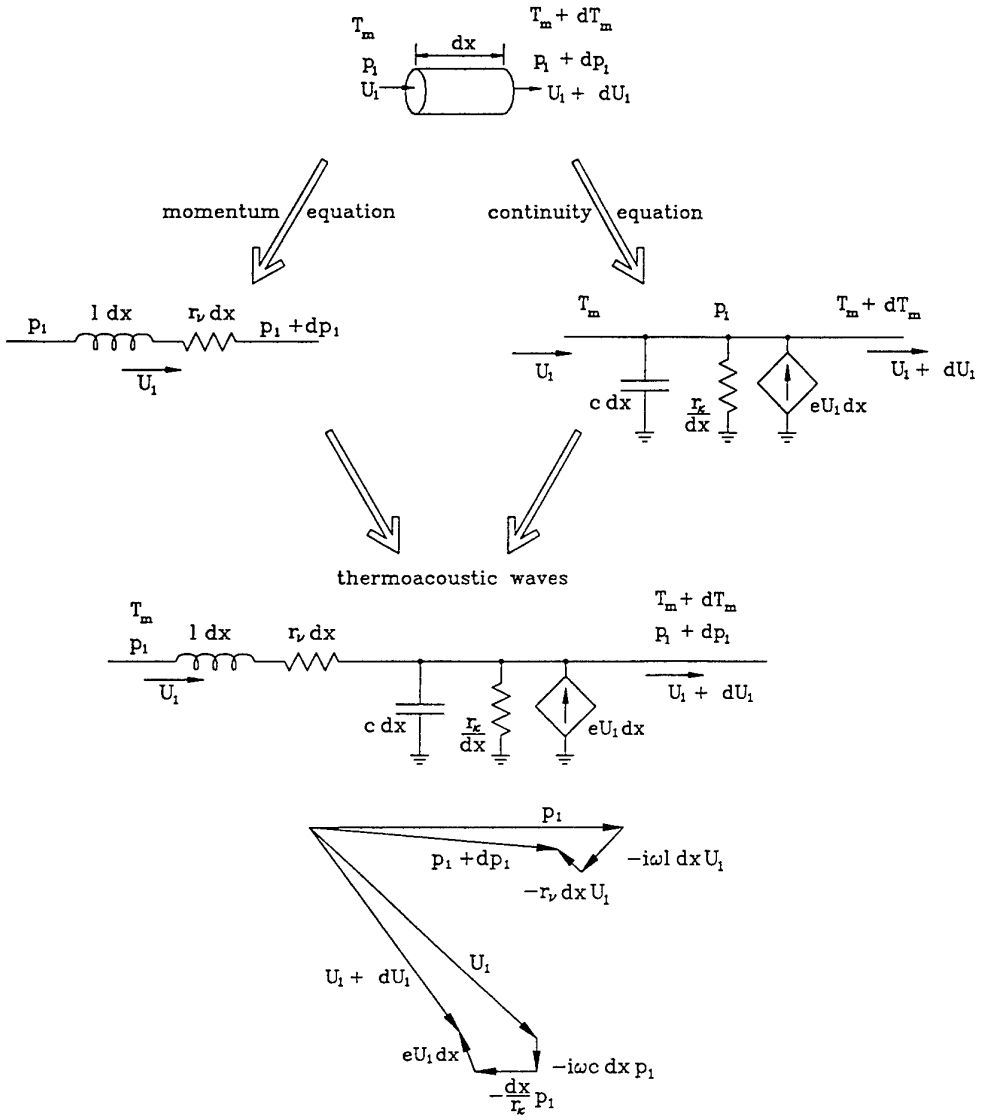

Fig. 7: Summary of the most important dynamic concepts of the thermoacoustic approach. The "channel" of length dx can be a piece of a regenerator, pulse tube, or any other component. This acoustic-impedance diagram is closely analogous to an ac electric circuit diagram. We can think of p_1, U_1, T_m, dT_m, and the geometry as given, so that the impedance diagram serves as a reminder of how the continuity and momentum equations yield dp_1 and dU_1. Combining the momentum and continuity pictures as shown at the bottom, we arrive at a complete, general impedance picture of thermoacoustics in any channel, leading to a general "phasor diagram" illustrating the spatial evolution of the complex functions $p_1(x)$ and $U_1(x)$. Sometimes, the relative sizes of $|p_1|$ and $|U_1|$ in a given component allow either the momentum equation or the continuity equation to be neglected, leading to further simplification.

the compliance of the segment of channel of length dx is $A\,dx/\gamma p_m = dV/\gamma p_m$. At the other extreme, if $f_\kappa = 1$, the thermal contact between gas and solid is perfect, so the gas is anchored at the local solid temperature. In this case, the isothermal compressibility $1/p_m$ is appropriate. For intermediate thermal contact, an effective compressibility $[1 + (\gamma - 1)f_\kappa]/\gamma p_m$, intermediate in magnitude and with nontrivial phase, describes the spatial average of the density oscillations in response to pressure oscillations.

The final term in Eq. (16) represents a controlled source $e\,dx\,U_1$ (or sink, depending on sign) of volume flow rate, proportional to the local volume flow rate U_1 itself, with proportionality constant

$$e = \frac{(f_\kappa - f_\nu)}{(1 - f_\nu)\,(1 - \sigma)}\,\frac{1}{T_m}\,\frac{dT_m}{dx}. \tag{18}$$

The symbol e represents a sort of complex gain/attenuation constant for volume flow rate, which arises only when the temperature gradient dT_m/dx along the channel is nonzero. The eU_1 term has no dependence on p_1, so it does not represent any sort of compressibility. To understand this term, let $p_1 = 0$ so that c and r_κ don't confuse the issue. The dependence of eU_1 on dT_m/dx is key. In a large-diameter pulse tube or thermal buffer tube, f_κ and f_ν are very small, so that $e \simeq 0$ even though $dT_m/dx \neq 0$. In this case, the eU_1 term in the continuity equation simply shows that whatever volume flow rate goes in one end comes out the other end—the behavior is essentially the same as the displacement of a solid piston (having a temperature gradient). At the opposite extreme, if a nonzero temperature gradient dT_m/dx exists along a channel with small pore size, such as in a regenerator, the volume-flow-rate source term eU_1 is very important. The small-channel limit of Eq. (18) is most important and most easy to appreciate: For $r_h \ll \delta_\kappa$ and $r_h \ll \delta_\nu$,

$$eU_1 \simeq \frac{1}{T_m}\,\frac{dT_m}{dx}\,U_1. \tag{19}$$

In this case, the eU_1 term in the continuity equation shows that $dU_1/U_1 = dT_m/T_m$: The volume flow rate is amplified in proportion to the temperature rise (or attenuated in proportion to a temperature drop). This is easy to understand as constancy of first-order mass flux $\rho_m U_1$, which for an ideal gas is equivalent to constancy of U_1/T_m : Whatever mass flux goes in one end must come out the other.

In most circumstances in a given location in a thermoacoustic-Stirling system, many or most of the components in this general impedance picture can be neglected. Recalling that $\delta_\kappa \sim \delta_\nu$ for ideal gases, we can summarize relative sizes and importance:

resonator, acoustic duct	$\delta \ll r_h$	$r_\nu \ll \omega l$	$1/r_\kappa \ll \omega c$	$e = 0$
pulse tube, thermal buffer tube	$\delta \ll r_h$	$r_\nu \ll \omega l$	$1/r_\kappa \ll \omega c$	$e \sim 0$
regenerator	$\delta \gg r_h$	$r_\nu \gg \omega l$	$1/r_\kappa \ll \omega c$	$e \simeq \nabla T_m/T_m$

Example: Acoustic-Stirling heat engine. The regenerator in the engine of **Figs. 1** and **2** is a bed of stainless-steel screen with $r_h = 42$ μm. At a typical operating point, at 80 Hz and with 3-MPa helium gas, and with the center of the regenerator at 650 K, the penetration depths are $\delta_\kappa = 300$ μm and $\delta_\nu = 250$ μm. Hence, we have $r_h \ll \delta$, so inertance and thermal-relaxation resistance are negligible, and the volume-flow-rate source is well described by Eq. (19). The regenerator is adequately modeled with the three impedance components labeled "regenerator" in **Fig. 8a**. The thermal buffer tube is 9 cm diam, so it has $\delta \ll r_h$, so its most important dynamic characteristic is its compliance, also shown in **Fig. 8a**. The rest of the torus is most roughly modeled as an inertance (the straight section) in series with a compliance (the 180-degree U bend); we neglect the resistances associated with these two components here. This LC network is responsible for ensuring that $|p_1|$ at the cold end of the regenerator is larger than, and in phase with, $|p_1|$ at the hot end. The resonator to the right of the junction is approximately an inertance (the uniform-diam section) in series with a compliance (the big volume on the end), with both of these components having associated resistances. Neither of these resonator components is really lumped, but we will neglect those details for now. The adjustable load on the system, comprising an adjustable valve in series with a tank, can be modeled as a resistance in series with a compliance. Hence, the impedance diagram of **Fig. 8a** shows the most important features of this system. [For accurate results, numerical integration [17] of Eqs. (12) and (13) is preferred.]

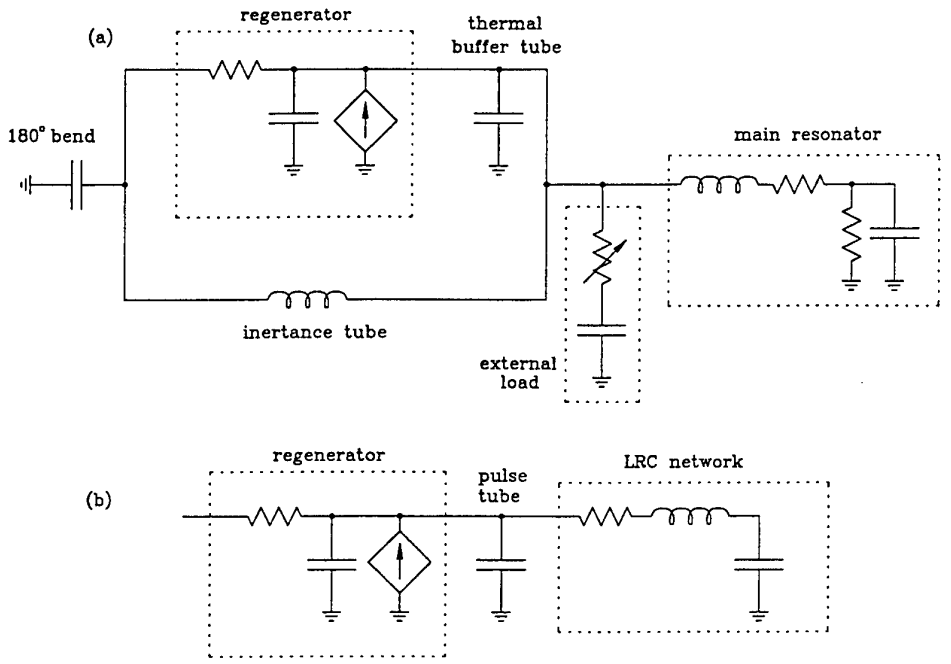

Fig. 8: Impedance diagram for (a) thermoacoustic-Stirling heat engine and (b) orifice pulse-tube refrigerator.

Example: Orifice pulse-tube refrigerator. The impedance diagram of **Fig. 8b** symbolically represents the most important dynamic features of the orifice pulse-tube refrigerator of **Figs. 3** and **4**. The rightmost compliance is the so-called compliance itself. The adjacent inertance and resistance represent the refrigerator's inertance tube and two valves. The compliance of the pulse tube is significant and is shown. With $r_h/\delta \sim 0.1$ in the regenerator, its compliance, viscous resistance, and volume-flow-rate source represent the regenerator well.

Acoustic Power

Products of first-order variables (such as p_1 and U_1) represent power, which is of paramount importance in engines and refrigerators. The acoustic power flowing in the x direction is

$$\dot{E}_2(x) = \frac{\omega}{2\pi}\oint \mathrm{Re}\left[p_1(x)e^{i\omega t}\right]\mathrm{Re}\left[U_1(x)e^{i\omega t}\right]\,dt = \frac{1}{2}\mathrm{Re}\left[\widetilde{p_1}U_1\right] = \frac{1}{2}\,|p_1|\,|U_1|\cos\phi_{pU}\,, \qquad (20)$$

where ϕ_{pU} is the phase angle between p_1 and U_1 and the tilde denotes complex conjugation. Note that $\dot{E}_2$ is a time average; we're not interested in *instantaneous* power delivered along x, only the power averaged over an integer number of cycles of the wave. The utility of $\dot{E}_2(x)$ is due largely to its intuitive appeal as describing a sort of flux of mechanical power past the location x. This interpretation is possible because the volume flow rate $U_1(x)$ is equal (to first order only) to the volume flow rate of the particular slab of gas whose average position is at x. Hence, $\dot{E}_2(x)$ can be interpreted as giving the work done by a slab of gas, whose average position is x, on the gas in front of it, as if that slab of gas were a solid piston.

The interaction of the sound wave with the channel walls leads to $d\dot{E}_2/dx \neq 0$. To find the time-averaged acoustic power $d\dot{E}_2$ produced in a length dx of the channel, we write

$$\frac{d\dot{E}_2}{dx} = \frac{1}{2}\,\mathrm{Re}\left[\widetilde{U_1}\frac{dp_1}{dx} + \widetilde{p_1}\frac{dU_1}{dx}\right] = -\frac{r_\nu}{2}\,|U_1|^2 - \frac{1}{2r_\kappa}\,|p_1|^2 + \frac{1}{2}\,\mathrm{Re}\left[e\widetilde{p_1}U_1\right]. \qquad (21)$$

In the second form, we obtained dp_1/dx and dU_1/dx from Eqs. (14) and (16).

The r_ν term in Eq. (21) is always negative, and represents the viscous dissipation of acoustic power. Naively, one can imagine layers of gas sliding relative to one another, with viscous "friction" between the layers turning mechanical energy into heat.

Compared to viscous dissipation, the dissipation of acoustic power by thermal relaxation, represented by the r_κ term in Eq. (21), is more difficult to appreciate. The temperature oscillates in phase with p_1 far from a solid wall; close to the wall, the wall's heat capacity provides a thermal anchor that reduces the amplitude of the temperature oscillation. In between, the gas approximately δ_κ from the surface experiences a complex, hysteretic cycle of density changes in response to the pressure oscillations: first an increase in density due to quasi-adiabatic compression by the sound wave, then a further increase in density as thermal relaxation to the surface removes heat from the gas, then a decrease in density due to quasi-adiabatic expansion by the sound wave, and finally a further decrease in density as thermal relaxation to the surface delivers heat to the gas. Since this gas experiences thermal expansion at low pressure and thermal contraction at high pressure, it absorbs work from the sound wave.

The e term in Eq. (21) exists only if $dT_m/dx \neq 0$. This term is difficult to fully understand, especially because e involves both f_κ and f_ν. To build understanding, our qualitative discussion will neglect viscosity, setting $f_\nu = 0$. In this limit, the third term of Eq. (21) can be written

$$\frac{1}{2}\,\mathrm{Re}\left[e\widetilde{p_1}U_1\right] = \frac{1}{2}\frac{1}{T_m}\frac{dT_m}{dx}\,\mathrm{Re}\left[\widetilde{p_1}U_1\right]\mathrm{Re}\left[f_\kappa\right] + \frac{1}{2}\frac{1}{T_m}\frac{dT_m}{dx}\,\mathrm{Im}\left[\widetilde{p_1}U_1\right]\mathrm{Im}\left[-f_\kappa\right]. \tag{22}$$

Expressing it this way shows that $\mathrm{Re}\left[f_\kappa\right]$ is important for acoustic power creation or consumption in Stirling engines and refrigerators, in which $\mathrm{Re}\left[\widetilde{p_1}U_1\right]$ is large. To make the most of the first term on the right side of Eq. (22), we should make $\mathrm{Re}\left[f_\kappa\right]$ as large as possible; examination of **Fig. 6** shows that this is accomplished at $r_h \ll \delta_\kappa$, where $\mathrm{Re}\left[f_\kappa\right] \simeq 1$. To generate (not dissipate) acoustic power requires that dT_m/dx and $\dot{E}_2$ share the same sign; *i.e.*, the temperature must increase through the regenerator in the direction of acoustic power flow in an engine, and decrease in a refrigerator.

Example: Acoustic-Stirling heat engine. For a typical operating point of the engine of **Figs. 1** and **2**, 1250 W of acoustic power flows into the ambient end of the regenerator and 3150 W of acoustic power flows out of the hot end of the regenerator. The dT_m/T_m factor in Eq. (22) shows that, ideally, the ratio of these two powers, 2.5, could be the ratio of the engine's hot and ambient temperatures, (1000 K)/(300 K) = 3.3. The other two terms in Eq. (21), especially the viscous term, account for this missing acoustic power in the regenerator. (In addition, some 400 W of acoustic power is dissipated in viscous and thermal-relaxation effects in the inertance and compliance that form the acoustic network.)

Example: Orifice pulse-tube refrigerator. For a typical operating point of the refrigerator of **Figs. 3** and **4**, 8800 W of acoustic power flows into the ambient end of the regenerator and 3000 W of acoustic power flows out of the cold end of the regenerator. The dT_m/T_m factor in Eq. (22) shows that, ideally, the ratio of these two powers, 2.9, could be the ratio of the engine's hot and ambient temperatures, (300 K)/(120 K) = 2.5. The other two terms in Eq. (21), especially the viscous term, account for additional absorption of acoustic power in the regenerator.

Total Power

Acoustic power is not the only power that is important in thermoacoustics; total power is perhaps of greater importance. The energy-flux density in fluid mechanics is $\mathbf{v}\left(\rho v^2/2 + \rho h\right) - k\nabla T - \mathbf{v}\cdot\boldsymbol{\Sigma}$, where h is the enthalpy per unit mass, $\rho v^2/2$ is the kinetic-energy density, and $\boldsymbol{\Sigma}$ is the viscous shear tensor. To simplify this to a usable form, we take the x component, substitute Eqs. (4)–(10) for all variables, keep terms through second order, take the time average, and integrate over the cross-sectional area of the channel. The viscous-shear term is generally much smaller than the other surviving terms. We call the result $\dot{H}_2$, the acoustic approximation to the total power flowing in the positive x direction in the channel—"total power" for short. This result is

$$\dot{H}_2(x) = \frac{1}{2}\rho_m \int \mathrm{Re}\left[h_1\widetilde{u_1}\right] dA - \left(Ak + A_{\mathrm{solid}}k_{\mathrm{solid}}\right)\frac{dT_m}{dx}. \tag{23}$$

The second term is simple conduction of heat, in which we've included conduction both in the gas and in whatever solid is present. There are many interesting ways to look at $\dot{H}_2$ given by Eq. (23):

Taking enthalpy as a function of temperature and pressure, $dh = c_p\,dT + (1-T\beta)\,dp/\rho = c_p\,dT$ (where β is the thermal expansion coefficient) and setting $\beta = 0$, which is true for an ideal gas, Eq. (23) becomes

$$\dot{H}_2(x) = \frac{1}{2}\rho_m c_p \int \mathrm{Re}\left[T_1\widetilde{u_1}\right]\,dA - \left(Ak + A_{\mathrm{solid}}k_{\mathrm{solid}}\right)\frac{dT_m}{dx}. \tag{24}$$

This point of view is useful for calculations of $\dot{H}_2$, and is especially useful for thinking about nearly ideal regenerators, in which $T_1 \simeq 0$.

Taking enthalpy as a function of entropy and pressure, $dh = T\,ds + dp/\rho$, the total power can be written

$$\dot{H}_2 = \frac{1}{2}\,\mathrm{Re}\left[\widetilde{p_1}U_1\right] + \frac{1}{2}\rho_m T_m \int \mathrm{Re}\left[s_1\widetilde{u_1}\right]\,dA - \left(Ak + A_{\mathrm{solid}}k_{\mathrm{solid}}\right)\frac{dT_m}{dx}. \tag{25}$$

The first term is acoustic power. The second term is T_m times the second-order hydrodynamic entropy flux, and the final term is simply conduction of heat. It is often intuitively helpful to identify the sum of the last two terms as a sort of heat-pumping power, with the s_1u_1 term generally largest.

If the total power through a good regenerator is approximately zero, then $\frac{1}{2}\rho_m T_m \int \mathrm{Re}[s_1\widetilde{u_1}]\,dA$ must be approximately equal and opposite to the acoustic power $\frac{1}{2}\,\mathrm{Re}[\widetilde{p_1}U_1]$ at each location x. This is another way of imagining the "cause" of a Stirling refrigerator's cooling power—as due to the large acoustic power flowing through the regenerator plus the fact that the total power flowing through the regenerator is nearly zero.

In a pulse tube or thermal buffer tube, s_1 is due almost entirely to $(u_1/i\omega)\,ds_m/dx$, so $\mathrm{Re}\left[s_1\widetilde{u_1}\right] \simeq 0$. Hence $\dot{H}_2 \simeq \dot{E}_2$ in a pulse tube or thermal buffer tube, if streaming (see below) is absent.

In the regenerators, $T_1 \simeq 0$, and hence $\dot{H}_2 \simeq 0$. Hence, if a heat exchanger is sandwiched between a regenerator and a pulse tube or thermal buffer tube, or between a regenerator and a resonator component, the heat-exchanger heat and the acoustic power flowing through it must be nearly equal.

3. TIME-AVERAGED FLOWS ("STREAMING")

In acoustics, the term "streaming" refers to second-order steady velocity that is superimposed on, and driven by, the larger first-order oscillating acoustic velocity and the oscillating pressure [18]. When streaming exists, it is useful to think of the motion of gas during each cycle as something like 102 steps forward and 98 steps backward, equivalent to the superposition of a steady drift forward of 4 steps and an oscillating motion with a peak–to–peak amplitude of 100 steps. In thermoacoustic-Stirling engines and refrigerators, streaming is important because it is a mechanism for convective heat transfer. Carrying heat, streaming can be either an undesirable loss mechanism or an essential heat-transfer method.

Pulse tubes and thermal buffer tubes are usually oriented vertically to avoid gravity-driven convection, which is one form of time-independent velocity superimposed on the oscillating velocity. Here, we will consider four other undesirable steady flows, illustrated in **Fig. 9**. Gedeon streaming [19] is a net time-averaged mass flux along x through a regenerator, pulse tube, etc. Rayleigh streaming [18] refers to a time-averaged toroidal circulation within a pulse tube or thermal buffer tube, driven by boundary-layer effects at the side walls [20]. Jet-driven streaming is a third type, which is also a toroidal circulation within a pulse tube or buffer tube, but which is driven by inadequate flow straightening at an end of the tube. A fourth type, toroidal streaming within a regenerator, presumably might also occur under some circumstances.

However, perhaps such steady flow can be used advantageously in some circumstances, to deliberately transfer heat. This steady flow could be either parallel or perpendicular to x, as illustrated in **Fig. 10**.

The quantitative understanding of both undesirable and deliberate streaming is an interesting challenge in future development of hybrid thermoacoustic-Stirling engines and refrigerators.

To discuss streaming, we extend the perturbation-series expansion of relevant variables ξ one step beyond the acoustic approximation:

$$\xi(t) = \xi_m + \mathrm{Re}\left[\xi_1 e^{i\omega t}\right] + \xi_{2,0} + \mathrm{Re}\left[\xi_{2,2}e^{2i\omega t}\right]. \tag{26}$$

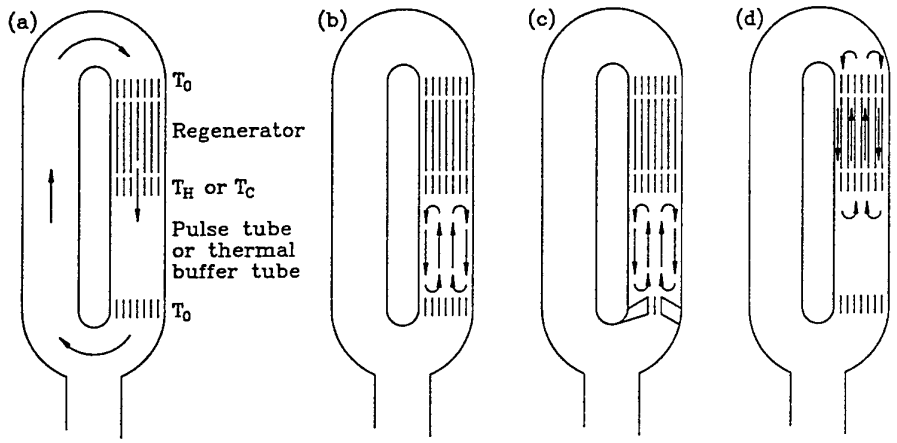

Fig. 9: Some types of streaming, generally harmful to thermoacoustic-Stirling engines and refrigerators. Arrows indicate the time-averaged velocity, which is superimposed on the much larger oscillating velocity. (a) Gedeon streaming. (b) Rayleigh streaming. (c) Jet-driven streaming. (d) Streaming within a regenerator.

The subscript "2,0" identifies the streaming term, which is independent of time. The second-order time-averaged mass-flux density $\dot{m}_{2,0}(x,y,z)$ is of primary interest, because it convects a time-averaged enthalpy-flux density $\dot{m}_{2,0}c_pT$.

Gedeon Streaming

It is important that the second-order time-averaged mass flow $\dot{M}_2 = \int \dot{m}_{2,0}\, dA$ in the x direction through a regenerator, pulse tube, etc. should be near zero, to prevent a large time-averaged convective enthalpy flux $\dot{M}_2 c_p(T_H - T_0)$ or $\dot{M}_2 c_p(T_0 - T_C)$ from flowing from hot to cold. In a refrigerator, such a steady energy flux adds an unwanted thermal load to the cold heat exchanger; in an engine, it wastefully removes high-temperature heat from the hot heat exchanger without creating acoustic power. This type of streaming is illustrated in **Fig. 9a**.

In a traditional orifice pulse-tube refrigerator such as shown in **Fig. 4**, $\dot{M}_2$ is exactly zero in steady-state operation: Otherwise, mass would gradually accumulate (or deplete, depending on sign) in the dead-end components. This phenomenon is discussed extensively in the literature on double-inlet pulse-tube refrigerators, in which $\dot{M}_2$ can be nonzero because the secondary orifice opens up a path having the toroidal topology of **Fig. 9a**.

To enforce $\dot{M}_2 c_p\, \Delta T = 0$, $\dot{M}_2$ must be zero. In terms of density and volume flow rate,

$$\dot{M}_2 = \frac{1}{2}\,\mathrm{Re}\,[\tilde{\rho}_1 U_1] + \rho_m U_{2,0}. \tag{27}$$

Hence, in a traditional orifice pulse-tube refrigerator, the two terms on the right side of Eq. (27) *must* be equal and opposite. The two first-order factors ρ_1 and U_1 are "known" from thermoacoustic considerations outlined above, so setting $\dot{M}_2 = 0$ in Eq. (27) determines what $U_{2,0}$ *must* be. The second-order time average of the momentum equation, which may be of the form

$$\omega\rho_1 \mathbf{v}_1 \text{ term } + \rho_m \mathbf{v}_1 \boldsymbol{\nabla}\mathbf{v}_1 \text{ term } = -\frac{dp_{2,0}}{dx} + r_\nu U_{2,0}, \tag{28}$$

must also be true, so a nonzero $dp_{2,0}/dx$ will generally also exist in a regenerator whenever $\dot{M}_2 = 0$ through it. It is helpful to think of the $\Delta p_{2,0}$ that exists across the regenerator as causing the viscous flow of $U_{2,0}$ through the regenerator.

However, as shown in **Fig. 9a**, any system with the topology of a torus, such as the thermoacoustic-Stirling heat engine of **Fig. 2**, can have $\dot{M}_2 \neq 0$ if the two terms on the right side of Eq. (27) are not

in perfect balance. To estimate how severe the time-averaged convective enthalpy flux carried by such streaming might be in a cryogenic refrigerator if $\dot{M}_2 \neq 0$, Gedeon [19] showed that

$$\frac{1}{2}\,\mathrm{Re}\,[\widetilde{\rho}_1 U_1] \simeq \rho_m \dot{E}_2 / p_m \tag{29}$$

in a regenerator, where $\dot{E}_2 = \frac{1}{2}\,\mathrm{Re}[\widetilde{p}_1 U_1]$ is the usual acoustic power passing through the regenerator. Hence, $\frac{1}{2}\,\mathrm{Re}[\widetilde{\rho}_1 U_1]$ *must* be nonzero in Stirling engines and refrigerators, and $U_{2,0}$ *must* be nonzero to achieve $\dot{M}_2 = 0$. The consequences of ignoring this requirement can be severe indeed. If $\dot{M}_2 \neq 0$, an undesired, streaming-induced enthalpy $\dot{Q}_{\mathrm{loss}} \sim \dot{M}_2 c_p\,(T_0 - T_C)$ flows from ambient to cold through the regenerator. For $U_{2,0} = 0$, the ratio of $\dot{Q}_{\mathrm{loss}}$ to the ordinary regenerator loss $\dot{H}_{2,reg}$ is of the order of

$$\frac{\dot{Q}_{\mathrm{loss}}}{\dot{H}_{2,reg}} \sim \frac{\gamma}{\gamma-1}\frac{(T_0 - T_C)}{T_0}\frac{\dot{E}_2}{\dot{H}_{2,reg}} \sim \frac{\gamma}{\gamma-1}\frac{(T_0 - T_C)}{T_C}\frac{\dot{Q}_{C,\mathrm{gross}}}{\dot{H}_{2,reg}}, \tag{30}$$

where $\dot{Q}_{C,\mathrm{gross}}$ is the gross cooling power, equal to $\dot{E}_2$ in the cold heat exchanger. In the final expression in Eq. (30), each of the three fractions is > 1 for cryocoolers; hence their product is $\gg 1$, and the unmitigated streaming-induced heat load would be very large.

Gedeon streaming can be suppressed either by a flexible membrane or bellows to enforce $\dot{M}_2 = 0$ or by using asymmetry in high-Reynolds-number minor-loss effects to produce enough $\Delta p_{2,0,reg}$ [8,6,7] to create the appropriate $U_{2,0}$.

Example: Acoustic-Stirling heat engine. The adjustable "jet pump" labeled in **Fig. 2** employed asymmetry of high-Reynolds-number flow to suppress Gedeon streaming. Temperature measurements in the center of the regenerator and measurements of $\dot{Q}_H$ required to maintain engine operation at constant amplitude both showed [6] that Gedeon streaming was stopped, but only when the jet area A was 2 to 3 times smaller than was estimated from tabulated steady-flow minor-loss coefficients and the flow resistance of the regenerator. Additional research is needed to resolve such disagreements.

Rayleigh Streaming

Ideally, the gas in a pulse tube or thermal buffer tube acts as a long (and slightly compressible) piston, transmitting pressure and velocity oscillations from one end to the other. The gas should also thermally insulate the ends of the tube from each other. Unfortunately, convection *within* the tube can carry enthalpy from one end to the other, adding a heat load to the cold heat exchanger in a refrigerator or consuming heat at the hot heat exchanger of an engine. If Gedeon streaming is eliminated, there can be no *net* mass flux $\dot{M}_2$ through the tube, but the possibility remains that enthalpy can be carried by mass flux density $\dot{m}_{2,0}(r)$ streaming upward near the side walls of the tube and downward in the central portion of the tube (or vice versa). Such streaming can be caused by jetting due to inadequate flow straightening at either end of the tube, as described in the next subsection, but here we review Rayleigh streaming, which is convection confined within the tube and driven by viscous and thermal boundary-layer phenomena at the side walls of the tube, as illustrated in **Fig. 9b**. The boundary-layer calculation [20] of streaming in such a geometry yields a prediction for the side-wall taper angle that suppresses this streaming.

This analysis is based entirely on laminar flow in the boundary layer, but at usefully high pressure amplitudes the oscillations in typical pulse tubes and thermal buffer tubes are near the transition to turbulence. Additional research is needed to determine how to suppress Rayleigh streaming in the turbulent regime.

Example: Orifice pulse-tube refrigerator. When the pulse-tube refrigerator of **Figs. 3** and **4** was being designed, Eq. (13) of Ref. [20] showed that a taper angle $\phi = 1.3°$ (with the cold end larger than the ambient end) would suppress Rayleigh streaming in the pulse tube at the design operating point, so the pulse tube was fabricated with that taper and care was taken to keep internal surface roughness much smaller than δ_κ and δ_ν. When the refrigerator was in operation [21], measurements showed that $\dot{H}_2/\dot{E}_2 = 0.96$ in the pulse tube at the design operating point, so the "heat leak" down the pulse tube was only 4% of the acoustic power flowing up the pulse tube into the LRC acoustic impedance network. This

value was extremely close to the design calculation, which included only the metallic thermal conductance of the tube wall ($\gtrsim 2\%$) and the second-order boundary-layer hydrodynamic entropy flux

$$\frac{1}{2}\rho_m T_m \int \mathrm{Re}\left[s_1 \widetilde{u_1}\right] dA. \tag{31}$$

Adjusting the acoustic-network orifice valves to change the phase of the complex acoustic impedance in the pulse tube just a few degrees from the design point, in either direction, caused the measured values of $\dot{H}_2/\dot{E}_2$ to drop below 0.9, as Rayleigh streaming convected enthalpy along the pulse tube.

Jet-Driven Tube Streaming

Ideally, the gas in a pulse tube or thermal buffer tube would do nothing more than oscillate in plug flow, transmitting $\dot{E}_2 \equiv \dot{H}_2$ from one end to the other. However, if either end of the tube has a small-diameter entrance, a jet may blow into the tube when gas enters, driving streaming within the tube, as illustrated in **Fig. 9c**. The spreading angle of a high-Reynolds-number jet in free space is roughly 10°, so such a jet can extend a large distance, and even the array of small jets formed by flow out of a heat exchanger or similar periodic structure requires some distance to "heal" into plug flow. Hence, flow straighteners are typically employed to break up such jets. A nonlinear impedance, such as that of a short stack of screens, is effective at straightening jets. Because such flow straighteners dissipate acoustic power, research leading to more quantitative design methods for flow straighteners will help improve the efficiency of thermoacoustic-Stirling engines and refrigerators.

Streaming Within a Regenerator

We know little about streaming *within* a regenerator as illustrated in **Fig. 9d**, except that it should be avoided for the same reasons that Rayleigh streaming should be avoided. We know it can occur, because we once suffered from harmful toroidal streaming within a regenerator when a narrow jet blew strongly on the heat exchanger at the ambient end of the regenerator, due to an abrupt transition from a small-diameter driver duct to the larger diameter of the ambient heat exchanger and regenerator. We fear that such toroidal time-averaged flows might also arise *spontaneously* in short, wide regenerators, as has been observed when two or more regenerators are operated in parallel [22].

Deliberate Streaming

In common with many other heat engines and refrigerators, Stirling systems suffer from a practical difficulty: They need heat exchangers to transfer heat between the thermodynamic working gas and the process fluid (usually air, combustion products, or water). Heat exchangers are expensive, and contribute to system inefficiency via temperature differences and viscous effects in the working fluid, in the process fluid, and often in an intermediate heat-exchange fluid. This difficulty is serious. For example, the decline of the Stirling and steam engines and the rise of the Diesel and other internal-combustion engines occurred in large part because the internal-combustion engines need no combustion-temperature heat exchangers (and also reject most of their waste heat in their exhaust instead of through heat exchangers).

For some applications, we hope that some or all of the heat exchangers can be eliminated from hybrid thermoacoustic-Stirling systems, by superposing the steady flow needed to deliver the process gas with the oscillating flow needed for the thermodynamic cycle in the gas. Steady flow can enter and leave the thermoacoustic resonator at pressure nodes, which sometimes already exist in the resonator but which can otherwise be created for this purpose.

Parallel flow. The superposition of deliberate steady flow parallel to the oscillating flow in a regenerator, as illustrated in **Fig. 10a**, could lead to increased efficiency, for two reasons. First, a heat exchanger, with its internal small temperature difference and its viscous losses, is eliminated. Second, a more subtle improvement in efficiency arises because a parallel-flow system essentially puts the flowing stream sequentially in thermal contact with a large number of refrigerators in series—a sort of continuum limit of staged refrigeration. To understand this point, first imagine that thermoacoustic-Stirling refrigerators are ideal, having Carnot's $COP = T_C/(T_0 - T_C)$. Then, in the case of a traditional refrigerator with the stream $\dot{m}$, initially at T_0, flowing through the cold heat exchanger, the refrigerator removes heat $\dot{m}c_p(T_0 - T_C)$ at temperature T_C and hence requires work

$$\dot{W} = \dot{m}c_p(T_0 - T_C)^2/T_C. \tag{32}$$

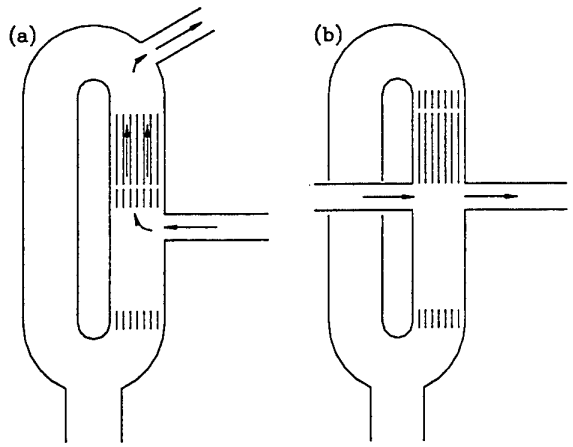

Fig. 10: Streaming that can be beneficial. Note the elimination of a heat exchanger in each case. (a) Flow parallel to x through a regenerator. Flow perpendicular to x across one end of a regenerator.

This is more than twice the minimum work required by the first and second laws of thermodynamics for this process, which is given by the difference between the outgoing and incoming flow availabilities:

$$\dot{W} = \dot{m}\left[(h_C - h_0) - T_0\,(s_C - s_0)\right] \tag{33}$$

$$= \dot{m}c_p[T_C - T_0 + T_0 \ln(T_0/T_C)]. \tag{34}$$

(The second expression results from using ideal-gas expressions for enthalpy h and entropy s.) The trouble with the simple, one-stage refrigerator is that it removes *all* the heat load at T_C, where every watt of cooling power requires the same amount of work. It is much more efficient to remove as much of the heat load as possible at higher temperatures T'_C, where each watt of cooling power requires less work because the Carnot $COP = T'_C/(T_0 - T'_C)$ is higher. The perfect embodiment of this idea would employ an infinite number of ideal refrigerators, each providing an infinitesimal cooling power $\dot{m}c_p\,dT'_C$ at T'_C and rejecting an infinitesimal amount of waste heat at T_0. The flow-through thermoacoustic-Stirling refrigerator of **Fig. 10a** has some features of this perfect situation, if we imagine each length dx of the regenerator to be a tiny refrigerator unto itself, lifting heat from T'_C to $T'_C + dT'_C$. The flow-through system removes each watt of heat from the flowing stream at the highest possible temperature, with an "infinite" number of tiny refrigerators, each of which must handle the waste heat of all its downstream neighbors in addition to the local heat load of the flowing stream.

We have made only a preliminary investigation [23] of these ideas. Much research and invention is needed to investigate practical use of such parallel steady flows.

Perpendicular flow. Further elimination of heat exchangers, and their associated viscous and thermal losses, could be accomplished by superposition of vigorous steady flow perpendicular to the oscillating flow, as illustrated in **Fig. 10b**.

REFERENCES

1. I. Urieli and D. M. Berchowitz, *Stirling Cycle Engine Analysis,* Adam Hilger, Bristol UK (1984).

2. G. Walker, *Stirling Engines,* Clarendon, Oxford (1960).

3. C. D. West, *Liquid Piston Stirling Engines,* Van Nostrand Reinhold (1983).

4. P. H. Ceperley, "A pistonless Stirling engine–the traveling wave heat engine," J. Acoust. Soc. Am. v. 66, pp. 1508–1513 (1979).

5. P. H. Ceperley, "Gain and efficiency of a short traveling wave heat engine," J. Acoust. Soc. Am. v. 77, pp. 1239–1244 (1985).

6. S. Backhaus and G. W. Swift, "A thermoacoustic-Stirling heat engine," Nature v. 399, pp. 335–338 (1999).

7. S. Backhaus and G. W. Swift, "A thermoacoustic-Stirling heat engine: Detailed study," submitted to J. Acoust. Soc. Am. (1999).

8. G. W. Swift, D. L. Gardner, and S. Backhaus, "Acoustic recovery of lost power in pulse tube refrigerators," J. Acoust. Soc. Am. v. 105, pp. 711–724 (1999).

9. G. W. Swift, *Thermoacoustics: A Unifying Perspective for some Engines and Refrigerators,* rough draft available at www.lanl.gov/thermoacoustics/ (1999).

10. Cryenco manufactures large-scale cryogenic hardware, such as cryogenic tank trucks, storage tanks, and cryogenic vessels for MRI systems. 3811 Joliet, Denver CO 80239.

11. G. W. Swift, "Thermoacoustic natural gas liquefier," *Proceedings of the DOE Natural Gas Conference,* Houston TX (March 1997). Also available at http://lib-www.lanl.gov/la-pubs/00412750.pdf.

12. G. W. Swift, "Thermoacoustic engines," J. Acoust. Soc. Am. v. 84, pp. 1145–1180 (1988).

13. N. Rott, "Damped and thermally driven acoustic oscillations in wide and narrow tubes," Z. Angew. Math. Phys. v. 20, pp. 230–243 (1969).

14. W. P. Arnott, H. E. Bass, and R. Raspet, "General formulation of thermoacoustics for stacks having arbitrarily shaped pore cross sections," J. Acoust. Soc. Am. v. 90, pp. 3228–3237 (1991).

15. G. W. Swift and R. M. Keolian, "Thermoacoustics in pin-array stacks," J. Acoust. Soc. Am. v. 94, pp. 941–943 (1993).

16. G. W. Swift and W. C. Ward, "Simple harmonic analysis of regenerators," J. Thermophysics and Heat Transfer v. 10, pp. 652–662 (1996).

17. W. C. Ward and G. W. Swift, Design environment for low amplitude thermoacoustic engines (DeltaE), J. Acoust. Soc. Am. v. 95, pp. 3671–3672 (1994). Fully tested software and user's guide available from Energy Science and Technology Software Center, US Department of Energy, Oak Ridge, Tennessee. To review DeltaE's capabilities, visit www.lanl.gov/thermoacoustics/. For a beta-test version, contact ww@lanl.gov (Bill Ward) or swift@lanl.gov (Greg Swift) by email.

18. W. L. M. Nyborg, "Acoustic Streaming," *Physical Acoustics, v. IIB, pp. 265–3331,* edited by W. P. Mason, Academic Press (1965).

19. David Gedeon, "DC gas flows in Stirling and pulse-tube cryocoolers," *Cryocoolers 9, pp. 385–392,* edited by R. G. Ross, Plenum, New York (1997).

20. J. R. Olson and G. W. Swift, "Acoustic streaming in pulse tube refrigerators: Tapered pulse tubes," Cryogenics v. 37, pp. 769–776 (1997).

21. G. W. Swift, M. S. Allen, and J. J. Wollan, "Performance of a tapered pulse tube," *Cryocoolers 10, pp. 315–320,* edited by R. G. Ross, Plenum, New York, (1999).

22. C. S. Kirkconnell, "Experimental investigation of a unique pulse tube expander design," *Cryocoolers 10, pp. 239–247,* edited by R. G. Ross, Plenum, New York, (1999).

23. R. S. Reid, W. C. Ward, and G. W. Swift, "Cyclic thermodynamics with open flow," Phys. Rev. Lett. v. 80, pp. 4617–4620 (1998).

RENEWABLE ENERGY IN THE 21ST CENTURY

Stanley R. Bull
Associate Director for Science and Technology
National Renewable Energy Laboratory, Golden, CO 80401
Email: stanley_bull@nrel.gov

Keywords: sun, wind, earth, plants

ABSTRACT. Energy is essential to our society. It is essential to our quality of life and underpins all other elements of our economy. As we approach the dawn of the 21st century, renewable energy technologies offer a tantalizing promise: clean, abundant energy gathered from continuously self-renewing resources such as the sun, wind, earth, and plants. Research conducted over the past 20 years has been bringing this promise closer to fruition, and progress towards realization of the full potential of renewable energy is accelerating.

> "For years, the renewables business has wanted to reach the point where, as sales volumes grew, prices dropped, making renewables more attractive and stimulating demand. This holy grail at last seems to be in sight."
>
> *The Economist*, April 18,1998, p. 57

This paper will briefly review the technical status, cost, and applications of major renewable energy technologies, and also discuss some of the socioeconomic impacts of wide-scale adoption of renewables.

PROGRESS IN RENEWABLE ENERGY TECHNOLOGIES

The term "renewable energy" encompasses a broad spectrum of technologies, all of which are based on self-renewing energy sources such as sunlight, wind, flowing water, the earth's internal heat, and biomass such as energy crops, agricultural and industrial waste, and municipal waste. These resources can be used to produce electricity for all economic sectors, fuels for transportation, and heat for buildings and industrial processes.

Renewable energy contributes as much today to U.S. energy consumption as nuclear power (7%) and contributes slightly more (8%) to worldwide energy consumption [1]. Each renewable energy technology is in a different stage of development and commercialization. Some technologies are already commercial, at least for some situations and applications [2]. Of the renewable energy consumed in the United States in 1998, hydropower comprised 55%; biomass, including municipal solid waste, 38%; geothermal, 5%; solar, 1%; and wind, 0.5% [3]. Detailed information on over 7,000 facilities that generate U.S. grid-connected electricity from renewable resources is available electronically [4].

Renewable energy technologies offer important benefits compared to those of conventional energy sources such as fossil fuels or nuclear power [5,6]. Renewable energy resources are abundant; worldwide, one thousand times more energy reaches the surface of the earth from the sun than is released today by all fossil fuels consumed. Table 1 gives the energy delivered per square meter of land for four renewable resources [7]. Similar to fossil fuels, renewable energy resources are not uniformly distributed throughout the world. However, every region has some renewable energy resource. And, because different renewable energy resources complement each other, taken together they can contribute appreciably to energy security and regional development in every nation of the world, without dependence on foreign energy sources that are subject to political instability or manipulation.

Table 1. Comparison of Renewable Energy Delivery per Unit Land Area

Resource	Annual Delivered Energy (kWh/m^2)
Wind Energy (intermittent)	11 (average wind speed) 18 (high wind speed)
Biomass (baseload)	15 (low efficiency) 45 (high efficiency)
Photovoltaics (intermittent)	50-100
Geothermal (The Geysers) (baseload)	160-200

Most renewable energy systems are modular, allowing flexibility in matching load growth. Today's markets for renewable energy technologies range from specialized niche markets, where they are already cost effective, to centralized energy production. For centralized energy production, renewable energy systems are relatively capital intensive compared to competing conventional technologies such as natural gas combined power plants. However, after the initial investments have been made, the economics of renewable energy technologies improve in comparison with conventional technologies because operating and maintenance costs are low compared with those incurred using conventional fuels. This is especially true in the regions of the world where world fuel prices are relatively high, and will be especially true in the future as fuel prices increase.

Renewable energy systems generate little if any waste or pollutants that contribute to acid rain, urban smog, and health problems, and do not require environmental cleanup costs or waste disposal fees. Potential global climate change, caused by excess carbon dioxide and other gases in the atmosphere, is the latest environmental concern; systems using solar, wind, and geothermal sources do not contribute any carbon dioxide to the atmosphere [8]. In fact, today renewable sources of electricity help the United States avoid about 70 million metric tons of carbon emissions per year that would have been produced had that electricity been generated by fossil fuels [9]. Biomass does release carbon dioxide when it is converted to energy, but because biomass absorbs carbon dioxide as it grows, the entire process of growing, using, and regrowing biomass results in very low to zero carbon dioxide emissions.

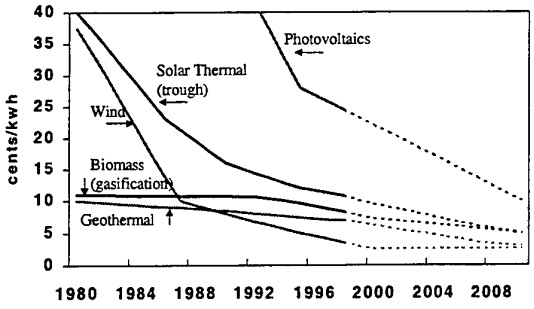

Fig. 1 Renewable Electricity Cost Trends and Projections

Although the energy of the sun and wind has been used by mankind for millennia, modern applications of renewable energy technologies have been under serious development for only about 20 years. In that period of research and development investment by industry and government (primarily the U.S. Department of Energy [DOE]), dramatic improvements have occurred in the cost, performance, and reliability of renewable energy systems (see Figure 1). A summary of these improvements is given below; many excellent reviews of the past two decades of progress in renewable energy technologies are available [10 - 19].

Photovoltaic Energy

Photovoltaic devices use semiconductor materials such as silicon to convert sunlight to electricity. They contain no moving parts and produce no emissions while in operation. Extremely modular, photovoltaic devices can be used in small cells, panels, and arrays. Photovoltaic systems require little servicing or maintenance and have typical lifetimes of about 20 years. Through the National Center for Photovoltaics at NREL, researchers in government, universities, and industry are working together to lower production costs. Their efforts are focused on developing more efficient semiconductor materials and device designs, while expanding production capacity, increasing production rates, and improving product quality [20 - 23].

Capital costs for photovoltaic panels have decreased from more than $50 per watt (W) in the early 1980s to about $5/W today; energy costs have declined from about 90¢ per kilowatt-hour (kWh) in 1980 to about 25¢/kWh. Although this is still higher than the cost of conventional baseload electricity, commercial markets are flourishing in developed countries for remote telecommunications, remote lighting and signs, remote homes and recreational vehicles, and in developing countries for remote power for village homes, clinics, and other uses (see Figure 2). Incorporating photovoltaic systems into roofing materials for generating power on buildings is another rapidly growing area [24].

Photovoltaic markets, which have been growing steadily, experienced a large boost the last two years. In 1997, sales grew by 42% and by 21% in 1998; the 1998 worldwide market for photovoltaic systems was greater than

$1 billion. Worldwide shipments of photovoltaic systems in 1998 were 152 megawatts (MW); of this, 54 MW was exported from the United States, for a 35% share; Japan captured 32% and Europe (mostly Germany), 20% [25]. The surge in sales in 1997 and 1998 came primarily from government programs in Japan and Germany that subsidize purchase of photovoltaics for residential use. In response to this growth, photovoltaic companies are expanding; considering only projects for which capital expenditures have been made, U.S. capacity grew from 50 MW in 1996 to more than 150 MW in 1998.

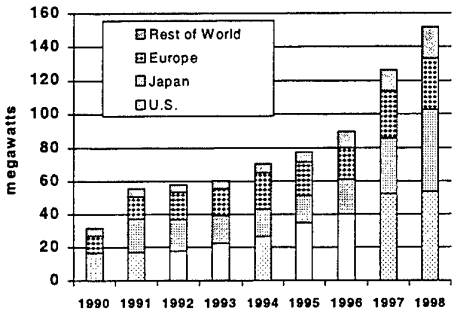

Fig. 2 Worldwide Photovoltaic Shipments

A new type of photovoltaics is now emerging, with the first commercial products now in development. Conventional solar photovoltaics, as discussed above, uses the energy of light to generate electricity. Thermophotovoltaics uses the energy of heat, or infrared radiation, to generate electricity, with the advantage that a generator can operate at night or when the sky is overcast, eliminating the need for batteries. Though it does need a fuel, such as natural gas, to provide the heat, using semiconductors for conversion rather than conventional diesel generators results in higher fuel-to-electricity conversion efficiencies, modularity, minimal pollutants, quiet operation, and high reliability. Applications under development include small power units to supply electricity in remote areas or for military troops; a U.S. company is also planning to market a thermophotovoltaic generator to run electrical equipment on sailboats. Ultimately, thermophotovoltaics could generate electricity from excess heat in hybrid electric vehicles or industrial processes [26,27].

Wind Energy

Wind power systems convert the kinetic energy of the wind into other forms of energy such as electricity. Although wind energy conversion is relatively simple in concept, turbine design can be quite complex. Most commercially available wind turbines use a horizontal-axis configuration with two or three blades, a drivetrain including a gearbox and generator, and a tower to support the rotor. Typical sizes for a wind turbine range from 200–600 kilowatts (kW), with electricity produced within a specific range of wind speeds.

Rapid progress in this technology has reduced costs until they are almost competitive with those of conventional power [28]. Capital costs have declined from about $2.2/W in the early 1980s to less than $1/W today. Energy costs have decreased from about 40¢/kWh to as low as 4¢-7¢/kWh today in areas with excellent wind resources. In the United States, cooperative research between DOE and manufacturing companies is aimed at increasing the aerodynamic efficiency and structural strength of wind turbine blades, developing variable-speed generators and electronic power controls, and using taller towers that allow access to the stronger winds found at greater heights. Projected energy costs for these advanced machines are 2¢-3¢/kWh [29,30].

Wind resources are abundant throughout the world. In the United States, good resources can be found in 34 of the 50 states. For example, the wind resources in North Dakota alone could supply as much as 36% of all the electricity consumed by the lower 48 states.

More than 2,200 MW of additional wind capacity, totaling $2.2 billion in sales, was installed worldwide in 1998 [31]. This reflects a 35% annual growth rate in total installations in 1998; international markets have been growing much more rapidly than U.S. markets (see Figure 3). Installed capacity in Europe, dominated by Germany and Denmark, has surpassed installations in the United States, and is rapidly increasing; the United States installed only 420 MW in 1998. China already has more than 100,000 wind turbines generating electricity and pumping water in rural areas far from existing power lines. According to the American Wind Energy Association, as much as 13,500 additional megawatts of wind capacity may be installed worldwide in the next decade.

The U.S. wind industry is thinly capitalized, except for the acquisition of one major wind company by Enron; there have been two bankruptcy filings recently. Europe has twice as many wind manufacturing and developing

companies; some have already established North American manufacturing facilities and are penetrating the U.S. market [32].

Biopower

Biomass power plants generate electricity from biomass resources ranging from agricultural and forest product residues to crops grown specifically for energy production. Direct-combustion systems burn biomass in a boiler to produce steam that is expanded to produce power; cofiring substitutes biomass for coal in existing coal-fired boilers; gasification converts biomass to a fuel gas that can be substituted for natural gas in combustion turbines. Today's U.S. biopower industry — nearly 1,000 plants — consists of direct-combustion plants with a small amount of cofiring. Plant size averages 20 MW with efficiencies of about 20% and electricity costs of 8¢-12¢/kWh. Grid-connected capacity has increased from less than 200 MW in 1978 to more than 7,300 MW in 1996. About 70% of this is in the forest products and sugarcane industries; municipal solid waste plants provide additional capacity of 3,300 MW [33]. Biopower capacity in the rest of the world is about 20,000–25,000 MW, and international markets are strong with at least six major multinational companies actively involved in the industry. Research focuses on doubling or tripling the conversion efficiency of commercial plants, reducing costs further, and resolving issues related to biomass residual ash [34,35].

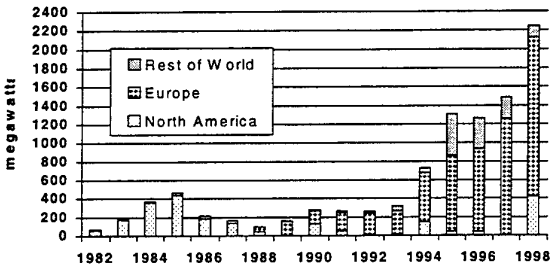

Fig. 2 Worldwide Wind Energy Installation

Geothermal Energy

Geothermal resources include dry steam, hot water, hot dry rock, magma, and ambient ground heat. Steam and water resources have been developed commercially for power generation and ambient ground heat is used commercially in geothermal heat pumps; methods of tapping the other resources are being studied. Research centers on lowering costs, improving methods for finding and characterizing reservoirs, and tapping broader resources [36,37].

The Geysers steam power plant in California is the oldest and largest geothermal power plant in the world, with a capacity of 2,000 MW. Hot-water plants have been developed more recently and are now the major source of geothermal power in the world. Total U.S. capacity is about 2,700 MW, enough electricity for 3 million people, at a cost of 5¢-10¢/kWh. Hot water from geothermal resources is also used directly to provide heat for industrial processes, dry crops, or heat buildings, for a total U.S. capacity of about 500 thermal MW. Many developing countries have geothermal resources, and continue to be an attractive market [38].

Geothermal heat pumps do not generate electricity, but they reduce the consumption of electricity by using heat exchangers and the constant temperature of the earth several feet under the ground to heat or cool indoor air. The market for geothermal heat pumps has been growing rapidly, and by 2000 expectations are that they will be installed on more than 400,000 homes and commercial buildings per year [39].

Solar Thermal Energy

Solar thermal systems use the sun's heat to meet a variety of needs, such as generating electricity; heating water for industrial processes, domestic water supplies, or community swimming pools; preheating building ventilation air; and direct heating of building interiors.

In California, nine commercial solar thermal electric plants with a total generating capacity of 354 MW having been operating since the mid-1980s. These systems consist of rows of highly reflective parabolic troughs. Each trough focuses and concentrates sunlight on a central tube filled with heat-absorbing fluid, which is used to generate electricity. When combined with natural-gas-fired turbines, parabolic-trough systems can produce electricity for about 9¢/kWh.

Two other options for solar thermal electricity include "power towers" and dish-Stirling units. Power towers generate large amounts of electricity using a tall, fluid-filled tower located at the focal point of a large field of mirrors. This technology has been demonstrated by DOE's Solar One and Solar Two projects near Barstow, California. Dish-Stirling units use a small array of mirrors to focus sunlight on a Stirling engine, which produces 5–50 kW of electricity for grid consumption or stand-alone applications. Dish-Stirling systems are currently being tested by several electric utilities in the southwestern United States as a way to add incremental capacity without constructing expensive new conventional power plants [40,41].

One of the most widespread uses of solar thermal technology is solar water heating. Significant progress has been made in improving the reliability and durability of these systems since the 1970s. According to the Solar Energy Industries Association, more than 200,000 businesses and 100,000 pools in the United States now use solar thermal systems to reduce their utility bills. Flat-plate collectors are used on residences, while more costly parabolic-trough systems make this technology suitable for moving the large volumes of water used by hospital laundries, institutional kitchens, swimming pools, or industrial processes [42 - 44].

The sun's heat can also be used to preheat building ventilation air using transpired solar collectors mounted on south-facing exterior walls. The first commercial systems were sold last year.

Biofuels

Ethanol is frequently used as a gasoline additive, or converted to another additive called ethyl tertiary-butyl ether, to raise the octane level of gasoline and promote cleaner combustion. According to the U.S. Environmental Protection Agency, the use of ethanol blended with gasoline can reduce motor vehicle emissions of carbon monoxide by 25% to 30% and also reduce ozone levels that contribute to urban smog. In addition, the combustion of ethanol produces 90% less carbon dioxide than gasoline.

A blend of 10% ethanol and 90% gasoline has been widely used throughout the nation for many years. Stronger blends of 85% and 95% ethanol are being tested in government fleet vehicles, flexible-fuel passenger vehicles, and urban transit buses. Although there are less than 100 such vehicles in operation, their use is expected to grow as federal, state, municipal, and private fleet operators seek to comply with the alternative fuel requirements of the Energy Policy Act of 1992 and the Clean Air Act Amendments of 1990.

Ethanol sold today is produced from corn kernels using traditional fermentation technology to meet a market demand of more than a billion gallons of fuel a year. Because corn requires high amounts of energy (as fertilizer and farm equipment fuel) to grow, renewable energy research has focused on producing ethanol — termed bioethanol — from corn waste, waste newspaper, rice straw, and grasses and trees cultivated as energy crops [45]. Biological production of ethanol involves hydrolysis of fibrous biomass, using enzymes or acid catalysts, to form soluble sugars, followed by microbial conversion of sugars to ethanol. The cost of bioethanol production has decreased from $3.60/gallon in 1980 to about $1.20 today (see Figure 4) due to technical breakthroughs, including genetic engineering of specialized enzymes and microbes. Ultimately, the goal is for bioethanol to become competitive with gasoline in price [46]. Research focuses on low-cost production of enzymes to break down cellulose, improve microorganism performance, produce suitable energy crops, and demonstrate ethanol production from a variety of biomass feedstocks [47,48].

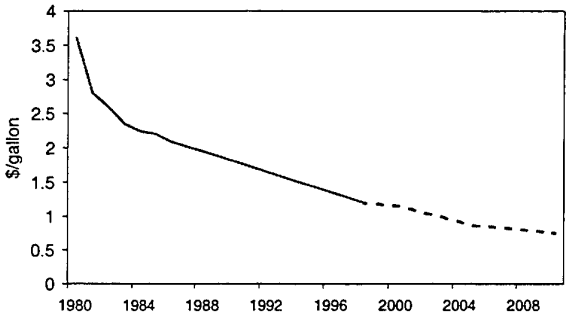

Fig. 3 Bioethanol Costs Will Continue to Decrease

Ethanol is not the only fuel that can be produced from biomass. About 1.2 billion gallons of methanol, currently made from natural gas, are sold in the United States annually, with about 38% of this used in the transportation

sector. (The rest is used to make solvents and chemicals.) Methanol can also be produced from biomass through thermochemical gasification. Diesel fuel, currently produced from petroleum, is also being produced in limited quantities from soybeans, but research has shown that diesel fuel can also be produced from less costly and more abundant sources, such as the natural oils occurring in algae and pyrolysis of biomass. Dimethyl ether is another fuel that can be produced from biomass as a diesel substitute. Federal support for research on biomass-derived methanol and diesel fuels has been de-emphasized recently to focus funding resources on ethanol.

Hydrogen and Fuel Cells

Hydrogen is today produced from natural gas for limited markets but it can be produced from renewable sources and promises substantial contributions to global energy supplies in the long term. Hydrogen is the most abundant element in the universe, the simplest chemical fuel (essentially a hydrocarbon without the carbon) that makes a highly efficient, clean-burning energy carrier. It has the potential to fuel transportation vehicles with zero emissions, provide process heat for industrial processes, supply domestic heat through cogeneration, help produce electricity for centralized or distributed power systems, and provide a storage medium for electricity from renewable energy sources. Some envision an entire economy based on hydrogen in the future [49 - 51].

> "The new solar-powered water splitter...converts about 12.5% of the energy in sunlight to gaseous fuel—nearly double the previous record achieved by a conventional process."
>
> *Science,* April 17, 1998, p. 382

Research challenges include cost-effective, energy-efficient production technologies and safe, economical storage and transportation technologies. Major breakthroughs have occurred this year in both production and storage technologies for hydrogen. Researchers have doubled the previous efficiency of producing hydrogen from water and have made major advances in carbon nanotube storage technology [52,53].

Fuel cells promise to be a safe and effective way to use hydrogen for both vehicles and electricity generation. Fuel cells convert hydrogen — as hydrogen gas or reformed within the fuel cell from natural gas, alcohol fuels, or some other source — directly into electrical energy with no combustion. Phosphoric acid fuel cells are already commercially available to generate electricity in 200-kW capacities selling for $3/W, using natural gas as the source of hydrogen; molten carbonate has been demonstrated at large (2-MW) capacities. Solid-oxide fuel cells are being demonstrated by major manufacturers for potential cogenerators in commercial and multifamily residential buildings. Proton exchange membrane cells using hydrogen (currently reformed from methanol) are being developed for both transportation and electricity applications [54,55].

Although hydrogen fuel cells are used routinely by NASA for space missions, terrestrial applications are still in their infancy. The lack of an economical process for hydrogen production and suitable storage methods are two of the greatest obstacles to commercialization, especially in the transportation sector. Research goals include developing technologies to produce hydrogen from sunlight and water and biomass; developing low-cost and low-weight hydrogen storage technologies for both stationary and vehicle-based applications, such as carbon nanotubes and metal hydrides; and developing codes and standards to enable the widespread use of hydrogen technologies.

TODAY'S TRENDS AND ISSUES AFFECTING RENEWABLES

As is evident from the preceding discussion, scientific and engineering advances continue to strongly influence the progress of renewable energy technology development, as do advances in information technology. Easily accessed World Wide Web sites relating to renewable energy technologies provide valuable and accurate information that is easily accessible by everyone. Real-time metering is opening up innovative electricity pricing [56]; sophisticated equipment and controls are improving the use of energy in buildings; and complex systems are being modeled in the laboratory, accelerating technology development.

But despite the excellent technical progress of the last 20 years, electricity and fuels from renewable energy are still generally more expensive than electricity and fuels from conventional fossil-fuel sources, with the exception of some niche markets. Table 2 summarizes the economic potential of major renewable energy electric systems. Although it is difficult to compare costs of electricity from renewable technologies to those of

conventional grid electricity, it should be noted that the average retail price of electricity in the United States is 7¢/kWh, which is less than most renewables. The cost of electricity and fuels from renewable energy would easily be less expensive than fossil fuels if the true, hidden costs of fossil fuels — environmental costs, health costs, and energy security costs — were considered. But our society has not yet found acceptable ways to incorporate these hidden costs into the cost of our energy.

Table 2. Economic Potential of Renewable Electric Systems in the U.S.

Resource	Application or Technology	Current Cost [57] (¢/kWh)	Next Generation Cost [57] (¢/kWh)	Grid-connected Generating Capacity, 1996 [58] (MW)	Timeframe for Major Market Penetration (years) [58]
Photovoltaics	All types	25-35	15 or less	10	5-15
Solar Thermal Energy	Dish-Stirling	10-15	4-6	0	5-10
	Trough	10-12	7-9	354	5-10
	Power Tower	6-9	3-5	0	5-10
Biopower	Direct Combustion	7-15	4-6	7,500	0
	Cofiring	2-3	2-3	500	0-3
	Gasification	8-10	4-5	0	3-8
Wind Energy	All types	5-10	2-4	1,850	0-5
Geothermal Energy	Steam and Hot Water	7-10	3	3,020	0-5

Although we have not yet incorporated hidden costs into our pricing structures, the support of the American public for renewable energy continues unabated. In surveys over the past 18 years, majorities of the public have chosen renewable energy and energy efficiency over other energy alternatives and expressed a desire for a national agenda of sustainable development with increasingly large portions of the nation's energy mix from renewables [59]. In addition, more than a dozen utilities in the United States and more in Europe are offering renewables as part of a "green" marketing campaign to attract consumers, with very positive results to date [60 - 63]. Renewable energy is also getting more attention as a valuable response to natural disasters to mitigate loss, aid in immediate relief, and promote rapid recovery [64]. Even the insurance community is paying greater attention to renewables as insurance companies take higher and higher losses from natural disasters that scientists suggest may be increasing due to the cumulative impact on the environment of mankind's use of energy.

The industrialized world, and particularly the United States, is currently undergoing rapid change in the fundamental structure of the electricity sector of our economies [65 - 67]. Following the experience of the airline, telecommunications, and other industries, regulated utility monopolies are giving way to a market-driven electricity industry. The challenges and opportunities of this restructuring affect utilities, independent developers, power marketers, energy users, investors — and the renewable energy community. The immediate effect has been to make it more difficult for renewable energy electric technologies to penetrate large U.S. markets, because of the newness and uncertainty surrounding investments in relatively new technologies, the expectation of stiff price competition, and the higher initial cost of renewable energy technologies. Although some opportunities have opened up because of consumer interest in "green" energy, wind energy companies in the United States have been hurt at a critical time for the industry.

To encourage the use of renewable energy electricity in the United States, policy measures will be needed [68,69]. The most prominent measure under consideration is the renewables portfolio standard, a market-based mechanism for ensuring a minimum level of renewable energy development in the electricity portfolios of power suppliers as determined by a state or other implementing entity. Electricity sellers could meet their obligation through direct ownership of renewable generation, contracts for power from renewable generating facilities, or purchase of credits for sufficient renewable electricity from another power supplier. The U.S. Department of Energy's proposed restructuring legislation [70] would establish a renewables portfolio standard which ensures that at least 5.5% of all electricity sales include generation from non-hydroelectric renewable energy sources by 2010 [71].

Because of the changing U.S. electricity marketplace, remote or distributed markets for renewable electricity, as noted in the individual technology discussions above, appear to be more promising today than centralized electricity markets [72]. Although central-station fossil and nuclear plants — which are, on average, 30 years old — supply 87% of the electricity used in the United States today, the Electric Power Research Institute expects that distributed markets will begin to emerge as early as 2000 [73]. Figure 5 indicates the large requirements for capacity replacement expected during the next 20 years [74]. Renewable energy electricity technologies will be competing with gas and diesel engines, gas turbines, microturbines, and fuel cells. Intermittent renewable electric systems (wind, photovoltaics, and solar thermal) should be helped by recent advances in battery and other storage technologies.

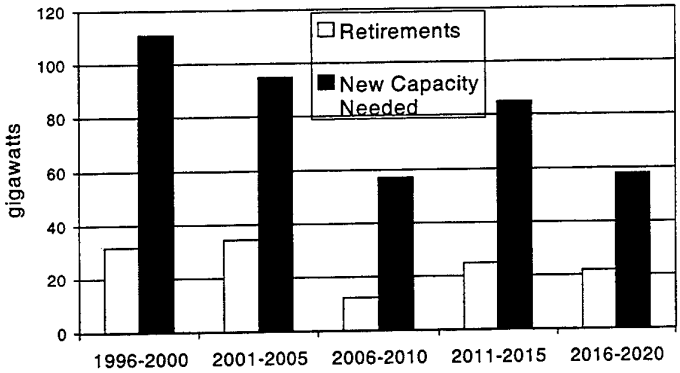

Fig. 4 New Electrical Capacity Presents Opportunities for Renewables

The electricity sector is not alone in its challenges; the transportation sector also faces major challenges in meeting the ever-growing demand for transportation goods and services while minimizing adverse energy security and environmental impacts. The total U.S. transportation sector remains over 97% dependent on petroleum fuels and consumes about two-thirds of the nation's oil demand. Reliable energy supplies are essential to national security and economic well-being, yet America now depends on other nations for 52% of its oil. According to DOE, that figure will likely rise to 70% in little more than 20 years [75]. Oil imports represent a major transfer of wealth — over $50 billion in 1998 [76] — from the United States to oil exporting countries. And while the world rests comfortably, with many energy forecasters predicting 50 years or more worth of petroleum left to find and produce, a recent article in *Scientific American* suggests that the end of cheap oil may come much sooner [77]. However, despite the predictions of rapidly rising oil prices in the next decade or two, today's petroleum prices (especially in the United States) have been the lowest in 20 years — presenting difficult challenges for bioethanol, biodiesel, hydrogen, renewable-powered fuel cells, and other alternative transportation fuels.

> "Our analysis of the discovery and production of oil fields around the world suggests that within the next decade, the supply of conventional oil will be unable to keep up with demand."
>
> *Scientific American, March 1998, p. 78*

Most renewable fuels, as well as biomass power, depend on various forms of biomass as feedstocks [78,79]. Therefore, the availability and price of biomass become key factors in the economic viability of both technologies. Agricultural, industrial, and municipal wastes are attractive near-term sources of biomass for these end uses; they have zero or low value today. But it will not take much market penetration of these new technologies to deplete economically attractive waste products. The longer-term solution is energy crops — plants such as fast-maturing species of trees and grasses that are grown on farms[80] to be harvested specifically for burning, gasifying, or fermenting into electricity or fuel. Although energy crops can bring many advantages to the American farmer and rural development, the emergence of farms growing energy crops will require some changes to the traditional policies affecting the American agricultural community.

Demand for energy in developing nations has been increasing more rapidly than in the industrialized nations for the past 20 years or more, and is projected to increase even more rapidly, especially in China, India, and other growing economies in Asia [81 - 84]. In addition, this century has seen the dawning of the independence of individual nations all over the world, including the former Union of Soviet Socialist Republics. Independent nations are looking to develop indigenous sources of energy and their own energy infrastructure, in contrast to fossil-fuel-based energy systems ultimately controlled by a very few nations [85]. Developing countries are also

looking to avoid the environmental problems created by conventional energy systems. In response, international lending institutions such as the World Bank have begun to target programs to environmentally friendly energy technologies such as renewables. All of these trends are quickly opening up strong international markets for renewables.

TOMORROW'S IMPACT OF RENEWABLE ENERGY ON THE WORLD

From the dawn of human civilization to about 100 years ago, the sources of energy used by mankind were predominantly human and animal muscle and wood, with lesser amounts of solar, wind, hydro, and geothermal. With the discovery of oil, the development of natural gas fields, and the widespread distribution of electricity from coal-powered central power plants, fossil fuels became the predominant sources of energy in the United States and the world. Is there another major transition ahead for energy? Can the renewable resources that sustained early civilization be harnessed with enough efficiency and availability and at a cost to meet a significant portion of the much higher energy needs of today's society?

Although there are always risks in predictions, the convergence of some of today's trends suggests interesting possibilities [86]. In summary, today's converging trends related to renewable energy include:

- Relevant scientific discoveries and engineering progress
- Emergence of a new economic structure in the electricity sector
- Trends towards decentralization and modularity
- Explosive advances in computers, information, and telecommunications
- Globalization of markets
- Persistent, pervasive support for a clean environment
- Limited future availability of inexpensive fossil fuels.

Do these converging trends mean that we are on the brink of a new energy transition from fossil fuels to renewables? Several independent entities have recently developed scenarios indicating that renewable energy will play a major role in the energy mix for the world, with increasing impacts beginning as early as 2000–2010 and major impacts by 2050 [87 - 92]. In both of the Shell International scenarios, energy contributions from conventional energy resources begin to level off in 20–30 years, with petroleum consumption actually decreasing [93]. (see Figure 6). According to these scenarios, the increases in world energy demand will be supplied by renewable energy technologies, which will provide 30%–50% of world energy by 2050.

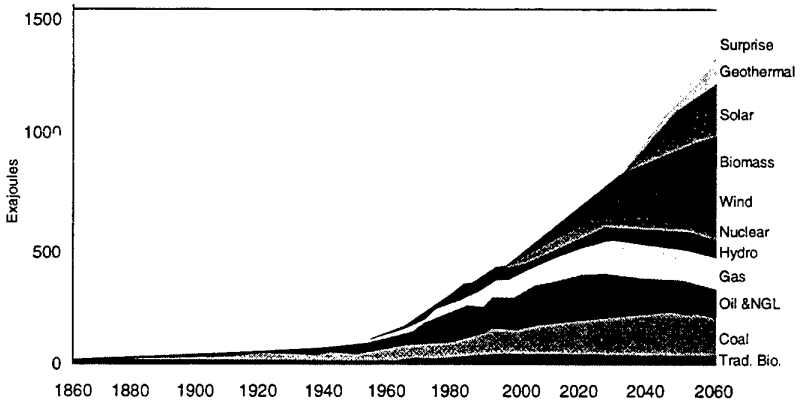

Fig. 5 Shell Sustained Growth Scenario

Although these scenarios are important, and should be studied and debated, it may be even more significant that four international companies have recently made major investments in renewables. In October 1997, the Royal Dutch/Shell Group created Shell International Renewables with a $500 million investment, focusing on solar, biomass, and forestry [94]. In January 1998, British Petroleum (BP), through its BP Solar subsidiary, opened a 10–15 megawatt photovoltaics facility (its sixth in the world) in California [95]. Enron Corporation, one of the world's largest natural gas companies, entered into a joint venture with Amoco Corporation in 1995 to form the

largest U.S.-owned producer of PV cells and the second largest in the world. Enron then acquired the largest U.S. wind energy company in 1997 and formed a new business unit, Enron Renewable Energy Corporation [96]. Most recently, Amoco and British Petroleum announced a merger. And Bechtel, the international engineering and project development giant, recently formed a joint venture with another U.S. firm to develop small, renewable energy systems including solar, wind, and hybrids.

Leaving aside the controversial question of *when* we might transition to an energy mix with significant proportions of renewable energy, but accepting the inevitability of the transition, what could be the impact on American and global society [97,98]? Although the topic is worthy of many pages of discussion, we will focus here on four areas relating most closely to the direct impact on human beings:

- U.S. rural economy
- Community planning and lifestyles
- International socioeconomic equity
- Environment

U.S. Rural Economy

The rural economy in the United States continues in a state of change and uncertainty. The typical modern farm concentrates on the production of one or two major commercial products such as corn, soybeans, milk, or beef; the net income is vulnerable to fluctuations in market demand, the weather, and other factors. The addition of crops grown specifically for energy — such as poplar trees or native switchgrass — will expand the horizons of the American farmer, providing flexibility with a greater diversity of crops to improve the economic potential and stability of the farm. Because it is most economical to build the power plant or fuel facility near the source of biomass, the energy facilities themselves will add non-farm jobs in rural areas. These businesses will bring other businesses, encouraging rural development and redirecting money spent on oil imports into local economies [99].

Community Planning and Lifestyles

Rural communities are only one type of community that will be radically affected by the advent of significant renewable energy usage. Urban and suburban communities are likely to be affected by two major changes: the restructuring of the electric industry and changes in the way people move about. The restructuring of the electric industry means that people will have much more choice than in the past about how they provide electricity, heating, and cooling for their homes. Consumers will be able to generate electricity on their own property and buildings using wind, photovoltaic, or micro-fuel-cell technology, or purchase electricity from a local network of small, interconnected generators. Local businesses will be able to use microturbine, fuel cell, or gasifier technologies. Heating and cooling options will increase as geothermal heat pumps and preheating solar collectors become commonplace among major builders. Energy requirements will decrease as the majority of builders respond to consumer awareness of energy's financial and other costs and incorporate widespread whole-building approaches to reduce energy requirements. Meanwhile, computers and information technology will allow customers to pay the lowest possible prices for electricity as suppliers institute real-time pricing. The convergence of advances in information technology, energy-efficient building equipment, and renewable energy technologies will result in "smart" buildings with sophisticated control systems that will optimize the use of energy while providing telecommunications, information services, and entertainment.

New generations of vehicles will increase fuel economy to three or four times today's levels — and dramatically lower or eliminate air pollution emissions — by taking advantage of lighter materials; new fuels; advances in gas turbines, fuel cells, and flywheels; and sophisticated computer technology for integration and control. Information and telecommunications technology will help reduce the miles traveled per day by controlling and directing traffic to avoid congestion, allowing people to work and shop from home, decreasing business travel, and suggesting the most efficient route and transportation mode for people when they do travel.

International Socioeconomic Equity

Changes in communities and lifestyles arising from widespread use of renewable energy will be even more profound in the developing world. Two billion people today are without access to electricity and efficient cooking fuels, contributing to a lack of medical services, lack of education, hunger, thirst, and environmental

degradation. Women suffer more from the current energy system than men [100]. Women and children spend long hours in energy-related activities — cooking, collecting fuelwood, carrying water, processing food — and expend more energy in work than men. Home by home and village by village, renewable energy technologies such as wind turbines, photovoltaic panels, and modular biomass gasifiers, will bring the benefits of electricity to disadvantaged people. The small, modular nature of these systems will also open up opportunities for individual entrepreneurs — including women — to manufacture, sell, and service the renewable energy systems, giving them valuable experience in business and economics. Lastly, by choosing renewable energy systems rather than centralized fossil-fuel systems, developing nations have the opportunity to avoid the environmental problems and costs that have plagued the industrialized world and take advantage of the window of economic opportunity as these technologies begin to expand rapidly throughout the world.

Environment

Energy production and use already does more environmental damage in the world than any other economic activity. Although the United States has made substantial progress in improving the environment since the mid-1970s, power plants are still responsible for 72% of all sulfur dioxide emissions and 33% of all nitrogen oxide emissions [101]. The public health implications of energy-related pollution present a serious challenge; recent studies link health problems with particulate matter, sulfur dioxide, nitrogen oxides, ozone, and carbon monoxide [102]. And, with respect to global warming, the burning of fossil fuels contributes three-fourths of the carbon dioxide emissions in the United States today. Meeting the rapidly growing demand for energy, while also maintaining a clean global environment, requires clean energy to power the economy. Higher oil prices and environmental and security concerns will eventually prompt the transition from oil-based fuels to renewables-based fuels and fuel cells. Restructuring, international markets, continuing technical advances, and public opinion will increase the use of renewable electric technologies, replacing coal-based, nuclear, and perhaps natural gas power plants. The advent of the substantial use of renewable energy will finally herald a time when energy production and use will no longer be so harmful to the environment.

CONCLUSIONS

Within the broad variety of technologies that constitute renewable energy, some are already making large inroads in the marketplace. Other technologies, perhaps those most beneficial to a sustainable future, are further from commercialization. Most, however, are progressing more quickly than ever; there are no technical stumbling blocks for renewable energy. Renewable energy *will* be a major force in America's future — the only question is when. The answer will depend only on the will of the American people for a clean environment and sustainable economy — or the next major political disruption in the Middle East.

REFERENCES

1. *Annual Energy Outlook 1999.* Department of Energy, DOE/EIA-0383(99), December 1998. Tables A1 and A2. Also see the *Renewable Energy Annual 1998,* DOE/EIA-0603(98), Dec. 98. Both are available through http://www.eia.doe.gov/
2. Web site http://solstice/crest.org/renewable/ has references and linkds to various trade associations for renenwable energy. Also see the *World Directory of Renewable Energy Suppliers and Services 1997*, James and James, ISBN 1-873936-68-0.
3. Annual Energy Review 1998. Department of Energy, DOE/EIA, July 1999. Table 10.1. http://www.eia.doe.gov/
4. Web site http://www.eren.doe.gov/repis
5. Web site http://www.nrel.gov/debate/issues.html
6. *Dollars from Sense – The Economic Benefits of Renewable Energy.* Department of Energy DOE/GO-10097-261, DE96000543, September 1997.
7. H. Chum, "Two Decades of Progress in Research, Development, and Commercialization of Renewable Energy," *The Enduring Nuclear Fuel Cycle*, edited by C. E. Walter, American Nuclear Society Winter Meeting, November 18, 1997.
8. *Climate Change 1995: Impacts, Adaptatiohs, and Mitigation of Climate Change.* Intergovernmental Panel on Climate Change, Cambridge University Press, Camridge, UK, 1996.
9. *Technology Opportunities to Reduce U.S. Greenhouse Gas Emissions.* National Laboratory Directors, October 1997, pp. 2-36, http://www.ornl.gov/climate_change

10. *Renewing Our Energy Future.* U.S. Congress, Office of Technology Assessment, OTA-ETI-614, September 1995.
11. *Energy Technologies for the 21st Century.* International Energy Agency, OECD/OCDE, Paris 1997. Pp. 177-207
12. F. Sissine, *Renewable Energy: Key to Sustainable Energy Supply*, Congressional Research Service Issue Brief for Congress #97031, September 26, 1997. http://www.cnie.org/nle/eng-29.html
13. A.K.N. Reddy, R.H. William,s and T.B. Johansson, *Energy After Rio: Prospects and Challenges*, United Nations Development Programme, New York, NY, 1997.
14. T.B. Johansson et al, *Renewable Energy: Sources for Fuels and Electricity*, Island Press, Washington, DC, 1996.
15. *Renewable Energy Technology Characterizations*, Electric Power Research Institute and Department of Energy, EPRI TR-109496, December 1997.
16. *Technology Opportunities to Reduce U.S. Greenhouse Gas Emissions Appendix B.* National Laboratory Directors, October 1997, http:www/ornl.gov/climate_change
17. *Federal Energy Research and Development for the Challenges of the Twenty*-First Century. President's Committee of Advisors on Science and Technology, November 5, 1997. http://www.whitehouse.gov/WH/EOP/OSTP/Energy/
18. N. Lenssen and C. Flavin, "Sustainable energy for tomorrow's world," *Energy Policy*, Vol. 24, No. 9, pp. 769-781, 1996. Elsevier Science Ltd, Great Britain.
19. A.A.M. Sayigh, Editor, *Proceedings of the World Renewable Energy Congress IV*, June 15-21, 1996. Pergamon, UK.
20. *Photovoltaic Energy Program Overview: Fiscal Year 1997*, Department of Energy, DOE/GO-10098-539, February 1998.
21. Photovoltaics: The Power of Choice: The National Photovoltaics Program Plan for 1996-2000, Department of Energy, DOE/GO-10096-017, DE95000214, January 1996.
22. Web site http://www.eren.doe.gov/pv
23. A. Barnett, "Solar Electric Power for a Better Tomorrow," *Proceedings of the 25th IEEE Photovoltaic Specialists Conference*, May 13-16, 1996, Washington, DC, pp 1-8.
24. J. Johnson, "The New World of Solar Energy," *Chemical and Engineering News*, March 30, 1998, pp. 24-28.
25. *PV News*, Vol. 18, No. 2, February, 1999.
26. T. Coutts and M. Fitzgerald, "Thermophotovoltaics: the potential for power," *Physics World*, August 1998, pp 49-52
27. T. Coutts and M. Fitsgerald, "Thermophotovoltaics," *Scientific Am*erican, September 1998, pp. 90-95.
28. D.C. Quarton, "The Evolution of Wind Turbine Design Analysis – A Twenty-Year Progresws Review," *Wind Energy*, Vol 1, pp. 5-24, 1998. John Wiley & Sons, Ltd.
29. *Wind Power Today: 1997 Wind Energy Program Highlights,* Department of Energy, DOE/GO-10098-550, April 1998.
30. Web site http://www.eren.doe.gov/wind
31. American Wind Energy Association press releases, January 30, 1998; http://www.igc.apc.org/awea/news/
32. H. Wasserman, "Inherit the Wind," *The Nat*ion, May 29-June 4, 1997.
33. See reference 1, Table A17.
34. *DOE Biomass Power Program Strategic Plan 1996-2015*, Department of Energy, DOE/GO-10096-345, DE97000081, December 1996.
35. Web site http://www.eren.doe.gov/biopower
36. *Strategic Plan for the Geothermal Energy Program*, Department of Energy, DOE/GO-10098-572, June 1998.
37. Web site http://www.eren.doe.gov/geothermal
38. *Geothermal Technologies Today and Tomorrow*, Department of Energy, March 1998
39. L. Lamarre, "Heating and Cooling," *EPRI Journal*, May/June 1998, pp. 24-31.
40. Concentrating Solar Power: Paths to the Future: Five-Year Program Plan 1998-2003, Department of Energy, April 1998.
41. Web sites http://www.ere.doe.gov/ste/ and http://www.energylan.sandia.gov/sunlab/documents/progov.htm

42. Solar Buildings Technology Program 5-Year Strategic Plan Draft, Department of Energy, January 31, 1998.
43. Solar Buildings: Overview: The Solar Buildings Program, Department of Energy, DOE/GO-10098-552, April 1998.
44. Web site http://www.eren.doe.gov/solarbuildings
45. M. M. Hamilton, "Pumping Up the Ethanol Option," *Washington Post*, May 6, 1998, page C-1
46. M. Zhang, C. Eddy, K. Deanda, M. Finkelstein, and S. Picataggio, "Metabolic Engineering of a Pentose Metabolism Pathway in Ethanologenic Zymomonas Mobilis," *Science*, 13 January 1995, Volume 267, pp. 240-243, American Association for the Advancement of Science.
47. Office of Transportation Technologies Strategic Plan, Department of Energy, October 1996.
48. J. D. McMillan, "Bioethanol Production: Status and Prospects," *Renewable Energy,* Vol. 10, No. 2/3, pp. 295-302, 1997. Elsevier Science Ltd, Great Britain.
49. *Strategic Plan for DOE Hydrogen Program*, Department of Energy, DOE/GO-10098-532, January 1998.
50. See reference 18, pp. 777-779
51. J. M. Ogden and R. H. Williams, *Solar Hydrogen: Moving Beyond Fossil Fuels*, World Resources Institute, Washington, DC,1989.
52. O. Khaselev and J. A. Turner, "A Monolithic Photovoltaic-Photoelectrochemical Device for Hydrogen Production via Water Splitting," *Science*, Vol. 280, 17 April 1998, p. 382 and pp. 425-428.
53. J. Winters, "Nanotanks," Discover, January 1998, p.
54. T. Moore, "Emerging Markets for Distributed Resources," *EPRI Journal,* March/April 1998, pp. 9-17.
55. Fuel Cell Handbook, DOE, 1993, Federal Energy Technology Center, Morgantown
56. S. Voien, "Pricing in Competitive Markets," *EPRI Journal,* Nov/Dec 1997, pp. 6-13.
57. See reference 1, Table A17; also private communications, National Renewable Energy Laboratory
58. See reference 11 pp. 190, 199; also private communications, National Renewable Energy Laboratory
59. B. Farhar, "Energy and the Environment: The Public View," Renewable Energy Policy Project Research Report, October 1996, No. 3; http://www.repp.org
60. S. Dunn, "Power of Choice," *World Watch,* September/October 1997, pp. 30-35
61. T. Peterson, *Green Pricing: Experience and Technology Options Assessment*, Electric Power Research Institute, EPRI TR-109204, March 1998.
62. L. Lamarre, "Utility Customers Go for the Green," EPRI Journal, March/April 1997, pp. 6-15.
63. E. A. Holt, "Green Power for Business: Good News from Traverse City," Renewable Energy Policy Project Research Report, July 1997, No. 1; http://www.repp.org
64. D.M. Katz, "Solar Technology Ripe for Loss Control: Experts," *National Underwriter Property & Casualty-Risk & Benefits Management*, August 10, 1998, p. 3
65. See reference 12.
66. "Competition in the Electric Power Industry," Edison Electric Institute, http://www.eei.org/Industry/structure/7competi.htm
67. Web site http://www.eren.doe.gov/electric
68. *New Policies Jump-Start Solar Markets,* Department of Energy, DOE/GO-10098-520, March 1998.
69. J. Fang, *Power Marketing and Renewable Energy*, NREL Topical Issues Brief 9701, DE97000244, NREL/SP-460-22080, September 1997
70. Web site http://www.hr.doe.gov/electric/
71. Web site http://www.ucusa.org/energy/rps.html
72. C. J. Weinberg, "Renewable Energy Policy: How Will Clean Energy Services Be Provided in the Future?" *Renewable Energy,* Vol. No. 2/3, pp. 423-431, 1997. Elsevier Science Ltd, Great Britain.
73. See Reference 53.
74. See Reference 1, Figure 56 and Table A9.
75. See Reference 1, Table A11.
76. See Reference 3
77. C. Campbell and J. Laherrere, "The End of Cheap Oil," *Scientific American,* Vol. 278, No. 13, pp. 78-83, March 1998.
78. R.P. Overend and E. Chornet, Editors, Making a Business from Biomass in Energy, Envrionment, Chemicals, Fibers, and Materials, Elsevier Science Ltd., 1997
79. R. P. Overend, C. M. Kinoshita, and M.J. Antal, Jr., "Bioenergy in Transition," *Journal of Energy Engineering*, 1996, pp. 78-92

80. Web site http://www.esd.ornl.gov/bfdp/
81. See References 11 and 13.
82. G. Williams and C. Bloyd, "Institutional Solutions for Renewable Energy," *Renewable Energy,* Vol. No. 2/3, pp. 309-314, 1997. Elsevier Science Ltd, Great Britain.
83. J. Sheffield, "The Role of Energy Efficiency and Renewable Energies in the Future World Energy Market," *Renewable Energy,* Vol. No. 2/3, pp. 315-318, 1997. Elsevier Science Ltd, Great Britain.
84. *International Energy Outlook 1997*, Department of Energy, DOE/EIA-0484(97), April 1997, Table 1.
85. K. Kozloff, "Electricity Sector Reform in Developing Countries: Implications for Renewable Energy," Renewable Energy Policy Project Research Report, April 1998, No. 2; http://www.repp.org
86. See Reference 18.
87. Renewable Energy Resources: Opportunities and Constraints 1990-2020, World Energy Council, 1993, London.
88. *Energy for Tomorrow's World,* World Energy Council, 1993, St. Martin's Press, New York.
89. Energy for our common world: what will the future ask of us? Conclusions and Recommendations, World Energy Council, 1995, London.
90. *Energy and Transportation Task Force Report*, The President's Council on Sustainable Development, 1996. http://www.whitehouse.gov/PCSD
91. *Energy Innovations: A Prosperous Path to a Clean Environment*, Alliance to Save Energy, American Council for an Energy-Efficient Economy, Natural resources Defense Council, Tellus Institute, and Union of Concerned Scientists. June 1997, Washington, DC. http://www.ase.org/
92. J. F. Coates, JB. Mahaffie, A. Hines. *2025: Scenarios of U.S. and Global Society Reshaped By Science and* Technology, Oakhill Press, Greensboro, North Carolina, February 1997.
93. *The Evolution of the World's Energy Systems*, Shell International Ltd, 1996, Group External Affairs, SIL, Shell Centre, London, SE1 7NA, United Kingdom.
94. *Connecting You to the Sun*, Shell International Ltd.; http://www.shell.com/h/renew/text/text.htm
95. Web sites http://www.bp.com/bpfinance/Rep_acc/report/main5/main4.html and http://www.bp.com/bpsolar/index.html
96. Web site http://www.enron.com/corppro/index.html
97. *Boosting Prosperity: Reducing the Threat of Global Climate Change Through Sustainable Energy Investments*, Energy Foundation, 1996. http://www.ef.org/reports/index.html
98. J.M. Kramer and C. D. Johnson, "Sustainable Development and Social Development: Necessary Partners for the Future," Journal of Sociology and Social Welfare, Volume 23, Number 1, 996, pp. 75-91
99. T*he American Farm: Harnessing the Sun to Fuel the World*, Department of Energy, NREL/SP-420-5877, DE94000217, March 1994.
100. See Reference 13.
101. I. Mintzer, A. Miller, and A. Serchuk, "The Environmental Imperative: A Driving Force in the Development and Deployment of Renewable Energy Technologies, Renewable Energy Policy Project Issue Brief, April 1996, No. 1; http://www.repp.org/
102. D.W. Dockery, et. Al, "An Associateion between Air Pollution and Mortality in Six U.S. Cities," *New England Journal of Medicine,* 1993, Vol. 326, pp. 862-866

LENGTH SCALES AND INNOVATIVE USE OF NONEQUILIBRIA IN COMBUSTION IN POROUS MEDIA

Massoud Kaviany and **Amir A. M. Oliveira**
Department of Mechanical Engineering and Applied Mechanics
The University of Michigan
Ann Arbor, MI 48109-2125
Email: kaviany@umich.edu; amirol@engin.umich.edu; Fax: (734)647-3170

Keywords: porous media, combustion, heat transfer

ABSTRACT. Combustion in porous media takes advantage of a large range of geometric and phenomenological length scales. These have allowed for the design of new combustion processes and systems, such as, catalytic reactors and converters, porous radiant burners, direct energy and gas conversion devices and systems, chemical sensors, and material synthesis processes. The improvement of the current and the design of yet newer and more innovative systems require further investigations into the gas-phase and surface chemistry, solid-state and condensed-phase physics, transport in disordered structures, and mathematical and numerical methods. This will allow for the development of a new generation of materials, devices, equipments and synthesis processes. Here, we summarize some new and innovative uses of porous media in combustion, the current understanding and modeling of these processes, and the modeling techniques that may allow for further improvements and development.

1. INTRODUCTION

The applications of porous media in combustion take advantage of the range of pore sizes, porosities, pore connectivity, and specific interfacial areas between phases which create the possibility of large thermal, chemical, and mechanical nonequilibria among and within phases. These nonequilibria processes increase the local reaction rates, redistribute heat and reactants over a larger section of the medium and allow for energy storage and recirculation. Nonequilibria may also be a result of intrinsic characteristics of the system, for example, nonuniform distribution of reactants, noncontinuos solid phase, large mismatch between the thermal properties of the fluid and solid phases, fast transient processes, strong reaction rates and strong variations in the inlet and outlet conditions. The geometric complexity and the existence of nonequilibria among and within phases allow for these many advantages in using a porous media in combustion systems, but also pose special challenges for the modeling of these processes.

Geometrically, a porous medium is composed of a solid phase and one or more fluid phases. The solid may have a periodic or random structure and each phase can be continuous or dispersed. Figure 1 presents a rendering of a porous medium composed of a continuous gas phase and a dispersed solid phase. The porous medium is represented with a single or multiple length scales. The single length scale is used for the unit-cells (periodic) or representative elementary volume (random) with nonporous solids. Two or more length scales are used when these solids are in turn porous (this is called the double or triple porosity), as shown in Fig. 1. These porous solids may also be nonuniform at the length scales of interest (this is sometimes called heterogeneity). The different length scales can differ by orders of magnitude (i.e., they are separated) or they can vary almost continuously in order of magnitude (i.e., they are nonseparated). The phases may be permanently continuous or may change with the reaction and a percolation threshold may be reached in which the transport of heat or mass along a phase is interrupted.

Chemically, the porous medium may be either inert or it may participate directly in the reactions as a catalytic surface or a source of fuel. Figure 1 also represents the different heat transfer (convection heat transfer $\mathbf{q}_u$, surface-convection heat transfer $\mathbf{q}_{ku}$, conduction heat transfer $\mathbf{q}_k$, radiation heat transfer $\mathbf{q}_r$) and mass transfer (reactants mass transfer $\dot{\mathbf{m}}_R$, products mass transfer $\dot{\mathbf{m}}_P$) vectors and energy and mass conversion and storage (energy conversion S, mass conversion $\dot{n}$) that are used to describe the transport and reaction during combustion in porous media. Figure 2 shows the different thermophysical and thermochemical processes of interest. These physical and chemical processes have phenomenological

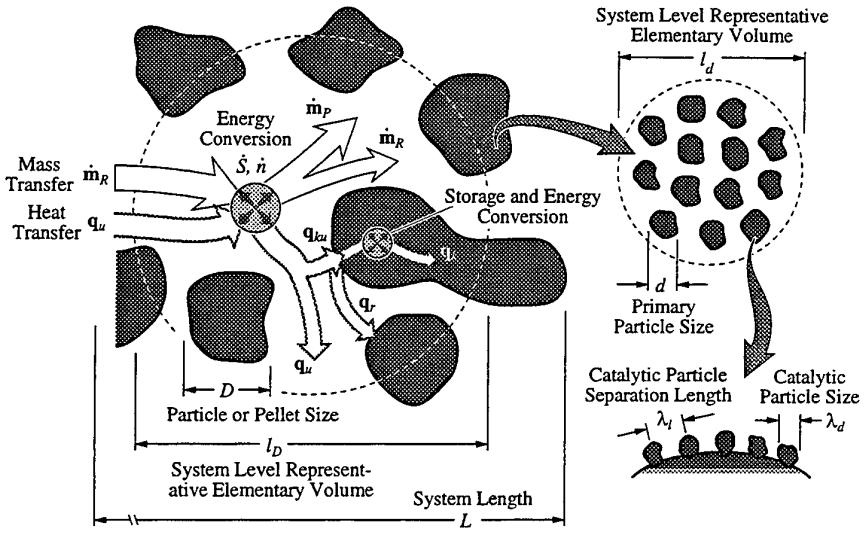

Fig. 1. Rendering of a porous media composed of a continuous gas phase and a dispersed solid phase showing the different length scales and the heat and mass transfer processes that may take place in the gas and solid phases.

length and time scales, such as flame thickness, penetration depth, residency time, etc. The phenomenological length scales can be of the same order of magnitude or much different from the geometric length scales. The interaction among the different phenomenological length and time scales and the geometric scales, results in different transport and reaction regimes and leads to thermal and chemical nonequilibria.

Figure 3 shows different examples of pore-level and system-level chemical nonequilibrium. They are classified accordingly to the distribution and to the physical process controlling the mixing of reactants. Fig. 3(a) is characteristic of the combustion of premixed gas mixtures inside a porous medium, as in the porous radiant burners [1-7,9], catalytic converters [10-13,20] and combustors [14-19,21-24], and energy regeneration devices [30-33,35-37,49]. Note that the solid phase may be either chemically inert or catalytic and both homogeneous and heterogeneous reactions may take place. The flow of reactants and products may be either pressure or diffusion driven. Only the last scale with a nonporous solid phase is

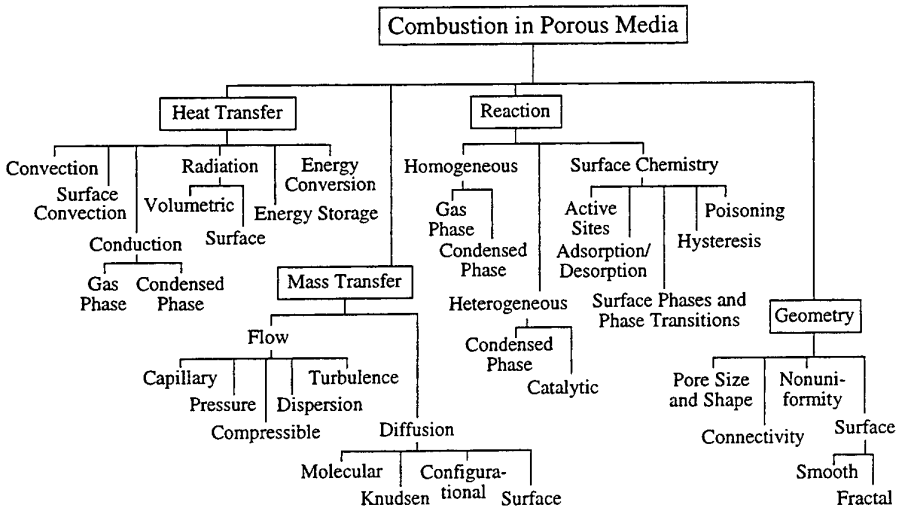

Fig. 2. Thermophysical and thermochemical processes and geometric characteristics of importance in the modeling of combustion in porous media.

(a) Homogeneous and Heterogeneous Reaction with Premixed Oxidant and Fuel Supply

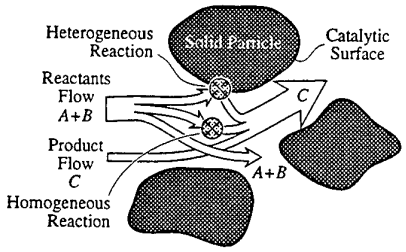

(b) Homogeneous Reaction with Continuous Oxidant and Distributed Fuel Supply

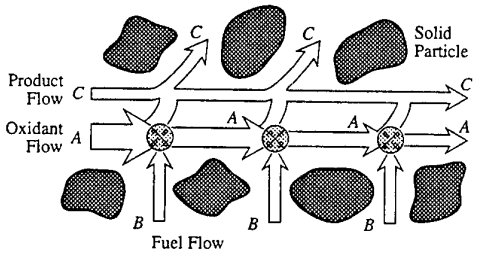

(c) Homogeneous Reaction with Transport Controlled Fuel Supply

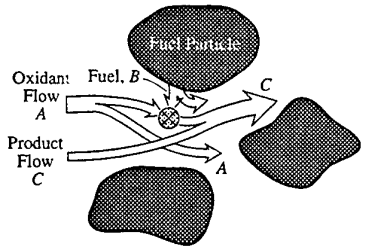

(d) Homogeneous Reaction with Transport Controlled Oxidant and Fuel Supply

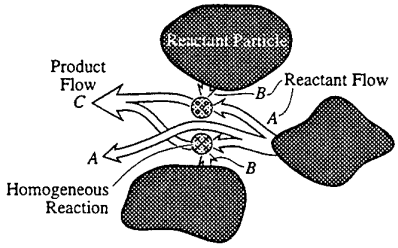

(e) Homogeneous and Heterogeneous Reaction with Transport Controlled Oxidant Supply or Product Removal

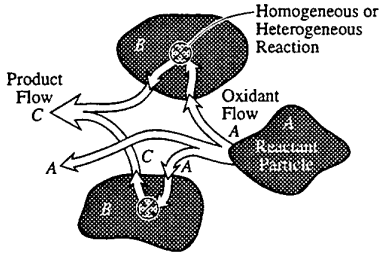

Fig. 3. Distribution and transport of reactants in chemical nonequilibrium processes.

represented. In Fig. 3(b) a porous burner for which the fuel supply is noncontinuos is depicted. This is useful in controlling the amount of heat generated per unit volume (or area) of the porous burner either to satisfy the demand for heat (the heat is radiated out from the burner surface) [40] or to control the maximum temperature in the burner [41]. The flow of reactants is pressure driven and good mixing is usually assumed. Figure 3(c) presents the case in which the fuel is provided from the pyrolysis of the solid, as in solid combustion or smoldering [45-49] and particulate trapp regeneration [41-43], or from evaporation of liquid in the form of droplets [41-43]. In this case, the rate of pyrolysis or evaporation may control the reaction. The reaction could also occur inside the solid phase (not depicted) and controlled by the transport of oxidizer or products. Figure 3(d) shows an example in which both the reactants come from the solid particles, with the reaction occurring in the gas phase. This is the case of some gas-solid and condensed-phase combustion synthesis [57, 58]. The reactants mixing may be controlled by the rates of generation or mass transfer. The product in the liquid or gas phase can then nucleate and crystallize as a solid product. Finally, Fig. 3(e) shows the reaction occurring inside one of the reactant particles, as in gasless combustion synthesis [53-55,59,60]. The reactants mixing is controlled by the transport in the pore space (by diffusion or capillarity) and within the reactant B particle (by diffusion). The product may be in the solid phase, growing around the reactant B particle, or in the liquid phase, later nucleating and growing as a solid phase. These mixing effects depicted in Fig. 3(a) to

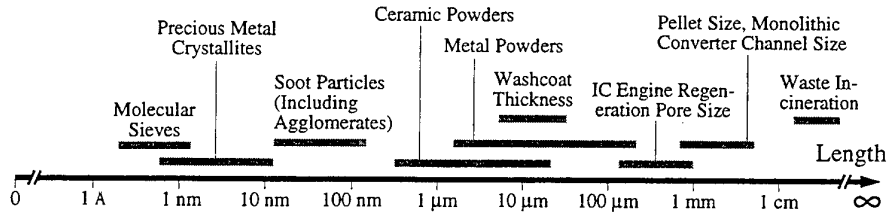

Fig.4. Length scales and characteristic dimensions for various systems.

(e) can be manipulated to some extent. For example, the control of the distribution of fuel in a porous burner, leads to distributed heating, and the maximization of reactant mixing in combustion synthesis by controlling the particle size and particle size distribution, leads to higher conversion rates. To better control the geometry of the medium and the processes occurring there, a fundamental understanding of the interaction among the various processes shown in Figure 2 is needed. The use of continuum (or volume-averaged, or homogeneous) models is common.

The derivation of volume-averaged conservation equations is available elsewhere [62-70]. Two- (and three-) medium treatments are used to model the thermal nonequilibrium among phases, for a given scale. For example, for a system composed of a fluid phase β and a solid (or porous) phase σ, two intrinsic volume-averaged equations are needed. The intrinsic phase-average of a scalar or vector quantity ϕ_β is defined as the volume average of that quantity for phase β over the volume V_β occupied by phase β inside an elementary representative volume, $V = V_\beta + V_\sigma$. The thermal energy equation for phase β may assume that it is transparent to thermal radiation (e.g., a transparent gas) and the volumetric energy generation assumes the presence of interphase heat transfer, homogeneous and heterogeneous (at the $\beta\sigma$ interface) chemical reaction. Usually, it is assumed that the chemical species absorbed at the $\beta\sigma$ interface and participating in the heterogeneous reactions are in thermal equilibrium with the σ phase. This may not be valid for fast transient processes. The modeling of the mass transport, requires a conservation equation for each chemical species i and a conservation of mass equation for each phase. Multicomponent diffusion is assumed and usually modeled with an extended form of Fick's equation. Phase σ may also be porous, having a fluid phase γ and a solid phase ψ. Interfacial mass fluxes then occur across the various areas available for flow (micro channels) and heterogeneous reactions may occur at the exposed solid surfaces. The surface reaction rate assumes the existence of N_r chemical reactions between N_c chemical species. These reactions occur at crystallites which may be nonuniformly distributed on the surface of the solid particles. Finally, the catalytic sites on the crystallites may also vary in activity. For example, the activity of noble metal crystallites depends on lattice orientation, presence of neighboring sites, interaction with the substrate, poisoning, etc. These form the last geometric length scales of interest here. Figure 4 shows a summary of these length scales and characteristic dimensions for various systems.

From the modeling perspective, volume-averaged equations are strictly valid when the length scales are sufficiently distinct. The use of volume-averaged equations assume length scale separation. Referring to Fig. 1, the requirements for length scale separation can be summarized as

$$L \gg l_D,\ D \gg l_d,\ d \gg \lambda_l \tag{1}$$

The first requirement is readily met. The second may not be met (e.g., in catalytic converters coated with thin washcoat layers formed by coarse agglomerates of alumina particles). When there is no distinction among the scales, detailed simulation is necessary and either network models or direct simulations are used. The treatment of nonuniformity is made using statistical methods, which ensemble average the effects before passing this information to the equations for the next length scale. The results of the detailed simulation for a scale, are incorporated into the volume-averaged model used for the subsequent (higher level) scale.

2. THERMAL NONEQUILIBRIUM

Intraphase thermal nonequilibrium results in heat transfer by conduction and radiation (volumetric and surface). Interphase thermal nonequilibrium results in heat transfer between phases. These processes when coupled are responsible for thermal regeneration and superadiabatic combustion. In the following, we review these processes and the radiant porous burners.

Superadiabatic Combustion

Combustion of a gas mixture in the presence of a chemically inert porous medium differs from combustion in a plain medium (i.e., gas phase only) because the thermal properties of the solid and gas phases are vastly different. The thermal conductivity of the solid phase and, as a result, the effective thermal conductivity of the medium, can be several orders of magnitude larger than that of the gas phase. Then, there is an enhanced conduction heat transfer along the solid phase, compared to the gas phase, and surface radiation exchange between particles. The large interfacial surface area between the gas and the solid results in a small resistance for surface-convection heat transfer, i.e., a large local (or pore) value for the number of transfer unit NTU. Thus, the heat generated by combustion is readily transferred to the solid phase and locally the surface of the solid phase reaches a temperature close to the gas phase temperature. As a result, for media which are not optically thick [5, 9, 76], there is surface radiation heat transfer along the flame. The combined effects of conduction, radiation and surface convection, cause a substantial preheating of the gas phase. This preheating adds to the energy released by combustion resulting in local temperatures in excess of the adiabatic flame temperature for the gas mixture. This is called superadiabatic combustion and has been applied to increase the burning rates of gas mixtures [2, 4, 9, 81] and condensed fuels [82], to allow for the combustion of low calorific fuels [4, 34], to recuperate energy from reaction processes [35], and to create large thermal gradients in the solid phase [36, 37, 40].

The superadiabatic effect is observed for both propagating [81, 82] and stabilized flames [4, 34, 81]. In a propagating flame, the superadiabatic effect occurs as a result of the overlap of the thermal and the combustion waves [50, 81, 82]. The velocity of propagation of a thermal pulse, when there is a gas flow with velocity $\langle u_g \rangle$ through the porous media (i.e., the thermal wave speed), is given by

$$u_T = \langle u_g \rangle \frac{\rho_g c_{p,g}}{\langle \rho c_p \rangle}, \tag{2}$$

where $\langle \rho c_p \rangle$ is the volumetric heat capacity of the porous medium (solid phase).

When there is also a combustion wave traveling at the speed u_F, the maximum excess temperature at the combustion wave, assuming an adiabatic medium and a complete combustion of the fuel, is given by [81]

$$\Delta T_{ex} \equiv T_{ex} - T_n = \Delta T_{ad} \frac{1}{1 - u_F/u_T}, \tag{3}$$

where the adiabatic temperature increase is given by

$$\Delta T_{ad} \equiv T_{ad} - T_n = \frac{\rho_F \Delta h_{r,F}}{\rho_g c_{p,g}}. \tag{4}$$

For stable propagation, $u_T > u_F$ is required. Note that when $u_F \to u_T$, i.e., there is a superposition of the two waves, the excess temperature may be very large, even for mixtures with a small heat of reaction $\Delta h_{r,F}$ or for diluted mixtures (small ρ_F). For example, a maximum temperature 2.8 times the adiabatic temperature for an air-methane mixture with air/fuel ratio $(A/F)_a = 62$ (stoichiometric ratio $\phi = (A/F)_s/(A/F)_a = 0.28$) has been observed [81]. Note that the flamability limits for methane-air mixtures (1 atm, 300 K) is $9 < (A/F)_a < 27$ ($0.6 < \phi < 1.9$) [112]. By adjusting the gas flow rate $\langle u_g \rangle$, stable propagation can be achieved over a large range of air/fuel ratios, $11 < (A/F)_a < 60$ ($0.28 < \phi < 1.6$).

The heat recirculation also results in the stabilization of the flame in the interior of the porous medium and reduces the susceptibility to extinguishment caused by flow rate fluctuations. There is a range of gas velocity for which the flame is stationary. Reciprocaing flow has also been used to create and hold high thermal gradients inside a porous medium at superadiabatic temperatures [4]. This has been used to burn extremely lean mixtures, either in porous burners as well as in combustion engines [34], in converting methane to hydrogen (autothermic reforming) [38] and in direct energy conversion [37]. In these systems, the flame is stabilized in the interior of the medium by periodically reversing the flow. The fuel can be premixed with the oxidizer or direct fuel injection can be used. For example, a direct energy conversion method [37] uses a combustion tube with reciprocating flow and direct fuel injection to create and stabilize a thermal gradient in the solid phase with maximum temperature above the adiabatic flame temperature for the mixture. This gradient is used to power a thermoelectric cell (Peltier effect) and produce electrical energy. Figure 5 shows a rendering of the combustion tube. The central part of the tube (combustor) is made of an inert material (alumina) and the ends are made of a high temperature resistant thermoelectric material (e.g., a Si-Ge alloy). Positioning of the fuel injection allows for better control of the flame position. Due to the relatively high thermal conductivity of the combustion section, the the exact position of the flame is not critical. Conduction along the thermoelectric section upstream the flame allows for heat recirculation (resulting in superadiabatic effect). However, this also increases the axial heat losses and the conduction heat loss from the hot junction to the cold junction, which reduces the thermoelectric efficiency of the cell. Increasing the length of the thermoelectric section, increases the preheating which leads to higher temperatures and higher thermal efficiency. But, the electrical resistance also increases resulting in higher Joule heating which leads to smaller thermoelectric efficiency. Therefore, an optimization of the length of the thermoelectric section to maximize the overall conversion efficiency is possible. For a cylindrical tube 1 mm in diameter, an overall conversion efficiency of 10% has been calculated. By decreasing the thermal conductivity of the thermoelectric material by 70% while keeping the electrical conductivity constant, efficiencies as high as 25% could be achieved. These would make this process competitive when compared to other high efficiency, direct electrical power generation methods.

For porous burners in general, increasing the specific heat of the medium increases the temperature gradient. The same effect is achieved when burning richer mixtures. The superadiabatic effect is increased for large radiation extinction coefficients. A small radiation extinction coefficient may lead to extinguishment due to heat transfer with the surroundings.

The presence of the porous matrix also affects the pore level flow and heat transfer. The fluid velocity at the walls is zero and Taylor-Aris dispersion [70] increases the heat and chemical species diffusion. The reactions are limited to the pore space and the local temperatures may be much higher (200 K [7]) than the volume-averaged gas temperatures. These high local temperatures affect the combustion and may increase the formation of thermal NO_x. The analysis of these effects require a pore level solution with multi-step chemistry.

The superadiabatic effect can also be used for thermal regeneration (i.e., heat recirculation).

Thermal Regeneration

A relatively new and innovative idea [30-32,38] is the use of an in-cylinder porous foam, or porous regenerator, to promote thermal regeneration and catalytic destruction of gaseous and particulate pollutants in diesel engines.

The porous regenerator is attached to a rod and moves up and down inside the cylinder, synchronized to the movement of the piston. Figure 6 shows a rendering of the cylinder of a diesel engine with the porous regenerator and the position of the piston and porous regenerator along the cycle. For most of the time, the regenerator is close either to the cylinder head or to the top of the piston. During the regenerative cooling stroke, the regenerator moves down, from the cylinder head to the piston top, and during the regenerative heating stroke the regenerator moves up, from the piston top to the cylinder head. Following combustion and expansion the products of combustion (exhaust gas) still have an appreciable amount

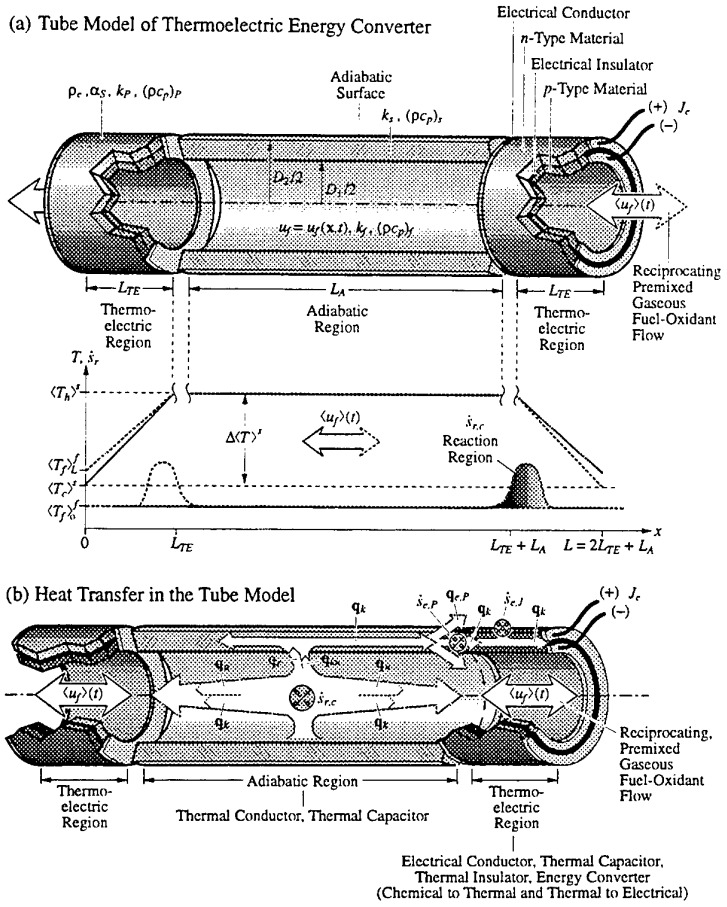

Fig.5. Combustion-thermoelectric tube.

of energy in the form of sensible heat. During the regenerative heating stroke, as the regenerator moves up, the hot exhaust gas flowing through it delivers part of its sensible heat to the regenerator (which has a large specific surface area) by surface-convection heat transfer. This amount of heat is stored as sensible heat. During the regenerative cooling stroke, as the regenerator moves downward, the cold air flowing through it is then heated by the regenerator. Therefore, there is a transfer of heat from the hot exhaust gas to the cold intake air via the regenerator. This principle is also used in the Stirling engines. But, in in-cylinder regeneration, the heating of the intake air does not affect the volumetric efficiency of the engine, because heating occurs after the intake air has been admitted to the cylinder.

The thermal regeneration depends on the choice of the material and geometry. High conductivity, high volumetric heat capacity and low effective thermal conductivity are desirable for optimal heat storage and recirculation. Comparison of the results for the non-regenerative and the regenerative engines using a SiC 12 ppi foam shows that there is a 50% increase in fuel efficiency and a 33% decrease in specific fuel consumption, for the same air/fuel ratio. There is also an increase in the average gas temperature for the top chamber (where combustion takes place). This high peak temperature is a result of the high initial temperature of the air (before injection starts) and the relatively smaller amount of air available for combustion. The local higher temperature of the gas in the top chamber may increase the production of thermal NO_x. However, the top-bottom volume averaged temperature is smaller than the volume averaged temperature for the nonregenerative engine.

Porous foams can also be used for trapping and combustion of particulates (soot). The porous insert

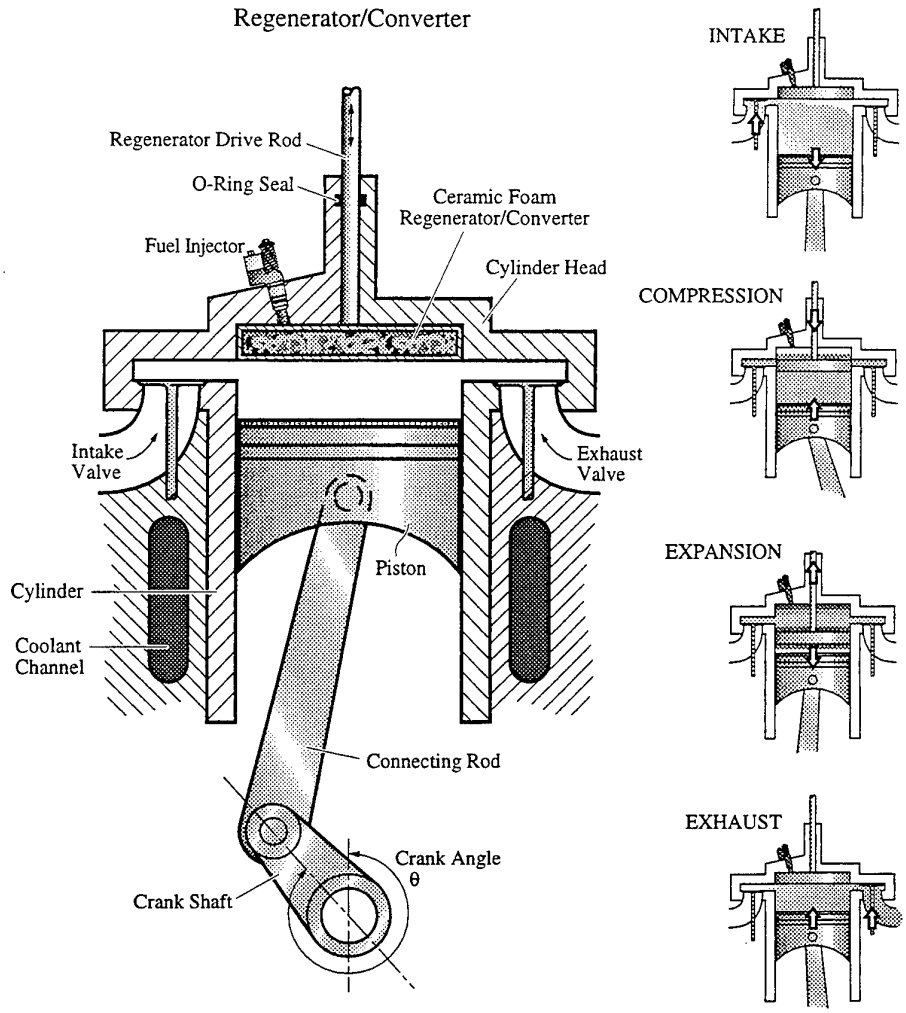

Fig.6.In-cylinder thermal regeneration for diesel engines.

trapps part of the soot before it leaves the cylinder and the high temperature reached by the solid phase promotes combustion of the particulates during each cycle.

Radiant Porous Burners

Radiant porous burners take advantage of superadiabatic stabilized flames and enhanced solid matrix emissivity to radiate heat to an external surface, for example, for infrared heating and drying of surfaces. The efficiency of the radiant burner is proportional to the radiation output [8, 9]. This depends on the heat generated by combustion, flame position and the thermal properties of the medium, especially, the radiation properties.

A rendering of the problem is shown in Fig. 7. The premixed gas flowing from the left to the right has the far upstream (nonreacted gas-phase only) conditions of T_n, u_{g_n} and fuel and oxidant densities ρ_{f_n} and ρ_{o_n}. The gas enters into the permeable slab at $x = 0$ and inside the slab the velocity (Darcean) is $\langle u_g \rangle$. The flame may be stabilized at a location x_F and the fluid- and solid intraphase heat flow occurs towards the upstream and downstream of the flame. The upstream heating, or preheating, is required for sustaining the reaction and the downstream heat flow occurs to supply the heat loss by radiation from the downstream surface at $x = L$.

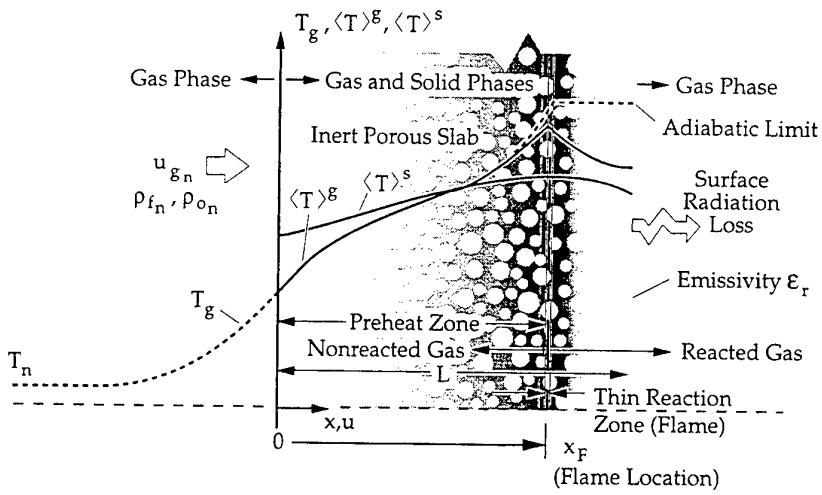

Fig.7. A radiant porous burner.

Depending on the choice of the solid material and matrix structure, the porous medium can significantly influence the flame speed for the combustion of a gaseous fuel u_F and, then, higher combustion rates are possible. This depends on the extent of the radiation and conduction preheating, the interfacial volumetric heat transfer rate, and the downstream radiation heat loss, among other parameters. In addition, for finite porous media, e.g., a permeable slab, the radiation heat loss from the surface of the slab can also influence the flame speed. The radiant output is maximized when the flame is near the exit of the medium, for optically thick media with high backward scattering [74]. The reduction of the scattering albedo can be achieved by reducing the fibers size [74] and by applying a thin coating over the fibers [8]. For different coating materials, there is an optimum coating thickness that maximizes the radiation output. The emissivity of silica fibers with diameter 2.5 μm coated with 6 nm thick platinum or 20 nm thick graphite is increased by a factor of 3 at $T = 1000$ K and 6 at $T = 1500$ K. Silicon oxide may be used to protect the platinum coating against oxidation [8]. In practice, the flame may be placed just outside the permeable slab (or layer), exposing it to the surroundings.

The internal radiation heat transfer can be modeled by considering emission and absorption [5] and by including scattering [3, 8, 74, 76, 77]. For porous burners, the optical thickness τ_r is usually larger than one, and the internal radiation heat transfer is significant [3, 8]. The Deissler approximation for the radiant heat flux is appropriate when $\tau_r > 1$. In this case, a radiant conductivity can be used [71-73,75,77] to obtain overall efficiency parameters for the porous burner. Thin media or spectral properties require the solution of the radiative transfer equation [8, 73, 76, 77] or the use of unit cells [78].

Direct local simulation [7] demonstrates the convenience and also the limitation of the volume-averaged treatments and the error expected when the constraints in the applicability of these treatments are not satisfied. The prediction of pollutant formation requires the use of detailed simulation and chemistry. A two-equation model, including dispersion effects on the conservation of energy and species mass equations, may be used for smaller thermal nonequilibrium. For strong thermal non-equilibrium or short burners, direct local simulation may be needed [6, 7]. These must be coupled with the appropriate radiation model (e.g., surface radiation exchange).

3. CHEMICAL NONEQUILIBRIUM

Chemical nonequilibrium may be imposed on the system to control combustion and heat transfer, or it may be a result of the inherent characteristics of the system, e.g., a nonuniform distribution (i.e., mixing) of reactants. Examples of the former are the distributed porous burners, and of the later, are solid pyrolysis and combustion synthesis.

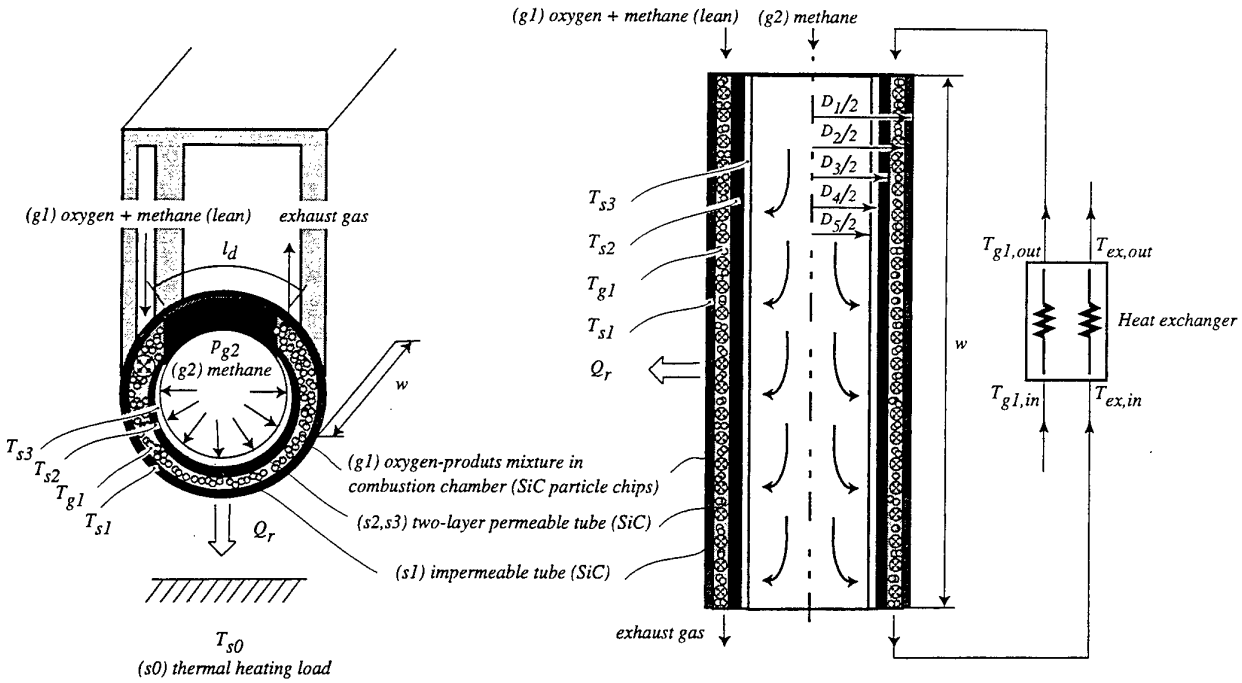

(a) (b)

Fig.8. Rendering of an annular radiant burner. (a) Cross-sectional view, and (b) model.

Distributed Porous Burners

In a conventional non-premixed and premixed oxygen-methane radiant burner, the combustion is confined to a small region near the fuel inlet, and therefore, only a small part of the burner surface contributes to the surface radiation heat delivery. This may result in excessive temperature and meltdown. To reduce the maximum temperature and have a more uniform heating, the fuel should be distributed over the entire volume of the combustion chamber. One method of achieving an optimum distribution of the fuel, is to burn the mixture in an annular combustion chamber with the fuel supplied through a permeable wall, as shown in Fig. 8 [40].

The optimum distribution of fuel is achieved by selecting the proper wall thickness, permeability, and pressure difference between the fuel supply line inside the permeable tube and the combustion chamber. For example, a nonuniform permeable wall thickness results in nonuniform fuel distribution (the flow is pressure driven), creating a nonuniform distribution of reaction rate along the burner which can then be tailored to the distribution of the thermal load. Heat exchange with the exhaust gas (preheating followed by superadiabatic effect) further increases the radiation output and overall burner efficiency. Radiation efficiencies around 90% are possible [40].

The high temperature in the permeable chamber may result in soot formation in the methane (fuel) stream near the inside surface, potentially blocking the fuel passage. To prevent the soot formation, the use of low-conductivity wall materials keeps the temperature of the inside surface of the permeable wall fairly low.

Fuel distribution has also been used to control the maximum temperature for catalytic combustors [41]. The fuel supply can be staged between sections of monolith to keep the adiabatic temperature for the fuel/air mixture below the catalytic surface meltdown temperature.

Catalytic Reactions

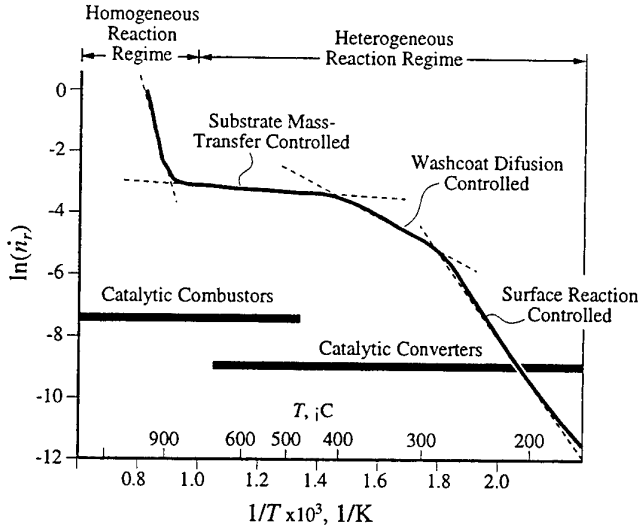

Fig.9. Reaction rate (arbitrary units) for CO oxidation on a Pt coated, monolith-type, catalytic converter [11].

Catalytic surfaces are used in catalytic reactors (converters) [10-13] and in complete [14-25] or partial catalytic combustors [26-29]. The catalytic reactors operate at a larger range of temperatures and are designed for improvement in synthesis rates of chemicals, purification and refining, and pollutant destruction. Catalytic combustors are designed for the production of power, heat (by radiation or convection), partial decomposition of heavier compounds, incineration, and regeneration and reforming. The catalytic converters and reactors are typically formed by a catalytic surface attached to a monolith, metallic mesh, screen or particles, in a packed or fluidized bed. In catalytic converters, frequently a washcoat is used as support of the catalytic surface. In the monolith-type automobile catalytic converters, the washcoat is made of sintered alumina agglomerates 10 to 100 nm in diameter, formed by primary alumina particles which are 1 to 2 nm in size. The precious metal (platinum, palladium and rhodium) crystallites are spread over the surface of the alumina particles. Manufacturing techniques for supported metal catalysts include precipitation and coprecipitation, impregnation, ion-exchange and sol-gel [85, 91] .

The conversion efficiency of gas pollutants depends on chemical reaction and transport limitations. Fig. 9 shows the reaction rate for the CO oxidation on a Pt coated, monolith-type, catalytic converter [11]. The reaction rate is initially controlled by the chemical kinetics of the reactions. As the temperature increases, the reaction rate increases exponentially and, for intermediate temperatures, diffusion through the washcoat becomes the controlling mechanism. With a further increase in temperature, the diffusion coefficient for gases increases and surface convection mass transfer through the large channels of the monolith (the flow is usually laminar) becomes the controlling mechanism. In the steady-state operational temperature range of underfloor catalytic converters (short excursions to high temperatures are possible), the kinetics of the chemical reactions and the transport in the washcoat control the pollutant conversion.

The modeling aims at a basic understanding of the reaction and transport which would ultimately allow for the optimization of the catalytic surfaces and substrates for a given application [93]. The modeling of the catalytic particles (pellets or washcoat) requires a description of the geometry of the porous structure and its change with time, and a treatment of the surface reactions and heat and mass transfer.

The description of the geometry of the support includes the size and shape of pores, connectivity of the network of pores and geometry of the surfaces (e.g., smooth or fractal). The selectivity and activity of a catalytic surface depends on the average size, geometry and distribution of crystallites, physical interactions between the metals, composition of the support and the presence of other promoters. Electron

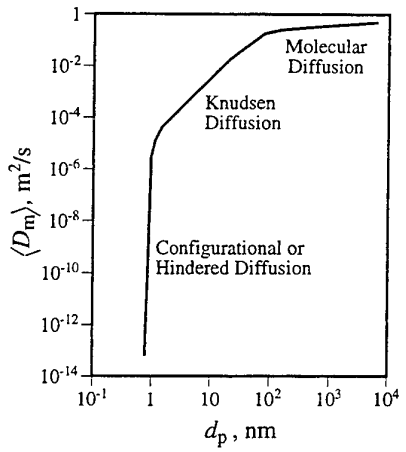

Fig.10. Effect of pore size on the effective diffusivity [86].

microscopy (with atomic resolution and transmission electron microscopy) allows for the visualization of the shape, size and distribution of crystallites down to the 1 nm size range [86]. X-ray diffraction can also give average diameter and scanning tunneling microscopy can give particle shape. Different lattice planes can be exposed at the crystallite surface and they may present line and point defects. The lattice planes and defects can be highly variable, depending on the pretreatment and environmental conditions [85]. During preparation, small amounts of oxide from the support may also be transported to the crystallite surface. Techniques using high-intensity fluxes of X-ray (e.g., from synchroton radiation sources) can provide information on metal-metal bond distance, metal coordination number, disorder of surface atoms and size and shape of supported metal clusters [85, 96]. The structure may change with time as a result of chemical reaction, poisoning, or thermal stress. The catalytic surface may lose its activity due to sintering and poisoning. Sintering depends on the temperature and composition of the gas mixture. Sintering of platinum particles supported on alumina occurs by crystallite migration and coalescence by surface diffusion, duct ripening and Ostwald ripening [92]. Pt and Rh particles are more stable under reducing conditions, while Pd particles are more stable under oxidizing conditions. This makes Pd the choice for lean-burn engines allowing for the placement of the converter closer to the engine which results in a faster light-off. Poisoning, mostly sulfur and phosphorus poisoning, occurs by the deactivation of active sites and plugging of the porous structure due to the growth of solid phases. The growth of solid phases is kinetic and transport controlled and occurs by a mechanism similar to the catalytic hydrodemetallation of crude oil process [93-95].

The surface reaction rates have been traditionally modeled following a Langmuir-Hinshelwood or Rideal-Eiley mechanism, extended to include multicomponent effects on the inhibition. The active sites are supposed to exist at a given surface concentration at the interface between the solid and gas phases, i.e., coating the solid particles. The predictions of these models are then compared to the integral conversion measurements and the reaction rate coefficients are adjusted to predict the measurements. Although these models are able to predicted steady-state results for different conditions, they do not provide an accurate description of multiple steady-states, oscillations, and chaotic behavior [85]. It has been shown that the chemical kinetics are sensitive to the geometry of the surface (lattice planes, defects) and to the distribution of crystallites [85]. A more basic understanding of the surface reactions requires theoretical and surface chemistry methods [97]. The theoretical methods include monte carlo simulations, molecular dynamics and quantum chemistry. The surface chemistry methods include infrared, Raman and NMR spectroscopy. These allow for the observation of the structure and composition of the adsorbed species. The observations are usually made on very well defined crystals under ultrahigh vacuum conditions.

The mass transfer involves bulk and surface multicomponent diffusion. The effective diffusivity of a gas in a porous medium $\langle \mathcal{D}_m \rangle$ depends on the geometry, the molecular diffusivity of the gas in the mix-

ture and the pore size. Fig. 10 shows the dependency of the effective diffusivity on pore size [86] for a given molecule and temperature. The effective diffusivity becomes a strong function of pore size in the Knudsen regime (when the mean-free path of the gas molecules is of the same order of magnitude as the pore size) and drops sharply as the pore size reaches the molecule size (hindered or configurational diffusion regime [108]). The diffusion through the washcoat is usually modeled using continuous models. The effective diffusivity accounts for the effect of the pore structure on the diffusion of the different components. The dusty-gas model is also used. It has been shown [99-101] that bulk pressure gradients can develop inside of the porous catalyst as a result of external pressure gradients and mass diffusion induced bulk flow due to the reaction stoichiometry. In modeling diffusion using networks, it is important to reproduce the connectivity and the conductance of the individual pores, statistically, as close as possible. The pore size distribution can be obtained from sorption experiments [109], mercury porosimetry [110], and image analysis [114]. Jerauld et al [101, 102] point that there are short-range correlations between the transport properties of the pores. However, they showed that as long as the average coordination number (a measure of connectivity) and distribution of conductances of the channels is reproduced correctly, the effective transport properties calculated from a regular network (e.g., a square network) are equal to the ones exhibited by a random network. One of the network models that has been used to model random pore structures is the Swiss-Cheese model, which leads to a Voronoi tessellation that represents the porous channels [103]. The mass transport through the channels of the monolith have been modeled using surface-convection correlations, assuming either plug or Poiselle flows and well-mixed sites (nodes). Transient effects are generally not included.

The accuracy of continuous models in describing transport and reaction in porous media has also been investigated. The questions are whether the effective diffusivity is a function of the reaction rate, if use of an effective diffusity fails near percolation thresholds and whether it is accurate enough in modeling diffusion of molecules with diameters approaching the pore size. The continuum models agree with network results when the multiscales are taken into account [93]. Zhang and Seaton [104] used a regular, three-dimensional network, with smooth cylindrical pores. At the pore level, they assumed one-dimensional, steady-state diffusion-reaction with first-order reaction and well-mixed sites. Their results show that the effective diffusivity calculated in absence of reaction is equal to the one calculated with reaction, as long as there is sufficient penetration of the diffusion front into the modeled network. This is due to the fact that the continuum model fails when the length scale for the penetration is of the same order of magnitude as the pore length. The continuum model also fails near the threshold of percolation caused by pore blockage during poisoning. The correlation length (i.e., the length scale over which the fluid phase is connected) is given by [103]

$$\xi \sim |P - P_c|^{-\upsilon}, \tag{5}$$

where P is the probability of a single pore being blocked, P_c is the critical probability (probability at the percolation threshold) and υ is an exponent which depends on the dimensionality ($\upsilon = 0.88$ for a three-dimensional network). The correlation length tends to infinity when the percolation threshold is reached and, therefore, becomes much larger than the system length L. As the pore size reaches the size of the molecules, a threshold for percolation may also be reached. From the results of Zhang and Seaton, these trends are summarized in Fig. 11(a). The Thiele modulus ϕ_l is defined as

$$\phi_l = \frac{l^2 a_1}{\langle \mathcal{D}_m \rangle} \frac{S_{\beta\sigma}}{\epsilon_\beta}, \tag{6}$$

where a_1 is the reaction rate constant (in m/s), l is the pore length, and $S_{\beta\sigma}$ is the interfacial specific surface area between the β and σ phases (e.g., solid and gas) (in m^2/m^3). For a smooth cylindrical pore with radius r_p, $S_{\beta\sigma}/\epsilon_\beta = 2/r_p$.

In the model of Zhang and Seaton [104], the reaction rate constant was uniform for the network. In practice, there may be nonuniformity in reaction constants due to variations in crystallite distribution and crystallite activity (related to size, shape, surface state, poisoning, etc). These nonuniformities have their own characteristic length scales which vary from crystallite, to pore, to system size. When the

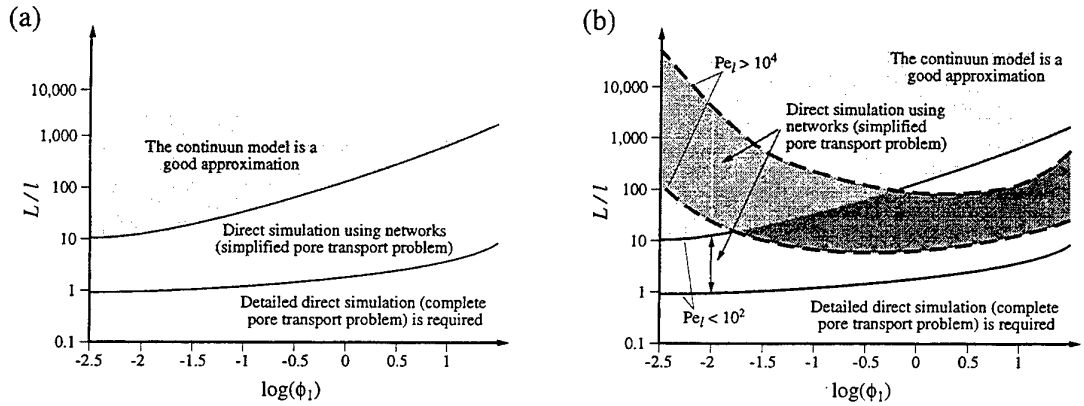

Fig. 11. Domains for the modeling of the diffusion and reaction in a porous pellet for (a) Uniform reaction rate constants, and (b) nonuniform reaction rate constants. ϕ_l is the pore Thiele modulus and L/l is the ratio of system to pore lengths.

nonuniformity is very pronounced, a percolation threshold may also be reached. Alvarado et al. [105] investigated the effect of a bimodal spatial nonuniformity on the reaction constant in transient diffusion and adsorption of a chemical species in a porous network. They used a two-dimensional square network of cylindrical pores with $l \gg r_p$ and assumed a pore-level one-dimensional diffusion-convection-reaction model. They concluded that for uniform reaction constants, the dispersion coefficient (which accounts fo the effect of effective diffusivity and flow in the spreading of a chemical species) is not a function of reaction rate (i.e., it is purely hydrodynamic) and the effective reaction constants are equal to the pore-level ones. However, when the reaction constants are nonuniform, the dispersion coefficient becomes a function of the reaction rate when the characteristic Damköhler number (where u is the pore average velocity and $a = a_2/a_1$ is the chemical equilibrium constant for an adsorption/desorption reaction)

$$\mathrm{Da}_l = \frac{la^2 a_1}{u} \frac{S_{\beta\sigma}}{\epsilon_\beta}, \tag{7}$$

is small ($\mathrm{Da}_l \to 0$). This condition is reached, for example, when the pore level Peclet number ($\mathrm{Pe}_l = ul/\mathcal{D}_m$) is large or when the reaction rates are small. They showed that for large Peclet numbers ($\mathrm{Pe}_l > 10^4$), the transport and reaction is dominated by both convection and reaction. When $\mathrm{Pe}_l \to 0$, diffusion dominates, and the reaction and transport effects are decoupled. Also, when the system size becomes very large ($L \gg l$) the dispersion coefficient approaches a purely hydrodynamic behavior. The Damköhler number is proportional to the ratio of the Thiele modulus and Peclet number, $\mathrm{Da}_l \sim \phi_l/\mathrm{Pe}_l$. Thus, in the presence of flow, a small Thiele modulus may also require detailed simulation, as summarized in Fig. 11(b). A pore with a fractal surface (large $S_{\beta\sigma}$) would increase the Thiele modulus and a surface effectiveness, which accounts for the accessibility of the surface to the gas molecules, can be defined. Coppens and Froment [106] show that the surface effectiveness of the fractal pore is smaller than the one for a circular pore with the same length. They also conclude that it is usually impossible to construct a smooth cylindrical pore which results in the same flux and end concentrations of a reactant species as the pore with a fractal surface.

The role of diffusion within the washcoat in the chemical conversion rates is not yet fully understood. The choice of agglomerate size used for the washcoat depends on design parameters such as activity of the washcoat, adherence to the substrate, mechanical strength under thermal loading, and other durability and reliability requirements. In most cases, a unity washcoat effectiveness is assumed and the precious metal loading is adjusted to predict the overall conversion rates for different operating conditions. Although the current generation of catalytic converters is overdesigned from a mass-transport perspective, the continuous decrease in the tolerable levels of emissions leads to the necessity of a closer examination of the effect of washcoat diffusion on the conversion of gas pollutants at low pollutant concentrations

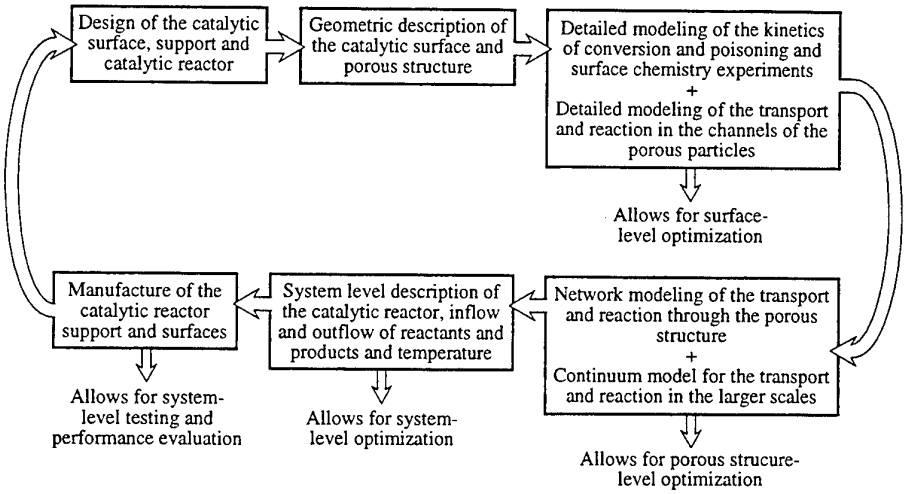

Fig. 12. Design and optimization of catalytic converters.

(to find ways of increasing the washcoat effectiveness for a given precious metal loading). This requires a detailed modeling of the reaction and transport in the washcoat. Also, the development of fast and accurate design tools for engineering treatment of washcoat diffusion that can be easily incorporated into existing design packages is necessary. Fig. 12 presents a summary of the modeling and experiments for the design and optimization of catalytic converters.

In the next two sections, systems with intrinsic chemical nonequilibrium are presented.

Solid Pyrolysis

Pyrolysis occurs as a result of the thermal degradation of a solid fuel. Wood burning for energy generation [44-46,49], waste incineration [49], and fire propagation [48] are examples of processes involving pyrolysis. Fig. 13 illustrates the coexisting gas- and solid-phase reactions in a combustible porous medium. The porous medium consists of a packed bed of randomly arranged spherical wood particles. The upward flow of the air against the gravitational field is in the opposite direction to that of the combustion wave. This is called reverse smoldering. The solid undergoes pyrolysis generating a volatile fuel to react with the oxygen available in the gas phase. Heterogeneous reactions can take place concurrently with the gas-phase reactions (homogeneous). The extent of the surface reactions depends on the rate of oxygen diffusion to the surface of the char produced subsequent to the pyrolysis. Four distinct regimes exist: heating and drying of the wood particles; pyrolysis; char oxidation; and gas-phase reaction regimes (flaming). For a given fuel bed porosity and particle size, the intensity, relative position, and width of the reaction zones are not known a priori and can vary greatly depending on the flow rate of the incoming gas, the initial concentration of the oxygen in the flow, and the chemical kinetics and thermal effects.

The pyrolytic reaction is initiated ahead of the char oxidation zone, generating the volatile fuel to burn in the gas phase further downstream. The pyrolysis takes place at a much faster rate than the char oxidation, being, usually, nearly complete at the start of the char oxidation. The pyrolysis zone may, however, extend over the char oxidation zone. In this case, while the char oxidation is taking place at the surface, the pyrolysis may still continue in the interior of the particle. The flow rate of the incoming air has negligible effect on the thickness of the pyrolysis zone. In contrast to the char oxidation, the pyrolysis is independent of the oxygen concentration in the gas and its availability. In the presence of nitrogen, it depends only on the local solid temperature. For wood particles, pyrolysis temperatures are typically from 625 K to 635 K. It is interesting to note that since the temperature gradient within the pyrolysis zone does not change significantly with variations in the incoming gas flow rate, the concentration of the volatiles in the solid phase also remains unaffected by the gas pore velocity.

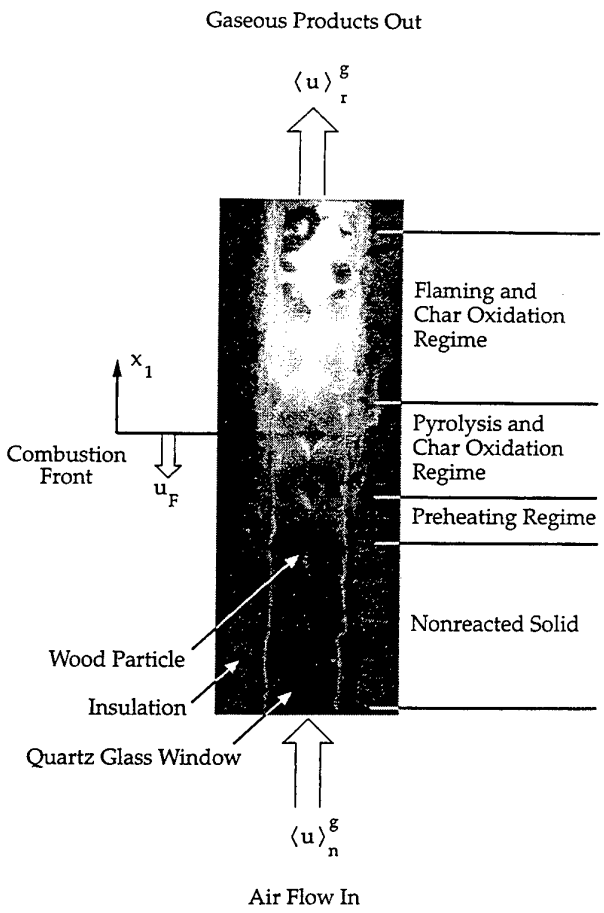

Fig. 13. Rendering of the coexisting gas- and solid-phase reactions in a combustible porous medium.

The solid surface can also suppress the gas phase reactions due to a third body recombination of the free radicals, which participate in the gas phase combustion. Thus, in a packed bed the gas-phase reactions can be inhibited because of the large specific surface area of the solid. In this situation, the smoldering is sustained by the char oxidation reactions.

The char oxidation reactions are kinetically controlled at low temperatures. At high temperatures, the rate-controlling path is the diffusion rate of oxygen from the bulk gas to the surface of the solid particle, i.e., it becomes mass transfer controlled. Mass diffusion to the particle surface is usually modeled using a solid-gas mass transfer coefficient. The overall local volume-averaged heterogeneous reaction rate is given by an Arrhenius expression [47, 50].

The condition of local thermal equilibrium between the gas and solid phases breaks down in the reaction zone. The transfer of some of the heat through the solid to the reactants in the gas phase causes a temperature increase in the flame (and in turn, heat transfer to the solid). The gas-phase thus exhibits a superadiabatic temperature. The excess temperature and the gas- and solid-phase temperatures throughout the combustion wave increase as the incoming air flow rate increases.

The combustion rate can be increased by reducing the thermal nonequilibrium. This can be done by decreasing the particle size. Smaller particle size increases the optical thickness and decreases the effective thermal conductivity. A maximum combustion rate can be achieved for an optimum particle

size. The use of a gas fuel to increase the rate of pyrolysis can be used for low calorific fuels.

Powder Combustion

In contrast to the gas-solid reactions in smoldering, the reactions between two components in the form of particles may be controlled by the interparticle rate of transfer of reactants. In the propagation mode of combustion synthesis (or SHS, self-propagating, high-temperature synthesis) [53-55], a compacted-powder specimen is ignited at one end and a combustion wave travels through it converting the reactants to products. This method has been used to produce ceramics, intermetallics, cermets, composites, functionally gradient materials, thin coatings, and to join materials. In gasless combustion synthesis (i.e., combustion with no participation or generation of a gas phase), it has been observed experimentally that complete conversion may not occur and the maximum temperature in the combustion region may be substantially below the adiabatic equilibrium temperature [59, 60]. This lack of complete reaction is related to the heterogeneous nature of the polysized, multicomponent particle mixture (affecting the heat transfer, diffusion, and phase transformation).

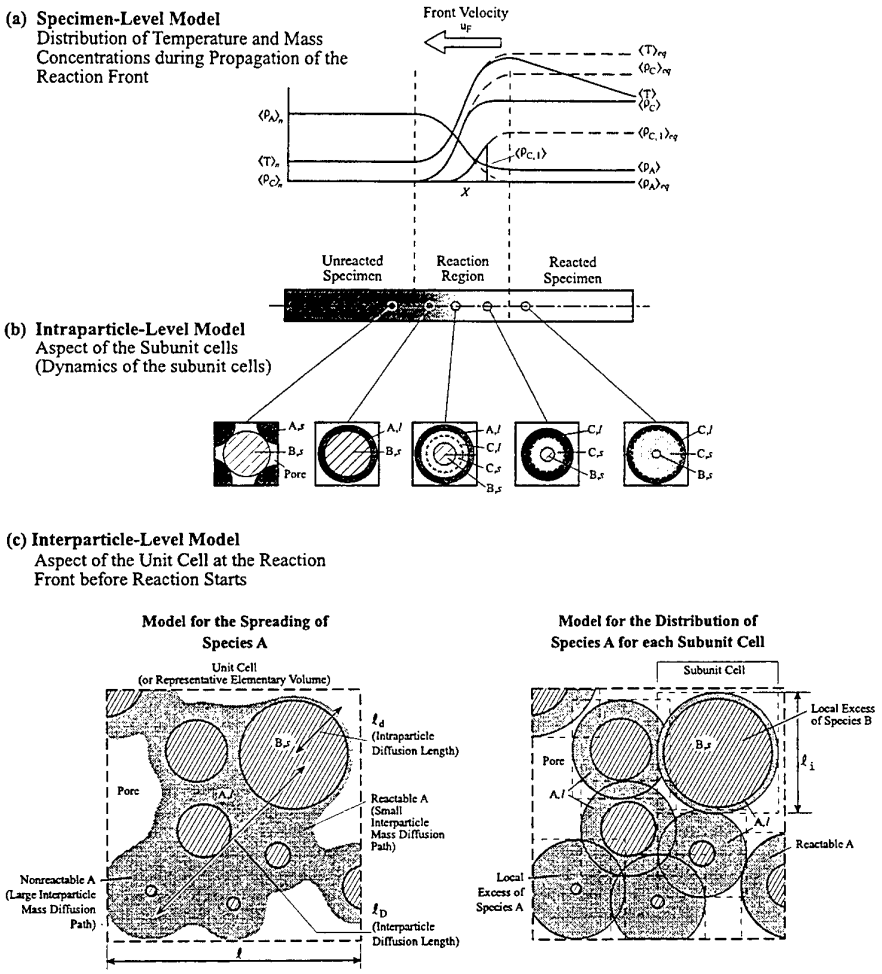

Fig. 14. (a) Rendering of the specimen-level temperature and mass concentration distributions, (b) variations in the structure of a particle along the specimen during reaction (using a shrinking-core model), and (c) modeling of the nonuniform particle-size distribution, showing the fraction of species A that may not reach the species B particles.

The modeling of gasless combustion synthesis requires descriptions at the specimen and particle scales, as shown in Fig. 14. At the specimen scale, the heat transfer, the volumetric heat generation, and the peripheral heat losses, determine the axial temperature distribution. The volumetric heat generation depends on the particle-level mass transfer, reaction rates, and phase transformations. The kinetics of these intraparticle processes depends on the temperature and chemical composition, which is affected by species diffusion and by the interparticle availability of reactants. This local (i.e., interparticle) stoichiometry may differ from the specimen-level average stoichiometry because of the inherent heterogeneity of the medium which increases in the presence of a particle size distribution. The interactions between specimen-level and particle-level processes determine the final microstructure, including the composition and distribution of product phases and the amount of reactants remaining, and the mechanical and morphological transformations during the combustion synthesis, including the formation and destruction of porosity (i.e., consolidation), the mechanical stability of the compacts during reaction, and the products mechanical and metallographic properties. The modeling of the mechanical transformations requires thermomechanical descriptions. A phase field formulation can be potentially used to model the particles transformations and motion [115, 116].

The powders commonly used present a nonuniform distribution of particle size and shape. This nonuniform particle-size distribution has two effects. First, since the chemical reaction is diffusion controlled, particles of different sizes experience different reaction rates and temperature evolution, thus, influencing the specimen-level temperature distribution and propagation speed. This effect depends primarily on the average particle size. Second, a nonuniform distribution of reactants changes the local stoichiometry and the distance separating the melt-rich regions from the melt-lean regions may be large. The peripheral heat losses would then prevent the timely migration of the melted reactant. This effect depends on the shape of the particle size distribution, especially the standard deviation. As a consequence, a uniform particle size distribution is needed for complete conversion and a small average particle size is needed for propagation. These would require screening of the powders which would then increase the production cost.

4. CONCLUSION

Surface science of adsorption, diffusion, and reaction need to be better understood for optimal design and innovative applications of catalytic combustion. The increase in the conversion rate of trace pollutants, depends on the optimization of the porous structure and catalytic-site distribution for large surface area and low resistance to mass diffusion. Bimodal pore-size distributions with axial and transversal nonuniform crystallite distribution may lead to an optimum performance. Catalytic surfaces and supports which are resistant to poisons and active in oxidizing exhaust conditions (e.g., the emission from diesel and lean-burn engines) need to be developed, especially NO_x catalysts. High-temperature catalytic surfaces for complete and partial combustion of methane are also needed. The understanding and modeling of chemical nonequilibrium in washcoats (and supports) is required for the development of these applications.

Superadiabatic combustion and local chemical nonequilibrium, including optimal fuel distribution, are very promising for innovative new combustion systems. The conduction and radiation along the porous media may be optimized by the proper choice of the material and structure, thus increasing the superadiabatic effect. Optimal fuel distribution is achieved by the proper design of the porous structure to attend the thermal load. The output of the radiant burners may be improved by a proper choice of the material and geometry near the surface. Thermal regeneration also depends on the choice of the material and geometry. High conductivity, high volumetric heat capacity and low effective thermal conductivity are desirable for optimal heat storage and recirculation.

The understanding of the solid pyrolysis allows for control and prevention of fire and a more efficient use of the solid fuel. The suppression or augmentation of the pyrolysis leads to a better control of the combustion rate.

The control of the nonuniform distribution of reactants in combustion synthesis and a better understanding of the mechanisms of dynamic phase nucleation and growth allows for a better control of the conversion rates. This allows for obtaining complete conversion, or producing a functionally gradient material. Also, the potential of the method as a near net-shape manufacturing strategy has not yet been exhausted.

REFERENCES

1. T. Takeno and K. Sato, Combust. Sci. Technol., v.20, pp.73-84 (1979).
2. Y. Yoshizawa, S. Kiyoshi and R. Echigo, Int. J. Heat Mass Transfer, v.31, pp.311-319 (1988).
3. S. B. Sathe, R. E. Peck and T. W. Tong, Int. J. Heat Mass Transfer, v.33, pp.1331-1338 (1990).
4. R. Echigo, R., "Radiation enhanced/controlled phenomena of heat and mass transfer in porous media," *Proceedings of the 1st ASME/JSME Joint Thermal Engineering Conference*, v.4, pp.xxi-xxxii (1991).
5. P. F. Hsu and J. R. Howell, Experimental Heat Transfer, v.5, pp.293-313 (1993).
6. P. Hsu and R. D. Matthews, Combustion and Flame, v.93, pp.457-466 (1993).
7. M. Sahraoui and M. Kaviany, Int. J. Heat and Mass Transfer, v.37, pp.2817-2834 (1994).
8. T. W. Tong and W. Li, J. Quant. Spectrosc. Radiat. Transfer, v.53, pp.235-248 (1995).
9. J. R. Howell, M. J. Hall and J. L. Ellzey, Prog. Energy Combust. Sci., v.22, pp.121-145 (1996).
10. R. W. Rice, *Porosity of Ceramics*, Marcel Dekker, New York (1998).
11. E. Koberstein and G. Wannemacher, *Catalysis and Automotive Pollution Control*, SAE, pp.155-172 (1987)
12. J.W. Beeckman and L. L. Hegedus, Ind. Eng. Chem. Res., v.30, pp.969-978 (1991).
13. K. Tamaru and G. A. Mills, Catalysis Today, v.22, pp.349-360 (1994).
14. J. N. Armor, Catalysis Today, v.26, pp.99-105 (1995).
15. W. C. Pfefferle adn L. D. Pfefferle, Prog. Energy Combust. Sci., v.12, pp.25-41 (1986).
16. W. C. Pfefferle and L. D. Pfefferle, Catal. Rev.-Sci. Eng., v.29, pp.219-267 (1987).
17. A. A. Barresi, S. L. Hung and L. D. Pfefferle, The Chemical Engineering Journal, v.50, pp.123-131 (1992).
18. H. Ikeda, P. A. Libby and F. A. Willians, Combustion and Flame, v.93, pp.138-148 (1993).
19. P. Markatou, L. D. Pfefferle and M. D. Smooke, Combustion and Flame, v.93, pp.185-201 (1993).
20. L. D. Pfefferle, Catalysis Today, v.26, pp.255-265 (1995).
21. R. A. Dalla Betta, J. C. Schlatter, D. K. Yee, D. G. Loffler and T. Shoji, Catalysis Today, v.26, pp.329-335 (1995).
22. H. Arai and H. Fukuzawa, Catalysis Today, v.26, pp.217-221 (1995).
23. S. Maruko, T. Naoi and M. Onedera, Catalysis Today, v.26, pp.309-317 (1995).
24. K. Eguchi and H. Arai, Catalysis Today, v.29, pp.379-386 (1996).
25. R. Jones, Surface and Coatings Technology, v.96-95, pp.118-122 (1997).
26. C. Niehorster, G. Arends and M. Schreiber, Combustion and Flame, v.110, pp.140-151 (1997).
27. D. A. Hickman and L. D. Schmidt, AIChE Journal, v.39, pp.1164-1177 (1993).
28. L. D. Schmidt, M. Huff and S. S. Bharadwaj, Chemical Engineering Science, v.49, pp.3981-3994 (1994).
29. S. S. Bharadwaj and L. D. Schmidt, Fuel Processing Technology, v.42, pp.109-127 (1995).
30. M. Ziauddin, A. Balakrishna, D. G. Vlachos and L. D. Schmidt, Combustion and Flame, v.110, pp.377-391 (1997).
31. A. Ferrenberg, SAE Transactions, SAE 900911 (1990).
32. A. Ferrenberg, AIAA Journal, AIAA 90-2510 (1990).
33. A. Ferrenberg, SAE Transactions, SAE 940946 (1994).
34. K. Hanamura, K. Bohda and Y. Miyairi, Energy Convers. Mgmt., v.38, pp.1259-1266 (1997).
35. G. A. Fateev and O. S. Rabinovich, Int. J. Hydrogen Energy, v.27, pp.915-924 (1997).
36. C.-W. Park and M. Kaviany, "Combustion Thermoelectric Tube," *Proceedings of the 1999 National Heat Transfer Conference*, Albuquerque, New Mexico (1999).
37. C.-W. Park and M. Kaviany, J. Heat Transfer, submitted (1999).
38. K. Hanamura, K. Akagi and K. Koyanagi, "Autothermic Reforming by Reciprocating-Flow Super-Adiabatic Combustion in Porous Media," *Proceedings of the 5th ASME/JSME Joint Thermal En-*

gineering Conference, pp.1-6, San Diego, California (1999).
39. M. Kaviany, *Principles of Heat Transfer*, ME370 Course Pack, Department of Mechanical Engineering and Applied Mechanics, The university of Michigan, Ann Arbor, MI (1999).
40. C.-W. Park and M. Kaviany, *Optimization of High-Temperature Radiant Burner*, Report to Air Liquide, CRCD, Joay-en-Josas, France (1999).
41. R. J. Farrauto, React. Kinet. Catal. Lett., v.60, pp.233-241 (1997).
42. A. C. MacIntosh, M. Bains, W. Crocombe and J. F. Griffiths, Combustion and Flame, v.99, pp.541-550 (1994).
43. M. Kaplan and M. J. Hall, Experimental Thermal and Fluid Science, v.11, pp.13-20 (1995).
44. V. V. Martynenko, R. Echigo and M. Yoshida, Int. J. Heat Mass Transfer, v.41, pp.117-126 (1998).
45. A. M. Kanury and P. L. Blackshear, Jr., Comb.Sci. and Tech., v.1, pp.339-355 (1970).
46. C. Di Blasi, Combust. Sci. and Tech., v.90, pp.315-340 (1993).
47. M. Fatehi adn M. Kaviany, Comb. Flame, v.99, pp.1-17 (1994).
48. D. A. Schult, B. J. Matkowski, V. A. Volpert and A. C. Fernandez-Pello, Combustion and Flame, v.104, pp.1-26 (1996).
49. C. Brereton, Resources, Conservation and Recycling, v.16, pp.227-264 (1996).
50. M. Fatehi and M. Kaviany, Int. J. Heat and Mass Transfer, v.40, pp.2607-2620 (1997).
51. C. P. Garner and J. C. Dent, SAE Transactions, SAE Paper No. 880007 (1988).
52. R. Noirot, P. Gilot, R. Gadiou, and G. Prado, Combust. Sci. Tech., v.95, pp.139-160 (1994).
53. G. C. Koltsakis and A. M. Stamelos, Ind. Eng. Chem. Res., v.35, pp.2-13 (1996).
54. Z. A. Munir, Ceramic Bulletin, v.67, pp.342-349 (1988).
55. A. G. Merzhanov, "Self-propagating high-temperature synthesis: twenty years of search and findings," *Combustion and Plasma Synthesis of High Temperature Materials*, Chap.1, edited by Z. A. Munir and J. B. Holt, VCH Publishers, New York (1990).
56. A. Varma and J.-P. Lebrat, Chem. Eng. Sci., v.47, pp.2179-2193 (1992).
57. K. Brezinski, "Gas-phase combustion synthesis of materials," *Proceedings of the Twenty-Sixth Symposium (International) on Combustion/The Combustion Institute*, pp.1805-1816 (1996).
58. M. Wooldridge, Prog. Energy Combust. Sci., v.24, pp.63-87 (1998).
59. A. A. M. Oliveira and M. Kaviany, Int. J. Heat Mass Transfer, v.42, pp.1059-1073 (1999).
60. A. A. M. Oliveira and M. Kaviany, Int. J. Heat Mass Transfer, v.42, pp.1075-1095 (1999).
61. R. Armstrong, Combust. Sci. Tech., v.71, pp.155-174 (1990).
62. S. Whitaker, "Simultaneous Heat, Mass, and Momentum Transfer in a Porous Media: A Theory of Drying," *Advances in Heat Transfer*, v.7, pp.119-203, edited by J. P. Hartnett and I. Irvine, Academic Press, New York (1977).
63. M. Quintard and S. Whitaker, Transport in Porous Media, v.3, pp.357-413 (1988).
64. M. Quintard and S. Whitaker, Transport in Porous Media, v.5, pp.341-379 (1990).
65. M. Quintard and S. Whitaker, "One- and two-equation models for transient diffusion processes in two-phase systems," *Advances in Heat Transfer*, v.23, pp.369-464, edited by J. P. Hartnett and T. F. Irvine, Academic Press (1993).
66. M. Quintard and S. Whitaker, Chem. Engng. Sci., v.48, pp.2537-2564 (1993)
67. M. Quintard and S. Whitaker, Transport in Porous Media, v.14, pp.163-177 (1994).
68. M. Quintard and S. Whitaker, Transport in Porous Media, v.14, pp.179-206 (1994).
69. M. Quintard, M. Kaviany and S. Whitaker, Advances in Water Resources, v.20, pp.77-94 (1997).
70. M. Kaviany, *Principles of Heat Transfer in Porous Media*, Springer-Verlag, Corrected 2nd Ed., (1999).
71. D. Vortmeyer, "Radiation in packed solids," *Proceedings of tht 6th International Heat Transfer Conference*, v.6, pp.525-539, Toronto, Canada (1978).
72. C. L. Tien and B. L. Drolen, "Thermal radiation in particulate media with dependent and independent scattering," *Annual Review of Numerical Fluid Mechanics and Heat Transfer*, v.1, pp.1-32, Hemisphere, Washington (1987).
73. R. Viskanta and M. P. Menguc, Appl. Mech. Rev., v.42, pp.241-259 (1989).
74. T. W. Tong, S. B. Sathe and R. E. Peck, Int. J. Heat Mass Transfer, v.33, pp.1339 (1990).
75. B. P. Singh and M. Kaviany, "Radiation in Porous Media," *Advances in Heat Transfer*, v.23,

pp.369-464, edited by J. P. Hartnett and T. F. Irvine, Academic Press (1993).
76. T. J. Hendricks and J. R. Howell, J. Heat Transfer, v.118, pp.79-87 (1996).
77. D. Doermann, and J. F. Sacadura, J. Heat Transfer, v.118, pp.88-93 (1996).
78. X. Fu, R. Viskanta,and J. P. Gore, Int. Comm. Heat Mass Transfer, v.24, pp.1069-1082 (1997).
79. P. Furmanski, S. Wisniewski and J. Banaszek, J., "Analysis of nonlocal character of radiation heat transfer in themal insulations," *Proceedings of the 11th International Heat Transfer Conference*, v.7, pp.379-384, Kyongiu, Korea (1998).
80. K. Kamiuto and T. Matsushita, "High-temperature radiative properties of open-cellular porous materials," *Proceedings of the 11th International Heat Transfer Conference*, v.7, pp.385-390, Kyongiu, Korea (1998).
81. S. Zhdanov, L. A. Kennedy and G. Koester, Combustion and Flame, v.100, pp.221-231 (1995).
82. A. P. Aldushin, I. E. Rumanov and B. J. Matkowsky, Combustion and Flame, v.118, pp.76-90 (1999).
83. A. A. Mohamad, S. Ramadhyani and R. Viskanta, Int. J. Heat Mass Transfer, v.37, pp.1181-1191 (1994).
84. S. S. Penner and A. L. Berlad, Energy, v.20, pp.311-324 (1995).
85. A. Bell, Chem. Eng. Science, v.45, pp.2013-2026 (1990).
86. B. C. Gates, *Catalytic Chemistry*, John Wiley (1992).
87. K.A. Bethke, M. C. Kung, B. Yang, M. Shah, D. Alt, C. Li, and H. H. Kung, Catalysis Today, v. 26, pp.169-183 (1995).
88. A. P. Walker, Catalysis Today, v.26, pp.107-128 (1995).
89. R. I. Masel, *Principles of Adsorption and Reaction on Solid Surfaces*, John Wiley (1996).
90. P. Gilot, M. Guyon and B. R. Stanmore, Fuel, v.76, pp.507-515 (1997).
91. R. D. Gonzales, T. Lopez,and R. Gomez, Catalysis Today, v.35, pp.293-317 (1997).
92. J. J. Chen and J. Ruckenstein, Journal of Catalysis, v.69, pp.254 (1981).
93. F. J. Keil and C. Rieckmann, Chemical Engineering Science, v.49, pp.4811-4822 (1994).
94. S. Arbabi and M. Sahimi,Chemical Engineering Science, v.46, pp.1739-1747 (1991).
95. S. Arbabi and M. Sahimi, Chemical Engineering Science, v.46, pp.1749-1755 (1991).
96. J. H. Sinfeld, G. H. Via and F. W. Lytle, Catal. Rev. Sci., v.26, pp.81 (1984)
97. F. J. Keil, Chemical Engineering Science, v.51, pp.1543-1567 (1996).
98. H. S. Nan, M. M. Dias and A. E. Rodrigues, Chem. Eng. J., v.57, pp.101-114 (1995).
99. D. Arnost and P. Schneider, Chem. Eng. J., v.57, pp.91-99 (1995).
100. J. W. Veldsink, R. M. J. Van Damme, G. F. Versteeg, and W. P. M. Swaaij, Chem. Eng. J., v.57, pp.115-125 (1995).
101. G. R. Jerauld, J. C. Hatfield, L. E. Scriven and H. T. Davis, J. Phys. C, v.17, pp.1519-1529 (1984).
102. G. R. Jerauld, L. E. Scriven and H. T. Davis, J. Phys. C, v.17, pp.3429-3444 (1984).
103. M. Sahimi, Physics Reports, v.306, pp.213-395 (1998).
104. L. Zhang and N. A. Seaton, Chemical Engineering Journal, v.49, pp.41-50 (1994).
105. V. Alvarado, H. T. Davis and L. E. Scriven, Chemical Engineering Science, v.52, pp.2865-2881 (1997).
106. M.-O. Coppens and G. F. Froment, Chem. Eng. Sci., v.50, pp.1027-1039 (1995). (1994).
107. W. C. Conner and C. O. Bennet, J. Chem. Soc. Faraday Trans., v.89, pp.4109-4114 (1993).
108. K. W. Limbach and J. Wei, AIChE Journal, v.36, pp.242-248 (1990).
109. N. A. Seaton, Chemical Engineering Journal, v.46, pp.1895-1909 (1991).
110. R. L. Portsmouth and L. F. Gladden, Chemical Engineering Journal, v.46, pp.3023-3036 (1991).
111. R. B. Bird, W. E. Stewart, and E. N. Lightfoot, *Transport phenomena*, John Wiley, New York (1960).
112. G. L. Borman and K. W. Ragland, *Combustion Engineering*, McGraw-Hill, New York (1998).
113. J. F. Griffiths, Prog. Energy Combust. Sci., v.21, pp.25-107 (1995).
114. P. C. Phillipi and H. A. Souza, Int. J. Multiphase Flow, v.21, pp.667-691 (1995).
115. J. W. Cahn, P. Fife and O. Penrose, Acta Mater., v.45, pp.4397-4413 (1997).
116. I. Steinbach, F. Pezzola, B. Nestler, M. Seeβelberg, R. Prieler and G. J. Schmitz, Physica D, v.94, pp.135-147 (1996).

References

[1] T. Takeno and K. Sato, Combust. Sci. Technol., v.20, pp.73-84 (1979).

[2] Y. Yoshizawa, S. Kiyoshi and R. Echigo, Int. J. Heat Mass Transfer, v.31, pp.311-319 (1988).

[3] S. B. Sathe, R. E. Peck and T. W. Tong, Int. J. Heat Mass Transfer, v.33, pp.1331-1338 (1990).

[4] R. Echigo, R., "Radiation enhanced/controlled phenomena of heat and mass transfer in porous media," *Proceedings of the 1st ASME/JSME Joint Thermal Engineering Conference*, v.4, pp.xxi-xxxii (1991).

[5] P. F. Hsu and J. R. Howell, Experimental Heat Transfer, v.5, pp.293-313 (1993).

[6] P. Hsu and R. D. Matthews, Combustion and Flame, v.93, pp.457-466 (1993).

[7] M. Sahraoui and M. Kaviany, Int. J. Heat and Mass Transfer, v.37, pp.2817-2834 (1994).

[8] T. W. Tong and W. Li, J. Quant. Spectrosc. Radiat. Transfer, v.53, pp.235-248 (1995).

[9] J. R. Howell, M. J. Hall and J. L. Ellzey, Prog. Energy Combust. Sci., v.22, pp.121-145 (1996).

[10] R. W. Rice, *Porosity of Ceramics*, Marcel Dekker, New York (1998).

[11] E. Koberstein and G. Wannemacher, *Catalysis and Automotive Pollution Control*, SAE, pp.155-172 (1987)

[12] J.W. Beeckman and L. L. Hegedus, Ind. Eng. Chem. Res., v.30, pp.969-978 (1991).

[13] K. Tamaru and G. A. Mills, Catalysis Today, v.22, pp.349-360 (1994).

[14] J. N. Armor, Catalysis Today, v.26, pp.99-105 (1995).

[15] W. C. Pfefferle adn L. D. Pfefferle, Prog. Energy Combust. Sci., v.12, pp.25-41 (1986).

[16] W. C. Pfefferle and L. D. Pfefferle, Catal. Rev.-Sci. Eng., v.29, pp.219-267 (1987).

[17] A. A. Barresi, S. L. Hung and L. D. Pfefferle, The Chemical Engineering Journal, v.50, pp.123-131 (1992).

[18] H. Ikeda, P. A. Libby and F. A. Willians, Combustion and Flame, v.93, pp.138-148 (1993).

[19] P. Markatou, L. D. Pfefferle and M. D. Smooke, Combustion and Flame, v.93, pp.185-201 (1993).

[20] L. D. Pfefferle, Catalysis Today, v.26, pp.255-265 (1995).

[21] R. A. Dalla Betta, J. C. Schlatter, D. K. Yee, D. G. Loffler and T. Shoji, Catalysis Today, v.26, pp.329-335 (1995).

[22] H. Arai and H. Fukuzawa, Catalysis Today, v.26, pp.217-221 (1995).

[23] S. Maruko, T. Naoi and M. Onedera, Catalysis Today, v.26, pp.309-317 (1995).

[24] K. Eguchi and H. Arai, Catalysis Today, v.29, pp.379-386 (1996).

[25] R. Jones, Surface and Coatings Technology, v.96-95, pp.118-122 (1997).

[26] C. Niehorster, G. Arends and M. Schreiber, Combustion and Flame, v.110, pp.140-151 (1997).

[27] D. A. Hickman and L. D. Schmidt, AIChE Journal, v.39, pp.1164-1177 (1993).

[28] L. D. Schmidt, M. Huff and S. S. Bharadwaj, Chemical Engineering Science, v.49, pp.3981-3994 (1994).

[29] S. S. Bharadwaj and L. D. Schmidt, Fuel Processing Technology, v.42, pp.109-127 (1995).

[30] M. Ziauddin, A. Balakrishna, D. G. Vlachos and L. D. Schmidt, Combustion and Flame, v.110, pp.377-391 (1997).

[31] A. Ferrenberg, SAE Transactions, SAE 900911 (1990).

[32] A. Ferrenberg, AIAA Journal, AIAA 90-2510 (1990).

[33] A. Ferrenberg, SAE Transactions, SAE 940946 (1994).

[34] K. Hanamura, K. Bohda and Y. Miyairi, Energy Convers. Mgmt., v.38, pp.1259-1266 (1997).

[35] G. A. Fateev and O. S. Rabinovich, Int. J. Hydrogen Energy, v.27, pp.915-924 (1997).

[36] C.-W. Park and M. Kaviany, "Combustion Thermoelectric Tube," *Proceedings of the 1999 National Heat Transfer Conference*, Albuquerque, New Mexico (1999).

[37] C.-W. Park and M. Kaviany, J. Heat Transfer, submitted (1999).

[38] K. Hanamura, K. Akagi and K. Koyanagi, "Autothermic Reforming by Reciprocating-Flow Super-Adiabatic Combustion in Porous Media," *Proceedings of the 5th ASME/JSME Joint Thermal Engineering Conference*, pp.1-6, San Diego, California (1999).

[39] M. Kaviany, *Principles of Heat Transfer*, ME370 Course Pack, Department of Mechanical Engineering and Applied Mechanics, The university of Michigan, Ann Arbor, MI (1999).

[40] C.-W. Park and M. Kaviany, *Optimization of High-Temperature Radiant Burner*, Report to Air Liquide, CRCD, Joay-en-Josas, France (1999).

[41] R. J. Farrauto, React. Kinet. Catal. Lett., v.60, pp.233-241 (1997).

[42] A. C. MacIntosh, M. Bains, W. Crocombe and J. F. Griffiths, Combustion and Flame, v.99, pp.541-550 (1994).

[43] M. Kaplan and M. J. Hall, Experimental Thermal and Fluid Science, v.11, pp.13-20 (1995).

[44] V. V. Martynenko, R. Echigo and M. Yoshida, Int. J. Heat Mass Transfer, v.41, pp.117-126 (1998).

[45] A. M. Kanury and P. L. Blackshear, Jr., Comb.Sci. and Tech., v.1, pp.339-355 (1970).

[46] C. Di Blasi, Combust. Sci. and Tech., v.90, pp.315-340 (1993).

[47] M. Fatehi adn M. Kaviany, Comb. Flame, v.99, pp.1-17 (1994).

[48] D. A. Schult, B. J. Matkowski, V. A. Volpert and A. C. Fernandez-Pello, Combustion and Flame, v.104, pp.1-26 (1996).

[49] C. Brereton, Resources, Conservation and Recycling, v.16, pp.227-264 (1996).

[50] M. Fatehi and M. Kaviany, Int. J. Heat and Mass Transfer, v.40, pp.2607-2620 (1997).

[51] C. P. Garner and J. C. Dent, SAE Transactions, SAE Paper No. 880007 (1988).

[52] R. Noirot, P. Gilot, R. Gadiou, and G. Prado, Combust. Sci. Tech., v.95, pp.139-160 (1994).

[53] G. C. Koltsakis and A. M. Stamelos, Ind. Eng. Chem. Res., v.35, pp.2-13 (1996).

[54] Z. A. Munir, Ceramic Bulletin, v.67, pp.342-349 (1988).

[55] A. G. Merzhanov, "Self-propagating high-temperature synthesis: twenty years of search and findings," *Combustion and Plasma Synthesis of High Temperature Materials*, Chap.1, edited by Z. A. Munir and J. B. Holt, VCH Publishers, New York (1990).

[56] A. Varma and J.-P. Lebrat, Chem. Eng. Sci., v.47, pp.2179-2193 (1992).

[57] K. Brezinski, "Gas-phase combustion synthesis of materials," *Proceedings of the Twenty-Sixth Symposium (International) on Combustion/The Combustion Institute*, pp.1805-1816 (1996).

[58] M. Wooldridge, Prog. Energy Combust. Sci., v.24, pp.63-87 (1998).

[59] A. A. M. Oliveira and M. Kaviany, Int. J. Heat Mass Transfer, v.42, pp.1059-1073 (1999).

[60] A. A. M. Oliveira and M. Kaviany, Int. J. Heat Mass Transfer, v.42, pp.1075-1095 (1999).

[61] R. Armstrong, Combust. Sci. Tech., v.71, pp.155-174 (1990).

[62] S. Whitaker, "Simultaneous Heat, Mass, and Momentum Transfer in a Porous Media: A Theory of Drying," *Advances in Heat Transfer*, v.7, pp.119-203, edited by J. P. Hartnett and I. Irvine, Academic Press, New York (1977).

[63] M. Quintard and S. Whitaker, Transport in Porous Media, v.3, pp.357-413 (1988).

[64] M. Quintard and S. Whitaker, Transport in Porous Media, v.5, pp.341-379 (1990).

[65] M. Quintard and S. Whitaker, "One- and two-equation models for transient diffusion processes in two-phase systems," *Advances in Heat Transfer*, v.23, pp.369-464, edited by J. P. Hartnett and T. F. Irvine, Academic Press (1993).

[66] M. Quintard and S. Whitaker, Chem. Engng. Sci., v.48, pp.2537-2564 (1993)

[67] M. Quintard and S. Whitaker, Transport in Porous Media, v.14, pp.163-177 (1994).

[68] M. Quintard and S. Whitaker, Transport in Porous Media, v.14, pp.179-206 (1994).

[69] M. Quintard, M. Kaviany and S. Whitaker, Advances in Water Resources, v.20, pp.77-94 (1997).

[70] M. Kaviany, *Principles of Heat Transfer in Porous Media*, Springer-Verlag, Corrected 2nd Ed., (1999).

[71] D. Vortmeyer, "Radiation in packed solids," *Proceedings of tht 6th International Heat Transfer Conference*, v.6, pp.525-539, Toronto, Canada (1978).

[72] C. L. Tien and B. L. Drolen, "Thermal radiation in particulate media with dependent and independent scattering," *Annual Review of Numerical Fluid Mechanics and Heat Transfer*, v.1, pp.1-32, Hemisphere, Washington (1987).

[73] R. Viskanta and M. P. Menguc, Appl. Mech. Rev., v.42, pp.241-259 (1989).

[74] T. W. Tong, S. B. Sathe and R. E. Peck, Int. J. Heat Mass Transfer, v.33, pp.1339 (1990).

[75] B. P. Singh and M. Kaviany, "Radiation in Porous Media," *Advances in Heat Transfer*, v.23, pp.369-464, edited by J. P. Hartnett and T. F. Irvine, Academic Press (1993).

[76] T. J. Hendricks and J. R. Howell, J. Heat Transfer, v.118, pp.79-87 (1996).

[77] D. Doermann, and J. F. Sacadura, J. Heat Transfer, v.118, pp.88-93 (1996).

[78] X. Fu, R. Viskanta,and J. P. Gore, Int. Comm. Heat Mass Transfer, v.24, pp.1069-1082 (1997).

[79] P. Furmanski, S. Wisniewski and J. Banaszek, J., "Analysis of nonlocal character of radiation heat transfer in themal insulations," *Proceedings of the 11th International Heat Transfer Conference*, v.7, pp.379-384, Kyongiu, Korea (1998).

[80] K. Kamiuto and T. Matsushita, "High-temperature radiative properties of open-cellular porous materials," *Proceedings of the 11th International Heat Transfer Conference*, v.7, pp.385-390, Kyongiu, Korea (1998).

[81] S. Zhdanov, L. A. Kennedy and G. Koester, Combustion and Flame, v.100, pp.221-231 (1995).

[82] A. P. Aldushin, I. E. Rumanov and B. J. Matkowsky, Combustion and Flame, v.118, pp.76-90 (1999).

[83] A. A. Mohamad, S. Ramadhyani and R. Viskanta, Int. J. Heat Mass Transfer, v.37, pp.1181-1191 (1994).

[84] S. S. Penner and A. L. Berlad, Energy, v.20, pp.311-324 (1995).

[85] A. Bell, Chem. Eng. Science, v.45, pp.2013-2026 (1990).

[86] B. C. Gates, *Catalytic Chemistry*, John Wiley (1992).

[87] K.A. Bethke, M. C. Kung, B. Yang, M. Shah, D. Alt, C. Li, and H. H. Kung, Catalysis Today, v. 26, pp.169-183 (1995).

[88] A. P. Walker, Catalysis Today, v.26, pp.107-128 (1995).

[89] R. I. Masel, *Principles of Adsorption and Reaction on Solid Surfaces*, John Wiley (1996).

[90] P. Gilot, M. Guyon and B. R. Stanmore, Fuel, v.76, pp.507-515 (1997).

[91] R. D. Gonzales, T. Lopez,and R. Gomez, Catalysis Today, v.35, pp.293-317 (1997).

[92] J. J. Chen and J. Ruckenstein, Journal of Catalysis, v.69, pp.254 (1981).

[93] F. J. Keil and C. Rieckmann, Chemical Engineering Science, v.49, pp.4811-4822 (1994).

[94] S. Arbabi and M. Sahimi,Chemical Engineering Science, v.46, pp.1739-1747 (1991).

[95] S. Arbabi and M. Sahimi, Chemical Engineering Science, v.46, pp.1749-1755 (1991).

[96] J. H. Sinfeld, G. H. Via and F. W. Lytle, Catal. Rev. Sci., v.26, pp.81 (1984)

[97] F. J. Keil, Chemical Engineering Science, v.51, pp.1543-1567 (1996).

[98] H. S. Nan, M. M. Dias and A. E. Rodrigues, Chem. Eng. J., v.57, pp.101-114 (1995).

[99] D. Arnost and P. Schneider, Chem. Eng. J., v.57, pp.91-99 (1995).

[100] J. W. Veldsink, R. M. J. Van Damme, G. F. Versteeg, and W. P. M. Swaaij, Chem. Eng. J., v.57, pp.115-125 (1995).

[101] G. R. Jerauld, J. C. Hatfield, L. E. Scriven and H. T. Davis, J. Phys. C, v.17, pp.1519-1529 (1984).

[102] G. R. Jerauld, L. E. Scriven and H. T. Davis, J. Phys. C, v.17, pp.3429-3444 (1984).

[103] M. Sahimi, Physics Reports, v.306, pp.213-395 (1998).

[104] L. Zhang and N. A. Seaton, Chemical Engineering Journal, v.49, pp.41-50 (1994).

[105] V. Alvarado, H. T. Davis and L. E. Scriven, Chemical Engineering Science, v.52, pp.2865-2881 (1997).

[106] M.-O. Coppens and G. F. Froment, Chem. Eng. Sci., v.50, pp.1027-1039 (1995).

[107] W. C. Conner and C. O. Bennet, J. Chem. Soc. Faraday Trans., v.89, pp.4109-4114 (1993).

[108] K. W. Limbach and J. Wei, AIChE Journal, v.36, pp.242-248 (1990).

[109] N. A. Seaton, Chemical Engineering Journal, v.46, pp.1895-1909 (1991).

[110] R. L. Portsmouth and L. F. Gladden, Chemical Engineering Journal, v.46, pp.3023-3036 (1991).

[111] R. B. Bird, W. E. Stewart, and E. N. Lightfoot, *Transport phenomena*, John Wiley, New York (1960).

[112] G. L. Borman and K. W. Ragland, *Combustion Engineering*, McGraw-Hill, New York (1998).

[113] J. F. Griffiths, Prog. Energy Combust. Sci., v.21, pp.25-107 (1995).

[114] P. C. Phillipi and H. A. Souza, Int. J. Multiphase Flow, v.21, pp.667-691 (1995).

[115] J. W. Cahn, P. Fife and O. Penrose, Acta Mater., v.45, pp.4397-4413 (1997).

[116] I. Steinbach, F. Pezzola, B. Nestler, M. Seeβelberg, R. Prieler and G. J. Schmitz, Physica D, v.94, pp.135-147 (1996).

PROSPECTS OF HIGHLY EFFICIENT POWER GENERATION TECHNOLOGIES BASED ON NATURAL GAS UTILIZATION TO REDUCE CO_2 EMISSION

Masaru Hirata
Professor, Shibaura Institute of Technology
Professor Emeritus, The University of Tokyo
President, Cogeneration Center of Japan
Vice President, Asian Pipeline Research Society of Japan
E-mail: hirata@se.shibaura-it.ac.jp Fax: (048) 687-5197

Keywords: CO_2 reduction, cogeneration, combined cycle, repowering, system energy, micro gas turbines, solid polymer fuel cells, natural gas pipelines

ABSTRACT. In order to reduce CO_2 emission to prevent global warming, the most promising way for electric generation in the Northeast Asia is to introduce highly efficient system technologies such as combined cycle, repowering, gas turbine integrated garbage incineration, gas turbine combined with coal fired steam power generation, gas turbine combined with nuclear power generation, and cogeneration including micro gas turbine and polymer fuel cell technologies. All of these energy system technologies should be based on natural gas as fuel. This paper presents a brief survey of these new technologies.

In accordance with the direction of introducing these highly efficient technologies of power generation, natural gas demand in the Northeast Asia should be drastically increased. To meet the big demand estimation, it is essential to have infrastructures as pipelines. As it is well known, in Europe, over 800,000km high pressure natural gas trunk pipelines have already been existed. In North America, there has been 440,000km in length existed. On the other hand, in Asia, there is nothing. This paper also proposes to construct the Northeast Asian Pipeline Network, by which natural gas is transported from candidate sources in East Siberia and in Central Asia to China, Mongolia, Korea, North Korea and Japan.

1. INTRODUCTION

Economic growth in the Asia-Pacific region is expected to bring about a conspicuous growth in energy demand. If the predicted rapid growth of energy consumption is met chiefly by coal, environmental pollution would be unavoidable. Oxide pollutants, especially sulfur oxides and nitrogen oxides, emitted in China have already begun to expose South Korea and Japan to acid rain and snow. Also a huge amount of carbon dioxide is emitted in the region, causing serious results to global warming. It should be essential to realize as soon as possible that natural gas be supplied to the countries in Asia-Pacific region, and that the energy saving system technologies described in this paper be spread there.

It is reported that the Asia-Pacific region has vast reserves of untapped natural gas. The development and utilization of these resources at sustainable levels constitutes a crucial issue in the future. In order to increase the intra-regional use of these vast reserves of natural gas, the National Pipeline Research Society of Japan proposed[(1)] the construction of international trunk pipelines, called the "Trans-Asian Natural Gas Pipeline Network", linking the gas fields with major consuming markets.

This Trans-Asian Pipeline will play a vital role in the international infrastructure of the 21st century and assist in finding a solution to problems involving the global environmental problems and a long-lasting security in Asia.

2. THERMODYNAMICALLY FUNDAMENTAL CONCEPT OF HIGHLY EFFICIENT POWER GENERATION SYSTEM TECHNOLOGIES

Everyone may envisage a plan to build series of dams and hydro-electric power stations along a river in different reaches from the top of a mountain to the bottom of sea water level so that the water head is used up completely, as shown in Fig.1. Water, after reaching the sea level, is no longer useful for power generation. As the proverb says, spilt water cannot be gathered again. In the case of heat utilization, temperature differences correspond to the water head differences and the ambient temperature corresponds to the sea water level. Effective utilization of heat energy requires arrangements to use up what corresponds to water head in a full

range of heat potential from a high temperature of more than 1,500°C generated by burning fuel to the ambient temperature of 15°C, as shown in Fug.1. Heat energy, after falling down to the ambient temperature, is no longer useful, but strangely, efforts have seldom been made to use up heat in decreasing order of temperature like the way water is used in hydro-electric power generation.

Once fuel is ignited, it should be considered firstly to operate a heat engine to produce motive power. It has been the past practice to install boilers when heat or steam is needed. From now on, we have to think firstly of installing engines or gas turbines whenever we want to get heat. The first step in rational use of heat energy is to change higher temperature heat into motive power by using a heat engine and then the lowered temperature heat discharged from the engine is utilized for baths or space heaters.

This kind of "series-flow" heat utilization system, in which higher temperature heat is utilized for electric power generation by adopting heat engines and lowered temperature heat discharged from the engines is utilized for heat applications, is called as "cogeneration." The technology according to the thermodynamic principle is the only way to materialize energy conservation technologically. With this in mind, the following paragraphs will propose some specific highly efficient technologies with priority on high-temperature gas turbines fueled by natural gas, which is the most effective key technology to turn high-temperature heat into motive power.

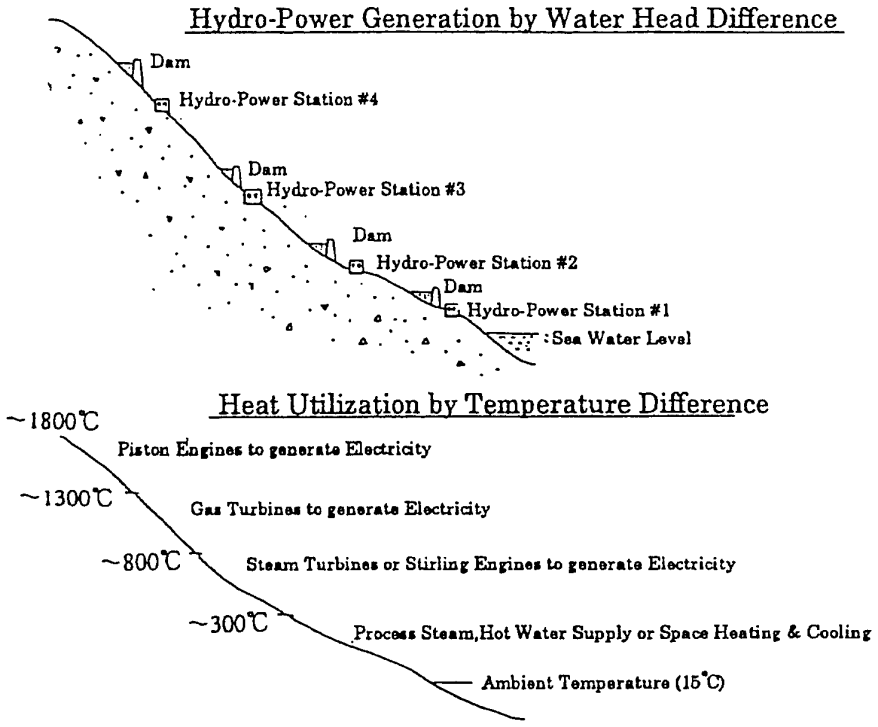

Fig.1. Similarity between water head utilization and temperature difference

3. RECENT ADVANCES IN HIGH TEMPERATURE GAS TURBINE TECHNOLOGIES

3.1. MHI's Air-Cooled 1,500 °C Class Gas Turbine

Natural gas-fired gas turbines use clean or low-pollution fuel and, therefore, their TIT - turbine inlet temperature - continues to rise steadily, reaching 1,350°C now in commercial installations. Mitsubishi Heavy Industries (MHI) has been developing 1,500°C class industrial gas turbine Type 501G• 701G from 1993. From February 1997, 501G (60Hz machine) has been test running at their Takasago factory, and 701G (50Hz machine) has been on test running from October 1998 and will be in commercial operation from July 1999 at Higashi-Niigata Combined-Cycle Power Station of Tohoku Electric Power Company of Japan. The output of gas turbine is

225MW and of steam turbine is 105MW, and in total 330MW. The efficiency of gas turbine unit is over 38% (LHV), and the overall efficiency of combined cycle will be over 58% (LHV). In this machine, the combustor is steam cooled and the rotor blade is full-coverage film cooled and also thermal barrier coated as shown in Fig.2.

3.2. Ceramic Gas Turbines

300kW class ceramic gas turbines for cogeneration application have been developed under the Japan's National New Sunshine Project from 1988, and was terminated in March 1999. The targets of this project are as that TIT is 1,350°C and the unit efficiency is over 42% (LHV). CGT302 unit developed by Kawasaki Heavy Industries Ltd. (KHI) cleared this target on March 14, 1999, by 2-shaft design of gas generator turbine of 64,000rpm and power turbine of 47,800rpm. They obtained power output of 322kW and thermal efficiency of 42.1% at TIT of 1,396°C under ISO conditions. NOx emission was 31.7ppm (O_2=16%) by adopting natural gas pre-mixed lean burn combustion. These values are the world champion record of these small sized gas turbines. Ceramic parts are made of Silicon Nitride (Si. N.) and are provided by Kyocera Corporation.

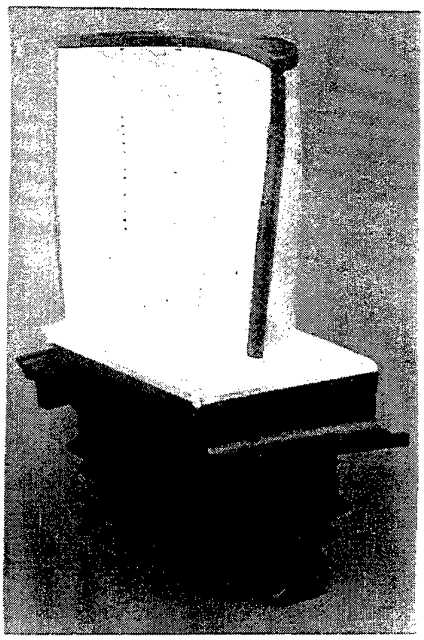

Fig.2. MHI's 1,500°C class gas turbine rotor blade with full coverage film cooling and thermal barrier coating

KHI is carrying on the endurance test under TIT of 1,200°C and at the end of June 1999, the total running hour reached 2,147 hours with 137 start and stop.

In U.S.A., CSGT (Ceramic Stationary Gas Turbine) project is going on from 1992 under the auspices of DOE. The 1st stage nozzle and rotor blade, and also the combustor, of Centaur 50 gas turbine (5MW) of Solar Turbines Inc. were replaced by ceramic components, and the target TRIT (Turbine Rotor Inlet Temperature) is 1,121°C. The nozzle is supplied by NGK Spark Plug Co. of Japan and the rotor blade is by AlliedSignal Inc., and both are made of Silicon Nitride. The combustor is made of Silicon Carbide CFCC (Continuous Fiber Reinforced Ceramic Composites) supplied by Dupont Co.. From April 1997, 4,000hr endurance field test has started under the TRIT of 1,010°C at the oil production site of ARCO (Atlantic Richfield Co.) in Bakersfield, California. After 948 hours running, in July 1999, the machine was stopped and found that 62 rotor blades were broken by the foreign object hitting.

3.3. ABB's "Sequential Combustion"

At the ASME Cogen Turbo '93, which was held in Bournemouth, UK, the inventor of ABB (Asea Brown Boveri

Power Generation Ltd.) 's "Sequential Combustion", Mr. Hans U. Frutschi, was attended in the booth of ABB's exhibition. It was the first release of this innovative technology. As shown in Fig.3, one single stage of turbine nozzle and rotor is provided just after the first combustor. The combustion gas after expanded at the first stage turbine immediately enters the second combustor, where the fuel (natural gas) is injected again and the gas is reheated and led into the remained turbine stages. The advantages of this system are: high exhaust temperature, high gas turbine output, and low NOx. ABB has now commercialized this concept as GT24/GT26. GT26 data (at ISO conditions and natural gas as fuel) are: Gross output 241MW, gross efficiency 38.2%(LHV), compression ratio 30, exhaust mass flow 543kg/s, exhaust gas temperature 610°C, Nox<25 (15% O_2). This technology is so useful for the highly efficient energy system technologies explained later in this paper.

4. HIGHLY EFFICIENT POWER GENERATION SYSTEM TECHNOLOGIES BASED ON HIGH TEMPERATURE GAS TURBINES FUELLED BY NATURAL GAS

Now some examples of highly efficient power generation system technologies based on high temperature gas turbines are proposed here. Those high-temperature gas turbines are adopted as the topping of a thermodynamic cycle and use turbine exhaust heat at the bottoming, as explained above in Fig.1 as the fundamental concept. High temperature gas turbines can be operated because the fuel is natural gas. Natural gas does not contain impurity as sulfur or heavy metals as vanadium. Those impurities may cause a serious corrosion problem on turbine materials at higher temperature range. Therefore natural gas is the most valuable fuel within fossil fuels compared with coal or oil, because of its softness to hardware as well as to environment.

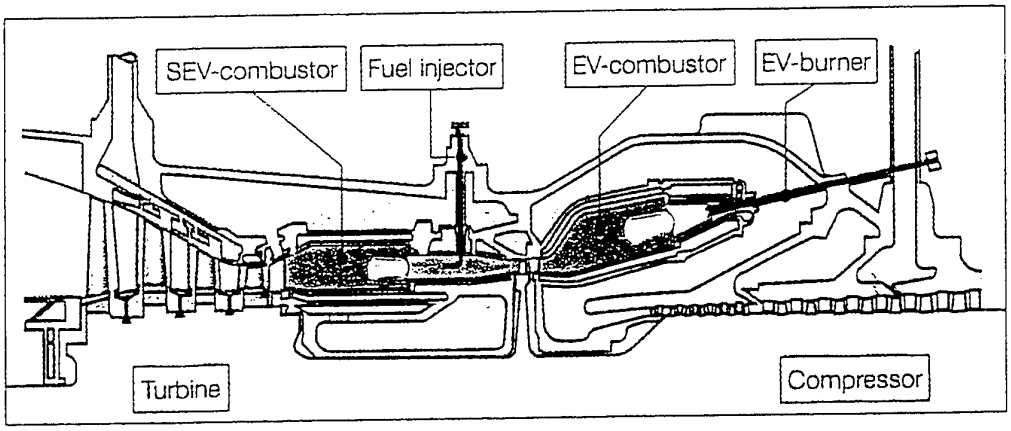

Fig.3. Concept of "Sequential Combustion" developed by ABB [2]

4.1. Combined Cycle

Recently it is usual for power generation industries to introduce combined cycle plants in case of utilizing natural gas as fuel. If the turbine inlet temperature is increased up to 1,500°C, the combined cycle efficiency is estimated to over 58% (LHV) as in the case of Japan's Higashi-Niigata power plant explained before.

In the case of ABB's sequential combustion, higher exhaust gas temperatures can be obtained with moderate gas turbine inlet temperatures, therefore the efficiency in the combined cycle process increases significantly compared with the case of conventional gas turbine. Fig.4 shows an example [2] of estimated comparison of the standard gas turbine process with the sequential combustion process. It shows the efficiency in the combined cycle process as a function of the power density (generated electric output in relation to the air mass flow). The resulting curve groups for both processes are based on the turbine inlet temperature and compressor pressure ratio. It can be seen that at similar turbine inlet temperatures, the gas turbine with sequential combustion achieves considerable efficiency advantages. In addition, the process with reheat indicates a higher potential for further development to efficiencies in the 60 percent range.

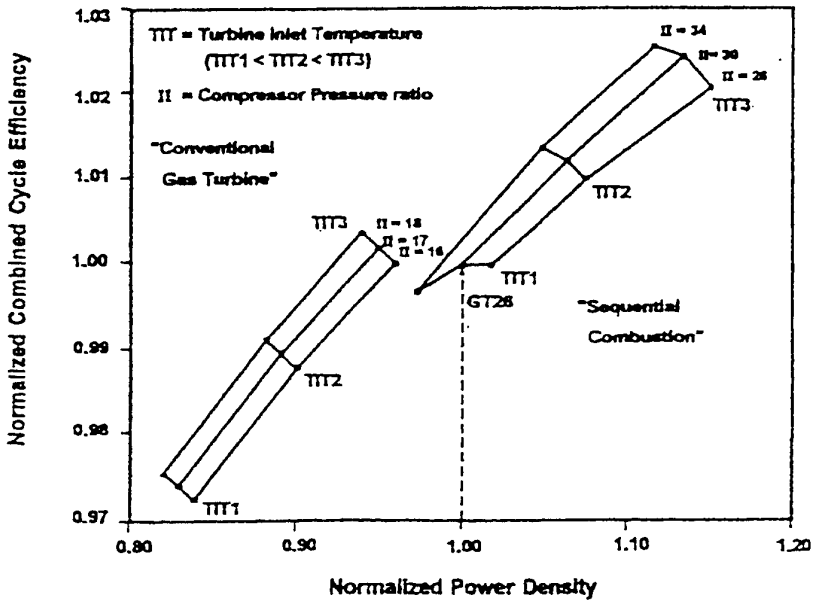

Fig.4. Efficiency increase due to sequential combustion in combined-cycle process

4.2. Cogeneration

Cogeneration systems in Japan reached 2,777 units with an installed capacity of 4,627MW at The end of March 1999. This accounts for some 2% of the total power generation capacity in Japan. The government decided to promote to introduce a cogeneration capacity of 10GW by the year 2010 through a mix of deregulation measures.

In Europe, they consider that cogeneration is the most promising measure to reduce CO_2 emission. For example, Denmark presented their national report to COP1 (The 1st Conference of the Parties of the United Nations Framework Convention on Climate Change) which was held in Berlin in March 1995, promising to reduce CO_2 emission until 2000 up to 7.9% of the level in 1990, and also the Netherlands up to 3.7%. The measure of the first priority stated in their reports is cogeneration. Fig.5 shows the propagation of the cogeneration into Europe. It is shown that these two countries, as well as Finland, are the leading countries of cogeneration in

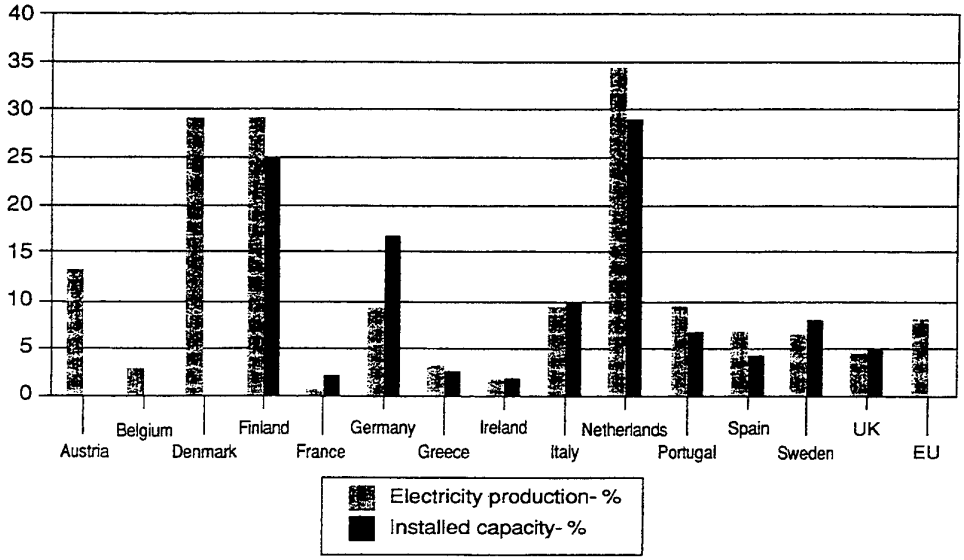

Fig.5. Cogeneration in Europe (data from"Cogen Europe")

Europe, that means around 30% of electric production and of installed capacity are supplied by cogeneration. The national reports of these countries promised that these figures of percentage should be increased over 40% until 2000. The major market of heat in these countries is district heating, and, in the Netherlands, greenhouses too.

4.3. Repowering

A method to retrofit existing boiler-steam turbine power plants improving thermal efficiency by introducing high temperature gas turbines is called "repowering." The underlying principle of this method is to use up all available heat from the top to bottom of its temperature range exactly in accordance with the fundamental concept of thermodynamics as previously explained.

Again ABB's sequential combustion is very useful for repowering. The first example [2] of GT26 application was to enter commercial service in July 1998 at the Rheinhafen steam power plant of the German utility Badenwerk AG, Karlsruhe. An old 100MW coal fired steam power plant commissioned in 1964 is repowered by GT26 and the power output in combined cycle mode will increase to 360MW (Steam Turbine : 120MW and Gas Turbine : 240MW). The old hard coal boiler is replaced by a gas turbine and a heat recovery steam generator, and the efficiency is increased from 38% to 58% (gross). The steam conditions are almost the same as before conversion as HP pressure of 153bar and temperature of 540°C, and reheat pressure of 40bar and temperature of 530°C. Fig.6 is a schematic process flow diagram.

A large number of similar plants are existing especially in the Northeast Asia, and if those plants are to be repowered as similar manner, a vast amount of CO_2 reduction is estimated.

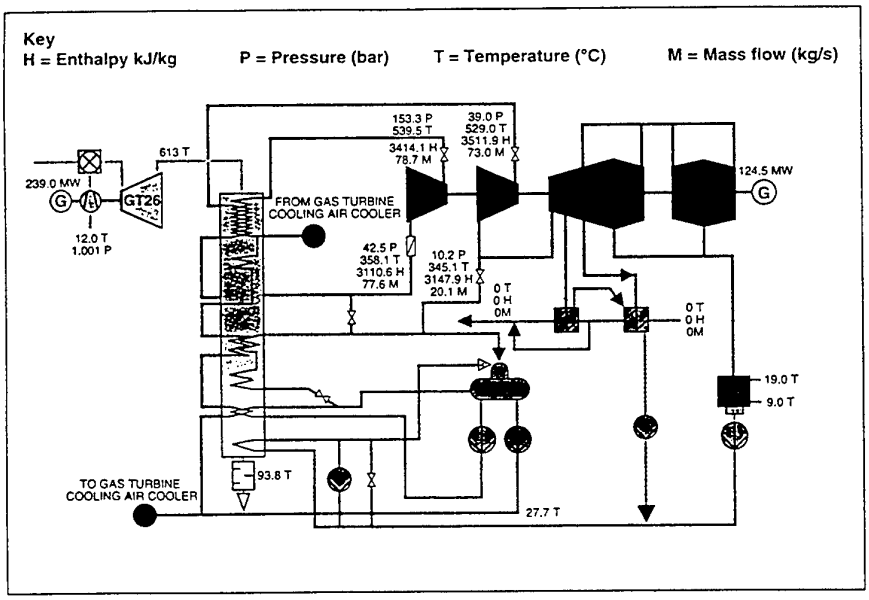

Fig.6. Schematic flow diagram of repowering of old coal-fired Rheinhafen steam power plant by GT26 advanced gas turbine

4.4. Gas Turbine Combined Garbage Incineration Plant

There are now some 1,900 garbage incineration facilities in Japan, but combustion heat from incinerators is seldom utilized, because of the serious corrosion problem of boiler tubes by hydrochloric acid contained in combustion gas. Currently combustion heat is utilized for power generation at only 180 incineration facilities, and at all other facilities the heat is discharged into the air. Even if the steam temperature is held down to the level which does not cause the corrosion of boiler tubes, i.e., about 290°C, a natural gas fueled gas turbine is installed additionally, and the exhaust gas of which is used to superheat the steam from the incinerator, resulted to become a combined cycle. Then the incineration facility would become changed into a highly efficient power generation plant. This proposal by the author has been promoted since fiscal 1993 as a Ministry of Home Affairs project under the name of "Super Waste-to-Energy Power Generation."

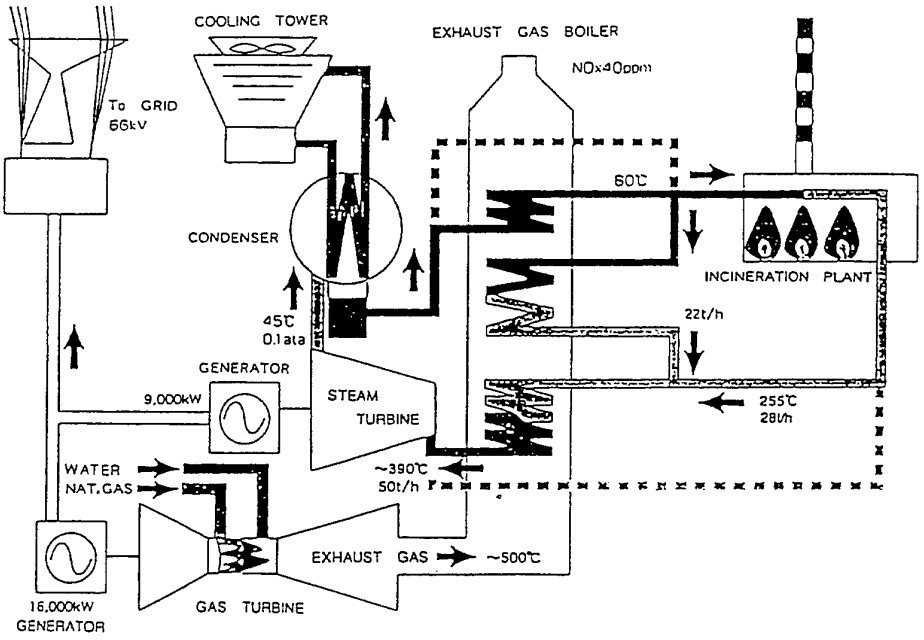

Fig.7. Schematic Flow Diagram of Takahama Power Plant as the 1st"Super Waste-to-Energy Power Generation"in Japan

The first super waste-to-energy power generation plant is the Takahama Plant in Gunma prefecture, which was started in commercial operation in November 1996. This plant is composed of 3 incinerators of 150T/D capacity, and 28t/h steam from this incineration plant, the temperature of which is limited as 255°C, is superheated up to the temperature of around 390°C by a 17MW gas turbine exhaust (temperature around 500°C) as shown schematically in Fig.7. This superheated steam drives a 10MW steam turbine. In total, 25MW electric output is obtained and the efficiency is increased from 7% up to 35%. Exhaust steam is used at the neighboring nursing home.

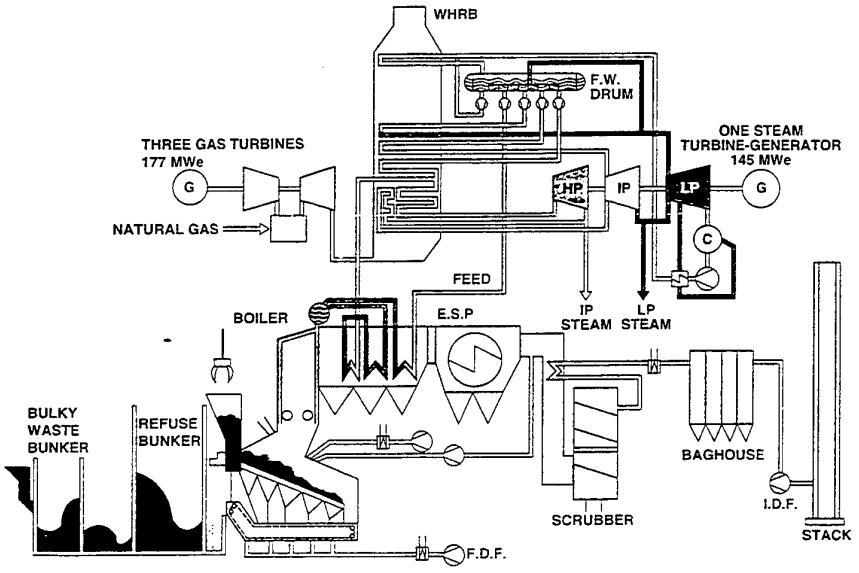

Fig.8. Schematic flow diagram of Moerdijk Gas Turbine combined incineration plant with industrial cogeneration

Fig.8 shows the process diagram [3] of the largest gas turbine integrated incineration plant in the world which was put into operation in February 1997 at Moerdijk in South-Netherlands by the Dutch electric utility N.V. Elektriciteits Produktiemaatschappij Zuid-Nederland (EPZ). The fundamental concept is completely same as Japanese plant. In Dutch plant, 280t/h of 100bar and 400°C steam from 3 garbage incinerators of a capacity of 550T/D is obtained, some steam of which is superheated to 510°C by the exhaust gas from 3 units of Siemens V64.3 gas turbine of 60MW each, and then sent into a 180MW steam turbine. The total electrical output is 339MW without extraction of process steam. Some 145t/h of 23.5bar and 322°C steam is extracted and sent to the neighboring Shell Chemical plant across a river, i.e., the system is operated as the industrial cogeneration. The electrical efficiency is over 52% and the overall efficiency of the plant becomes over 69%.

4.5. Natural Gas Fired Gas Turbine Combined With Nuclear Power Plant

A similar idea should be applied to nuclear power generation. At present Japan has 51 nuclear power reactors with a total installed capacity of 45GW. The allowable limit of steam cycle temperature for nuclear power plant is around 340°C because the maximum pressure of the plant is limited by the strength of the reactor pressure vessel and the maximum temperature is limited by the saturation temperature corresponding to the system pressure.

It is desirable, therefore, that nuclear power plants be repowered by installing high-temperature gas turbines in their sites. Rough estimation has shown that an 1GW nuclear reactor should be repowered by gas turbines of 1.2GW in total and the steam turbine becomes 1.5GW, and the total output should become 2.7GW. Thermal efficiency is increased up to 44~45% compared with 30% of conventional nuclear reactors. Similar idea has been presented by the Battelle Memorial Institute in USA as shown in Fig.9.

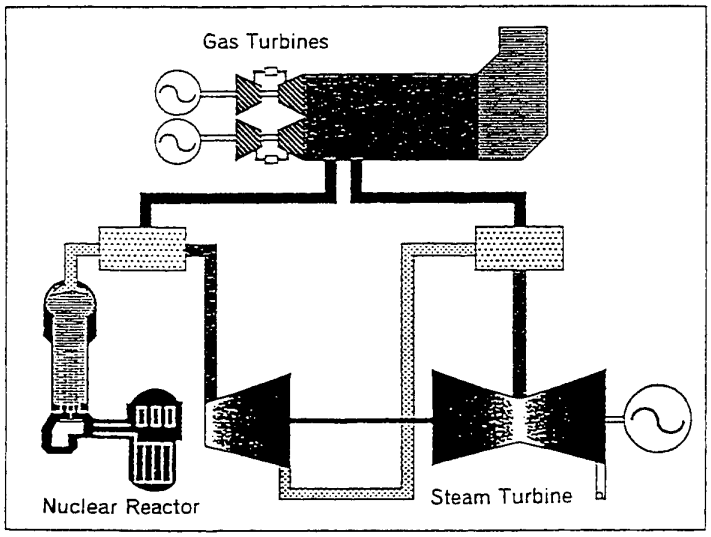

Fig.9. Repowering of nuclear reactor by natural gas fired high temperature gas turbines (Battelle Memorial Institute)

5. RECENT DEVELOPMENTS OF MICRO COGENERATION BASED ON MICRO GAS TURBINES AND SOLID POLYMER FUEL CELLS

Recently it is remarkable that the development of micro gas turbines ranged 20~100kW. Fig.10 is the Pint-Size"28kW gas turbine package developed by Capstone Turbine Corporation in California, U.S.A.. TIT is approximately 700°C and the efficiency is 26%. The rotor shaft spins at 96,000rpm and air bearing is eliminating the need for lubricating oil and related maintenance. The dimensions of the package is 710W×1350L×1900H (mm) and the weight is 489kg. Their technology is an extension of the turbocharger. The target price would be around 550$/kW.

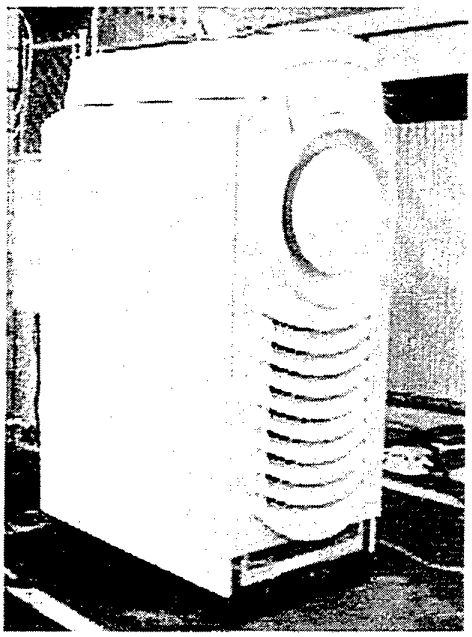

Fig.10. Capstone's 28kW gas turbine

Fig.11. AlliedSignal's 75kW gas turbine

Fig.11 is 75kW gas turbine package developed by AlliedSignal Power Systems Inc. in California, U.S.A.. Again the rotor speed is 116,000rpm and the generator is driven directly. TIT is 1,010°C and the unit efficiency becomes 28.5% with recuperator. The dimension of the package is 1220W×2330L×2370H (mm) and the weight is 1,540kg. The exhaust gas temperature is around 250°C.

Fig.12 is the schematic view of a 60kW$_e$ gas turbine cogeneration unit developed by Mega Limburg of Maastricht, Netherlands. The electric output is 60kW$_e$ and the thermal output is 238kW$_{th}$, and the overall efficiency as cogeneration becomes 87%. A radial compressor and a generator is driven directly by a radial turbine and the shaft speed is 105,000rpm. The exhaust gas temperature is 527°C. The supplier of this gas turbine is Bowman Power Systems Ltd. of U.K..

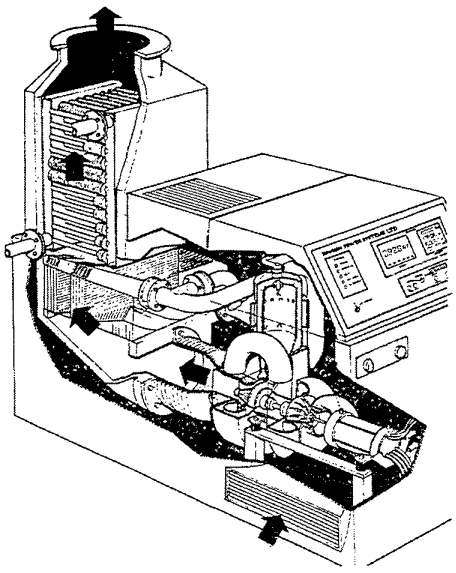

Fig.12. Mega Limburg's 60kW$_e$ gas turbine cogeneration package

In November 1998, the German automotive company, Daimler-Benz AG, has advertised on a Japanese newspaper that they will complete the mass production lines of fuel cell driven hybrid cars until 2004. Their partner in the fuel cell technology is Ballard Power Systems Inc. in Vancouver, Canada, and the author visited them in March 1998. Fig.13 shows the polymer membrane of 0.2mm thick which exchange protons. The membrane is coated with a platinum catalyst and an electrode made of gas-permeable graphite paper. Gas channels are milled on both sides of bipolar graphite plates, with hydrogen being fed into one channel and air being fed into the other. With the help of the catalyst, the hydrogen is ionized and broken down into positive hydrogen ions(protons) and negatively charged electrons. The protons can then migrate through the permeable film, so that the anode acquires a negative charge from the electrons left behind. In turn, the oxygen molecules on the cathode side, likewise excited by the catalyst, take on electrons. This process generates oxygen ions, and causes the cathode to acquire a positive charge.

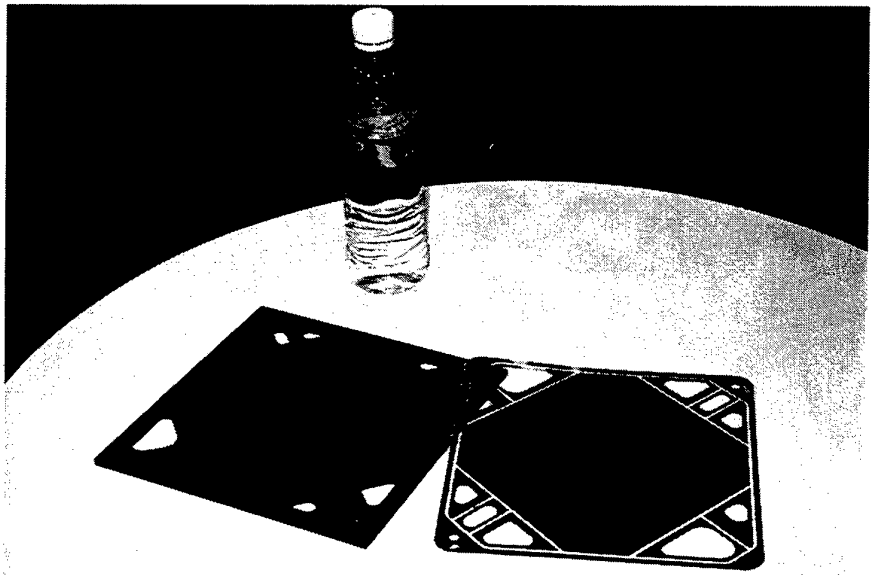

Fig.13. Proton exchange membrane (right) and graphite plate (left)

A potential difference can now build up between the cathode and the anode. If the electrodes are connected via an electric motor, for example, the electrons flow from the anode back to the cathode. The motor receives its power in this manner. At the same time, hydrogen and oxygen bond to form the reaction product water. In addition to this reaction product, heat is also generated. The latter can be used as cogeneration. The unit cell can produce around 0.7V, and the stack is formed of housing tightly packed unit cells as shown in Fig.14.

If the automotive industries go into mass production of the fuel cells, the cost should be drastically reduced. The Ballard people said that the fuel cell stack including reformer which produces hydrogen from methanol as fuel will be 50 Canadian dollars/kW for the car application and 1,500 Canadian dollars/kW for electric generator. The lifetime of the stack for car application is around 5,000 hours and 40,000 hours for generators.

Then the micro cogeneration unit for household application might become available up to 2010 at around 1,000 to 1,500US$/kW, and its lifetime should be estimated as around 20,000 hours. The lifetime is mainly decided by CO attack for catalyst. CO is produced as impurity during the process of reforming of fuel.

6. CO_2 REDUCTION POSSIBILITIES BY"SYSTEM ENERGY"TECHNOLOGIES

Almost all of the highly efficient energy systems explained above, except fuel cell technology, are the systems

Fig.14. Solid polymer fuel cell stacks developed by Ballard Power Systems Inc. for Daimler Benz AG (left : 40kW, right : 54kW)

composed of the elements based on"proven"technologies. Proven technologies do not require additional technological innovations, but original idea or concept is required to develop a new system. The increase of efficiency of primary energy utilization has the same meaning of new energy production without increase CO_2 emission. So these kind of technologies should be called as"system energy"technologies. Fuel cells are not heat engines and do not obey thermodynamic principles shown as Fig.1. But if the exhaust heat is used as cogeneration, it should be integrated into this category.

As a preparation for COP3 held in December 1997 in Kyoto, the Environmental Agency of Japan has organized a committee to make an estimation for the CO_2 reduction possibilities in Japan by adopting feasible technologies in these 10 years. The author has been working as the chairman of this committee. Table 1 shows the calculated results indicated by contribution % of each technology to the total amount. The Japan's total CO_2 emission in 1990 was 307Mt in carbon equivalent, and the total possible amount of CO_2 reduction in 2010 was estimated by this committee as around 20% of this value. But this value is based on quite reliable estimation of diffusion probability of each technology, and if some political incentives are given to some particular technology, the diffusion probability will be much increased and CO_2 reduction will be much accelerated.

It can be seen in Table 1 that the contribution of"system energy"technologies such as combined cycle, repowering, cogeneration, or gas turbine combined incineration, is significant and the total amount should be around 30% of the total reduction. In this estimation, the repowering of the nuclear reactors and also micro cogenerations based on micro gas turbines or solid polymer fuel cells are not included. If these terms are integrated, the reduction potential should be significantly increased. In conclusion, according to the COP3 decision in Kyoto, Japan's target of 6% CO_2 reduction from 1990 in 2010 should be cleared by technological approach. In addition, natural gas based, highly efficient power generating "system energy"technologies mentioned above in this paper should become much popular in Asia in near future. Then natural gas demand will become much more increased.

7. NATURAL GAS TRANSPORTATION BY NORTHEAST ASIAN PIPELINE NETWORK

In order to introduce these highly efficient technologies of power generation, natural gas demand in the Northeast Asia should be drastically increased. China, Korea and Japan have organized "The Northeast Asian

Gas and Pipeline Forum (NAGPF)", and had five times of International Conferences. Through the papers [4-7] presented at the past Conferences, the demand in 2010 is estimated as 3.6 times from now. To meet this big demand estimation, it is essential to have infrastructures as pipelines. As it is well known, in Europe, over 800,000km high pressure natural gas trunk pipelines have already been existed. In North America, there has been 440,000km in length existed. On the other hand, in Asia, there is nothing.

Table 1. Possibilities of CO_2 Reduction in 2010 (Environmental Agency of Japan)

SECTOR	CO_2 REDUCTION TECHNOLOGIES AND EACH CONTRIBUTION (%)	TOTAL(%)
ENERGY CONVERSION	CO_2 REDUCTION DUE TO DEMAND SIDE STRUCTURE ALTERATION(11), POWER STRETCHING OF NUCLEAR REACTORS(10), EFFICIENCY INCREASE OF COAL FIRED POWER PLANTS (ULTRA-SUPERCRITICAL, IGCC, PRESSURIZED FLUIDIZED BEDS, REPOWERING)(5), REPOWERING OF OIL FIRED POWER PLANTS (2), EFFICIENCY INCREASE OF NATURAL GAS FIRED POWER PLANTS (ACC, REPOWERING)(2), PROMOTION OF NATURAL GAS UTILIZATION(8), REDUCTION OF NETWORK LOSSES(3), HIGHLY EFFICIENT INCINERATION POWER GENERATION(3), DECREASE OF OIL REFINING(2), CONVERSION OF CITY GAS TO NATURAL GAS(0.5), INCREASE OF RENEWABLE ENERGY(0.5)	47
INDUSTRY	IMPROVEMENT OF PROCESSES (STEEL(9), CEMENT(4), PAPER/PULP(2), PETRO-CHEMICAL(1)), INTRODUCTION OF COGENERATION(4), INTRODUCTION OF COMBINED-CYCLE(1), INTRODUCTION OF INVERTERS & HIGHLY EFFICIENT MOTORS(2), EFFICIENCY INCREASE OF BOILERS & FURNACES(3), INTRODUCTION OF SOLAR CELLS(1), RECYCLING(2)	29
HOUSEHOLD	THERMAL INSULATION & AIR TIGHTNESS OF HOUSES(2), REDUCTION OF STAND-BY POWER(2), EFFICIENCY INCREASE OF HEAT-PUMP AIR-CONDITIONER(1), INTRODUCTION OF EFFICIENT FLUORESCENT LAMP(0.5), INTRODUCTION OF SOLAR CELLS(0.5), OTHERS(1)	7
COMMERCIAL	INTRODUCTION OF COGENERATION(2), ENERGY CONSERVATION OF NEW BUILDINGS(1), EFFICIENT ILLUMINATION(1), INTRODUCTION OF LATENT HEAT ABSORPTION BOILERS(0.5), INTRODUCTION OF SOLAR CELLS(0.5), OTHERS(0.5)	5
TRANSPORTATION	DECREASE OF SPECIFIC FUEL CONSUMPTION (LEAN BURN, DIRECT INJECTION, LIGHT WEIGHT BODY, REDUCTION OF AIR DRUG, LOCK UP OF AUTOMATIC TRANSMISSION, INTER-COOLER TURBO, ETC.)(3), INTRODUCTION OF LOW EMISSION VEHECLE (ELECTRIC CARS, NATURAL GAS VEHECLES, HYBRID CARS)(2), MODAL SHIFT FROM CARS TO RAIL OR SHIPS(2), SHIFT FROM PERSONAL CARS TO PUBLIC TRANSPORTATION(2), INCREASE OF AVERAGE SPEED OF CARS(1), OTHERS(2)	12
TOTAL		100

The National Pipeline Research Society of Japan proposed [1] the construction of international trunk pipelines, called the "Trans-Asian Natural Gas Pipeline Network", linking the gas fields with major consuming markets, as shown conceptually in Fig.15. This proposal is the core of the concept of"Asian Pacific Energy Community".

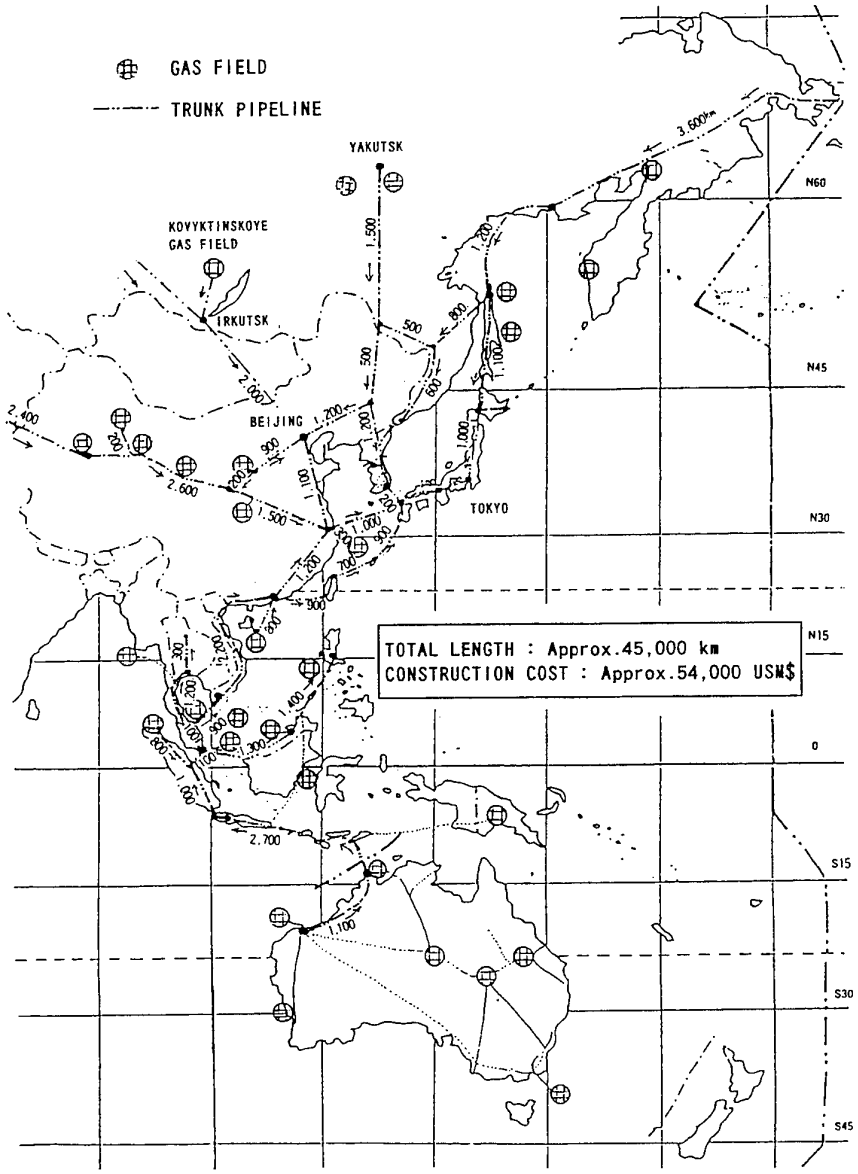

Fig.15. Fundamental Concept of Trans-Asian Natural Gas Pipeline Network

The"Asian Pacific Energy Community"should aim to develop; securing and stable supply of energy; efficient use of energy and environmental protection; strengthening of security of energy based on intra-regional interdependence; promotion of economic and technical cooperation among Asian Pacific countries, in order to contribute to the permanent peace and economic development of this region. The completion of these trunk lines would bring into being a network extending a total length of 45,000 km and linking a total of 15 supplying, consuming, and transit countries. The total construction cost is estimated at about 7 trillion yen (approximately 54 billion U.S.$), excluding the cost of right of way.

8. CONCLUSIONS

In November 1994, the Worldwatch Institute in USA published a book entitled "Power Surge" [8], in which they pointed that if, at the beginning of the next century, the highly efficient energy systems as cogeneration fueled by natural gas should be distributed, and the fuel is gradually changing to a mixture of natural gas and hydrogen. Around 2020, the gas fuel so called as"Hythane", which is a mixture of around 15% hydrogen and 85% natural gas or methane, should be introduced. Hydrogen is to be produced by electrolysis of water, and the electricity is generated by using renewable energy as solar or hydraulic power generation. According to their scenario, CO_2 concentration within atmosphere will take a peak value of 450ppm at around 2050, and after that it will gradually decrease as shown in Fig.16.

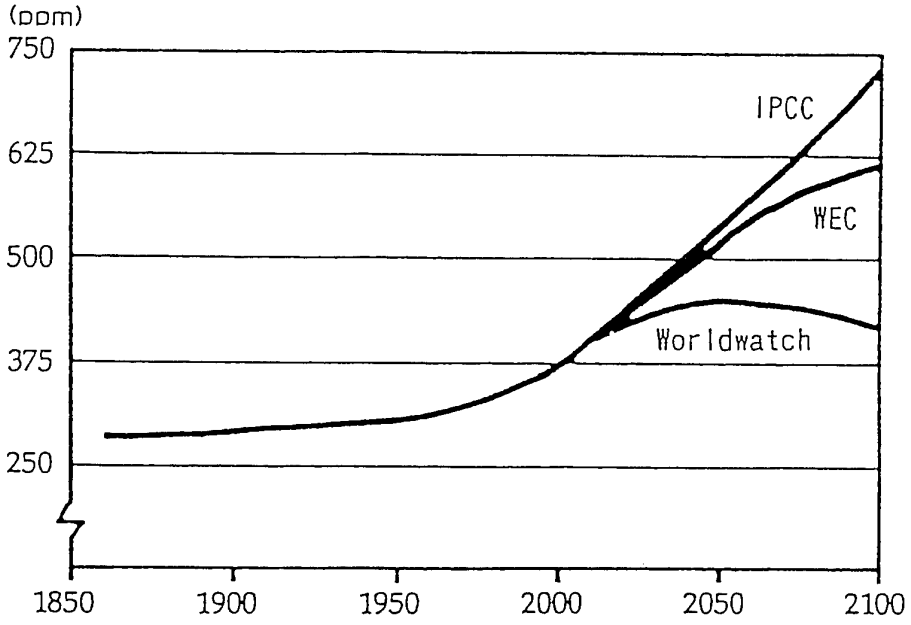

Fig.16. Forecast of CO_2 concentration in atmosphere by scenario of Worldwatch Institute

East Siberia has a vast potential of hydro-power generation undeveloped. For example, there are so many famous big rivers as Angara, Yenisei, Lena or Amur River, and if such potential should be developed to produce electricity and to use for the production of hydrogen, the pipelines will become most effective infrastructure for the transportation of hythane.

Each country in the region must fully discuss the role of energy supply and demand and take action based on a consensus. Each country must understand that natural gas plays an important role in the energy policies and that the promotion of intra-regional distribution of natural gas through the development of a pipeline network contributes to the sustainable development of the region. Each country will need to study which project is feasible and essential for the region, and arrange the projects in order of priority.

The Trans-Asian Natural Gas Pipeline is a public infrastructure that spans across the country. The realization of the projects will crucially depend on the cooperation of each country, or government and private sectors. In the construction phase, the required construction funds and pipeline technology will be actively transferred across the borders. Meanwhile in the operation phase, intra-regional interdependence in the field of energy will be heightened. Just as the pipeline network in Europe is a symbol of intra-regional unification, the"Trans-Asian Natural Gas Pipeline"will widely contribute to the peace and security of the Asia-Pacific region as a symbol of cooperation.

ACKNOWLEDGEMENTS

The author wishes to acknowledge the members of The National Pipeline Research Society of Japan and also of

Asian Pipeline Research Society of Japan, for their remarkable contributions described in this paper.

REFERENCES

1. Masaru Hirata:"A Proposal on Trans-Asian Natural Gas Pipeline Network", Int. Conf. on Northeast Asian Natural Gas Pipeline, Tokyo, March 1995.
2. M. Brandauer, et al.:"GT26 repowers Rheinhafen", Modern Power Systems, Vol.16, No.5, pp.39• 48 (1996)
3. "Moerdijk combines waste burning with GTCC cogeneration", ibid., Vol.17, No.7, pp.29• 36 (1997)
4. Xunzhi Shi:"Present Situation and Forecast of Natural Gas Exploitation and Utilization in China", Int. Conf. on Northeast Asian Natural Gas Pipeline, Tokyo, March 1995.
5. H.B. Sunwoo:"Present and Future Trend of Natural Gas Utilization in Korea", Int. Conf. on Northeast Asian Natural Gas Pipeline, Tokyo, March 1995.
6. Meng Muyao:"Strategy for China Onshore Natural Gas Utilization and Development", The Second Int. Conf. on Northeast Asian Natural Gas Pipeline, Beijing, September 1996.
7. Hoesung Lee:"Long-Term Energy Demand 2030", The Second Int. Conf. on Northeast Asian Natural Gas Pipeline, Beijing, September 1996.
8. C. Flavin & N. Lenssen:"Power Surge", W.W. Norton & Co., Inc., N.Y.(1994)

EFFECT OF FLUID PROPERTIES ON POOL BOILING, BUBBLE DYNAMICS AND THERMAL PATTERNS ON THE WALL

G. Hetsroni, A. Mosyak and R. Rozenblit
Department of Mechanical Engineering
Technion-Israel Institute of Technology
Email: hetsroni@tx.technion.ac.il; Fax: (972)-4-8324533

Keywords: boiling, bubble dynamics, thermal pattern, heat transfer

ABSTRACT. During nucleate pool boiling of pure water and water with cationic surfactants, the motion of bubbles and the temperature of the heated surface were recorded by both a high-speed video camera and an infrared radiometer. All experiments were performed at saturated boiling conditions. The boiling curves for various solutions were obtained and compared. The results show that the bubble behavior and the heat transfer mechanism for the surfactant are quite different from those of clear water. In this study the examples of the irregular behavior of nucleation sites and their interactions are presented.

1. INTRODUCTION

A goal of research in the field of boiling heat transfer is to transfer the largest heat flux by applying the smallest temperature difference between the heating surface and the boiling liquid, and to maximize the critical heat flux. Various means have been developed with this aim in mind, including the use of additives to modify the fluid properties. The process of nucleate boiling is the total sum of the processes of bubble initiation, growth and departure. Though these individual processes have been much studied during the past years, it is difficult to predict the effect of the physical properties of surface-active agents (surfactants) on the main boiling characteristics, such as the relationship between the heat flux and the temperature difference. In contrast to the momentum and scalar transfer in turbulent pipe flow with surfactants, which shows a reduction in the friction factor and the heat transfer coefficient (Hetsroni et al. [1]), the study of surfactant solutions in the pool boiling shows a significant enhancement of the boiling mechanism. The role of surface active solutes was explored by Morgan et al. [2], for 0.1–1.0% aqueous solutions of a commercial surfactant. They found that the boiling curves (q vs. Δt) were shifted laterally in varying degrees, such that heat transfer was higher than that for pure water, (q is the heat flux, Δt is the superheat, $\Delta t = t_w - t_{sat}$, t_w – the wall temperature, t_{sat} – the saturation temperature of the solution). This is an important discovery because, if proved to be applicable under industrial boiling conditions, it will lead to a considerable increase in the power level of all boilers without any increase in size or operating temperature. One interesting field of application of boiling and evaporation is in desalination of seawater, which is becoming essential in some arid regions. It has been shown by Sephton [3] that addition of small amounts of surfactants to seawater can substantially enhance the boiling process, and reduce the price of the desalinated water to an acceptable level. At that time the research has been discontinued because the environmental impact of surfactants was not known. Because the concentrations are usually low, addition of the surfactant to water causes no significant change in saturation temperature and the majority of other physical properties, except for the surface tension and maybe the viscosity. There have been a large number of studies to determine the boiling enhancement mechanism caused by addition of surfactants to water. Frost and Kippenhan [4] investigated boiling of water with varying concentrations of surfactant "Ultra Wet 60L". They found an increase in heat transfer and concluded that it resulted from the reduced surface tension. Heat transfer in nucleate pool boiling of dilute aqueous polymer solutions was measured by Kotchaphakdee and Williams [5] and compared with results for pure water. Photographs showed distinct differences in bubble size and dynamics, between polymeric and non-polymeric liquids. Gannett and Williams [6] concluded that surface tension was not relevant in explaining the enhancement effect, and reported that viscosity could be a generally successful correlating parameter. Nucleate boiling curves for aqueous solutions of drag-reducing polymers have been measured experimentally by Shah and Darby [7] and by Paul and Abdel-Khalik [8]. The explanation of observed changes in the boiling curves was based only on how the polymer additives changed the solution viscosity. Polymer type, concentration and molecular weight were important only insofar as they affect the solution viscosity. Yang and Maa [9] studied pool boiling of dilute surfactant solutions. The surfactants used in this study are sodium lauryl benzene sulfonate and sodium lauryl sulfate. Because all experiments were carried out under very low concentrations it was concluded that these additives had no noticeable influence over the physical properties of the boiling liquid, except surface tension, which was significantly reduced. That study showed that the surface tension of the boiling liquid had

significant influence on the boiling heat transfer coefficient. Pool boiling experiments were carried out by Tzan and Yang [10], for relatively wide ranges of surfactant concentration and heat fluxes. The results verify again that a small amount of surface-active additive makes the nucleate boiling heat transfer coefficient of water considerably higher. It was also found that there is an optimum additive concentration for highest heat flux. Beyond this optimum point, further increase in the additive concentration lowers the boiling heat transfer coefficient. Wu et al. [11] reported experimental data of surfactant effect on nucleate boiling heat transfer in water with nine additives. Anionic, cationic, and nonionic surfactants were studied with the highest concentration up to 400 ppm. The enhancement of heat transfer was related to the depression of static surface tension. Boiling heat transfer coefficients were measured by Ammerman and You [12] for an electrically heated platinum wire immersed in saturated water, and in water mixed with three different concentrations of sodium dodecyl sulfate (an anionic surfactant). Their results showed that addition of an anionic surfactant to water caused an increase in the convection component and a corresponding reduction in the latent heat component of the heat flux in the fully developed boiling region. The boiling enhancement of water, due to the addition of an anionic surfactant, appears to be influenced by this relative change in these heat flux components. Unfortunately, although enhancement of nucleate pool boiling can usually be achieved by the addition of surfactants to working fluid, these surfactants were not suited for recirculation systems because of the susceptibility of high molecular weight component to degradation in high shear or extensional flows. In the present study we used the cationic surfactant Habon G (trade name Hoe S4089, Hoechst AG) for the boiling enhancement. It was shown by Zakin et al. [13] that although microstructure of Habon G was also mechanically degraded under high shear conditions, it recovered quickly–no matter how many times it was broken up by shear. The objective of the present study is to determine how the nucleate boiling is affected by the addition of Habon G to water. Saturated pool boiling on a heated surface and on a heated tube has been studied and the effect of the surface tension and Prandtl number on the heat transfer coefficient has been examined.

2. PHYSICAL PROPERTIES OF SOLUTIONS

Taking into account the effect of physical properties of the surfactant solutions on the heat transfer, we, together with the US research group of Prof. J.L. Zakin., carried out such measurements. We concentrated on measurements of thermal conductivity and Prandtl number, in the wide temperature range. The shear viscosity data and temperature dependence of the surface tension were obtained by the research group at Ohio State University.

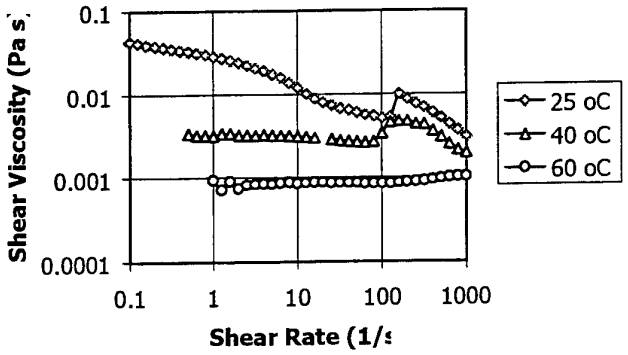

Fig.1. The shear viscosity of 530 ppm Habon G solution vs shear rate

All solutions used were prepared by dissolving the powdered solution in deionized water with gentle stirring over a period of several days. Concentrations investigated here were 65–1060 ppm (parts per million weight).The shear viscosity of all surfactant solutions used was determined in the temperature range 25-60°C by Rheometrics Fluids Spectrometer RFS II and a Couette system. Figure 1 shows the dependence of shear viscosity vs shear rate for 530 ppm Habon mixture. It can be seen from Fig. 1, that shear velocity value does not change significantly depending on shear rate for temperature range more than 60°C. Moreover, the curves come closer for higher shear rate values. Based on this result we studied the viscosity behavior by capillary viscometer with high value of shear rate

at temperature more than 55 °C. For this purpose the Cannon-Fenske viscometer was used. The measurement uncertainty does not exceed ±4%.

Fig.2 shows the behavior of kinematic viscosity of surfactant solution depending on the temperature at various Habon G concentrations. One can see here the similar tendency of curves go toward pure water viscosity value near the saturation temperature. Such behavior is more pronounced as the solution concentration decreases.

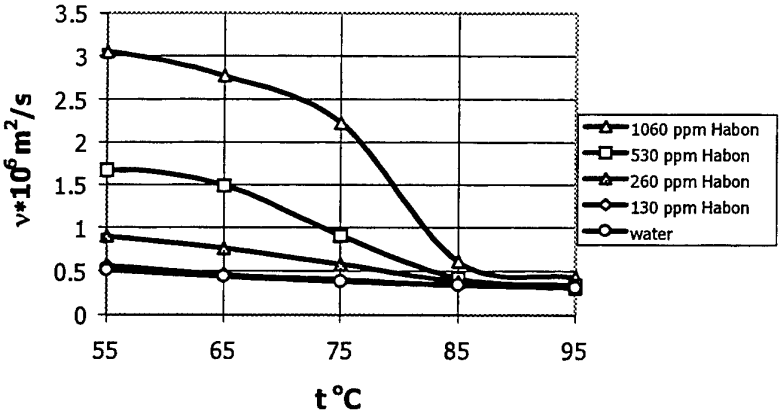

Fig. 2. Kinematic viscosity of solution vs temperature at various Habon G concentration

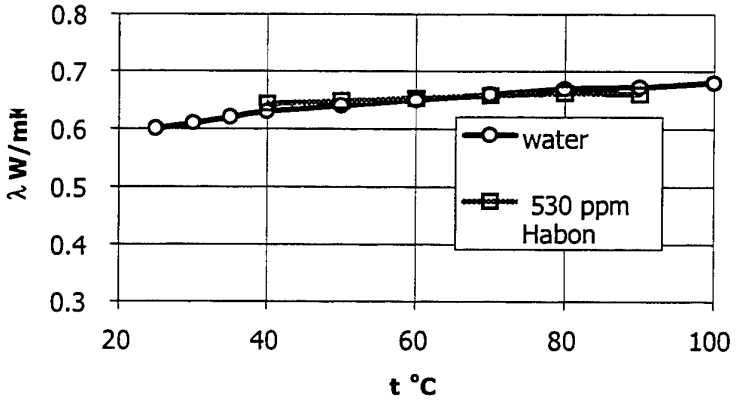

Fig. 3. Thermal conductivity vs temperature

We carried out also the measurements of thermal conductivity of Habon G solution. The apparatus is of the steady state type. Both the clear water and the tested surfactant solution were enclosed in two identical cells. The cell width is 5.0 mm. The top of each cell is made of 50μm stainless steel foil, heated by DC current. The bottom of each cell is cooled by water. The difference between inlet and outlet temperature did not exceed 0.2°C. The thermal field of the cell top was measured by IR radiometer. The average uncertainty of thermal conductivity measurement is 2%. The measured conductivity deviates only slightly (Fig. 3) from that of pure water at low surfactant concentrations that we used.

The effect of above mentioned characteristics can be summarized by the Prandtl number (Pr). The dependence of Prandtl number on the temperature at various concentrations of Habon G solution is shown in Fig. 4.

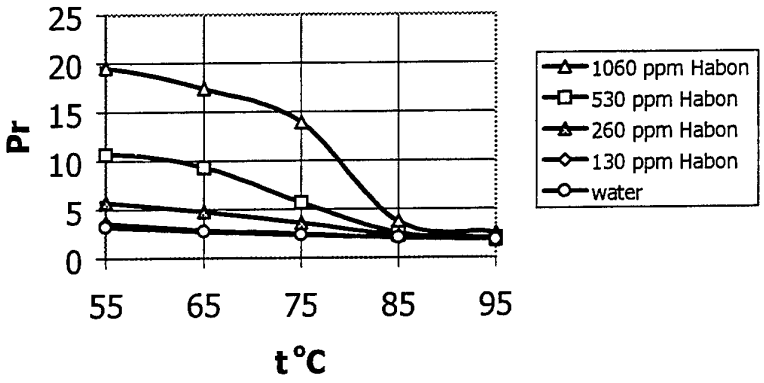

Fig. 4. The variation of Prandtl number vs temperature at various concentration of Habon G

The surface tension was measured in the temperature range from 25 to 70°C with standard deviation of 2%. The data have been received using ScnsaDyne PC500-LV Surface Tensiometer System, which measure surface tension within the body of a test fluid by blowing bubble of gas through two probes of different diameters inside the body.

Figure 5 shows the magnitude of surface tension as a function of the temperature at various concentration of

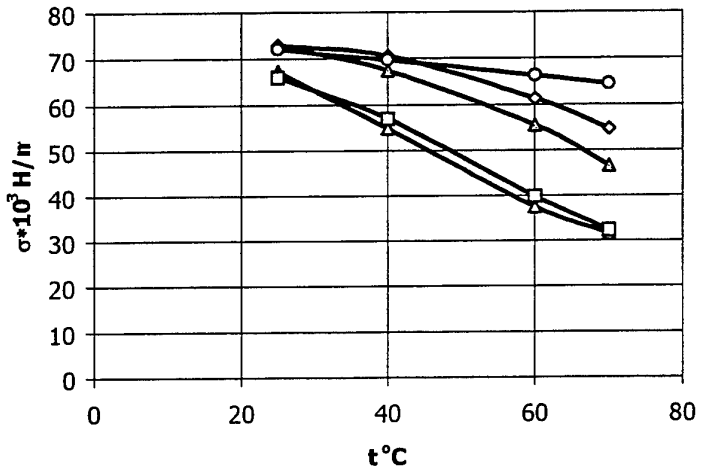

Fig. 5. The surface tension as a function of temperature at various Habon G concentrations

Habon G. As seen in this figure, the surface tension is decreased with both the concentration and the temperature increasing. But the temperature effect is much stronger for the high temperatures, whereas for viscosity the opposite trend is observed.

3. EXPERIMENT

3.1 Apparatus

Two sets of apparatus were used. Figure 6 shows the one designed for the study of pool boiling from a horizontal heating surface facing upward. Boiling occurred over a constantan foil, 50μm thick, attached to the window at the bottom of the vessel. The foil was heated by DC current and the heat flux on the wall could be regulated. The infrared image of the heater was recorded from below by an Infrared Radiometer. The radiometer has typical minimum detectable temperature difference of 0.1K, time response of 25 frames per second and horizontal resolution of 256 pixels per line for the recording data.

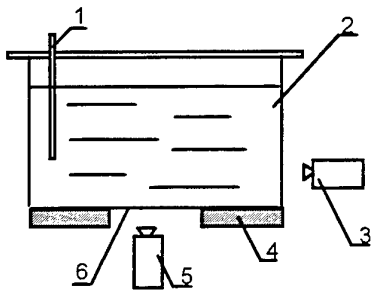

Fig. 6. Apparatus for pool boiling on a horizontal surface.
1 – supplementary heater, 2 – window, 3 – video camera,
4 – insulation, 5 – IR camera, 6 – foil heater

Since the foil was very thin, the temperature difference between the two sides of the foil does not exceed 0.2K at heat flux of 100 kWm^{-2}. Therefore, the time-averaged temperature was almost the same on both sides of the foil. The image had 256 intensity levels and was recorded on videotape. Heat losses were reduced by proper insulation and did not exceed 1%. Boiling on the heated foil was illuminated and photographed through view windows on the sides of the apparatus.

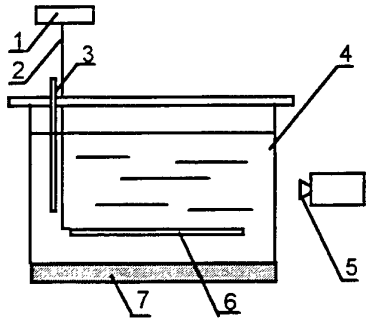

Fig. 7. Apparatus for pool boiling on a tube.
1 – temperature measurements, 2 – thermocouple,3 – supplementary heater, 4 – window,
5 – high-speed camera, 6 – heating tube, 7 – insulation

The second apparatus, as shown in Fig. 7 was designed for the studies of the heat flux q > 100 kWm^{-2}. The construction of this apparatus was similar to the one described above except that the heating element was made of a stainless steel tube of outer diameter of 1.5 mm. The electric current was supplied to this heating element through two copper bars and DC power supply. Calibrated Teflon coated T–type thermocouple was inserted inside of the tubular heating element. The joint of the thermocouple could be adjusted exactly to any desired position in the heating element. The temperature of the outer surface was calculated from the power generation per unit volume of the electrically heated tube. The measurements showed that the temperature distribution along the tube was uniform, within the accuracy of 0.1°C.

3.2 Instrumentation

The growth of bubbles and the bubble motion near the heated surface was recorded by a high-speed video camera with recording rate up to 10,000 frames per second. The playback speed can be varied from a single frame to 250 frames per second. An IR radiometer was used in the investigation of thermal patterns. It has a typical resolution of 256 pixels per line. The radiometer allows obtaining a quantitative thermal profile in the line mode, the average temperature in the area mode, and the temperature of a given point in the point mode. We had to consider the frequency response of the system to changes in the heat transfer coefficient. It was shown by Hetsroni and Rozenblit (1994) that temperature distortions and phase shift in temperature fluctuations on the heated wall begin at $f=15\text{-}20s^{-1}$. In the present study the highest frequency of the bubble departure was higher, then we confine ourselves measurement of average temperature and qualitative observation of thermal structure on the heated bottom. The thermal pattern was saved on videotape. The video was then used in a playback mode to analyze the data. The surface temperature and the surfactant mixture temperature were measured with an accuracy of $\pm 0.1°C$. Electrical power was determined by means of a digital wattmeter with an accuracy of $\pm 0.5\%$.

3.3 Procedure

The heating surface was cleaned routinely before and after each set of three data points with a sequence of operations involving application of constantan cleaner and washing with hot tap water and deionized water. Only a soft sponge and absorbent paper tissues contacted the constantan, which remained smooth and completely wettable. During a typical run, the boiler was loaded with 1500 ml of liquid to bring the surface to a level 70–80 mm above the heater. Steady state boiling was achieved in 10–20 min after the supplementary heater was turned on, this was determined by monitoring the temperature of the solution. Surfactant solutions were replaced with fresh samples after three runs. This precaution was taken in order to minimize change of solution properties, which might have occurred at high temperature due to evaporation over long periods of time. These occasions of sample renewal permitted regular observations of the heater surface. No visible deposits formed under test conditions, this was visible in the test runs and after draining the boiler. Room temperature was maintained at 23°C, so that heat losses from the boiler would be nearly constant in all runs.

4. BOILING BEHAVIOR

4.1 Bubble Visualization

The evolution of vapor bubbles in a boiling liquid, in particular the rate of growth of bubbles, is one of the parameters determining the intensity of the heat transfer from a heated surface. The growth of the bubble in the liquid containing surfactants is accompanied by manifestation of a number of specific factors. The pool boiling experiments were carried out under atmospheric pressure. The phenomenon of foaming often was observed during boiling in the presence of surfactant, was found also for all Habon G solutions used. The foam formed on the surface of the solution, and the foam height increased with the heat flux. In the present study, the height of liquid phase over the heater was no less than 60 mm throughout all experiments. The bubble behavior was recorded with speed of 1000 frames per second by high-speed camera. The typical stages of bubble growth analyzed for this study are shown in Figs. 8, 9. The field of view is 40 x 30 mm in the horizontal and vertical direction, respectively.

In order to provide a description of the flow pattern under high heat fluxes, we studied pool boiling on the stainless steel tube of outer diameter 1.5mm. Figure 8 (a,b,c) shows typical pictures for water boiling at heat fluxes $q = 150; 450; 750\ kWm^{-2}$, respectively. There was observed a population of bubbles in the vicinity of the heated tube. The bubble dynamics for water depends on heat flux and is similar to well-known data of boiling visualization. After the onset of nucleate boiling, the regime of single bubble occurs close to the heated wall (Fig. 8a). As the heat flux increases, the bubble coalescence takes place (Fig. 8b). This phenomenon is more pronounced at $q = 750\ kWm^{-2}$, (Fig. 8c). For pure water, the average bubble size was observed slightly increasing with increasing heat flux. The bubbles have an irregular shape at all values of heat flux. Figure 8(d,e,f) shows boiling of 530 ppm Habon G solution under the same conditions. The Habon G additive reduces significantly the tendency of coalescence between vapor bubbles. Hence, these bubbles are smaller in size but

larger in number than the case of pure water. They settle on the heated tube in a quite orderly manner. There is a weak tendency to increasing in the average diameter size too. The shape of bubbles in this case becomes closer to spherical one, than for pure water.

To study the bubble dynamics and the thermal pattern on a horizontal surface, the experimental setup, shown in Fig. 6, was used. The process of single bubble growth, at heat flux q = 90kWm^{-2} is presented in Fig. 9(a-f) for

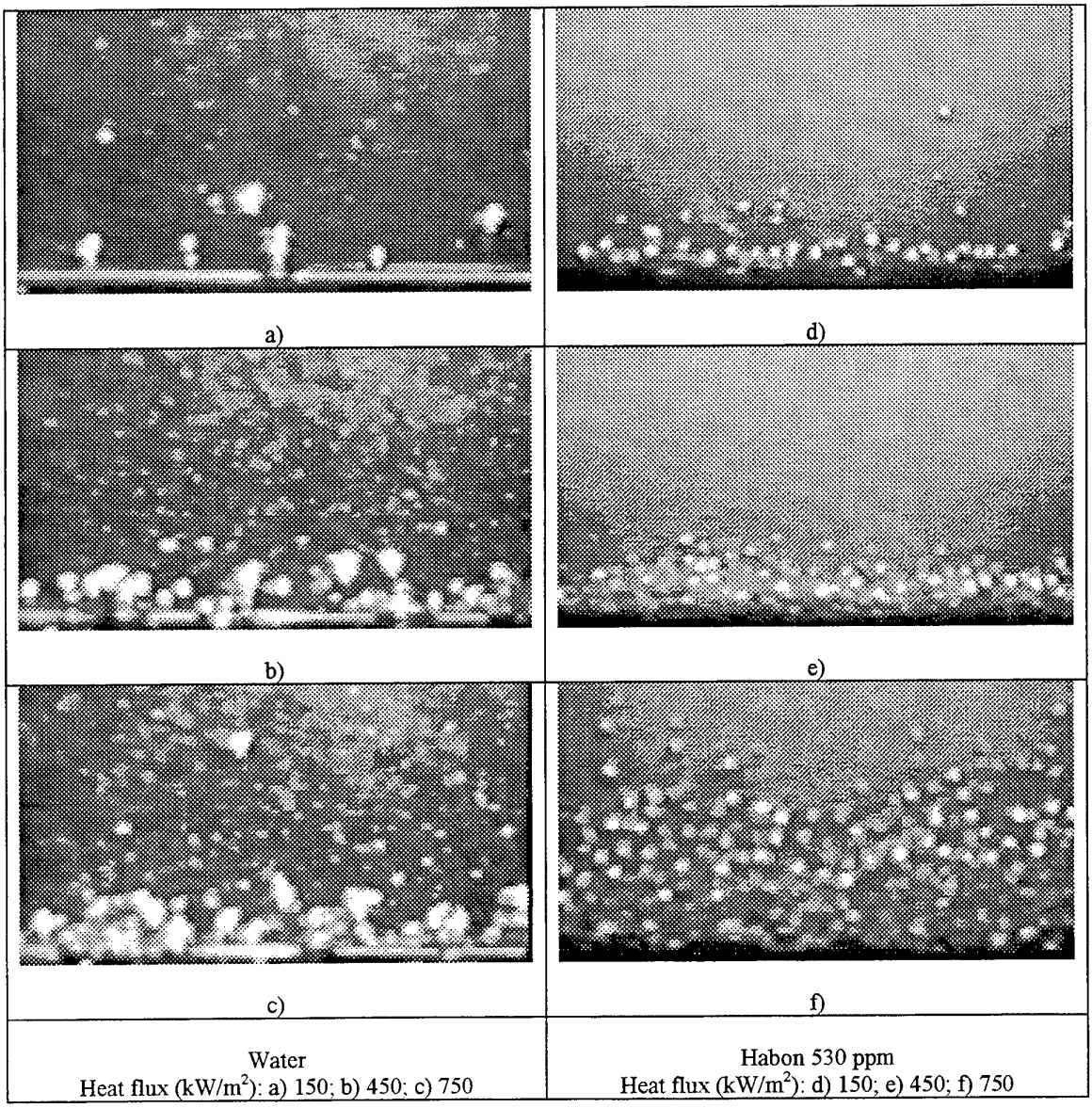

Fig. 8. Boiling of water (a,b,c) and 530 ppm Habon G (d,e,f) on the pipe at various heat fluxes

water and Habon G solution. Figure 9(a-c) shows the bubble initiation, the bubble growth after 7ms and the bubble departure after 17 ms for water pool boiling. In the case of boiling 530 ppm Habon G solutions (Fig. 9(d-f), the time from the bubble initiation to its departure is about two times longer as much as that for the pure water. For the Habon G solutions, boiling on the horizontal heating surface facing upward, we sometimes can observe the phenomenon of an origin of large number secondary bubbles (Fig. 9f) at the departure time of the initial bubble.

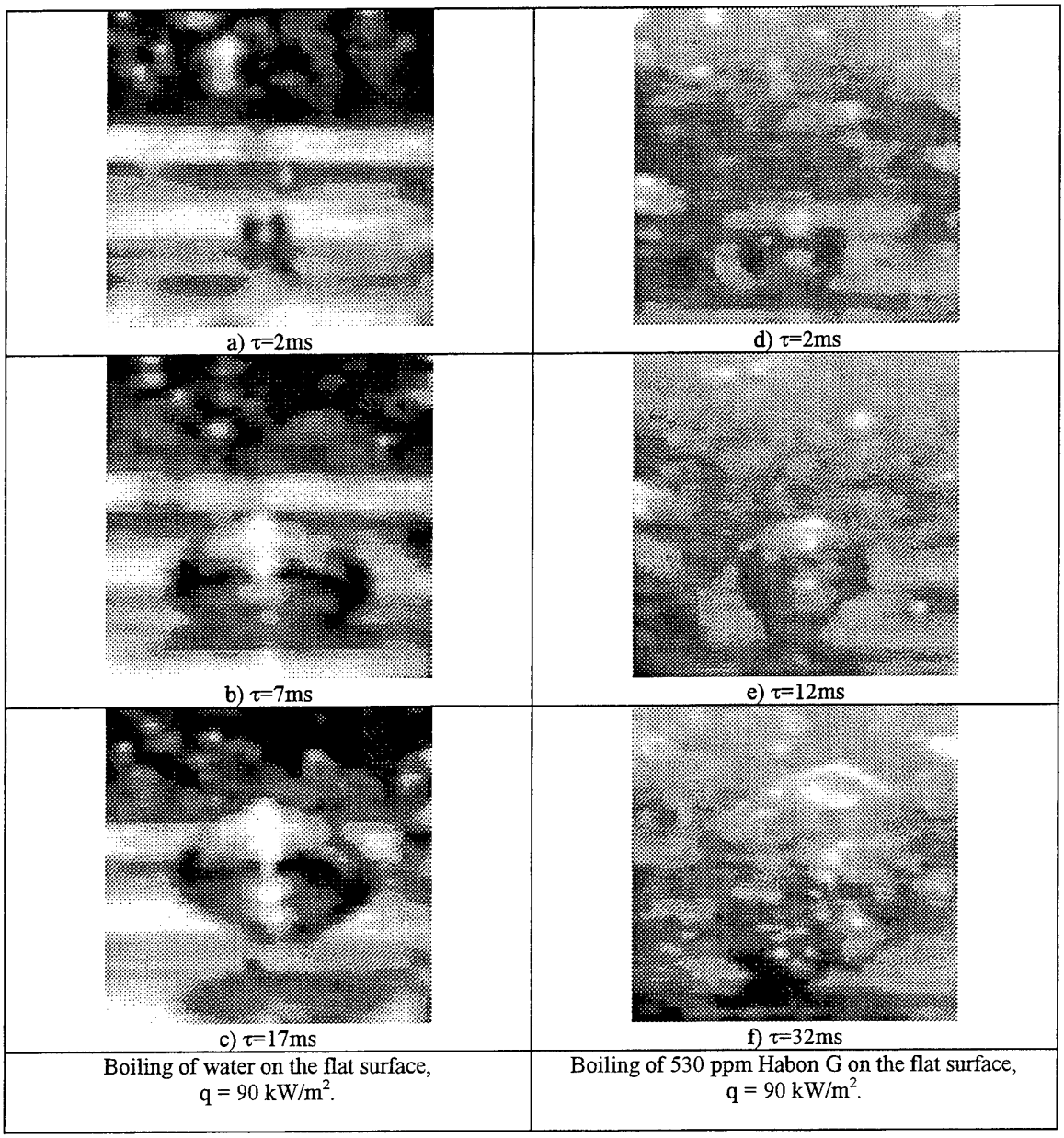

Fig. 9. The dynamics of bubble growth in clear water and 530 ppm Habon G

4.2 Visualization of Thermal Pattern on the Heated Wall

Although IR thermography applied to boiling has relatively low frequency response, it is still more accurate than surface temperature measurement by micro thermocouples or resistance thermometers. Its advantages are the extensive nature of the measurements and the absence of disturbance to the microgeometry of the boiling surface. The examples given in this paper are a small sample of the information contained in the recordings. They illustrate the advantages and limitations of IR thermography combined with video recording for the study of boiling heat transfer. The technique is necessarily limited to boiling on very thin walls, conditions that maximize the local variations in wall temperature and minimize lateral conduction. There may indeed be smaller variations in wall superheat during boiling on thick walls, but many industrial applications and

laboratory experiments involve boiling on materials of low thermal conductivity ranging from stainless steel to coated glass.

The spatial distributions (Fig. 10) show variations of wall temperature of about 17K for water and 25K for surfactant. With such wide ranges, it is clear that models for the bubble nucleation and growth that assume uniformity of wall superheat cannot be realistic. The histograms of thermal field of the heated wall show the decrease in the average temperature for Habon G solution (Fig. 10b). The magnitude of standard deviation value of temperature is higher for Habon G solution, than for water. It means that the heat transfer coefficient in the surfactant solution increases and vaporization is more intensive, compared to water boiling.

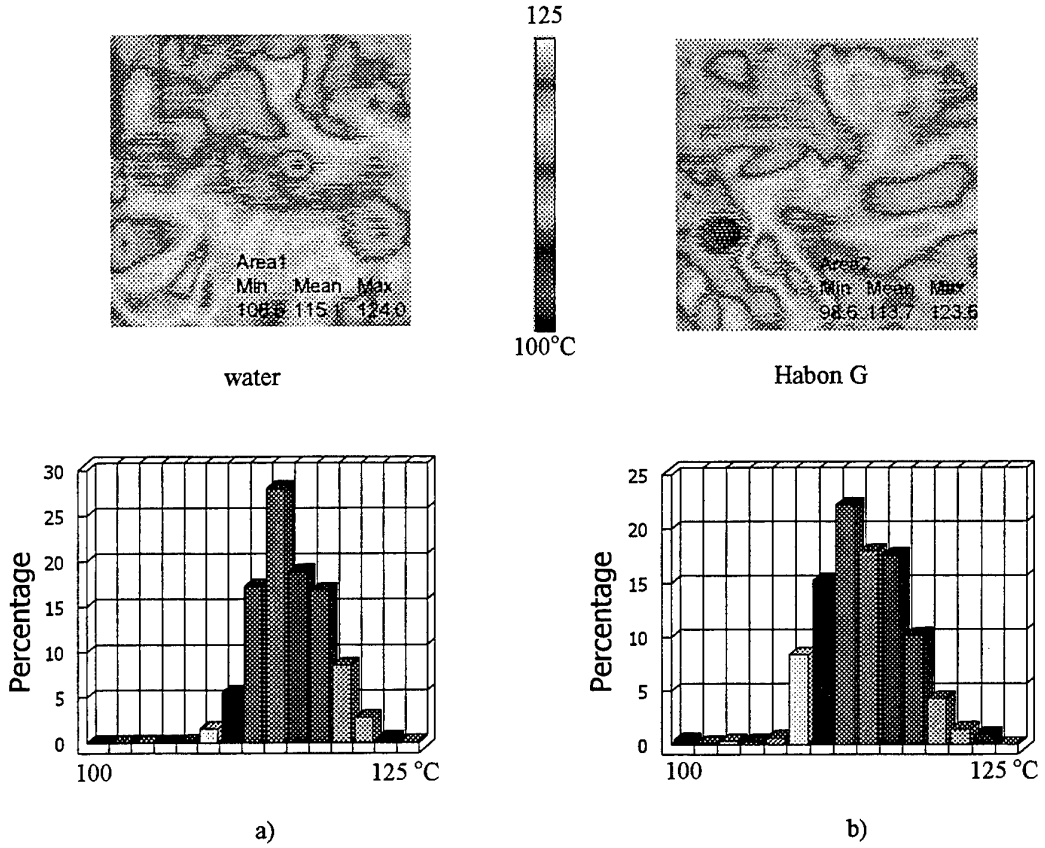

Fig. 10. Thermal patterns and histograms of the temperature at pool boiling of water and Habon G on the flat plate ($q = 90$ kW/m^2)

4.3 Boiling Curves and Heat Transfer Coefficients

In Fig. 11, experimental boiling heat transfer data are presented as a function of heat flux vs. wall superheat (space–time average values at the fluid–solid interface). As the heat flux increases, the boiling curve shifts left as the concentration of Habon G increases. It can be seen that the boiling curve at concentration of 1060 ppm is close to the curve for 530 ppm Habon G solution, and at high values of heat flux shifts rightward. It is evident that the influence of surfactant on the boiling curve behavior has an optimum, depending on the concentration.

The effect of heat flux and additive concentration on the nucleate boiling heat transfer coefficient of Habon G solutions is more evident if the experimental data are expressed as a plot of heat transfer coefficient versus heat flux, as shown in Fig. 12. The heat transfer coefficient increases as the heat flux and concentration are increased, except when the heat flux level is lower than about $q = 300$ kWm^{-2} and the concentration is higher than 530 ppm. Of these two trends, the former is consistent with results observed previously (e.g., Shah and

Darby [7], Yang and Maa [9], Tzan and Yang [10]). The latter has seldom been reported. This may be attributed to the fact that the solutions tested were usually too dilute and/or the heat flux level conducted was too low in most of the past experiments reported in the literature.

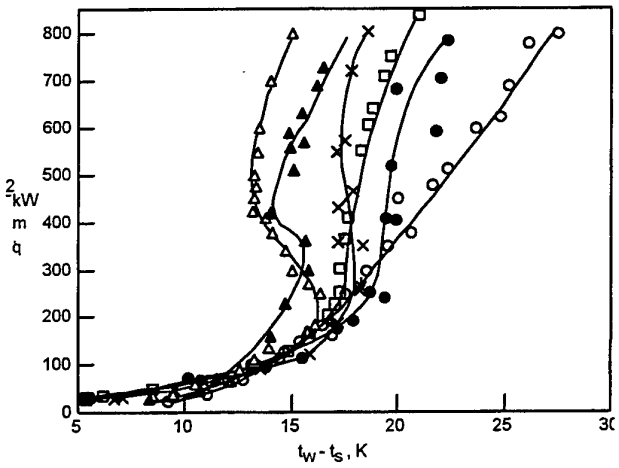

Fig. 11. Boiling curves of water and aqueous Habon G solutions: o – water; Habon G: • – 65 ppm, □– 130ppm, x – 260ppm, ▲– 530 ppm, Δ– 1060 ppm.

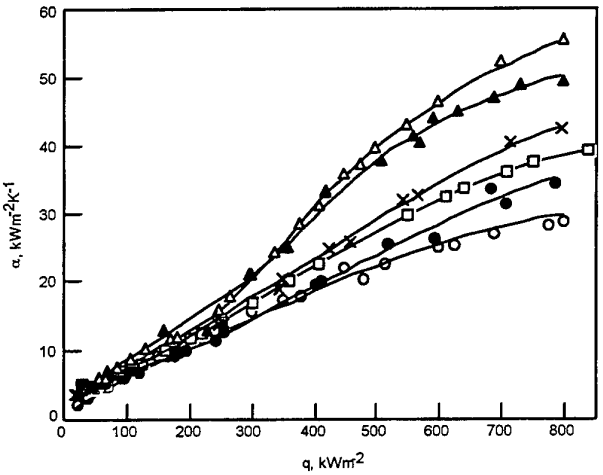

Fig. 12. Boiling heat transfer coefficient (symbols as in Fig. 11)

Our data of heat transfer for 1060 ppm Habon G solution agree qualitatively with boiling heat transfer results reported by Tzan and Yang [10]. They demonstrated that the effect of surfactant additives on nucleate boiling heat transfer decreases, when the concentration of SLS solution was higher than 700 ppm.

5. THE EFFECT OF PHYSICAL PROPERTIES OF HABON G SOLUTION ON HEAT TRANSFER

Detailed investigation of physical characteristics of surfactant mixture let made it possible to demonstrate the effect of different properties of the mixture on the heat transfer. In Fig. 13 is shown the dependence of the non-dimensional surface tension σ/σ_w and the Prandtl number as a function of Habon G concentration, where σ is the surface tension, Pr is the Prandtl number for Habon G solution. The value of surface tension σ_w and the

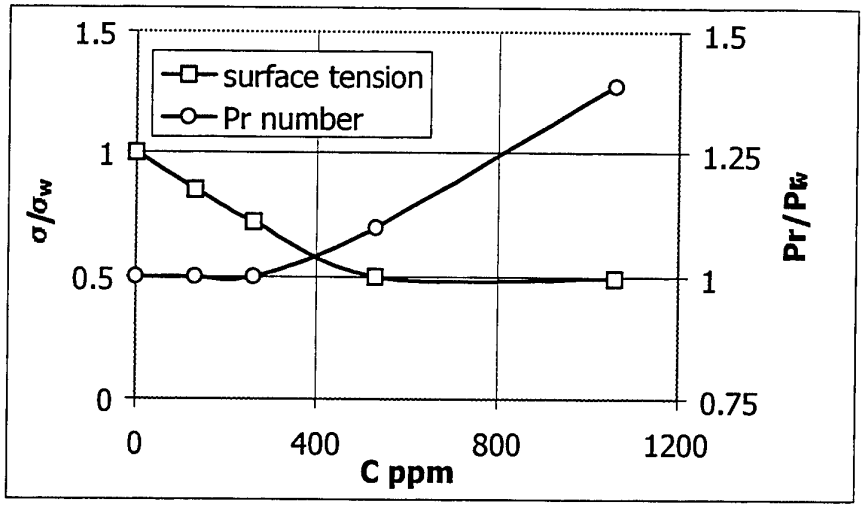

Fig. 13. The non-dimensional surface tension σ and Pr number as a function of Habon G concentration

Prandtl number Pr_W for pure water at the same conditions were used for normalization. It should be noted that

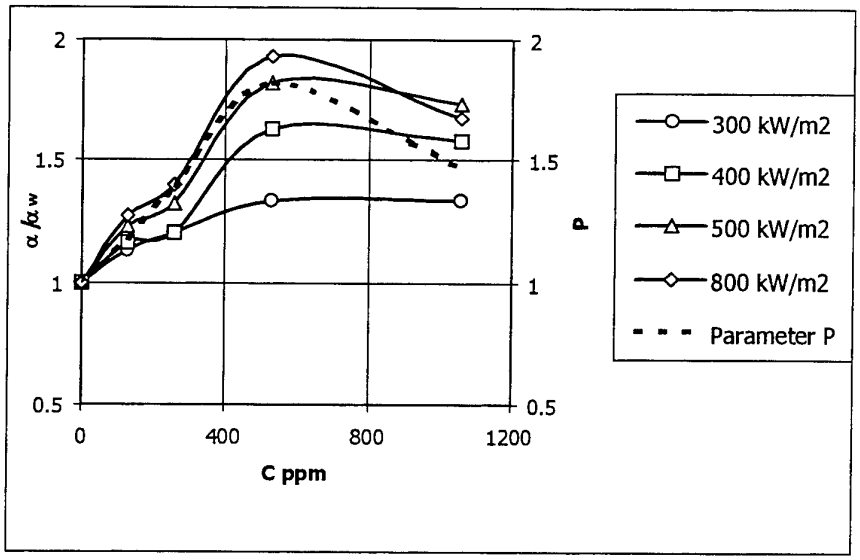

Fig. 14. Relative heat transfer coefficient and parameter of physical properties as a function of Habon G concentration

we used the values of surface tension at 70°C and kinematic viscosity at 95°C, because a limitation of the instruments. One can see that the magnitude of relative surface tension decreases gradually from 1.0 for pure water to value about 0.5 at 500 ppm surfactant solution. Further increase in the surfactant concentration does not result in a significant change of the value of the surface tension. On other hand, the value of relative Prandtl number is practically equal to one of pure water at small amount of surfactant (<300 ppm of Habon G), whereas further increase in additive concentration leads to increasing in the viscosity. Such complicated behavior of physical properties inevitably involves the complex behavior of the heat transfer coefficient in boiling. In Fig. 14 the heat transfer enhancement as a function of Habon G concentration is demonstrated.

It can be seen that the curves are shifted upward when the heat flux increases, and the main enhancement of heat transfer occurred with increasing in the concentration up to 530 ppm Habon G solution. Further increase in the additive amount leads to faint decrease in heat transfer. The enhancement of heat transfer up to 530 ppm solution is connected to the decrease in the surface tension value, because in this range of concentration the Pr number does not change significantly. On other hand the decrease in heat transfer at further surfactant addition may be related to the increase viscous characteristics (Fig. 13). We assume that the product of the non-dimensional surface tension and the relative Pr number becomes the main parameter characterizing the ability of surfactant solution to enhance heat transfer in pool boiling. The dashed line in Fig.14 shows the dependence of parameter $P=\sigma_w Pr_w/\sigma Pr$ (the magnitude of this composite parameter presented on secondary axis) on surfactant concentration. It can be seen that the behavior of this parameter qualitatively agrees with behavior of relative heat transfer coefficient.

6. CONCLUSIONS

The experimental results are summarized as follows:
The Difference in Boiling Behavior. The addition of small amount of cationic surfactant Habon G makes the boiling behavior quite different from that of pure water. For water, bubble action is seen to be extremely chaotic, with extensive coalescence during the rise. Bubbles formed in Habon G solutions were very much smaller than those in water and the surface was covered with them faster. It is known that reduced surface tension results in a decrease of energy required to create a bubble and thus in more bubbles and smaller ones. The boiling excess temperature becomes smaller and the vapor bubbles are formed more easily.

Thermal Pattern on the Heated Surface. Pool boiling of both water and Habon G solutions on a thin, electrically–heated constantan plate in a pool was investigated by infrared thermography in combination with video recording. The experiments show that the limitations of the IR technique with respect to frequency response are outweighed by its unique capacity to measure wall temperature distribution with high spatial resolution over an area encompassing many nucleation sites and over long periods. The measurements confirm the importance of variations in wall temperature for the removal of heat by bubbles.

Heat Transfer. The boiling curves of surfactant are quite different from the boiling curve of pure water. Experimental results demonstrate that the heat transfer coefficient of the boiling process can be enhanced considerably by the addition of a small amount of Habon G. This effect is more pronounced when the surfactant concentration is higher. This effect diminishes as surfactant concentration is increased. There exists an optimum concentration, probably near 530 ppm Habon G.

ACKNOWLEDGEMENTS

This research was supported by the Fund for the Promotion of Research at the Technion. A. Mosyak and R. Rozenblit are supported by The Ministry of Absorption, State of Israel. This research was also supported by the Israeli Ministry of Science.

REFERENCES

1. G. Hetsroni, J.L. Zakin and A. Mosyak, Phys. Fluids v.8, pp.2397-2404 (1997).
2. A.I Morgan,. L.A. Bromleyand and C.R Wilke,. Ind. Eng. Chem. v.41, pp.2767- 2771 (1949).
3. H. Sephton, US Patent No. 3846254, (1974).
4. W. Frost and C.J Kippenhan, Int. J. Heat Mass Transfer v.10, pp.931-949 (1967).
5. P.Kotchaphakdee and M.C. Williams, Int. J. Heat Mass Transfer v13: pp.835-848 (1970).
6. H.J. Gannet, Jr. and M.C Williams, Int. J. Heat Mass Transfer v.14, pp.1001-1005 (1971).
7. B.H Shah. and R.Darby, Int. J. Heat Mass Transfer v.16, pp.1889-1903 (1973).
8. D.D. Paul and S.I. Abdel-Khalik, Journal of Rheology v.27, pp.59-76 (1983).
9. Y.M Yang and J.R. Maa,. Journal of Heat Transfer v.105, pp.190-192 (1983).
10. Y.L. Tzan and Y.M Yang,. Journal of Heat Transfer v.112, pp.207-212 (1990).
11. W.T Wu, Y.M. Yang and J.R. Maa, Journal of Heat Transfer v.117, pp.526-529 (1995).
12. C.N. Ammerman and S.M You, Journal of Heat Transfer v.118: pp.429-435 (1996).
13. J.L. Zakin, J Myska and Z. Chara, AIChE Journal, v.42, pp.3544-3546 (1996).

HEAT TRANSFER ASPECT TO UPGRADE THE QUALITY OF PLASTICS

Yasuo Kurosaki
Department of Mechanical Engineering and Intelligent Systems
The University of Electro-Communications
Email: kurosaki@mce.uec.ac.jp; Fax: +81-424-80-1085

Isao Satoh, Takushi Saito
Department of Mechanical and Intelligent Systems Engineering
Tokyo Institute of Technology
Email: satohi@mep.titech.ac.jp; Fax:+81-3-5734-3917
Email: tsaito@mep5.mep.titech.ac.jp; Fax:+81-3-5734-3917

Keywords: polymer injection, infrared radiation, birefringence, transcribability, moldability

ABSTRACT. The lecture delivers an innovative injection molding process whose concept was developed from the heat transfer point of view. The process is able to improve the optical quality and the transcribability of injection molded components by applying infrared radiation on the moving polymer melt injected in the mold cavity. The birefringence generated in the skin-layer of molded products can be reduced by radiative heating, and the feasibility of this technique was investigated experimentally using a CO_2 laser beam as a radiation source. The numerical simulation clarified the effects of CO_2 laser radiation on the quality of molded polymer. The effects of radiative heating on the skin-layer of the molded polymer were observed using the mold with transparent windows, and the residual birefringence frozen in the molded specimen was measured. The results clearly showed that the birefringence in the skin-layer of injection molded polymer strips was reduced by CO_2 laser heating. In addition, the transcribability from the surface nature of mold to the surface of polymer product by the proposed method was experimentally confirmed. It was noted to be upgraded so as to be applicable to products requiring a high quality. Another advantage is that the processing time is only slightly increased to process high quality components.

1. INTRODUCTION

Plastics have been used in various fields in industry, electric devices, automobiles, housing elements and so on. Polymer injection moldingprocess is one of the most cost-effective production processes to fabricate plastics. Heat transfer in injection molding process plays an important roleon the quality of molded components.

In a typical injection molding process, resin material which is (usually supplied as pellets) is melted in a heating barrel to a temperature of about 523 K by electric heaters so as to become a viscoelastic fluid. As shown in Fig. 1, the molten polymer is then injected with a high flow rate under high pressure into a cold mold cavity, of which the temperature is usually maintained between 303 and 373 K. During the filling stage the polymer melt is cooled from its surface through contact with the cold mold wall, and a "solidified surface layer" is formed in the vicinity of the mold wall. Because of the high viscosity in this layer, injection molded polymer products inherently suffer many different problems such as shape deformation, residual stresses, low moldability, bad transcription and birefringence. These problems are fatal defects for precise products such as photo memory disks, camera lenses, electronic devices and micro-machine parts[1.2].

To avoid these problems, a number of techniques have been proposed and investigated. Jansen and Flaman[3, 4]

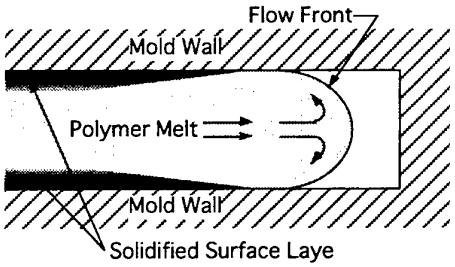

Fig.1. Polymer melt behavior in the mold cavity for the case of the conventional injection molding process

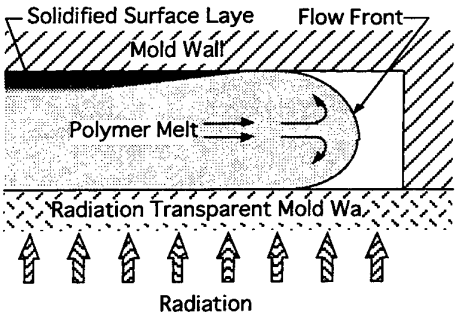

Fig.2. Polymer melt behavior in the mold cavity for the case of the innovative injection molding process

used thin electric heaters pasted on the mold walls to prevent the temperature drop of the molten polymer during the filling stage. Liou and Suh [5] proposed a technique for reducing the residual stress in the molded polymer by applying a PTFE (Teflon) layer on the mold wall. These techniques do result in a quality improvement of the molded products, but they also increase the cycle time because they also hinder the cooling of the polymer during the cooling stage. In these techniques, the generation of the solidified layer is controlled by avoiding heat transfer between the mold wall and the molten polymer. After completion of the filling stage, the molten polymer should be cooled as fast as possible in order to minimize the cycle time, but high temperature/low thermal conductivity mold walls hinder the cooling of the molded polymer also after the filling stage. In order to satisfy these two competing factors, namely, quality improvement and cycle time minimization, the authors[6,7] have proposed an "Injection Molding Process Assisted by Radiation Heating", developed from the heat transfer point of view.

In the proposed injection molding process, the temperature of a skin layer generated adjecent to the mold wall is raised by an infrared (IR) radiation heating. In this situation, the mold wall is not heated directly by the irradiation and continuously cools the molded polymer during the filling and cooling phases of the process. Consequently, the temperature of the molded polymer decreases sharply when the radiation heating is stopped. The elongation of the cycle time due to the radiation heating is therefore very small.

To realize this concept, a CO_2 laser was used as a radiation heating source, and Zinc Selenide (ZnSe) as transparent window material for the radiation. ZnSe is almost completely transparent to CO_2 laser light (wave length = 10.6 mm). On the other hand, most polymers are semi-transparent to the IR radiation. For example, the absorptivity of polystyrene for CO_2 laser irradiation is about 3000 times higher than that of ZnSe. Consequently, the CO_2 laser radiation heats only a very thin layer of polymer the molded polymer in the cavity as shown in Fig. 2.

In this paper the feasibility of the proposed injection molding process was investigated numerically, as well as experimentally by using an experimental mold. Experiments focused on reduction of the birefringence frozen in the skin layer, improving the transcription of minute mold surface markings onto the molded polymer surface, and finally improving the moldability of the melt in very thin flow passages.

2. NUMERICAL SIMULATION OF POLYMER TEMPERATURE APPLIED BY CO_2 LASER RADIATION

Modeling and Formulation

The temperature profiles in the molded polymer were numerically estimated using an unsteady-state heat transfer model before experimental examination was done. The purpose of this simulation was not to obtain accurate temperature distributions in the molded polymer but to estimate whether the CO_2 laser irradiation has sufficient effect for preventing the temperature drop of the molded polymer surface. Conduction heat transfer is predominant in this system because the injection velocity of the molten polymer is relatively small, and the thermal conductivity of the mold wall is much larger than that of the molded polymer. The authors therefore assumed the heat transfer in this simulation to be two-dimensional as shown in Fig. 3. Also the polymer melt is assumed to flow at constant mean velocity between the two parallel mold walls. On the outer side (not the melt side) of each mold wall is assumed to be maintained at a constant temperature corresponding to the cooling water temperature in the practical molding situation. Actually, since molten polymer is injected into an empty cavity, a melt front exists in the mold cavity during the filling stage. In the present calculation, however, the existence of a melt front was ignored in order to simplify the numerical calculation: polymer melt having an uniform inlet temperature T_{in}, continuously flows into the mold gap, and is transiently cooled by the mold walls having an initial

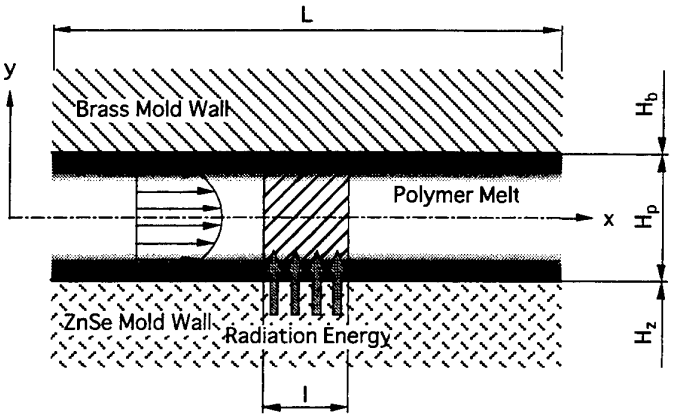

Fig.3. A model for numerical calculation of the temperature of the polymer melt with radiation heating

temperature T_w. In the present calculation, polystyrene is used as the polymer material, and the top and bottom of mold walls are made of brass and ZnSe respectively.

Under these circumstances, the governing equations for the polymer melt flow and temperature can be written as:

* conservation of mass:

$$\frac{\partial u}{\partial x} + \frac{\partial v}{\partial y} = 0 \tag{1}$$

* conservation of X momentum:

$$\rho_p\left(\frac{\partial u}{\partial t} + u\frac{\partial u}{\partial x} + v\frac{\partial u}{\partial y}\right) = -\frac{\partial P}{\partial x} + \frac{\partial}{\partial x}\left(\eta\frac{\partial u}{\partial x}\right) + \frac{\partial}{\partial y}\left(\eta\frac{\partial u}{\partial y}\right) \tag{2}$$

* conservation of Y momentum:

$$\rho_p\left(\frac{\partial v}{\partial t} + u\frac{\partial v}{\partial x} + v\frac{\partial v}{\partial y}\right) = -\frac{\partial P}{\partial y} + \frac{\partial}{\partial x}\left(\eta\frac{\partial v}{\partial x}\right) + \frac{\partial}{\partial y}\left(\eta\frac{\partial v}{\partial y}\right) \tag{3}$$

* conservation of thermal energy:

$$\rho_p c_p\left(\frac{\partial T_p}{\partial t} + u\frac{\partial T_p}{\partial x} + v\frac{\partial T_p}{\partial y}\right) = \kappa_p\left(\frac{\partial^2 T_p}{\partial x^2} + \frac{\partial^2 T_p}{\partial y^2}\right) + Q_r + \eta\Phi \tag{4}$$

where the second term on the right hand side of eq. (4) is the heat generation due to radiation absorption within the polymer melt in the irradiated region shown in Fig. 3, and is given by the following equation:

$$Q_r = \left|\frac{dI}{dy}\right| = \left|-\beta I_0 \exp\left(-\beta\delta\right)\right| \tag{5}$$

where I_0 is the incident CO_2 laser intensity, b the absorption coefficient of the polymer and d the radiation penetration depth (i.e. $d = y + H/2$). The third term on the right hand side of eq. (4) is the viscous dissipation function defined as

$$\Phi = 2\left[\left(\frac{\partial u}{\partial x}\right)^2 + \left(\frac{\partial v}{\partial y}\right)^2\right] + \left(\frac{\partial v}{\partial x} + \frac{\partial u}{\partial y}\right)^2 \tag{6}$$

Thermal properties including the absorption coefficient of the polymer are assumed to be constant except for the viscosity. The authors considered the temperature dependence of the viscosity to be given by

$$\eta = \eta_0 \exp\left(-A \frac{T - T_r}{T_r} \right) \tag{7}$$

Governing equations in the mold walls are

* conservation of thermal energy in the brass mold wall:

$$\rho_b c_b \frac{\partial T_b}{\partial t} = \kappa_b \left(\frac{\partial^2 T_b}{\partial x^2} + \frac{\partial^2 T_b}{\partial y^2} \right) \tag{8}$$

* conservation of thermal energy in the ZnSe mold wall

$$\rho_z c_z \frac{\partial T_z}{\partial t} = \kappa_z \left(\frac{\partial^2 T_z}{\partial x^2} + \frac{\partial^2 T_z}{\partial y^2} \right) \tag{9}$$

The boundary conditions for the model shown in Fig. 3 are as follows:

* inlet of the polymer melt

$$T_p = T_{in}, \quad u = \text{given (parabolic)}, \quad v = 0 \qquad \text{at } x = 0, \; -\frac{H_p}{2} \le y \le \frac{H_p}{2}$$

* the outer sides of the mold walls

$$T_b = T_z = T_w \qquad \text{at } 0 \le x \le L, \; y = \frac{H_p}{2} + H_b; \; 0 \le x \le L, \; y = -\frac{H_p}{2} - H_z$$

$$\frac{\partial T_b}{\partial x} = 0, \; \frac{\partial T_z}{\partial x} = 0 \qquad \text{at } x = 0, \; x = L, \; -\frac{H_p}{2} - H_z \le y \le -\frac{H_p}{2}, \; \frac{H_p}{2} \le y \le \frac{H_p}{2} + H_b$$

* boundary between molten polymer and mold wall

$$T_b = T_p, \; \kappa_b \frac{\partial T_b}{\partial y} = \kappa_p \frac{\partial T_p}{\partial y}, \; u = v = 0 \qquad \text{at } 0 \le x \le L, \; y = \frac{H_p}{2}$$

$$T_p = T_z, \; \kappa_p \frac{\partial T_p}{\partial y} = \kappa_z \frac{\partial T_z}{\partial y}, \; u = v = 0 \qquad \text{at } 0 \le x \le L, \; y = -\frac{H_p}{2}$$

The initial conditions for the present simulation was that the molten polymer flow was fully developed. At $t = 0$ the polymer was assumed to be at an uniform temperature, T_{in}. At $t > 0$ the polymer melt was suddenly cooled by the mold walls at temperature T_w and the radiation heating was simultaneously started. At $t = 0$ the mold walls were assumed to be at an uniform temperature, T_w.

The governing equations were solved with the Finite-Difference Method with control volume approach, subject to the molding conditions cited in Table 1 and material properties summarized in Table 2. To calculate the temperature profiles within the polymer melt and the mold walls, the authors used 80 uniform control volumes in the X direction and 140 control volumes in the Y direction. The dimensions of the computational domain and the size of the control volumes are summarized in Table 3. The time step for each successive calculation was set at 0.02 sec. It was confirmed that these grids and time-step are sufficiently fine to obtain accurate temperature fields.

TABLE 1.Molding conditions used for the present numerical calculation

Initial Mold Temperature	(℃)	30
Initial Melt Temperature	(℃)	240
Injection Velocity	(m/s)	0.10
Radiation Intensity	(W/m^2)	8.0×10^5
Time Step	(s)	0.02

Estimated Temperature Distribution in the Molten Polymer

Figure 4 shows the time dependent temperature change in the molded polymer whose one surface is partially irradiated by IR radiation. In these figures the molten polymer flows from left to right, and one quarter part of the calculated domain is omitted from both the left and right ends so as to show the gap-wise temperature profile within the polymer melt more clearly. As shown in this figure, the injected polymer melt is cooled immediately from its surface by unsteady heat transfer to the cold mold wall, but the temperature drop of the polymer surface is sufficiently prevented in the region where the IR radiation heating is applied.

To obtain more detail on the temperature distribution within the polymer melt in the gap-wise direction, the time dependent temperature change at the right end of the irradiated region (dashed line in Fig. 4) is plotted in Fig. 5. The left and right ends of this figure correspond to the irradiated and not irradiated surfaces respectively. The dashed line in Fig. 5 shows the lowest desirable temperature for easy molding of polystyrene (453K). As shown on the right hand side of Fig. 5 (the region which was not irradiated), the polymer melt temperature of the surface region decreases monotonously and rapidly with elapsed time. This result corresponds to the temperature profiles within the polymer molded by the conventional injection molding process. In this case various problems induced by the generation of the solidified surface layer may occur. On the other hand, as shown on the left hand side of Fig. 5 (irradiated region), the temperature in the irradiated region is maintained at a temperature sufficiently higher than the glass transition temperature of polystyrene. Note that the temperature in the vicinity of the surface is higher than T_{in}. This can be explained by the fact that the heat generation due to absorption of radiation occurs not in the mold wall but in the polymer itself. This result typically indicates the characteristics of the current injection molding process which directly supplies the energy to the polymer melt in the cavity. Careful inspection of Fig. 5 shows that the melt temperature just inside the irradiated region decreases with elapsed time. This is because the polymer melt cooled from the mold wall flows into the irradiated region from the upper region which was not irradiated. In addition, it should be pointed out that the temperature of the mold wall surface (or temperature of the polymer surface) is only slightly affected by the IR radiation. This suggests that the polymer temperature near the mold wall can be quickly controlled by the IR radiation heating without any significant increase in process duration.

3. EXPERIMENTAL INVESTIGATION OF QUALITY

Experimental Setup and Procedure

A schematic diagram of the experimental setup is shown in Fig. 6. It consisted of two optical systems, one for heating, and one for observation of the birefringence distributions. In the present study a CO_2 laser (NAL-10D,

TABLE 2. Material properties

		Polystyrene	Brass	Zinc-Selenide
Density	(kg/m^3)	950	8500	5270
Specific Heat	(J/kg/K)	2070	370	340
Thermal Conductivity	(W/m/K)	0.185	106	16.0
Absorptivity (at $\lambda = 10.6$ μm)	(1/m)	8500	–	2.3
Arrhenius Empirical Constant		10.85	–	–
Reference Temperature	(℃)	151.3	–	–
Glass Transition Temperature	(℃)	100.5	–	–
Reference Viscosity	(Pa-s)	15770	–	–

TABLE 3. Dimensions of the computational domain and the size of control volumes

	x direction	y direction
Polymer Melt	Lp = 40 mm, 80 div. (0.5 mm/div.)	Hp = 3mm, 60 div. (0.05 mm/ div.)
Brass Mold Wall	Lb = 40 mm, 80 div. (0.5 mm/div.)	Hb = 20 mm, 40 div. (0.5 mm/div.)
ZnSe Mold Wall	Lz = 40 mm, 80 div. (0.5 mm/div.)	Hz = 20 mm, 40 div. (0.5mm/div.)
Irradiation Region	l = 4.0 mm	

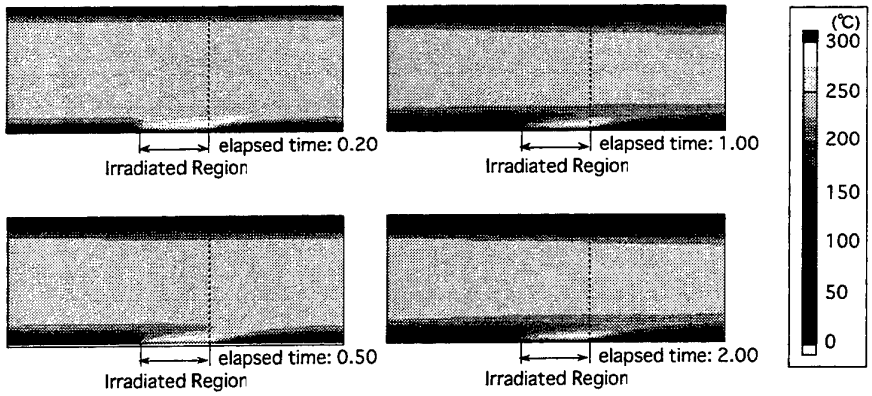

Fig. 4. Temperature profiles within the flowing polymer melt with radiation heating

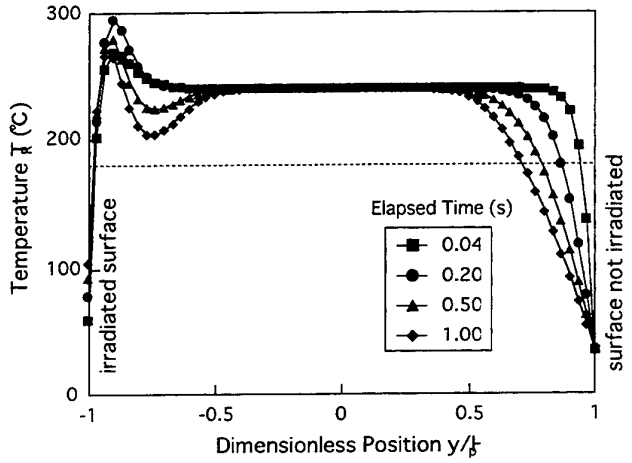

Fig. 5. Time dependent temperature distribution in the gap-wise direction with radiation heating

Nihon Kagaku Engineering Co.) was used as the IR radiation heating source. The laser specifications of the CO_2 laser are shown in Table 4. The laser beam introduced from the side of the mold was reflected by a metal mirror installed in the mold, and then guided to the polymer melt inside the mold cavity. Details of the test mold is shown in Fig. 7. Basically, the mold walls consisted of brass, but one mold wall had a ZnSe window for the IR radiation. The other two side walls were fabricated from acrylic resin plates in order to observe the flow and birefringence in the polymer. To observe the birefringence pattern an optical setup similar to that used in the photo-elastic method was used. The time-dependent birefringence pattern was observed and recorded by a video camera.

The sizes and shapes of the products molded in the present study are shown in Fig. 8. The reduction of residual birefringence due to IR irradiation was examined using the simplest product (Fig. 8 (a)). To measure the residual birefringence distribution in the gap-wise direction, a thin specimen was cut out from the molded strip (Fig. 9) with a diamond cutter. As shown in Fig. 10, for examining the improvement of the transcribability, micro scale grooves (10 mm in width) engraved on the ZnSe transparent mold surface were used. This was followed by SEM observation and surface geometry measurements were performed on the micro protrusions caused by the transcription of the micro grooves. Lastly the improvement of the moldability was investigated by using a mold cavity having a thin flow passage 180 mm thick, and 3 mm wide (Fig. 8(c)). The improvement of the moldability in the thin flow passage was examined by measuring the polymer volume which flowed into the upper cavity of the mold. The laser beam irradiation was initiated just before the polymer melt passed over the heated area, and ceased just after the melt flow stopped. The irradiated region of the polymer surface was limited to the circular area of the laser beam diameter (ϕ 4 mm).

Polystyrene ST 970 K supplied by Sumitomo Chemical Co. LTD. was used as the molding material. The material properties are summarized in Table 2. All polymer products were molded using an injection molding machine

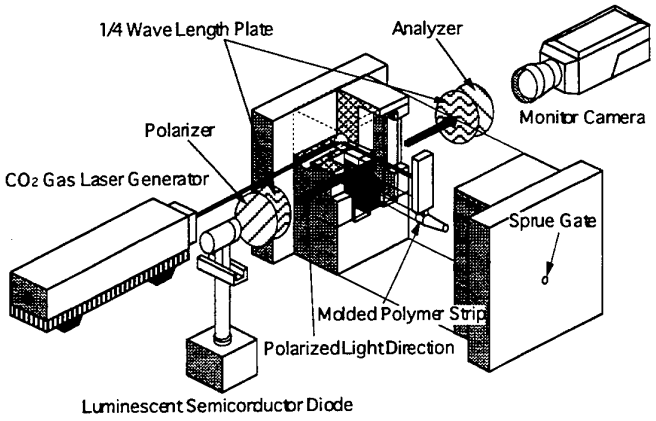

Fig.6. Experimental setup

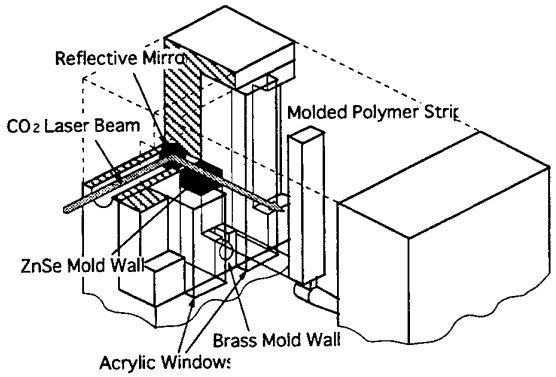

Fig. 7. Detail of the experimental mold having a ZnSe window

TABLE 4. Specifications of the CO_2 laser used in the present study

Generated Wave Length	(μm)	10.6
Max. Output Power	(W)	10
Beam Diameter	(mm)	4
Max. Power Density	(W/cm^2)	80

(Minimat 8/7, Sumitomo Heavy Industries Co.) with a maximum clamping force of 7 tons. The molding conditions are summarized in Table 5. It should be noted that the injection pressure applied in this study was substantially lower than that normally used in practical processes, so as to avoid destruction of the IR transparent (ZnSe) window.

Reduction of the Birefringence in the Molded Polymer

Molecular orientation is inherent in injection molded polymer products, since the polymer molecules near the mold wall are stretched by the polymer flow during the filling stage, and are frozen in this stretched condition by rapid cooling through contact with the cold mold wall. The birefringence due to the molecular orientation seriously affects the optical quality of injection molded such as CD-ROMs, mirrors and lenses[1,8]. In order to try and reduce the residual birefringence in the molded polymer, the authors applied IR heating to the injection

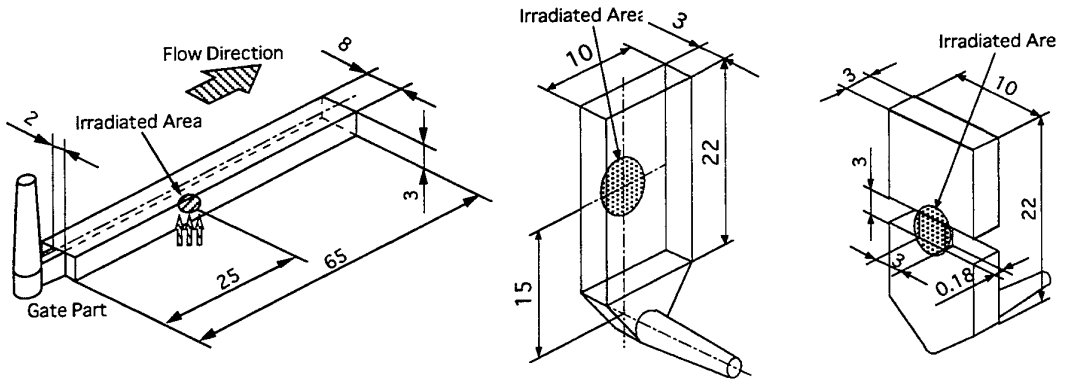

(a) for reducing the residual birefringence

(b) for improving the surface transcription

(c) for improving the moldability in the very

Fig. 8. Dimensions and shapes of the molded polymer specimens (dimensions are in mm)

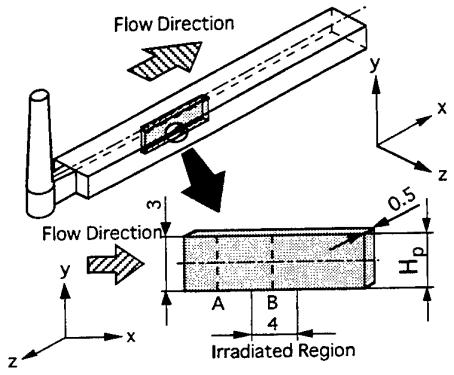

Fig.9. Specimen cut out from the molded polymer strip for the birefringence measurement. The measured positions A and B are indicated. (dimensions are in mm)

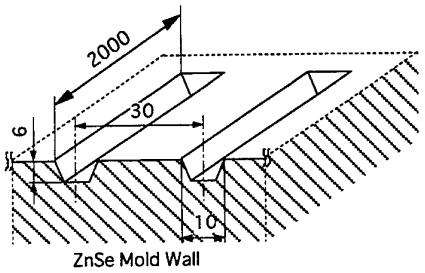

Fig.10. Detail of the micro scale grooves engraved on the ZnSe window surface (dimensions are in μm)

molding process.

Figure 11 shows typical birefringence patterns in the entirely solidified polymer in the mold cavity, both without, and with IR radiation heating. As shown in Fig. 11 (a), a large number of fringes exist near the surface of the molded polymer. These fringes correspond to the iso-birefringence lines, and this means that the polymer molecules are highly oriented in this region. As shown in Fig. 11 (b), however, the highly oriented layer, i.e. the "solidified surface layer," disappears in the vicinity of the surface in the irradiated region, and the birefringence is effectively reduced. This is explained by the fact that the polymer temperature in the irradiated region rises with the CO_2 laser heating and consequently the relaxation of molecular orientation is enhanced in this region, even during the filling process.

Figure 12 shows the birefringence distributions measured by a polarizing microscope on a specimen cut out from an irradiated polymer strip as shown in Fig. 9. Figure 12 shows the magnitude of birefringence in the x-y plane. The left end of the figure corresponds to the irradiated surface of the molded polymer. As shown in Fig. 12 (a), birefringence near both surfaces is quite large at the location which received no irradiation (location A in Fig. 9), and this birefringence corresponds to the solidified surface layer. On the other hand, as shown in Fig. 12 (b), the residual birefringence on the irradiated surface which was measured at location B in Fig. 9 was effectively reduced by the CO_2 laser heating.

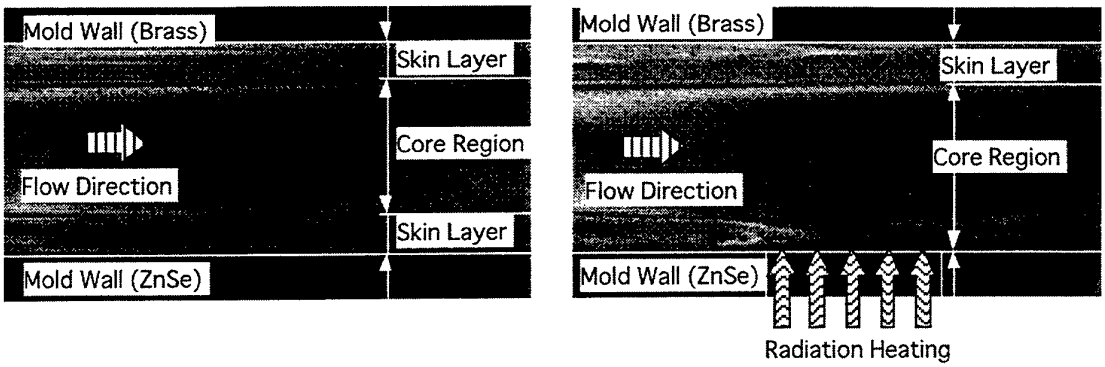

(a) without radiation heating (b) with radiation heating

Fig.11. Residual birefringence pattern within the molded polymer strip

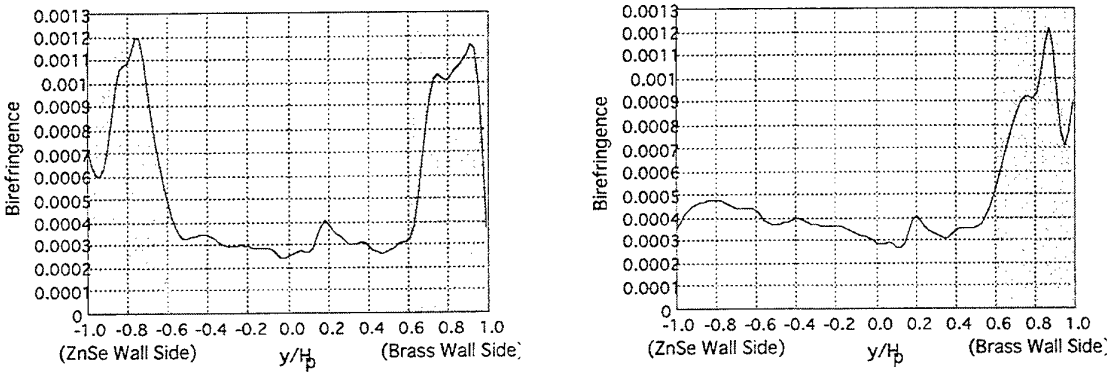

(a) without radiation heating (b) with radiation heating

Fig.12. Residual birefringence distribution in the gap-wise direction

TABLE 5. Molding conditions used in the present experiments

Mold Wall Temp.	(K)	302~352
Melt Temp.	(K)	512
Injection Velocity	(cm/s)	3.7~15
Holding Pressure	(MPa)	12~44
Holding Time	(s)	10
Radiation Intensity	(W/cm^2)	80

Improvement of Transcribability of the Molded Polymer Surface

Good surface transcription is very important for optical and photoelectronic products where highly precise surface geometries are required. For example, a photo memory disk has a large number of micro scale pits on the surface. It is very difficult to manufacture these highly precise polymer devices through the conventional injection molding process. Specifically, the generation of the solidified surface layer lowers transcribability of the

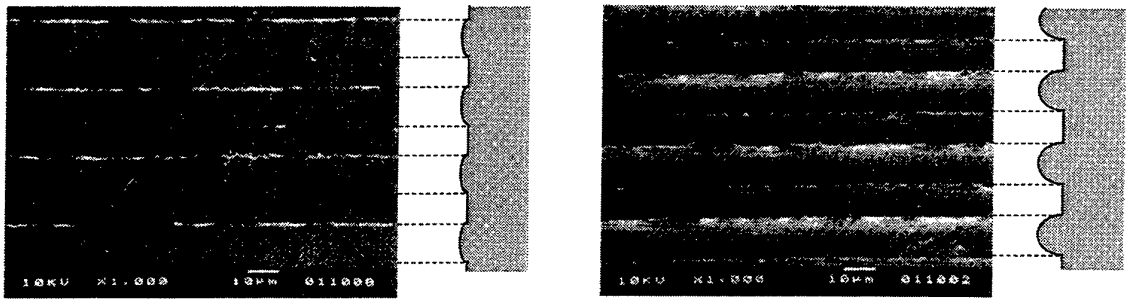

(a) without radiation heating (b) with radiation heating

Fig.13. Scanning electron micrographs of the protrusions formed by transcription of the micro scale grooves engraved on the ZnSe window surface

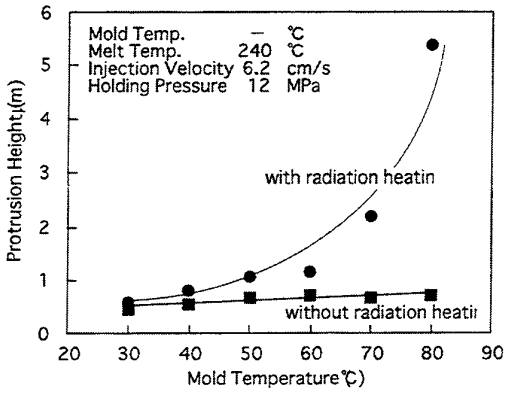

Fig.14. Effect of mold wall temperature on the height of the protrusions transcribed onto the molded

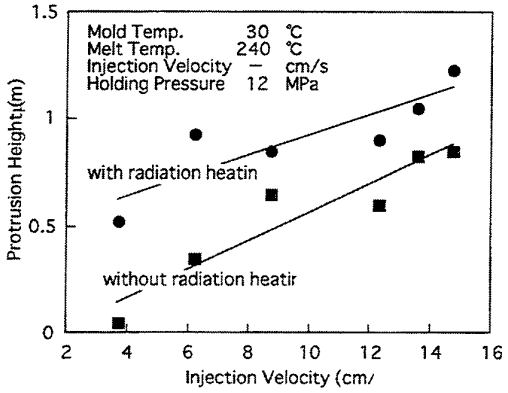

Fig.15. Effect of injection velocity on the height of the protrusions transcribed onto the molded surface

polymer surface because the cooled polymer on the mold surface is not so flexible so as to duplicate the micro scale geometry on the mold surface accurately enough.

As mentioned previously, the ZnSe window assembled in the test mold had micro scale grooves on its surface. Figure 13 shows the SEM photographs of the polymer surface transcribed from the grooves. Figures 13 (a) and (b) show the polymer surface molded without and with IR radiation, respectively. Comparing these two photo groups, one can see that the transcribability of the molded polymer surface was effectively improved by applying the radiation heating. In order to investigate the influence of the molding conditions on the transcribability, the height of the protrusions on the polymer surface was measured for various mold wall temperature and injection rate settings. The results are shown in Figs. 14 and 15. As shown in these figures, with no irradiation, the transcribability of the molded polymer surface is not sufficient, even when the mold wall is heated up to 343K. However, when the radiation heating is applied, the protrusion height is effectively increased, especially in the case where the mold wall temperature is higher than 343K .

Improvement of the Moldability for Very Thin Mold Gaps

In the conventional injection molding process, the generation of the solidified surface layer induces the "short shot" problem and/or large pressure drop during mold filling, especially when the mold gap thickness is thin. In practical injection molding, higher mold wall temperature and/or higher injection rate settings are often applied to solve these problems. However, these countermeasures may result in other problems such as lower productivity and/or decomposition of the polymer material due to excessive viscous heating. In this study, therefore, the authors intended to improve the moldability of injection molded polymer products for very thin mold gaps by applying IR radiation heating.

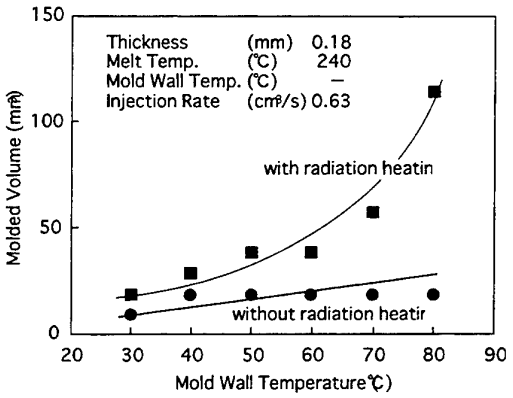

Fig.16. Polymer melt volume that passed through the very thin mold gap as a function of mold wall temperature

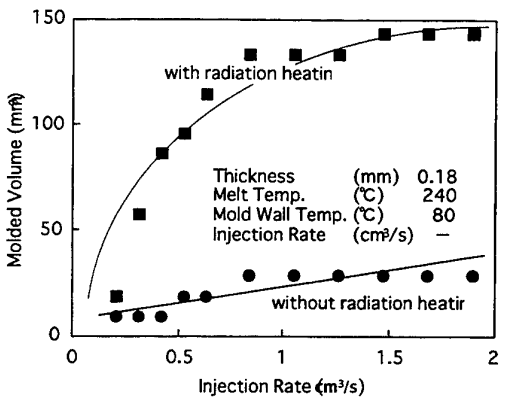

Fig.17. Polymer melt volume that passed through the very thin mold gap as a function of injection rate (injection velocity)

As described previously, the improvement of the moldability was investigated by measuring the polymer volume which flowed into the upper cavity through a very thin passage (180 mm). Figures 16 and 17 show the effect of the mold wall temperature and the flow rate on the polymer volume flowing through the very thin passage, respectively. One can see that the moldability for a very thin mold gap (180 mm) is hardly improved without radiation heating, but significantly improved with irradiation. This result indicates that the moldability of injection molded polymer products is sufficiently improved by applying the IR irradiation even if the thickness of the product is much thinner than that of the products which is difficult to mold by the conventional injection molding process.

4. CONCLUDING REMARKS

The concept for an innovative injection molding process assisted by IR radiation heating to suppress cooling during the filling process is proposed. The effect of the radiation heating on the temperature profiles within the molten polymer was numerically estimated, and the validity of the proposed process was experimentally confirmed for three major problems associated with injection molded polymer products, namely: residual birefringence in the skin layer, transcribability of the molded surface for micro scale geometries, and moldability in the case of very thin mold gaps. Although the proposed innovative process requires an IR radiation heat source and a mold wall transparent to IR radiation, the authors believe that the process proposed in this paper is practically feasible for improving the quality of high precision polymer products having micro scale configurations because this process hardly affects the process time required for the molding.

NOMENCLATURE

A	Arrhenius empirical constant	[−]
c	specific heat	[J/kg/K]
H	thickness	[m]
I_0	initial laser power density	[W/m²]
l	width of the irradiated region	[m]
L	length of the cavity	[m]
P	pressure	[Pa]
Q_r	heat generation due to the radiation absorption	[W/m³]
t	time	[sec]
T	temperature	[℃]
T_{in}	molten polymer temperature at the inlet of the mold	[℃]
T_w	initial mold wall temperature	[℃]
T_r	reference temperature	[℃]
u, v	x and y velocity components	[m/s]
x, y, z	coordinates	[m]

β	absorption coefficient of polymer	[1/m]
δ	laser absorption thickness	[m]
Φ	viscous dissipation function	[W/m^3]
κ	thermal conductivity	[W/mK]
η	viscosity	[Pa-s]
η_0	reference viscosity	[Pa-s]
ρ	density	[kg/m^3]

Subscripts

b	brass
p	polymer (polystyrene)
R	with radiation heating
z	Zinc-Selenide

ACKNOWLEDGMENT

This work was supported in part by the Ministry of Education, Science and Culture of Japan under the grant No. 05239104 and by the New Energy and Industrial Technology Development Organization under the grant of the Proposed-Based Promotion Program on Immediate R & D.

REFERENCES

1. M. Takeshima and N. Funakoshi, Journal of Applied Polymer Science, v.32-2, pp. 3457-3468 (1986).
2. W. R. Friedel, Polymer Engineering and Science, v.30, No.14, pp. 813-820 (1990).
3. K. M. B. Jansen and A. A. M. Flaman, Polymer Engineering and Science, v.34-11, pp. 894-897 (1994).
4. K. M. B. Jansen and A. A. M. Flaman, Polymer Engineering and Science, v.34-11, pp. 898-904 (1994).
5. M.J. Liou and N.P. Suh, Polymer Engineering and Science,v 29-7, pp. 441-447 (1989).
6. Y. Kurosaki and I. Satoh, "Visualization of Flow and Solidification of Polymer Melt in the Injection Molding Processes," Heat Transfer Manufacturing and Materials Processing. ASME HTD,v.113, pp. 63- 70 (1989).
7. Y. Kurosaki, I. Satoh and T. Saito, "Reduction of Birefringence in a Skin-Layer of Injection Molded Polymer Strips Using CO_2 Laser Irradiation," ASME HTD, v. 306, pp. 201-208 (1995).
8. J. P. Wu and J. L. White, Polymer Engineering and Science, v.31-9, pp. 652-660 (1991).

THERMAL AND NON-THERMAL REGIMES OF GLIDING ARC DISCHARGES

Ozlem Mutaf-Yardimci, Alexei V. Saveliev
Alexander A. Fridman, Lawrence A. Kennedy
Department of Mechanical Engineering
University of Illinois at Chicago, Chicago, USA 60607
Email: lkennedy@uic.edu ; Fax : (312) 9968664

Keywords: non-equilibrium plasma, gliding discharges

ABSTRACT. The sliding arc discharge starts at the shortest distance between the electrodes, then moves with the gas flow at a velocity about 10 m/s and the length l of the arc column increases together with the voltage. When the length of the gliding arc exceeds its critical value l_{crit}, heat losses from the plasma column begins to exceed the energy supplied by the source, and it is not possible to sustain the plasma in a state of thermodynamic equilibrium. As a result, a fast transition into a non-equilibrium phase occurs. The discharge plasma cools rapidly to a gas temperature of about T_0 = 1000 K and the plasma conductivity is maintained by a high value of the electron temperature T_e = 1 eV (about 11,000 K). After this fast transition, the gliding arc continues its evolution, but under non-equilibrium conditions ($T_e >> T_0$). Gliding discharges comprising both equilibrium and non-equilibrium plasma conditions offer high energy efficiency and selectivity for chemical processes. Prevailing parameters satisfying non-equilibrium plasma conditions at relatively high power levels should be well understood and characterized. In the present work, gliding discharges formed between diverging electrodes in air flow are discussed. These were studied experimentally over a wide range of gas velocities and power levels. Depending on the system parameters the following discharge regimes were observed: low power non-equilibrium discharge; thermal quasi-equilibrium discharge; and gliding discharge with equilibrium to non-equilibrium transition. The effect of system parameters on discharge characteristics is analyzed. The equilibrium to non-equilibrium transition was experimentally observed as a change of voltage increase rate with discharge length growth. The local electric field, defined as dV/dl, increased up to three times, indicating the change of plasma conditions. However, previously reported phenomenon of length explosion was not supported by our experimental data. The co-existence of equilibrium and non-equilibrium phases is also discussed in the frame of phenomenological theory, assuming formation of a growing non-equilibrium fragment inside the gliding discharge channel. It was found that high flow velocities provide intensive cooling, an increase of electric field, and a decrease of gas temperature, promoting equilibrium to non-equilibrium transition at high power levels.

I. INTRODUCTION

The number of industrial applications of plasma technologies is extensive and involves many industries. High energy efficiency, specific productivity, and selectivity may be achieved in plasmas for a wide range of chemical processes. As an example, for CO_2 dissociation in non-equilibrium plasmas under supersonic flow conditions, it is possible to selectively introduce up to 90% of total discharge power in CO production when the vibrational temperature is about 4,000 K and the translational temperature is only 0(100) K. The specific productivity of a such a supersonic reactor achieves 1,000,000 liter/hour, with power levels up to 1 MW. The key point for practical use of any chemical process in a particular plasma system is to find the proper regime and optimal plasma parameters among the numerous possibilities intrinsic to systems far from equilibrium. In particular it is desired to provide high operating power for the plasma chemical reactor together with high selectivity of the energy input while simultaneously maintaining non-equilibrium plasma conditions.

Generally, two very different kinds of plasmas are used for chemical applications. Thermal plasma generators have been designed for many diverse industrial applications covering a wide range of operating power levels from less than 1 kilowatt to over 50 Megawatts. However, in spite of providing sufficient power levels, these are not well adapted to the purposes of plasma chemistry, where selective treatment of reactants (through the excitation of molecular vibrations or electron excitation) and high efficiency are required. The main drawbacks of using thermal plasmas for plasma chemical applications are overheating of the reaction media when energy is uniformly consumed by the reagents into all degrees of freedom and hence, high energy consumption required to provide special quenching of the reagents, etc. Because of these drawbacks, the energy efficiency and selectivity of such systems are rather small (only one of many plasma chemical processes developed in the first decades of the century remains, e.g. the production of acetylene from light hydrocarbons in Germany, Hülls).

An alternative approach for plasma-chemical gas processing is the non-thermal one. Silent, glow, corona, short pulse, microwave or radio-frequency (RF) electrical discharges are directly produced in the processed gas, mostly under low pressure. The glow discharge in a low pressure gas is a simple and inexpensive way to achieve a non-thermal plasma. Here, the ionization processes induced by the electric field dominate the thermal ones and give relatively high energy electrons as well as excited ions, atoms and molecules which promote selective chemical transitions. However, the power of glow discharges is limited by the glow to arc transition. Gas, initially below 1 000 K, becomes hot (> 6,000 K), and the electron temperature, initially high enough (> 12,000 K), cools close to the gas temperature. The discharge voltage decreases during such a transition making it necessary to increase the current in order to keep the power on the same level which in turn leads to thermalization of the gas. Thus, cold non-equilibrium plasmas created by conventional glow discharges offer good selectivity and efficiency, but at limited pressure and power levels.

In these two general types of plasma discharges, it is impossible to simultaneously keep a high level of non-equilibrium, high electron temperature and high electron density, whereas most perspective plasma chemical applications simultaneously require high power for high reactor productivity and a high degree of non-equilibrium to support selective chemical process.

These parameters are somewhat achievable in microwave discharges. Skin effect here permits simultaneous achievement of a high level of electron density and a high electric field (and hence a high electronic temperature as well) in the relatively cold gas. Existing super high frequency discharge technology can be used to generate dense (lg n_e (electrons/cm^3) = 13) non-equilibrium plasmas (T_e = 1-2 eV, T_V = 3,000 - 5,000 K, T_0 = 800 - 1,500 K, for super sonic flow $T_0 \leq 150$ K and less) at pressures up to 200 - 300 Torr and at power levels reaching 1 MW.

Recently, a simpler technique offering similar advantages has been proposed, the Gliding Arc. Gliding discharge is an auto-oscillating periodic phenomenon developing between at least two diverging electrodes submerged in a laminar or turbulent gas flow. Self-initiated in the upstream narrowest gap, the discharge forms the plasma column connecting the electrodes of opposite polarity. This column is further dragged by the gas flow towards the diverging downstream section. The discharge length grows with the increase of inter-electrode distance until it reaches a critical value, usually determined by the power supply limits. After this point, the discharge extinguishes but momentarily re-ignites itself at the minimum distance between the electrodes and a new cycle starts. An overview of the early work is given in ref [3].

Plasma generated by the gliding discharge has thermal or non-thermal properties depending on the system parameters such as power input and flow rate. Along with completely thermal and completely non-thermal discharges, it is possible to obtain the transition regimes of the gliding discharges. Powerful and energy efficient transition discharges combine the benefits of both equilibrium and non-equilibrium discharges in a single structure. They can provide plasma conditions typical for non-equilibrium plasmas but at elevated power levels.

The Gliding Arc is a well-known example of a gliding discharge. It was first used in chemical applications in the beginning of this century for the purpose of nitrogen based fertilizer production [1]. In the early 1990's, the Gliding Arc again became popular after A. Czernichowski demonstrated the successful use of it in number of chemical processes[2]. Most of the recent applications are focused on gas conversions and decontamination processes[3] such as carbon dioxide[4] or steam[5,6] reforming of methane to produce synthesis gas ($CO+H_2$); oxidation of low concentration H_2S into SO_2 for pollution control[7,8]; and volatile organic compounds treatment for environmental protection.[2] The Gliding Arc plasma is significantly non-thermal. The electronic, vibrational and translational gas temperatures in the non-equilibrium regime of a Gliding Arc discharge were measured to be approximately 10000 K, 2000-3000 K and 800-2100 K, respectively [9]. These plasma conditions were obtained with the power levels of up to 40 kW and are considered favorable for stimulation of chemical processes.
Although numerous industrial applications have been attempted, the physical mechanisms governing the Gliding Arc evolution remain poorly understood. Further the development of non-equilibrium conditions at high power levels is the most intriguing phenomenon among them.

To date, experimental studies of gliding discharges were focused on optical and electrical measurements of discharge parameters, including neutral, electron and vibrational temperatures; discharge column length and diameter; current, voltage, electric field and power per unit length. Diagnostic methods include high-speed

photography and CCD imaging, emission spectroscopy and time-resolved electrical measurements. For example, a multi-shot camera with a very short exposure time combined with the electrical measurements was used to analyze the arc motion relative to the flow motion[10] Following this work, the same technique was used to describe the properties of the discharge and its changes by using the measurements of electrical parameters as well as temperatures, velocities and length of discharge[8]. Also, the effect of voltage, flow rates and frequency of the power supply was determined in another work and plasma treatment efficiency was studied in the same process of H_2S destruction[12].Temperature measurements included the time-space averaged translational temperatures of the gliding plasma determined from OH band spectra[12]. Similarly, translational, rotational, vibrational and electronic temperatures were measured in another well-developed spectroscopic technique by using N_2 and OH molecular emission spectra where a distinction between equilibrium and non-equilibrium plasma conditions could be done[9].

In the present paper, gliding discharges formed in a parallel flow are studied experimentally in a wide range of gas velocities and input power levels. Employed measurement techniques combines continuous recording of discharge column evolution by a high-speed video camera (up to 1000 frames per second) and synchronized current-voltage measurements. Time-resolved values of discharge length, current and electric field provide the necessary data on critical plasma parameters during evolution of the gliding discharge. A simple model is used to analyze the physical and electrical characteristics of the discharge. Non-thermal, thermal and transition types of gliding discharges are observed depending on power input, gas velocity and blade geometry. Particular attention is given to the transition from equilibrium to non-equilibrium regime observed in a number of experimental conditions.

II. EXPERIMENTAL SETUP

The experimental setup is shown in Fig. 1. The gliding discharge reactor consists of two thin diverging steel electrodes, fixed in a transparent container. In order to achieve a uniform drag of the plasma column by the surrounding flow, a rectangular cross-section (90x13-mm) parallel flow gliding discharge reactor was built. The processing gas is passed through stages of different size fillings and flow diffusers before it is introduced to the section with blades to ensure parallel flow around the blades with controllable flow rates. The power is delivered by a high voltage power supply (Universal Voltronics-BRC 10,000). It has output powers up to 10 kW with no-load voltage variable from 1 to 10 kV with less than 1% ripple on the output voltage. An internal resistance bank was designed that has variable resistance values of 25 to 100 kΩ.

The evolution of the plasma column was recorded continuously by using a high-speed video camera (Kodak EktaPro Motion Analyzer, Model 1000HRC) which has a recording rate of up to 1000 frames per second and an adjustable exposure rate of 0.05 to 1 millisecond. In order to obtain the time-resolved length and position diagnostics of the moving plasma channel, digitally stored images were subsequently analyzed in a personal computer by using a image processing and analysis software (Image Analyst™, AM 3300). A digital oscilloscope (HP 54616B, 500 MHz, 2 GSa/s) was used to record the electrical characteristics of the plasma column during its evolution. Digitized electrical waveforms were transferred to a personal computer via a GPIB interface and then processed using software (HP34801A, BenchLink Scope) that handles the oscillograms and gives output as time-amplitude pairs for further processing. A homemade external trigger ensures the perfect synchronization of the electrical and visual recordings.

The oscillograms were analyzed to obtain discharge electrical characteristics such as average current and voltage values, average power and histograms of all these parameters during individual cycles or overall process. The analysis of the geometrical parameters of the discharge gives the time dependent length, position and diameter values of the moving plasma channel. Finally, the coupling of the electrical and video diagnostic data provides necessary information for developing theoretical or numerical models to relate system parameters to each other.

III. OBSERVATION OF GLIDING DISCHARGE REGIMES

The evolution of gliding discharge plasma (Fig. 2) starts at the shortest distance (usually 2-5 mm) between two diverging electrodes when the applied voltage reaches to the breakdown voltage value (3 kV/mm at atmospheric pressure for air). Immediately after breakdown, the spark channel is formed crossing the gap between the

blades. If the discharge current is limited, the discharge remains non-equilibrium and continues its evolution as spark-like narrow blue string dragged by the gas flow. With sufficiently high power input, a short quasi-equilibrium plasma column is formed and supported by thermal ionization. The gas flow drags the column downstream and the length of the plasma column increases. The equilibrium gas temperature lies in the range 7000-10000 K for powerful discharges. For the experiments with lower electric current and lower power, the temperature in this zone could be as low as 2300 K. The surrounding flow cools the arc column and the power supply compensates the heat losses until the maximum power available from the power supply is reached. If the conditions are appropriate, high electric field values support a small portion of the column to be transferred into the state of thermodynamic non-equilibrium. Some of these conditions are; sufficient cooling supported by the surrounding fluid, adequately high current values for the discharge, high values of breakdown voltages defined by the minimum distance between the electrodes. Further expansion of this non-equilibrium discharge segment inside the equilibrium discharge column causes the translational temperature of the gas to drop gradually to the values around 800-2100 K, while the electric field values are maintained at elevated levels. The plasma conductivity thereafter is sustained by a relatively high electron temperature of about 1 eV (~12000 K). After the maximum possible discharge length is reached, the discharge disappears and a new cycle starts again at the minimum distance between the electrodes.

A picture of the gliding discharge taken by a regular camera can be seen in Fig. 3. Because of the fast repetition rates of cycles (usually 20-100 Hz), the individual elongating plasma columns are not distinct.
Depending on the power input, gas flow rate and blade geometry, three major types of gliding discharges are observed: (i) Thermal (quasi-equilibrium) gliding discharge (Thermal Gliding Arc); (ii) Non-thermal (non-equilibrium) gliding discharge; (iii) Gliding discharge with transition from equilibrium to non-equilibrium state (Non-thermal Gliding Arc).

Gliding quasi-equilibrium discharges, i.e. thermal gliding arcs, have usually high current values and intensive specific power consumption. Gliding non-equilibrium discharges on the other hand retain very low specific power consumption and remains non-equilibrium throughout their evolvement. Transition discharges have both distinct equilibrium and non-equilibrium regimes as well as a smooth transition from one to the other supported by high values of the electric field in a single cycle of plasma column. Transition discharges are most attractive in plasma chemistry due to high power levels and non-equilibrium plasma conditions. In the upcoming sections, these discharges will be discussed in detail.

A. Thermal (Quasi-Equilibrium) Gliding Arc

Thermal (or equilibrium) plasmas are created by thermal heating of the bulk gas in devices like electric arcs. The main ionization mechanism is the thermal ionization of neutral particles, where the translational temperature of the gas and the temperatures of ions and electrons are in equilibrium.

For stationary constant length discharge configurations, arc discharges have current values as low as 0.1-0.2 A, current densities of 10 A/cm^2 or higher, and electric field values from 10V/mm to 40 V/mm[4,14]. In our experiments, the maximum current value is 1 A or lower and although the discharge length and discharge radius altered during the evolution of arc, the current density value is 10-15 A/cm^2. We observed electric field values as low as 30 V/mm.

Thermal gliding arcs are identified by their compact structure that holds the plasma column in a well-preserved form throughout their evolution. The cycle duration and maximum arc length are bigger for higher specific power (power per unit flow rate) inputs. Figure 4 shows four snapshots of the arc evolution for the same cycle. In our experiments, equilibrium discharges were recorded in the limit of high specific power levels corresponding to either low flow rates or high power levels. The flow rates considered in this study were between 0-400 SLM (standard liter per minute) of air and up to 10 kW of power. Maximum arc lengths observed were as high as 20 cm with cycling times of up to 100 ms.

A typical voltage-current histogram of a gliding equilibrium discharge can be seen in Fig. 5. Initial arc development corresponds to the maximum current and minimum voltage values. During the arc evolution, the voltage increases due to increases in discharge length. Also, typical to equilibrium discharges, the power per unit length of discharge appears to be constant. For the particular case given in Fig. 5, this value is close to 5 W/cm. Because of the intense energy deposition to the system, electrodes and surrounding reactor components

are heated and prolonged operation in the quasi-equilibrium regime of gliding discharges requires cooling. During experimentation, it was observed that the period of cycling decreases with increasing flow rate of the processed gas. If the electrodes are positioned sufficiently close, before transition to non-equilibrium occurs, the discharge 're-ignites itself' and a new equilibrium discharge cycle starts[13].

Voltage values as a function of discharge length can be seen in Fig. 6. For this particular case, power source voltage is 7 kV, power source internal resistance is 50 kΩ, and the average cycle time is about 90 ms with a volumetric flow rate of 110 SLM. From the slope of the curve, the electric field value is found to be 33 V/mm. The voltage drop near the electrodes is found from the voltage value corresponding to the zero length of the discharge and all voltage values are corrected accordingly.

B. Non-Thermal (Non-Equilibrium) Gliding Discharge

The non-equilibrium conditions arise from the fact that the temperature of electrons is very much higher than the temperature of the ions and neutral gas. In our experiments, the bulk gas flow temperature was measured on the exit plane of the reactor, and the measurements showed temperatures only on the levels of tens of degrees centigrade. Non-equilibrium gliding discharges are easy to attain with low power levels and high flowrates. But with the low power levels (only tens of Watts) their possible application in plasma chemistry are limited.

Gliding non-equilibrium discharges are different in physical appearance from the quasi-equilibrium ones and the maximum discharge length observed is shorter. The discharge appears smeared by the high flow rate surrounding it. Flow velocities considered in this study were as high as 6 m/s of air at room temperature. Power levels were kept low on the order of tens of Watts to satisfy the low specific power requirement of non-equilibrium discharges. In some cases, addition of another gas, e.g. helium, to the main airflow lowered the breakdown voltage value and made it easy to obtain non-equilibrium conditions. Voltage and current histograms are similar to the one given in Fig 5; for each cycle, after an initial breakdown, a quasi-linear increase in voltage and a quasi-linear decrease in current were observed. Also, duration of cycles was reduced to 7-12 ms which was shorter in comparison to equilibrium gliding discharges. In some cases, blank intervals between cycles without any discharge were also recorded.

C. Transition Gliding Discharge (Non-Thermal Gliding Arc)

Transition gliding discharges are the ones that hold the largest potential among the gliding discharges for practical applications in chemistry. They support high power levels by containing both equilibrium and non-equilibrium phases. Depending on the chemical process under consideration both phases may be useful[14], but most of the time a powerful non-equilibrium discharge is required to improve the selectivity and energy efficiency of plasma chemical reactions. Energy depositions during equilibrium and non-equilibrium expansion of the plasma column may vary depending on the working conditions. Theoretical models predict that in the limiting case, up to the 75% of the total energy can be delivered in the non-equilibrium part of the gliding transition discharge[15].

In these discharges, the formation of an equilibrium plasma column occurs shortly after breakdown. The corresponding values of current are high and the electric fields are low. In this regime, as the discharge length grows, power increases linearly in such a way that equilibrium is maintained until the power supply reaches its limit. After that point, the discharge length keeps growing due to the flow drag, but the power supply is no longer able to support this growth for equilibrium conditions. Hence transition to non-equilibrium conditions starts. When transition occurs, the discharge plasma cools gradually to a gas temperature of about 800-2100 K while the electron temperature is around 1 eV. The voltage keeps increasing although the power level remains constant. The high values of electric field sustain the growth of the non-equilibrium discharge until the end of the cycle.

Detailed spectroscopic and electrical measurements are available in the literature[9] including vibrational and rotational molecular gas temperatures as well as free electron temperatures and concentrations in a low current gliding discharge. It was observed that the discharge begins as a quasi-equilibrium discharge with 2300-4000 K translational and rotational, 3100-4000 K vibrational and 6000 K electron temperatures. These values in the non-equilibrium zone are 800-2100 K for translational and rotational, 2000-3000 K for vibrational and 10000 K for electron temperatures with similar electrical parameters used in our experiments.

The 'length explosion' phenomenon, which is associated with fast equilibrium to non-equilibrium transition (FENETRE),[3,9]was not observed in our experiments in spite of the fact that we continuously recorded the discharge evolution for about 1.3 seconds each run. On the contrary, experimental results lead us to believe that when transition starts, a small non-equilibrium plasma portion within the equilibrium one is created. It is believed that, the high values of electric field sustain the growth of this non-equilibrium portion much faster than the equilibrium one until the end of the cycle. Video recording of the discharge also shows that beginning from the midpoint of the discharge column a less compact and smeared appearance is detected. Therefore, instead of FENETRE, which should cause discontinuities in electrical parameters, it is more reasonable to conclude that a rather slow and smooth transition to non-equilibrium occurs as the discharge length increases.

The major mechanism known to trigger the equilibrium to non-equilibrium transition is an ionization instability mechanism involving the electric circuit instability. In the case that power is not sufficient to support the plasma in the equilibrium regime as the length increases, the gas temperature drops and thermal ionization disappears. Since the resistance of the discharge is decreasing, according to Ohm's law the electric field can be increased. If the electric field is sufficiently high to support non-thermal ionization, non-equilibrium conditions for the plasma are achieved. Previously the physical phenomenon of transition was thoroughly discussed by the authors[3].

A quantitative criterion to distinguish the equilibrium and non-equilibrium regimes was chosen based upon observations of the rate of voltage increase during the discharge evolution (Fig. 7). It is known that the electrical field, which is defined here as the slope of the voltage-discharge length curve, has a higher value in non-equilibrium discharges than it has in equilibrium discharges. For the case given in Fig. 7, the power source voltage was 10 kV, power source internal resistance was 100 kΩ, breakdown current value was 0.1 A, the minimum distance between the electrodes was 3 mm, and the volumetric flow rate was 210 SLM. For this specific case, the electrical field value increased about 2.7 times, showing that after the critical discharge length of approximately 55 mm, transition to non-equilibrium discharge regime started. The energy fraction dissipated by the discharge during the non-equilibrium phase of its evolution is about 30%, while other 70% of the electrical energy is dissipated during the equilibrium phase. Total evolution of each cycle is approximately 30 ms with an average power consumption of 116 W.

IV. EFFECT OF INTERNAL RESISTANCE AND FLOW VELOCITY

The observations given in the previous section shows that particular parameters characterize the discharge regimes. The internal resistance of power supply is one of them and can be set to 25, 50 and 100 kΩ in our experiments. The effect of internal resistance was investigated keeping the other parameters constant. Power source no-load voltage was fixed at 9 kV and volumetric flow rate was set to 330 SLM. The electrode configuration remained unchanged. Results are presented in Fig. 8 and Fig. 9. As one can observe in Fig. 8, the maximum current value (occurring shortly after breakdown) decreases as the resistance value increases.

A stable equilibrium arc can be supported until the plasma resistance becomes equal to the resistance of the power supply[3]. This critical point has the following electrical parameters:

$$I_{crit} = U_0/2R_0 \ , \quad w_{crit} = U_0^2/4R \ , \quad V_{crit} = U_0/2$$

For the highest value of power supply internal resistance (100 kΩ), the discharge starts with maximum current equal to 0.085 A and continues its evolution beyond the point of critical current value ($I_{max}/2$=0.0425 A) before its extinction (Fig. 8). Also, more points are recorded beyond the critical current value with 100 kΩ resistance than with 25 kΩ. Another interesting effect of power supply internal resistance is observed in the voltage versus discharge length characteristics of the discharge. Figure 9 clearly shows that the measured electric fields are higher for high resistance values, and, as a consequence, the maximum attainable discharge length is shorter.

The effect of power source's internal resistance value is dramatic because of the fact that the maximum current available determines the discharge regime achievable for that particular configuration. For comparison, values of voltage divided by discharge length are shown as a function of current in Fig. 10 for different values of internal resistance. According to the previous discussions, as the resistance value decreases from 100 to 25 kΩ, the discharge seems to proceed towards the equilibrium regime.

The effect of cooling was also studied by changing the flow rate of air entering the reactor. All other parameters, e.g. power source voltage, electrode configuration, maximum current applied, were kept constant and flow rate values of 110, 280 and 370 SLM of air were employed. In the parallel flow reactor, these flow rate values correspond respectively to gas velocities of 1.6, 4.1 and 5.4 m/s of air at room temperature. Maximum power level was kept constant at the level of 500 W with an average value of about 340 W.

Figure 11 shows the effect of flow rate (or specific power input) on discharge length-voltage characteristics. Attainable maximum discharge length was increased at least 30% by decreasing the flow from 5.4 to 1.6 m/s confirming the fact that discharge becomes dominantly equilibrium as the cooling is reduced. Corresponding electric field values also decreased from 96 V/mm to 34 V/mm.

Also, for a constant value of the discharge length, faster cooling promotes faster transition to non-equilibrium by maintaining higher electric field values. Meanwhile, higher electric field values allow lower current values that help to convey the discharge faster into the non-equilibrium state (Fig. 12). It is also interesting to observe that for a constant value of the discharge length, as the cooling is increased (or as specific power input is decreased), power per unit length at the beginning of cycles increases as well. This is due to the fact that an effective convective cooling requires increased compensating power for heat losses to keep the discharge stable.

V. MODELING AND DISCUSSION

In order to optimize the plasma conditions for gliding discharges, detailed physical modeling is needed. However, due to the complexity of the gliding discharges,- unsteady behavior in time and space, high temperatures in the discharge, viscous effects, non-equilibrium temperatures, effects of flow patterns, the electrode geometry, and power supply's internal characteristics, etc.- there are no detailed numerical models available. Instead, simple physical models for different configurations were thought to be more practical to estimate the quantities (temperature, electron density, etc.) that are difficult to measure[3,10,16]

The simple one-dimensional analytical consideration was used by Fridman et al. [15] to analyze the arc plasma behavior and evolution. Within this approach the equilibrium and non-equilibrium stages of the Gliding Arc were distinguished. The consideration of the equilibrium stage is based on the Elenbaas-Heller equation, and ionization instability is considered to initiate fast transition to non-equilibrium stage. The model shows that up to 75% of the electrical energy could be deposited in the non-equilibrium stage of the gliding discharge[15]. The possible mechanism of ionization instability leading to non-equilibrium transition was also discussed by Rusanov and co-workers[17]. The Elenbaas-Heller equation was used also by Pellerin et al.[16] to estimate NO_x production in Gliding Arc discharges, assuming the radius of plasma channel to be constant. A similar approach was employed for estimation of the conducting plasma radius.[10]. This analytical model, developed by Richard et al.[10], distinguishes two arc regions - the plasma core (plasma string) and the outer weakly ionized mantle. The temperature profile of the plasma string and conduction radius were assumed to be constant and the convection, as a main source of plasma cooling, was expressed in terms of an axially symmetrical convection flow. It was found experimentally, that increases in the gas velocity resulted in an almost linear rise of power dissipated per unit length of the discharge and in the essential increase of the electric field values.

Despite the fact that the relative velocity of the arc and the gas flow is often small relatively to the gas velocity, this strongly affects plasma conditions in the equilibrium and non-equilibrium phases.[3,15,18]. Although the arc motion is not well defined geometrically and the reported flow measurements are not extensive, studies indicated that the relative arc propagation could be explained as a purely hydrodynamic effect[18]. It was also suggested that when the relative velocity of the arc with respect to the gas flow is high, the mechanism of arc stabilization is changing from diffusive to convective [18].

In the present study, a new approach to model the gliding discharges is presented by establishing the relations between the electrical parameters of the circuit and plasma characteristics of the discharge. Beginning from the electrical circuit characteristics and definition of the plasma discharge column, this model is able to predict the critical circuit parameters promoting the transition to non-equilibrium regime. It is now possible to determine quantitatively the length of the non-equilibrium discharge portion inside the column after the transition point is reached. This transition point was first identified based on the electrical and visual measurements in an early work of authors[19].

Based on our experimental results, we assume that the plasma column is composed of two parts: an equilibrium part and non-equilibrium part. It can be totally equilibrium as in the quasi-equilibrium (arc) gliding discharge or it can be totally non-equilibrium as in the last part of a transition gliding discharge.
At any instant of the discharge evolution, total power consumption can be written as

$$P = l_1 w + l_2 E I \tag{1}$$

where l_1 is the length of the equilibrium part and l_2 is the length of the non-equilibrium part; w represents the power per unit length, which is assumed to be constant for equilibrium part of discharge; E is the electric field and I represents current. For the given electrical circuit (Fig. 13) one can write using Ohm's law

$$U_0 = R_0 I + \frac{P}{I} \tag{2}$$

where U_0 is the power source no-load voltage; R_0 is the power supply internal resistance. Substituting Eq. (1) into Eq. (2) and rearranging gives

$$R_0 I^2 - (U_0 - E l_2) I + w l_1 = 0 \tag{3}$$

From the definition of l, total length of the plasma column (l_1+l_2), Eq. (3) has a solution for the current as

$$I = \frac{U_0 - E l_2}{2R_0}\left(1 \mp \sqrt{1 - \frac{4wR_0(l - l_2)}{(U_0 - E l_2)^2}}\right) \tag{4}$$

Knowing that the current can take only real positive values, which means that the term inside the square root must be a positive value, the solution with plus sign gives the stable solution. Therefore, the existing limit of l_2 as a function of l can be written as:

$$l_{2,\mathrm{lim}} = \frac{U_0 E - 2wR_0}{E^2}\left(1 \mp \sqrt{1 - \frac{(U_0^{\,2} - 4wR_0 l)E^2}{(U_0 E - 2wR_0)^2}}\right) \tag{5}$$

In order for l_2 to exist as a real value, the term in square root in Eq. (5) must have a positive value, which leads us to define the parameter

$$l_{\mathrm{crit}} = \frac{U_0^{\,2} E - (U_0 E - 2wR_0)^2}{4wR_0 E^2} \tag{6}$$

This can be interpreted as a critical value of discharge length above which the plasma can not be supported in the equilibrium regime. Graphical representation of above formulas is given in Fig. 14 with w representing power per unit length of the discharge. The triangular-like area cornered by 0AB is the only area that the discharge can exist. The line that bounds the area on right hand side is function of the electrical parameters and deduced from the formula given in Eq. (4). The equilibrium discharge length lays on the line 0B and non-equilibrium discharge length on 0A. For transition discharges, the discharge length could be anywhere in the area OAB, including the borders. As an example, for the case given in Fig. 7, the discharge length characteristics are also shown in the same figure. Here, the whole discharge column stays in equilibrium up to the point where it has the length close to 55 mm, and thereafter the non-equilibrium part grows much faster. The line restricting the total discharge length on the right hand side is a function of power per unit length. It shifts upward as the discharge length increases.

The formulation given above is useful also to determine the stability regimes of the gliding discharges. For this purpose, we need to study the change in discharge power as a function of non-equilibrium and total lengths of the discharge.

Rewriting the Eq. (1) using the definition $l=l_1+l_2$ gives

$$P = (l - l_2)w + l_2 EI$$

and by using the definitions

$$w = \frac{P_{max}}{l_{1,max}} \qquad P_{max} = \frac{U_0^2}{4R_0} \qquad I_{max} = \frac{U_0}{R_0} \qquad E = \frac{U_0}{l_{2,max}}$$

the following is obtained:

$$P = (l - l_2)\frac{U_0^2}{l_{1,max} 2R_0} + l_2 \frac{U_0}{l_{2,max}} I \tag{7}$$

Non-dimensional parameters can be defined as follows:

$$P^* = \frac{P}{P_{max}} \qquad l_2^* = \frac{l_2}{l_{2,max}} \qquad I^* = \frac{I}{I_{max}} \qquad l^* = \frac{l}{l_{1,max}} \qquad \alpha = \frac{l_{2,max}}{l_{1,max}}$$

The values of first three parameters are bounded by 0 and 1. The limits of l* and α will be discussed later in this section. By using these non-dimensional parameters, Eq. (7) can be rearranged as follows:

$$P^* = (l^* - l_2^* \alpha) + 4 l_2^* I^* \tag{8}$$

Power can also be written from Eq. (2) as:

$$P = U_0 I - R_0 I^2$$

and dividing both sides by P_{max} leads to the second non-dimensional equation

$$P^* = 4I^* - 4I^{*2} \tag{9}$$

taking I^* from Eq.(8) and substituting into Eq. (9) gives a quadratic equation of P^* as a function of l^* and l_2^*. Solving for P* gives the solution as

$$P^* = -2l_2^{*2} + 2l_2^* + (l^* - l_2^* \alpha) + \sqrt{[2l_2^{*2} - 2l_2^* - (l^* - l_2^* \alpha)]^2 - [4(l^* - l_2^* \alpha) l_2^* + (l^* - l_2^* \alpha)^2]} \tag{10}$$

the solution with plus sign is the stable solution.

The maximum value that l^* can have is either 1 or α (if α is greater than 1). Unity value of α corresponds to the condition that both equilibrium and non-equilibrium discharge has maximum lengths equal to each other. Graphical representation of power surface in terms of isopowers is given in Fig. 15. In this figure, on the x-axis representing total discharge length, thermal (quasi-equilibrium) gliding discharge has an increase in power as expected. According to minimization of power principle, if power suddenly increases due to a disturbance in the system, the system proceeds to a new position (or to a new power level) depending on the magnitude of the disturbance and the current spacial position of the arc over the surface. In order to have both equilibrium and non-equilibrium discharges together; the system should be able to overcome the plateau between the P*=0.9 constant lines. After that point, following the slope towards lower power levels, the discharge can be sustained in a state where the non-equilibrium portion grows faster than the equilibrium. Otherwise, the discharge will be forced to return to lower power levels, perpendicular to the x-axis in Fig. 15, for constant discharge length and

becomes a stable equilibrium discharge again. This particular case was observed during the experimentation (Fig. 16). An unstable condition was created due to the power supply; following a regular transition period, the discharge became equilibrium again when it was expected to diminish.

The cases where α takes values smaller than 1.0, the maximum equilibrium length is also the maximum possible length of the discharge. Isopower curves as a function of non-equilibrium and total lengths are given in Fig. 17 for α=0.75 case. For the high values of α, maximum discharge length is determined by the value of α. As an example, the α=2 case is shown in Fig. 18. Although equilibrium discharge length can take values up to 2.0, total length can grow up to 4.0 for this particular case determined by the value of α.

VI. CONCLUSIONS

Gliding discharges formed between diverging electrodes in air flow were studied experimentally over a wide range of gas flow rates and power levels. Depending on the system parameters the following discharge regimes were observed:

1. Non-equilibrium gliding discharge exists in the limit of low currents and high flow velocities. This discharge retains very low specific power consumption and remains in non-equilibrium throughout the whole evolution cycle. The electric field inside developing plasma column remains practically constant. The maximum attainable discharge length is short and determined by the voltage limits of power supply.

2. Thermal Gliding Arc is a quasi-equilibrium discharge observed at low gas velocities and high current values. The power per unit length remains practically constant throughout discharge evolution. The maximum achievable length is limited by power rating of the high voltage source.

3. Transition Gliding Discharge (Non-thermal Gliding Arc) is observed for moderate current values and high flow velocities. Transition discharge contains two phases: equilibrium and non-equilibrium. At the first phase, developing as a thermal arc, the discharge is supported by thermal ionization. Further, approaching the critical power limits, this discharge develops high electric fields, strong enough to induce transition to the non-equilibrium conditions. At this point the ionization mechanism is changed to non-equilibrium supported by high electron temperature.

The equilibrium to non-equilibrium transition is experimentally observed as a change of voltage increase rate with discharge length growth. The local electric field defined as dV/dl is increasing up to three times, indicating the change of plasma conditions. However, previously reported phenomenon of length explosion is not supported by our experimental data. It is found that high flow velocities provide intensive cooling, with an increase of electric field, and decrease of gas temperature. It was experimentally shown that these conditions promote equilibrium to non-equilibrium transition at high power input values. Experimental data is interpreted as a formation of non-equilibrium fragment inside extending plasma column. Based on this assumption, the phenomenological model was developed to determine the existences limits and relative power input to the non-equilibrium stage. The existence of non-equilibrium phase is important for the optimization of related plasma chemical processes, and critically affects the selectivity and energy efficiency of plasma chemical reactions.

ACKNOWLEDGEMENT

This work has been supported by National Science Foundation under grant (SGER #9810784); The corporate support of Texaco, Kodac and Dupont are gratefully acknowledged.

REFERENCES

1. A.A. Naville, C.E. Guye, French Patent 350, 120,(1904)
2. Czernichowski, Pur & Applied Chem.66,1301 (1994)
3. A. A.Fridman, S. Nester, L. A. Kennedy, A. Saveliev, O. Mutaf-Yardimci, J. Prog. Energy and Comb. Sci. v25, 211 (1999).
4. H. Lesueur, A. Czernichowski and J. Chapelle, Int. J. Hydrogen Energy, v19,139 (1994).
5. K. Meguernes, A. Czernichowski and J. Chapelle, VDI-Berichte, v1166, 495 (1995).

6. A. Czernichowski, K. Meguernes, Proc. 12th Int. Symp. Plasma Chem. V2, 729 (1995).
7. A. Czernichowski, Non-Thermal Plasma Tech. for Pollution Control, Part B: Electron 7 7. Beam and Elec. Discharge Processing, NATO ASI Series G: Ecological Sci. v34B, 371, Springer-Verlag (1993).
8. V. Dalaine, J. M. Cormier, and P. Lefaucheux, J. Appl. Phys. V83, 2435 (1998).
9. A. Czernichowski, H. Nassar, A. Ranaivosoloarimanana, A. A. Fridman, M. Simek, K. Musiol, E. Pawelec and L. Dittrichova, Acta Physica Polonica A, v89, 595 (1996).
10. F. Richard, J. M. Cormier, S. Pellerin, J. Chapelle, J. Appl. Phys. V79, 2245 (1996).
11. V. Dalaine, J. M. Cormier, S. Pellerin, P. Lefaucheux, J. Appl. Phys. V84, 1215 (1998).
12. S. Pellerin, J. M. Cormier, F. Richard, K. Musiol, J. Chapelle, J. Phys. D: Appl. Phys. V29, 726 (1996).
13. Y. P. Raizer, *Gas Discharge Physics*, (Springer-Verlag, Berlin, 1997).
14. O. Mutaf-Yardimci, L. A. Kennedy, S. A. Nester, A. V. Saveliev, A. A. Fridman, Plasma Exhaust Aftertreatment, SAE SP-1395, 1 (1998).
15. A. A. Fridman, A. Petrousov, J. Chapelle, J. M. Cormier, A. Czernichowski, H. Lesueur, J. Stevefelt, J. Phys. III v4,1449 (1994).
16. S. Pellerin, J.M. Cormier, J. Chapelle, and F. Kassabji, 13th Int. Symp. Plasma Chem. V2, 813 (1997).
17. V. D. Rusanov, V. V. Liventsov, B. V. Potapkin, A. A. Fridman, A. Czernichowski and J. Chapelle, Phys.-Doklady v40, 623 (1995).
18. M. A. Deminskii, B.V. Potapkin, J. M. Cormier, F. Richard, A. Bouchoule, and V. D. Rusanov, Phys.-Doklady, v42, 337 (1997).
19. A. Fridman, S. Nester, O. Yardimci, A. Saveliev and L. A. Kennedy, Proc. 13th Int. Symp. Plasma Chem. V2, 819 (1997).

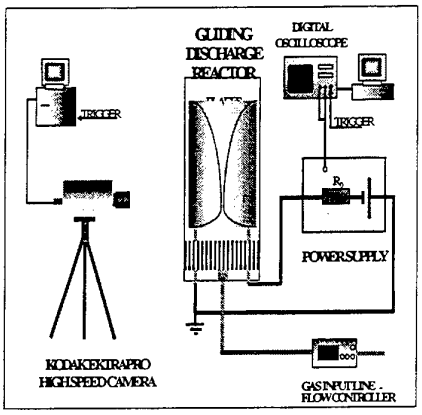

Fig. 1. Gliding discharge experimental setup.

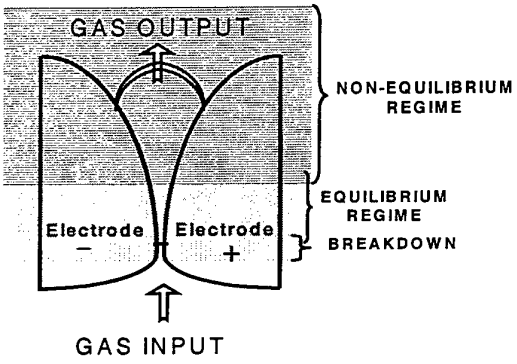

Fig. 2. Evolution of gliding discharge column.

Fig 3. Picture of gliding arc discharge.

Fig. 4. Gliding arc evolution

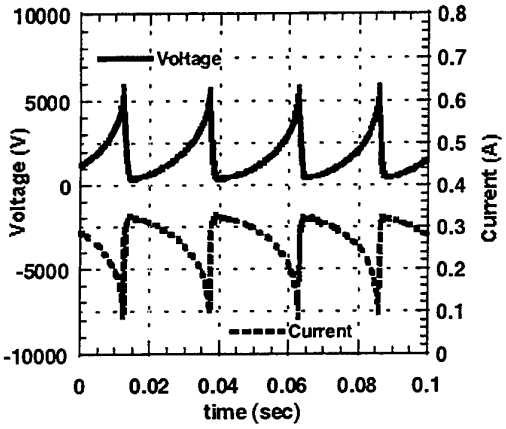

Fig. 5. A typical voltage-current oscillogram of gliding arc.

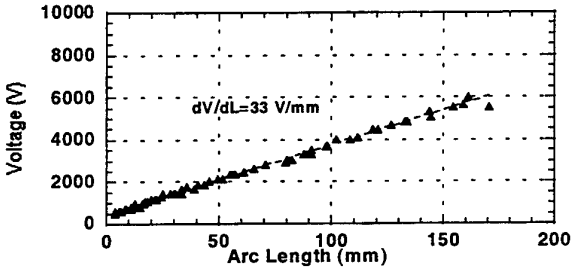

Fig. 6. Voltage-arc length characteristics of thermal gliding arc discharge.

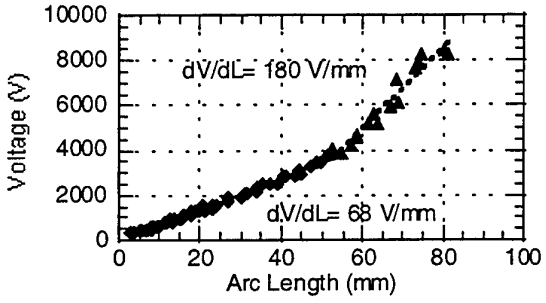

Fig. 7. Voltage-discharge length characteristics of a gliding transition discharge.

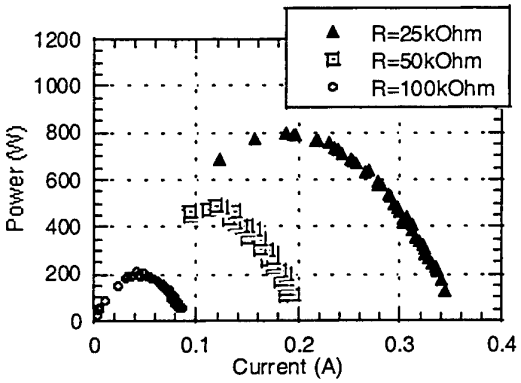

Fig. 8. Effect of power source internal resistance on power.

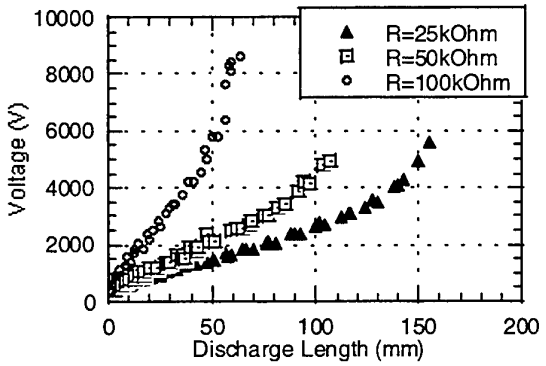

Fig. 9. Effect of power source internal resistance on voltage-discharge length characteristics of discharge.

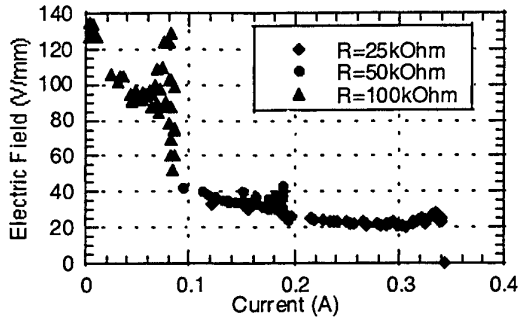

Fig. 10. Effect of power supply resistance on gliding discharge characteristics.

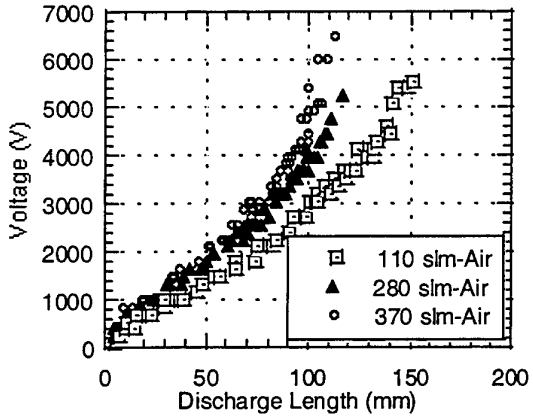

Fig. 11. Effect of flow rate on electric field (U_0=10 kV, R_0=50 kΩ).

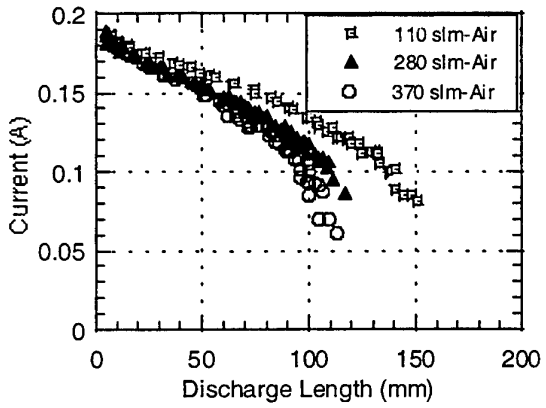

Fig. 12. Effect of specific power on discharge length-current characteristics (U_0=10 kV, R_0=50 kΩ).

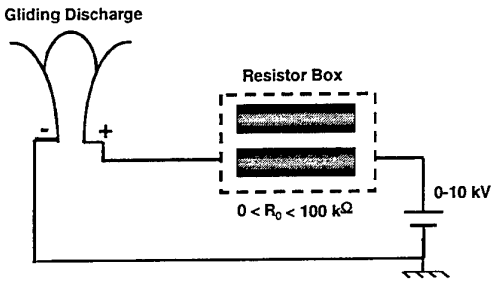

Fig. 13. Schematic of electrical circuit.

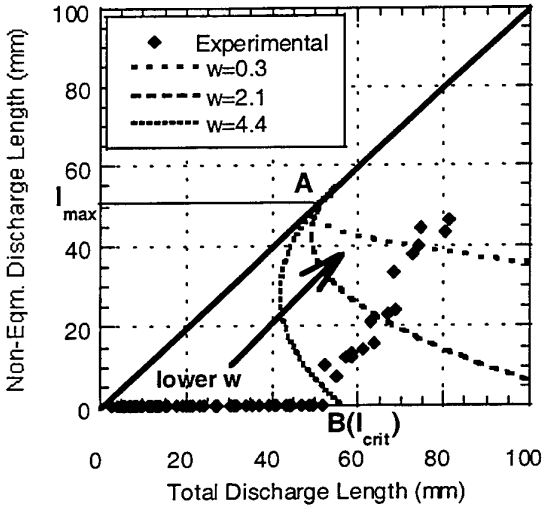

Fig. 14. Graphical representation of non-equilibrium discharge length as a function of total discharge length showing non-equilibrium plasma growth in gliding plasma column. (U_0=10 kV, R_0=100 kΩ)

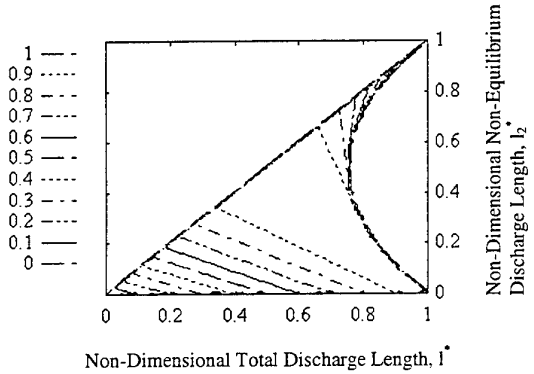

Fig. 15. Power level contours for gliding discharges for the case α=1.0.

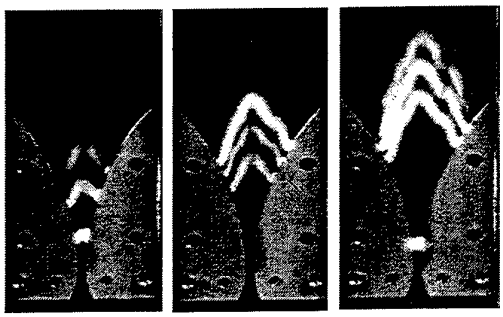

Fig. 16. Gliding discharge instabilities causing stable equilibrium discharge to reappear.

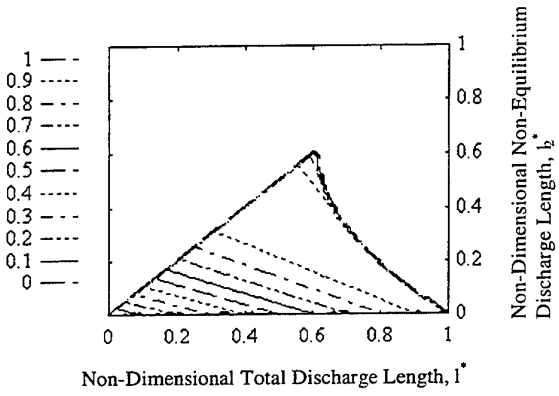

Fig. 17. Power levels contours for gliding discharges for the case α=0.75.

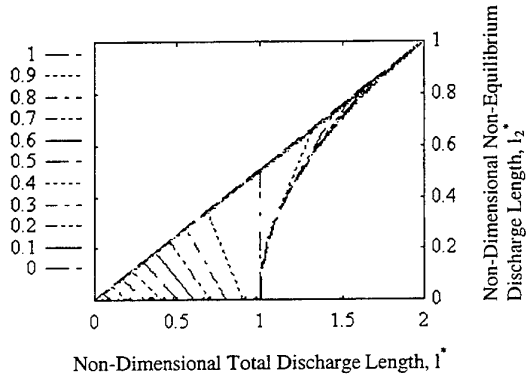

Fig. 18. Power levels contours for gliding discharges for the case α=2.0.

MULTICOMPONENT GAS-LIQUID FLOWS WITH CHEMICAL REACTIONS AND PHASE TRANSITIONS IN TUBULAR REACTORS OR FURNACES

R. Nigmatulin
Ufa-Bashkortostan Branch of Russian Academy of Sciences
Email: nigmar@anrb.ru; Fax: (73472)-223-569

Keywords: dispersed-annular flow, hydraulic resistance, entrainment, deposition, plugging

ABSTRACT. In this paper two-phase multicomponent dispersed-film flow with phase transition (evaporation) and chemical reactions is considered. A mathematical model is presented. The closed system of equation includes mass conservation equations for each component of each phase (gas, drops, film), momentum and energy conservation for whole mixture. Also it includes equations for kinetics of the chemical reactions, evaporation and experimental correlations for drop entrainment and deposition of the near wall film. This system of equation was used for modeling of oil refinery tubular furnace.

1. INTRODUCTION

A combined motion of gas and liquid in channels is widely used in chemical technology, petroleum refining, and other related industries. In particular, many technological processes are associated with an intensive heating of large masses of multicomponent liquid accompanied by phase transitions and chemical reactions. Tubular furnaces with the internal diameter of tube, D ~ 0.1 m, are often used in these processes; these tubes convey gas-liquid multicomponent flows with heat input through tube walls by burning fuels outside the tubes (Fig. 1). The level of heat fluxes in petroleum processing reaches 50 kW/m^2. With the volumetric concentrations of gas α_G>0.8 and velocities v > 10 m/s (when Froude number, Fr = v^2/gD > 100), the flow may be close to axis-symmetric dispersed-film regime even in horizontal tubes.

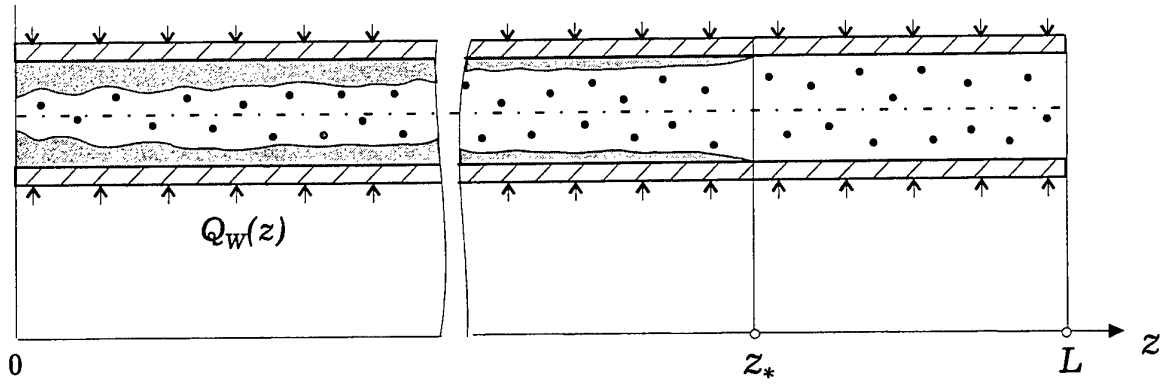

Fig. 1

The presence of the liquid film on the channel wall affects the hydraulic resistance (pressure drop) along the gas-liquid flow, since the structure of the film wave surface (or the "film roughness"), and, consequently, the viscous friction between the flow core and the film, depend on its thickness. The so-called crisis of hydraulic resistance may occur when, with the gas-phase velocity growth the hydraulic resistance decreases rather than grows due to reduction of the "film roughness".

The presence of a liquid film plays a predominant role also for heat exchange, particularly, for heat removal from the heating channel-wall responsible for the film vaporization. Under intensive evaporation, when drops from the flow core have no time to additional feed the film, the later can vanish (the flow becomes dispersed) or lose its continuity. In this case, because of the luck of required contact between the heating wall and liquid phase, the heat exchange detoriates, and the wall is overheated. This phenomenon is referred to as a heat-transfer crisis due to the wall liquid film drying-up. A crisis of heat transfer during bubbly boiling also exists. This crisis may occur under heavy heat loading due to the agglomeration of vapor film. This also contributes to

a distortion of a contact between a liquid and heating wall that may result in emergency overheating (burnout) of the later.

The dispersed-film flows, together with film, foamy, drop, and partially inverse disperse-annular and bubbly flows, represent varieties of flows of disperse-annular structure. This structures of gas-liquid flow in channels, are the most widespread in nuclear-power plants, chemical plants used in petroleum refining, industries dealing with processing of raw materials, and also in the transporting of a gas-condensate and petroleum products from the oil fields.

It is noteworthy that in steam generating channels, to whose inlets a saturates or subcooled water is fed, there is at the outlet a vapor-liquid mixture with maximum vapor concentration which can be obtained with no heat-transfer crisis, the dispersed-film regime may occur 90% of the channel. The single-phase, bubbly and slug flows account only for the remaining 10%.

It should be remembered that large pressure drops take place in intensive processes, and the process of a chemical reaction depends not only on heating but also on purely hydrodynamic effects defining, in particular, pressure variation and interrelated with it, intensity of evaporation or condensation. But evaporation and condensation influence the velocities that in their turn influence the pressure drop along the flow. These are precisely the situations specific for a number of modern intensive and energy-consuming processes whose analysis and design require a coupled or joint solution of a complete system of equations of mass, momentum, energy, and kinetics of both interphase and intraphase processes.

2. BASIC CONCEPTS

In tubular furnaces for petroleum refinery process each phase of a two-phase gas-liquid flow - gas, drops, and near-wall film – is a homogeneous mixture of a number of components. Parameters related to different (j-th) phases: gas and vapor (j = 1), drops (j = 2), and near-wall film (j = 3), are denoted hereafter by first subscripts j = 1, 2, 3, respectively. Parameters related to intensities of interphase interactions and corresponding to interface mass (J), momentum (F) and heat (Q) transfer from the j-th to the i-th phase are denoted by double subscripts ji, i.e. J_{ji}, F_{ji}, Q_{ji} (j, i = 1, 2, 3; $j \neq i$). Parameters related to different (k-th, k = 0, 1, 2, 3, ...) components in the j-th phase or in the interphase transfer from the j-th to the i-th phase are denoted by an additional subscript (k) in parentheses, i.e. $m_{j(k)}$, $J_{ji(k)}$, etc.

For long tubular channels which are typical in petroleum refinery ($L \sim 10^2 - 10^3$ m) the averaged velocities of gas and drops (core of the flow), and the temperatures of all three phases of the flow can be assumed equal:

$$v_1 = v_2 = v_c,\ T_1 = T_2 = T_3 = T \qquad (1)$$

since in the process the inherent times, t_{12}^{v}, t_{12}^{T}, t_{13}^{T}, of the equalization of, respectively, velocities of gas and droplets, temperatures of gas and droplets and temperatures of gas and film are much smaller than the inherent residence time $t_{j0} = L/v_{j0}$ of a fixed mass of any phase (j = 1, 2, 3) in the channel. It means that this liquid-vapor flow may be considered as thermodynamically equilibrium.

In tube furnaces for heating petroleum raw liquid material the gas phase (j = 1, k = 0, 1, 2) consists of a light volatile component V (j(k) = 1(1)) with molecular weight $\nu_m \approx 100$, heavy oil vapor component O (j(k) = 1(2)) with molecular weight $\nu_m \approx 400$, and inert water vapor component W (j(k) = 1(0)) with molecular weight $\nu_m \approx 18$. The latter does not participate in phase transitions and chemical reactions. Each component of the liquid phase (droplet, j = 2, or film, j = 3) consists of four components (k = 2, 3, 4, 5), namely: oil O ($\nu_m \approx 400$, j(k) = 2(2), or 3(2)), resin R ($\nu_m \approx 700$, j(k) = 2(3), or 3(3)), asphaltene A ($\nu_m \approx 700$, j(k) = 2(4), or 3(4)), carboid C ($\nu_m \approx 1000$, j(k) = 2(5), or 3(5))undergoing chemical transformations as follows:

$$\begin{array}{l} \overset{(k=0)}{W}, \ [\quad \overset{(k=1)}{V} \quad] \qquad \text{–gas phase } (j=1;\, k=0,1) \\ \quad \uparrow \quad \uparrow \quad \uparrow \\ \underset{(k=2)}{O} \leftrightarrow \underset{(k=3)}{R} \leftrightarrow \underset{(k=4)}{A} \leftrightarrow \underset{(k=5)}{C} \quad \text{– liquid phase } (j=2,3;\, k=2,3,4,5) \end{array} \tag{2}$$

Chemical reaction rates for 9 presented chemical reactions was prescribed by the Arrhenius law:

$$K_{j(kn)} = K^{\circ}\kappa_{j(k)} \exp\left(\frac{T_{(kn)}}{T}\right), \tag{3}$$

$$j = 2, 3; \quad (kn) = (21, 23, 32, 31, 34, 43, 41, 45, 54),$$

where $K_{j(kn)}$ (s^{-1}) is the mass rate of formation of the n-th component from the k-th component in unit mass of liquid phase (j = 2, 3) per unit time; $\kappa_{j(k)}$ is the mass fraction of the k-th component in the j-th phase.

We shall consider, in the interests of simplicity, that the gas phase is a mixture of thermally perfect gas components with gas constants $R_{1(k)}$, constant specific heat capacities $c_{1(k)}$ (k = 0, 1, 2), specific heat of evaporation $l_{(1)}$ and $l_{(1)}$ of components O and V (k = 1, 2), and that the liquid phase is incompressible fluid with constant specific heat capacity c_2:

$$p = \tilde{n}_1^{\circ} R_1 T, \quad R_1 = \sum_{k=0}^{2} \hat{e}_{1(k)} R_{1(k)}, \quad i_1 = \sum_{k=0}^{2} \hat{e}_{1(k)} i_{1(k)}$$

$$i_{1(0)} = c_{1(0)}(T - T_0), \quad i_{1(1)} = c_{1(1)}(T - T_0) + l_{(1)}, \quad i_{1(2)} = c_{1(2)}(T - T_0) + l_{(2)}$$

$$i_2 = i_3 = c_2(T - T_0) + \frac{p - p_0}{\rho_L^{\circ}} \tag{4}$$

$$(\rho_1^{\circ} \equiv \rho_G^{\circ}, \ \rho_2^{\circ} = \rho_3^{\circ} = \rho_L^{\circ}, \ c_2 = c_3 = c_L)$$

Here i_j (j = 1, 2, 3) and $i_{1(k)}$ (k = 0, 1, 2)) are specific enthalpy of the j-th phase and specific enthalpy of the k-th gas component, respectively.

3. MASS CONSERVATION EQUATIONS

Let us consider a steady flow using one-dimensional approximation. Then the conservation equations for mass flow rates (m_j) of gas, drops, and film can be written in the form:

$$\frac{dm_1}{dz} = J_{21} + J_{31}, \quad \frac{dm_2}{dz} = -J_{21} + J_{32}, \quad \frac{dm_3}{dz} = -J_{31} - J_{32} \tag{5}$$

where $m_1 = \rho_G^{\circ} \alpha_1 v_c S_c, \quad m_2 = \rho_L^{\circ} \alpha_2 v_c S_c, \quad m_3 = \rho_L^{\circ} v_3 S_f,$

with $\alpha_1 + \alpha_2 = 1, \ S_c + S_f = S = \frac{1}{4}\pi D^2, \ S_c = \pi(\frac{1}{2} D - \delta)^2, \ S_f \approx \pi D\delta$

Here S is the internal cross section of the channel, $S_c \equiv S_1 \equiv S_2$, and $S_f \equiv S_3$ are the cross sections of the channel occupied by the core and by the film, respectively; δ is an averaged thickness of the film which is thin ($\delta << D$); α_1 and α_2 are the volume fractions of the core occupied by the gas and drops, respectively; J_{ji}, are the intensities of the interface mass exchange processes from the j-th to the i-th phase of the flow per unit time and per unit length of the channel. In this case J_{21} and J_{31} are the intensities of evaporation, respectively, from the surface of the drops and from the surface of the film; J_{32} is the intensity of mass transfer from the film to the droplet phase which takes place due to two opposite processes: entrainment (J_{32}°) and deposition (J_{23}°):

$$J_{32} = J^{\circ}_{32} - J^{\circ}_{23} \tag{6}$$

From (5) the mass conservation equation follows for the mixture with the constant mass flow rate, m_0:

$$m_1 + m_2 + m_3 = m_0 = \text{const}, \quad \text{or } m_c + m_f = m_0 = \text{const} \tag{7}$$

$$(m_1 + m_2 = m_c,\ m_3 \equiv m_f)$$

The mass conservation equations for the components in each of the three phases are:

$$\frac{dm_{1(0)}}{dz} = 0, \quad \frac{dm_{1(1)}}{dz} = J_{21(1)} + J_{31(1)}, \quad \frac{dm_{1(2)}}{dz} = J_{21(2)} - J_{31(2)},$$

$$\frac{dm_{2(k)}}{dz} = -J_{21(k)} + J_{32(k)} + \rho^{\circ}_L S_c \sum_{\substack{n=2 \\ n\neq k}}^{5} (K_{2(nk)} - K_{2(kn)}) \tag{8}$$

$$\frac{dm_{3(k)}}{dz} = -J_{31(k)} - J_{32(k)} + \rho^{\circ}_L S_c \sum_{\substack{n=2 \\ n\neq k}}^{5} (K_{3(nk)} - K_{3(kn)})$$

where $m_{j(k)} = \kappa_{j(k)} m_j$; $j = 1, 2, 3$; $k, n = 0, 1, 2, 3, 4, 5$

Here $m_{i(k)}$ is the mass flux of the k-th component in the j-th phase; $J_{32(k)}$ is the intensity of mass transfer of the k-th component from the film to the droplet phase which takes place due to two opposite processes (6): transfer of the k-th component by entrainment ($J^{\circ}_{32(k)}$) and by deposition ($J^{\circ}_{23(k)}$):

$$J_{32(k)} = J^{\circ}_{32(k)} - J^{\circ}_{23(k)} \tag{9}$$

$$J^{\circ}_{32(k)} = \kappa_{3(k)} J^{\circ}_{32}, \quad J^{\circ}_{23(k)} = \kappa_{2(k)} J^{\circ}_{23} \qquad (j = 2, 3)$$

In accordance with (2) the evaporation takes place only for components V (k = 1) and O (k = 2):

$$J_{j1} = J_{j1(1)} + J_{j1(2)} \qquad (j = 2, 3) \tag{10}$$

The intensity of evaporation of the component L (k = 1) therewith is determined by its chemical production rate because of its instant vaporization ($\kappa_{2(1)} = \kappa_{3(1)} = 0$) assumed:

$$-J_{j1(1)} + \rho^{\circ}_L S_c \sum_{n=2}^{4} K_{j(n1)} = 0, \ K_{j(1n)} = 0 \qquad (j = 2, 3) \tag{11}$$

The intensities of evaporation of the second component O from the droplets ($J_{21(2)}$) and the film ($J_{31(2)}$) is determined by the equation of thermodynamic equilibrium approach:

$$p_{1(2)} = p_{S(2)}(T) \tag{12}$$

4. MOMENTUM AND ENERGY CONSERVATION EQUATIONS

The momentum conservation equations for the core and film can be written in the following form:

$$\frac{d}{dz}(m_c v_c) = -S_c \frac{dp}{dz} - F_{13} - P_{cf} + \rho_c S_c g^z$$

$$\frac{d}{dz}(m_f v_f) = -S_f \frac{dp}{dz} + F_{13} + P_{cf} - F_W + \rho_L^\circ S_f g^z \tag{13}$$

with $\rho_c = \rho_G^\circ \alpha_1 + \rho_L^\circ \alpha_2$, $P_{cf} = J_{23}^\circ v_c - (J_{31} + J_{32}^\circ) v_f$

where F_{13} is the friction force between the gas core and film; P_{cf} is the momentum transfer intensity between the core and film due to mass exchange; F_W is the intensity of external surface force between the film and channel wall; g^z is the intensity of external body forces (gravity) along the channel.

For tubular furnace conditions kinetic energy and its dissipation is usually negligibly small as compared with the change of internal energy (or enthalpy) due to external heating (from external volume through the tube wall) with intensity Q_W. Then the energy conservation, or heat flux, equations for the core, for the film and for the film interface can be written as follows:

$$m_1 \frac{d_i i_1}{dz} + m_2 \frac{di_2}{dz} - v_c S_c \frac{dp}{dz} = -Q_{13} - (J_{21(1)} l_{(1)} + J_{21(2)} l_{(2)})$$

$$m_3 \frac{di_3}{dz} - v_3 S_f \frac{dp}{dz} = -Q_{31} + Q_W \tag{14}$$

$$Q_{13} + Q_{31} = J_{31(1)} l_{(1)} + J_{31(2)} l_{(2)}.$$

Here Q_{13} and Q_{31} are the intensities of heat fluxes to the film interface (per unit time and unit length of the tube), respectively, from the gas phase and from the liquid of the film to the film interface where evaporation ($J_{31(1)} + J_{31(2)}$) may take place. It is shown [1] that the heat flux equations may be simplified when intensive heating with large Q_W takes place, namely: $Q_{13} << Q_{31}$, and left sides of the differential equations are much smaller than Q_W. It means:

$$J_{31(1)} l_{(1)} + J_{31(2)} l_{(2)} = Q_W,\ J_{21(2)} << J_{31(2)} \tag{15}$$

5. INTERFACIAL MASS, FORCE, AND HEAT EXCHANGE CORRELATIONS

Following Nigmatulin [1, 2] let us consider experimental correlations for interfacial interaction terms (F_{13}, F_W, Q_W, J_{32}°, J_{23}°) based on corresponding measurements mainly for air-water and steam-water dispersed-film flow for a wide range of pressures (p = 1 - 100 bar) and some theoretical schemes proposed by Hewitt & Hall-Taylor [3], McCoy & Hanratty [4], Whalley [5], Hewitt & Govan [6]. In so doing some physical characteristics will be used, namely: viscosity coefficients, $\mu_1 = \mu_G$ and $\mu_2 = \mu_3 = \mu_L$, thermal conductivity coefficients, $\lambda_1 = \lambda_G$ and $\lambda_2 = \lambda_3 = \lambda_L$, and surface tension coefficient, Σ.

The friction force between the film and tube for turbulent film can be assumed as analogous to the Blausius formula:

$$F_W = \pi D \tau_W,\ \tau_W = C_W \frac{\rho_3^\circ v_3^2}{2}$$

$$C_W = \frac{0.0589}{Re_3^{0.25}},\ \left(Re_3 \equiv \frac{\rho_3^\circ v_3 \delta}{i_3} = \frac{m_3}{\pi D \mu_L} > 300\right) \tag{16}$$

The friction force between the film and well developed turbulent gas-droplet core can be presented similarly to the friction in a rough tube when the coefficient of friction is independent of the Reynolds number, depending only on the effective "roughness" of the film which is unequivocally defined by its thickness δ:

$$F_{13} = \pi(D - 2\delta)\tau_{13}, \quad \tau_{13} = C_{13}\frac{\rho_G^\circ (v_1 - v_3)^2}{2} \tag{17}$$

$$C_{13} = 0.005\left(1 + 120\frac{2\delta}{D}\right), \left(Re_{13} \equiv \frac{\rho_G^\circ (v_1 - v_3)(D - 2\delta)}{\mu_G} \approx Re_1 = \frac{\rho_G^\circ v_1 D}{\mu_G} \geq 10^5\right)$$

The intensity of heat exchange between the film and tube wall is related to the temperature gradient between the temperature of the wall, T_W, and temperature of the film, T:

$$Q_W = \pi D\, q_W,\ q_W = \lambda_L Nu_W \frac{T_W - T}{\delta} \tag{18}$$

$$Nu_W = 0.010\ Re_3^{0.83} Pr_L^{0.5}, \quad \text{for } Re_3 \equiv \frac{m_3}{\pi D \mu_L} > 300, \quad \text{and } Pr_L \equiv \frac{\mu_L c_L}{\lambda_L}$$

Usually external heat flux, Q_W, is given, then on calculating the temperature of the flow, T(z), one may calculate the tube wall temperature, $T_W(z)$, along the flow using the last correlations. The intensity of droplet deposition is described by a semi-theoretical formula:

$$J_{23}^\circ = \pi D \rho_L^\circ \alpha_2 v_1 J_{23}^* \tag{19}$$

$$J_{23}^* = 9.6\cdot 10^{-3}(1 - 7.5\alpha_2) Re_1^{0.95} We_1^{-1.2}\left(\frac{\rho_G^\circ}{\rho_L^\circ}\right)^{0.2}, \quad We_1 \equiv \frac{\rho_G^\circ v_1^2 D}{\Sigma}$$

Here surface tension, Σ, reveals itself due to the influence on the size of droplets in the core of the flow.

The intensity of entrainment of droplets from the film is characterized by the Weber number of the film, We_3. This number equals the ratio of dynamic or shear stress, τ_{13}, to capillary force, Σ/δ. The entrainment has a threshold character, i.e., entrainment takes place only if Weber number exceeds some critical value, We_{3*}:

$$J_{32}^\circ = \frac{m_3}{f\hat{I}D} J_{32}^*,\ J_{32}^* = \begin{cases} 0, & \text{if} \quad We_3 < We_{3*}; \\ 91\dfrac{We_3}{Re_3}\left(\dfrac{\rho_L^\circ}{\rho_G^\circ}\right)^{1/2}, & \text{if} \quad We_3 > We_{3*}; \end{cases} \tag{20}$$

$$We_3 = \frac{\tau_{13}\delta}{\Sigma},\ \frac{We_{3*}}{(\mu_L/\mu_G)(\rho_G^\circ/\rho_L^\circ)^{1/2}} = \begin{cases} 2{,}5\cdot 10^{-3} Re_3^{0,2}, & \text{when } Re_3 \leq 300; \\ 2{,}8\cdot 10^{-5} Re_3, & \text{when } Re_3 > 300. \end{cases}$$

The thermodynamic data on hydrocarbon raw materials in [4], namely: $R_{1(k)}$, $c_{1(k)}$, $l_{(1)}$, $l_{(2)}$, c_2, ρ_L°, transport coefficients, μ_G, μ_L, Σ, in (16) - (20), together with kinetic constants (K°, $T_{(qk)}$) in (3) and saturation pressure (12) are presented in [1].

6. NUMERICAL CALCULATION RESULTS FOR OIL REFINARY TUBULAR RURNACE

Finally, if external heat flux, $Q_W(z)$, is given, we have a closed system of equations. For this system of ordinary differential equations the Cauchy problem with the inlet parameters predetermined may be solved.

Fig. 2 (where $x_j = m_j/m_0$ is the mass flow rate fraction) illustrates the results of numerical and experimental investigations of the two-phase multicomponent flow in a tubular (D = 0.1 m, L ≈ 1000 m) furnace for petroleum

coke production. We shall discuss an operation regime with the mixture flow rate m_0 = 10 kg/s, inlet (z = 0) gas mass flow rate fraction $x_1(0) = m_1(0)/m_0 = 0.03$, inlet pressure p(0) = 2.5 MPa, a heat distribution $Q_W(z)$ shown by a dashed line, that corresponds to the experiment. One may see good coincidence of numerical and experimental pressure, p(z), gas velocity, $v_1(z)$, gas mass flow rate fraction, $x_1(z)$, flow temperature, T(z), and liquid component contents, $\kappa_{(k)}(z)$, distributions. The analysis has shown satisfactory agreement between theoretical and experimental data also with all other regimes (other m_0, $x_1(0)$, p(0), and $Q_W(z)$). Thus, it has been proved that an adequate "numerical experiment" based on the proposed model is possible and relevant in studying tubular furnace process.

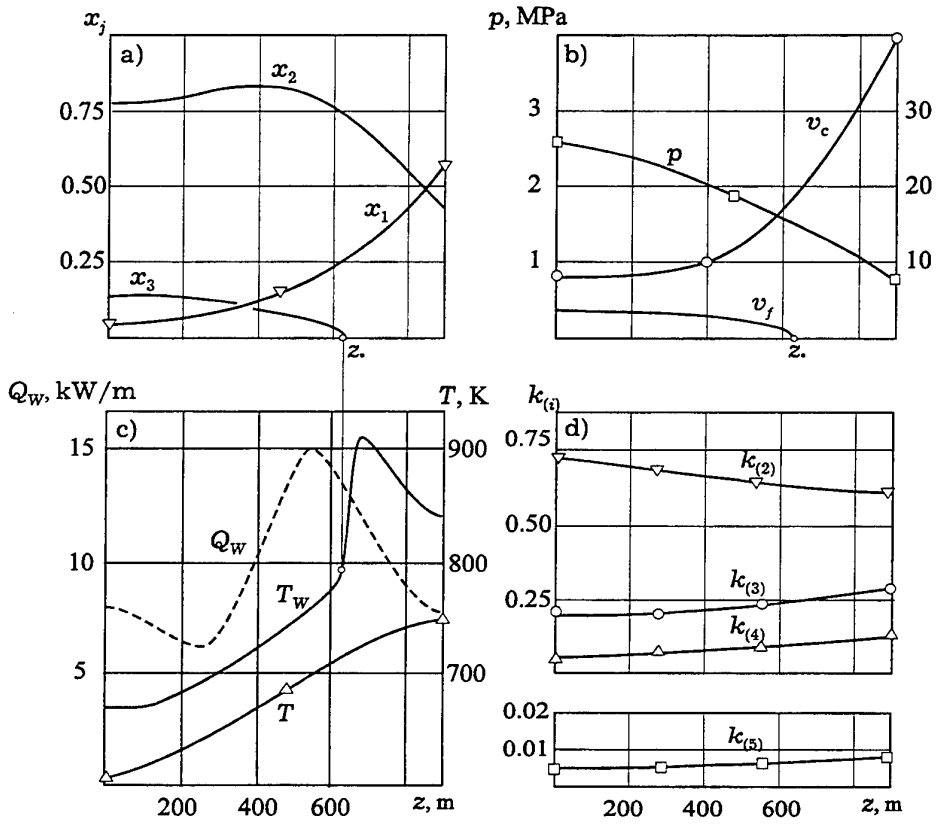

Fig. 2

The investigation was initiated by the production problem on periodical plugging of a tube by coke ("coke sclerosis") along final 100 m of the channel. This plugging forced to stop the process for a very hard operation of burning out the coke plug by oxygen blowing.

Our analysis predicts the presence of a heat transfer crisis because of reduction of liquid near-wall film flow rate, x_3, and film thickness, δ, at section $z = z_*$ approaching zero ($x_3 \to 0$, $\delta \to 0$) because of evaporation. This must lead to deterioration of heat transfer from the tube wall and the rise of the wall temperature T_W for $z > z_*$. It is this near-wall film dry-out that causes the observed overburning of tubes and gradual plugging of internal section by coke ("sclerosis") as a consequence of drop deposition on a hot tube wall unprotected by the near-wall film. This is confirmed by the data which show that overburning and plugging by coke are specific mostly for the tube segment $z > z_*$, where the flow, according to predictions, is totally dispersed and film-free. It is noteworthy that the film vanishes in spite of the presence of a great amount of liquid phase at section $z = z_*$ ($x_{2*} \approx 0.7$; see Fig. 2, where $z_* \approx 650$ m is marked by a cross). The point is that a predominant part of liquid flows in the form of droplets in a core, and its velocity is very close to the gas velocity ($v_1 \approx v_2 = 2$ - 50 m/s). This fact found from theoretical analysis is substantiated by coincidence of residence time of both liquid phase and gas phase in a

tube.

By means of the "numerical experiment", the optimum values of the parameters (D, L, pressure and gas flow rate fraction at the entrance, p_0, and x_0, mass flow rate m, heat power distribution, Q(z), along the channel are obtained. Some new ideas for preventing dry-out crisis are proposed.

This method for predicting the gas-liquid flows of multicomponent mixtures with chemical reactions and heat-transfer processes in a reactor battery discussed in this section by way of example is applicable to processes of thermal cracking, petroleum refinery, pyrolysis of oil products, etc.

REFERENCES

1. R.I. Nigmatulin, *Dynamics of Multiphase Media, v.2,* Hemisphere (1990).
2. R.I. Nigmatulin, B.I. Nigmatulin, Ya.D. Khodzaev, V.E. Kroshilin, "Entrainment and Deposition Rates in a Dispersed-Film Flow", *Int. J. of Multiphase Flow, v.22 (1), pp.19-30* (1996).
3. G.F. Hewitt, & N.S. Hall-Taylor, *Annular Two-Phase Flow,* Pergamon Press (1972).
4. D.D. McCoy, & T.J. Hanratty, "Rate of Deposition of Droplets in Annular Two-Phase Flow", *Int. J. Multiphase Flow, v.3, pp.319-331* (1977).
5. P.B. Whalley, *Boiling, Condensation, and Gas-Liquid Flow,* Clarendon Press, Oxford (1987).
6. G.F. Hewitt, & A. Govan, "Phenomenological Modelling of Non-Equilibrium Flows with Phase Change", *Int. J. Heat Mass Transfer,* v.33, pp.229-242 (1990).

NOVEL CONCEPT AND APPROACHES OF HEAT TRANSFER ENHANCEMENT

Z. Y. Guo S. Wang
Department of Engineering Mechanics
Tsinghua University, Beijing 100084, P.R. China
Email: demgzy@mail.tsinghua.edu.cn; Fax: (86)-10-62781610

Keywords: analogy of convection and conduction, heat transfer enhancement

ABSTRACT. According to the analogy between convection and conduction with heat sources, three ways are used to enhance convective heat transfer, including the increase of Re and Pr numbers, uniformity of velocity and temperature profiles, and the included angles of velocity and temperature vectors. With the latter two ways, further understanding can be obtained for the conventional heat transfer enhancement techniques on the one hand and some new approaches of heat transfer enhancement techniques have been suggested on the other hand. Analytical and experimental studies show that the enhancement approaches aimed at improving the coordination of flow and temperature fields or direct improvement of uniformity of fluid temperature profile can remarkably enhance heat transfer with less additional pressure drop.

1. INTRODUCTION

In the development of modern industrial world, there is always a pressure to reduce the capital and running costs for heat transfer process. The goals of enhanced heat transfer can be stated as the desire to have the encouragement and accommodation of high heat fluxes [1]. Tremendous work on enhancement has been conducted and a large number of techniques of convective heat transfer enhancement have been developed since 1970's. These techniques are segregated into two groups, passive and active techniques [2-4]. The passive techniques cover the use of extended surfaces, surface roughness and treatment, turbulent promoter, jet impingement, swirl flow and fluid additives. The surface vibration, fluid vibration, fluid blow or suction, and applying electric or magnetic field are named the active techniques, which require the external power.

The mechanism of heat transfer enhancement for conventional passive techniques can be attributed to the increase of the heat transfer area and/or convective heat transfer coefficient. One of following ways will result in the rise of the heat transfer coefficient: (a) mixing the main flow and/or the flow in the wall region by using rough surface, inserts, etc.; (b) reducing the flow boundary layer thickness by using offset strip fins, jet impingement, etc.; (c) creating the rotating and/or the secondary flow by using swirl flow device, duct rotation, etc.; (d) raising the turbulence intensity by using surface roughness, turbulence promoter, etc.

The problem for the existing techniques lies in the large additional pressure drop associated with heat transfer enhancement. This is why many high efficient techniques of heat transfer enhancement have no practical application. Furthermore, it seems that less attention was paid to the further discussion on the principle of convection heat transfer and its enhancement. In this paper, starting from governing equations of heat transfer, a second look at the mechanism of convective heat transfer is given based on the analog between heat convection and heat conduction. As a result, a novel concept of heat transfer enhancement — coordination of flow and temperature fields — is advanced. With this concept, a number of heat transfer phenomena and conventional heat transfer enhancement techniques may be understood from a different angle. More important is, it can be expected to develop some new approaches of heat transfer enhancement with less additional pressure drop.

2. NEW CONCEPT OF HEAT TRANSFER ENHANCEMENT

2.1 Analog of Convection and Conduction

Convective heat transfer is essentially the conductive heat transfer under fluid motion condition [5]. Consider the energy equation for 2-D boundary-layer steady flow over a cold flat plate at zero incident angle:

$$\rho C_p\left(u\frac{\partial T}{\partial x}+v\frac{\partial T}{\partial y}\right)=\frac{\partial}{\partial y}\left(k\frac{\partial T}{\partial y}\right) \tag{1}$$

It is easy to find according to the analog between heat convection and heat conduction [6] that the convection

term in the energy equation for the boundary layer flow corresponds to the heat source term in the heat conduction equation. The presence of heat sources leads to the increase of heat flux at boundary for both the conduction and convection problems. The integral of the equation (1) over the thermal boundary layer thickness leads to

$$\int_0^{\delta_t} \rho C_p \left(u\frac{\partial T}{\partial x} + v\frac{\partial T}{\partial y} \right) dy = -k\frac{\partial T}{\partial y}\bigg|_w \tag{2}$$

which indicates the wall heat flux is equal to the overall strength of heat sources inside the thermal boundary layer. This implies that the convective heat transfer can be enhanced by raising the value of the integral of convection term (heat sources) over the thermal boundary layer.

2.2 Various Ways to Enhance Heat Transfer

The energy equation in general form for heat convection is given as follows:

$$\rho c_p (u\frac{\partial T}{\partial x} + v\frac{\partial T}{\partial y} + w\frac{\partial T}{\partial z}) = k(\frac{\partial^2 T}{\partial x^2} + \frac{\partial^2 T}{\partial y^2} + \frac{\partial^2 T}{\partial z^2}) + s \tag{3}$$

where S is the heat source term. Integrating Eq.(3) across the thermal boundary layer or the tube radius , we have

$$\int_0^{\delta_t} \rho c_p (u\frac{\partial T}{\partial x} + v\frac{\partial T}{\partial y} + w\frac{\partial T}{\partial z})dy + \int_0^{\delta_t} k(\frac{\partial^2 T}{\partial x^2} + \frac{\partial^2 T}{\partial z^2})dy + \int_0^{\delta_t} (-s)dy = -k\frac{\partial T}{\partial y}\bigg|_w \tag{4}$$

convection source conduction heat source

where δ_t is the thermal boundary layer or the tube radius.

It is evident that intensifying the real source term can considerably improve heat transfer. For example, the heat transfer coefficient becomes much larger for the hot flow over cold plate boundary layer with exothermic chemical reaction or for the humid air flowing over the hot surface. Similarly, the multi-dimensional term in Equation (4) stands for the impact of 2-D or 3-D conduction on the heat transfer coefficient. This paper will focus on the investigation on the heat transfer enhancement in terms of variation of convection term.

For the case of 2-D boundary-layer steady flow over a flat plate at zero incident angle, Equation (4) reduces to the Equation (2) which may be rewritten with the convection term in the vector form:

$$\rho C_p \int_0^{\delta_t} (U \cdot \nabla T) dy = -k\frac{\partial T}{\partial y}\bigg|_w \tag{5}$$

where the thermal properties ρ , C_p are assumed constant. The dimensionless form of Equation (5) is given as:

$$Re_x Pr \int_0^1 (\overline{U} \cdot \nabla \overline{T}) d\overline{y} = Nu_x \tag{6}$$

or

$$I = \int_0^1 (\overline{U} \cdot \nabla \overline{T}) d\overline{y} = St_x \tag{7}$$

where dimensionless variables:

$$\overline{U} = \frac{\bar{U}}{U_\infty}, \quad \nabla \overline{T} = \frac{\nabla T}{(T_\infty - T_w)/\delta_t}, \quad \overline{y} = \frac{y}{\delta_t}, \quad T_\infty > T_w \tag{8}$$

In Equation (6), $Re_x Pr\left(\overline{\overline{U}}\cdot\nabla\overline{T}\right)$ represents the strength of the local dimensionless heat source in the thermal boundary layer flow. Equation (7) indicates that the physical essence of Stanton number is the integral of dimensionless convection term over the thermal boundary layer. It is clear that Stanton number is a function of Reynolds as well as Prandtl numbers and usually smaller than unity.

Equation (6) indicates that there are three ways to enhance heat transfer: (a) increasing Reynolds or/and Prandtl number; (b) increasing the uniformity of dimensionless velocity or/and temperature profiles; (c) increasing the included angle between the dimensionless velocity and temperature gradient vectors. It is noted that Stanton number may have large variation in the way (a) or (b) because it is proportional to the integral I.

It is well known that Nusselt number depends on Reynolds number and Prandtl number intensively. However, to author's knowledge, no heat transfer techniques based on the way (b) and (c) were reported before. The following discussion will be emphasized on the effects of the uniformity of velocity and temperature profiles and the included angle between two vectors on heat transfer enhancement.

3. FURTHER UNDERSTANDING OF SOME HEAT TRANSFER PHENOMENA

3.1 Effect of Profile Uniformity

For the laminar flow past a wedge, the exact solution of governing equations shows that Nusselt numbers become larger, compared with that for flow over a flat plate. For example, $Nu_x = 0.332 Re_x^{1/2} Pr^{1/3}$ for the flat plate , $Nu_x = 0.57 Re_x^{1/2} Pr^{1/3}$ for the stagnation point as $Pr \geq 0.7$ [7]. The reason for the difference between the coefficients of above correlations can be attributed to the different uniformity of velocity and temperature profiles. To describe the uniformity of velocity and temperature profiles, a uniformity factor is defined as:

$$\gamma_T = \left|\frac{T_b - T_w}{T_m - T_w}\right|, \qquad \gamma_U = \left|\frac{U_b - U_w}{U_m - U_w}\right| \tag{9}$$

where subscript b and m hold for the mean and maximum (or minimum) value over the cross section, w is the value at the wall. Obviously, the more uniform the profile is, the larger the uniformity factor, γ, becomes.

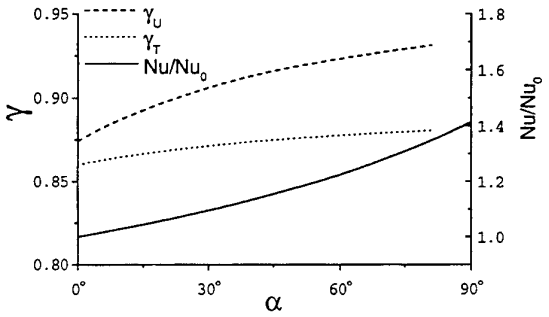

Fig. 1. γ_U, γ_T, and Nu/Nu_0 versus wedge angle (Nu_0—for flow over a flat plate)

The variations of Nusselt number and corresponding uniformity factor γ with the wedge angle are shown in Fig. 1. It can be seen that Nusselt number increases with increasing uniformity factor. The underlined mechanism lies in the fact that the favorable pressure gradient makes the velocity profile fuller, and consequently the strength of heat source is higher in the boundary layer heat transfer is enhanced as well.

For the boundary layer flow with Pr<1, the uniformity of the velocity profile is greater than that for the cases of Pr>1 because the thermal boundary layer is thicker than the flow boundary layer, as shown in Fig. 2. It turns out that the value of the integral, $I = \int_0^1 \left(\overline{U}\cdot\nabla\overline{T}\right)d\overline{y}$, increases with decreasing the Prandtl number.

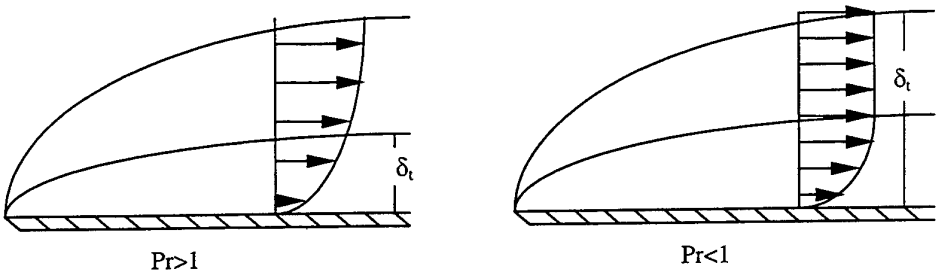

Fig. 2 The velocity Profiles in the flow boundary layer for Pr>1 and Pr<1

Fig. 3 shows the numerical results of uniformity factors of velocity and temperature profiles, and their relation with Nusselt number. This is why the Nusselt number is proportional to $Pr^{1/2}$, as $Pr \ll 1$, and to $Pr^{1/3}$, as $Pr \geq 0.6$ [6]. It can be also expected from this point of view that the power index of Pr in the heat transfer correlation should have a continuos change from 0.5 to 0.333 as Pr varies from 0 to ∞.

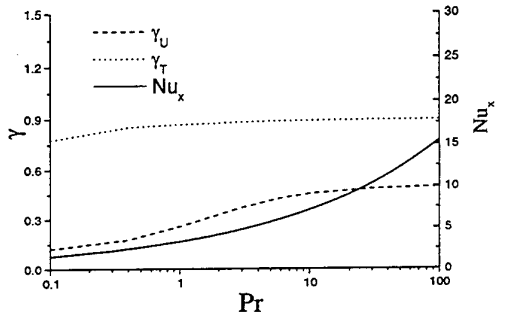

Fig. 3. γ_U, γ_T, and Nu_x/Re_x versus Pr

3.2 Effect of Included Angle

(1) Effect of the included angle between the velocity and temperature gradient vectors plays a key role in some heat transfer phenomena. Consider a hydrodynamically and thermally developed laminar flow between parallel flat plates, as shown in Fig. 4. The lower and upper plates are kept at uniform temperatures T_c and T_h, respectively. It is easy to know from the governing equation that all fluid particles are moving in the direction parallel to the plates and temperature varies in the direction normal to the plates only, that means, the streamlines are parallel to the isotherms. Consequently, the included angle between velocity and temperature gradient reaches ninety degree. As a result, the convection term/heat source term in the energy equation (1) disappears and the convective problem then reduces to a conduction problem as follows.

$$U \cdot \nabla T = u\frac{\partial T}{\partial x} + v\frac{\partial T}{\partial y} = 0 \tag{10}$$

$$Nu = \frac{hD}{k} = \frac{\left(k\frac{\partial T}{\partial y}\right)_0 \cdot D}{\Delta T} = \frac{k\frac{\Delta T}{D} \cdot D}{\Delta T} = 1 \tag{11}$$

Here the heat transfer coefficient is defined by temperature difference T_h-T_c. It means that the fluid motion has no contribution to heat transfer for this specific problem. In other cases, for instance, heat transfer will be augmented intensively in the stagnation region of jet impingement because the velocity is nearly parallel

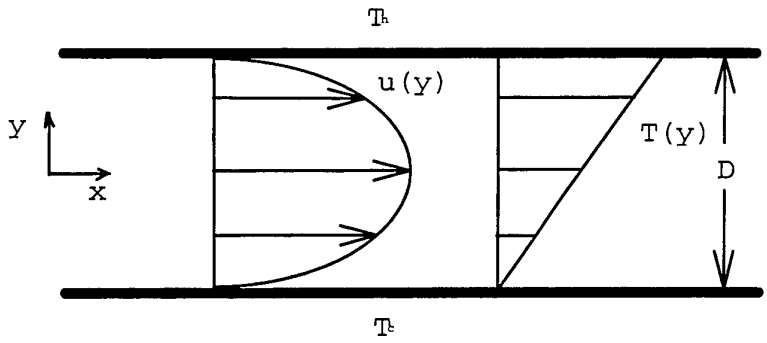

Fig. 4 Fully developed laminar flow between two parallel plates at different temperatures

to the temperature gradient. The effect of included angle shows that the common belief that fluid motion enhances the heat flux is not always true. In other words, not only the absolute value of velocity and temperature gradient, but also their included angles determines the intensity of heat transfer.

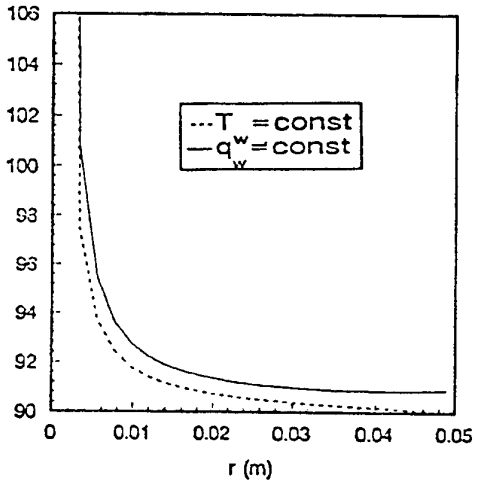

Fig. 5. Included angle for the isoflux and isothermal boundary conditions

(2) For a fully developed laminar tube flow Nu is equal to 4.36 for the isoflux thermal boundary condition, while Nu is equal to 3.66 for the isothermal boundary condition. The difference between these two cases can be well explained based on the concept of the included angle between the velocity and temperature gradient vectors. It had been verified that the included angles are only the function of radial coordinate r for the fully developed tube flow as follows [6]:

$$tg\beta = \frac{\dfrac{\partial T}{\partial r}}{\dfrac{\partial T}{\partial x}} = \frac{\dot{m} \cdot C_p \cdot D}{Nu \cdot k \cdot P} \cdot \frac{d\theta}{dr} \tag{12}$$

where P is tube perimeter, θ is dimensionless temperature.

So, it is sufficient to calculate the angles, β, on one cross section. Numerical results indicate that the included angles, β, of the U and ∇T, for the tube flow subject to the isoflux boundary condition are larger than that for the isothermal boundary condition at the given Reynolds number if wall temperature is greater than fluid temperature, as shown in Fig. 5. Hence, the larger included angle of velocity and temperature vectors leads to the larger Nusselt number for the isoflux boundary condition than for the isothermal boundary condition.

4. NOVEL APPROACHES OF HEAT TRANSFER ENHANCEMENT

Based on discussion above, some novel approaches of heat transfer enhancement have been suggested, which are expected to enhance heat transfer with less pressure drop because they are aimed at control of the included angle between velocity and temperature gradient and/or the uniformity of temperature profiles.

(1) Consider the problem shown in Fig. 6. Laminar flow with uniform velocity U passes through two parallel porous plates. The velocity is normal to the plates and the isotherms in between. The plates are kept at uniform temperatures T_c and T_h, respectively, with $T_h > T_c$. Assuming that the heat transfer between the porous plate and fluid in the pores is intensive enough, the energy equation for the fluid between two plates can be simplified as:

$$\frac{d(\rho UT)}{dy} = \frac{d}{dy}\left(\frac{k}{C_p}\frac{dT}{dy}\right) \tag{13}$$

boundary conditions:

$$U(0)=U \qquad U(D)=U;\ T(0)=T_c \qquad T(D)=T_h \tag{14}$$

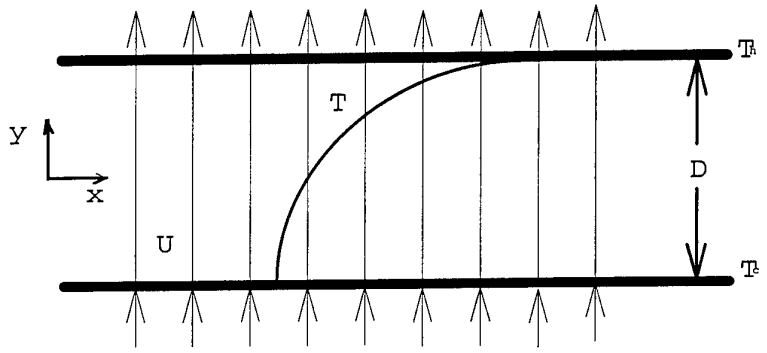

Fig. 6. velocity parallel to temperature gradient

the analytical solution of equation (13) gives:

$$\frac{T-T_c}{T_h-T_c} = \frac{\exp(Re_D \cdot Pr \cdot \frac{y}{D}) - 1}{\exp(Re_D \cdot Pr) - 1} \tag{15}$$

where $Re=\rho UD/\mu$.

In this case the isotherms are parallel to the porous plates, that is, the included angles between U and ∇T always equal to 0 degree. But the convection term acts a heat source for the upper plate because it is cooled, and as a heat sink for a the lower plate because it is heated. Based on the temperature profile given by equation (15) we have Nusselt numbers for the upper and lower plates as follows:

for the upper plate
$$Nu_D = \frac{\exp(Re_D \cdot Pr)}{\exp(Re_D \cdot Pr) - 1} \cdot Re_D \cdot Pr \tag{16}$$

if $Re_D \cdot Pr >> 0$ $\quad Nu \to Re_D \cdot Pr$ or $St \to 1$ (17)

As is well known, Nusselt number is usually proportional to $Re^{0.5}$ and $Pr^{0.5\sim0.33}$. Here Nusselt number can

be so large up to the value proportional to Re and Pr. Nusselt number given by equation (17) should be its upper limit for convection heat transfer from the viewpoint of the coordination of flow and temperature fields. This implies that heat transfer can be enhanced as long as the improvement of the coordination of flow and temperature fields, although it is impossible in practice to reach such upper limit of Nusselt number.

for the lower plate:
$$Nu_0 = \frac{\exp(Re_D \cdot Pr)}{\exp(Re_D \cdot Pr) - 1} \tag{18}$$

if $Re_D \cdot Pr >> 0$ $\quad Nu \to 0$ (19)

Then heat transfer will be greatly reduced when the included angle is close to 0 degree. It means heat transfer in this case is even worse than heat conduction.

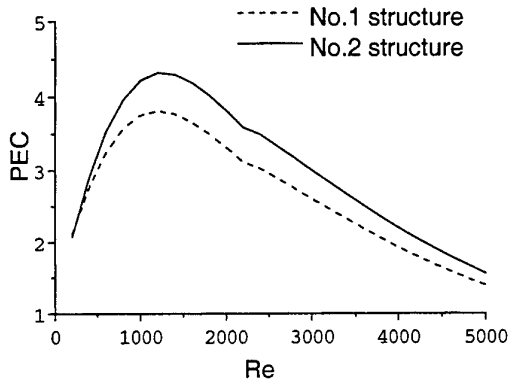

Fig.7. Experimental results on PEC for tube flow with special designed inserts

(2) In the conventional techniques heat transfer is usually enhanced through varying the velocity field. This is an effective approach but inevitably introduces considerable additional pressure drop. Based on the present novel concept, heat transfer can also be enhanced by improving the uniformity of temperature profile directly. For this purpose, specially designed inserts composed of sparse metal filaments are used to increase heat transfer in laminar tube flow [8]. The filaments were made with high conductivity metal which can be expected to increase the uniformity of fluid temperature profile. At the same time, the filaments were thin enough to produce only slight additional pressure drops. Experimental results of such a novel device are plotted in Fig. 7. Performance evaluation criteria (PEC), defined by $(Nu/Nu_0)/(\xi/\xi_0)^{1/3}$, represents the heat transfer enhancement for a given pumping power. As shown in Fig. 7, PEC reaches its acme at Re=1500 and then goes down. Compared with most conventional enhanced tubes with air as the working medium in which the PEC usually less than 2 [9,10], such an enhanced tube based on novel concept has PEC values much larger than 2 at Re ranging from 200 to 3500. It seems very promising to be applied in various kinds of heat exchangers.

(3) If the included angles between velocity and temperature gradient vector are close to 90 degree, heat transfer will be deeply weakened. Fluid rotation can be utilized to enhance the heat transfer for some cases, while reduce the heat transfer for other cases based on the concept of included angle between U and ∇T vectors [11].

Consider air in the annulus between horizontal concentric cylinders. The inner cylinder is rotating and kept at uniform temperature T_i. Outer cylinder is stationary and kept at uniform temperature T_o. $T_i > T_o$. Fig.8 shows the velocity vector at difference Re. Free convection governs heat transfer when Re=0. With the increase of Re, free convection is mixed with force convection produced by inner cylinder rotation. When the rotation speed is high enough, fluid movement is dominated by rotation.

Define mean equivalent conductivity k_{eqm} as ratio of convective and conductive heat fluxes. k_{eqm} is no other than Nusselt number. The curve of k_{eqm} versus Re is shown in Fig. 9, in which, k_{eqm} decreases with the increase of Re. And, k_{eqm} will fall to 1 when Re is sufficient larger That means fluid rotation reduces heat transfer. This can be well explained by included angle between U and ∇T vectors. It can be easily found that the direction of fluid rotating velocity is normal to that of temperature gradient. That is, heat transfer will be weakened as soon as fluid rotation takes place. When Re reaches its critical value, free convection can be neglected and the convection problem reduces to a pure conduction problem.

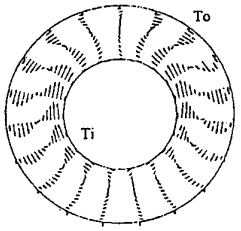

(a) Re=0

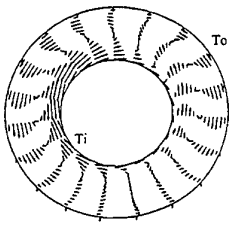

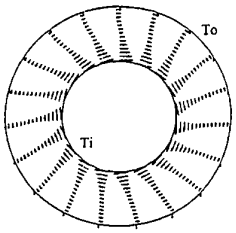

(b) Re=100 (c) Re=1000

Fig. 8. Velocity distribution in annulus ($Gr=10^5$)

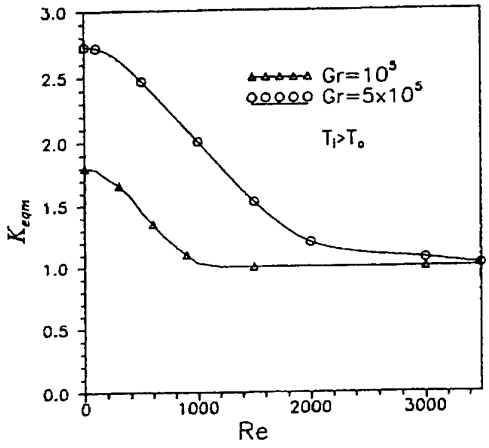

Fig. 9. k_{eqm} versus Re

5. CONCLUDING REMARKS

1. Convective heat transfer can be regarded as conduction with heat sources (sink) includidng real heat source, convection source and multi-dimension source. With such an analog, heat transfer can be enhanced as the sources are intensified.
2. There are three ways to raise the strength of heat source and, consequently, to enhance heat transfer: (a)

increasing Reynolds or/and Prandtl number; (b) increasing the uniformity of dimensionless velocity or/and temperature profiles; (c) increasing the included angle between the dimensionless velocity and temperature gradient vectors. Hence, convective heat transfer is dependent not only on the velocity and temperature gradient, but also on the coordination of flow and temperature field.

3. The present concept can be applied not only to explain physical mechanism of many existing heat transfer enhancement techniques, but also to develop some novel enhancement approaches.
4. Analytical and experimental studies show that, novel enhancement approaches aimed at improving the coordination of flow and temperature fields or direct improvement of uniformity of fluid temperature profile can remarkably enhance heat transfer with less additional pressure drop.

NOMENCLATURE

U_b, T_b mean value over cross-sectional area of the profile
U_m, T_m the maximum (or minimum) value of the profile
U_w, T_w the value on the wall of the profile
C_p specific heat capacity at constant pressure
D space between plates, diameter
Gr Grashof number
k thermal conductivity
k_{eqm} mean equivalent conductivity
Pr Prandtl number
PEC performance evaluation criteria
r radius
Re Reynolds number
S source term
St Stanton number
T Temperature
T_w wall temperature
T_∞ free-steam fluid temperature
T_c, T_h temperature of plates
T_i, T_o temperature of inner and outer cylinders
u,v,w velocity component along x, y and z coordinate, respectively
U velocity vector
∇T temperature gradient
$\overline{U}$ dimensionless velocity vector
$\nabla \overline{T}$ dimensionless temperature gradient

Greek symbles
α wedge angle
β included angle between fluid velocity and temperature gradient
θ dimensionless temperature
δ_f flow boundary layer thickness
δ_t thermal boundary layer thickness
ρ density
γ_U, γ_T uniformity factor of velocity and temperature
ξ frictin factor
μ dynamic viscosity

REFERENCES

1. A. E. Bergles, *Heat Transfer Enhancement—The Encouragement and Accommodation of High Heat Fluxes.* Journal of Heat Transfer, v.119, pp. 8-19 (1995)
2. A. E. Bergles, *Application of Heat Transfer Augmentation*, Hemisphere Pub. Co., (1981)
3. J. P. Gupta, *Fundamentals of Heat Exchanger and Pressure Vessel Technology*, Hemisphere Pub. Co., (1985)
4. R. L. Webb, *Principles of Enhanced Heat Transfer.* Hemisphere Pub. Co., (1995)
5. F. M. White, *Heat Transfer.* Addison-Wesley Pub. Co. Inc., (1984)
6. Z. Y. Guo, D. Y. Li and B. X. Wang, *A Novel Concept for Convective Heat Transfer Enhancement.* Int. J. Heat Mass Transfer, v.41, pp. 2221-2225 (1998)
7. E. R. G. Eckert, and R. M. Drake, *Heat and Mass Transfer*, McGraw-Hill Book Co., (1959)
8. S. Wang, Z. X. Li and Z. Y. Guo, *"Novel Concept and Device of Heat Transfer Augmentation"*, Proceedings of the 11th International Heat Transfer Conference.v.5. pp405-408, edited by J. S. Lee, Kyongju, Korea (1998)
9. H. M. Li, K. S. Ye, Y. K. Tan, S. J. Deng, Investigation on Tube-Side Flow Visualization, Friction Factors and Heat Transfer Characteristics of Helical-Ridging Tubes, Heat Transfer 1982, Hemisphere Pub. Co., Vol. 3, p75, (1982)
10. M. D. Donne, Convective Heat Transfer from Rough Surfaces, Turbulent Forced convection in Channels and Bundles, Hemisphere Pub. Co., Vol. 2, p911, (1978)
11. Z. Y. Guo, C. M. Zhang, *Thermal Drive in Centrifugal Fields—Mixed Convection in a Vertical Rotating Cylinder,* Int. J. Heat Mass Transfer. Vol. 35, No. 7. pp. 1635-1644, (1992)

BOILING HEAT TRANSFER IN NORMAL AND QUANTUM LIQUID HELIUM

Maurice-Xavier François, Fathi Jebali, Marie-Christine Duluc
Laboratoire d'Informatique pour la Mécanique et les Sciences de l'Ingénieur
CNRS
Email: mxf@limsi.fr; Fax: 33 1 69 85 80 88

Keywords: heat transfer, boiling and superfluid helium

ABSTRACT. The use of superfluid helium as the cooling mechanism for superconducting cavity or superconducting magnet is a key point for many years and recently for the Large Hadron Collider (LHC) which will be built at CERN (Switzerland), stimulating complementary studies on its heat transfer properties. Topics are now likely such as two phase flow of a quantum liquid helium II and its vapour, heat transfer in the very narrow geometry filled by helium II of the electrical insulation of superconductor cable, or peak heat flux and boiling configurations for surfaces wetted by either the normal liquid helium I or the quantum liquid helium II. On the other hand, these applied researches provide new information on complex and fundamental phenomena encountered with liquid helium II, as two-phase flow, heat and mass flow in porous media and boiling heat transfer. It is thus interesting to look at them on a basic point of view and compare the behaviour of a normal and a quantum fluid subjected to a boiling process. In this short review of the few experimental and theoretical works on the subject, widely using our experimental results on boiling configurations by means of photographs and high speed camera, the attention is focused on the quite complex phenomena of boiling heat transfer from a heated surface or more specially a thin cylindrical wire immersed in helium II. We then try to get the special feature of a boiling quantum fluid in configurations often referred as silent and noisy boiling regimes. A special attention is given to the silent boiling states as shown in the movie presented at the conference.

1. INTRODUCTION

Boiling heat transfer in classical fluids has been extensively studied and there are several excellent reviews or books on the subject [1]. In spite of that, numerous data are analysed in terms of empirical correlation. A few exact theoretical analyses are available for some simplified experimental situations. Although the growth and collapse of a single bubble are fully understood, the mechanism of coalescence of bubbles are not so clear. For applications, the very efficient heat transfer nucleate boiling regime still stimulates studies in order to increase the " peak heat flux " value. But the role of the bulk thermal properties of the heating surface on the burn out onset is clearly important and still difficult to model in a 3D configuration. Some recent results [2] obtained with a heated thin wire (suppressing the influence of the heater) show indeed that they can be different than those obtained with other heater configurations. On the other hand, it seems likely that the pressure field induced by the nucleation of the boiling system itself and the convection phenomena associated with the heat transfer in the liquid phase, play also a dominant role on nucleation process, intermediate boiling states, and transition to film boiling regime. Few studies have tried to take into account these wave characteristics of boiling heat transfer, but this is probably the main promising way for a better understanding of the phenomena. Boiling heat transfer is thus concerned at least by two different points: 1. the nucleation process itself which is controlled by the heated surface with cavities filled by dissolved gas and the saturation conditions required for the boiling onset. 2. the fluid heat transport properties by means of temperature, velocity and pressure fields surrounding the heated surface. Note that in a classical fluid, the convection field associated with the boiling heat transfer is rather complicated and, as said above, difficult to model as far as several growing bubbles are concerned.

On the contrary, in the quantum fluid helium II, the heat flow is in a sense very simple as we recall below and may occur without any net mass flux. Then, we may expect a different behaviour and encounter some simple and extraordinary configurations of boiling states. The studies of boiling heat transfer in helium II started in the seventies with the work of Leonard and his co-workers [3]. At that time, using a 76 micron diameter wire, they gave a first description of the different typical boiling regimes which may be found in helium II, providing good pictures of boiling states using focused shadowgraph and Schlieren visualisation techniques. Quantitative data in terms of heater superheating versus the heat flux densities were also provided but with a rough interpretation. It is interesting to note that in the same period, Allen J.[4] recorded a wonderful movie on the phenomenon of Superfluidity giving a visual evidence of the exceptional character of the quantum liquid helium II. The second

important work done on this topic was made in the eighties by the team of Labuntsov [5] and somewhat latter by the team of Francois [6-8]. A very good experiment on the possible superheating of helium II made by Tough [9] in 1981 is also useful for a complete understanding of these phenomena. More recently, these experimental studies have been repeated by the group of Murakami [10] providing some useful confirmation of the different boiling configurations occurring in the quantum fluid helium II in terms of silent or not silent boiling systems.

In this paper, we present some unpublished visualisations and data concerning the boiling states in helium II. In a first paragraph, we underline some key points of the boiling heat transfer phenomenon for a classical fluid and give typical values for liquid helium I using our data and the good reviews of Smith [11] and Pfotenhauer [12]. We then describe a typical experimental set up for a boiling heat transfer experiment and stress the main parameters controlling the phase change process. Comparing the heat transport properties of the two fluids, mainly the quantum fluid helium II, one may thus understand the difference between helium I and helium II for a boiling heat transfer experiment performed in the same cryostat. Then, we look at the results visualised in helium II and give some direction to understand these unusual results.

2. POOL BOILING CHARACTERISTICS

The Case of Liquid Helium I.

Liquid-vapour phase transition occurs when the liquid phase reaches an unstable thermodynamic state. For a given local pressure, the superheating necessary to get the formation of a vapour bubble in the bulk liquid, may be much higher that the one required by the same issue on a heated surface. In the first case, referring to the so called homogeneous nucleation, the superheated state characterised by an overheating ΔT_{hom} is rather difficult to obtain because the higher temperature is in front of the heater leading to the second case referring to an heterogeneous nucleation process for which the overheating is noted ΔT_{het}.

For helium, Sihna [13] propose an empirical expression for ΔT_{hom} :

$$\Delta T_{hom} = 4.322\left(1 - \frac{T_b}{T_c}\right)^{1.534} = T_{fluid} - T_{sat} \qquad (1)$$

where $T_c = 5.2$ K is the critical temperature, T_b the bath temperature, T_{sat} the saturation temperature. This leads to an overheating of 0.345 K at 4.2 K and 1.6 K at $T_\lambda = 2.176$ K.

It may be shown that in the second case, ΔT_{het} and the critical radius r^* of the vapour bubble are given by:

$$\Delta T_{het} = \left(\frac{8\sigma T_{sat} q}{L_v \rho_v k_l}\right)^{0.5} \text{ and } r^* = \left(\frac{2\sigma T_{sat} k_l}{q L_v \rho_v}\right)^{0.5} \qquad (2)$$

where L_v is the latent heat of vaporisation, k_l the liquid thermal conductivity, ρ_v the vapour density, σ the liquid surface tension, and q the heat flux density at the surface. As an example, for $q = 10^4$ W/m^2, at 4.2 K, one can calculate: $r^* = 0.25$ μm and $\Delta T_{het} = 0.028$ K. This is of course a minimum value which indicates that, if there are cavities whose size is of the order of r^*, such a bubble may be nucleated for such an overheating of the wetted liquid at the interface.

Experimental Set uU.

In most experimental set up, the sample is immersed in a saturated bath of liquid helium as schematised on Fig. 1. A cut in the silvered Pyrex walls of the cryostat allows visualisation. The cold source is the vaporisation of the liquid at the free surface liquid vapour. Then the overheating of the fluid, due to the flow of heat from the heated element (flat surface or wire) towards the cold source is larger close to the solid surface where heterogeneous nucleation is indeed reached prior any homogeneous one in the bulk. *And in a classical fluid with low thermal conductivity*, it is easily achieved for small heat flux density. Note that *any sub-cooling* ΔT_{sub} of the sample adds its contribution to the needed overheating. The corresponding phase diagram, Fig. 2, shows clearly

the effect of the hydrostatic overpressure in terms of ΔT_{sub}. But again, the corresponding heat flux density is only controlled by the heat flow according to *the heat transport properties of the surrounding liquid.*

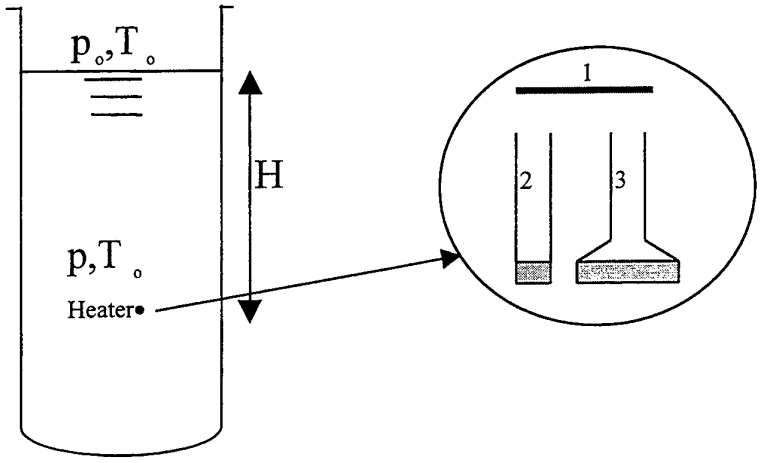

Fig. 1. Experimental set-up with different heating configurations: horizontal wire immersed in a free bath: case 1 - copper block linked by a vertical channel of uniform cross section: case 2 – channel with non-uniform cross section: case 3.

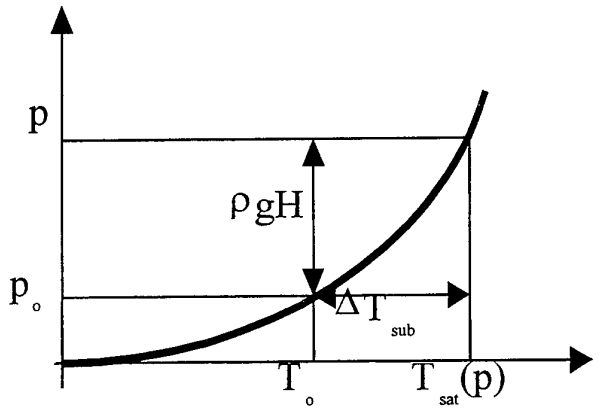

Fig. 2. Typical phase diagram. The effect of the overall hydrostatic pressure ρgH on the overheating needed to reach the phase transition.

3.BOILING IN A NORMAL FLUID

The so called Nukiyama (q, ΔT) characteristic for helium I, after Schmidt [10], reported in Fig. 3, indicates that, at saturated vapour pressure, that is, with no overpressure, heterogeneous nucleation occurs for heat flux density as small as 10^2 W/m^2 (point B) or less. Due to the very small value of the surface tension and thus of the bubble radius, the nucleate boiling regime stands till the peak heat flux 10^4 W/m^2 where flow of bubbles as well as flow of liquid become unstable and a direct transition CD to the film boiling regime occurs. However, as demonstrated by Duluc and al. [2], if the heating surface has got negligible thermal inertia, this transition region CD between peak heat flux and fully developed film boiling may be made by mixed boiling states as shown for liquid nitrogen in Fig. 4

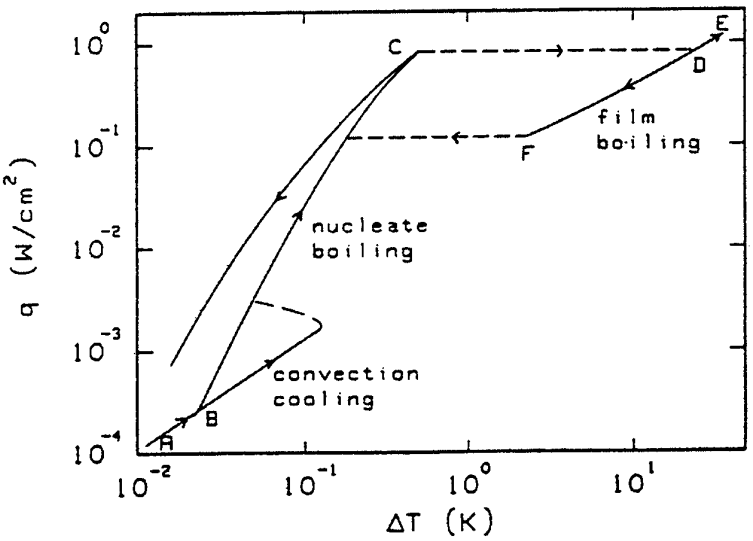

Fig. 3. Boiling curve of the classical liquid helium I. after Schmidt [11]

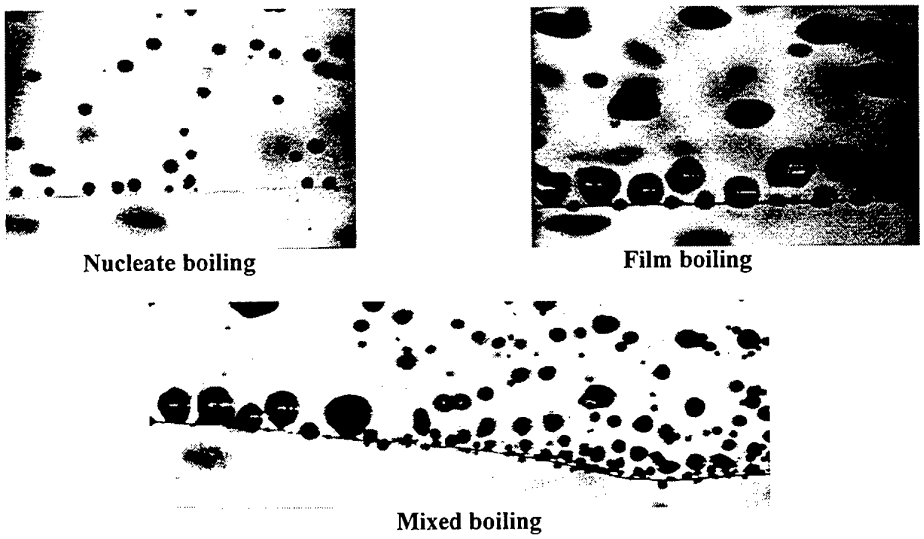

Fig. 4. Boiling regimes for a normal fluid (LN_2) and on a thin wire

The film boiling regime is characterised by a thin vapour layer blanketing the heated surface, with a vapour-liquid interface where a Taylor instability may grow [14] and whose the so-called dominant wavelength λ_d is given, for a wire of radius r_0, by:

$$\lambda_d = 2\pi \frac{\sqrt{3}}{\sqrt{\frac{g(\rho_l - \rho_v)}{\sigma} + \frac{1}{2r_0(r_0 + a)}}} \tag{3}$$

Finally, upon decreasing the heat flux while in the film boiling region, this state of heat transfer persists until the minimum film boiling point F, (ΔT_F), is attained where the vapour layer breaks allowing new liquid flow

on the heater. Note for applications that it means that a heated source, immersed in liquid helium at 4.2K, may never be wetted by liquid phase if the heat flux density q applied is larger than this small minimum value q_F. The heated solid will indeed remain surrounded by a vapour blanket and overheated. For helium I, at 4.2 K, (ΔT_F) is of the order of 1 or 2 K and $q_F \geq 10^3$ W/m^2. Moreover, for a wire $r_0 = 16$ μm, and negligible wave amplitude a << r_0, we have $\lambda_d = 0.25$ mm.

4. MAIN HEAT TRANSPORT PROPERTIES OF HELIUM II

To understand it, one must stress two special features of the quantum liquid helium II (more details may be found in the review of Pfotenhauer [12]).

Heat Flow

The hydrodynamic behaviour of the quantum liquid helium II may be approached in terms of a mixture of two components (so-called two fluid model), one normal, because like any common liquid having a density ρ_n, an entropy s_n and a viscosity μ_n, and the other said superfluid ρ_s because with no viscosity and no entropy. Then, if heat is supplied to liquid helium II by a heated surface, it can be only given to the entropic component. This one is thus brought to a non zero velocity $\mathbf{V}_n$ in the thin layer wetting the solid surface according to the temperature gradient simultaneously created by the heat flow and towards the cold source. It follows then a counter-flow of the quantum component, that is the superfluid part of the fluid, towards the heater at velocity $\mathbf{V}_s$ with no net mass flux. The heat flux density is mainly driven by the normal component and, because the thermal conductivity k_l of the liquid is negligible, one get :

$$q = \rho \,.\, s \,.T \,.\, \mathbf{V}_n + k_l \nabla T \cong \rho \,.\, s \,.T \,.\, \mathbf{V}_n, \quad \text{with} \quad \rho_s \,.\, \mathbf{V}_s + \rho_n \,.\, \mathbf{V}_n = 0 \tag{4}$$

As an example, q = 10^4 W/m^2, T = 2 K, $\mathbf{V}_n \cong 4\ 10^{-2}$ m/s.

A tremendous demonstration of the pertinence of this useful approximation is given by the fountain effect experiment for which the flow of the two component are separated. A short movie is presented at the conference to show clearly the heat transport process.

Using the two-fluid model, in the case of small heat flux, that is with no superfluid turbulence, the flow of $\mathbf{V}_n$ is only subjected to the viscous forces. In terms of equivalent thermal conductivity, one may show the well known following expression:

$$k_l = \frac{(\rho s d)^2 T}{\beta \mu_n} \qquad \text{with } \beta = 32 \text{ for cylindrical channel} \tag{5}$$

The corresponding Fourier law gives the local temperature gradient :

$$\nabla T = -\frac{1}{k_l} q \,. \tag{6}$$

Superfluid Turbulence

For heat flux larger than a "critical" value q_C^* which is a complex function of, at least, temperature and duct diameter, the superfluid component starts to be filled by a tangle mass of vortex lines or rings which is seen as an homogeneous turbulence. The main consequence is to couple the superfluid component to the viscous flow of the normal component driven by the heat, leading to an increase of the effective viscosity, ant thus to a decrease of the apparent thermal conductivity. If we accept the results of many experiments [12]and Vinen theory [17] which had shown that the vortex density is proportional to the square of the heat flux density, one may understand the new expression k_2 :

$$k_2 = \left(\frac{(\rho_s T)^3 s^4}{A(T) \rho_n} \right) q^{-2} \tag{7}$$

The corresponding heat transport model referred as the Gorter Mellink law is:

$$\nabla T \cong -\left(\frac{A(T)\rho_n}{(\rho_s T)^3 s^4}\right) q^2 q \quad = \; - \; F(T) \, . \, q^3 \tag{8}$$

Typically, for a channel diameter as small as 1 mm, at $T = 2$ K, k_1 is 10^6 W/m.K. At a large heat flux $q = 10^4$ W/m^2, $k_2 = 10^3$ W/m.K and this leads to a temperature gradient of 10^{-3}K/m. Remember that the normal liquid helium thermal conductivity k_l is about 2.10^{-2} W/ m. K.

Consequences

Using these brief comments for our purpose, we may note:

1. The equivalent thermal conductivity of helium II is so high than the overheating needed to nucleate a bubble could never be achieved locally on the surface.
2. For the same reason, and on the contrary of helium I, the heater is now thermally linked to the cold source by the whole bulk liquid. The link is approximately a wide "channel" of cryostat diameter if the test sample is a wire (Fig. 1,case 1) immersed in the bath. Or, as for many experiments with copper block heater (Fig. 1, case 2), it is a "channel" of small diameter put in order to increase the heat flux density for a given heat flux acceptable for the pumping refrigeration facility.
3. Any overhead pressure leads to an overheating which must be achieved by this "channel". It is thus clear that one may obtain the phase transition for a large range of heat flux density and thus expect various behaviours.
4. *The characteristic thermal time constant* τ_2 of a helium II filled channel of length L is of the order of L/ U_2, U_2 being the speed of second sound or entropy wave. Typically, at 1.9 K, for $L = 0.2$ m, $\tau_2 = 10^{-3}$ s. This means that the whole bath is thermally connected not only in amplitude but also in phase to the boiling process. And thus the remark on the possible influence of the pressure and convection waves takes now more evidence.

Reminding of these quite simple characteristics must not hide the real quantum and complex nature of helium II but allows going quickly to the essential differences between the two fluids facing boiling phenomena. In fact, it must be emphasised that these differences occur both in amplitude and phase.

5.BOILING CONFIGURATIONS IN HELIUM II

The Nukiyama Curve

(q, ΔT) obtained with liquid helium II is thus very different because *no nucleate boiling may occur*. A typical result is plotted on Fig. 5. T_0, p_0 correspond to the saturation conditions at the free surface, p (H) is the local pressure near the heater with:

$$p(H) = p_0 + \rho g H \tag{9}$$

and a corresponding overheating ΔT_s (H) calculated from equations (5) or (8).

For increasing heat flux up to A, the overheating of the heater surface $\Delta T_{solid} \leq \Delta T_A$ is mainly due to the so–called Kapitza thermal resistance R_k associated to the phonon transmission from the solid to the liquid. And if R_k is simply written as:

$$q = \frac{\Delta T_{Kapitza}}{R_k} \tag{10}$$

One gets:

$$\Delta T_{solid} = \Delta T_{Kapitza} + \Delta T_A \text{ , with } \Delta T_{kapitza} >> \Delta T_A \tag{11}$$

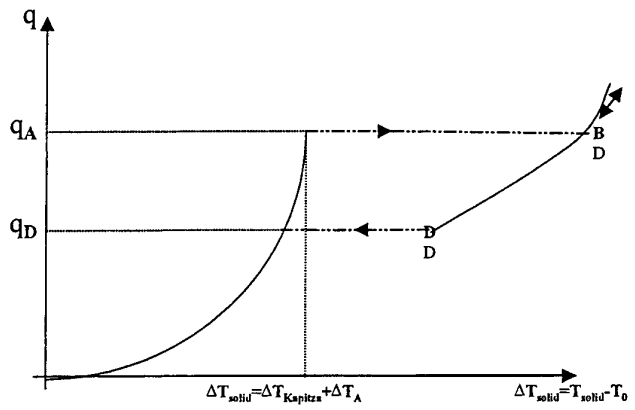

Fig. 5. Heat transfer characteristic curve in heliumII. The overheating OA corresponds both to the Kapitza and Gorter Mellink contribution. Saturation conditions are obtained for q_A.

Note that the phonon transmission does not concern the boiling phenomenon which only requires saturation conditions. On the movie the wire does not look affected by the eventually high heat flux density.

Once $q \geq q_A$, the overheating of the solid increases as expected from the appearance of a vapour layer on the heater surface point B. If this event is quite normal it is interesting to note that it can be very different for cases 1 and 2. In case 1, the temperature field of the quantum fluid all around the thin wire is perfectly uniform and very few 2-dimensional effect exist because the solid does not participate. We will see on the movie and on fig $5a_1$ that the vapour layer is perfectly uniform, the temperature gradient in the liquid side being concentrated close to the wire according to the logarithmic profile of the boundary thermal resistance.

In case 2, the temperature field in the solid is often not uniform due to many well understood reasons of the very complex thermal links between the heating solid and its environment. One thus get a partial vaporisation of the liquid wetting the heater, and reaches the complete vapour blanket for a larger heat flux density. (This phenomenon is better observed is the expecting phase transition is the second order one He II – He I, because for it there is no net decrease of the density).

Such an effect may be easily emphasised with an experimental set up (case3) whose results are given in [5]. The periodic instabilities, which then appear, will be commented elsewhere. Note that the temperature gradient is this time distributed all along the small diameter "channel".

When decreasing the heat flux density q, it is indeed obvious that the collapse of the vapour layer occurs for a lower value q_D. The amplitude of the hysteresis effect depends on several parameters such as surface tension, possible superheating of the liquid phase and stability of the vapour layer. In cases 2 and 3 this last effect is dominant.

Typical Results Obtained With a Heated Wire of 32μm Diameter

As mentioned 2 times above, the major interest of the cylindrical configuration and the thinness of the diameter is to provide an experimental heat source with no inertia, no heat capacity, short thermal time constant, and a so small cross section than the temperature distribution along the wire has no effect on the radial heat flux density transmitted to the surrounding liquid by means of joule effect. In particular, this last fact allows the existence of a distribution of mixed boiling states along the wire (Fig 3c), but is also a guaranty of the intrinsic character of the obtained boiling configurations. Moreover the mean temperature of the heater is easily known by the measurement of its electrical resistance.

Transition for moderate immersion depth H and thus heat flux density q. The result (referred as *regime 1*) is shown Figure 6. A high-speed movie of the uniform and quiet vapour layer confirms the existence of zero net mass flux at the interface. This configuration is one of those named "silent boiling" by the different

investigators. Note that this heat flux close to q_A in Fig. 6, corresponds to the maximum value transportable by the helium II " channel" to the cold source. It means that as $q_A = q_A (T_0,H)$, any larger value of q supplied to the heater at the solid gas interface will now correspond to this constant value. This is physically realised by the corresponding increase of the vapour layer diameter d, such as, if a designs the wire diameter:

$$q \cong q_A \, . \, \{ d / a \}$$

In fact q_A is not strictly constant as the increase of d modify a little bit (by few 10^{-3}) the characteristic of the "channel". An exact model of the boundary layer -vapour liquid he II, first proposed by Labuntzov [15], developed and experimentally verified by Jebali [16] will be published elsewhere.

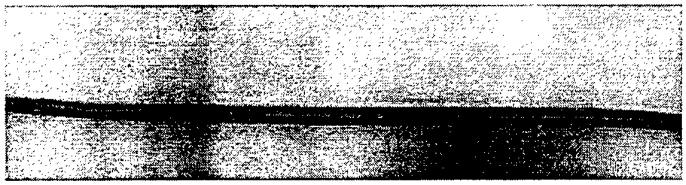

Fig 6 : Film boiling around an horizontal wire. The vapour layer is remarkably stable and no net mass flux is observed.

<u>Increasing the heat flux after the transition</u> As shown on the movie, the "silent boiling" regime may take some other unexpected and extraordinary shapes. Increasing the heat flux density drives the vapour layer to larger size for which the effect of gravity starts to be effective. First the shape of the vapour cylinder is no more symmetrical around the wire. Second the buoyancy forces balanced by the surface tension forces induce the appearance of a Taylor instability. A typical example of this new configurations (referred as *regime 2*), widely detailed in the movie, is given in Figures 7a and 7b. The measured wavelength, ranging from 0.5mm and 1 mm, is in good agreement with the equation (3). Although the surface tension coefficient is quite small for liquid helium, the result indicates that there exists stationary modes of the vapour liquid interface Taylor instability. The interfacial waves and the process of vaporisation – condensation with no net mass flux are also clearly seen on the high-speed camera movie.

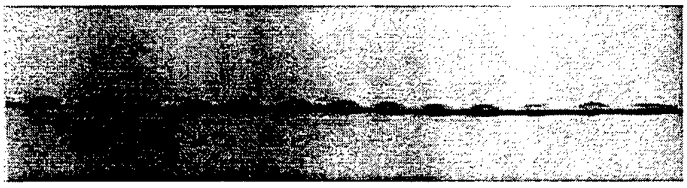

Fig 7a: For larger heat flux, the vapour liquid interface starts to underwear stationary modes of Taylor instability.

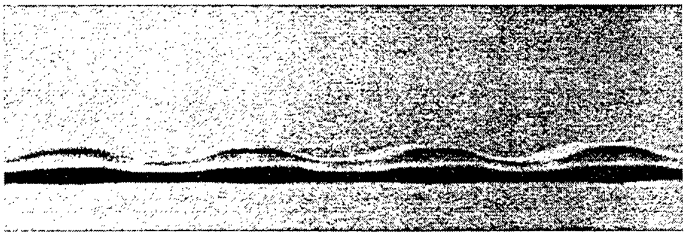

Fig 7b: Details of Fig 7a

A kind of classical film boiling for the quantum fluid ? For larger heat flux density and thus bigger value of d, the amplitude of the interfacial waves becomes too big to avoid the tearing of the interface under the buoyancy force. The new feature (referred as *regime 3*) shown in Figure 8 may look like classical film boiling except that the lifetime of the expulsed vapour pocket is very short, i.e. of the order of few ms. The 2000 frame/sec movie will give more information one the dynamic of this regime.

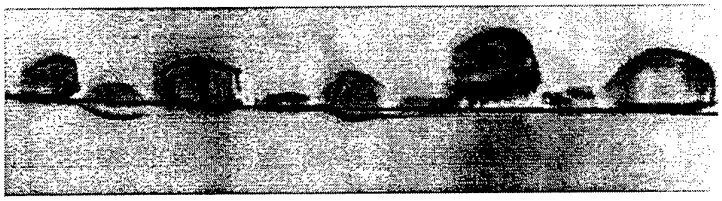

Fig. 8: A typical kind of film boiling in helium II . Note that there are no vapour pocket in the liquid phase.

Transition for high flux density q_A If the immersion depth H of the heater is large (more than 20 cm) at constant bath temperature T_0, q_A becomes high and the configuration is modify in Fig. 9 (referred as *regime 4*). It is clearly seen and better on the movie that the upper part of the vapour – liquid interface is burst in many places by the very hot atoms of gas restoring a kind of noisy film boiling at the liquid – vapour interface.

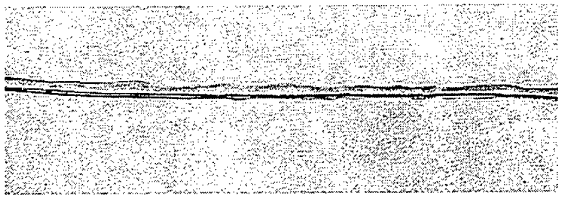

Fig. 9 : If the phase transition occurs for a high heat flux density, the silent film boiling (Fig 6) is replaced by noisy film boiling.

The Role of The Quantum Fluid.

The helium II properties are so strongly temperature dependant than it is interesting to span the maximum temperature range for T_0 to try to understand its particular contribution to the boiling process. The conclusion may be summarised in a H,T plane. In fact, as said above, the easily measured immersion depth H, that is ρgH is directly related to the overheating and thus to q_A by means of the Gorter Mellink law (7). It has been shown by Vinen [17] that the critical heat flux density q_C^* of the nucleation and development of these vortices, nearly constant till 2 K , decreases and vanishes when the bath temperature reaches T_λ.

Note that if one fixes a value of q, H becomes an equivalent parameter to look for the transition, because there is an unique value for it $q_A = q_A(H, T_0)$, and thus, for a given value of q, there exist curves $H(T_0)$ corresponding to the appearance of regime 1, regime 2, regime 3. In fact it is easier to give the portion of H,T plan where each regime may occur.

It is then possible to read the Fig. 10 in the following way: by what boiling regime 1,2 3 or 4, heat may be transmitted to quantum liquid helium at the vapour liquid interface? Atoms in the gas are indeed replacing the phonons of the solid liquid helium II conventional heat transfer.

In Fig. 10, for a given heat flux imposed here of $3.5.10^4$ W/m^2, it can be seen that when T is approaching T_λ, regime 1 is only obtained for more and more large value of H in order to fit the decrease of q_C^* and k_2 . This shows clearly that the quantum fluid drives or imposes the heat flow at and after the vaporisation.

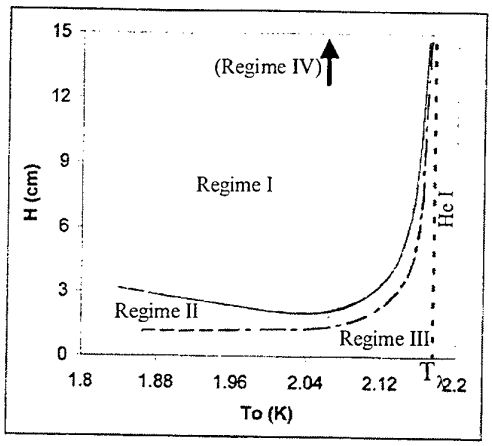

Fig 10 For a given heat flux density, the different regimes occur for given values of the overhead pressure. The effect of mean bath temperature is clearly seen. In particular, as T approaches the lambda temperature, the quantum liquid behaviour disappears progressively.

This is in agreement with the idea that the contribution of the quantum fluid is to suppress any net mass flow at the interface of condensation – vaporisation. In that sense, the transition to regime 3 is probably related to the hydrodynamic of superfluid and normal flows with a strong mutual friction due to the presence of a increasing density of superfluid vortices. This indeed transforms progressively as the temperature is approaching T_λ the boiling regimes of the quantum fluid in the classical ones of the liquid helium I.

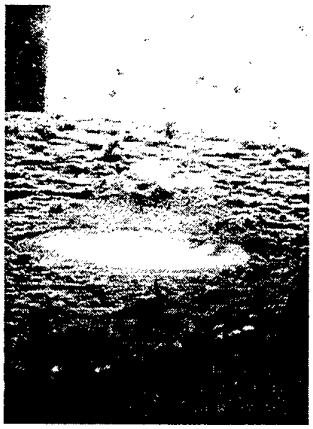

Fig 11. Boiling on a thin and horizontal copper layer of 1 mm^2 at 1.9 K. and H = 510^{-2}m. The vapour liquid interface is wrinkled. The particles of ice are dragged by the normal fluid flow.

In conclusion, it must be emphasised that, not to close to T_λ, the quantum fluid provides many unique experimental configuration of "film boiling". One may indeed vary the thickness d of the vapour layer without modifying the interfacial heat flux density, which controls the normal and superfluid velocity fields at the interface and all around. There are no net mass fluxes all around the vapour layer, and the temperature field on the liquid side of the interface is remarkably uniform. It is likely an ideal experimental configuration to study the phase transition of a superheated liquid for various q_A and understand the stability modes of a vapour – liquid interface subjected to various heat flux density. This work has also been done with plane heater and the same four regimes have been obtained. In Fig. 11, we show a regime2 for the large vapour pocket obtained on a

horizontal 1mm^2 heater surface. The particles of ice moving inside the helium II bath are dragged by the normal fluid flow. The shape of the interface is wrinkled for those case but can be much more regular for different T_0 and H value.

REFERENCES

1. S. Van Stralen and R. Cole, *Boiling phenomena*, Mac Graw Hill, (1979).
2. M.C. Duluc and M.X. François, "Steady-State Transition Boiling on Thin Wires in Liquid Nitrogen. The Role of Taylor Wavelength, Cryogenics v.37, pp.631-638 (1998).
3. A.C. Leonard, " Helium II noisy film boiling and silent film boiling heat transfer coefficient values. *Proceedings of the International Cryogenics Engineering Conference* ICEC3, pp.109-114 (1970).
4. J.F.Allen, the University of St. Andrews, Scotland, UK.
5. D.A. Labuntsov, E.V. Ametistov, A.G. Spiridonova, "Investigation of Film Boiling of Superfluid Helium (He-II), Thermal Engineering, v. 28 (4), pp.212-214, (1981).
6. M.X. François, D. Gentile, G. Defresne, L.J. Challis, "Observation of Nucleate Boiling in Helium II and its Effect on Heat Transfer", *Proceedings of the Workshop on the Stability of Superconductors*, Saclay, France pp. 85-88, (1981). IIF, 177 Bv. Malsherbes – F75017 Paris - France
7. F. Jebali, J. Maza, M.X. François, F. Vidal, "Noiseless Film Boiling in Superfluid Helium on a Heated 30 μm diameter wire", Adv. Cryog. Eng., v.33, pp 425-431, (1988), edited by R.W.Fast, Plenum Press.
8. F. Jebali, M.X. François, "Vapour Liquid heII Interface Subjected to Heat Flow", Cryogenics, v.30, pp 355-359 (1990).
9. L.J. Rybarcyk and J.T. Tough, "Superheating in He II and the Extension of the Lambda Line". J.Low Temp Phys. v.43, No ½,pp.197-202 (1981).
10. see for example Y. Katsuki, M. Murakami, T. Iida, T. Shimazaki, T. Sato, "Visualisation Study of Noisy and Silent Film Boiling Phenomena on a Plane Heater in He II", Cryogenics v.34, pp.333-336 (1994) ICEC supplement.
11. C. Schmidt, "Review of steady state and transient heat transfer in pool boiling helium I" *Proceedings of the workshop on the Stability of Superconductors*, Saclay, France pp.17-31(1981). IIF, 177 Bv. Malsherbes – F75017 Paris - France
12. J.M. Pfotenhauer, R.J. Donnelly, "Heat Transfer in Liquid Helium", Advances in heat transfer, Academic Press, Inc. v. 17,pp.66-159 (1985).
13. D.N. Shina and al., "Homogeneous Nucleation in He^4: C corresponding-States Analysis", Phys. Rev. A v. 26, 2, pp1048-1061 (1982).
14. H. Lamb , *Hydrodynamics*, 6th edition, Dover Publications, New York, N.Y. (1945), p.455.
15. D.A. Labuntzov, Ye. V. Ametistov., "The theory of He-II film boiling on horizontal cylinders", Cryogenics 21 (1981).
16. F. Jebali, PhD dissertation, "Contribution à l'étude des propriétés de l'interface vapeur-hélium superfluide créée autour d'un fil horizontal chauffé", The Paris 6 University, 28 Oct. 1991.
17. W. F. Vinen, "Proc.Roy. Soc. A 240 , p.114 (1957).

MEETING CALIFORNIA'S AIR-QUALITY GOALS: THE ROLE OF NEW TECHNOLOGIES AND FUELS

Alan C. Lloyd, Ph.D.
Chairman
California Air Resources Board
E-mail: Alloyd@arb.ca.gov; Fax: (916) 327-5748

Keywords: pollution, low emission vehicle, gasoline, fuel cell, hybrid

ABSTRACT. Air pollution is responsible for a variety of respiratory ailments. Motor vehicles produce about 60 percent of smog-forming emissions in California. While pollution levels have decreased in the last 30 years, further steps must still be taken to reduce pollution from motor vehicles. California already has the world's cleanest standards for new light-duty motor vehicles and gasoline. Low-emission vehicle regulations will require conventional vehicles to become steadily cleaner until 2010. This will largely result from refinements to existing technologies. Further refinements to gasoline are under consideration. California will require the marketing of zero and near-zero emission vehicles in 2003. Battery-powered electric vehicles are already available. Fuel cell vehicles show great promise and will be the focus of a major demonstration project in California. Hybrid electric vehicles and advanced internal-combustion engines also show substantial promise. Heavy-duty vehicles will be subject to new emission standards in 2004, but California is looking for additional strategies to reduce emissions from those vehicles. The use of low-sulfur diesel fuel and incentives for fleet operators to use alternative fuels are desirable strategies.

I. AIR POLLUTION IN CALIFORNIA

California has the worst air quality in the United States. While air pollution levels have decreased significantly during the last 30 years, smog continues to hang over many California cities during summer months. The lungs of the average Californian are regularly exposed to significant levels of ozone, hydrocarbons and other volatile organic compounds, oxides of nitrogen, and a bewildering variety of microscopic particles. In total, more than 90 percent of California's 32 million people breathe unhealthy air at some time during a typical year.

High levels of ozone have long been known to exacerbate asthma, bronchitis and other respiratory ailments. In recent years, studies have confirmed that high levels of airborne particulates can cause death in people already suffering from respiratory ailments. Children with chronic exposure to severe air pollution appear to have higher rates of asthma, wheezing and other respiratory ailments, and are more likely to have diminished lung function. Continuing research into the health effects of air pollution reinforce the importance of improving air quality in a timely and cost-effective manner.

Much has been written about the ironic nature of California's air-quality problems: The same amenities that attracted millions of people to California are also responsible for its air pollution. The state's world-famous sunny climate readily converts volatile organic compounds and oxides of nitrogen into ozone. Stable weather patterns and mountain ranges prevent pollutants from dispersing. But weather and mountains by themselves do not pollute the air. California's automobile-dependent transportation system ensures the introduction of a considerable volume of pollutants into its emission-sensitive environment. On-road motor vehicles produce about 60 percent of smog-forming emissions in California; off-road mobile equipment contributes another 10 percent, and stationary sources account for the remainder.

Even though California still faces significant air-quality challenges, the state has enjoyed considerable success in reducing air pollution. Between 1980 and 1997, peak ozone levels in California decreased by 49 percent while the state's population grew by 39 percent and vehicle use increased by 78 percent. Much of this success has been due to the ability of the California Air Resources Board (CARB) to use the regulatory process to push the development of cleaner motor vehicle and fuel technologies. Future improvements in air quality will continue to rely in large part on continued technological improvements in motor vehicles

and fuels. California's current goal is to attain U.S. national ambient air-quality standards for ozone and particulates by 2010 or within a few years thereafter.

In general, California regulators view greenhouse-gas emissions as a global issue that is better addressed at the national and international level, rather than at the state level. CARB does not regulate carbon-dioxide emissions from motor vehicles. However, it should be noted that continuing excessive emissions of greenhouse gases will likely contribute to global warming, and that higher average temperatures will tend to increase the conversion of tailpipe and smokestack pollutants into ground-level ozone. The ability to reduce carbon-dioxide emissions from motor vehicles through the use of improved technologies will play an indirect role in future efforts to minimize ozone levels.

II. MOTOR VEHICLE AND FUEL REGULATIONS

California scientists and regulators since the 1950s have recognized that cars and trucks play a key role in air pollution. In the last decade, regulators have gained a greater appreciation of the role that clean fuels can play in improving air quality. At the present time, California has the world's cleanest new motor vehicles and cleanest gasoline. The average 1999 model-year car sold in California produces emits 0.113 grams of non-methane organic gases (NMOG) per mile -- less than one-half of the 0.250 gram/mile standard for NMOG in the rest of the United States. The 0.113 standard represents a 95 percent reduction in NMOG emissions from new vehicles since the early 1970s.

California vehicles employ the same basic pollution-control devices – catalytic converters, computerized fuel controls, fuel injection and on-board diagnostics -- as vehicles in the other 49 states and many other countries. Motor vehicle emission standards established by CARB have pushed vehicle manufacturers to further refine these technologies and improve their efficiencies. New emission standards to be phased in during the next decade are pushing further improvements in these familiar technologies. The average new 2010 California motor vehicle will meet an NMOG emission standard of 0.035 grams per mile -- 70 percent less than a 1999 vehicle. Just a few years ago, few believed that a gasoline-burning engine could meet such a standard. However, CARB staff now expects that 2010 cars with conventional engines will meet the new standards, primarily with improved catalysts and fuel controls.

Cleaner gasoline also has played a major role in reducing emissions. Since 1996, CARB has required the use of a special low-sulfur reformulated gasoline that reduces emissions of volatile organic compounds by 17 percent and oxides of nitrogen by 11 percent. Vehicle manufacturers have designed emission-control systems in California vehicles around the use of this gasoline, known in oil-industry and regulatory circles as CARB Phase 2 gasoline.

Low-Emission Vehicle Program

CARB approved its original Low-Emission Vehicle (LEV) regulations in 1990, and approved a second set of regulations, known as LEV-II, in 1998. These two regulatory packages cover light- and medium-duty vehicles. Viewed as a single package, the regulations:

1. Define emission requirements for various classes of vehicles, known as "Tier 1" vehicles, "Transitional Low Emission Vehicles (TLEVs), Low Emission Vehicles (LEVs), Ultra-Low Emission Vehicles (ULEVs), Super Ultra-Low Emission Vehicles (SULEVs) and Zero Emission Vehicles (ZEVs). Each vehicle category contains its own set of exhaust-emission standards for NMOG, oxides of nitrogen (NOx) and carbon monoxide (CO). A ZEV is defined as a vehicle that produces no NMOG, NOx or CO emissions. Emissions from a Tier 1 vehicle are equivalent to a standard U.S. motor vehicle.

2. Allow vehicle manufacturers to choose the mix of vehicle classes that they sell, but the overall fleet marketed by a manufacturer must meet a "fleet-average" NMOG standard that gets steadily lower each year between 1994 and 2010. The 1994 fleet-average NMOG standard was .250 g/mile; the 2000 standard is .073 g/mile, the 2004 average is .053 g/mile, and the 2010 average is .035 g/mile. In 1999, the "average" vehicle

marketed in California met the TLEV standard. Eventually, vehicles meeting the ULEV and SULEV standards will dominate the California vehicle market.

3. Require sport-utility vehicles, pickups and minivans weighing less than 8,500 pounds to meet the same emission standards as passenger cars, beginning in 2004. Traditionally, vehicles exceeding 3,750 pounds in weight have been considered work vehicles and have been subject to less-stringent emission standards. Larger vehicles currently are allowed to emit as much as 2-1/2 times as passenger cars. In recent years, the popularity of larger vehicles in the United States has grown; sport-utility vehicles, pickups and minivans accounted for almost 46 percent of new vehicle sales in 1997. These vehicles are now used primarily as passenger vehicles, and CARB's position is that they should meet passenger-car standards.

4. Require all vehicles to meet stringent evaporative-emission standards. Until 2004, passenger cars subject to a standardized three-day test measuring diurnal and hot soak emissions are allowed evaporative emissions of 2.0 grams. The standard is reduced to 0.5 grams in 2004. In addition, vehicles will remain subject to CARB's current running loss standard of 0.05 g/mile.

5. Require vehicles, beginning in 2004, to meet CARB emission standards for their first 120,000 miles. Emission standards will be relaxed somewhat after 50,000 miles. For example, a vehicle certified as a LEV will have to meet a 0.075 g/mile NMOG standard for its first 50,000 miles, and then 0.090 g/mile standard until it attains 120,000 miles. CARB operates an in-use compliance program in which it tests vehicles owned by everyday Californians; if a certain percentage of vehicles of a particular make and model fail emission tests, CARB can order a recall or take enforcement action against the manufacturer. Until 2004, vehicles are subject only to a 50,000-mile standard.

6. Call for manufacturers selling (and/or leasing) 3,000 or more vehicles per year in California to meet a Zero-Emission Vehicle (ZEV) requirement, beginning in 2003. A manufacturer will meet the requirement if 10 percent of its vehicles for sale or lease are ZEVs. An alternative is for at least 4 percent of a manufacturer's fleet to be pure ZEVs, and an additional percentage to be "near Zero-Emission Vehicles" that utilize advanced technologies. The actual percentage of near-ZEVs needed is based on the emissions of the vehicles and the percentage of pure ZEVs that a manufacturer markets. Given the continued anticipated growth in the number and usage of motor vehicles, CARB believes the commercialization of ZEVs and near-ZEVs is essential to get the Los Angeles region and other regions of the state into compliance with air-quality standards. ZEVs do not deteriorate with age, nor do they emit evaporative emissions. Battery-powered electric vehicles have been marketed by major manufacturers in California since 1996 and are the only pure ZEVs currently on the market. CARB is currently participating in a demonstration project involving electric vehicles powered by fuel cells using on-board hydrogen, which also qualifies as a ZEV. In the last several years, manufacturers have made promising advances with hybrid electric vehicles, fuel cell vehicles using methanol and gasoline, and also advanced internal-combustion engines using natural gas and gasoline. These vehicles could qualify as near-ZEVs under CARB regulations.

Reformulated Gasoline Program

CARB views the vehicle and its fuel as a single, integrated system. By treating the vehicle/fuel system as one entity, it is possible to achieve emission reductions that would not occur through vehicle regulations alone. For example, vehicle manufacturers rely on the low-sulfur requirements for California gasoline to design catalysts that enable the vehicle to meet CARB emission standards.

CARB's first comprehensive gasoline regulation (known officially as CARB Phase 1 reformulated gasoline) took effect in 1992, when a reid vapor pressure specification of 7.8 PSI took effect. Current California gasoline must meet CARB Phase 2 reformulated gasoline regulations, which took effect in

Spring 1996. In addition to producing 17 percent fewer VOC and 11 percent fewer NOx emissions, relative to conventional gasoline, Phase 2 gasoline also reduces cancer risk from exposure to motor vehicle toxics by about 40 percent. This is due to an approximate 50 percent reduction in benzene emissions and 30 percent reduction in emissions of 1,3-butadiene. Phase 2 gasoline produces greater emission benefits than reformulated gasoline used in other parts of the United States in accordance with U.S. Environmental Protection Agency (U.S. EPA) regulations.

Phase 2 gas contains a sulfur specification of 30 parts per million. Other specifications require relatively low levels of benzene, aromatic hydrocarbons and olefins, as well as lower distillation temperatures. There is also a reid vapor pressure limit of 7.0 PSI. There is also an oxygen specification of 2.0 percent by weight, but CARB allows refiners to reduce or eliminate oxygen (and vary from most other Phase 2 specifications) as long as there is no decrease in emission benefits. Most cleaner-burning gasoline since 1996 has contained the oxygenate MTBE. But due to concerns about the remediation of MTBE-contaminated groundwater, California will prohibit MTBE use beginning in 2003. Future California gasoline most likely will contain ethanol or be formulated without oxygenated additives.

CARB staff in 1999 worked with refiners, vehicle manufacturers and others to develop specifications for Phase 3 reformulated gasoline. CARB was scheduled to consider approval of the Phase 3 specifications in December 1999. As of this writing, CARB staff had not yet developed a detailed proposal, but the staff was considering a further reduction of the sulfur standard to approximately 20 parts per million, as well as other modifications that could give refiners more flexibility to produce non-oxygenated gasoline without sacrificing air-quality benefits.

The impact of reformulated gasoline has been far-reaching. In the early 1990s, many people believed that gasoline-powered vehicles would not be able to meet CARB's Low-Emission Vehicle standards. The use of reformulated gasoline has helped vehicle manufacturers to meet ambitious CARB standards without a costly investment in infrastructure for alternative fuels.

Fuel-Neutral Policy

The success of reformulated gasoline should not overshadow the fact that CARB adheres to a strict "fuel neutral" policy. CARB has no policy favoring any fuel over any other fuel. Vehicle manufacturers can design vehicles around the use of any fuel they choose. While gasoline and diesel remain the dominant fuels in California, there has been progress in the use of alternative fuels, particularly natural gas. Several vehicle manufacturers have developed light- and medium-duty natural-gas vehicles that meet CARB's ULEV and SULEV standards. In particular, natural gas is an extremely promising fuel for urban buses and heavy-duty truck fleets that are fueled at a central location. While maintaining an official policy of fuel neutrality, CARB recognizes the real and potential benefits of alternative fuels and encourages both manufacturers and customers to seriously consider their use.

Heavy-Duty Vehicles and Diesel Fuel

CARB's current heavy-duty vehicle standard of 4.0 grams/brake-horsepower-hour for NOx emissions is consistent with the U.S. national standard. CARB worked with the U.S. EPA and diesel-engine manufacturers to develop a national standard of 2.0 grams/brake-horsepower-hour that will take effect in 2004. Engine manufacturers will introduce the cleaner engines in California beginning in 2002. The cleaner engines also are expected to produce significantly fewer particulate emissions.

Further emission reductions from heavy-duty trucks and buses will be needed to enable California to achieve its clean-air goals. The technologies needed to achieve these reductions have not yet been defined. A discussion on the technologies needed to meet heavy duty-vehicle standards of 0.5 g/b-hp-hr for NOx and .01g-bhp-hr for particulates was scheduled for a CARB-sponsored symposium in October 1999.

Further improvements in diesel fuel are crucial in order to reduce emissions beyond the 2004 national standard. In 1993, CARB implemented a 500 ppm sulfur limit and a 20 percent limit for aromatic hydrocarbons in diesel fuel. While these diesel-fuel specifications are the cleanest in the United States, CARB no longer believes they are satisfactory. CARB has asked the U.S. EPA to consider a U.S. national

standard of 30 ppm for sulfur in diesel fuel. Low-sulfur diesel fuel would permit effective afterburner treatment of diesel exhaust similar to a catalytic converter.

The potential for the use of alternative fuels is best in the heavy-duty sector, due to the use of central fueling for fleets. Several public-transit systems in California have made major commitments to the use of buses running on compressed natural gas. CARB and local air districts have begun a cooperative program to provide financial assistance to public and privately owned fleets that wish to purchase alternative fuel (or clean-diesel) equipment that is at least (25 percent) cleaner than CARB requirements.

An additional issue related to the use of diesel equipment is the toxicity of both gaseous and particulate components of diesel exhaust. In 1998, CARB officially declared diesel particulates to be a Toxic Air Contaminant; about 40 other substances found in diesel exhaust also are listed as toxic air contaminants. CARB staff is currently performing an analysis to determine if current ozone-control regulations will be sufficient to protect Californians from the toxic properties of diesel exhaust. If more regulations are deemed to be necessary, they most likely will take the form of emission standards and/or fuel specifications, but it would be premature to dismiss other kinds of regulations. While CARB encourages the use of alternative fuels where appropriate, no bans or legal restrictions on the use of diesel technology are envisioned.

III. MEETING THE STANDARDS WITH NEW TECHNOLOGIES

Conventional Technologies For Conventional Vehicles

While there has been outstanding progress in zero and near-zero emission technologies, most California light-duty vehicles will likely run on gasoline for the foreseeable future. The basic technologies that are reducing emissions from conventional vehicles to once-unthinkable levels are familiar to the knowledgeable auto enthusiast. But these technologies are not remaining static – they are steadily evolving and improving as the motor vehicle industry responds to the need for cleaner vehicles in California and elsewhere.

The cleanest conventional vehicles currently in California meet CARB's Ultra-Low Emission Vehicle (ULEV) standard (0.04 g/mile NMOG and 0.2 g/mile NOx for passenger cars, and less-stringent standards based on weight for heavier vehicles). The Honda Accord and Mazda Protégé both have engine families that meet ULEV standards. In addition, there are compressed natural gas versions of the Ford Crown Victoria and Honda Civic that meet ULEV standards. A Ford Windstar minivan engine family currently is the only medium-duty vehicle to be certified as a ULEC. In addition, Ford is producing a line of F250, E250 and E350 pickups and vans using compressed natural gas that meet the SULEV standard for medium-duty vehicles.

Low-emission vehicles now on the market are utilizing a variety of technologies. Improved fuel control results from dual or universal exhaust-gas oxygen sensors that maintain the air/fuel ratio at the best level. New software algorithms also are helping to improve fuel control. Vehicle manufacturers are improving fuel atomization and delivery with use of sequential multi-point fuel injection that delivers the precise amount of fuel needed to each cylinder. Air-assisted fuel injectors and heated fuel injectors also are being used. A variety of technologies are being utilized to assist catalyst performance, including close-coupled and underfloor catalysts, heat-optimized exhaust pipes, improved software for better engine calibration, leak-free exhaust systems, electrically heated catalysts, electric air injection and hydrocarbon adsorber systems. To reduce engine-out emissions, manufacturers are turning to electronic exhaust-gas recirculation, reduced crevice volume in the combustion chamber, and improved designs for cylinders and pistons to reduce oil consumption.

Manufacturers generally will need to employ further measures to meet the cleaner emission standards taking effect by 2004. Typical expected actions include increasing the volume and metal content of the catalyst. At the time that the second set of LEV regulations were adopted in November 1998, much debate centered around how the larger sport-utility vehicles, pickups and minivans could meet passenger-car emission standards. ARB technicians outfitted two large sport-utility vehicles with advanced catalyst systems and oxygen sensors that were bench-aged to simulate use at 50,000 miles. With some difficulty,

the technicians were able to achieve acceptable emissions performance in vehicle tests. One key challenge was that ARB technicians could not modify the vehicle software to achieve optimum performance. ARB staff concluded that the use of advanced catalysts and other equipment, along with appropriate software, will enable large vehicles to meet passenger-car standards.

Manufacturers are expected to meet the evaporative emission standards through the use of steel or improved plastic fuel tanks, the use of carbon steel and fluropolymer fuel lines, improvements to fuel canisters and fuel caps, and the use of an activated carbon filter in the intake manifold to reduce running losses.

Battery-Powered Electric Vehicles

For most of the 1990s, battery-powered electric vehicles (EVs) were seen as the only ZEV technology that could be ready for commercialization in the foreseeable future. Even the recent promising advances in fuel cells do not diminish the important role that EVs will play in the next several years as a zero-emission alternative to the internal-combustion engine.

Many observers are quick to point out that there is no such thing as an absolute zero-emission vehicle; even the use of EVs result in power-plant emissions from producing the electricity to power an EV. In California, those power-plant emissions are equivalent to approximately 0.004 g/mile NMOG, or about one-tenth the emissions of a ULEV. While recent developments indicate that advanced internal-combustion engines may soon reach such low emissions levels, EVs still hold an inherent advantage from an environmental standpoint. All internal-combustion engines deteriorate over time and produce more emissions; EVs do not. Also, there are substantial emissions associated with the production, refining and distribution of gasoline, and these emissions are avoided with the use of EVs. For these reasons, the EV (and its zero-emission cousin, the hydrogen fuel cell vehicle) is considered the "gold standard" for the clean-air vehicle. Even the very promising near-ZEV technologies discussed later in this paper cannot provide all the environmental benefits of a true ZEV.

Under CARB's current ZEV rule, a minimum of 4 percent of vehicles marketed in California in 2003 by most manufacturers must be pure ZEVs. Battery-powered EVs are still the only ZEV technology that will be commercially available in 2003. There are still concerns that the limited range of EVs will limit their appeal in the marketplace. For much of the past decade, EVs relied on traditional lead-acid batteries that offer only a 80- to 110-kilometer range before they need recharging. Since 1996, CARB has tried to focus efforts on the development of advanced batteries with ranges of 160 kilometers or longer. CARB has signed agreements with major vehicle manufacturers for the marketing of 3,750 EVs with advanced batteries by 2000. The objective of the agreements is to use the 3,750 EVs as a pilot-test fleet and gain sufficient information to fully commercialize one or more advanced-battery technologies by 2003. Many of these vehicles have already been marketed to fleets and individuals. Virtually all of the advanced batteries marketed to date have been nickel-metal-hydride. Honda introduced the battery in its EV Plus sedan in 1997. Other major manufacturers now are marketing EVs with nickel-metal-hydride batteries, although Nissan is introducing a demonstration fleet of EV station wagons containing lithium-ion batteries.

The other major questions concerning EVs are both vehicle and battery costs. At present, the cost of vehicles and batteries remains somewhat greater than for conventional vehicles. Costs should decrease when vehicles and batteries are produced in greater quantities and economies-of-scale are realized. The lower fuel and maintenance costs of EVs should also be considered when comparing the cost of EVs with conventional vehicles. CARB will examine cost, range and other EV-related issues when it conducts its next biennial review of its ZEV requirement later in 2000.

A total of 10 makes and models of factory-built EVs have been available to California motorists since late 1996, when General Motors introduced its EV-1 sports car. Several months later, Honda introduced its EV Plus sedan. GM and Honda remain the only manufacturers to market their vehicles to the general public. Unfortunately, consumer response has been somewhat tepid, due to high vehicle costs (they have been leased to customers at $400 to $500 a month) and limited battery range. Honda stopped marketing its EV Plus sedan in 1999, despite evidence that there were still customers interested in leasing the vehicle. Other manufacturers are marketing EVs to fleets.

The 10 EVs marketed as of this writing in California, along with their battery types, are: Dodge Caravan (lead-acid and nickel-metal-hydride); Ford Ranger pick-up (lead-acid); General Motors EV-1 (lead-acid and nickel-metal-hydride); General Motors S-10 pickup (lead acid and nickel-metal-hydride); Honda EV Plus (nickel-metal-hydride); Hyundai Accent EV (nickel-metal-hydride); Nissan Altra EV (lithium-ion); Plymouth Voyager Epic EV (lead-acid and nickel-metal-hydride); Toyota RAV-4 EV (nickel-metal-hydride); and Solectria Force (lead-acid).

The success of EVs hinges as much on consumer education as reducing vehicle costs and improving range. Given the large distances often traveled in California, motorists have natural skepticism about the limited range of EVs. Efforts to market EVs focus on the fact that EVs do not have to fully replace consumer vehicles and that, in fact, they make excellent commuter vehicles. CARB and local agencies have been working with utilities on the installation of public charging stations at shopping centers and other prominent locations. More recently, CARB and several local agencies began working with the car-rental industry to have EVs available for rent at major California airports. The availability of EVs as rental cars should give them greater exposure to potential buyers.

Even though questions remain about the future of EVs, there is little doubt that the 1990s were a tremendously productive period for EV technology. In 1990, EVs were still largely garage-built prototypes. By the end of the decade, they were an increasingly common sight on California's highways. Surveys of vehicle and battery developers have confirmed that CARB's ZEV rule helped accelerate the advancement of EVs and other EV-based vehicle technologies. As these technologies have developed, our vision of zero and near-zero emission vehicles has likewise expanded. It now appears to be simply a matter of time before fuel cell- and hybrid-electric vehicles take their place alongside battery-powered EVs as the vehicles of the future.

Fuel Cell Vehicles

Just a few years ago, fuel cell vehicles were still deemed to be decades away from practicality. Rapid advances have made decreased the size and weight of fuel cells and made them a promising alternative to batteries as the power source for an electric vehicle. Most major vehicle manufacturers have undertaken fuel cell-development projects. In the most visible development effort, DaimlerChrysler, Ford and a leading fuel cell manufacturer, Ballard Power Systems of Canada, have embarked on a $950 million project to commercialize a fuel cell vehicle by 2005. Those three companies also have joined with three oil companies and the State of California on a major fuel cell demonstration project.

A fuel cell produces electricity through a chemical reaction involving hydrogen (from on-board fuel) and oxygen. Emissions resulting from fuel cells depend on the fuel used. If the on-board fuel is pure hydrogen, the only emission is water vapor, and the vehicle would qualify as a pure ZEV. Hydrogen can also be derived through an on-board reformer from more familiar fuels, such as methanol, ethanol or gasoline. In those cases, there are low levels of hydrocarbon emissions from the reforming of the fuels, and the vehicle would likely qualify as a near-ZEV under CARB regulations. It is worth noting that there is no combustion, and therefore no NOx or CO emissions, from any fuel cell vehicle.

While the use of on-board hydrogen would be ideal from an emissions standpoint, there would be practical difficulties associated with the widespread commercialization of hydrogen fuel. The use of methanol, ethanol or gasoline would compromise the elegance of the fuel cell vehicle as a pure ZEV, but such fuels likely will be more practical in the short term. Emissions from the use of gasoline are expected to be higher than from methanol or ethanol, but a gasoline fuel cell could take full economic advantage of the vast gasoline infrastructure that exists worldwide. The widespread use of methanol or ethanol might require modifications to that infrastructure, with the benefit being lower emissions.

Whether as pure ZEVs or near-ZEVs, fuel cell vehicles have exciting potential. They offer most or all of the emission benefits of a ZEV with the range and refueling convenience of a conventional vehicle. It should be noted that the fuel cell vehicle benefits from the rapid acceleration of EV technology during the 1990s. Because fuel-cell vehicles are powered by electric engines, the successful development of EV drivetrains, software and aerodynamic designs can be applied directly to fuel-cell vehicles.

As always, a critical factor governing the future of fuel cells is vehicle cost. A fuel-cell engine costs significantly more than an internal-combustion engine. Improved technology, mass-production volumes and the likelihood of lower maintenance costs should make fuel cells more competitive with conventional vehicles. Fuel costs will also play a key role in determining the commercial viability of fuel cells.

The California Fuel Cell Partnership

Fuel cell technology for light-duty vehicles as well as urban buses has reached the stage where it is ready for rigorous testing under real-world conditions. In early 1999, CARB joined with seven other private and public entities with an interest in fuel cells to form the California Fuel Cell Partnership. This cooperative partnership will demonstrate and test fuel cells in about 50 fuel-cell cars and urban buses during the next three years.

Joining CARB, Ford Motor Company, DaimlerChrysler and Ballard Power Systems in the partnership are ARCO Products Company, Shell Oil Company, Texaco and the California Energy Commission. Other companies and agencies can join if they wish. The goal of the partnership is to raise public awareness of fuel cells and demonstrate the viability of fuel cell vehicles by testing vehicle performance and operating a fueling infrastructure. The partnership also will identify and attempt to resolve barriers to the commercialization of fuel cells.

California Governor Gray Davis announced the formation of the partnership in April 1999. The demonstration of 10 passenger cars and as many as five buses will begin in 2000. An additional 30 passenger cars and 10 buses will join the demonstration fleet before the project concludes in 2003. DaimlerChrysler's NECAR 4 and Ford's P2000 Prodigy will likely be the two passenger vehicles used in the demonstration.

Current plans call for the initial demonstration fleet to use on-board hydrogen. This demonstration should provide important information on the ability of a fleet manager to operate and maintain a fleet of pure zero-emission fuel cell vehicles. Other fuels may be tested later in the project. The participation of three major fuel companies in the program is important, as they will gain valuable information that will eventually be needed for establishing a commercial fueling infrastructure.

In addition to developing information on the relative cost and feasibility of different fuels, the demonstration project also will produce important data on the maintenance needs and costs of fuel cell vehicles. Because fuel cell vehicles have fewer moving parts than conventional vehicles, it is expected that maintenance costs will be lower than for internal-combustion engines. To better determine costs for fuel cell buses, data from the California project will be added to data from bus-demonstration projects in Chicago and Vancouver to better determine bus operation and maintenance costs.

The fuel cell partnership represents another milestone in California's efforts to accelerate the introduction of clean, advanced-technology vehicles. A successful demonstration may play a critical role in winning consumer acceptance of fuel-cell vehicles.

Hybrid-Electric Vehicles

Progress with hybrid electric technologies also has advanced in recent years. A hybrid contains both an electric engine and a gasoline (or diesel) engine. The use of two engines allows the hybrid to overcome the range limitations of battery-powered EVs while still providing for extremely low emissions and very high fuel economy. In modern hybrids, software controls the functioning of both engines by having each engine operate when it is most efficient. The electric engine would operate during periods of constant speed or when the vehicle is "idling"; the gasoline engine would operate during periods of acceleration or if the vehicle is traveling uphill.

Hybrid electric vehicles would be expected to qualify as near-ZEVs under CARB regulations. The range of the electric engine would be a critical factor in determining how many hybrids a manufacturer would have to market to meet CARB's ZEV requirement. Hybrids with longer electric ranges would be presumed to emit less than a hybrid with a shorter range. The gasoline engine also would have to meet SULEV standards.

Toyota's hybrid electric vehicle, the Prius, has been well received since its recent introduction in Japan. Toyota has plans to introduce a hybrid in the United States in 2000. Honda and other automakers also are developing hybrid electric vehicles.

Near-Zero Emission Internal-Combustion Engines

While the excitement over fuel cell and hybrid vehicles is justified, it would be premature to assume that conventional internal-combustion engine vehicles could not approach near-zero emission levels. Both Honda and Nissan have announced the development of gasoline-powered engines that could meet the SULEV standard. Nissan has announced it would seek CARB certification for its vehicle in late 1999 and begin marketing the vehicle in 2000. Honda is already marketing a natural gas vehicle with extremely low emissions. The ability of the auto industry to produce near-zero emission conventional vehicles at competitive costs would have a profound long-term impact on future clean-vehicle markets.

Heavy-Duty Vehicles

As stated earlier in this paper, the regulatory strategy for heavy-duty vehicles is not as clear as for light-duty vehicles. Heavy-duty vehicles have gotten significantly cleaner in the last decade, but more must be done to reduce emissions. One strategy already underway is to seek a national low-sulfur standard for diesel fuel, which would make possible the use of catalyst-like technologies to treat diesel exhaust. Another strategy underway is to create incentives for the use of natural gas and other alternative fuels, which are feasible for many heavy-duty fleets because of the use of central fueling facilities.

CARB was scheduled in October 1999 to consider new regulations for urban buses. At the time of this writing, CARB staff had not released a specific regulatory proposal.

Technology developers have shown interest in adapting advanced technologies for use in heavy-duty vehicles. As stated earlier, demonstration projects for fuel cell buses are already underway in Chicago and Vancouver, and a third demonstration will begin soon in California. Electric and hybrid technologies also show some promise in the heavy-duty sector. One California company has developed an electric-natural gas hybrid truck that shows considerable promise. Future CARB policies in the heavy-duty sector may embrace these advanced technologies.

IV. STATIONARY SOURCES

Stationary sources produce approximately 30 percent of ozone-forming emissions in California. Emission reductions over the years from these sources have contributed significantly to the state's improved air quality; further reductions from stationary sources are essential for California to meet its air-quality goals. Point sources (ranging from dry cleaners to power plants and oil refineries) are regulated by California's 35 local air pollution control districts. These local agencies establish regulations for businesses within their jurisdiction, and also set emission limits and other operating conditions for specific facilities and power plants.

One stationary-source technology with exciting potential is the use of fuel cells for power generation. While fuel-cell costs still need to come down, many observers believe they can become viable for a reasonably large group of applications. Fuel cells operate relatively cleanly and silently, they can use a variety of fuels, and they are generally unaffected by storms and other calamities. The most promising application for stationary fuel cells in the immediate future lies with smaller units, ranging from less than 50 kilowatts to several hundred kilowatts, that could supply power to individual homes or commercial buildings. A number of facilities in the United States receive their power from fuel cells; the most successful units have operated successfully for tens of thousands of hours. In contrast, larger experimental units exceeding one megawatt have had mixed results.

One family of stationary sources that falls directly under CARB's regulatory purview is consumer products. These products, which range from deodorant and hair spray to carpet cleaners, household pesticides, aerosol paints and automotive-care products, accounted for 15 percent of volatile organic compound emissions in California in 1990. As of this writing, CARB had enacted regulations for 46 categories. These

regulations typically place limits on the VOC content of specific products. Manufacturers have shown the ability to develop innovative water-based formulations that perform as well as traditional VOC-based formulations.

V. CONCLUSION

Urban air pollution results largely from the use of technology. People of the 20th century were more mobile and generated energy more efficiently than their ancestors, but the downside was the advent of modern air pollution. By the end of the century, government and the private sector had both invested considerably in the development of cleaner technologies that could provide the same services for society with less impact on air quality. Many of these cleaner technologies are now coming to fruition as we enter the 21st century. Undoubtedly, the path of further technological development will take some unexpected turns as the century progresses.

When the 1990s began, the battery-powered EV was, at best, a promising prototype. Most EVs were still made by hobbyists in garages. As 2000 begins, EVs are on the road, and hybrids, fuel cell vehicles and near-zero emission internal-combustion engines are not far behind. California gasoline and diesel pollute much less now than in 1990. These advances resulted in part from the ingenuity of engineers and entrepreneurs, and in part from the willingness of agencies like CARB to use the regulatory process to push those engineers and entrepreneurs to higher levels of creativity. As these technologies mature and enter the marketplace, air pollution will continue to subside, creating a healthier environment for all. The effort will have been well worthwhile.

Acknowledgment. The author wishes to acknowledge the assistance of Allan Hirsch of the California Air Resources Board staff in preparing this paper.

B. Forced Convection

A NOVEL FINITE DIFFERENCE METHOD FOR FLOW SIMULATION AND VISUALIZATION

Kunio Kuwahara
The Institute of Space and Astronautical Science
Yoshinodai, Sagamihara-shi, Kanagawa 229-8510, Japan
Email: kuwahara@pub.isas.ac.jp; Fax: 81-42-759-8231

Keywords: simulation, unsteady flow, transition, visualization, multi-directional scheme

ABSTRACT. Incompressible high-Reynolds-number flows are simulated by solving the Navier-Stokes equations. A finite-difference method with third-order upwinding are employed without using any turbulence model. Validity of this method is discussed. Also, a newly developed multi-directional formulation is applied for improved accuracy. Examples are presented to show the applicability of the present approach to variety of problems.

1. INTRODUCTION

Many of the high-Reynolds-number, turbulence simulations have been based on Reynolds-averaged Navier-Stokes equations using a turbulence model [1]. Some use a large-eddy simulation based on a Smagorinsky-type model. However, a usual turbulence model or a large-eddy simulation is not suitable for high-Reynolds-number-flow computation because, there, the effect of turbulence mixing is usually replaced by second-order diffusion. This diffusion is similar to viscous diffusion. It means that we are simply computing a locally low-Reynolds-number flow.

There are some real direct numerical simulation in which most of the small-scale structure are resolved, but the computations can be done only at relatively small Reynolds numbers. We can not use enough grid points for high-Reynolds-number flows of practical interest. We have rather to use a very coarse grid system. In many applications, large structures are most important and we usually are not interested much about in small structures. What we want to do is to capture the large-scale structure using a coarse grid system. On the other hand, quit a few simulations [2], show that large structures of high-Reynolds-number, turbulent flow can be captured using relatively coarse grid, if the numerical instability, usually unavoidable for high-Reynolds-number-flow simulation, is suppressed. Most successful simulations in these approaches are based on the third-order upwind formulation [3]. An approach similar in philosophy but different in method is adopted by Boris et. al. [4].

In the present paper, we summarize the third-order upwind scheme for high-Reynolds-number-flow computations. To increase the accuracy, we have developed a new finite-difference scheme named as multi-directional finite-difference method. All the results in the present paper is based on this new scheme. The following five examples are presented in this paper to show the applicability of the approach:

(1) Two-dimensional flow around a circular cylinder at the Reynolds numbers 50000 and 1000000.
(2) Two-dimensional flow around NACA0012 and an arcairfoil at Reynolds number 100000.
(3) Three-dimensional transition to turbulence in the wake of a bluff body
(4) Thermal convection at high Rayleigh numbers
(5) Free surface problems

2. COMPUTATIONAL METHOD

The governing equations are the unsteady Navier-Stokes equations and the equation of continuity as follows:

$$\frac{1}{\rho}\left\{\frac{\partial \rho}{\partial t}+u_j\frac{\partial \rho}{\partial x_j}\right\}=-\frac{\partial u_j}{\partial x_j} \tag{1}$$

$$\frac{\partial u_i}{\partial t}+u_j\frac{\partial u_i}{\partial x_j}=-\frac{1}{\rho}\frac{\partial p}{\partial x_i}+\frac{1}{\rho}\frac{\partial}{\partial x_j}\left\{\mu\left(\frac{\partial u_i}{\partial x_j}+\frac{\partial u_j}{\partial x_i}\right)\right\}+K_i \quad (i=1,2,3) \tag{2}$$

$$\frac{\partial C_v T}{\partial t}+u_j\frac{\partial C_v T}{\partial x_j}=\frac{1}{\rho}\frac{\partial}{\partial x_j}\left(\kappa\frac{\partial T}{\partial x_j}\right)-\frac{1}{\rho}p\frac{\partial u_j}{\partial x_j} \tag{3}$$

where $\boldsymbol{K}=(K_1,K_2,K_3)$ is the external force.

We simplify the equations under the condition that the pressure difference is small, that means we do not treat a shock wave.

The equation of state of perfect gas is

$$\rho=\frac{p}{RT}.$$

The change of the density can be expressed by that of the temperature, because the pressure is nearly constant.

$$\rho=\frac{1}{\alpha T} \quad \left(\alpha=\frac{R}{p_m}\right)$$

Therefore, the LHS of Eq.(1) becomes

$$\frac{1}{\rho}\frac{D\rho}{Dt}=-\frac{1}{T}\frac{DT}{Dt}. \tag{4}$$

Then,

$$\frac{\partial u_j}{\partial x_j}=\frac{1}{T}\frac{DT}{Dt}. \tag{5}$$

Putting Eq.(5) into Eq.(3), we obtain

$$C_p\frac{DT}{Dt}=\alpha T\frac{\partial}{\partial x_j}\left(\kappa\frac{\partial T}{\partial x_j}\right) \quad (C_p=C_v+R). \tag{6}$$

From Eq.(5) and Eq.(6), Eq.(1) is

$$\frac{\partial u_j}{\partial x_j}=\frac{\alpha}{C_p}\frac{\partial}{\partial x_j}\left(\kappa\frac{\partial T}{\partial x_j}\right). \tag{7}$$

We can get the basic equations as follows:

$$\frac{\partial u_j}{\partial x_j}=\frac{\alpha}{C_p}\frac{\partial}{\partial x_j}\left(\kappa\frac{\partial T}{\partial x_j}\right) \tag{8}$$

$$\frac{\partial u_i}{\partial t}+u_j\frac{\partial u_i}{\partial x_j}=-\alpha T\frac{\partial p}{\partial x_i}+\alpha T\frac{\partial}{\partial x_j}\left\{\mu\left(\frac{\partial u_i}{\partial x_j}+\frac{\partial u_j}{\partial x_i}\right)\right\}+K_i \ (i=1,2,3) \tag{9}$$

$$\frac{\partial T}{\partial t}+u_j\frac{\partial T}{\partial x_j}=\frac{\alpha T}{C_p}\frac{\partial}{\partial x_j}\left(\kappa\frac{\partial T}{\partial x_j}\right) \tag{10}$$

where $\boldsymbol{K}=(0,0,\alpha g\Delta T)$ is the gravitational force.

The numerical procedure is based on the projection method [5,6]. Thus, the pressure field is obtained by solving the Poisson equation. The equation for the pressure is as follows;

$$\frac{\partial}{\partial x_j}\left(\alpha T \frac{\partial p}{\partial x_j}\right) = \frac{\partial}{\partial x_k}\left[-u_j \frac{\partial u_k}{\partial x_j} + \alpha T \frac{\partial}{\partial x_j}\left\{\mu\left(\frac{\partial u_k}{\partial x_j} + \frac{\partial u_j}{\partial x_k}\right)\right\} + K_k\right] + \frac{1}{\Delta t}\left\{\frac{\partial}{\partial x_k} u_k - \frac{\alpha}{C_p}\frac{\partial}{\partial x_j}\left(\kappa \frac{\partial T}{\partial x_j}\right)^{n+1}\right\}. \quad (11)$$

For high-Reynolds-number flows, time-dependent computations are required owing to the strong unsteadiness. These equations are solved by a finite-difference method. To stabilize the computation, a third-order upwind scheme has been found to be most suitable for high-Reynolds-number-flow computation.

The accuracy decreases when the flow direction is not well parallel to one of the coordinate lines. This introduces a serious error especially on the boundary of the two fluids. To overcome this problem we introduced the multi-directional upwind method. For all the spatial derivatives, the multi-directional finite-difference method is used.

In cases 1, 2, a boundary fitted computational mesh is employed, so that enough grid points can be concentrated near the body surface where the no-slip condition is imposed.

All the spatial derivative terms are represented by the central difference approximation except for the convection terms. For the convection terms, the third-order upwind difference is used. This is the most important point for high-Reynolds-number computations and the detail is given below.

Strong numerical instability caused by the aliasing error occurs at high Reynolds numbers, owing to the non-linear convection terms, if enough grid points are not used to resolve the small-scale structures. When digitizing a continuous function into a finite number of the values, it is very important to filter out the high-frequency part of the original function which can not be resolved by the digital system. If not, aliasing error makes the approximation meaningless. Usually a turbulence model or a large eddy simulation is used to get rid of this instability. The diffusion coefficients increased by the added turbulent viscosity reduce the aliasing error and suppress the numerical instability. In most of the models ,this diffusion has the same form as the viscous diffusion and the diffusion coefficient is usually much larger than that of the viscous diffusion. Therefore, the effect of physical diffusion is concealed, resulting no dependency of the flow on the Reynolds number is captured.

Another way to stabilize the computation is to use an upwind scheme. The first-order upwind scheme is widely used because of the very good stability but the leading numerical error caused by this upwinding is second order and similar to the physical diffusion. This should be avoided because of the same reason just mentioned above. The second-order upwind scheme has a dispersion type leading error, which makes the computation unstable generally. For the discretization of the non-linear convection terms, the order of accuracy is odd or even has special importance for stable computation. In case of even order of accuracy, the leading numerical-error term is the odd-order derivative which is dispersive. Once some error is created, the error never diffuses but moves around in the computational domain until the computation blows up. Eventually no stable solution can be obtained in this case. On the other hand, in case of odd order of accuracy, the leading error term is the even-order derivative which is diffusive. This makes the computation very stable by reducing the aliasing error well. A third-order upwind scheme has been found to be most suitable for high-Reynolds-number-flow computation. The leading numerical error terms are the fourth-order derivative terms, where the effects of the second-order numerical diffusions are carefully removed. The numerical diffusion of forth-order derivatives is of short range and does not conceal the effect of molecular diffusion but well stabilizes the computation.

One simple explanation why the fourth-order diffusion does not conceal the effect of second-order diffusion is as follows. A finite-difference representation of the fourth-order diffusion term is as follows:

$$(u_{i+2} - 4u_{i+1} + 6u_i - 4u_{i-1} + u_{i-2})/\delta x^4 \quad (12)$$

This can be written as,

$$4\delta x^{-2}\left(\frac{u_{i+2}-2u_i+u_{i-2}}{(2\delta x)^2}-\frac{u_{i+1}-2u_i+u_{i-1}}{\delta x^2}\right). \tag{13}$$

The two terms in Eq.(13) represent the second-order diffusion and their effects are canceled each other except near the point i. This means fourth-order diffusion is very independent from second-order diffusion. In general, the effects of lower-order diffusion are not concealed by higher-order diffusion. Similarly, fifth-order upwinding is possible and some computations have been done but it requires seven points in each direction to approximate the local derivative. This means to require a wider range of analyticity to the solution of the equations. High-Reynolds-number flows are not so analytical, therefore it is not necessarily better than third-order unwinding.

There are several third-order upwind schemes. We use the following scheme. Initially, the one-sided second-order finite difference approximation is employed for the convection terms.

$$u\frac{\partial u}{\partial x}=\begin{cases} u_i\left(\frac{3u_i-4u_{i-1}+u_{i-2}}{2\delta x}\right) & (u_i>0) \quad (14)\\ u_i\left(\frac{-u_{i+2}+4u_{i+1}-3u_i}{2\delta x}\right) & (u_i<0) \quad (15)\end{cases}$$

We can rewrite the above equations to a symmetrical form by using the formula:

$$\frac{u_i+|u_i|}{2}=\begin{cases} u_i & u_i>0\\ 0 & u_i<0\end{cases}, \qquad \frac{u_i-|u_i|}{2}=\begin{cases} 0 & u_i>0\\ u_i & u_i<0\end{cases}$$

Then, Eq.(14) and (15) can be written

$$u\frac{\partial u}{\partial x}=\frac{u_i+|u_i|}{2}\left(\frac{3u_i-4u_{i-1}+u_{i-2}}{2\delta x}\right)+\frac{u_i-|u_i|}{2}\left(\frac{-u_{i+2}+4u_{i+1}-3u_i}{2\delta x}\right).$$

Finally, we get

$$u\frac{\partial u}{\partial x}=u_i(-u_{i+2}+4(u_{i+1}-u_{i-1})+u_{i-2})/4\delta x+|u_i|(u_{i+2}-4u_{i+1}+6u_i-4u_{i-1}+u_{i-2})/4\delta x. \tag{16}$$

If the first term of Eq.(14) is developed into Taylor series, it becomes

$$u\frac{\partial u}{\partial x}-\frac{1}{3}\delta x^2 u\frac{\partial^3 u}{\partial x^3}+O(\delta x^4). \tag{17}$$

Similarly the second term becomes

$$\delta x^3 u\frac{\partial^4 u}{\partial x^4}+O(\delta x^5). \tag{18}$$

Therefore, the leading error of Eq.(14) is order δx^3 and its coefficient includes third-order derivative. As mentioned above, odd order-derivative is not desirable, but this error term is eliminated if the second term of Eq.(18) is replaced by

$$|u_i|(-u_{i+2}+8(u_{i+1}-u_{i-1})+u_{i-2})/12\delta x. \tag{19}$$

As a result, the present third-order upwind scheme is represented by five grid points as follows:

$$u\frac{\partial u}{\partial x}=u_i(-u_{i+2}+8(u_{i+1}-u_{i-1})+u_{i-2})/12\delta x+|u_i|(u_{i+2}-4u_{i+1}+6u_i-4u_{i-1}+u_{i-2})/4\delta x \tag{20}$$

There is another version of third order upwind schemes for example as follows:

$$u\frac{\partial u}{\partial x}=u_i(-u_{i+2}+8(u_{i+1}-u_{i-1})+u_{i-2})/12\delta x+\alpha|u_i|(u_{i+2}-4u_{i+1}+6u_i-4u_{i-1}+u_{i-2})/4\delta x \tag{21}$$

where $\alpha=1/3$ is called UTOPIA scheme by Leonard [7]. We compared these schemes and as well as QUICK scheme [7] by comparing the energy spectrum in one-dimensional Burgers turbulence and found the above Kawamura-Kuwahara scheme is the best (Fig.1). When we use a very fine grid as 4096 points, the three schemes agree completely with each other and theoretical prediction. However,

with reducing the number of grid points, the difference become clear. Only the present method give the good agreement with the result of very fine computations. For the theoretical validation based on the digital-filter theory has been given by Hashiguchi [8].

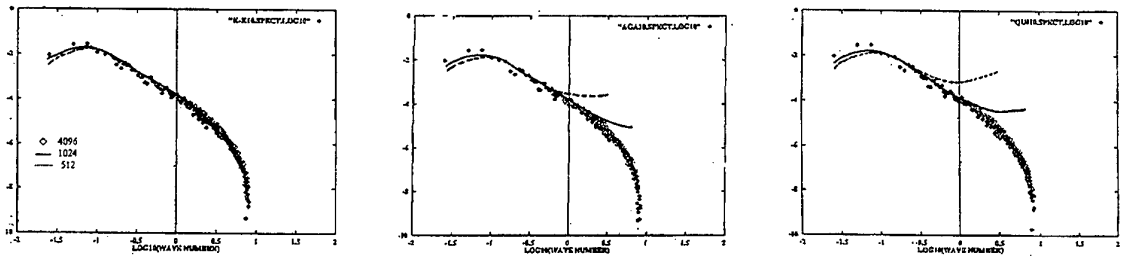

(a) The present scheme (Kawamura-Kuwahara) (b) UTOPIA (c) QUICK

Fig.1. Energy spectrum for Burgers turbulence

There is another important problem in high-order upwind schemes. That is, the accuracy decreases when the flow direction is not well parallel to one of the coordinate lines. If we use generalized coordinate system, near the boundary, the flow direction and one of the coordinate lines are almost parallel, and this problem is not serious. However, in general, flow direction is not always parallel to a coordinate line and the problem become very important.

To overcome this problem we introduced the multi-directional upwind method. This method is summarized as follows;

When structured grid points are given, the black points in Fig.1(a) are usually used to approximate the derivatives at the central point (system A). If we introduce the other 45 degrees-rotated local grid points, the white ones in Fig.1(b), which can be used to approximate the derivatives at the central point (system B). In order to improve the derivative value at the central point, we mix the derivative values calculated from both systems (A and B) at a proper ratio. We adopt the ratio A : B = 2/3 : 1/3. Using this ratio, for example, resulting finite-difference scheme for the Laplacian coincides with the well-known 9-points formula with forth-order accuracy. This method improves the rotational invariance of the coordinate system. Then those flows where flow direction is not parallel to the grid direction are better simulated.

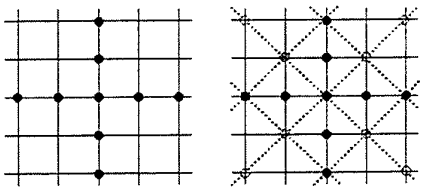

(a) system A (b) system B

Fig.2. Grid for multi-directional scheme

For all the spatial derivatives, the multi-directional finite-difference method is used. This method has another advantage. In MAC method, usually a staggered mesh is used to remove the unphysical oscillation of the pressure. This oscillations is caused by the decoupling of the computed values within the nearest two points. These values couples more tightly with the second nearest points. This decoupling become less if we use third-order upwind scheme because of the five-point differencing, but there remains some. However, if we use multi-directional finite-difference method, every point becomes tightly coupled and the oscillation disappears. Therefore, a non-staggered mesh system is employed where the defined positions of velocity and pressure are coincident.

For the temporal integration of the Navier-Stokes equations, the Crank-Nicolson implicit scheme is utilized. This scheme has second-order accuracy in time. These equations and the Poisson equation are iteratively solved at each time step by the successive overrelaxation (SOR) coupled with a multigrid method.

3. COMPUTATIONAL RESULTS

3.1. CIRCULAR CYLINDER

The dependence of the drag coefficients on Reynolds numbers is shown in Fig.3. The number of grid points are 32*16, 64*32, 128*64. If the Reynolds number is less than 100, all the computations and experiments agree very well. At high Reynolds numbers even 64*32 computation can capture the drag crisis qualitatively. The 128*64 computations agrees much better with the experiments as expected. The drag sharply decreases at about Reynolds number 400000, which is called drag crisis, is well captured even using this coarse grid. Instantaneous and time-averaged flow patterns clearly show the difference as shown in Fig.4. After drag crisis, flow separation delays and the wake becomes narrower, which makes the drag less.

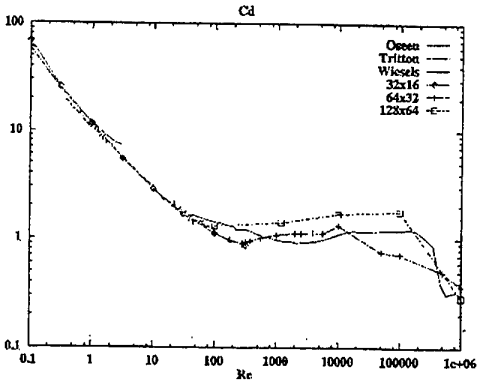

Fig.3. Drag coefficients of circular cylinder

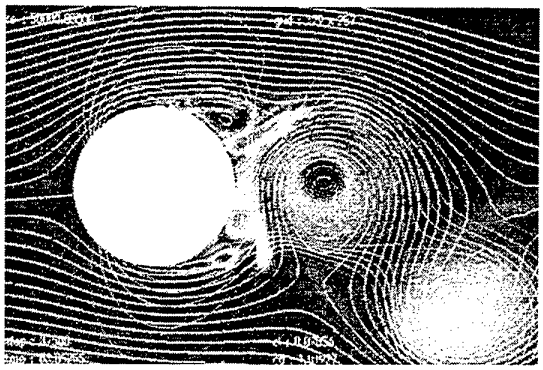

(a) Re=50000, before drag crisis

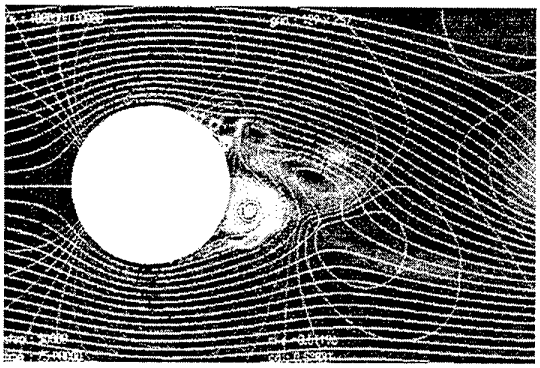

(b) Re=1000000, after drag crisis

Fig.4. Flow past a circular cylinder, streamlines and pressure contours, background color shading shows, the vorticity distribution. Instantaneous flow field, 128*256 grid system

3.2. FLOW AROUND AN AIRFOIL

Flow around an airfoil is a standard problem, but unsteady computations have rarely been done. At high angle of attack, the flow becomes very unsteady and to understand the flow well we need an unsteady simulation. For airfoil simulation, C-grid is usually used to avoid the trailing edge singularity. To make C-grid is not easy for very high angle of attack, and this is another reason of the difficulty to simulate the flow at very high angle of attack. Also C-grid needs unnecessarily concentrated grid points in the near wake region beginning from the trailing edge. This make the computation more unstable.

On the other hand O-grid is, in every sense, much better if the computation converges. The multi-directional finite-difference method makes the computation very stable even near the singular points.

Computed lift coefficients agree well with experiments.

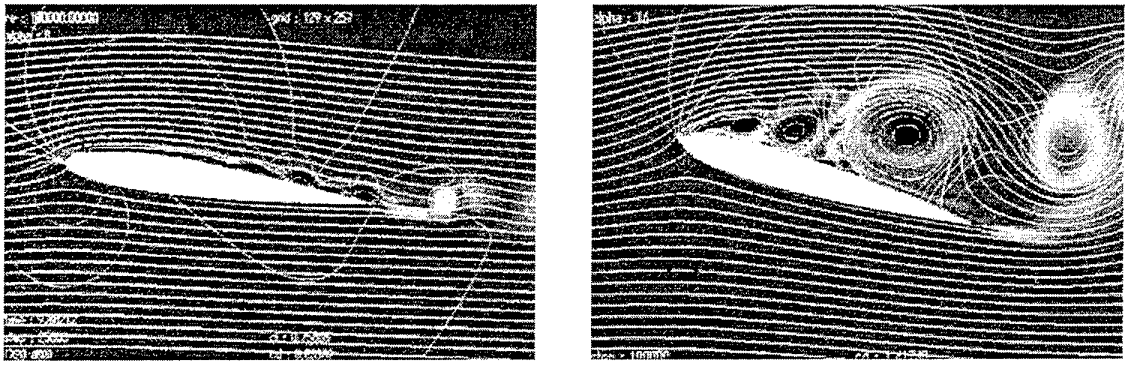

(a) Angle of attack 8 degrees (b) Angle of attack 16 degrees

Fig.5. Flow around NACA0012 airfoil at Re=100000, 128*256 O-grid system, instantaneous streamlines and pressure contours, background color shading shows the vorticity distribution.

If the O-grid computation around a airfoil is possible it is easy to compute a flow around a circular arc airfoil which has a singularity at the leading edge also (Fig.6). Even we can compute a flow around an arcairfoil of negative thickness (Fig.6(b)) All the computations around a two dimensional body were done here by using O-grid.

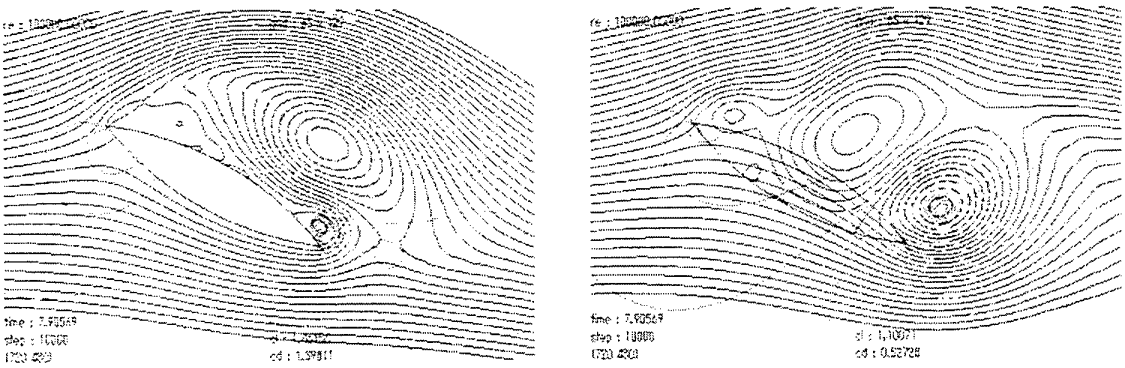

(a) Positive thickness (b) Negative thickness

Fig.6. Flow around a circular arc-airfoil at Re=100000, 128*64 O-grid system, angle of attack 30 degrees, instantaneous streamlines and pressure contours

3.3. TRANSITION IN BLUFF BODY WAKE

It is impossible to compute transitional flow by using turbulence model. Even large-eddy simulation can not handle this type of problem, because it assumes the flow is turbulent from the beginning. However, transition phenomena is very important at high-Reynolds number flow. In the present approach, this is not a special thing, we can compute any transitional flow without any special consideration. In Fig.7, development of turbulence behind a sphere is shown; the sphere has impulsively started from rest. Fig.8 show a flow around a ski jumper. This is a more streamlined body than the sphere. The turbulent area is much less. Fig.9 shows a flow around a protoceratopus. This is as bluff as a sphere, then the wake turbulence is very similar to the sphere. The visualization was done by showing the surface pressure of the body and the volume rendering of absolute value of the vorticity.

The number of the grid point is 288*144*144=5,971,968 in the case of sphere and 256*128*128=4,194,304 in the case of protoceratopus. These numbers are not enough to see the smallest structures but look to be good enough to see the large structure in the transitional stage. In this computation, only cartesian

grid with equal grid spacing is used. Body fitting type grid system is not only difficult to make but uniformity of the grid is not possible. To see the behavior of the transition to turbulence, this uniformity is crucial.

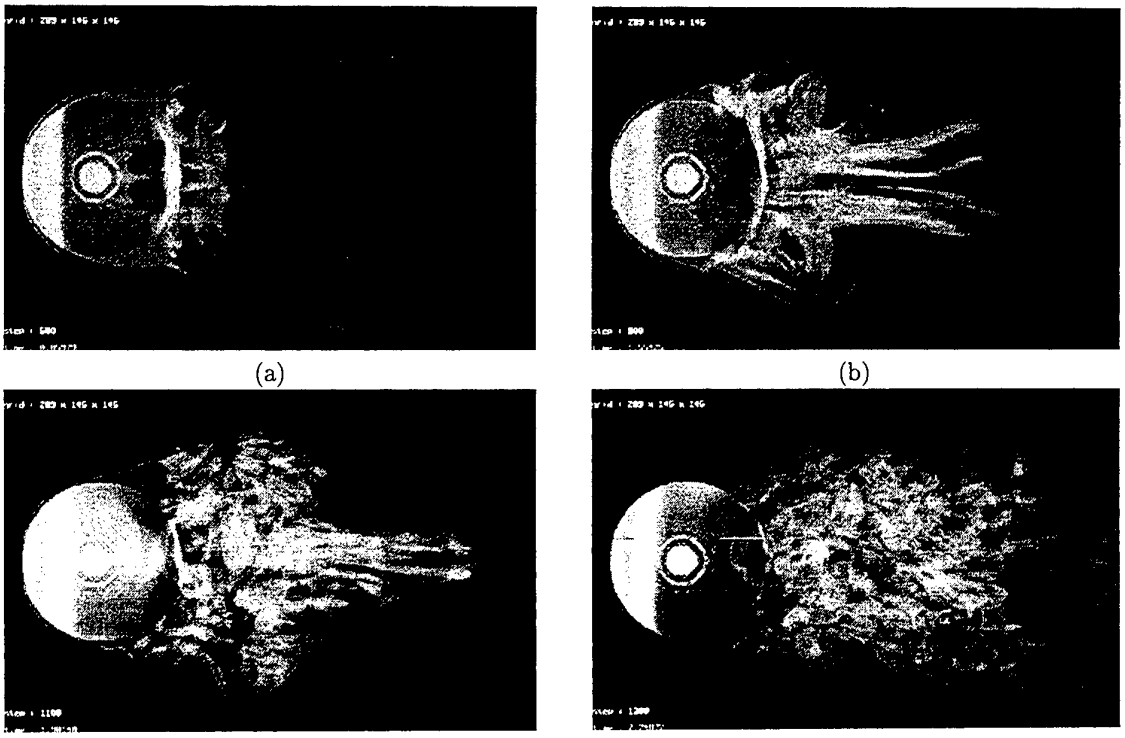

(a) (b)

(c) (d)

Fig.7. Development of turbulence behind a sphere at Re=20000, 288*144*144 grid system

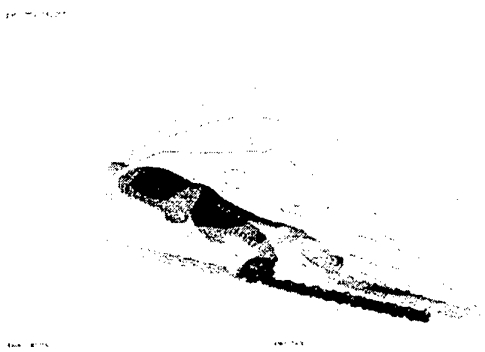

Fig.8. Flow around a ski jumper at Re=200000, 288*144*144 grid system

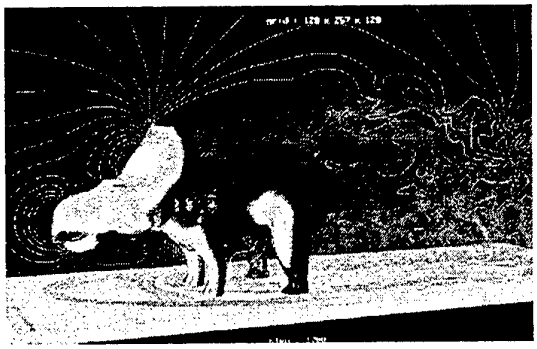

Fig.9. Flow around a protoceratopus at Re=100000, 256*128*128 grid system

3.4. THERMAL CONVECTION

Using this approach, we have obtained numerical solution for thermal convection at high Rayleigh number. Fig. 10 shows the convection patterns and the isotherms.

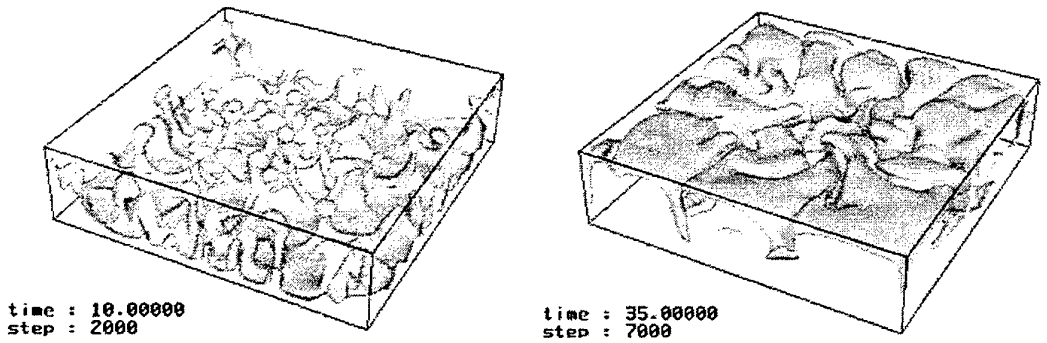

Fig.10. Thermal convection at Rayleigh number=$1.08*10^6$, equi-temperature surface [10]

3.5. FREE SURFACE

We shall now apply the method to solve problems involving free surfaces. To keep the sharpness of the boundary of immiscible fluids, we impose a negative diffusion as follows:

$$T := T_{high} + \varepsilon \cdot (T_{high} - T) \cdot |T_{high} - T|/T_c, \qquad \text{if } T > T_c$$

$$T := T_{low} + \varepsilon \cdot (T_{low} - T) \cdot |T_{low} - T|/T_c, \qquad \text{if } T < T_c$$

where $T_c = (T_{high} + T_{low})/2.0$ and ε is a small number of order of non-dimensional time increment. T_c can be a little modified so that the mass conservation be kept.

In low gravity condition, the surface tension becomes a dominant force. The surface tension is treated as follows;

$$\boldsymbol{K} = \sigma \cdot \tau \cdot \boldsymbol{n}$$

σ is corefficient of surface tension. τ is curvature of the free surface. $\boldsymbol{n}$ is the unit normal vector of the surface.

$$\tau = \mathrm{div}\boldsymbol{n}$$

$$\boldsymbol{n} = \frac{\mathrm{grad}T}{|\mathrm{grad}T|}$$

This formulation is very general and need not to track the free surface. Therefore, this method can be used with Cartesian coordinates system and we have applied to the following four problems:

1. Formation of a bubble under zero gravity
2. Motion of a bubble
3. 2D falling drop from a ceiling
4. 3D deformation of a liquid drop by surface tension in zero gravity

Under micro gravity condition, because of the surface tension, liquid climbs up along the wall and forms a circular bubble. In the present formulation, the wet wall is substituted by the low temperature wall. Fig. 11 (a) shows the initial condition of the present 2D simulation. The liquid stays in the lower part of the box. After the bubble is formed it continues to oscillate. Figure 12 shows a motions of a

3D bubble. An initially spherical bubble is going up. It deforms and oscillates and finally it attaches to the ceiling. In the next example, the liquid initially attached on the ceiling drops because of the gravity (Fig. 13). At first, it forms a bell shape and then most of part of the liqid began to fall and it is divided into two parts, namely a falling drop and the remaining liquid on the ceiling. A cubic liquid drop becomes to a spherical drop by surface tension under micro gravity condition (Fig. 14). Surface tension is stronger around the corners. Then initially sharp corners become rounded; this movement overshoots and the drop oscillates but finnally it becomes a sphere because of the viscous damping.

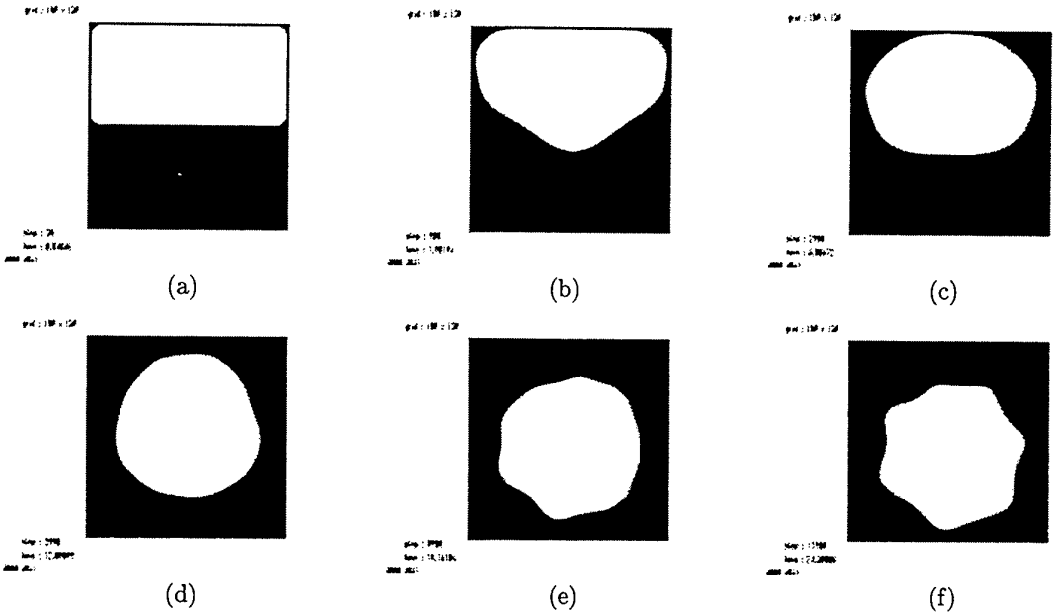

Fig.11. Formation of a bubble under zero gravity

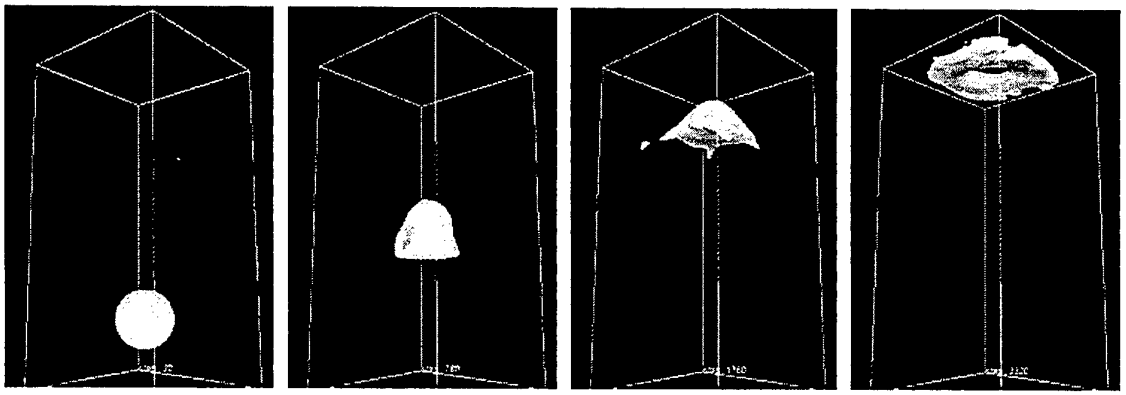

Fig.12. Motion of a bubble

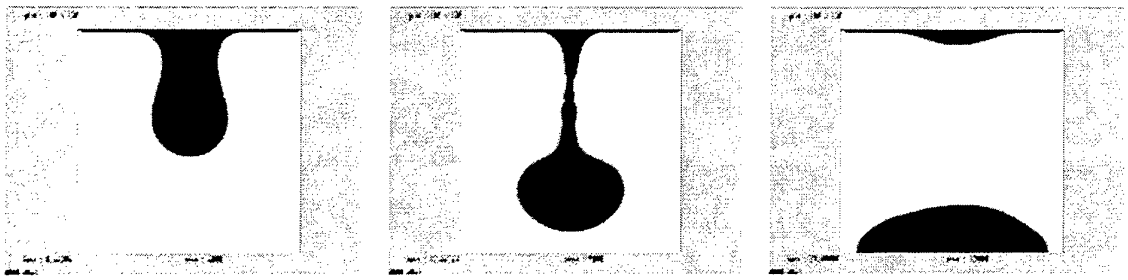

(a) (b) (c)

Fig.13. 2D falling drop from a ceiling

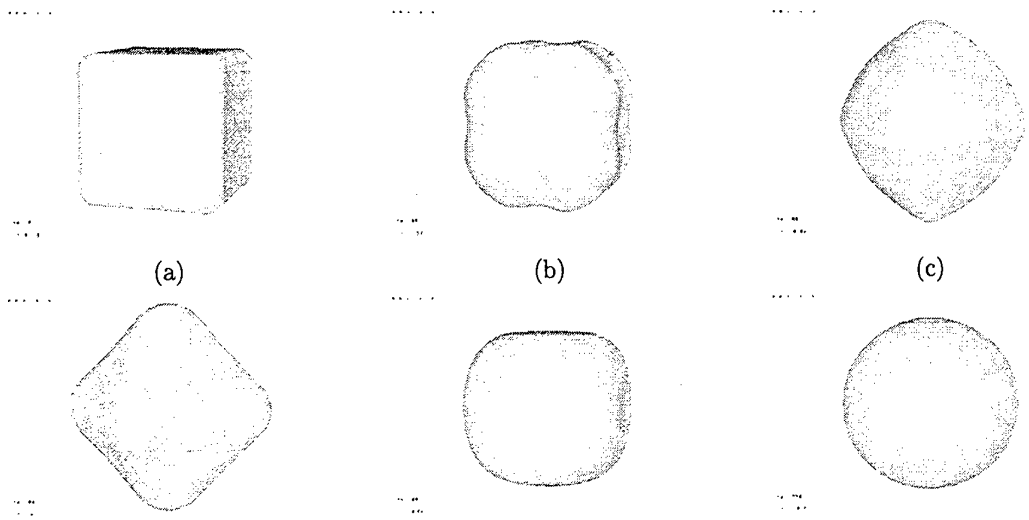

(a) (b) (c)

(d) (e) (f)

Fig.14. 3D deformation of liquid drop by surface tension in zero gravity

4. VISUALIZATION

The amount of computed data is becoming bigger and bigger and without visualization system understanding of underlying flow mechanism is very difficult. What is needed is a means of properly visualizing the computed flow field. The key points are real-time visualization and animation. A flow simulation takes a large amount of CPU time, therefore it is desirable to visualize it while computing it. This saves a lot of time especially while debugging. This should be called real-time visualization. Moreover, still pictures are insufficient when the flow becomes essentially unsteady as those at high Reynolds numbers, since it is impossible to understand the transient flow in total only from a set of instantaneous flow pictures. Visualization by animated graphics is a necessity in this case. Only by using such a system it becomes possible to observe the essentially unsteady flow field and to understand the fundamental flow mechanism underlying it. The visualization software used here is Clef2D and Clef3Dvr developed by Institute of Computation Fluid Dynamics, which satisfies the above requirements [9].

5. CONCLUSIONS

It is becoming clear that we need not resolve the small-scale structure of high-Reynolds-number flow to capture the large structure, which is most important for application. We should not use standard models to simulate any high-Reynolds-number, turbulent flows. Only without using turbulence models we are able to capture the dependence of the flow on the Reynolds number. To avoid the numerical instability we can simply use a third-order upwind difference. Multi-directional finite-difference makes the dependence of the solution on the flow direction less and the computation more reliable.

REFERENCES

1) J.W. Deardorff, 1970, "A Numerical Study of Three-Dimensional Turbulent Channel Flow at Large Reynolds Numbers," J. of Fluid Mechanics, Vol. 41, Part 2, pp. 453-480

2) K. Kuwahara, 1992, "Flow Simulation on Supercomputers and Its Visualization," International Journal of High Speed Computing, Vol.4, No.1, pp. 49-70.

3) T. Kawamura, and K. Kuwahara, 1984, "Computation of high Reynolds number flow around a circular cylinder with surface roughness," AIAA Paper 84-0340.

4) J.P. Boris, F.F. Grinstein, E.S. Oran, and R.L. Kolbe, 1992, "New insights into large eddy simulation," Fluid Dynamics Research 10, pp. 199-228

5) H. Takami, and K. Kuwahara, 1974, "Numerical Study of Three-Dimensional Flow within a Cubic Cavity," J. Phys. Soc. Japan, Vol. 37, No. 6

6) K. Kuwahara, 1984, "Computation of Thermal Convection with a Large Temperature Difference," Proc. International Conf. on Applied Numerical Modeling, Taiwan, R.O.C.

7) B.P. Leonard, 1979, "A Stable and Accurate Convective Modeling Procedure Based on Quadratic Upstream Interpolation," Computer Methods in Applied Mechanics and Engineering, Vol. 19, pp. 59-89

8) M. Hashiguchi, 1996, "Turbulence simulation in the Japanese automotive industry," Engineering Turbulence Modeling and Experiments 3, pp. 291-308.

9) K. Kuzuu, and H. Kaizaki, and K. Kuwahara, 1997, "Real Time Visualization of Flow Fields Using Open GL System," AIAA Paper 97-0235.

10) T. Tsuchiya, and K. Kuwahara, 1997 "Three-Dimensional Computation of Natural Convection in an Enclosure at High Rayleigh Numbers," AIAA Paper 97-0436.

NUMERICAL STUDY ON THREE-DIMENSIONAL FLOW AND HEAT TRANSFER CHARACTERISTICS OF TURBULENT FLOWS OVER A BACKWARD-FACING STEP IN A RECTANGULAR DUCT

Hiroshi Iwai, Eng Chong Neo and Kenjiro Suzuki
Department of Mechanical Engineering
Kyoto University, Kyoto 606-8501, Japan
Email: iwai@htrans.mech.kyoto-u.ac.jp

Keywords: backstep flow, non-linear eddy viscosity model, aspect ratio, 3-D simulation, heat transfer

ABSTRACT. Two- and three-dimensional numerical simulations were carried out for turbulent flows over a backward-facing step in a rectangular duct and related heat transfer employing a non-linear eddy viscosity model proposed by the UMIST group(Craft, Launder and Suga). Reynolds number and the expansion ratio were kept constant at Re=5,200 and ER=2, respectively. The wall downstream of the step was heated at a constant heat flux and the other walls were treated to be adiabatic. The computations were carried out for two different aspect ratios in the 3-D simulations. The objectives of the present study include the comparison of 2-D and 3-D computational results. Examination is also made for the effects of the duct sidewalls on the flow and thermal fields. It is found that the statistical quantities calculated in the centerplane in the case of AR=12 agree satisfactory with the results obtained by 2-D simulations. Two-dimensional region however is not observed around the duct center region in the case of AR=4. Calculated results also indicate significant differences of characteristic values on the heated wall in the spanwise direction. Transverse counter rotating eddies are observed in the relatively low velocity region right after the step, resulting the highly three-dimensional flow and thermal fields in the recirculation region. This three-dimensionality is more prominent for the smaller aspect ratio(AR=4).

1. INTRODUCTION

In many flows of practical interests, flow separation and reattachment to a solid surface is unavoidable. The flow past a backward-facing step is one of the simplest geometries to produce separation and reattachment of flows. Thus, the fundamental characteristics of such flow have been investigated experimentally and numerically by many researchers. From experimental observations, de Brederode and Bradshaw [1] showed that the flow was primarily two-dimensional away from the sidewalls for an aspect ratio greater than 10. Recently, Papadopoulos and Ötügen [2] gave a relatively comprehensive picture of an interesting three-dimensional flow structure in a suddenly expanding rectangular duct. However, almost all numerical computation of the flow over a backward facing step reported so far assumed that the flow was two-dimensional. As for the turbulence model, the $k-\varepsilon$ model is still widely used because of its numerical stability and smaller demands on computer resources. Recently, the UMIST group (Craft, Launder and Suga) proposed a non-linear eddy viscosity model (CLS model)[3] in which strain and vorticity tensors to the cubic level are retained. Comparisons over a range of complex shear flows have shown that this model performs consistently better than a linear eddy-viscosity scheme.
The authors have previously carried out two- and three-dimensional numerical simulations for the flows over a backward-facing step at low Reynolds numbers, and reported the effects of the aspect ratio [5], the buoyancy level [6] and the duct inclination angle [7] on the flow and thermal fields. In the present study, two- and three-dimensional numerical simulations were carried out for turbulent flows over a backward-facing step and related heat transfer employing above mentioned CLS model. The computations were carried out for two different aspect ratios(AR=4 and 12). The objectives of the present study include the comparison of 2-D and 3-D computational results. Examination will also be made for the sidewall effects on the flow and thermal fields.

2. NUMERICAL METHOD

Figure schematically illustrates the computational domain presently adopted for three-dimensional computations. Two-dimensional computations were carried out in a plane where z/WD=0.0. The computational domain was set to cover $-5 \leq x/S \leq 30$ in the streamwise direction, where S is the step height. The governing equations are the time-averaged continuity equation, the Navier-Stokes equations and the energy equation. The Reynolds stresses were modeled using a non-linear eddy viscosity model recently proposed by the UMIST group (Craft, Launder and Suga) [3,4], hereafter referred as CLS model,

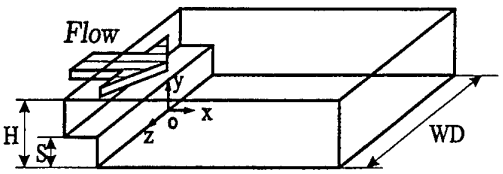

Figure 1: Computational domain

in which strain and vorticity tensors to the cubic level were retained. The turbulent heat flux was assumed to be proportional to the temperature gradient. The finite-volume method was used to discretise the governing equations, employing the 5th-order upwind scheme for the convective terms, the 4th-order central difference scheme for the diffusion terms in the U, V, W equations. As for the k, ε, h equations, the 1st-order upwind scheme and the central difference scheme were adopted for the convective terms and the diffusion terms respectively. The fully implicit scheme was adopted for the unsteady terms, and computations were performed using the SIMPLE algorithm. A total grid number of $100 \times 40 \times 45$ was allocated non-uniformly in the computational domain. The first grid point from the bottom wall was located at $y^+ \simeq 3.5$. The computational conditions were set to be as close to the experiment of Papadopoulos and Ötügen [2], i.e., expansion ratio, ER=$H/(H-S)$=2 and boundary layer thickness at the upstream boundary (x/S=-5), $\delta/S \simeq 0.16$. The Reynolds number based on the freestream mean velocity, U_{ref} and the step height, S was set at Re=5,200, five times smaller than the experimental value of 26,500 to reduce computing costs. All variables except for temperature were set equal to zero at all wall surfaces. The wall downstream of the step was assumed to be heated at a uniform heat flux, while all other walls were treated thermally adiabatic. Streamwise gradients of all quantities at the duct exit were set to be zero. 3-D computations were carried out for two different values of the aspect ratio,AR(= WD/S)= 4 and 12. It should be noted here that all 3-D computation results to be presented are time mean values averaged over an arbitrary long period of time.

3. RESULTS AND DISCUSSIONS

Comparison between 2-D and 3-D Results

Figure compares mean velocity, velocity fluctuation intensities and Reynolds shear stress obtained from 2-D computation and the centerplane counterparts of 3-D computation(AR=12) at various streamwise locations. U_{ref} refers to the inlet freestream mean velocity, while X^* is the normalized streamwise distance defined as $(x - x_r)/x_r$. x_r here is the mean reattachment length along the duct centerline on the bottom wall. Negative values of X^* indicate the locations to be within the recirculation region while its positive values represent positions downstream the recirculation region. The experimental results of Papadopoulos and Ötügen [2] for the case of AR=12 are also included in this figure for comparison. According to the experimental finding by de Brederode and Bradshaw [1] that the flow is primarily two-dimensional away from the sidewalls for an aspect ratio greater than 10, results of 2-D and 3-D computations in Fig. are expected to match each other. Present 2-D and 3-D computations predicted exactly the same mean reattachment length,x_r/S=9.5, which is approximately 15% larger than the value of x_r/S obtained by Papadopoulos and Ötügen. It can be observed in this figure that the distribution patterns at each streamwise location obtained from 2-D simulation agree quite well with those obtained in the centerplane in 3-D simulation. Especially the mean streamwise velocity profiles obtained by 2-D and 3-D simulations are almost identical to each other at all streamwise locations. Only slight differences can be seen between 2-D and 3-D results both on the velocity fluctuation intensities,u', v' and the Reynolds shear stress,$\overline{uv}$ inside the recirculation region, which may suggest innegligible three-dimensionality of flow structure in this region. The values of u', v' predicted in 2-D computation, for instance, take higher values than that of 3-D computation within the recirculation region($0.0 < y/S < 1.0, X^* < 0$). Quantitative agreements with the experimental counterparts cannot be obtained except for the mean streamwise velocity profile. This is probably due to the difference in the Reynolds number between the experiment(Re=26,500) and the present computations(Re=5,200). It is confirmed that the results obtained from 2-D and 3-D simulations agree satisfactory with each other if the aspect ratio in 3-D simulation is large enough (AR=12), suggesting that the effects of three-dimensionality are minor in the central region of the duct at AR=12, except for the recirculation region.

Effect of Aspect Ratio on Characteristic Values in the Centerplane

In experimental studies, various characteristic quantities of the fluid flow are often measured in the

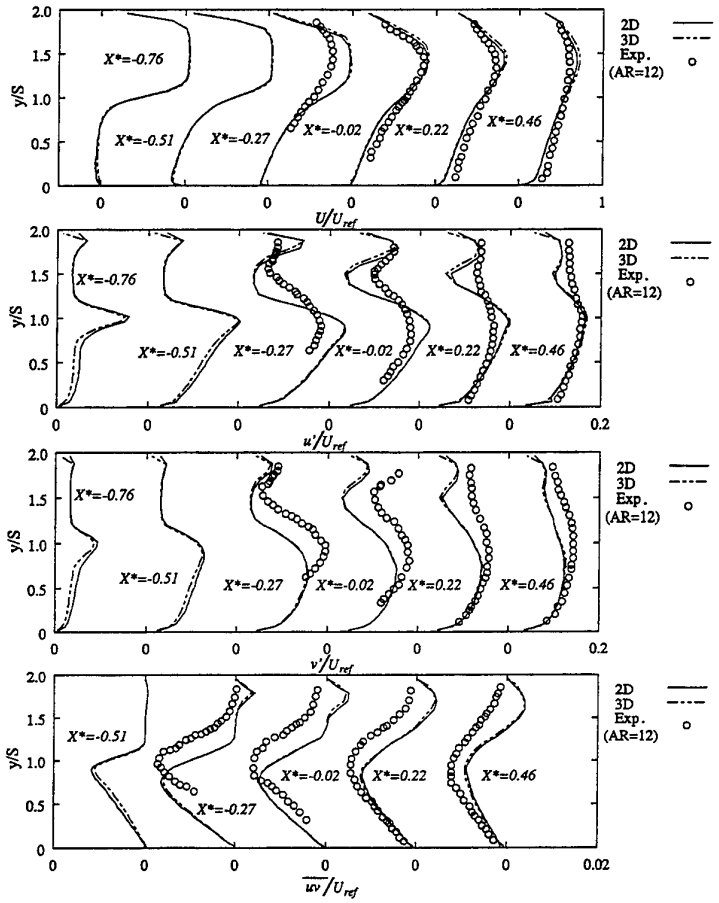

Figure 2: Comparison between 2-D and 3-D (AR=12) simulations for mean streamwise velocity, velocity fluctuation intensities and Reynolds shear stress

Table 1. Mean reattachment lengths(x_r/S) along the centerline

	2-D	3-D,AR=12	3-D,AR=4
Experiment of Papadopoulos and Ötügen		8.2	8.1
CLS model	9.5	9.5	9.0
LS + Yap model	7.9	7.9	8.0

centerplane of the duct. The effect of the aspect ratio,AR, on the characteristic values in the centerplane is now discussed. Predicted mean reattachment lengths,x_r along the duct centerline on the bottom wall for two aspect ratios(AR=4,12) are tabulated in Table 1 with the result of 2-D simulation. The results obtained using Launder-Sharma model [8] with Yap correction(LS + Yap) [9], which is a well known linear eddy viscosity model for its capability to describe the flow separation and reattachment phenomenon [10], are also shown in this table as a reference. Results with LS + Yap model show quantitatively better agreement with the experimental data by Papadopoulos and Ötügen [2]. CLS model predicts mean reattachment length approximately 10-15% larger than experimental data. x_r is, however, predicted to be smaller for the smaller aspect ratio with CLS model, which is consistent with the reported experimental observations [1] [2]. Contrary, LS + Yap model predicts a slightly larger mean reattachment length for the smaller aspect ratio.

Figure illustrates the profiles of the centerplane mean streamwise velocity, streamwise and transverse velocity fluctuation intensities and the Reynolds shear stress for two aspect ratios calculated with CLS

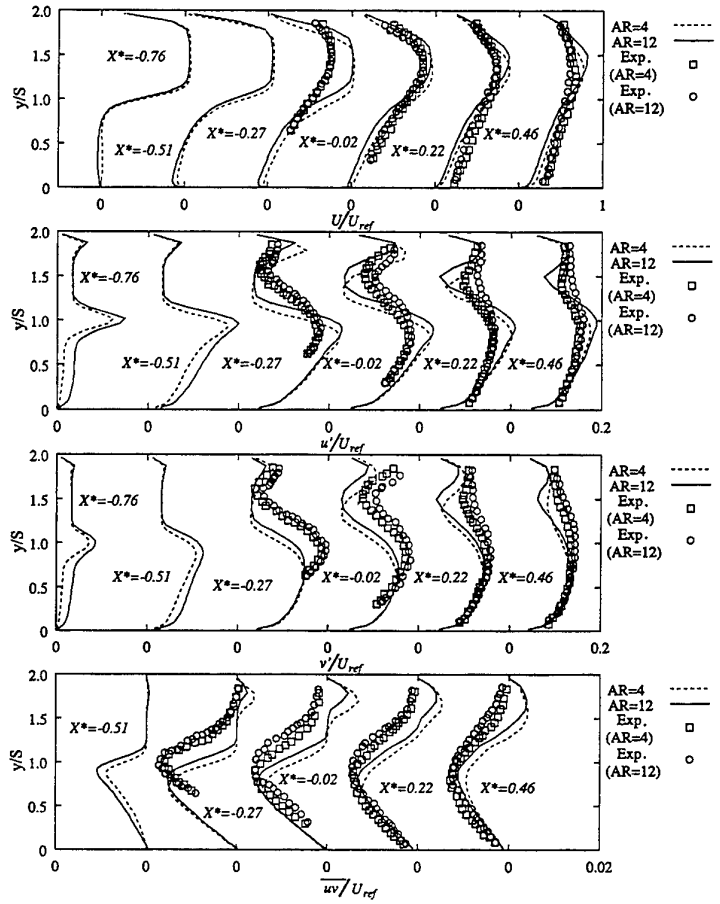

Figure 3: Effect of aspect ratio on mean streamwise velocity, velocity fluctuation intensities and Reynolds shear stress

model. The results of experiment by Papadopoulos and Ötügen [2] are also included.It is shown in this figure that the general shapes of the distribution patterns of the characteristic values are basically similar between two aspect ratios calculated. The distributions of the velocity fluctuation intensities, u', v', show maxima around the locations where maximum mean shear rate is observed and in contrast, minimum values of u' and v' are obtained at locations where the mean streamwise velocity gradient$(\partial U/\partial y)$ is zero. The distributions of Reynolds shear stress, $\overline{uv}$ also show large negative value around the location of maximum velocity gradient. The differences between the case of AR=4 and the case of AR=12 are also observed in Fig.. The values of u', v' in the case of AR=4, for example, are predicted to be smaller than those in the case of AR=12 within the recirculation region $(0.0 < y/S < 1.0, X^* < 0)$. As for the Reynolds shear stress, a slightly smaller negative peak value of $\overline{uv}$ is predicted for smaller aspect ratio. This trend is also consistent with the experimental data. Quantitative agreement with the experimental data is not quite good, probably because of the different vaules of Re between the experiment and the computations. Qualitatively, however, it is confirmed that the present CLS model is able to capture the differences of the flow and turbulence characteristics between two aspect ratios studied.

Three-Dimensionality of Flow and Thermal Fields

The contours of the mean skin friction coefficient,C_f, and the mean Nusselt number,Nu, on the heated bottom wall are illustrated for two different aspect ratios in Fig. and Fig.. In Fig. the shaded area

corresponds to the region where the skin friction coefficient is positive. As for Fig. , gray tone levels correspond to the level of Nusselt number. Darker tone means higher Nusselt number. In the case of AR=12, the two-dimensional zone, where contours of both C_f and Nu are parallel to the z-axis, can be observed around the duct center region, while no such region can be seen in the case of AR=4. When

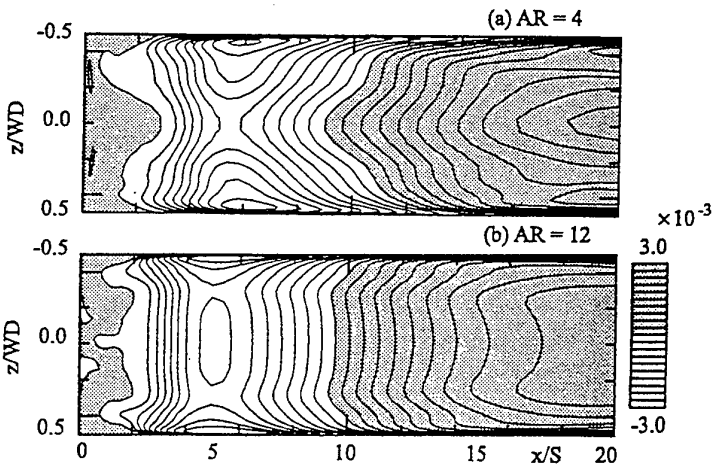

Figure 4: Mean skin friction coefficient contour on the bottom wall

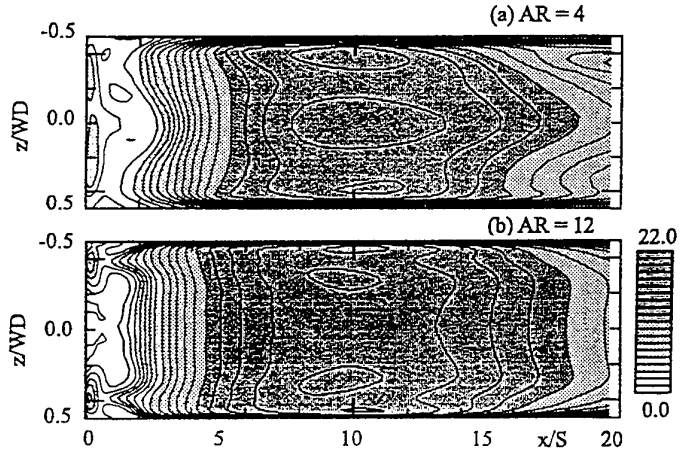

Figure 5: Mean Nusselt number contour on the bottom wall

AR=4, spanwise non-uniformity of C_f and Nu distributions around the centerplane is prominent particularly in the downstream region after the flow reattachment point (x/S >9.00). In Fig. , high Nu area widely expands in the region of $5 < x/S < 15$ in both AR cases. Three peaks of Nu are observed in the case of AR=4 around $x/S \simeq 10$, one in the duct center region and two near the sidewalls($|z/WD| \simeq 0.4$). In the case of AR=12, two pairs of peaks are symmetrically observed with respect to the duct centerline around (x/S,$|z/WD|$)=(9.0,0.3) and (10.0,0.45). In the laminar flows, two distinct peaks in Nu distribution are symmetrically obtained near both sidewalls due to the downwash flows directed toward the heated wall at such spanwise positions[4]. In turbulent flows, heat transfer can be enhanced as the effects of turbulence. Figure shows the distributions of turbulent heat flux,$\overline{v\theta}$, near the heated wall (y/S=0.02). Darker tone means higher value of turbulent heat flux. A peak is observed around (x/S,z/WD)=(9.0,0.0) in the case of AR=4 while two peaks are symmetrically observed in the case of AR=12 around (x/S,$|z/WD|$)=(8.0,0.3). The positions of these peaks are located roughly close to the positions of peak Nu in Fig. , suggesting that heat transfer enhancement due to the turbulence is one

of the causes of producing Nu peaks at such positions.

Slightly complicated distribution patterns are observed in Fig. and Fig. in the region immediately after the step ($0 < x/S < 2$). In order to see the detailed velocity field in this region, magnified velocity

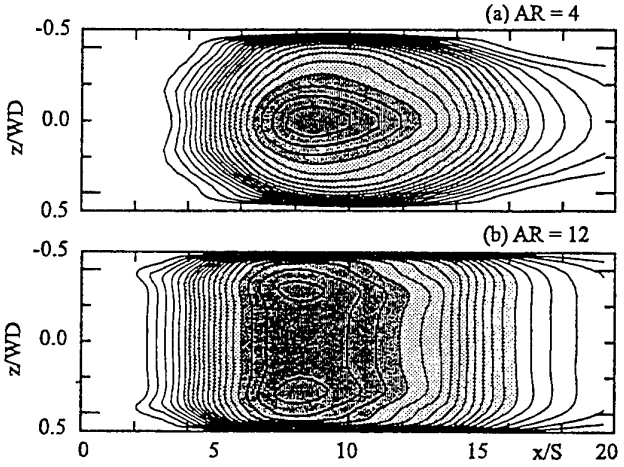

Figure 6: $\overline{v\theta}$ contours near the bottom wall(y/S=0.02)

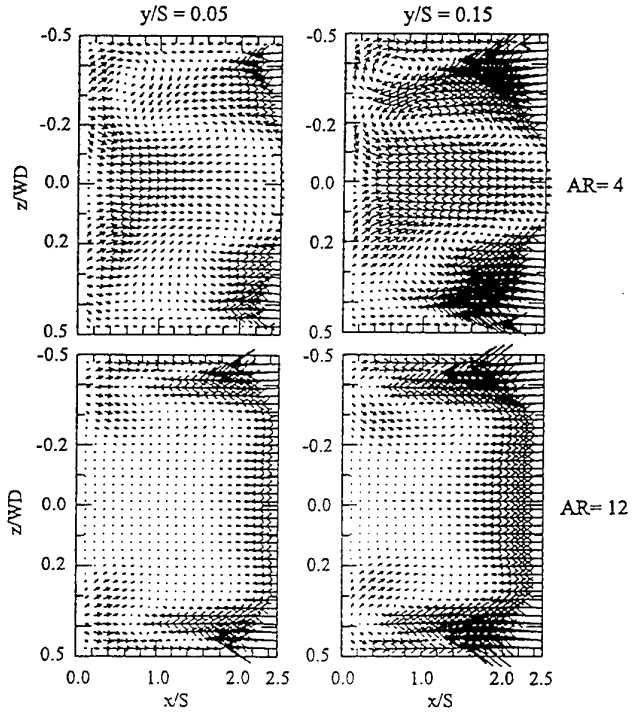

Figure 7: U-W vector plot in the secondary recirculation region

-vector maps in two x-z planes are shown in Fig. for two aspect ratios. It can be seen in Fig. that there exist pairs of counter rotating eddies whose axes are normal to the bottom wall. In the case of AR=4, a pair of counter rotating eddies can be observed around $(x/S,|z/WD|)$=(1.4,0.2). It is clear that two-dimensionality does not hold even in the duct center region for the case of AR=4. In the case of AR=12, those eddies are slightly weaker and are situated at positions around $(x/S,|z/WD|)$=(1.0,0.3). In the duct center region, there exists a zone where fluid is almost stagnant in this case. A near wall flow model immediately after the step was proposed based on results of the surface visualization for different

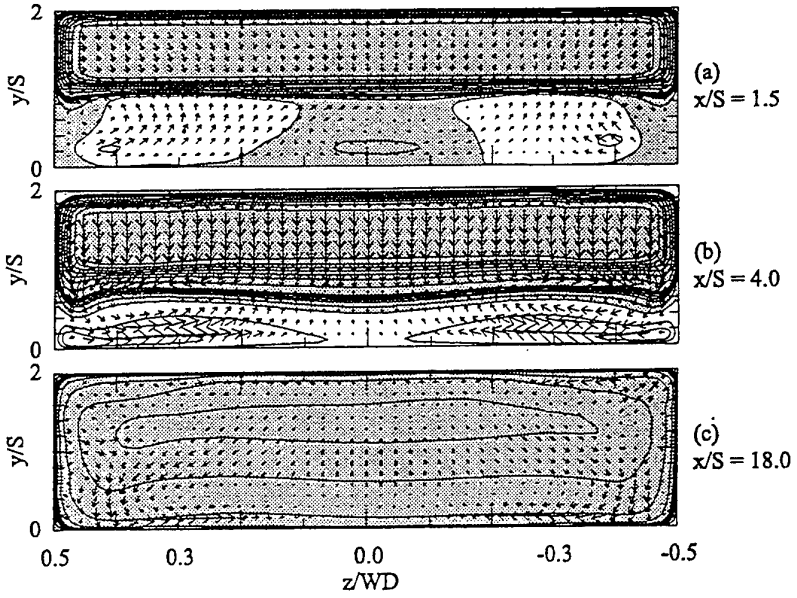

Figure 8: U contours and $V - W$ vector plot at various streamwise-locations (AR=4)

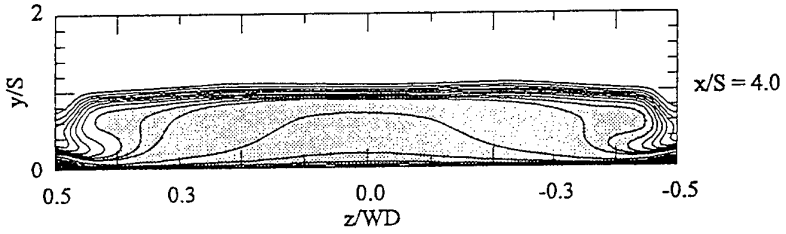

Figure 9: Temperature contour at x/S=4.0 (AR=4)

aspect ratios by Papadopoulos and Ötügen [2]. According to their results, the nearly dead flow zone on the bottom wall immediately after the step is dominated by a pair of primary eddies situated near the sidewalls, whose axes are normal to the bottom wall. The sense of rotation of the eddies predicted by the present simulations basically matches that obtained from the surface visualization results.

To discuss the three-dimensionality of the flow and thermal fields in detail, profiles of the flow velocity and temperature in the y-z cross-sections of the duct are examined for the case of AR=4. Figure shows the upstream view of the velocity vectors (V,W) together with the contours of the streamwise velocity U in three cross-sections of different streamwise positions. Shaded areas in the figures correspond to the positive U velocity regions and white areas to negative U. Figure, on the other hand, shows the profile of the temperature contours similar to those for velocity contours shown in Fig.. Only one cross-section,x/S=4.0, is shown in Fig. because of the space limitation. Darker tone means higher value of temperature in this figure. It is observed in Fig. (a) that the longitudinal vortices like flows are formed after the step near the sidewalls $|z/WD|$=0.42. Further downstream at x/S=4.0, the existence of the secondary flow is more clearly confirmed by the upstream view of the velocity vectors. Counter-clockwise rotating flow is observed on the left hand side of the figure ($z/WD > 0$), directing toward the duct center near the bottom wall. In Fig., the contours of fluid temperature protrude toward the bottom wall near both sidewalls. Comparison between Fig. (b) and Fig. shows that the above mentioned rotating secondary flow transports relatively cold fluid toward the heated wall near both sidewalls. Secondary flows of this nature persist even at the locations considerably downstream at x/S=18. The existance of

such secondary flow is the cause of higher Nusselt number being observed near the sidewalls at $|z/WD| \simeq 0.4$ as can be seen in Fig..

4. CONCLUSIONS

Two- and three-dimensional simulations were performed for turbulent flows over a backward-facing step in a duct. The computations were carried out for two different aspect ratios (AR=4 and 12) in 3-D simulation to investigate three-dimensionality of the flow and thermal fields. The following conclusions were obtained:

(1) In the case of AR=12, the two-dimensional region is observed around the duct center region, while no such region is seen in the case of AR=4. The statistical quantities calculated in the centerplane in the case of AR=12 agree satisfactory with the results obtained by 2-D simulations. The general belief that two-dimensionality can be assumed along the centerplane for the backward-facing step flows in a duct with an aspect ratio greater than 10 is tolerably correct.

(2) High Nu region is observed over the streamwise positions of $5 < x/S < 15$ for both of the aspect ratios. Those high Nu regions are obtained not only as the result of heat transfer enhancement due to the turbulence, but also as the result of the rotationg secondary flow directing toward the duct center near the heated wall.

(3) Transverse counter rotating eddies are observed in the relatively low velocity region right after the step, resulting in the highly three-dimensional flow and thermal field there. This is more prominent for the smaller aspect ratio(AR=4).

NOMENCLATURE

AR:WD/S, C_f:$2\tau_w/\rho U_{ref}^2$, ER:$H/(H-S)$, H:Duct height, Nu:$q_w S/\lambda(T_w - T_{in})$, Re:$U_{ref}S/\nu$, S:Step Height, U_{ref}:Inlet freestream mean velocity, u', v':Velocity fluctuation intensities, $\overline{uv}$:Reynolds shear stress, X^*:$(x-x_r)/x_r$, x_r:Reattachment length, y^+:$\rho u_\tau y/\mu$, WD:Duct width

REFERENCES

1. V. de Brederode and P. Bradshaw, "*Three-Dimensional Flow in Nominally Two-Dimensional Separation Bubbles; I. Flow Behind a Rearward-Facing Step*", Imperial College of Science and Technology, Aero Report 72-19(1972)
2. G. Papadopoulos and M. V. Ötügen, J. Fluids Engineering v.117, pp.17-23(1995).
3. K. Suga, "*Development and Application of a Non-linear Eddy Viscosity Model Sensitised to Stress and Strain Invariants*", UMIST, Dept. of Mech. Eng., Report TFD/95/11(1995).
4. T.J. Craft, B.E. Launder and K. Suga, Int.J.Heat and Fluid Flow v.17,no.2, pp.108-115(1996).
5. H. Iwai, K. Nakabe, K. Suzuki, "A Three Dimensional Numerical Study on Heat Transfer Characteristics of Backward Facing Step Flow in a Rectangular Duct", *Proceedings of the 4th International Symposium on Heat Transfer, pp.541-546*,edited by W.Buxuan,Beijing,China(1996).
6. H. Iwai, K. Matsubara, K. Nakabe, K. Suzuki, "Numerical Simulation on Flow and Heat Transfer of Buoyancy Assisting Backward-Facing Step in a Rectangular Duct", *Proceedings of the 10th International Symposium on Transport Phenomena, v.2 pp.475-480*, Kyoto, Japan(1997).
7. H. Iwai, K. Matsubara, K. Nakabe, K. Suzuki, "A three-dimensional numerical study on the effects of inclination angles on buoyancy affected backward-facing step flow and heat transfer", *Proceedings of 5th International Conference on Advanced Computational Methods in Heat Transfer, pp.327-336*, edited by A.J.Nowak,C.A.Brebbia, R.Bialecki and M. Zerroukat, Cracow, Poland(1998).
8. B. E. Launder and B. I. Sharma, Letters in Heat and Mass Transfer v.1, pp.131-138(1974).
9. C. R. Yap, "*Turbulent Heat and Momentum Transfer in Recirculating and Impinging Flows*", PhD Thesis, Faculty of Technology, University of Manchester(1987).
10. B. E. Launder, J. Heat Transfer v.110,pp.1112-1128(1988).

NEAR-WALL MODELING OF TURBULENT HEAT TRANSFER WITH DIFFERENT PRANDTL NUMBERS

C. Y. Zhao and R. M. C. So
Mechanical Engineering Department
The Hong Kong Polytechnic University
Hung Hom, Kowloon, Hong Kong
Fax: 852-2365-4703
E-mail: mmcyzhao@polyu.edu.hk

Keywords: Heat transfer modeling, turbulence modeling, near-wall heat transfer, variable Prandtl number

ABSTRACT. Near-Wall modeling of the turbulent temperature field is much more complicated, because the boundary conditions are not as well defined as those for the velocity field. Up to now, most computational and theoretical investigations are still based on the hypothesis of a constant turbulent Prandtl number in order to remove the uncertainty of the turbulent temperature boundary condition. However, strictly speaking, the physical arguments for these assumptions are applicable only for fluids whose Prandtl number, Pr, is approximately 1. Near-wall asymptotes of the turbulence statistics show that these properties are Pr dependent. Another difficult in the modeling of near-wall heat transfer is the irregular geometries often encountered in heat transfer prblems. If the heat-flux models fail to reflect the Pr dependence and are geometry dependent, they would not be able to replicate the thermal asymptotes correctly as a wall is approached. The main objective of this paper is to develop a geometry independent near-wall two-equation heat-flux model for fluids with different Pr. In this paper, a geometry independent near-wall Reynolds stress turbulence model and the proposed two-equation heat-flux model are used to calculate heat transfer problems. As a first attempt, the proposed model is validated against fully developed turbulent channel flow with variable Pr. The mean temperature, turbulent kinetic energy, temperature variance, heat flux and the time scale ratio together with the near-wall characteristics are calculated and compared with direct numerical simulation (DNS) data. Good correlation with data is obtained.

INTRODUCTION

The wall boundary conditions of the thermal field are quite a bit more complicated than the velocity field in any turbulent heat transfer problem. For example, in the case of an incompressible flow, the fluid equation of state is automatically satisfied. Therefore, if the assumption is made that the temperature fluatuations vanish at the wall, that will lead to the conclusion that the fluctuating pressure also goes to zero at the wall [1]. Obviously, this is not true physically. The difficulty can be bypassed by invoking Reynolds analogy. In other words, the transport of heat is assumed to be similar to that of the transport of momentum [2]. As a result, a turbulent Prandtl number, Pr_t, can be defined and assumed to be given by a constant not too different from unity. This assumption is probably valid for simple heat transfer problems, such as fully-developed pipe and channel flow with a molecular Prandtl number, Pr, not too different from one [2]. If the Pr is much greater or smaller than one, the assumption of the heat and momentum transport process being similar is no longer valid [3, 4]. The heat transfer problem, even in the case of fully-developed flows, has to be investigated using higher level closure schemes [2].

The wall boundary condition is one of many difficulties encountered in complex heat transfer modeling. Another is the unavailability of models that are truly geometry independent. There are two components to the modeling of heat transfer problems; one is the velocity field model, the other is the thermal field model. Both models have to be geometry independent before the resultant model can be claimed to be one that is truly independent of geometry. Among the available velocity field models, the high Reynolds-number models are usually geometry independent while most near-wall models are not [5]. This is true for both two-equation and Reynolds-stress models. The reason is that wall unit normals and wall normal coordinate are frequently used to help devise near-wall damping functions to account for the effects of viscosity near a wall. Recently, a few geometry independent near-wall Reynolds-stress models have been put forward and they are shown to be quite valid for a range of flows with geometries that vary from the simple to the rather complex [6-8]. The other component is the heat flux model. As in the case of high Reynolds number velocity field models, the high Reynolds number heat flux

models are also geometry independent. On the other hand, not many near-wall heat transfer models, be it two-equation or second order, are geometry independent [2]. In fact, even the more recently proposed near-wall models for flows with different Pr are either dependent on wall unit normals or wall normal coordinate [3, 4]. Therefore, if a truly geometry independent model for flows with different Pr is to be proposed for turbulent heat transfer problems, a new near-wall model has to be derived. The alternative is to modify one of the existing near-wall models to rid its dependence on wall unit normals and wall normal coordinate.

In heat transfer modeling, it is advisable to use a heat flux model that is at least one level lower than that of the velocity field model [9]. If the geometry independent near-wall Reynolds-stress models are used to calculate the velocity field, this means that the heat flux model should be limited to either a two-equation model or a constant Pr_t assumption. For incompressible heat transfer problems, the velocity field affects the thermal field but not the other way around. In isothermal flows, there is only one turbulence time scale,. This is given by the ratio of the turbulent kinetic energy, k, over its dissipation rate, ε. For non-isothermal incompressible flows, another time scale given by the ratio of the temperature variance, θ^2, and its dissipation, ε_θ, is also important. As a result, a time scale ratio, $R = \theta^2\varepsilon/(2\ k\ \varepsilon_\theta)$, can be defined. Strictly speaking, if R is assumed constant, the model is essentially a constant Pr_t model because it can be shown that $Pr_t = \sqrt{R}$ [2]. On the other hand, if R is to be determined, two equations governing the transport of θ^2 and ε_θ have to be solved. Consequently, there is no one-equation model for the heat flux [2]. There are many different types of near-wall two-equation models. Some are formulated for a particular Pr, while others can account for different Pr. However, none is geometry independent. Even the more recent proposals [3, 4] have damping functions in the heat flux model that are dependent on the wall unit normal and the wall normal coordinate. In the work of So and Sommer [3], a Reynolds-stress and a two-equation model were used to calculate the velocity field and both models have near-wall corrections that rendered them geometry dependent. On the other hand, Nagano and Shimada [4] only used a two-equation model to resolve the velocity field. However, their model is not geometry independent either. The present approach is to attempt to modify one of the two heat flux models to make it geometry independent and to use it in conjunction with a near-wall Reynolds-stress model that is also geometry independent. That way, a truly geometry independent heat transfer model that can account for fluids with different Pr is available.

The choice of models for both the velocity and temperature fields is dictated by the desire to have relatively simple models, the least modifications need be made to the heat flux model and a fairly accurate prediction of Pr effects. Among the near-wall Reynolds-stress models that are geometry independent, the model by Craft and Launder [7] is very complex, however, their predicted results of simple flows are not too much different from those given by Durbin [6] and So and Yuan [8]. The model proposed by Durbin [6] relies on the solution of an additional second order tensor equation. Since the So and Yuan [8] model is fairly simple, the choice for the present study is quite straightforward. As for the heat flux, the models of So and Sommer [3] and Nagano and Shimada [4] give equally good results for the prediction of Pr effects. The selection of the So and Sommer [3] model is based on the fact that it only involves the modification of a single damping function, while the model of Nagano and Shimada [4] requires the revision of several damping functions in order to rid its dependence on wall unit normals and wall normal coordinate. Therefore, the present approach to formulate a geometry independent model for heat transfer calculations is to adopt the So and Yuan [8] model for the velocity field and to modify the So and Sommer [3] model for the thermal field. Thus formulated, the model will be suitable for complex heat transfer problems with variable Pr. The present paper only attempts to verify the model calculations against the direct numerical simulation (DNS) data of Abe *et al.* [10] where fully-developed channel flows with different Pr have been reported. A full validation of the model against complex flows with different Pr will be reported in a subsequent paper.

VELOCITY FIELD MODEL

The detailed derivation of the geometry independent near-wall Reynolds-stress model has already been reported by So and Yuan [8]. Therefore, for the sake of brevity, only the modeled equations and the associated constants are given here. The interested readers should go to [8] for details. For incompressible flows, the exact Reynolds-stress equations can be written as

$$\frac{D\,\overline{u_i u_j}}{Dt} = \frac{\partial}{\partial x_k}\left(\nu \frac{\partial \overline{u_i u_j}}{\partial x_k}\right) + D_{ij}^{T} + P_{ij} + \Pi_{ij}^{*} - \varepsilon_{ij} \quad , \tag{1}$$

where U_i, u_i are the mean and fluctuating velocity vectors, x_i is the coordinate vector, t is time, ν is the fluid kinematic viscosity and the models proposed for the turbulent diffusion tensor, the production tensor, the velocity pressure-gradient correlation tensor and the dissipation rate tensor, D_{ij}^{T}, P_{ij}, Π_{ij}^{*}, ε_{ij}, respectively, are given by

$$D_{ij}^{T} = \frac{\partial}{\partial x_m}\left[C_s \frac{k}{\varepsilon}\left(\overline{u_i u_l}\frac{\partial \overline{u_j u_m}}{\partial x_l} + \overline{u_j u_l}\frac{\partial \overline{u_m u_i}}{\partial x_l} + \overline{u_m u_l}\frac{\partial \overline{u_i u_j}}{\partial x_l}\right)\right] \quad , \tag{2}$$

$$P_{ij} = -\left[\overline{u_i u_m}\,\partial U_j/\partial x_m + \overline{u_j u_m}\,\partial U_i/\partial x_m\right] \quad , \tag{3}$$

$$\Pi_{ij}^{*} = \Pi_{ij} + \Pi_{ij}^{w} + D_{ij}^{p} \quad , \tag{4}$$

$$\varepsilon_{ij} = \frac{2}{3}\varepsilon\,\delta_{ij} + \varepsilon_{ij}^{w} \quad . \tag{5}$$

Here, C_s is the model constant. In (4), the tensor has been split into three parts, a pressure strain part, Π_{ij}, a wall correction part, Π_{ij}^{w}, and a pressure diffusion part, D_{ij}^{p}. As for ε_{ij}, near the wall, a correction, ε_{ij}^{w}, is added to account for the anisotropic behavior of the dissipation rate tensor. The pressure strain part is given by the high Reynolds number model of Speziale *et al.* [11], or

$$\Pi_{ij} = -\left(C_1\varepsilon + C_1^{*}\widetilde{P}\right) b_{ij} + C_2\varepsilon\left(b_{im}b_{mj} - \frac{1}{3}II_b\,\delta_{ij}\right) - \alpha_1\left(P_{ij} - \frac{2}{3}\widetilde{P}\,\delta_{ij}\right)$$
$$- \beta_1\left(D_{ij} - \frac{2}{3}\widetilde{P}\,\delta_{ij}\right) - 2\left(\gamma_1 + \frac{C_3^{*}}{2}II_b^{1/2}\right) k\,S_{ij} \quad . \tag{6}$$

The near-wall correction for Π_{ij}^{w} derived by So and Yuan [8] is given by

$$\Pi_{ij}^{w} = f_{w1}\left[\left(C_1\varepsilon + C_1^{*}\widetilde{P}\right) b_{ij} - C_2\varepsilon\left(b_{im}b_{mj} - \frac{1}{3}II_b\,\delta_{ij}\right) + \alpha^{*}\left(P_{ij} - \frac{2}{3}\widetilde{P}\,\delta_{ij}\right) + 2\gamma^{*}k\,S_{ij}\right] \quad . \tag{7}$$

Only one near-wall correction is proposed for the combined term, $D_{ij}^{p} + \varepsilon_{ij}^{w}$. This term is again written as ε_{ij}^{w} and is given by

$$\varepsilon_{ij}^{w} = -(2/3) f_{w1}\delta_{ij}\varepsilon + f_{w1}(\varepsilon/k)\,\overline{u_i u_j} + \varepsilon_{ij}^{*} \quad , \tag{8}$$

where ε_{ij}^{*} is modeled by the function

$$\varepsilon_{ij}^{*} = \frac{1}{2}\left[\frac{\partial}{\partial x_m}\left(\nu\frac{\partial \overline{u_i u_j}}{\partial x_m}\right) - \frac{\overline{u_i u_j}}{k}\frac{\partial}{\partial x_m}\left(\nu\frac{\partial k}{\partial x_m}\right)\right] \quad . \tag{9}$$

One damping function has been introduced and this is $f_{w1} = exp\left[-(Re_t/200)^2\right]$ where $Re_t = k^2/\varepsilon\nu$. The other unknown functions are defined by $D_{ij} = -\left[\overline{u_i u_m}\,\partial U_m/\partial x_j + \overline{u_j u_m}\,\partial U_m/\partial x_i\right]$, $b_{ij} = \left\{\overline{u_i u_j} - (2/3)\,k\,\delta_{ij}\right\}/2k$, $II_b = b_{ij}\,b_{ij}$ and $2\widetilde{P} = P_{ii}$, and the model constants are given by $C_1 = 3.4$, $C_2 = 4.2$, $C_1^{*} = 1.8$, $C_3^{*} = 1.3$, $\alpha_1 = 0.4125$, $\beta_1 = 0.2125$, $\gamma_1 = 0.01667$, $\alpha^{*} = -0.29$ and $\gamma^{*} = 0.065$.

Finally, the modeled ε-equation can be written as

$$\frac{D\varepsilon}{Dt} = \frac{\partial}{\partial x_j}\left(\nu\frac{\partial \varepsilon}{\partial x_j}\right) + \frac{\partial}{\partial x_j}\left[C_\varepsilon\frac{k}{\varepsilon}\overline{u_i u_j}\frac{\partial \varepsilon}{\partial x_i}\right] + C_{\varepsilon 1} f_1 \frac{\varepsilon}{k} P_k - C_{\varepsilon 2} f_2 \frac{\varepsilon\,\widetilde{\varepsilon}}{k} \quad , \tag{10}$$

where $\widetilde{\varepsilon} = \varepsilon - \left(C_{\varepsilon 3}/f_2 C_{\varepsilon 2}\right)\nu\left(\partial k^{1/2}/\partial x_j\right)^2$ and the damping functions are defined as $f_1 = \left(1 - \alpha\, f_{w2}\right)$ and $f_2 = 1 - (2/9)\exp\left[-(Re_t/6)^2\right]$. The constants are specified as $C_\varepsilon = 0.12$, $C_{\varepsilon 1} = 1.50$, $C_{\varepsilon 2} = 1.9$, $C_{\varepsilon 3} = 2.9556$ and $\alpha = 1$. It can be seen that all modeled equations are not dependent on any wall unit normals or wall

normal coordinate. As such, the near-wall corrections only depend on local variables, hence the model is geometry independent.

THERMAL FIELD MODEL

The near-wall heat flux model selected for improvement is the two-equation model proposed by So and Sommer [3]. This model could re-produce the near-wall heat transfer effects correctly for fluids with different Pr. It is also versatile enough to handle different wall thermal boundary conditions, whether they are given by a constant wall heat flux or a constant wall temperature or a mixed of both. The important thing is that the model could even replicate the thermal field fairly correctly under the assumption of a vanishing wall fluctuating temperature in spite of the fact that its prediction of ε_θ in the near-wall region is in error [1]. The only drawback of this model is its geometry dependence.

So and Sommer [3] assumed the turbulent thermal diffusivity to be given by $\alpha_T = C_\lambda f_\lambda k \left[k \overline{\theta^2}/\varepsilon \varepsilon_\theta\right]^{1/2}$, where a mixed time scale is invoked and f_λ is the near-wall correction proposed to mimick the viscous damping effects near a wall. If the model has to reproduce the *Pr* effects correctly, f_λ has to be parametric in Pr. Their proposal not only reflects the dependence of f_λ on Pr, but is also parametric in y, the wall normal coordinate. In addition, some terms in their proposed near-wall correction to the modeled ε_θ-equation also depends on y. As a result, their model is not coordinate independent and modifications are needed in order to render the modeled equations to be completely dependent on local properties.

The present approach is to modify the damping function and the near wall correction to the ε_θ-equation, so that their dependence on *y* could be eliminated. An asymptotic analysis similar to that used by Lai and So [12] to derive near-wall corrections to the modeled Reynolds-stress equations is used to deduce an f_λ and a near-wall correction for the ε_θ-equation that are independent of y. Instead of using the wall coordinate as a length scale, a turbulence length scale given by $k^{3/2}/\varepsilon$ is taken to be the characteristic length scale near a wall. Without going into details, the equations for the modified heat flux model can be written as

$$\frac{\partial \overline{\theta^2}}{\partial t} + U_j \frac{\partial \overline{\theta^2}}{\partial x_j} = \frac{\partial}{\partial x_j}\left(\alpha \frac{\partial \overline{\theta^2}}{\partial x_j}\right) + \frac{\partial}{\partial x_i}\left(C_{\theta^2}\, \overline{u_i u_j}\, \frac{k}{\varepsilon} \frac{\partial \overline{\theta^2}}{\partial x_j}\right) - 2\overline{u_j\theta} \frac{\partial \Theta}{\partial x_j} - 2\varepsilon_\theta \quad , \tag{11}$$

$$\frac{\partial \varepsilon_\theta}{\partial t} + U_j \frac{\partial \varepsilon_\theta}{\partial x_j} = \frac{\partial}{\partial x_j}\left(\alpha \frac{\partial \varepsilon_\theta}{\partial x_j}\right) + \frac{\partial}{\partial x_i}\left(C_{\varepsilon\theta}\, \overline{u_i u_j}\, \frac{k}{\varepsilon} \frac{\partial \varepsilon_\theta}{\partial x_j}\right) + C_{d\,1} \frac{\varepsilon_\theta}{\overline{\theta^2}} P_\theta + C_{d\,2} \frac{\varepsilon}{k} P_\theta$$

$$+ C_{d\,3} \frac{\varepsilon_\theta}{k} \widetilde{P} - C_{d\,4} \frac{\widetilde{\varepsilon}_\theta}{\overline{\theta^2}} \varepsilon_\theta - C_{d\,5} \frac{\widetilde{\varepsilon}}{k} \varepsilon_\theta + \xi_{\varepsilon\theta} \quad , \tag{12}$$

where Θ and θ are the mean and fluctuating temperature, respectively, and $P_\theta = -\overline{u_j\theta}\left(\partial\Theta/\partial x_j\right)$ is the production of $\overline{\theta^2}$. Similar to $\widetilde{\varepsilon}$, the reduced ε_θ is defined as $\widetilde{\varepsilon}_\theta = \varepsilon_\theta - \alpha\left[\partial\left(\overline{\theta^2}\right)^{1/2}/\partial x_j\right]^2$. This definition still gives the correct asymptotic behavior for $\widetilde{\varepsilon}_\theta$ near a wall because the derivatives along the stream and transverse directions are of higher order than that along the normal direction. Therefore, the two leading terms in $\widetilde{\varepsilon}_\theta$ are contributed by the normal derivative only. Finally, the near-wall correction function is given by

$$\xi_{\varepsilon\theta} = f_{w,\varepsilon\theta}\left[\left(C_{d\,4} - 4\right)\frac{\widetilde{\varepsilon}_\theta}{\overline{\theta^2}}\varepsilon_\theta + C_{d\,5}\frac{\widetilde{\varepsilon}}{k}\varepsilon_\theta - \frac{\widetilde{\varepsilon}_\theta^2}{\overline{\theta^2}} + \left(2 - C_{d\,1} - C_{d\,2}\mathrm{Pr}\right)\frac{\varepsilon_\theta}{\overline{\theta^2}} P_\theta^*\right] \quad . \tag{13}$$

The C's in these equations are model constants to be specified. Here, P_θ^* is P_θ due to a streamwise mean temperature gradient alone and $f_{w,\varepsilon\theta} = \exp\left[-\left(R_t/80\right)^2\right]$ is a damping function proposed to render (11) zero far away from the wall. The P_θ^* term is a consequence of the constant wall heat flux boundary condition, where $\partial\Theta/\partial x$ is finite. Once $\overline{\theta^2}$ and ε_θ are known, α_T can be evaluated provided f_λ is properly specified, and the heat flux vector is then given by $-\overline{u_i\theta} = \alpha_T\left(\partial\Theta/\partial x_i\right)$.

The heat flux model is complete by specifying f_λ and the model constants. Following So and Sommer [3], the damping function $f_\lambda = C_{\lambda\,1}\left(1 - f_{\lambda\,1}\right)/\mathrm{Re}_t^{1/4} + f_{\lambda\,1}$ is assumed. In this expression, $C_{\lambda 1}$ is assumed to be

parametric in Pr, while $f_{\lambda 1}$ is taken to be a function of the dimensionless characteristic length $\eta = k^{3/2}u_\tau/\varepsilon\nu$ and Pr. Here, u_τ is the friction velocity. Again, using asymptotic analysis, $f_{\lambda 1}$ can be shown to be given by $f_{\lambda 1} = [1 - \exp\{- g(\eta)/A^+\}]$. The function g is determined to be

$$g(\eta) = 1.313 + 0.249\,\eta - 0.0045\,\eta^2 + 7.643 \times 10^{-5}\,\eta^3 \quad , \tag{14a}$$

for $\eta < 65$ and

$$g(\eta) = 0.991\,\eta - 45.0 \quad , \tag{14b}$$

for $\eta \geq 65$. The quantities A^+ and $C_{\lambda 1}$ are parametric in *Pr* and are defined as $A^+ = 10/Pr$ for $Pr < 0.25$ and $A^+ = 39/Pr^{1/16}$ for $Pr \geq 0.25$; $C_{\lambda 1} = 0.4/Pr^{1/4}$ for $Pr < 0.1$ and $C_{\lambda 1} = 0.07/Pr$ for $Pr \geq 0.1$. Other constants are given by $C_{d1} = 1.80$, $C_{d2} = 0$, $C_{d3} = 0.72$, $C_{d4} = 2.20$, $C_{d5} = 0.80$, $C_\lambda = 0.10$, $C_{\theta 2} = 0.11$ and $C_{\varepsilon\theta} = 0.11$. Again, it can be seen that, after modifications, the modeled equations are not dependent on the wall unit normal or the wall normal coordinate. Hence, this modified two-equation heat flux model is geometry independent.

RESULTS AND DISCUSSION

The second order velocity field model and the two-equation heat flux model are used to calculate different kinds of heat trtansfer problems. Since the velocity field model has been verified to give good results for a variety of complex flows without heat transfer [8], its credibility needs no further validation. However, the performance of the heat transfer model needs verification. Two steps are taken to verify the model; the first is its ability to predict flows with different Pr after the modifications, and the second is its performance in the prediction of heat transfer problems with complex geometry. This paper reports on the first attempt using DNS data derived from Abe *et al.* [10], while leaving the second to a more detailed study using reliable data.

The available DNS heat transfer data is usually derived from fully-developed channel and pipe flows calculations at different *Pr* and either constant wall heat flux or constant wall temperature boundary conditions. Under these assumptions, the governing mean flow equations for channel/pipe flows can be written in a combined form as

$$\frac{1}{y^j}\frac{d}{dy}\left[y^j\left(\nu\frac{dU}{dy} - \overline{uv}\right)\right] - \frac{1}{\rho}\frac{dP}{dx} = 0 \quad , \tag{15}$$

$$\frac{1}{y^j}\frac{d}{dy}\left[y^j\left(\alpha\frac{d\Theta}{dy} - \overline{v\theta}\right)\right] - S = 0 \quad , \tag{16}$$

where $S = 2(2^j)\,U q_w / (\rho C_p U_m D)$ is the source term for (16) with constant wall heat flux, q_w, specified, $S = - q''/(\rho C_p)$ is the source term for (16) with constant wall temperature specified, j = 0 denotes channel flows, j = 1 denotes pipe flows and dP/dx is related to the wall shear. Here, q" is the heat source per unit volume, C_p is the specific heat at constant pressure, U_m is the mean velocity and D is either the pipe diameter or the channel height. Similarly, the modeled turbulence equations are also reducible to ordinary differential equations. As a result, the governing equations can be solved by standard numerical techniques and the numerical errors are essentially the same for all calculated cases. The results to be compared [10] covered a range of Pr, from 0.025 to 5.0 at a Reynolds number based on the friction velocity, u_τ, and D of $Re_\tau = 180$.

The results are reported in wall variables, which are defined as $U^+ = U/u_\tau$, $k^+ = k/u_\tau^2$, $y^+ = yu_\tau/\nu$, $\Theta^+ = \Theta/\Theta_\tau$, $\theta^+ = \overline{\theta^2}/\Theta_\tau^2$, $-v\theta^+ = - \overline{v\theta}/u_\tau\Theta_\tau$, and the time scale ratio R. Here, Θ_τ is the friction temperature. In order to show that the seond order velocity field model is indeed giving a correct prediction of the velocity and turbulence field, the calculated U^+ and k^+ are also compared with the DNS data [13] which was reported at an $Re_\tau = 180$. Some sample plots of the results are shown in Figs. 1 through 5. In these figures, besides the present model predictions, the results of the calculations using the model of So and Sommer [3] and the second order velocity field model of So and Yuan [8] are also shown for comparison. The present calculations are designated as "present model" while those using the model of So and Sommer [3] and the DNS data are simply indicated by the reference numbers. This comparison is intended to show that the modifications made to the So and Sommer [3] model do not cause any deterioration in the model performance as far as its ability to replicate Pr effects.

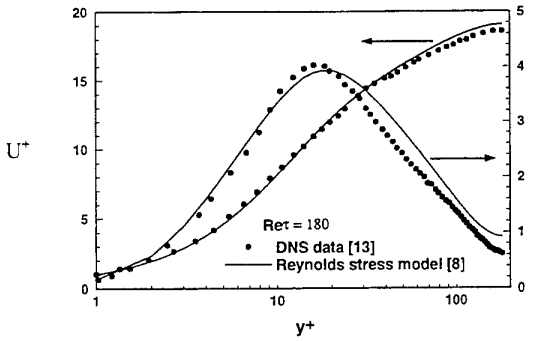

Fig. 1 Comparisons of U^+ and k^+ with DNS data.

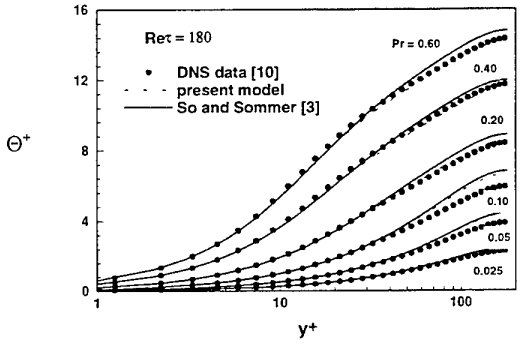

Fig. 2a Comparison of Θ^+ with DNS data at Pr varying from 0.025 to 0.60.

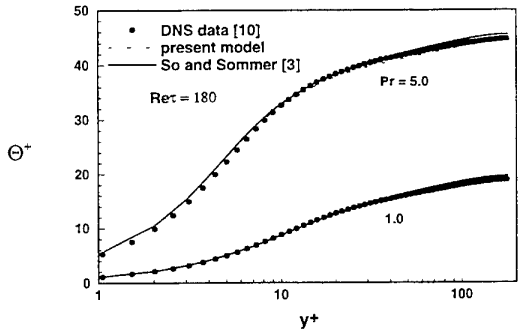

Fig. 2b Comparison of Θ^+ with DNS data at Pr = 1and 5.

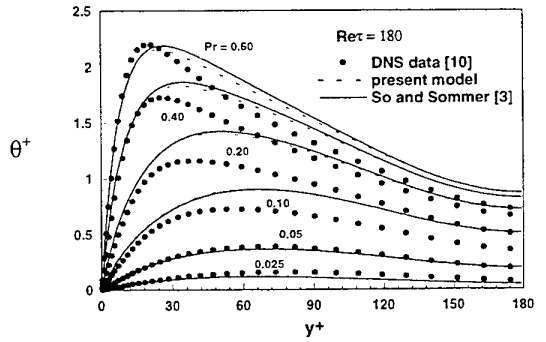

Fig. 3a Comparison of θ^+ with DNS data at Pr varying from 0.025 to 0.60.

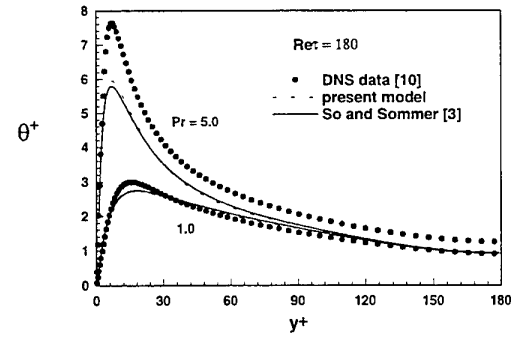

Fig. 3b Comparison of θ^+ with DNS data at Pr = 1 and 5.

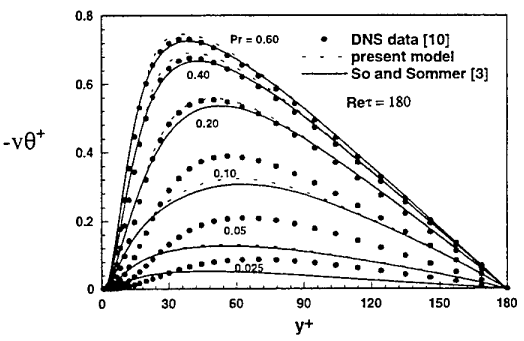

Fig. 4a Comparison of $-v\theta^+$ with DNS data at Pr varying from 0.025 to 0.60.

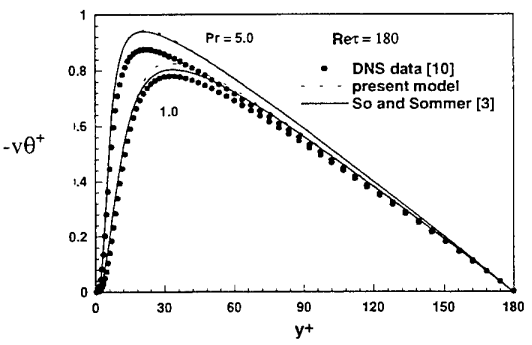

Fig. 4b Comparison of $-v\theta^+$ with DNS data at Pr =1 and 5.

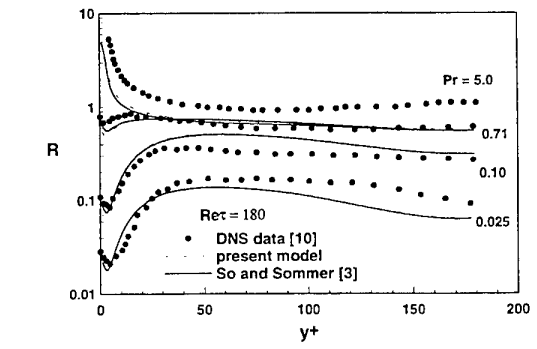

Fig. 5 Comparison of R with DNS data at four different Pr.

The comparisons of U^+ and k^+ are shown in Fig. 1 and they simply verify that the second order model is giving good results for this fully developed channel flow. Mean temperature Θ^+ is compared in Fig. 2 for eight different Pr. In this and subsequent figures, the comparisons with *Pr* less than one are shown in part (a) of the figure while the comparisons with Pr greater or equal to one are given in part (b). Both the present model and that of So and Sommer [3] yield the same result for the whole range of Pr calculated and the Pr effects are predicted correctly. In fact, the discrepancy is so small that it is not noticeable in the plots. The temperature variance predictions for the range of Pr considered are compared in Fig. 3. Here, differences between predictions and the DNS data show up at large Pr. At Pr = 5.0, a subatantial under-prediction of the θ^+ peak is noticed, while differences between predictions and DNS data also occur at other Pr in the range, 0.1 to 1.0. In spite of this, there is still not much discrepancies between the calculations of the present model and that of [3]. The normal heat flux is compared next in Fig. 4. In general, the discrepancies between predictions and DNS data occur either at Pr < 0.20 or at Pr = 5.0, while there is little difference between the two model calculations. Finally, the time scale ratio is compared in Fig. 5. The trend predicted by the models is essentially correct, even though there are minor differences between calculations and DNS data. For Pr < 1.0, the models yield a fairly correct prediction of R in the near-wall region. On the other hand, the predicted R is lower than the DNS data for Pr = 5.0. These results, therefore, verify that the modifications made to render the heat flux model geometry independent do not unnecessarily affect the ability of the model to replicate the Pr effects in an incompressible flow with heat transfer.

CONCLUSIONS

The present study attepts to formulate a geometry independent turbulence model for incompressible heat transfer problems that involve fluids with different Pr. Two different components are required; they are the velocity field model and the thermal field model. Both models have to be independent of the flow geometry before the combined model can be claimed to be truly geometry independent. Furthermore, it is advisable to have a thermal field model that is at least one level lower than the velocity field model. In view of these constraints, it is decided to formulate a heat transfer model that is based on a second order velocity field model and a two-equation thermal field model. The alternative is to have a two-equation model for the velocity field and to invoke a constant Pr_t assumption for the thermal field, which is not a viable alternative for complex heat transfer problems. Since the second order model of So and Yuan [8] is geometry independent, the proposed approach is to adopt this model for the velocity field and to modify the two-equation model of So and Sommer [3] for the heat flux. This latter model has been formulated for different Pr, but it is not geometry independent because of the presence of wall unit normals and wall normal coordinate in the near-wall correction functions. Asymptotic analysis is used to derive alternative near-wall correction functions that are capable of mimicking the Pr effects and yet are truly geometry independent. Validation of the combined model has been carried out in two steps, the first is against simple channel/pipe flows with different Pr and the second is against complex flows at a fixed Pr. The calculations are compared with DNS data over a wide range of Pr. Good correlation with mean temperature is obtained. However, for the turbulence statistics, minor differences exist at either Pr = 5.0 or Pr < 0.2. The comparison with flows having complex geometries will be carried out later.

ACKNOWLEDGEMENTS

The authors wish to acknowledge the support given to them through Grant No. Y-W18 of The Hong Kong Polytechnic University, Hong Kong.

REFERENCES

1. T. P. Sommer, R. M. C. So and H.S. Zhang, Heat Transfer Modeling and the Assumption of Zero Wall Temperature Fluctuations. J. Heat Transfer v.116, pp. 855-863 (1994).
2. R. M. C. So and C. G. Speziale, A Review of Turbulent Heat Transfer Modeling. *Annual Review of Heat Transfer - X* (Editor: C. L. Tien), Published by Begell House, Inc., New York, pp. 177-219, 1999.
3. R. M. C. So and T. P. Sommer, A Near-Wall Eddy Conductivity Model for Fluids with Different Prandtl Numbers. J. Heat Transfer v.116, pp. 844-854 (1994).

4. Y. Nagano and M. Shimada, Development of a Two-Equastion Heat Transfer Model Based on Direct Simulations of Turbulent Flows with Different Prandtl Numbers, Physics of Fluids v.8, pp. 3379-3402 (1996).
5. C. G. Speziale and R. M. C. So, Turbulence Modeling and Simulation. *The Handbook of Fluid Dynamics* (Editor: Richard W. Johnson), CRC Press LLC, Boca Raton, Florida, pp. 14.1 - 14.111 (1998).
6. P. A. Durbin, A Reynolds-Stress Model for Near-Wall Turbulence, J. Fluid Mechanics v.249, pp. 465-498 (1993).
7. T. J. Craft and B. E. Launder, A Reynolds Stress Closure Designed for Complex Geometries, Int. J. Heat Fluid Flow v.17, pp. 245-254 (1996).
8. R. M. C. So and S. P. Yuan, A Geometry Independent Near-Wall Reynolds-Stress Closure. Int. J. Engineering Science v.37, pp. 33-57 (1999).
9. Cebeci, T. and Bradshaw, P. *Physical and Computational Aspects of Convective Heat Transfer*, Springer-Verlag, New York, pp. 13, 19-31, 150-151 (1984).
10. H. Abe, H. Kawamura and Y. Matsuo, DNS of Turbulent Heat Transfer in Channel Flow: Near-Wall Turbulence Quantities, Proceedings of the 13th Australasian Fluid Mechanics Conference, Monash University, Melbourne, Australia, pp. 849-852 (1998).
11. C. G. Speziale, S. Sarkar and T. B. Gatski, Modeling the Pressure-Strain Correlation of Turbulence: An Invariant Dynamical Systems Approach. J. Fluid Mechanics v.227, pp. 245-272 (1991).
12. Y. G. Lai and R. M. C. So, On Near-Wall Turbulent Flow Modelling, J. Fluid Mechanics v.221, pp. 641-673 (1990).
13. J. Kim, P. Moin and R. D. Moser, Turbulence Statistics in Fully Developed Channel Flow at Low Reynolds Number, J. Fluid Mechanics v.177, pp. 133-186 (1987).

A METHOD FOR VISCOUS INCOMPRESSIBLE FLOWS WITH A SIMPLIFIED COLLOCATED GRID SYSTEM

J.H. Nie, Z.Y. Li, Q.W. Wang, W.Q. Tao
School of Energy and Power Engineering, Xi'an Jiaotong University
Xi'an, Shaanxi 710049, P. R. China

Keywords: collocated grid; underralaxation factor; SIMPLE algorithm

ABSTRACT. A simplified version of collocated grid system is proposed, which is characterized by adopting the momentum interpolation only for the discretization of mass conservation equation, while the interface velocity used for determining the discretization coefficient is obtained by linear interpolation. To eliminate the effect of the underrelaxation factor on the numerical results, it is suggested that the value of the underrelaxation factor resume to 1 in the computation of momentum interpolation. Three cases are computed and the results are compared with the existing literature, showing the feasibility of the proposed methods.

1. INTRODUCTION

When fluid flow and heat transfer problems are to be solved by a finite volume approach with primitive variables, a staggered grid is often adopted to eliminate the checkerboard pressure field. In the staggered grid arrangement, the velocities are stored at the cell-faces, whereas the pressure and other scalars are stored at the cell-centers or the main grid nodes. Because the velocity components and pressure are located at displaced or staggered locations in the staggered grid [1,2], it is quite inconvenient when this grid system is to be extended to curvilinear non-orthogonal coordinates or to 3-D coordinates. Moreover, the staggered grid has obvious disadvantages when the multi-grid technique is to be implemented to accelerate the convergence rate of solving algebraic equation because different multi-grids and the related interpolation operators must be applied to different variables. In recent years, efforts have been devoting to solve Navier-Stokes equations on a non-staggered grid, in which the velocities and the pressure are stored at the same grid nodes. Though practically attractive, the arrangement is beset with by major difficulty in eliminating the checkerboard pressure field.

The cures for the checkerboard pressure were proposed by several researchers [3-6]. Rhie and Chow firstly proposed a method, in which the cell-face velocities are interpolated via what is called the momentum interpolation practice rather than linear interpolation. In the Rhie-Chow's method, momentum interpolation for the face velocity is used in two procedures: the one for determining the coefficients of the momentum discretized equations, and the other for deriving the pressure-correction equation. Numerical practices have shown that the Rhie-Chow's interpolation method may lead to some uncertainty of the final numerical solution, dependent on the values of under-relaxation factors for velocities. Some techniques have been proposed to overcome this difficulty [7-9]. Other methods used to cure the checkerboard difficulty may be found in [3] and [5]. Over the last decade, the momentum interpolation method is probably the most extensively adopted in the CFD/NHT community. In present paper, a method for viscous incompressible flows with collocated grid system is presented. In this method, the momentum interpolation to calculate the interface velocities is only used for deriving and computing the pressure correction equation while for the determination of coefficients the linear interpolation is adopted. In order to eliminate the role of under-relaxation factor, a simple and efficient method is proposed. Special computation is performed to demonstrate the ability of this method to eliminate the checkerboard pressure field. Through the numerical computations of six standard test problems with benchmark solutions, it can be concluded that this method is feasible.

2. DISCRETIZATION EQUATIONS AND SOLUTION ALGORITHM

Governing Equations

Consider 2-D, steady state, no internal heat sources, laminar fluids flow and heat transfer problems. In the Cartesian coordinates, the governing equations can be written as

$$\frac{\partial(\rho uu)}{\partial x}+\frac{\partial(\rho uv)}{\partial y}=-\frac{\partial p}{\partial x}+\frac{\partial}{\partial x}\left(\mu\frac{\partial u}{\partial x}\right)+\frac{\partial}{\partial y}\left(\mu\frac{\partial u}{\partial y}\right)+S_u \tag{1}$$

$$\frac{\partial(\rho uv)}{\partial x}+\frac{\partial(\rho vv)}{\partial y}=-\frac{\partial p}{\partial y}+\frac{\partial}{\partial x}\left(\mu\frac{\partial v}{\partial x}\right)+\frac{\partial}{\partial y}\left(\mu\frac{\partial v}{\partial y}\right)+S_v \tag{2}$$

$$\frac{\partial(\rho uT)}{\partial x}+\frac{\partial(\rho vT)}{\partial y}=\frac{\partial}{\partial x}\left(\frac{k}{c_p}\frac{\partial T}{\partial x}\right)+\frac{\partial}{\partial y}\left(\frac{k}{c_p}\frac{\partial T}{\partial y}\right)+S_T \tag{3}$$

$$\frac{\partial(\rho u)}{\partial x}+\frac{\partial(\rho v)}{\partial y}=0 \tag{4}$$

The finite difference forms of equations (1)~(3) are now derived using the control volume method with a collocated grid showed in Fig.1. In contrast with the staggered grid, in the collocated grid all the variables are stored at the same location. Therefore, only one set of control volume is needed. The details of derivation may be found in [1] or [5]. The forms of the discretization equations for u, v and T are almost identical, except the expression of the source term. For the purpose of simplicity, only the discretized u-momentum equation is enumerated. It reads

$$a_P u_P=\sum a_{nb}u_{nb}+b+(1-\alpha)a_P u_P^0-\Delta y_P(p_e-p_w) \tag{5a}$$

where a_{nb} represents the coefficients a_E, a_W, a_N and a_S.

For simplicity, set

$$B_P=\left(\sum a_{nb}u_{nb}+b+(1-\alpha)a_P u_P^0\right)/a_P \tag{5b}$$

Then we have

$$u_P=B_P-\left(\Delta y_P/a_P\right)\cdot\left(p_e-p_w\right) \tag{5c}$$

The pressure at the control volume interface will be determined by linear interpolation between the pressure of its two neighbor grid points.

Interpolation Formulas of Velocity Components at Interfaces for Coefficient Determination

As shown in Fig.1, in the collocated grid, the velocities are calculated at the same grid points as those for pressure and temperature. Thus to calculate the coefficient a_{nb}, the velocities at the control volume interface must be interpolated. In this study, the linear interpolation method is implemented, that is to say,

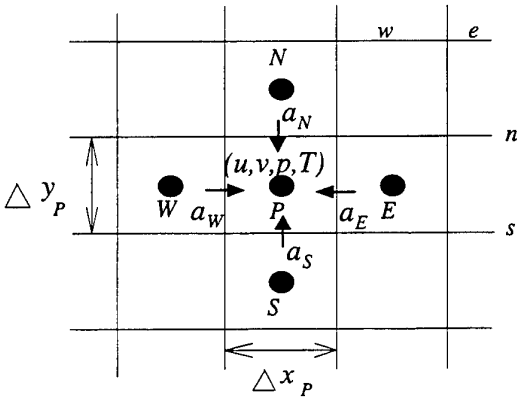

Fig. 1 Collocated grid

$$u_e = f_e^+ u_E + f_e^- u_P \tag{6}$$

where f_e^+, f_e^- are the linear interpolation factors defined as

$$f_e^+ = \frac{\overline{Pe}}{\overline{PE}}, \quad f_e^- = \frac{\overline{eE}}{\overline{PE}} \tag{7}$$

Similarly,

$$u_w = f_w^+ u_P + f_w^- u_W ; v_n = f_n^+ u_N + f_n^- u_P ; v_s = f_s^+ u_P + f_s^- u_S \tag{8}$$

Discretized Continuity Equation and Pressure Correction Equation

The discretized continuity equation may be written as

$$(\rho u_e - \rho u_w)\cdot \Delta y_P - (\rho v_n - \rho v_s)\cdot \Delta x_P = 0 \tag{9}$$

where the velocities at the control volume interfaces, u_e, u_w, v_n and v_s, must be interpolated. According to Peric et al. [4], for determined the interfacial velocity u_e, following interpolation technique is used.

First, by using equation (5c) at nodes P and E, we have

$$u_P = B_P - [(\Delta y/a_P)\cdot(p_e - p_w)]_P \tag{10}$$

$$u_P = B_E - [(\Delta y/a_P)\cdot(p_e - p_w)]_E \tag{11}$$

Then, using the same formula as Eqs. (12)-(19), the interface velocity, u_e, is expressed as:

$$u_e = B_e - [(\Delta y/a_P)\cdot(p_E - p_P)]_e \tag{12}$$

where B_e is the linear interpolation of B_P and B_E in equations (12) and (13), and $(a_P)_e$ is the harmonious interpolation of $(a_P)_P$ and $(a_P)_E$, i.e.

$$B_e = f_e^+ \cdot B_E + f_e^- \cdot B_P ; \frac{1}{(a_P)_e} = \frac{f_e^+}{(a_P)_E} + \frac{f_e^-}{(a_P)_P} \tag{13}$$

Set $d_e = \Delta y/a_P$, we have

$$u_e = B_e - d_e(p_E - p_P) \tag{14}$$

Similarly

$$u_w = B_w - d_w(p_P - p_W); v_n = B_n - d_n(p_N - p_P); v_n = B_n - d_n(p_N - p_P) \tag{15}$$

In equations (15), $d_n = (\Delta x/a_P)_n$, and $d_s = (\Delta x/a_P)_s$. It is to be noted that the introduction of Eqs. (14)-(15) is the key point of the success of the momentum-interpolation, which includes the two-neighboring pressure values aside of the interface into the interface velocity determination, thus guarantee the linkage between pressure and velocity. In addition, the pressure correction equation related point *P* and its four neighbors may also be easily derived from continuity by using equation (14)-(15). The derivation procedure is the same as for the staggered grid system. The details of the derivation may be found in [1]. Only the resulting pressure correction equation is

given below:

$$A_P p'_P = A_E p'_E + A_W p'_W + A_N p'_N + A_S p'_S + S_p \tag{16}$$

where p' is the pressure correction value and

$$\begin{aligned} &A_P = A_E + A_W + A_N + A_S \\ &A_E = \rho_e d_e \Delta y_e ; A_W = \rho_w d_w \Delta y_w ; A_N = \rho_n d_n \Delta x_n ; A_S = \rho_s d_s \Delta x_s \end{aligned} \tag{17}$$

$$S_p = (\rho u^*)_w \Delta y_w - (\rho u^*)_e \Delta y_e + (\rho v^*)_s \Delta x_s - (\rho v^*)_n \Delta x_n \tag{18}$$

In equation (18) u^* and v^* are the resulting velocities based on a guessed pressure field p^*, and the interface values are also interpolated by momentum interpolation method.

3. ROLE OF UNDER-RELAXATION IN AN ITERATIVE ALGORITHM

According to Majumdar's analysis, when an iterative algorithm is used and under-relaxation technique is incorporated, equations (14)~(15) for determining the interfacial velocities are actually mixed expressions which include two portions: α portion of the momentum interpolation and (1-α) portion of the linear interpolation. Therefore, the converged solution of the interfacial velocity does not converge to the desired value of the full momentum interpolation, leading to some dependence of the numerical solution with the value of α. To eliminate this inconsistency, Majumdar proposed a method [7] with a more complicate expression which can ensure that for whatever value of α, the converged value of interface velocity is the one of the full momentum interpolation (α=1). Thus we may exclude the effect of the under-relaxation factor by simply setting its value equal 1 in the d's equation. For example, the equation for d_e may expressed as:

$$d_e = \Delta y_e \frac{(a_P)_P (a_P)_E}{f_e^+ (a_P)_P + f_e^- (a_P)_E} \cdot \alpha \tag{19}$$

Similar equations may be written for other d-terms .

4. RESULTS AND DISCUSSIONS

In this section, the results of three test problems will be presented. The three problems (see Fig. 2)are natural convection in a square enclosure, lid-driven flow in a polar-cavity, and sudden enlarge flow in a tube. For the three tested problems, three coordinate systems, i.e. Cartesian, 2-D cylindrical and polar coordinate are used. The convection-diffusion terms in the momentum and energy equations are discretized by the central difference scheme (CDS). The resulting algebraic equations are solved by the SLUR method incorporated with the block correction technique. The iteration is considered to be converged if the following two criteria are both satisfied.

$$S_{max} \le 10^{-6}; \left| \phi - \phi^0 \right| \le 10^{-3} \tag{20}$$

where S_{max} is the maximum value of the residual in each control volume and ϕ stands for one of the variables u, v, T and p.

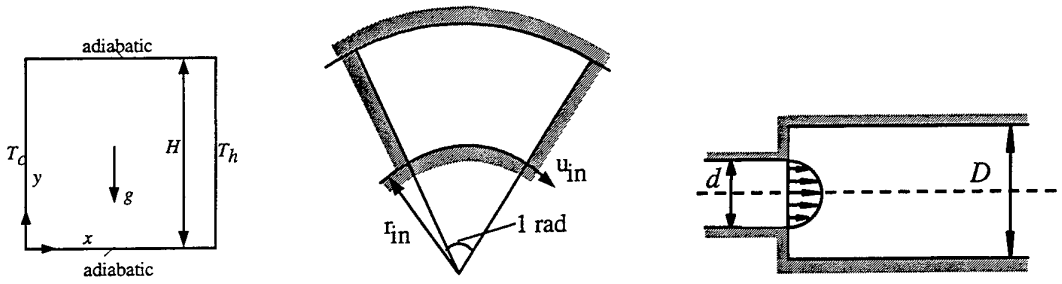

(a) Natural convection in enclosure

(b) Lid-driven flow in a polar cavity

(c) Sudden enlarge flow in a tube

Fig. 2 Three tested cases

Problem 1: Natural Convection in a Square Enclosure

Natural convection in a square enclosure is a standard problem in numerical heat transfer. The Boussinesq hypothesis is adopted and the numerical calculations are conducted under the conditions of $Ra=10^3$, 10^4, 10^5 and 10^6 with grid numbers 82×82. For comparison, the results and the benchmark solutions [10] are listed in Table 1.

Table 1 Comparison of Heat Transfer Characteristics of Problem 1

	This work	De Vahl Davis[10]
$Ra=10^3$		
Nu_{mean}	1.121	1.118
Nu_{max} (y/H)	1.504(0.0880)	1.505(0.092)
Nu_{min} (y/H)	0.702(0.9993)	0.692(1.000)
$Ra=10^4$		
Nu_{mean}	2.245	2.243
Nu_{max} (y/H)	3.520(0.1457)	3.528(0.143)
Nu_{min} (y/H)	0.599(0.9993)	0.586(1.000)
$Ra=10^5$		
Nu_{mean}	4.526	4.519
Nu_{max} (y/H)	7.675(0.0778)	7.717(0.081)
Nu_{min} (y/H)	0.7659(0.9993)	0.729(1.000)
$Ra=10^6$		
Nu_{mean}	8.840	8.799
Nu_{max} (y/H)	17.447(0.0420)	17.925(0.0378)
Nu_{min} (y/H)	1.105(0.9993)	0.989(1.000)

Problem 2: Lid-Driven Flow in a Polar Cavity

In the polar coordinate, driven flow in a polar cavity is used as a benchmark solution [11]. For the coaxial annulus, its inner diameter is r_1 and its outer diameter is r_2. The angle of the annulus is 1 radian. The inner circle rotates along the axial. Computation was conducted for the case of Re=350 on the grid of $80(\theta)\times80(r)\times4(z)$. Comparison of profiles of u- and v- velocities along the central line of θ- directions was given in Fig. 3.

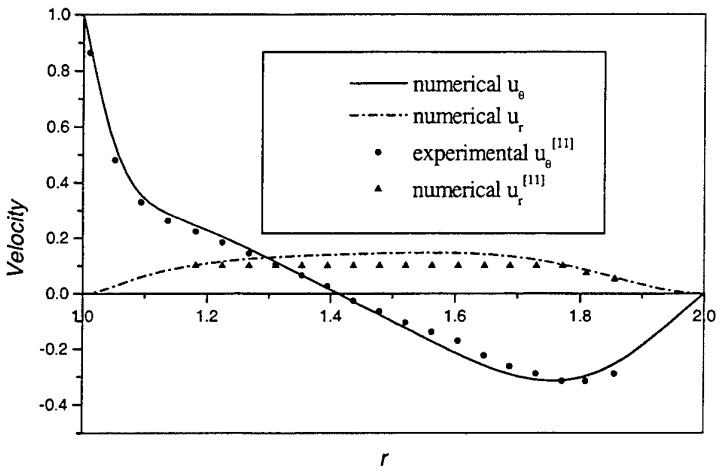

Fig.3 Comparison of profiles of u- and v- velocities along the central line of θ - directions

Problem 3: Sudden Enlarge Flow a Cylindrical Tube

The third tested problem is a sudden enlargement in a cylindrical system. The ratio of a small and large cylinder, d/D, is 0.5. The inlet velocity is in distribution of parabolic. A code developed for three dimensional coordinates was used. In the computation, the grid used is $4(\theta)\times31(r)\times41(z)$. Comparison of computed reattachment point length with those in [12] is shown in Table 2.

Table 2 Comparison of Computed Reattachment Point Length with those in [12]

Re	Computed results	Reference[9]	Deviation (%)
50	2.38	2.2	8.4
100	4.488	4.3	4.4
150	6.73	6.5	3.6
200	9.14	8.8	3.9

The numerical results of the above three problems show the feasibility and reliability of the present simple method for the collocated grid system. To ensure that the proposed method can effectively eliminate the checkerboard pressure fields and discard the effect of the under-relaxation factor, special computations were performed. The results are presented in the subsequent paragraphs

Ability to Eliminate the Checkerboard Pressure Field

To demonstrate the ability of the present collocated grid to eliminate checkerboard pressure field, computation test was performed for problem 1 by taking a checkerboard field as initial pressure field and the converged velocities as the initial distribution. Numerical computations reveal that the present collocated grid method can eliminate the unrealistic pressure fields in a few iterations and the converged solutions of both velocity and pressure are the same as the pre-conducted solutions (Fig.4).

Role of Under-Relaxation

As aforementioned, when an iterative algorithm is used and under-relaxation technique is incorporated, the equations (14)~(15) for determining the interfacial velocities are mixed expressions of linear momentum interpolations. In this study, equation (19) is adopted to eliminate the role of under-relaxation. For problem 1, computations were conducted with the grid points 22×22 and $Ra=10^4$ while α varied from 0.4 to 0.8 respectively. The distribution of the local Nusselt number along the high temperature wall is listed in Table 3. It can be seen that the role of under-relaxation can be neglected.

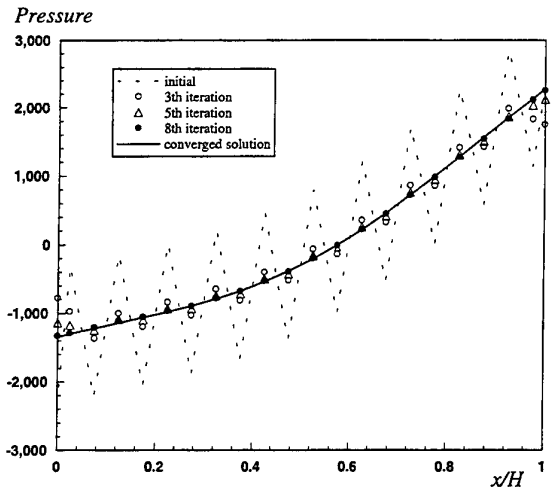

Fig.4 Change of pressure field during iteration

Table 3 The Distribution of the Local Nusselt Number Along the High Temperature Wall

y/H	Local Nusselt Number	Local Nusselt Number
	α=0.4	α=0.8
0.025	3.55591	3.55592
0.125	3.68047	3.68049
0.225	3.55164	3.55165
0.325	3.21263	3.21265
0.425	2.76445	2.76447
0.525	2.28930	2.28931
0.625	1.79999	1.80001
0.725	1.32044	1.32045
0.825	0.91227	0.91229
0.925	0.66961	0.66963

5. CONCLUSION

In the present work, SIMPLE algorithm is implemented with a simplified collocated grid scheme. The momentum interpolation is only used for the discretization of the continuity equation. The effect of the under-relaxation factor is discarded by setting its value equal to 1 in the momentum interpolation expression. The numerical results of three test cases show that the proposed numerical methods are feasible and reliable,

REFERENCES

1. S. V. Patankar,, *Numerical Heat Transfer and Fluid Flow*, Hemisphere (1980).
2. W. Q. Tao, *Numerical Heat Transfer*. Xi'an Jiaotong University Press (1998).
3. M. Rhie and W. L. Chow, AIAA J. v.21, pp.1525-1532 (1983).
4. G. D. Thiart, Numerical Heat Transfer v.18, pp.81-95 (1990).
5. A. W. Date, Int. J. Heat Mass Transfer v.36, pp.1913-1922 (1993).
6. M. Peric, R. Kessler, and, G. Scheuerer, Computers & Fluids v.16, pp.389-403 (1988).
7. S. Majumdar, Numerical Heat Transfer v.13, pp.125-132 (1988).
8. T. F. Miller and F. W. Schmidt, Numerical Heat Transfer v.14, pp.213-233 (1988).
9. W. Rodi, S. Majumdar and B. Schonung, Comput. Meth. Appl. Mech. Eng. v.75, pp.369-392 (1982).
10. G. De Vahl Davis, Int. J. Numer. Methods fluids v.3, pp.249-264 (1994).
11. Fuch, N. Tillmark, Int. J. Numer. Methods Fluids v.5, pp.311-329 (1985).
12. E. Q. Macagno and T. K. Hung, J. Fluid Mech. v.28, pp.43-61 (1967).

EFFECT OF ASPECT RATIO ON MIXED CONVECTIVE HEAT TRANSFER IN A HORIZONTAL RECTANGULAR DUCT

Koichi Ichimiya
Department of Mechanical System Engineering
Yamanashi University
Email: ichimiya@ccn.yamanashi.ac.jp; Fax: +81-(0)55-220-8434

Koji Toriyama
Department of Mechanical System Engineering
Yamanashi University
Email: toriyama@ccn.yamanashi.ac.jp

Keywords: mixed convection, rectangular duct, aspect ratios, numerical analysis

ABSTRACT. The characteristics of heat transfer and flow on three-dimensional mixed convection in horizontal rectangular ducts with heated lower wall and cooled upper wall were examined numerically for five kinds of aspect ratios. The working fluid was water and the flow was assumed to be laminar and incompressible. The SIMPLE procedure and QUICK scheme were used to solve the governing equations through a control volume. The kinematic viscosity and the thermal conductivity of the water depend on temperature. The aspect ratios affected the generation and the number of the recirculated flows. The local and averaged Nusselt numbers corresponding to the flow were examined on the heated and the cooled walls, respectively.

1. INTRODUCTION

In the present technologies, many sophisticated small size machines and devices can be found. In such a facility, laminar flow should be utilized because of low noise and vibration. Therefore, it is important to study how laminar mixed convection works under various thermal flow conditions. One of the authors has studied systematically on laminar mixed convection in a horizontal square channel with various heat transfer conditions. For constant wall temperatures, the flow reversal at the entrance section was analyzed [1,2] and was recognized by flow visualization [3]. For side wall heating and cooling, the swirl flow existed along the flow direction and the shear stress increased with increase of Gr/Re^2 [4]. In addition, effect of fluid temperatures was also evaluated numerically [5]. In the practical application, effect of aspect ratio of a rectangular duct was reported by Chou et al. [6] and Abou-Ellail et al. [7]. However, three-dimensional behavior has not discussed sufficiently. In the present study, three-dimensional laminar mixed convection in a horizontal rectangular duct with lower heated wall and upper cooled wall was analyzed numerically for five kinds of aspect ratios. Heat transfer on the upper and lower wall and the flow were examined for each aspect ratio.

2. NUMERICAL ANALYSIS

Fig. 1 shows the physical model and the coordinate system. The flow passage is a horizontal rectangular duct whose size is a height and b width. The aspect ratio is AR=b/a and the equivalent hydraulic diameter is L=2ab/(a+b). The water as a working fluid flows along the x-axis and the gravity acts along the negative direction of y-axis. The thermally insulated section (x/L=0~2) is set at the entrance. The heat transfer section (x/L=2~14) has the high temperature (T_H) lower wall and the low temperature (T_L) upper wall. The kinematic viscosity and the thermal conductivity of water depend on temperature. Buoyancy force is expressed by Boussinesq approximation. The high and low wall temperatures, T_H and T_L for various ratios were determined at constant Grashof number $Gr=2.91\times10^5$.

Governing equations, the conservation of mass, momentum and energy, are expressed by equations (1), (2) and (3).

$$\frac{\partial u_j}{\partial x_j}=0 \tag{1}$$

$$\frac{\partial u_i}{\partial t}+\frac{\partial u_j u_i}{\partial x_j}=-\frac{1}{\rho}\frac{\partial p}{\partial x_i}+\frac{\partial}{\partial x_j}\nu\frac{\partial u_i}{\partial x_j}-g\beta(T-T_0) \tag{2}$$

$$\frac{\partial \rho C_p T}{\partial t}+\frac{\partial u_j \rho C_p T}{\partial x_j}=\frac{\partial}{\partial x_j}\lambda\frac{\partial T}{\partial x_j} \tag{3}$$

Boundary and initial conditions are as follows:

(1) Entrance and initial velocities are fully developed laminar profile [8] corresponding to Re=200.

(2) Entrance section (x/L=0~2) is thermally insulated. Entrance temperature T_0 is 30 °C. Wall temperatures (T_H and T_L) were determined at $Gr=2.91\times10^5$, shown in Table 1. Therefore, Richardson number Gr/Re^2 is 7.3 for all of the aspect ratios.

(3) At the exit, the velocity gradient and the second derivative of temperature along the axial direction are zero.

The unsteady three-dimensional governing equations were solved numerically by finite difference method. Velocity and pressure were obtained by using the pressure correction method (SIMPLE algorithm) [9]. QUICK scheme [10] was implemented to calculate the convection flux through the cell face of control volumes. Temperature dependence of the kinematic viscosity and the thermal conductivity (Table 1) was considered in the analysis. The state was approached to be steady.

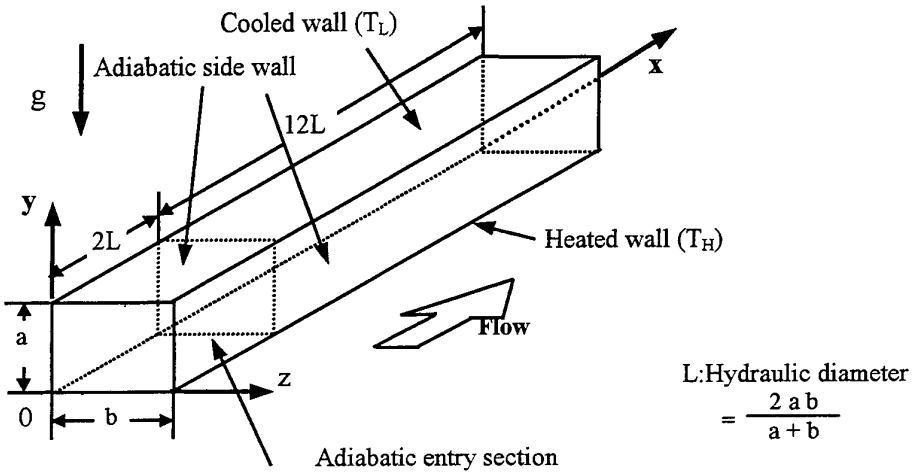

Fig. 1. Coordinate system

Table 1. Channel Size, Wall Condition and Thermal Properties

Aspect Ratio	0.25	0.5	1	2	4
Size (m)	0.187×0.033×0.0083	0.187×0.02×0.01	0.28×0.02×0.02	0.187×0.01×0.02	0.187×0.0083×0.033
Mesh	224×40×10	280×30×15	280×20×20	280×15×30	224×10×40
L (m)	0.0133	0.0133	0.02	0.0133	0.0133
T_H (°C)	46.88	46.88	35.0	46.88	46.88
T_L (°C)	13.13	13.13	25.0	13.13	13.13
T_0 (°C)	30.0				

3. RESULTS AND DISCUSSIONS

Flow Field

Velocity vectors at x/L=10 are presented in Figs. 2. Height and width of the cross section divided by equivalent hydraulic diameter L are dimensionless. In the case of AR=1, two rising flows are produced along both side walls from the lower wall and two falling flows along the side walls from the upper wall. These rising and falling flows impinge near the center of the flow passage. As the result, four recirculating flows are generated symmetrically. In the case of AR=0.5, symmetry is broken up and three different recirculating flows are generated. In the case of AR=0.25, four symmetrical recirculating flows can be found like them at AR=1. On the other hand, in the case of AR=2, a rising flow is produced from the center of the lower wall and large clockwise and anticlockwise recirculating flows are symmetrically constructed along the whole height. In the case of AR=4, the flow state at AR=2 is expanded horizontally.

Fig. 3 shows the intensity of the secondary flow defined as the ratio of the root of the maximum value of summation of v and w square across the section and the average velocity. The absolute values of the secondary flows for AR=0.25, 0.5, 2 and 4 are higher than that for AR=1. The intensities at AR<1 are higher than those at

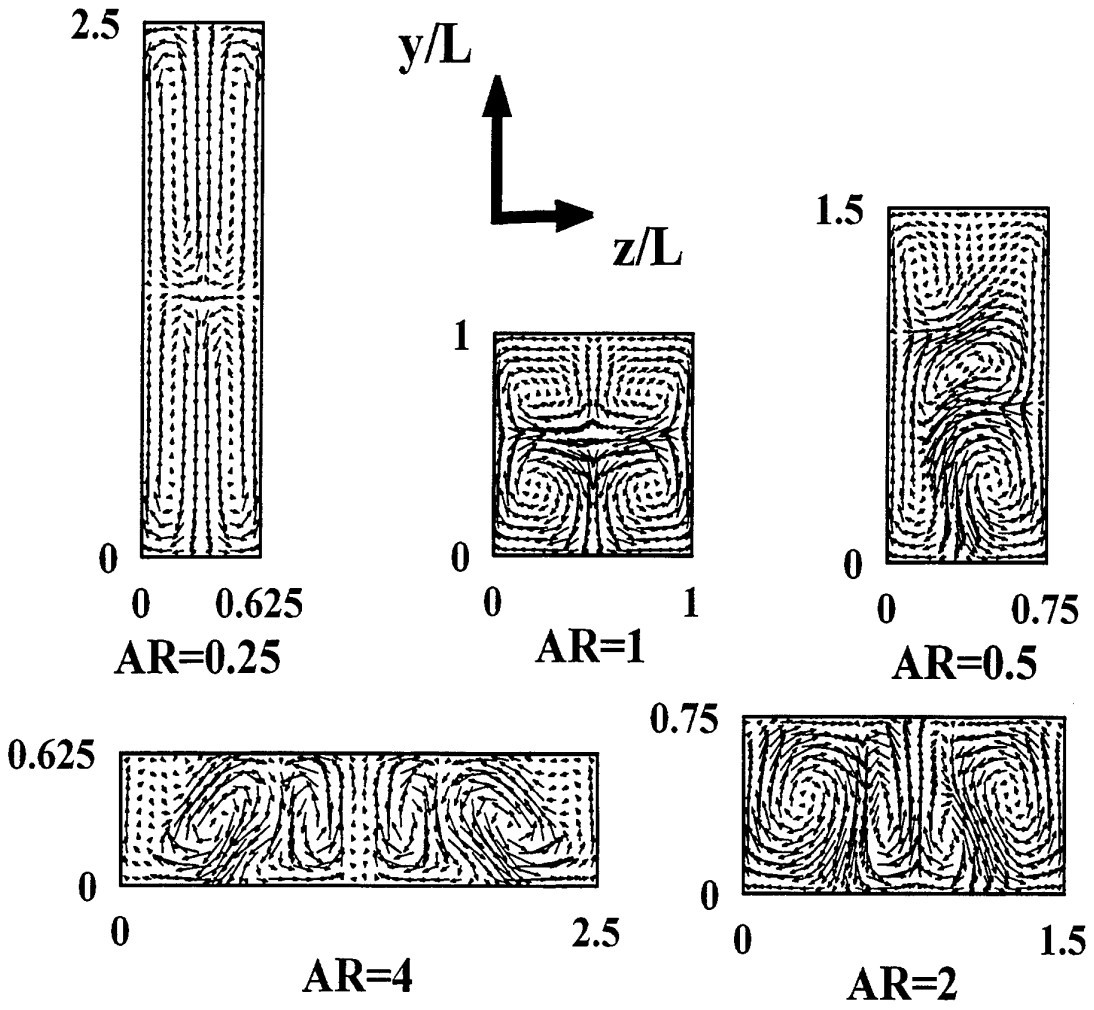

Fig. 2. Velocity vector at x/L=10

AR>1 along the first half of the flow passage (2<x/L<8). However, the state is inverse along the latter half of the flow passage (8<x/L<12). This depend on the development of the recirculating flows. The intensities at AR=0.25 and 1.0 increase near exit (12<x/L<14). The velocity vectors and isotemperature lines at x/L=13 are presented in Fig. 4. The symmetry of the secondary flow is broken up for AR=0.25. Two large recirculating flows due to the rising flows along the side walls dominate the secondary flow.

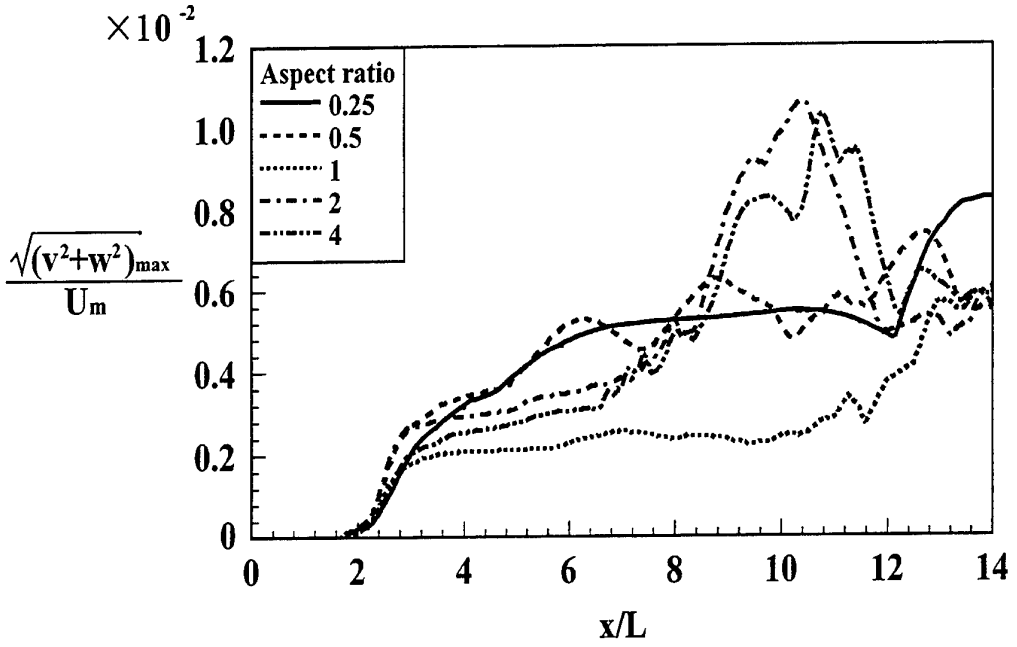

Fig. 3. Secondary flow

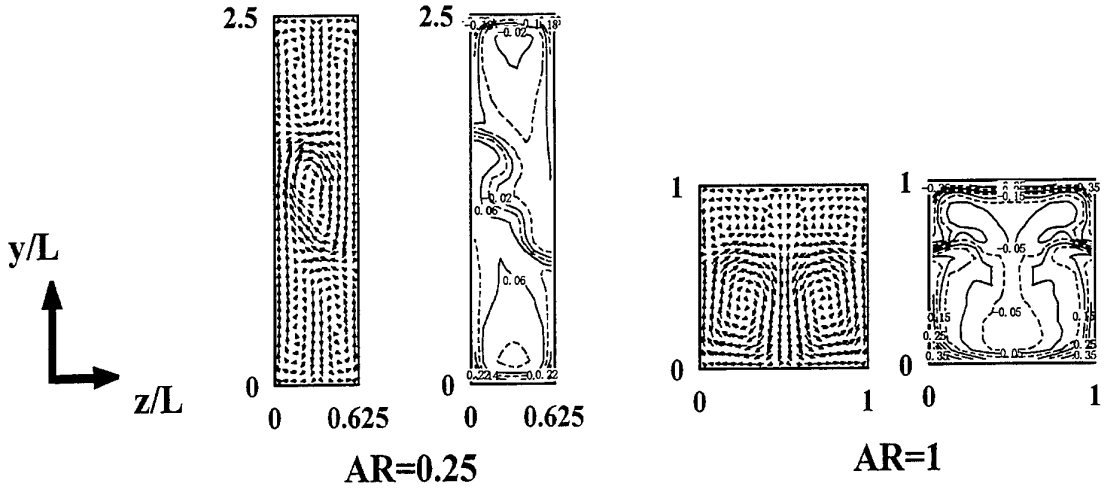

Fig. 4. Velocity vector and isothermal lines at x/L=13

Heat Transfer

Figs. 5 show the isothermal lines at x/L=10 corresponding to Fig. 2. Dimensionless temperature Θ is defined by $\Theta=(T-T_L)/(T_H-T_L)$. Therefore, dimensionless temperatures at upper wall and lower wall are $\Theta=0$ and $\Theta=1$, respectively. Temperature gradients at the impingement point of rising and falling flows become high at AR<1.

In the case of AR=2, one thermal plume rises and in the case of AR=4, two thermal plumes separate from the center of the lower wall. The highest temperature regions at the top of the thermal plumes are closed.

Local Nusselt numbers on the lower wall and the upper wall are represented in Fig. 6(a) and Fig. 6(b), respectively. Local heat transfer is stable at low aspect ratio. The closed regions of iso-Nusselt number appears periodically as AR increases. Two peaks exist on the lower wall at about x/L=10 due to the impingement of cooled fluid for AR=2 (Fig. 6(a)) and on the other hand, two peaks at about x/L=9 and one peak at about x/L=10 appear on the upper wall (Fig. 6(b)). Several peaks of local Nusselt number can be found corresponding to the local recirculating flows along the latter half of the flow passage. Four peaks are produced at both edges of upper wall due to the impingement of hot rising fluid along the side walls (Figure 6(b)).

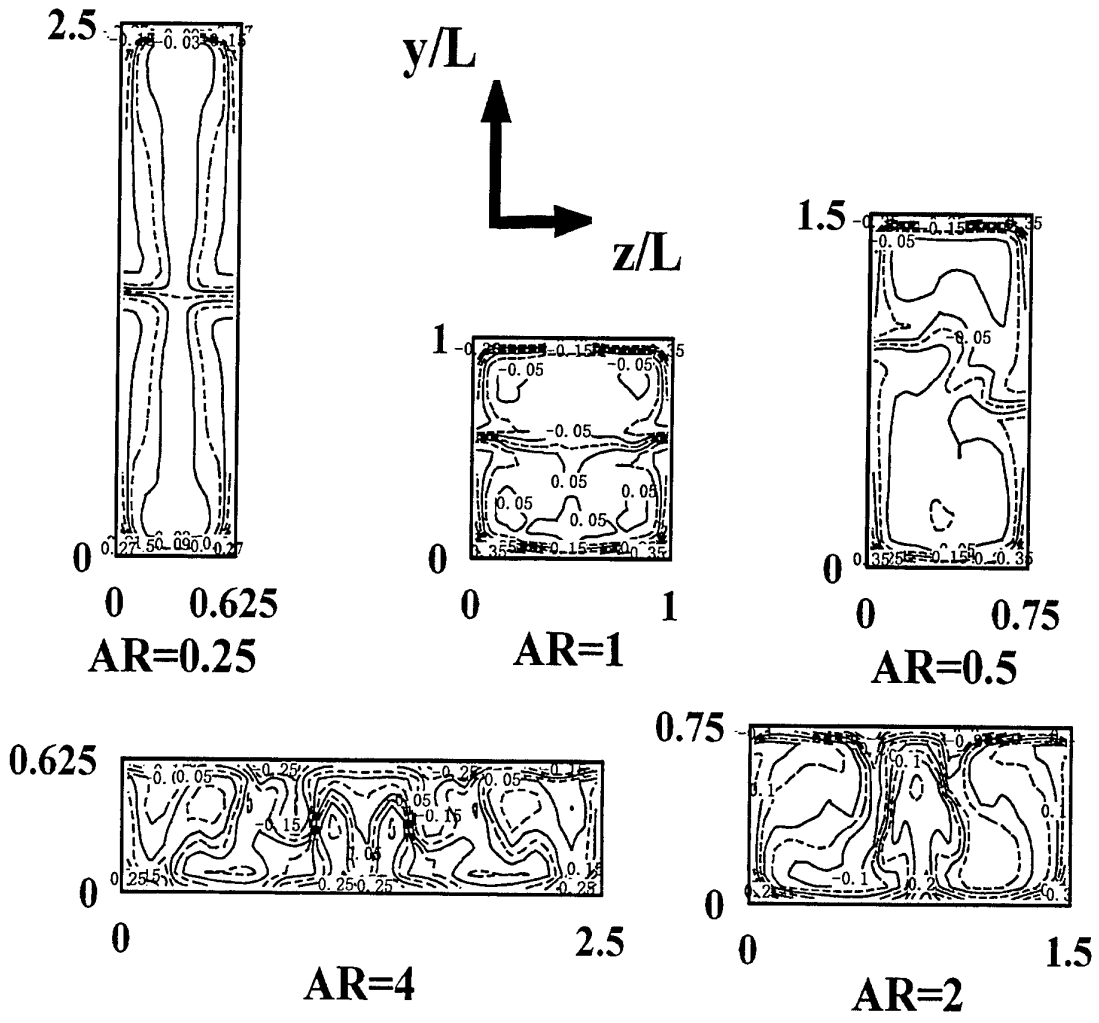

Fig. 5. Isothermal line at x/L=10

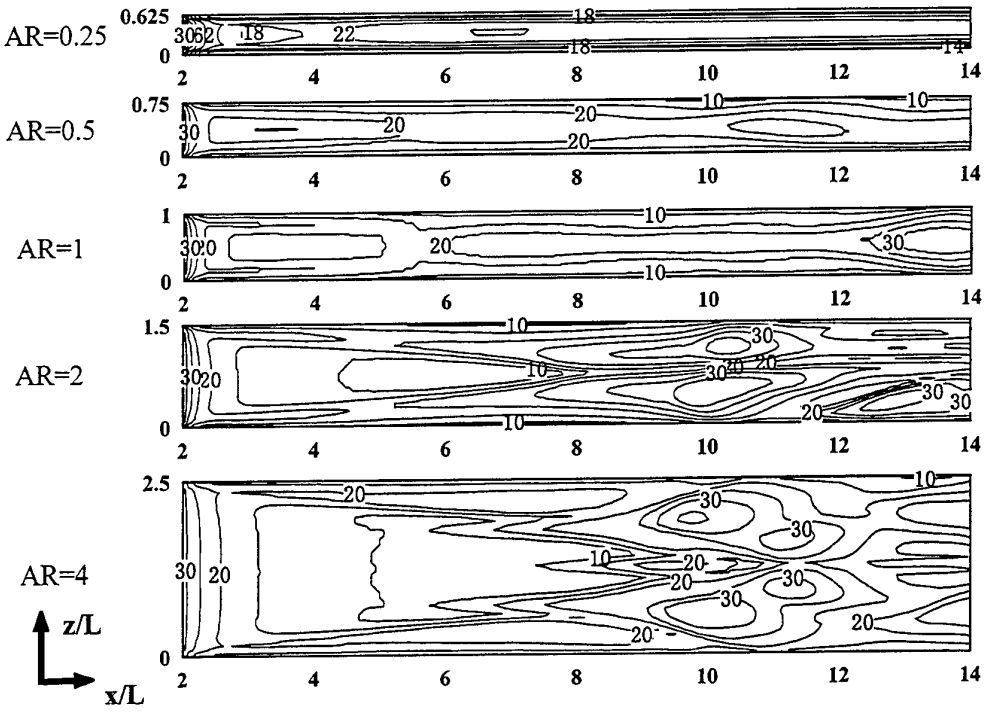

(a) On lower heated wall

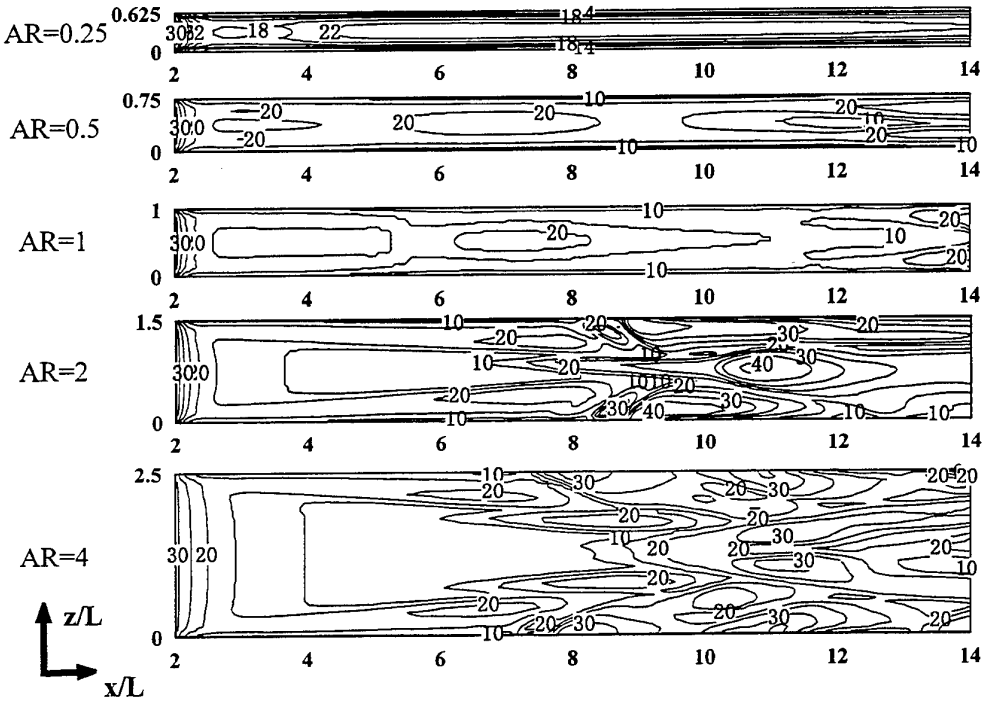

(b) On upper cooled wall

Fig. 6. Local Nusselt number

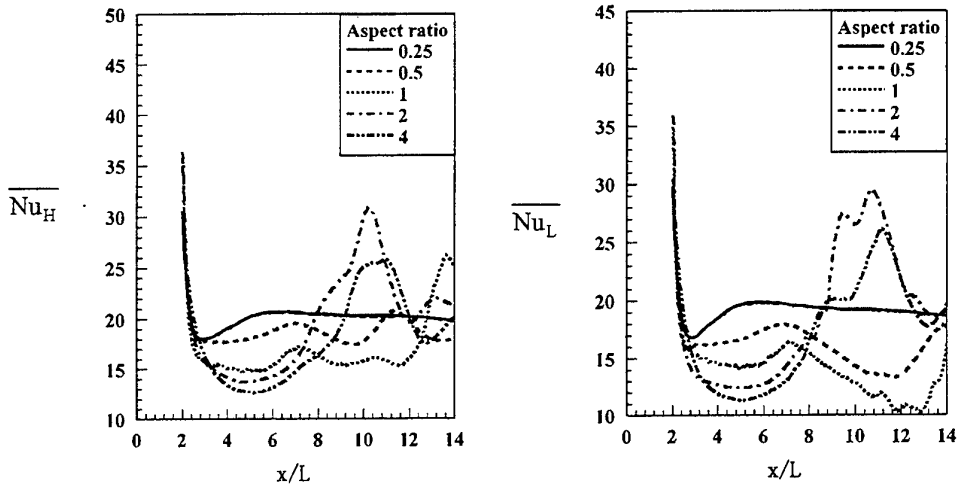

(a) On lower heated wall (b) On upper cooled wall

Fig. 7. Average Nusselt number along flow direction

Figs. 7 (a) and (b) show the longitudinal Nusselt numbers averaged along the width on the lower wall and the upper wall, respectively. The Nusselt numbers $\overline{Nu_H}$ and $\overline{Nu_L}$ on both walls increase with decrease of AR along the first half of the flow passage. This depend on the development of boundary layer with decrease of width and means that forced convection is dominant locally. Along the latter half of the flow passage, effect of the natural convection appears. $\overline{Nu_H}$ and $\overline{Nu_L}$ for AR=2 and 4 increase and peak at about x/L=10 (Fig. 7 (a)) and about x/L=11 (Fig. 7(b)), respectively. Both Nusselt numbers for AR=1 are lowest in those for other aspect ratios.

4. CONCLUSIONS

The characteristics of heat transfer and flow on three-dimensional mixed convection in horizontal rectangular ducts with heated lower wall and cooled upper wall were examined numerically for five kinds of aspect ratios at constant Richardson number. Conclusions of this study are as follows:

1. Various aspect ratios affect the generation of the recirculating flows and the number of them.
2. Rising flows are produced along the side walls for AR>1.
3. Nusselt numbers on both walls are longitudinally divided into two regions, namely, along the first half and the latter half of the flow passage. $\overline{Nu_H}$ and $\overline{Nu_L}$ have the dependency of aspect ratio along the first half of the flow passage. They peak at a certain point along the latter half of the flow passage for AR>1.

REFERENCES

1. T. Kunugi, K. Ichimiya and Y. Sakamoto, Proceedings of the 10th International Heat Transfer Conference (Brighton, U.K.), v.5, pp.501-506 (1994).
2. K. Ichimiya, T. Kunugi and Y. Sakamoto, Proceedings of the 4th ASME/JSME Thermal Engineering Joint Conference (Maui, U.S.A.), v.1, pp.131-138 (1995).
3. Y. Sakamoto, T. Kunugi and K. Ichimiya, Proceedings of the 10th International Symposium of Transport Phenomena (Kyoto, Japan), v.1, pp.535-539 (1997).
4. Y. Sakamoto, T. Kunugi and K. Ichimiya, Transactions of JSME (B), v.61, No.586, pp.2228-2234 (1995).
5. K. Ichimiya and K. Toriyama, Proceedings of the 5th International Conference on Advanced Computational Method in Heat Transfer (Krakow, Poland), v1, pp.317-326 (1998).
6. F.C. Chou and W.Y. Lien, Warme und Stoffubertragung, v.26, pp.121-127 (1991).
7. M.M.M. Abou-Ellai and S.M. Morcos, Journal of Heat Transfer, v.105, pp.925-928 (1983).
8. R.K. Shah and A.L. London, Advanced in Heat Transfer, Academic Press, 197 (1978).
9. S.V. Patankar, Numerical Heat Transfer and Fluid Flow, Hemisphere, (1980).
10. B.P. Leonard, Computer Methods in Fluid, Pentech Press, Plymouth, pp.159-195 (1980).

NUMERICAL PREDICTION OF CONVECTIVE HEAT TRANSFER AND SECONDARY FLOW CHARACTERISTICS IN A CURVED RECTANGULAR DUCT WITH CONCAVE HEATING

Tilak T Chandratilleke, Nursubyakto and Ala Altraide
School of Mechanical Engineering, Curtin University of Technology
GPO Box U1987, Perth WA6845, Western Australia
Tel: +61 8 9266 7661, Fax: +61 8 9266 2681
Email: tilak@vesta.curtin.edu.au

Keywords: secondary flow, convective heat transfer, curved channel

ABSTRACT. A numerical simulation is developed to examine the secondary flow characteristics in a curved rectangular duct with external heating on the concave wall of the duct. The general governing equations of momentum, mass continuity and energy of the flow are non-dimensionalised and transformed into vorticity-stream function formulation. The equations are discretised using finite volume method and the dynamical variables are defined on a stagger grid. The resulting penta-diagonal system of linear algebraic equations is solved using Strongly-Implicit-Procedure. Numerical simulation is performed on ducts of aspect ratios between 1 to 8 and selected curvature. The external wall heating is varied up to 200 W/m^2 and the numerical solutions are obtained for Dean number ranging from 20-500. Results are presented to illustrate the effects of Dean number, aspect ratio, buoyancy force and external heating on the flow parameters.

NOMENCLATURE

a	Channel width
b	Channel height
C	Streamwise pressure drop
D_e	Hydraulic diameter
K	Dean number, $Re(D_e/R)^{1/2}$
k	Thermal conductivity
P, p	Pressure and dimensionless pressure
Pe	Peclet number
Pr	Prandtl number
q''	Heat flux
R	Channel radius of curvature
Re	Reynolds number, $\frac{\overline{W}D_e}{\nu}$
T	Temperature
U, V, W	Velocity components
u, v, w	Dimensionless velocity components
$\overline{W}$	Average axial velocity
X, Y, Z	Displacement coordinates
x, y, z	Dimensionless coordinates
α	Thermal diffusivity
β	Dimensionless radius of curvature, R/D_e
$\tilde{\beta}$	Temperature coefficient
ε	Infinite norm
γ	Channel aspect ratio, b/a
μ	Kinematic viscosity
ν	Dynamic viscosity
θ	Dimensionless temperature
ρ	Density
ξ	Vorticity
ψ	Streamfunction

1. INTRODUCTION

The centrifugal forces acting on a fluid flowing in a curved duct cause generation of a pair of counter-rotating vortices and development of secondary flow in the passage. Beyond a certain critical flow condition, additional secondary vortices appear at the outer concave wall of the flow passage. This is commonly referred to as Dean's hydrodynamic instability and the additional vortices are termed as the Dean vortices. It is evident that these vortices tend to promote turbulence in the flow and have a profound influence on the heat transfer characteristics in the fluid [1]. Attempts have been made to exploit these effects in the design of compact heat exchanger for improved effectiveness in waste heat recovery [2,3].

The early work of Dean [4] relates the behaviour of secondary flow to a single parameter, K, called the Dean number which is defined as, $K = Re\left[\frac{D_c}{R}\right]^{\frac{1}{2}}$. The critical requirement for the onset of secondary flow instability is primarily dependent on the aspect ratio of the channel [5], as shown in Fig. 1, where increased aspect ratio leads to formation of more pairs of Dean vortices. Majority of the published research in curved channels is limited to experimental investigations of flow characteristics under isothermal condition [6] for aspect ratio of 1 to 12 and curvature ratio of 0.2 to 0.025. Largely due to the difficulties associated with the measurement of fluid temperature profile, studies on non-isothermal cases are limited [7,8].

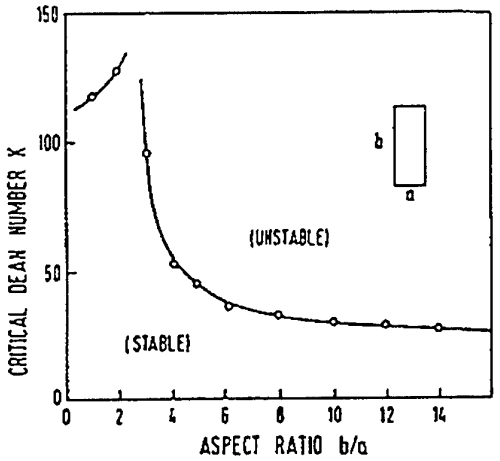

Fig 1: Variation of critical Dean Number with aspect ratio

Analytical methods have had a limited success, as the governing equations are highly non-linear. In order to avoid convergence instability in computations, most of these solution schemes neglect either the buoyancy effects caused by temperature field or consider passages of small curvature and low aspect ratio. Some of the significant studies include Hwang et.al. [9] who obtained fluid and heat flow characteristics for the forced laminar convection in a curved isothermal square duct under hydrodynamically and thermally fully developed conditions, Ru et.al.[10] who considered combined free and forced convection for developed flow in uniformly heated curved pipes, Wang [11] who applied finite volume method for steady fully developed flow in curved rotating channels and examined the buoyancy-driven transitions in flow structures, Ligrani [12] who studied channels of aspect ratio 40 and showed that the secondary vortex formation is more affected by external heating at the concave wall than on the convex wall.

In this paper, a numerical simulation is presented where fully developed laminar flow through a curved rectangular duct with uniform external heating on the outer concave wall. The convective and buoyancy forces are taken in to account in the formulation. The flow characteristics for channels of moderate curvature are studied for a range of aspect ratios and external heat fluxes.

2. NUMERICAL FORMULATION

Using the system of toroidal coordinates shown in Fig. 2, the governing equations of mass continuity, momentum and energy are written for a steady and fully developed laminar flow through a curved rectangular duct in the form given below.

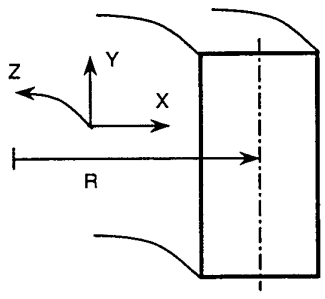

Fig. 2: Coordinate system for the governing equations

Mass continuity equation:

$$\frac{1}{(R+X)}\frac{\partial[(R+X)U]}{\partial X}+\frac{1}{(R+X)}\frac{\partial W}{\partial Z}+\frac{\partial V}{\partial Y}=0 \tag{1}$$

X-momentum equation:

$$U\frac{\partial U}{\partial X}+V\frac{\partial U}{\partial Y}=-\frac{1}{\rho}\frac{\partial P}{\partial X}+\upsilon\left[\nabla^2 U-\frac{U}{(R+X)^2}\right]-\frac{W^2}{(R+X)} \tag{2}$$

where, the term, $\frac{W^2}{(R+X)}$ is the centrifugal force driving the flow in the x-direction.

Y-momentum equation:

$$U\frac{\partial V}{\partial X}+V\frac{\partial V}{\partial Y}=-\frac{1}{\rho}\frac{\partial P}{\partial Y}+\upsilon\nabla^2 V+g\beta(T-T_z) \tag{3}$$

where, the term $g\beta(T-T_z)$ represents the buoyancy force acting in the main flow.

Z-momentum equation:

$$U\frac{\partial W}{\partial X}+V\frac{\partial W}{\partial Y}+\frac{UW}{(R+X)}=-\frac{1}{\rho}\frac{\partial P}{\partial Z}+\upsilon\left[\nabla^2 W-\frac{W}{(R+X)^2}\right] \tag{4}$$

Energy equation:

$$U\frac{\partial T}{\partial X}+V\frac{\partial T}{\partial Y}+\frac{R}{(R+X)}W\frac{\partial T}{\partial Z}=\alpha\left[\nabla^2 T+\frac{R^2}{(R+X)^2}\frac{\partial^2 T}{\partial Z^2}\right] \tag{5}$$

where, $\frac{\alpha R^2}{(R+X)^2}\frac{\partial^2 T}{\partial Z^2}$ represents axial heat conduction and $\nabla^2=\frac{1}{(R+X)}\left[\frac{\partial}{\partial X}(R+X)\frac{\partial}{\partial X}\right]+\frac{\partial^2}{\partial Y^2}$.

The boundary conditions are $U = V = W = 0$ at the walls and $-k\frac{\partial T}{\partial X}=\dot{q}_w$ at the outer channel wall. The equations are simplified using the following assumptions:

(1) Steady incompressible fully developed laminar flow
The fluid velocity profile is considered to have fully developed in the Z direction. Therefore the terms containing $\frac{\partial W}{\partial Z}$ are omitted from the governing equations.

(2) Fully developed temperature profile that increases linearly in the streamwise (Z) direction.
As a constant heat flux is applied on the outer wall of the curved channel, it can be shown that the bulk temperature in the flow (Z) direction increases linearly. Thus, $\left(\frac{\partial T}{\partial Z}\right)$ can be treated as a constant. Furthermore as the hydrodynamic profile is fully developed the temperature profile remains unchanged in the Z direction even though the bulk temperature increases linearly.

(3) Viscous heat dissipation
The viscous heat dissipation is negligible because of the low viscosity of air and low flow velocities.

(4) Constant physical properties

Within the range of temperatures concerned the change in physical properties of air are within 3% of the calculated value at the mean temperature. Hence, for computational simplicity physical properties are taken to be constant at 330K with the exception of density.

(5) Boussinesq approximation
The variation of density with temperature is represented by the Boussinesq approximation,

$$\rho_{(T)} = \rho_0\left[1-\tilde{\beta}(T-T_0)\right] \tag{6}$$

Using $X-D_e x, Y=D_e.y, Z=L.z, U=K^2\left(\frac{\upsilon}{D_e}\right)u, V=K^2\left(\frac{\upsilon}{D_e}\right).v, W=\overline{W}.w, P=P_z(z)+\rho K^2\left(\frac{\upsilon}{D_e}\right)^2.p, \beta=\frac{R}{D_e}$

$\theta=\frac{T-T_o}{\left(\frac{q_w''.Z}{k.Pe_a}\right)}$, $u=\frac{\beta}{\beta+x}\frac{\partial\psi}{\partial y}$ and $v=-\frac{\beta}{\beta+x}\frac{\partial\psi}{\partial x}$, the set of equations is non-dimensionalised and transformed into the vorticity-stream function formulation as given below:

Vorticity-stream function equation:

$$\left(\frac{\beta+x}{\beta}\right)^2\xi=-\left(\frac{\partial^2\psi}{\partial x^2}+\frac{\partial^2\psi}{\partial y^2}\right)+\frac{1}{\beta+x}\frac{\partial\psi}{\partial x} \tag{7}$$

Vorticity-transport equation:

$$K^2\left[u\frac{\partial\xi}{\partial x}+v\frac{\partial\xi}{\partial y}\right]=\frac{1}{(\beta+x)}\frac{\partial}{\partial x}\left[(\beta+x)\frac{\partial\xi}{\partial x}\right]+\frac{\partial^2\xi}{\partial y^2}+\frac{2}{(\beta+x)^2}\frac{\partial\xi}{\partial x}-2\left(\frac{\beta}{\beta+x}\right)^2 w\frac{\partial w}{\partial y}+\left(\frac{Gr}{K^2Pe_a}\right)\frac{\partial\theta}{\partial x} \tag{8}$$

Z-momentum equation:

$$K^2\left[u\frac{\partial w}{\partial x}+v\frac{\partial w}{\partial y}\right]=\frac{\beta C}{(\beta+x)}+\frac{1}{(\beta+x)}\frac{\partial}{\partial x}\left[(\beta+x)\frac{\partial w}{\partial x}\right]+\frac{\partial^2 w}{\partial y^2}-\frac{w}{(\beta+x)^2}-K^2\frac{uw}{(\beta+x)} \tag{9}$$

where, $C=-\frac{D_e^2\left(\frac{\partial P_z}{\partial Z}\right)}{\mu\overline{W}}$, which will be determined by considering the global continuity condition $\overline{w}=\int\int((\beta+x)w/\beta)dxdy=\frac{a.b}{D_e^2}$ in any cross section.

Energy equation:

$$PrK^2\left[u\frac{\partial\theta}{\partial x}+v\frac{\partial\theta}{\partial y}\right]=\frac{1}{(\beta+x)}\frac{\partial}{\partial x}\left[(\beta+x)\frac{\partial\theta}{\partial x}\right]+\frac{\partial^2\theta}{\partial y^2}-\frac{\beta}{(\beta+x)}\left[\frac{Pe_a.De}{L.z}\right]w\theta \tag{10}$$

In terms of the dimensionless variables, the boundary conditions are expressed as (n is normal to channel wall)

$$\frac{\partial\psi}{\partial n}=0,\ \psi=0,\ w=0,\ \frac{\partial\theta}{\partial x}=-\frac{Pe_a.D_e}{L.z}\ \text{at the outer concave wall} \tag{11}$$

Using the control volume method and convection-diffusion concept [13] the governing equations (7), (8), (9) and (10) are discretised and written in the general form,

$$a^{P}_{i,j}\phi_{i,j} + a^{W}_{i,j}\phi_{i-1,j} + a^{E}_{i,j}\phi_{i+1,j} + a^{S}_{i,j}\phi_{i,j-1} + a^{N}_{i,j}\phi_{i,j+1} = S_P \qquad (12)$$

where, superscript P represents centre of control volume, superscripts W,E,S and N represent west, east, south and north surfaces of control volume, respectively, and S_P is a source term. The resulting equations with five-diagonal coefficients and the boundary conditions given in (11) are solved by Strongly Implicit Procedure [14].

The solution process is started by evaluating the vorticity values at the wall from the stream function solution near the wall. The computation is then continued to evaluate ψ, u, v, w and θ for all internal nodes of the grid until the convergence is achieved. Convergence of the numerical scheme is tested by computing the infinite norm, ε which is defined as, $\varepsilon = \dfrac{\max\left|F_{i,j}^{\tau+1} - F_{i,j}^{\tau}\right|}{\max\left|F_{i,j}^{\tau}\right|}$ where F is a general function. For cases where the infinite norm exhibits a periodic behaviour, the solution was obtained by a false transient algorithm.

3. RESULTS AND DISCUSSION

The iterative process was initiated by assigning a zero value for all variables except w and θ which were introduced as uniform profiles. The solution deemed to have converged when the largest of ε in the vector field (ξ, ψ, u, v, w, θ) during successive iterations did not change by more than a prescribed amount, which is typically of the order 10^{-5}.

The numerical simulation was carried out for representative curved rectangular ducts of aspect ratio ranging from 1 to 8. The curvature ratio was set at 5. The Dean number, K was varied in the range 20 to 500 and the external heat fluxes up to 200 W/m^2 were considered. This selection enables a direct comparison to be made with the available experimental data for airflow through a curved passage [15].

Fig. 3 shows typical results of the numerical solution for stream function contours for a channel of $\gamma = 5$, $\beta = 5$ without external heating and with a heat flux of 25 W/m^2. The contours clearly indicate the secondary flow in the channel with the occurrence of single-pair and multiple-pair vortices.

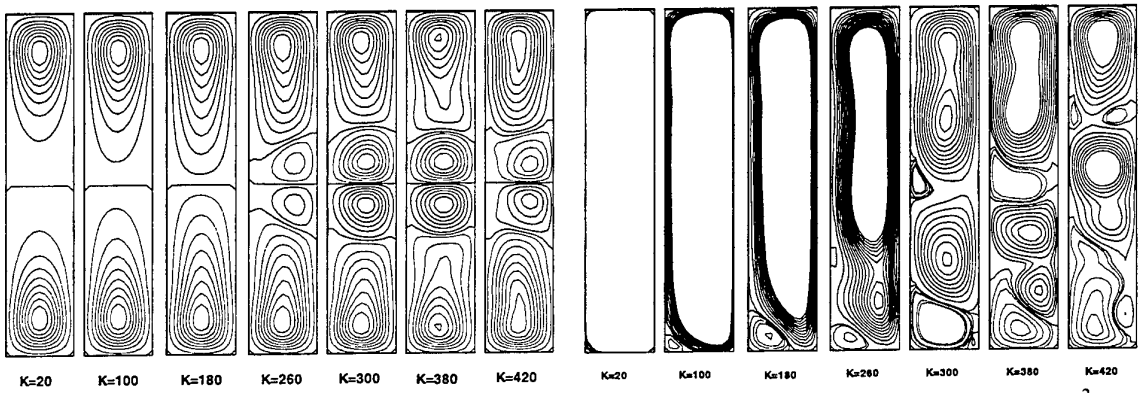

(a) With no heating at the wall (b) With external wall heat flux q" = 25 W/m^2

Fig. 3. Stream function ψ contours for $\beta = 5$ and $\gamma = 5$

Under the isothermal flow conditions shown in Fig. 3(a), the secondary flow is generated in the channel in the absence of temperature-induced buoyancy forces. The stream function contours tend to be more symmetrical. Above a certain critical value of K additional Dean vortices appear in the mid-section of the channel. When external wall heating is applied, buoyancy forces are set up due to density variation and convection currents are established in the flow. As shown in Fig. 3(b), for flow with low Dean number, the entire channel is

predominantly occupied by one temperature-induced vortex. With the increased flow rate, centrifugal forces become stronger and a second counter-rotating vortex is formed at the bottom of the channel. This then develops in strength for higher Dean number giving secondary flow characteristics to the channel flow. When the flow rate is increased further, an additional pair of vortices known as Dean vortices appears in the mid-channel. However, the flow pattern tends to be unsymmetrical unlike in the case of isothermal channel flow. These observations are well supported and vindicated by the flow visualisation data reported in literature for airflow through curved heated channels [15].

The effects of external wall heating on the stream function ψ, fluid velocity, w in streamwise direction and the temperature field are illustrated in Figs. 4, 5 and 6, respectively. As illustrated, both the velocity fields and the temperature profile are highly affected by the buoyancy forces generated by the wall heating.

For the isothermal flow with no external heating, symmetrical profiles are indicated in Figs. 4 and 5 for the streamfunction and the streamwise velocity of the flow. The streamwise velocity contours, however, differ significantly from the idealistic parabolic profiles for laminar flow due to the presence of secondary vortices and broadly indicates two distinct peak velocity points. With the applied external heating, it is seen from Fig. 4 that the thermally induced convection currents tend to suppress the additional Dean vortices. Also the external heat flux causes the peak velocity points of the streamwise velocity distribution to be shifted towards the top of the channel as seen in Fig.5.

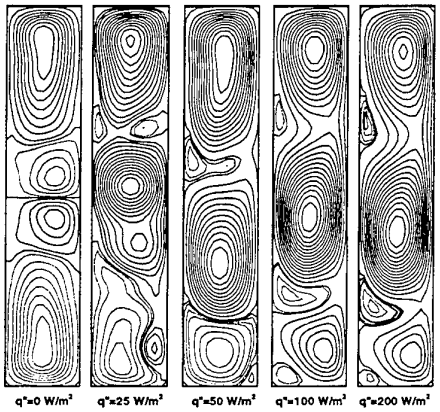

Fig. 4 Effect of heating on stream function
K = 420, γ = 5, β = 5

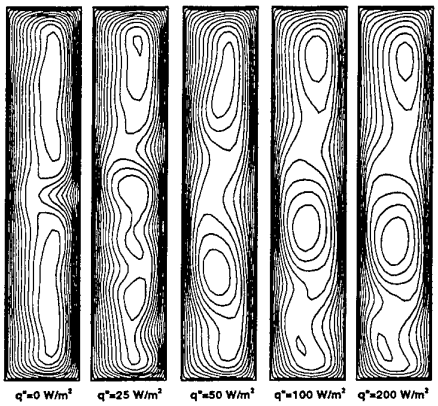

Fig.5 Effect of heating on streamwise velocity
K = 420, γ = 5, β = 5

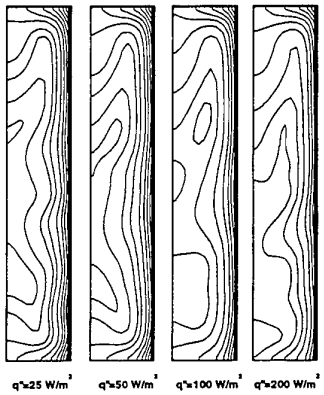

Fig.6 Effect of heating on temperature distribution
K = 420, γ = 5, β = 5

Fig. 6 shows the temperature distribution in the flow for selected values of external heating. With increased heat fluxes the low temperature contours residing near the bottom of the channel tend to move towards the upper end of the channel hence, becoming more and more unsymmetrical.

The effect of aspect ratio on the secondary flow patterns is depicted in Fig. 7. Increased secondary flow activities are evident in channels with higher aspect ratio where multiple vortex cell formations are seen. It is noticed that the number of Dean vortices present in the fluid is very much dependent on the aspect ratio of the channel. Channels with higher aspect ratios seem to yield more pairs of vortices at the outer wall. They usually appear in pairs and tend to be unsymmetrical for non-isothermal flows. For the range of K values examined, the additional Dean vortices are seen to appear in channels having aspect ratio more than 2.

Fig. 8 illustrates the variation of Nusselt number with the Dean number for the convective heat transfer process in the flow for channel aspect ratio 1 to 8. It is seen that, with the increasing channel aspect ratio the Nusselt number exhibits rapid improvement indicating the heat transfer enhancement due to the secondary flow. However, the degree of this enhancement becomes lesser for higher values of the channel aspect ratios.

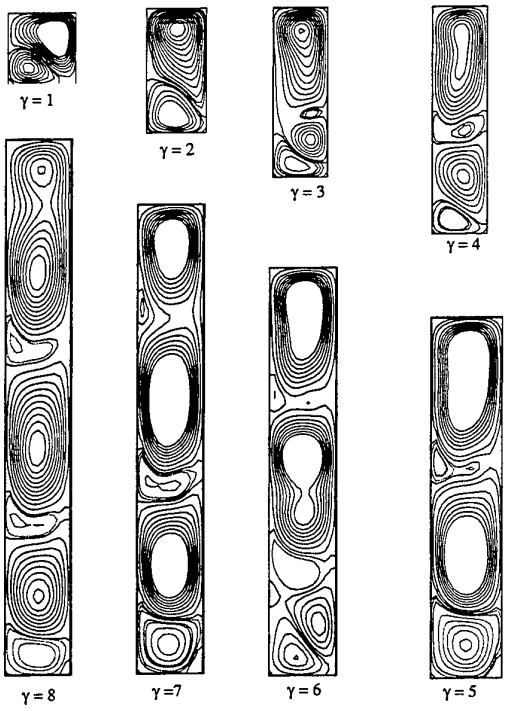

Fig. 7 Effect of aspect ratio on stream function
K = 420, γ = 5, β = 5, q″ = 50 W/m²

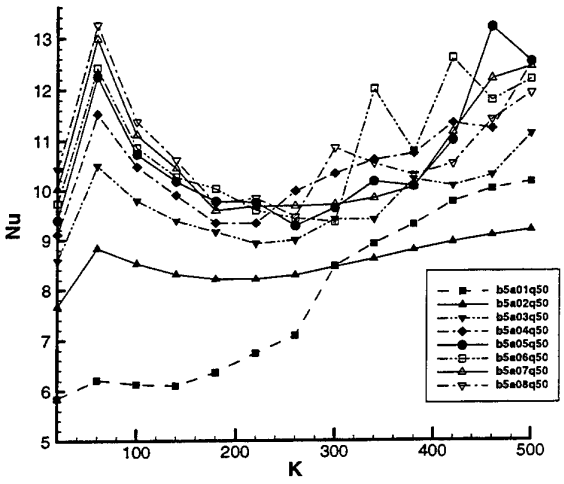

Fig. 8 Variation of Nusselt Number with Dean Number
q″ = 50 W/m², γ = 5 and β = 5

4. CONCLUSION

The numerical procedure developed takes in to account the temperature-induced buoyancy forces and, predicts stable solutions for the generation of Dean vortices and the associated flow patterns well. Application of external heating at the outer wall of the rectangular curved channel causes deformation of secondary vortex contours and yields asymmetric flow patterns. Additional Dean vortices still appear in the flow. However, a highly interactive and complex behaviour is exhibited between the main secondary vortices and the additional Dean vortices. Unlike in isothermal flow, it is generally difficult to identify and present Dean vortices as vortex pairs appearing in channels.

REFERENCES

1 P.D. McCormack, H. Welker and M. Kelleher, Taylor Goertler vortices and their effect on heat transfer, ASME, J.of Heat Transfer, Vol 92, pp101-112 (1970).

2 T.T. Chandratilleke and J.C. Ho, Performance study of a heat exchanger with streamwise curvature, American Society of Mechanical Engineers Singapore Chapter Yearbook 91/92, Singapore, Vol. 1, pp.68-72 (1992).

3 J.C. Ho, N.E. Wijeysundera, S. Rajasekar and T.T. Chandratilleke, Performance of a spiral coil heat exchanger, ASEAN Journal on Science and Technology for Development, Thailand, Vol. 9, No. 2, pp. 129-141 (1992).

4 W.R, Dean, Fluid motion in a curved channel, Pro.Roy.Soc. London, Ser.A, 121, pp 402-420 (1928).

5. K. C. Cheng, J. Nakayama, M. Akiyama, Effect of finite and infinite aspect ratios on flow patterns in curved rectangular channels, flow visualisation Tokyo, Japan, pp. 181 – 186 (1977).

6. S. Sugiyama, T. Hayashi, K. Yamazaki, Flow characteristics in the curved rectangular channels, Bulletin of the JSME, vol. 26, No. 216, pp. 961 – 969 (1983).

7. K. C. Cheng, A. Mitsunobu, Laminar forced convection heat transfer in curved rectangular channels, Int. Journal Heat Transfer, Vol 13, 471 (1970).

8. Y. Komiyama, F. Mikami, K. Okui, Laminar forced convection heat transfer in curved channel of rectangular cross section, Trans. JSME, Series B, Vol 50, pp. 424 – 434 (1984).

9. G. J. Hwang, C.-H. Chao, Forced laminar convection in a curved isothermal square duct, Trans. of the ASME, Vol 113, 48-55 (1991).

10. Y. Ru, S. F. Chang, Combined free and forced convection for developed flow in curved pipes with finite curvature ratio, Int. Journal Heat and Fluid Flow, Vol. 15 No. 6 (1994).

11. L. Wang, Buoyancy-force-driven transitions in flow structures and their effects on heat transfer in a rotating curved channel, Int. Journal Heat Mass Transfer, Vol. 40, No. 2, pp. 223-235 (1997).

12. P. M. Ligrani, S. Choi, A. R. Scallert, P. Skogerboe, Effects of Dean vortex pairs on surface heat transfer in curved channel flow, Int. Journal Heat Mass Transfer, Vol. 39, pp. 27-37 (1996).

13. S. V. Patankar, Numerical Heat Transfer and Fluid Flow (Hemisphere Publishing Corporation, Washington D.C., 1980).

14. M. Peric, Efficient semi-implicit solving algorithm for nine-diagonal coefficient matrix, Numerical Heat Transfer, Vol. 11, pp. 251-297 (1987).

15. T.T. Chandratilleke, Performance enhancement of a heat exchanger using secondary flow effects, Proc. of 2nd Pacific-Asia Conf. Mech Eng, Manila, Philippines, 9-11 Sept (1998).

NUMERICAL ANALYSIS ON LAMINAR FLOW AND HEAT TRANSFER IN STAGGERED ELLIPTIC TUBE BANKS

Hiroyuki Yoshikawa, Kaixin Yang and Terukazu Ota
Department of Machine Intelligence and Systems Engineering, Tohoku University, Japan
E-mail: yoshi@cc.mech.tohoku.ac.jp; Fax: 81-22-217-6933
yang@cht.mech.tohoku.ac.jp; Fax: 81-22-217-6933
ota@cc.mech.tohoku.ac.jp; Fax: 81-22-217-6931

Keywords: tube bank, elliptic cylinder, heat transfer, pressure loss, laminar flow

ABSTRACT. Numerical analysis based on the finite difference method has been made on laminar flow and heat transfer in staggered elliptic tube banks at low Reynolds number. Details of the flow and heat transfer characteristics are clarified for the fully developed flow state under the condition of uniform heat flux. The pressure loss coefficient, the local and mean heat transfer coefficients are presented along with the flow and temperature fields. Effects of the longitudinal and transversal pitch ratios and the axis ratio of elliptic cylinder upon them are made clear. It is found that a decrease of the longitudinal pitch ratio results in an increase of the pressure loss and the heat transfer. On the other hand, a decrease of the transversal pitch ratio causes a drastic increase of the pressure loss. In the case of a large axis ratio, the heat transfer coefficient first increases with a decrease of the transversal pitch ratio, becomes maximum within a range from 1.1 to 1.2 of the transversal pitch ratio, and then decreases. The axis ratio greatly effects these characteristics. These results suggest that an appropriate arrangement of the elliptic tube enhances the heat transfer performance of the tube bank.

1. INTRODUCTION

The understanding of the flow and heat transfer characteristics in tube banks relates closely to the design of the high performance and compact heat exchanger. Many experimental investigations on the pressure loss and heat transfer coefficients of circular tube banks have been conducted to improve the performance of the heat exchanger [1, 2]. Various empirical formulae have been proposed for these coefficients [3]. On the other hand, in order to make the heat exchanger small, decrease the flow resistance and prevent the noise, it is important to clarify these characteristics at low Reynolds number. Recently, numerical simulations have been also conducted to clarify the complicated flow and heat transfer characteristics in circular tube banks [4-10].

The circular cylinder has been used for many heat exchangers. It is well known that the flow resistance of the circular cylinder is remarkably larger than that of a streamlined one [11]. An elliptic cylinder of a certain axis ratio may be considered as a streamlined one, and the use of the elliptic cylinder may improve the heat exchanger performance. From such a standpoint, experimental investigations on the in-line tube composed of 2 to 4 elliptic cylinders have conducted by the present author [12-14]. There are, however, few papers about elliptic tube banks [15-17], and most of them have treated only a single axis ratio.

From the background described above, in the present study, staggered tube banks composed of the elliptic cylinder of the axis ratio ranged from 1.0 to 3.0 are numerically analyzed at low Reynolds number. The distance between neighboring cylinders is relatively short. It is a main objective of this study to make clear the effects of the axis ratio of elliptic cylinder and the pitch ratios on the flow and heat transfer characteristics.

2. NUMERICAL PROCEDURE

In the present study, the flow is assumed to cross the short axis of elliptic cylinder at a right angle, as shown in Fig. 1, and to be two-dimensional one of incompressible fluid, because the Reynolds number is relatively low ($10 \leq Re \leq 133$) and the pressure loss is small. Fundamental equations analyzed are the continuity, Navier-Stokes, and energy equations described in the following.

$$\frac{\partial u_j}{\partial x_j} = 0 \tag{1}$$

$$\frac{\partial u_i}{\partial t}+\frac{\partial}{\partial x_j}\left(u_i u_j\right)=-\frac{\partial p}{\partial x_i}+\frac{1}{Re}\frac{\partial^2 u_i}{\partial x_j \partial x_j} \tag{2}$$

$$\frac{\partial T}{\partial t}+\frac{\partial}{\partial x_j}\left(T u_j\right)=\frac{1}{Re\,Pr}\frac{\partial^2 T}{\partial x_j \partial x_j} \tag{3}$$

In the equations, the velocities, pressure, temperature, coordinates and time are non-dimensionalized by u_0, ρu_0^2, $q_w d/\lambda$, d and d/u_0, respectively. d is an equivalent diameter based on the cylinder circumference, q_w the uniform heat flux on the cylinder surface, and u_0 the mean velocity at the inlet of tube bank. The physical coordinates are projected to the general curvilinear coordinates because various pitch ratios and axis ratios of elliptic cylinder are treated in the present study. As for the time derivative, the Crank-Nicolson method for the convection and viscous terms, and the Euler backward difference for the pressure terms are used, respectively. As for the space derivative, the QUICK method [18] for the convection terms and the second order central difference for the other terms are used. Resulting finite difference equations are solved using the HSMAC method [19] along with the collocation method [20, 21].

The hatching area in Fig. 1 is analyzed. It is assumed that the flow and temperature fields are fully developed under the condition of uniform heat flux on the cylinder surface. The periodic boundary conditions are imposed for the pressure following the method of Segal et al. [10], and for the temperature following the method of Launder et al. [5], respectively. On the top and bottom boundaries, the symmetric condition is imposed. For the grid generation, the method of Hsu et al. [22] is improved so that the grid distance and inclination on the whole boundaries are specified.

In the following, the pressure loss coefficient per one cylinder row C_d, the surface friction coefficient C_f, the pressure coefficient C_p, local Nusselt number Nu, and Reynolds number Re are defined as $C_d=\Delta p/(1/2)\rho u_0^2$, $C_f=\tau_w/(1/2)\,\rho u_0^2$, $C_p=(p-p_s)/(1/2)\,\rho u_0^2$, $Nu=q_w d/\lambda(T_w-T_b)$, $Re=u_0 d/\nu$, respectively. p_s is the pressure at the front stagnation point on the cylinder, and T_b is the bulk temperature at the cross-center upstream of the cylinder. Further, the axis ratio of elliptic cylinder, the longitudinal and transversal pitch ratios are defined as $\Lambda=a/b$, $P_L=L/d$, $P_T=H/d$, as shown in Fig. 1.

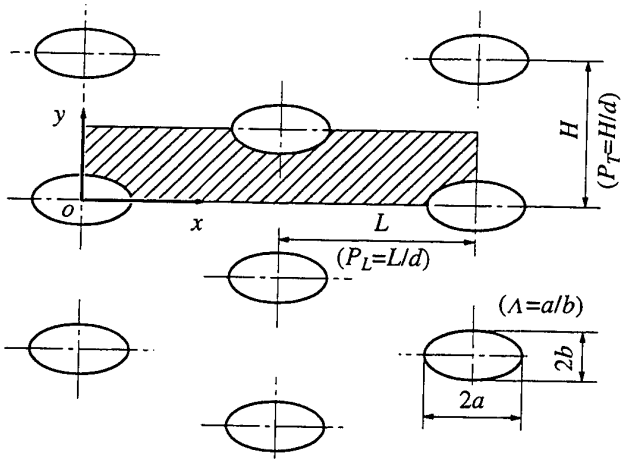

Fig. 1. Staggered elliptic tube bank, geometrical factors and coordinates

3. RESULTS AND DISCUSSION

Preliminary calculations were conducted using three kinds of grids in the case of the axis ratio $\Lambda=2.0$, the pitch ratios $P_L \times P_T=1.5\times1.5$, Reynolds number Re=66.7, Prandtl number Pr=0.7. Their grid points are 51×51,

101×101, and 201×201. There is no essential difference between the results with two fine grids. Accordingly, following results are obtained using the grids whose points are (181~221)×(65~129) depending on the pitch ratios. In the present study, unsteadiness of the flow and temperature fields was not observed in the Reynolds number range treated.

The pressure loss coefficient C_d of the circular tube bank is compared with previous experimental and numerical results for the case of $P_L \times P_T = 1.3 \times 1.5$ in Fig. 2. The present results are a little smaller than experimental results of Bergelin et al. [2] at high Reynolds number, but their agreement is reasonably well. A numerical result in the core region of Fujii et al. [7] agrees well with the present results.

Figure 3 presents the pressure, vorticity and temperature distributions in the tube banks. In the figure, the axis ratio varies from 1.0 to 3.0, under the condition of $P_L \times P_T = 1.5 \times 1.5$, Re=66.7, Pr=0.7. Results in the upstream half region are presented because all of the pressure, vorticity and temperature distributions are periodic, and the pressure and temperature are put zero at the left upper corner. The solid black line in the figure is the separated streamline. In the case of the circular cylinder, the channel width is narrower than that of others and the recirculation region is considerably wide. The flow is accelerated in the narrow region of the channel and the high-speed flow impinges to the front surface of the cylinder. As a result, the pressure becomes very high at the front stagnation point. The flow is largely reflected along the cylinder surface and accelerated gradually as the channel width decreases. The pressure decreases rapidly in the narrow region of the channel. As the axis ratio increases, the channel width becomes wide and the surface shape near the cross-center becomes gently. Accordingly, the separation point moves downstream, the recirculation region reduces, and the separation does not occur in the cases of Λ=2.5 and 3.0. It is clear that the pressure change in the tube bank becomes small as the axis ratio increases. The vorticity on the front surface of the circular cylinder is very high because the fluid is reflected rapidly there and the effective channel width is narrow. A high vorticity area spreads to the upstream of the separation point. As the axis ratio increases, the vorticity clustered near the cylinder surface is diffused. In the case of Λ=3.0, the high vorticity area is restricted in the vicinity of the front stagnation point. It is clear that the thermal boundary layer on the front surface becomes thick as the axis ratio increases. It is originated from that the channel width becomes wide, the flow on the channel center does not contribute the heat transfer strongly, the flow acceleration becomes weak, and the vorticity on the cylinder surface decreases.

The surface friction coefficient C_f, the pressure coefficient C_p on the cylinder surface, and the local Nusselt number Nu are presented in Fig. 4(a) in the cases of Λ=1.5, P_T=1.5, Re=66.7, Pr=0.7 for P_L=1.3 and 1.6. Nu takes maximum value at the front stagnation point because the accelerated cold flow approaches the front

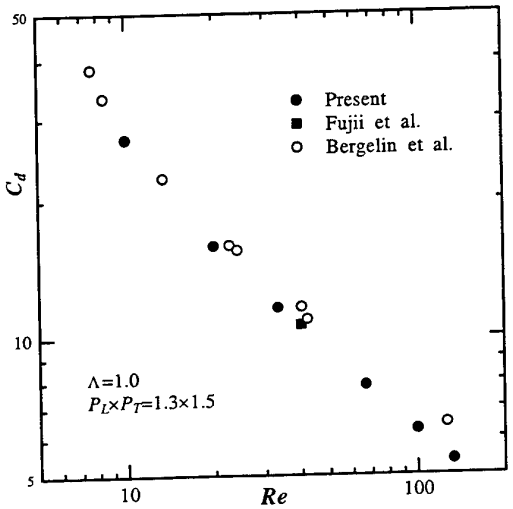

Fig. 2. Comparison of C_d of circular tube bank (Λ=1.0, $P_L \times P_T$=1.3×1.5)

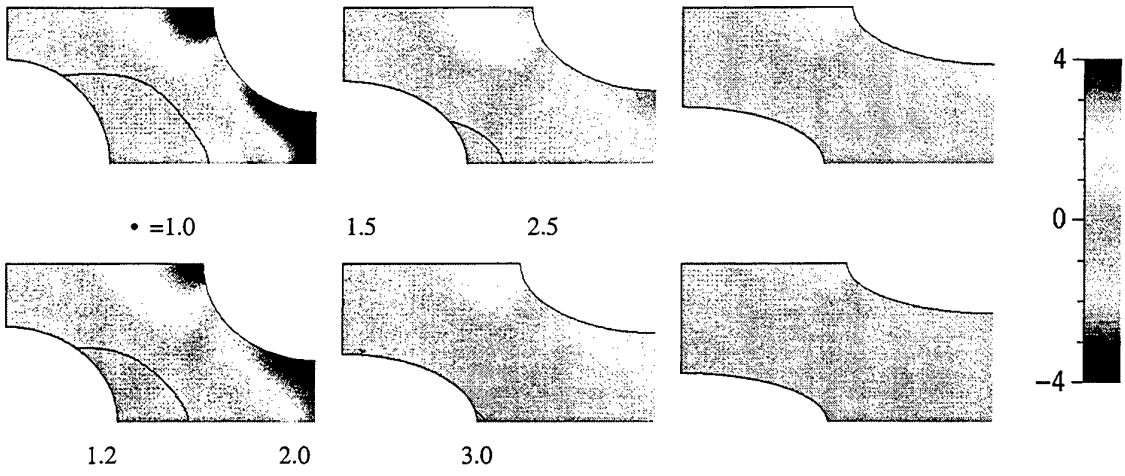

(a) Pressure distribution

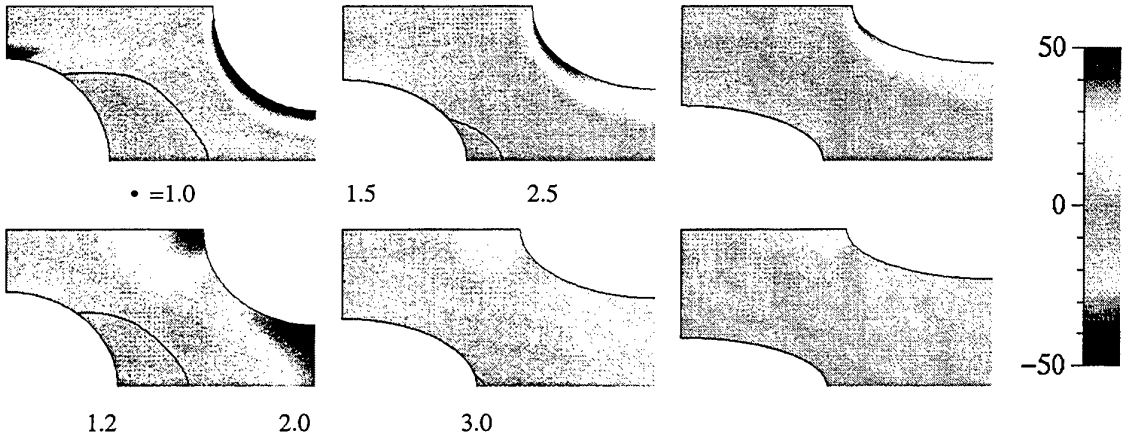

(b) Vorticity distribution

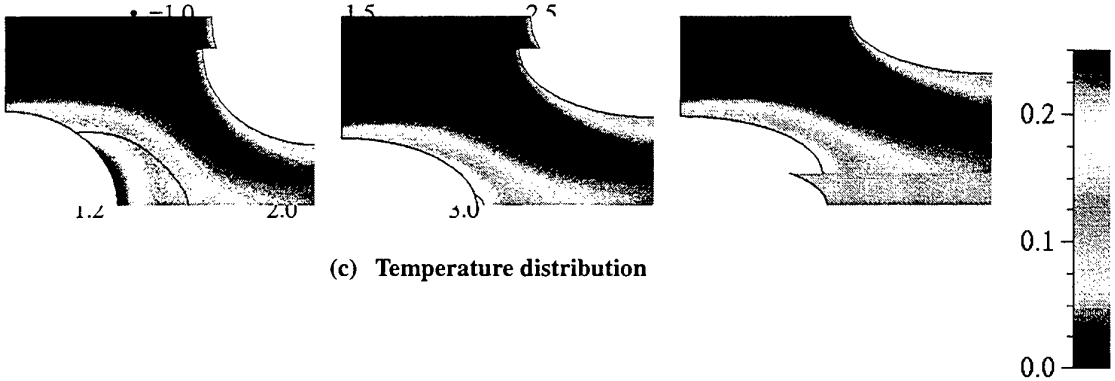

(c) Temperature distribution

Fig. 3. Pressure, vorticity and temperature distributions ($P_L \times P_T = 1.5 \times 1.5$, Re=66.7, Pr=0.7)

surface. Nu decreases monotonically with the flow direction. C_f reaches a peak at a slightly downstream of the front stagnation point where the flow is accelerated. C_{fmax} of P_L=1.3 is larger by 10 percent than that of P_L=1.6 because the channel width of P_T=1.3 is narrower than that of P_L=1.6. At the rear part of the cylinder, C_f of P_L=1.3 is a little larger than that of P_L=1.6, and the heat transfer of P_L=1.3 is enhanced there. In the case of P_L=1.3, the separation point moves downstream because the flow is accelerated and the separation region is reduced. C_p decreases suddenly in the downstream of the front stagnation point where C_f is large, and becomes minimum at S/S_0=0.55. At the further downstream, C_p increases slightly. C_{pmin} and the pressure recover of P_L=1.3 is smaller than that of P_L=1.6.

C_f, C_p on the cylinder surface, and Nu are presented in Fig. 4(b) in the cases of Λ=1.5, P_L=1.5, Re=66.7, Pr=0.7 for P_T=1.2 and 1.6. In the case of P_T=1.2, Nu_{max} at the front stagnation point is larger by 36 percent than that of P_T=1.6 because the flow speed of P_T=1.2 is higher than that of P_T=1.6. C_{fmax} of P_T=1.2 is 1.8 times larger than that of P_T=1.6 and its point locates at the upstream of that of P_T=1.6. In the case of P_T=1.2, C_f first increases rapidly with the flow direction, becomes maximum, decreases to the local minimum, increases again and subsequently becomes local maximum at S/S_0=0.43. The heat transfer is slightly enhanced there, similar to the results shown in Fig. 4(a). The separation point of P_T=1.2 moves upstream and the recirculation region increases. C_p suddenly decreases at the downstream of the front stagnation point. C_{pmin} of P_T=1.2 is 2.5 times lower than that of P_T=1.6.

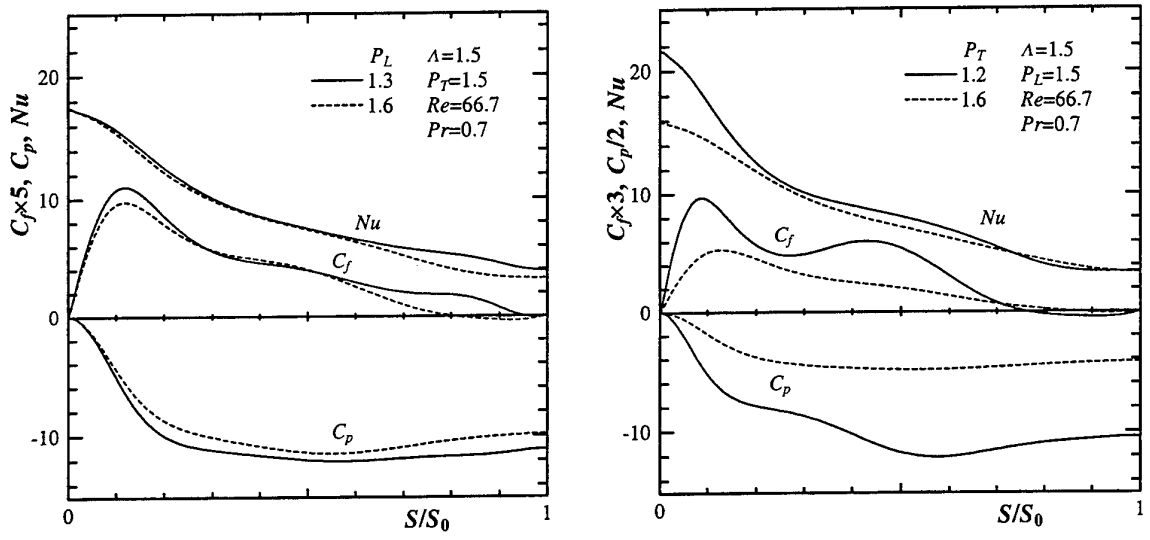

(a) Effect of P_L **(b) Effect of P_T**

Fig. 4. Effects of P_L and P_T on C_f, C_p and Nu distributions (Λ=1.5, Re=66.7, Pr=0.7)

The relation of the mean Nusselt number Nu_m and the pressure loss coefficient C_d for the various axis ratios Λ and the Reynolds numbers Re is shown in Fig. 5. In the cases of Re≤33.3, Nu_m varies little with the axis ratio. However, Nu_m increases with a decrease of the axis ratio in a range of Re≥66.7. The increase of Nu_m becomes large as the Reynolds number becomes large. In the case of Re=133, Nu_m of Λ=1.2 is smaller by 8.5 percent than that of the circular cylinder, but its value of C_d is smaller by 35 percent than that of the circular tube bank.

The relation of Nu_m and C_d for the various values of Λ and P_L is shown in Fig. 6. Both Nu_m and C_d increase with a decrease of the axis ratio and it is independent of the longitudinal pitch ratio. This increase becomes large as the axis ratio becomes small. Nu_m increases with a decrease of the longitudinal pitch ratio and its increasing rate becomes large as the axis ratio becomes small. In the case of an elliptic cylinder, C_d increases with a decrease of the longitudinal ratio. In the case of a circular cylinder, in contrast, C_d varies little with the longitudinal pitch ratio in the range treated.

The relation of Nu_m and C_d for the various values of Λ and P_T is shown in Fig. 7. C_d increases rapidly with a decrease of the transversal pitch ratio independently of the axis ratio. In the cases of Λ=1.0 and 1.2, Nu_m

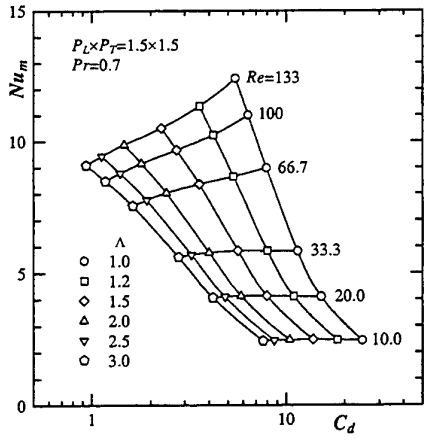

Fig. 5. Variations of Nu_m and C_d with Λ and Re ($P_L \times P_T$=1.5×1.5, Pr=0.7)

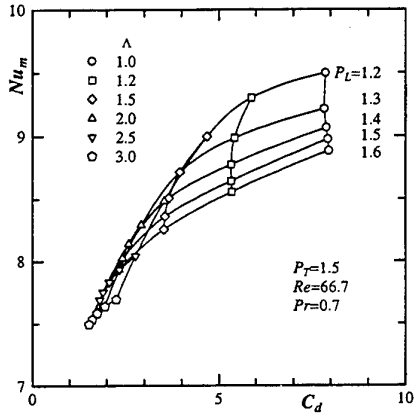

Fig. 6. Variations of Nu_m and C_d with Λ and P_L (P_T=1.5, Re=66.7, Pr=0.7)

increases with a decrease of the transversal pitch ratio. In the cases of 1.5≤Λ≤3.0, Nu_m first increases with a decrease of the transversal pitch ratio, becomes maximum in a range of 1.1≤P_T≤1.2, and then decreases. The maximum value increases with a decrease of the axis ratio.

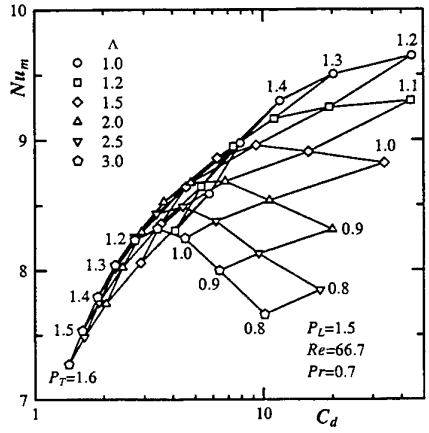

Fig. 7. Variations of Nu_m and C_d with Λ and P_T (P_L=1.5, Re=66.7, Pr=0.7)

4. CONCLUSIONS

Numerical analysis was made on laminar flow and heat transfer in the staggered elliptic tube banks in cross flow at low Reynolds number. Details of the flow and heat transfer characteristics in the tube banks are clarified. Main results obtained are as follows.

1. A decrease of the axis ratio results in an increase of the pressure loss and the heat transfer. Such an increase is independent of the longitudinal and transversal pitch ratios.
2. The heat transfer is enhanced with a decrease of the longitudinal pitch ratio. Such an enhancement becomes remarkable as the axis ratio becomes nearly unity. The pressure loss increases gradually with a decrease of the longitudinal pitch ratio in the case of a large axis ratio.
3. The pressure loss increases drastically with a decrease of the transversal pitch ratio. In the case of a relatively large axis ratio, the heat transfer becomes maximum within a range from 1.1 to 1.2 of the transversal pitch ratio. The maximum value increases with a decrease of the axis ratio.
4. These results suggest that an appropriate arrangement of the elliptic tubes enhances the heat exchanger performance.

The present calculations were conducted using an SX-4/128H4 supercomputer at the Computer Center, Tohoku University.

REFERENCES

1. O. P. Bergelin, G. A. Brown, H. L. Hull and F. W. Sullivan, Trans. ASME v.72, pp.881--888 (1950).
2. O. P. Bergelin, G. A. Brown and S. C. Doberstein, Trans. ASME v.74, pp.953-960 (1952).
3. A. Źukauskas, *Advances in Heat Transfer*, 8, Academic Press, pp.93-160 (1972).
4. R. F. LeFeuvre, "Laminar and Turbulent Forced Convection Processes through In-Line Tube Banks", *Imperial College London, Mech. Eng. Dept., HTS/74/5*, (1973).
5. B. E. Launder and T. H. Massey, Trans. ASME, J. Heat Transfer v.100, pp.565-571 (1978).
6. M. Fujii, T. Fujii and T. Nagata, Num. Heat Transfer v.7, pp.89-102 (1984).
7. M. Fujii, T. Fujii and T. Aramaki, Trans. JSME v.52B, pp.1694-1701 (1986).
8. M. N. Dhaubhadel, J. N. Reddy and D. P. Telionis, Int. J. Non-Linear Mechanics v.21-5, pp.361-373 (1986).
9. T. Ota and S.-K. Park, "Numerical Analysis of Heat Transfer and Flow in Tube Banks", *Proc. 2nd KSME-JSME Fluids Eng. Conf.*, v.1, pp.269-274, Seoul, Korea (1990).
10. G. Segal, K. Vuik and K. Kassels, Int. J. Num. Methods Fluids v.18, pp.1153-1165 (1994).
11. V. J. Modi and E. Wiland, AIAA J. v.8, pp.1814-1821 (1970).
12. T. Ota and H. Nishiyama, Trans. ASME, J. Fluids Eng. v.108, pp.98-103 (1986).
13. T. Ota, H. Nishiyama, J. Kominami and K. Sato, Trans. ASME, J. Heat Transfer v.108, pp.525-531 (1986).
14. H. Nishiyama, T. Ota and T. Matsuno, JSME Int. J. v.31, pp.410-419 (1988).
15. S.-K. Park and T. Ota, "Numerical Analysis of Laminar Heat Transfer and Flow around Staggered Elliptic Tube Banks", *Proc. 2nd JSME-KSME Thermal Eng. Conf.*, v.2, pp.49-54, Kitakyushu, Japan (1992).
16. S.-K. Park and T. Ota, "Numerical Analysis of Laminar Flow and Heat Transfer around In-line Elliptic Tube Banks", *Proc. 6th Int. Symp. Transport Phenomena in Thermal Eng.*, pp.964-969, Seoul, Korea (1993).
17. H. Yoshikawa, A. Tatamitani and T. Ota, Trans. JSME v.64B, pp.3337-3342 (1998).
18. B. P. Leonard, Comp. Methods Appl. Mech. Eng. v.19, pp.59-98 (1979).
19. C. W. Hirt, B. D. Nichols and N. C. Romero, "SOLA - a Numerical Solution Algorithm for Transient Fluid Flow", *LA*-5852, (1975).
20. C. M. Rhie and W. L. Chow, AIAA J. v.21-11, pp.1525-1532 (1983).
21. Y. Zang, R. L. Street and J. R. Koseff, J. Comp. Phys. v.114, pp.18-33 (1994).
22. K. Hsu and S. L. Lee, J. Comp. Phys. v.96, pp.451-469 (1991).

EFFECTS OF TIP CLEARANCE AND ROTATION ON THREE DIMENSIONAL FLOW FIELDS IN TURBINE CASCADES

B. Han and **R. J. Goldstein**
Department of Mechanical Engineering
University of Minnesota, USA
Email: rjg@me.umn.edu; Fax: (612)-624-1398

Keywords: turbine cascade passage, numerical analysis, tip clearance, rotating frame, leakage vortex

ABSTRACT. The effect of tip clearance and rotation on the flow field in an annular turbine passage is studied numerically. Three-dimensional Navier-Stokes equations are solved with respect to the rotating frame of reference. The results indicate that the leakage flow through the tip gap induces a leakage vortex along the suction side of the blade. The leakage vortex interacts with the passage vortex and suppresses its development. Another vortex, referred as a tip vortex, at the edge between the tip and the pressure side of the blade is observed. With a larger gap, the strengthened leakage vortex pushes the passage vortex away from the suction side of the blade. With rotation, the leakage and passage vortex are pushed toward the suction side of the blade.

1. INTRODUCTION

To improve the performance of gas turbines, an understanding of the flow and heat transfer phenomena in turbine passages is essential. A number of numerical and experimental studies have already been done. However, the complex geometry, tip clearance between the blade tip and the casing, and rotation of the rotors make understanding such flow a challenging problem in fluid mechanics and heat transfer. Due to the complexity of flow field within a real turbine rotor passage, most previous studies were performed with some simplification including no gap, no rotation, and a linear cascade.

Experimental studies on flow patterns through turbine passages are reviewed by Langston [1] and Sieverding [2]. Comparison with numerous results indicates that there is general agreement on the flow patterns, but disagreement on the number of the vortices in the passage. Jabbari, Goldstein, Marston, and Eckert [3] clarify the flow patterns by comparing results of flow visualization and mass transfer measurements. Their results showed the initiation and evolution of horseshoe and passage vortices in the passage. Even though those studies improve the understanding of the flow patterns in the turbine passage, most of them are performed in linear cascade without tip clearance. The influence of the tip gap on flow and heat transfer is studied by Metzger, Dunn, and Hah [4], and Moore, Moore, Henry, and Chaudhry [5]. Their studies are focused on the flow pattern in the gap, but the interaction between the leakage flow and the flow in the passage is not fully studied. Several three-dimensional numerical analyses on the flow in the turbine passage are performed. Liu and Bozzola [6] calculate the three-dimensional flow field in the passage with tip clearance and rotation, but the computational domain is for a linear cascade. The computation by Basson, Kunz, and Lakshiminarayana [7] is carried out in an annular passage with tip clearance, but the rotation is not considered.

In the present study, the three-dimensional flow field in an annular turbine rotor passage is numerically studied. Calculations with three different tip gap - 1%, 4%, and 10% of blade span - are performed to find out the effects of tip clearance. Effects of rotation are indicated by comparing the calculation results with and without rotation. The results are verified by comparison with experimental flow visualization.

2. NUMERICAL ANALYSIS

A three dimensional CFD code, TASCflow developed by AEA technology, was used in the present study. This code solves Reynolds-averaged time-dependent three dimensional Navier-Stokes equations in stationary and rotating coordinates. A standard k-ε model was employed to calculate turbulent quantities. In all computations, the properties of fluid are assumed to be constant.

An axial turbine rotor passage is constructed as the calculation geometry. The passage geometry is based on the Axial Flow Turbine Research Facility at the Pennsylvania State University [8]. Numerical analysis is performed

in one of the annular passages. The blade profile and grid in the calculation domain are shown in Fig. 1. The computational grid of 52×23×27 in streamwise, spanwise, and pitchwise direction was used. At the inlet of the domain, uniform velocity boundary condition is employed. Boundaries in pitchwise direction are treated with periodic boundary conditions. The Reynolds number based on relative inlet velocity and the chord length is 3.6×10^5. The detailed geometry and other computational parameters are summarized in Table 1.

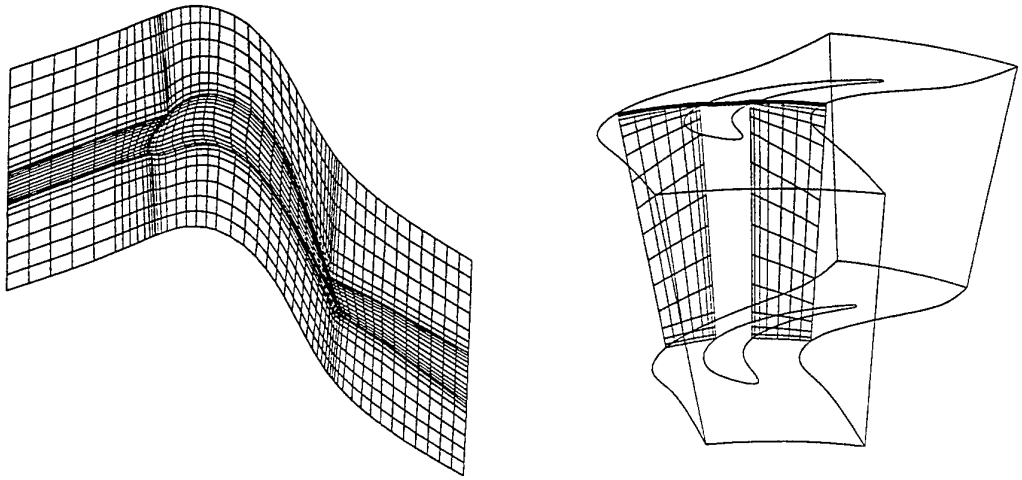

Fig. 1. Calculation domain and computational grids

Table 1. Detailed Geometry of Calculation Domain and Calculation Parameters

Geometry of Calculation Domain	
Hub Radius	0.335 m
Blade Span	0.123 m
Axial Blade Chord	0.129 m
Number of Blades	29
Computational Parameters	
Tip Clearance	1, 4, and 10 % of Span
Rotational Speed	1,000 rpm
Relative Inlet Velocity	42.4 m/s
Inlet Flow Angle	43.17 °

As indicated in Table 1, computations with three different tip clearances were carried out to investigate the effects of tip clearance on flow fields in turbine rotor passage. The effects of rotation were studied by comparing the results with and without rotation for 4% span clearance.

3. RESULTS AND DISCUSSIONS

Relative velocity vectors in three cross sectional planes which are parallel to the inlet are presented as the results. The locations of the planes are depicted in Fig. 2. The planes are located at 20%, 50%, and 80% of chord respectively.

3.1 Effect of Tip Clearance

Relative velocity vectors with respect to the rotating frame of reference around the tip clearance for 4% span clearance are plotted in Fig. 3. At section A-A, the leakage flow from the pressure side to the suction side of the blade is observed. At this location, no vortex is detected, but a small separated region on the edge between the

tip and the pressure side of the blade exists which implies the initiation of vortex. In the vicinity of the casing, very thin shear layer caused by the relative motion of the casing is noticed. This shear layer develops into a passage vortex downstream.

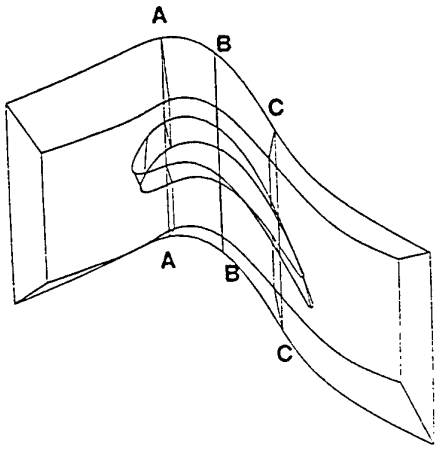

Section A-A: 20% of Chord

Section B-B: 50% of Chord

Section C-C: 80% of Chord

Fig. 2. Location of cross sections

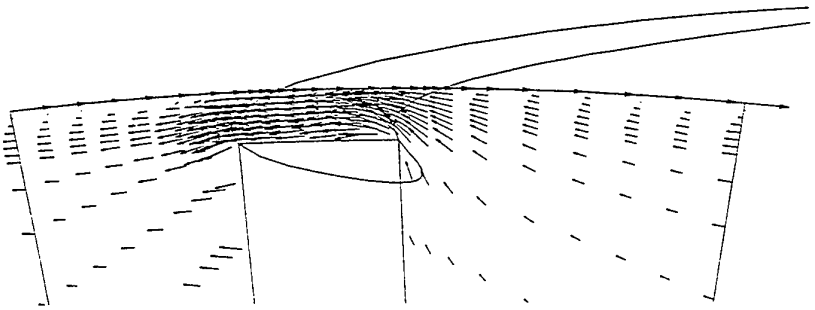

(a) Section A-A

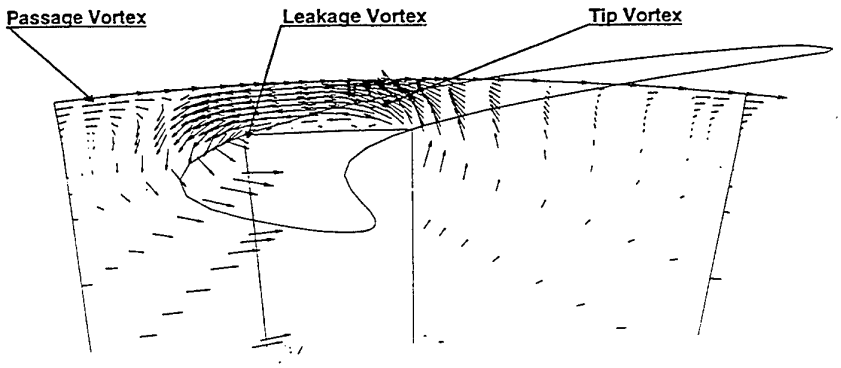

(b) Section B-B

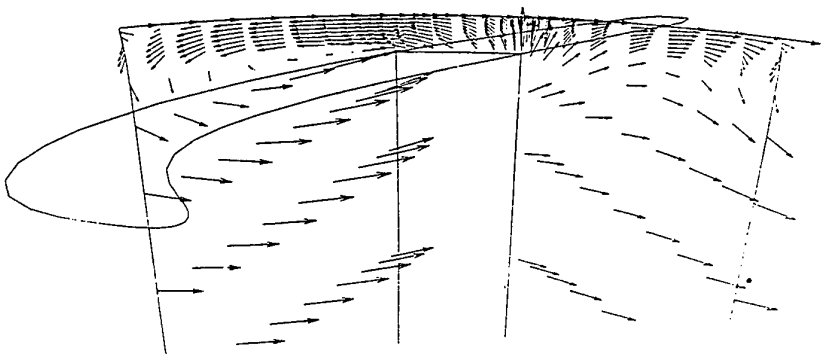

(c) Section C-C

Fig. 3. Velocity vector plots near tip clearance (4% of Span)

As flow goes downstream (section B-B), the developed leakage flow forms a leakage vortex close to the suction side of the blade. Within the tip clearance, another small vortex, called a tip vortex, is observed where the separation is detected at upstream location. At this section, the passage vortex is also observable near the casing. Since the rotational directions of leakage and passage vortex are opposite, both vortices tend to suppress each other. Further downstream (section C-C), the size of the leakage and passage vortices are bigger, but the tip vortex is disappeared.

The velocity vector plots for the other tip clearances, 1% and 10% of span, are shown in Fig. 4 (a) and (b) respectively. Because of the decreased leakage flow due to the smaller tip clearance, the development of the leakage vortex is slower than when the clearance is 4%. For 1% clearance, the tip vortex cannot observed, but it could be due to the limitation of resolution in the current computational gird.

For larger tip clearance (10% of span), the leakage vortex is strengthened because of increased leakage flow. In Fig. 4 (b), notice that the center of the passage vortex is moved away from the suction side of the blade and the shape of the passage vortex is squeezed. These imply that the increased leakage flow pushes the passage vortex away from the suction side of the blade and suppresses it. Increased leakage flow also affects the tip vortex. The size of the tip vortex is larger than that with 4% clearance and its shape is rounder.

3.2 Effect of Rotation

The velocity distribution without rotation for 4% tip clearance case is presented in Fig. 5. The distance between the center of the passage vortex and the suction side of the blade is larger than with rotation. This means that rotation moves the passage vortex close to the leakage vortex, and intensifies the interaction between the vortices. As a result of the intensified interaction, the size and the strength of the leakage vortex is reduced. Similar results were reported in [6].

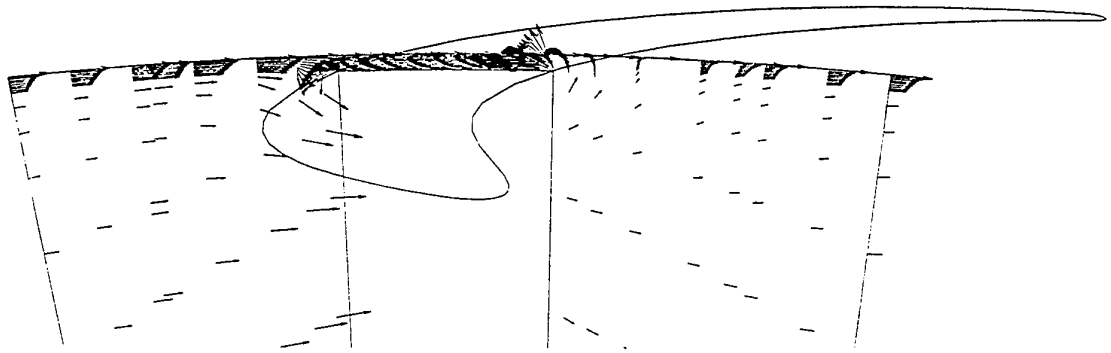

(a) Tip clearance of 1% of span at section B-B

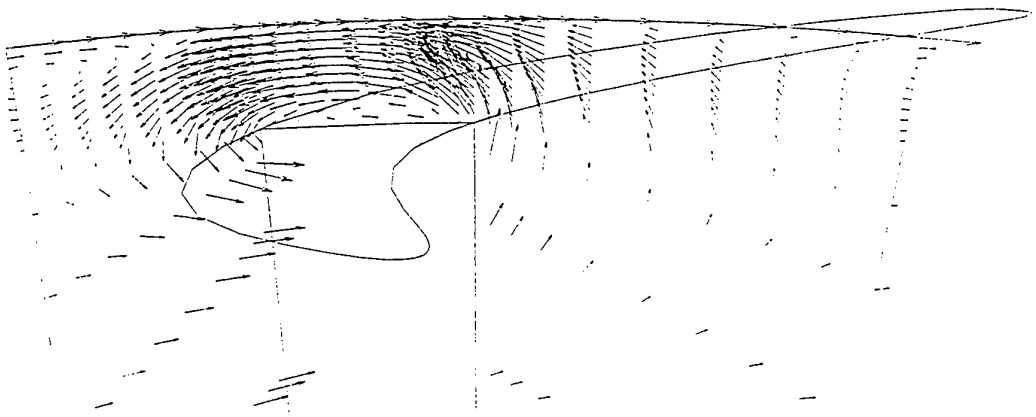

(b) Tip clearance of 10% of span at section B-B

Fig. 4. Velocity vector plots near tip clearance

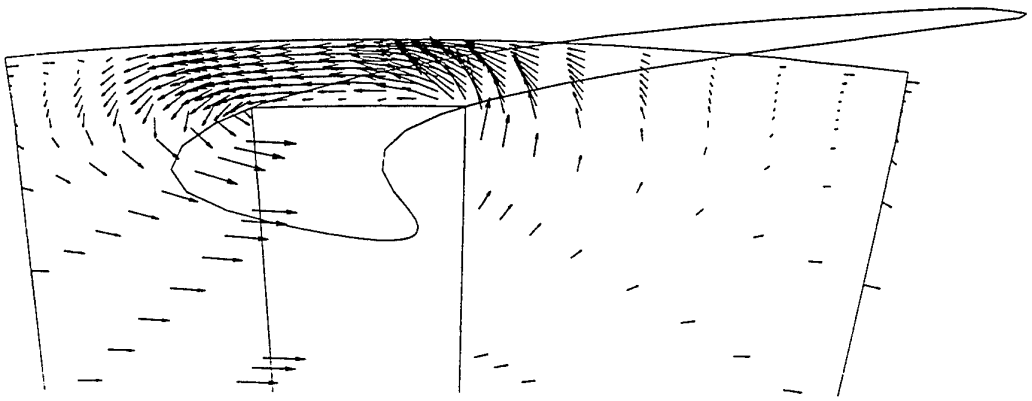

Fig. 5. Velocity vector plots without rotation at section B-B (4% tip clearance)

3.3 Comparison with Flow Visualization

The flow pattern around the tip clearance is compared with smoke-wire flow visualization by Goldstein, Eckert, Patankar, and Camci [9]. Fig. 6 shows the passage, leakage and tip vortex which are predicted in computations. Even though the visualization is performed in a linear-cascade, the qualitative comparison between the calculation and flow visualization shows good agreement in flow pattern.

(a) Leakage and passage vortex

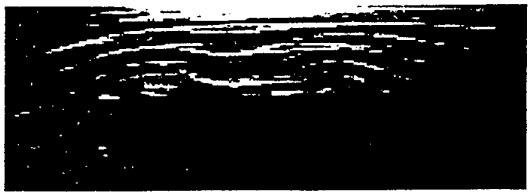

(b) Tip vortex

Fig. 6. Comparison with flow visualization in linear cascade

4. SUMMARY AND CONCLUSIONS

The flow fields in a turbine cascade is studied numerically. Three dimensional Navier-Stokes equations are solved with tip clearance and rotation. Calculations with three different tip clearance - 1%, 4%, and 10% of span - are performed to investigate the effect of tip clearance. The effect of rotation is studied by comparing the results with and without rotation for one tip clearance (4% of span). The conclusions can be summarized as follows:

1. The flow from the pressure side to the suction side of the blade through the tip clearance induces a leakage vortex. The leakage vortex interacts with the passage vortex near the casing, and tends to lessen the development of the passage vortex. Increased leakage flow due to the larger tip clearance suppresses the passage vortex and pushes the passage vortex away from the suction side of the blade.

2. In the tip clearance, another vortex (tip vortex) can be observed on the tip of the blade near the edge between the tip and the pressure side. The size of the tip vortex increases with tip clearance.

3. The rotation of blades affects the development of the leakage vortex. The distance between the center of the leakage vortex and the blade is smaller when the rotation is included in the computation. The interaction between the leakage and passage vortex is also intensified by rotation.

ACKNOWLEDGMENTS

The present study is supported by U.S Department of Energy through the Advanced Gas Turbine System Research (AGTSR) program. The authors would like thank to AEA technology for providing TASCflow, and Dr. C. Camci for providing information on the turbine passage geometry. All the computations in this work were performed in Scientific Development and Visualization Laboratory (SDVL) at the University of Minnesota Supercomputing Institute.

REFERENCES

1. L. Langston, AGARD No. 496 (1990).
2. C. Sieverding, J. Eng. Gas Turbines Power, v. 107, pp. 248-257 (1985).
3. M. Jabbari, R. Goldstein, K. Marston, and E. Eckert, Wärme- und Stoffübertragung, v. 27, pp. 51-59 (1991).
4. D. Metzger, M. Dunn, and C. Hah, Journal of Turbomachinery, v. 113, pp. 502-507 (1991).
5. J. Moore, J. Moore, G. Henry, and U. Chaudhry, Journal of Turbomachinery, v. 111, pp. 301-309 (1989).
6. J. Liu and R. Bozzola, AIAA Journal, v. 31, pp. 2068-2074 (1993).
7. A. H. Basson, R. F. Kunz, and B. Lakshminarayana, Journal of Propulsion and Power v. 9, pp. 59-66 (1993).
8. B. Lakshminarayana, C. Camci, I. Halliwell, and M. Zaccaria, Int. Journal of Turbo and Jet Engines v.13, pp. 155 - 172 (1996)
9. R. Goldstein, E. R. G. Eckert, S. V. Patankar, and C. Camci, "Edge Cooling Heat Transfer on Turbine Blades", *AGTSR Semi-Annual Progress Report* (1999)

FILM COOLING FROM TWO ROWS OF HOLES WITH OPPOSITE ORIENTATION ANGLES : INJECTANT BEHAVIORS

Joon Ahn
Department of Mechanical Engineering
Seoul National University
Email: mariposa@heat3.snu.ac.kr; Fax: +82-2-883-0179

In Sung Jung
Turbo and Power Machinery Research Center
Seoul National University
Email: isjung@heat3.snu.ac.kr; Fax: +82-2-883-0179

Joon Sik Lee
Department of Mechanical Engineering
Seoul National University
Email: jslee@gong.snu.ac.kr; Fax: +82-2-883-0179

Keywords: film cooling, compound angle, TLC (Thermochromic Liquid Crystal), boundary layer temperature, adiabatic film cooling effectiveness

ABSTRACT. For film cooling from two rows of holes with opposite orientation angles, injectant trajectory behaves differently and affects film cooling performance. The inclination angle was fixed at 35°, and orientation angles were set to 45° for downstream row and -45° for upstream row. Four film cooling hole arrangements including inline and staggered configurations were investigated. The blowing ratios studied were 0.5, 1.0 and 2.0. Film cooling performance depends on the relative location of injectant center with respect to the film cooled surface and the ability of the injectant to absorb and store thermal energy. Boundary layer temperature distributions were measured to investigate these characteristics. Detailed distributions of adiabatic film cooling effectiveness were measured as well using TLC (Thermochromic Liquid Crystal). At $M = 0.5$, the injectant was centered near film cooled surface irrespective of hole configurations, and it showed higher film cooling effectiveness. As the blowing ratio increases, the film coolant shows different characteristics depending on hole configurations. When the blowing ratio exceeds unity, the injectant tends to lift off from the wall. With inline configuration, however, the injectant is located near the film cooled surface even at higher blowing ratios and inline configuration thus showed higher adiabatic film cooling effectiveness than staggered one.

1. INTRODUCTION

The efficiency of gas turbine engine depends highly on the turbine inlet temperature, but the inlet temperature is limited to the allowable temperature of blade material. Film cooling is commonly used to prevent thermal failure in turbine blades that could result from the operation in high temperature. In film cooling, cooling air bled from the compressor is discharged through holes in the turbine blade wall or the end wall. The injected coolant from holes form a thin thermal insulation layer on the blade surface to protect the blade from being overheated by the hot gas. The film cooling effectiveness is influenced by blade geometry, coolant injection geometry, approaching flow characteristics, coolant to approaching flow velocity ratio, to name a few.

The compound angle injection hole has two characteristic angles as illustrated in Fig. 1. The inclination angle(α) is defined as the angle between the injection vector and its projection on x-z plane whereas the orientation angle(β) is defined as the angle between the streamwise direction and the projection of the injection vector on x-z plane. In the compound angle orientation system, the coolant is injected with a spanwise momentum component. Thus, the compound angle holes provide more uniform film coverage. There exist complex three-dimensional flows in the film cooled area in the case of compound angle injection. As the orientation angle increases the counter-rotating vortices, which usually observed in simple angle injection, turn to a single strong vortex and the strength of downstream secondary flow depends strongly on the velocity ratio [1]. The past studies, in general, show that compound angle injection provides significantly improved effectiveness compared

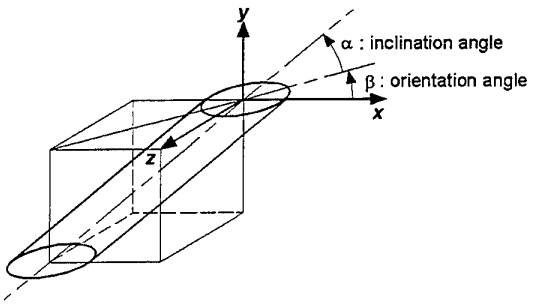

Fig. 1 Configuration of compound angle injection hole

with simple angle injection for the same spanwise hole spacing, normalized streamwise location and blowing ratio [2, 3]. It is also noteworthy that the film coolant injected from compound angle holes interacts with the mainstream fluid more vigorously to increase the heat transfer coefficient [4].

Past studies on the film cooling from two rows of holes with compound angle orientation adopted staggered configuration. They made each row of holes have the same orientation angles. Since the injectant from the compound angle holes possesses lateral momentum component, the injectant center moves in the z-direction as it flows downstream. Thus, effects of configuration on film cooling can be different from that of simple angle injection. In the present study, two rows of holes with opposite orientation angles were adopted to investigate the interactions of injectant flow with vortices. Four hole configurations including inline and staggered ones were investigated. For all configurations effects of three blowing ratios of 0.5, 1.0, and 2.0 are studied.

2. EXPERIMENTAL APPARATUS AND PROCEDURES

An open type subsonic wind tunnel is used to generate the free-stream(Fig. 2(a)). A boundary layer trip wire of 1.8mm diameter is located at $20D$, where D is the hole diameter, upstream from downstream holes to provide a turbulent boundary layer flow at the exit of the holes. The air, used as the injectant, first flows through an orifice followed by two heat exchangers that control the injectant temperature. Then, the air is ducted to a plenum chamber and discharged through the injection holes. The bottom plate of the duct consists of an upstream plate, an injection plate, and a measurement plate(Fig. 2(b)). Injection plates are prepared for each configuration(Fig. 3). The measurement plate starts at $x/D = 1.0$.

The boundary layer temperature distribution can reveal information about injectant behaviors and has a close relation with effectiveness distribution on the wall. In the measurement of boundary layer temperature distribution and the adiabatic film cooling effectiveness measurements, free-stream temperature is fixed at 20°C while the injectant is heated to 40°C.

The boundary layer temperature distribution is described in terms of dimensionless temperature defined as follows:

Table 1. Experimental Conditions

U_∞	10 m/s
D	10 mm
δ / D	1.50
H (= δ^*/θ)	1.36
L / D	4.0
M (= $\rho_c U_c / \rho_\infty U_\infty$)	0.5, 1.0, 2.0
Re_D (= $U_\infty D / \nu$)	6570

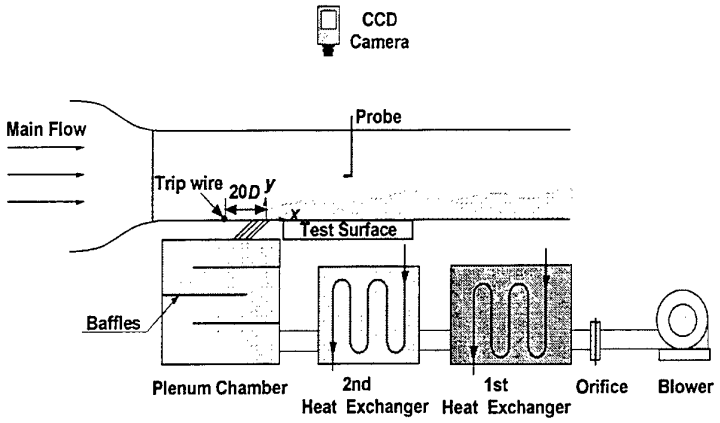

(a) Schematic diagram of wind tunnel and coolant supply system

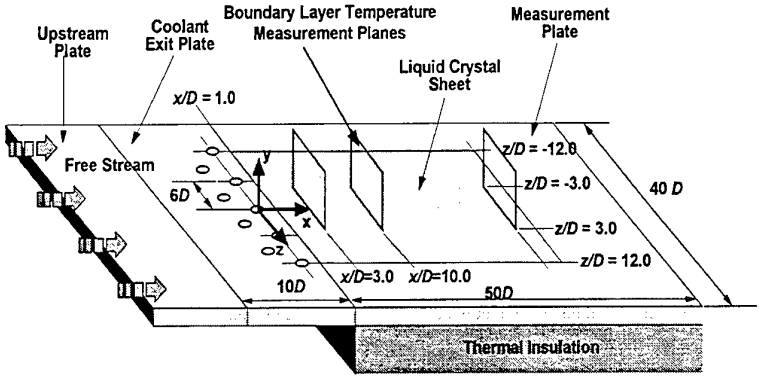

(b) Configuration of measurement plate

Fig. 2 Schematic diagram of experimental setup

$$\Theta = \frac{T - T_\infty}{T_c - T_\infty} \tag{1}$$

Boundary layer temperature distributions were measured using a T-type thermocouple calibrated in a constant temperature bath with a precision platinum resistance thermometer. The boundary layer temperature distribution is measured at $x/D = 3.0$, in $-3.0 \le z/D \le 3.0$.

The adiabatic film cooling effectiveness is defined as follows:

$$\eta = \frac{T_{aw} - T_\infty}{T_c - T_\infty} \tag{2}$$

where, T_{aw} denotes the adiabatic wall temperature. The effectiveness value of 1.0 implies that the adiabatic wall temperature is the same as the coolant temperature which implies that the wall is perfectly protected by the coolant. An effectiveness value of 0.0 means that the adiabatic wall temperature is the same as the main-stream temperature such that the wall is not covered by the coolant at all.

For the effectiveness measurements, the injectant is heated by 20°C higher than the free-stream temperature. Both T_∞ and T_c are measured with T-type thermocouples that are calibrated in constant temperature bath with precision platinum resistance thermometer. Adiabatic wall temperature is measured with TLC (Thermochromic

Liquid Crystal). The TLC sheet is covered in the range $1.0 \leq x/D \leq 31.0$, and $-12.0 \leq z/D \leq 12.0$. This measuring technique provides temperature distributions of the entire surface of interest at a time. Prior to the data acquisition, the wind tunnel and the injectant blower were activated to allow the surface temperature to reach a steady state. The process typically takes 2 hours. The TLC color image is then captured by a CCD camera for 30 seconds. From the captured images, the hue values are calculated and time-averaged simultaneously. The hue values are then converted to temperature.

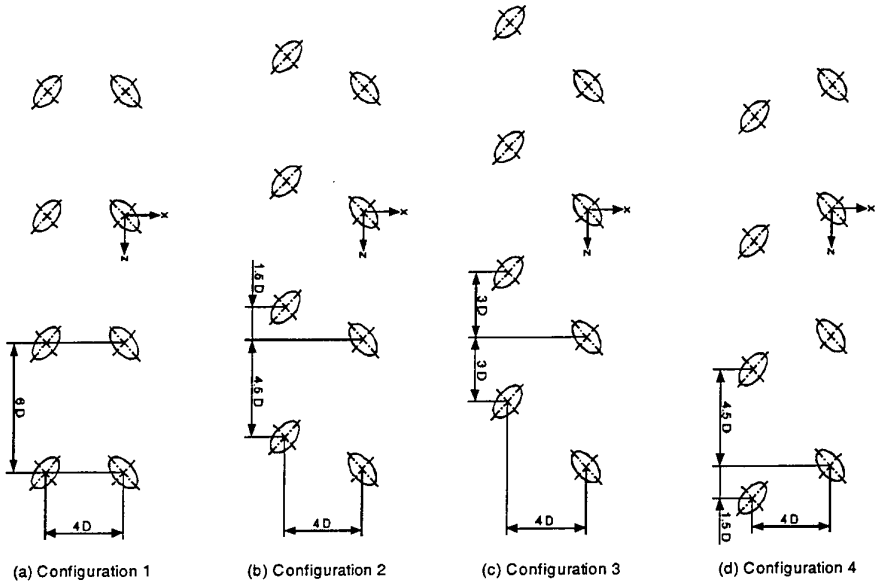

Fig. 3 Injection hole geometries

In the present study, the uncertainty analysis is evaluated on 20 to 1 odds (95% confidence level). All the uncertainty values are evaluated based on single-sample experiments proposed by Kline and McClintock [5]. The uncertainty of the dimensionless boundary layer temperature is estimated at a typical dimensionless boundary layer temperature value of 0.25. The uncertainty of dimensionless temperature is 5.7%, and of the adiabatic film cooling effectiveness is 6.8% at a typical η value of 0.2.

3. RESULTS AND DISCUSSION

Boundary Layer Temperature Distribution

The injectant concentration distributions (boundary layer temperature distributions) at downstream hole exits are measured prior to the measurement of temperature fields of each configuration (Fig. 4). Clockwise vortices exist – there is downwash flow on the right side of the jet and upwash flow on the left (Fig. 3)- since the upstream holes have orientation angles of –45 deg. The jet center moves in the z-direction as it flows downstream since the injectant from a compound angle hole has lateral momentum. Accordingly, the downwash regions of the upstream jets were located at the downstream-hole exits for configuration 1. For configuration 4, however, jets from downstream holes became to meet upwash flow at the hole exit. For the staggered configuration (configuration 3), the jet concentration was small at the downstream hole exit for low blowing ratios. But, jets from downstream holes met upwash flow at a blowing ratio of 2.0. For configuration 2, downwash flow was located at downstream hole exits at a blowing ratio of 0.5. However, jet concentration at the location became smaller as the blowing ratio increased.

As depicted above, each configuration has different flow condition at the downstream hole exit according to the blowing ratio. Jet from downstream holes behaved differently for each blowing ratio and configuration (Fig. 5). At $M = 0.5$ (Fig. 5(a)), the injectant was attached fairly well to the wall and confined to $y/D \approx 1.5$ irrespective of

configurations. The jet is less attached to the wall at M = 1.0 comparing to those at M = 0.5. This is simply because the injectant at M = 1.0 has a larger normal momentum components than at M = 0.5. For inline configuration (configuration 1), however, the jet was centered near the surface at M = 1.0 due to downwash flow at the hole exit. As the blowing ratio increases to 2.0, injectant penetration is so great that Θ = 0.05 contour line rises to $y/D \approx 3.0$.

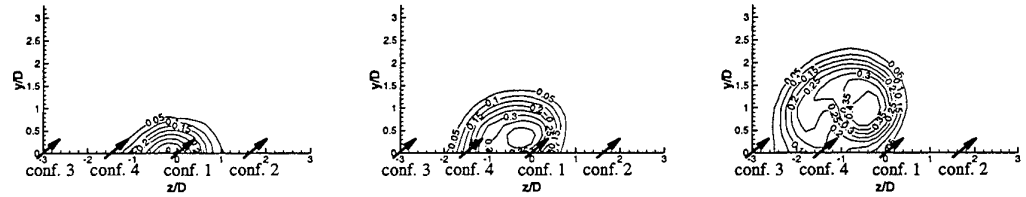

(a) $M = 0.5$ (b) $M = 1.0$ (c) $M = 2.0$

Fig. 4 Boundary layer temperature distributions at downstream hole exit

Near wall values of Θ are particularly important because they approach local magnitude of the surface adiabatic film cooling effectiveness. At the blowing ratio of 0.5, the maximum Θ value that met the surface was about 0.5 for all configurations. Thus, the area of unprotected region is important to the film cooling performance. High spanwise-averaged film cooling effectiveness is expected for the configuration 2 and 3. Configuration effects are more significant at higher blowing ratios. For configuration 1, the area occupied by Θ of 0.5 increased at M =1.0, compared to that at M = 0.5. For the other configurations, however, Θ values at y/D = 0 decreased with the blowing ratio because the injectant trajectory was less attached to the wall. At M = 2.0, the configuration effects are most distinct. The injectant well attached to the wall with inline configuration, but wide range of unprotected region was observed with configuration 3 and 4. An interesting characteristic to be noted is that the jet distribution of configuration 4 at M = 1.0 is similar to that of configuration 3 at M = 2.0. It is because the jet distributions from the upstream holes are changed according to the blowing ratios.

Adiabatic Film Cooling Effectiveness Distributions

The film cooling effectiveness distributions for M = 0.5 are shown in Fig. 6. The overall characteristic of the

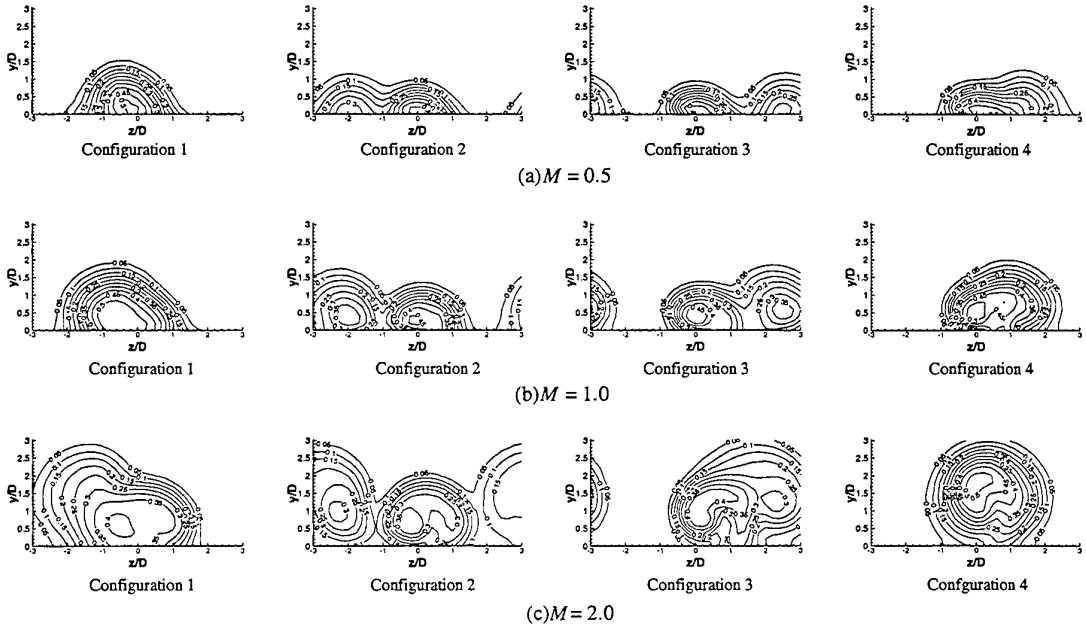

Fig. 5 Temperature distributions with tow rows of holes at x/D = 3.0

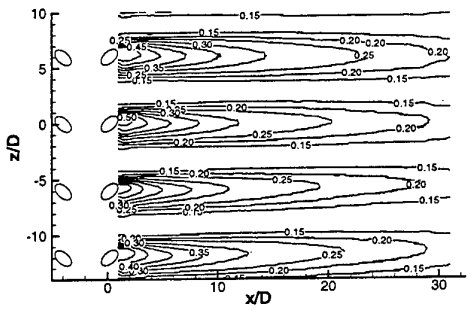

(a) Configuration 1

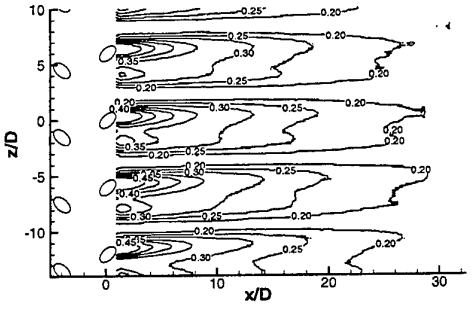

(b) Configuration 2

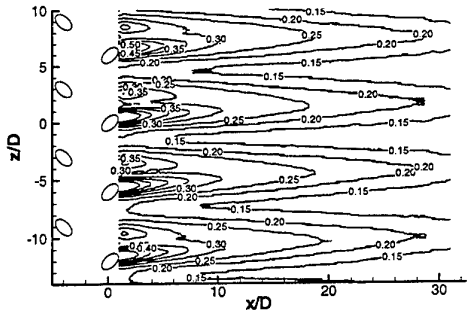

(c) Configuration 3

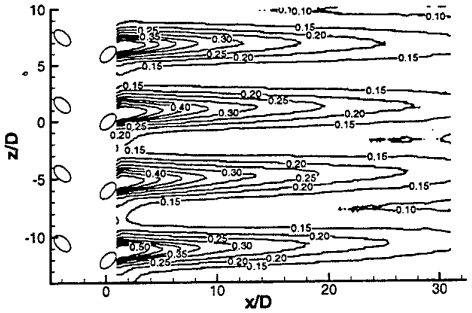

(d) Configuration 4

Fig. 6 Adiabatic film cooling effectiveness distributions for $M = 0.5$

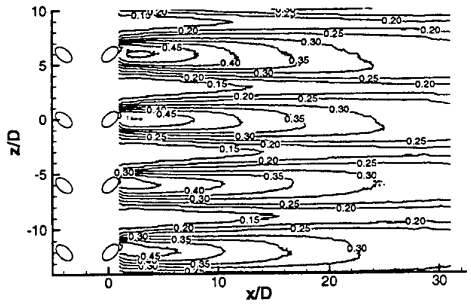

(a) Configuration 1

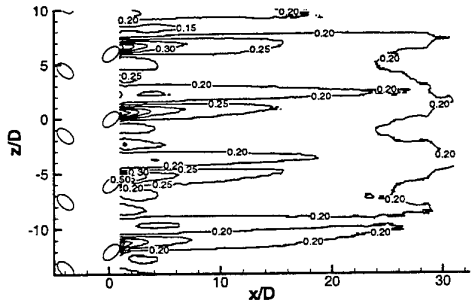

(b) Configuration 2

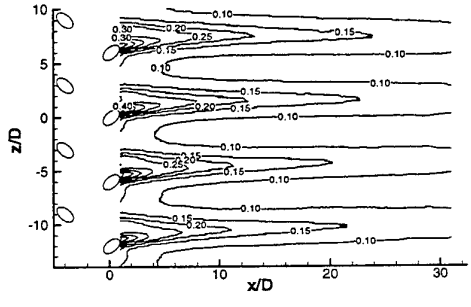

(c) Configuration 3

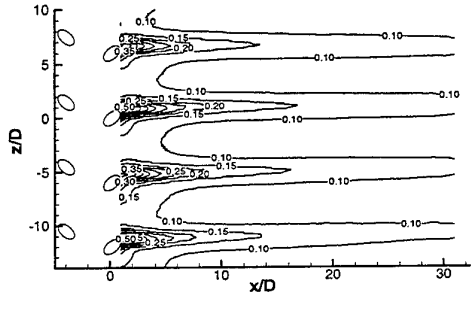

(d) Configuration 4

Fig. 7 Adiabatic film cooling effectiveness distributions for $M = 1.0$

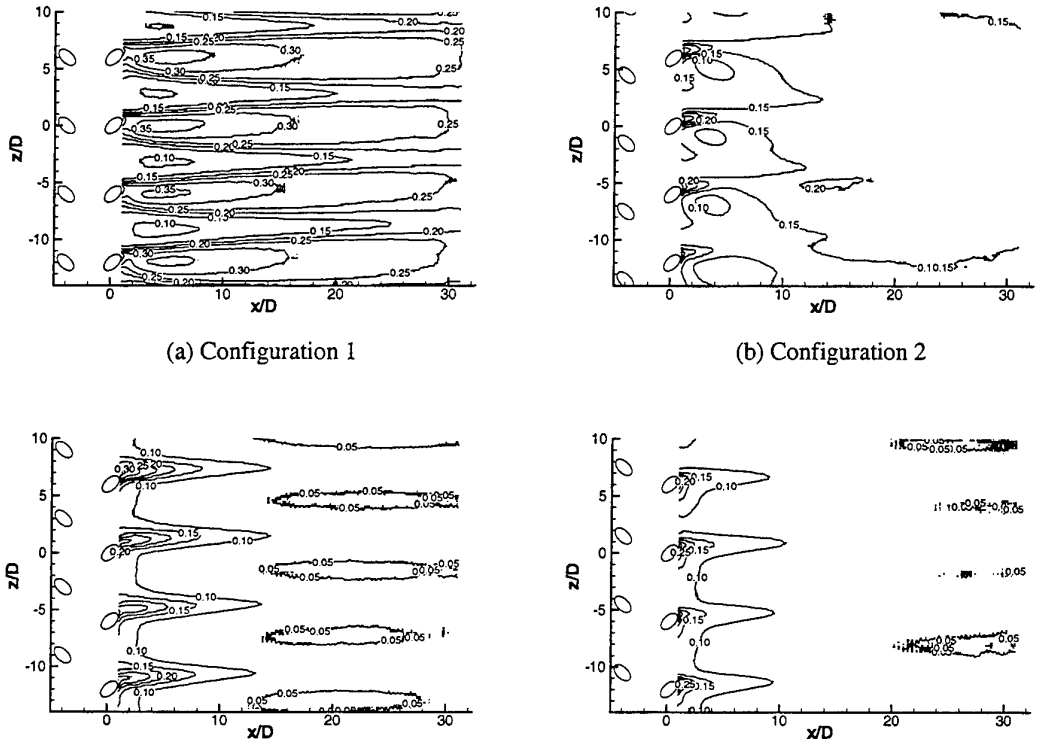

(a) Configuration 1

(b) Configuration 2

(c) Configuration 3

(d) Configuration 4

Fig. 8 Adiabatic film cooling effectiveness distributions for $M = 2.0$

effectiveness distribution is the high level of effectiveness compared to the other blowing ratios. The high level of effectiveness results from the attachment of the injectant to the wall as shown in the boundary layer temperature distributions (Fig. 5). The differences with respect to the configurations are not significant because jet is well attached to the wall for all investigated configurations.

When the velocity ratio increases to 1.0, the film cooling characteristic of each configuration becomes distinct (Fig. 7). The injectant started to separate from the wall for configuration 3 and 4 while jet was well attached to the wall with inline configuration at the blowing ratio. Consequently, configuration 1 showed high film cooling effectiveness. Between holes, however, low effectiveness level could be observed with the configuration. The effectiveness distribution near the holes is more uniform than that of inline configuration for configuration 2. But the overall effectiveness level is lowered compared with that of configuration 1. The lift-off of injectant causes a decrease in effectiveness value more significantly with configuration 3 and 4. The high blowing ratio of 2.0 brings about the strong vortex motion downstream of the injection holes and for this reason, the effectiveness distributions depend sensitively on the configurations (Fig. 7). Configuration 1 showed high effectiveness level because of the downwash flow at the hole exits. Another interesting feature of M = 2.0 is re-increase of effectiveness. For configuration 1, $\eta = 0.35$ contours (the highest effectiveness level) were observed from $x/D \cong 3.0$. The re-increase of effectiveness can be found at $x/D \cong 10.0$ for configuration 2. But it can be hardly observed with configuration 3 and 4.

To compare the effectiveness of the different configurations over a full range of blowing ratios, a space averaged adiabatic effectiveness was used. The space-averaged effectiveness is determined by averaging the effectiveness in the region of $-3.0 \leq z/D \leq 3.0$ and $1.0 \leq x/D \leq 31.0$. As blowing ratio increases, the space-averaged effectiveness decreases in general. This is a result of the injectant lift-off with the high blowing ratio. For inline

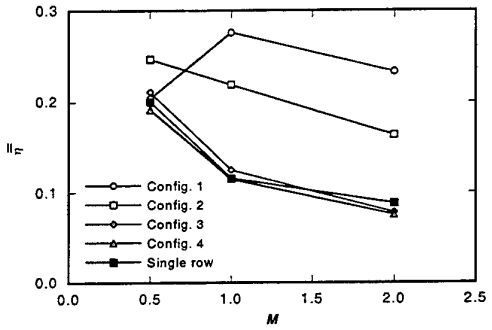

Fig. 9 Space-averaged film cooling effectiveness

configuration (configuration 1), however, the space-averaged effectiveness is higher at $M = 1.0$ than that at $M = 0.5$ by 40%. The space averaged effectiveness decreased with blowing ratio for configuration 2. But the configuration yields higher effectiveness compared with those of configuration 3 and 4. Since the upwash flows at the hole exits enhance injectant lift-off at the high blowing ratio for configuration 3 and 4, the effectiveness decreases drastically as the blowing ratio increases.

4. CONCLUSIONS

The effects of configurations and blowing ratios on boundary layer temperature distribution and adiabatic film cooling effectiveness were studied. Four configurations including inline and staggered configuration are investigated. The adopted blowing ratios are 0.5, 1.0, and 2.0. With heated injectant, the boundary layer temperature distributions were measured. The adiabatic film cooling effectiveness distributions were measured in detail with thermochromic liquid crystal. From the results, some important conclusions are drawn and summarized as below.

1. At the blowing ratio of 0.5, jet is centered near the surface regardless of the configuration.
2. For configuration 1 and 2, there exist downwash flows at the downstream hole exits and they showed high adiabatic film cooling effectiveness with the blowing ratios of 1.0 and 2.0.
3. Upwash flows are present at the downstream hole exits for configuration 3 and 4, which results in injectant lift-off and low effectiveness.

REFERENCES

1. S. W. Lee, Y. B. Kim and J. S. Lee, "Flow Characteristics and Aerodynamic Losses of Film Cooling Jets with Compound Angle Orientations," ASME J. of Turbomachinery, v.119, pp. 310-319 (1997).
2. D. L. Schmidt, B. Sen and D. G. Bogard, "Film Cooling with Compound Angle Holes: Adiabatic Effectiveness," ASME J. of Turbomachinery, v.118, pp. 807-813 (1996).
3. S. Honami, T. Shizawa and A. Uchiyama, "Behavior of the Laterally Injected Jet in Film Cooling: Measurements of Surface Temperature and Velocity/Temperature Field within the Jet," ASME J. of Turbomachinery, v.116, pp. 106-112 (1994).
4. B. Sen, D. L. Schmidt and D. G. Bogard, "Film Cooling with Compound Angle Holes: Heat Trnasfer," ASME J. of Turbomachinery, v.118, pp. 800-806 (1996).
5. S. J. Kline and F. A. McClintock, "Describing Uncertainties in Single Sample Experiments," Mechanical Engineering, v.75, pp. 3-8 (1953)

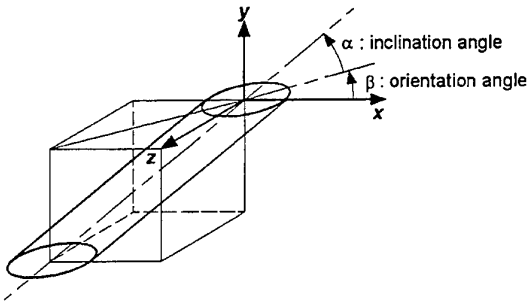

Fig. 1 Configuration of compound angle injection hole

with simple angle injection for the same spanwise hole spacing, normalized streamwise location and blowing ratio [2, 3]. It is also noteworthy that the film coolant injected from compound angle holes interacts with the mainstream fluid more vigorously to increase the heat transfer coefficient [4].

Past studies on the film cooling from two rows of holes with compound angle orientation adopted staggered configuration. They made each row of holes have the same orientation angles. Since the injectant from the compound angle holes possesses lateral momentum component, the injectant center moves in the z-direction as it flows downstream. Thus, effects of configuration on film cooling can be different from that of simple angle injection. In the present study, two rows of holes with opposite orientation angles were adopted to investigate the interactions of injectant flow with vortices. Four hole configurations including inline and staggered ones were investigated. For all configurations effects of three blowing ratios of 0.5, 1.0, and 2.0 are studied.

2. EXPERIMENTAL APPARATUS AND PROCEDURES

An open type subsonic wind tunnel is used to generate the free-stream(Fig. 2(a)). A boundary layer trip wire of 1.8mm diameter is located at $20D$, where D is the hole diameter, upstream from downstream holes to provide a turbulent boundary layer flow at the exit of the holes. The air, used as the injectant, first flows through an orifice followed by two heat exchangers that control the injectant temperature. Then, the air is ducted to a plenum chamber and discharged through the injection holes. The bottom plate of the duct consists of an upstream plate, an injection plate, and a measurement plate(Fig. 2(b)). Injection plates are prepared for each configuration(Fig. 3). The measurement plate starts at $x/D = 1.0$.

The boundary layer temperature distribution can reveal information about injectant behaviors and has a close relation with effectiveness distribution on the wall. In the measurement of boundary layer temperature distribution and the adiabatic film cooling effectiveness measurements, free-stream temperature is fixed at 20°C while the injectant is heated to 40°C.

The boundary layer temperature distribution is described in terms of dimensionless temperature defined as follows:

Table 1. Experimental Conditions

U_∞	10 m/s
D	10 mm
δ / D	1.50
$H (= \delta^* / \theta)$	1.36
L / D	4.0
$M (= \rho_c U_c / \rho_\infty U_\infty)$	0.5, 1.0, 2.0
$\mathrm{Re}_D (= U_\infty D / \nu)$	6570

EFFUSION COOLED COMBUSTOR LINERS OF GAS TURBINES – AN ASSESSMENT OF THE CONTRIBUTIONS OF CONVECTIVE, IMPINGEMENT, AND FILM COOLING

Achmed Schulz, Sigmar Wittig
Lehrstuhl und Institut fuer Thermische Stroemungsmaschinen
Universitaet Karlsruhe
76128 Karlsruhe, Germany
Email: achmed.schulz@its.uni-karlsruhe.de

Moritz Martiny
Dr.Ing. h.c. F. Porsche AG
71287 Weissach, Germany
Email: moritz.martiny@porsche.de

Keywords: combustor linear cooling, effusion cooling, cooling effectiveness

ABSTRACT. The requirement for an effective cooling of thermally high loaded combustor walls at little coolant consumption leads to effusion cooled combustor liners. Since effusion cooling is always a combination of convective cooling on the back of the wall and within the ejection holes and film cooling on the hot surface, the present study concentrates on the contributions of the various cooling methods to the total cooling effectiveness.

In a comprehensive experimental investigation the thermal behaviour of an effusion cooled test plate was analysed under real engine conditions, i.e. realistic Reynolds numbers, blowing rates, and density ratios. For an indepth understanding of the local heat transfer phenomena the test plate was geometrically scaled up. Two effusion hole patterns were investigated with and without impingement cooling on the cold side of the test plate. Moreover, two materials with different thermal conductivities were chosen for the test plates. Detailed effectiveness distributions were gained from highly resolved surface temperature distributions measured with an infrared camera. The effect of blowing rates on local as well as on laterally averaged effectiveness was addressed.

The experimental results show that the lateral averaged effectiveness is comparatively high with low blowing rates at the beginning of the effusion cooled area, i.e. the area of developing cooling film, due to attached coolant flow. Further downstream high blowing rates perform better. They form a thick and long effective layer of coolant. The relative poor preformance right at the beginning of the effusion cooled area in case of high blowing rates can be improved by applying impingement cooling on the back.

To get an instant information on the contributions of the various cooling methods a one-dimensional calculation procedure was developed. The calculation procedure accounts for different effusion geometries described by hole density, ejection angle, and hole length-to-diameter ratio. Aero-thermal parameters like blowing ratio, density ratio, Reynolds number, and thermal conductivity may be varied in a wide range as well. Comparisons between calculated and measured coolant and wall temperatures showed good agreement.

1. INTRODUCTION

Improvements in thermal efficiency of gas turbines depend on higher turbine inlet temperatures and higher compressor pressure ratios. The higher temperature level together with increased coolant temperatures, due to higher pressure levels, result in an increased heat load to the combustor wall. The walls of modern combustion chambers are effusion cooled. The pressure difference between coolant and hot gas flow drives cooling air through a huge number of slanted cooling holes on the inner hot gas surface of the combustor liner. In contrast to the ejection from one row of holes, many consecutive rows of cooling holes are applied with effusion cooling. The coolant forms a stable cooling film which is steadyly replenished. A major advantage of effusion cooling is the high amount of convectively transferred heat. Heat is not only drawn from the cold back surface, as in the case of slot film cooling, but also from within the cooling holes themselves. An illustration of an effusion cooled combustor liner together with typical thermodynamic and geometrical data is given in Figure 1. Shingles form the inner wall of a double walled flame tube.

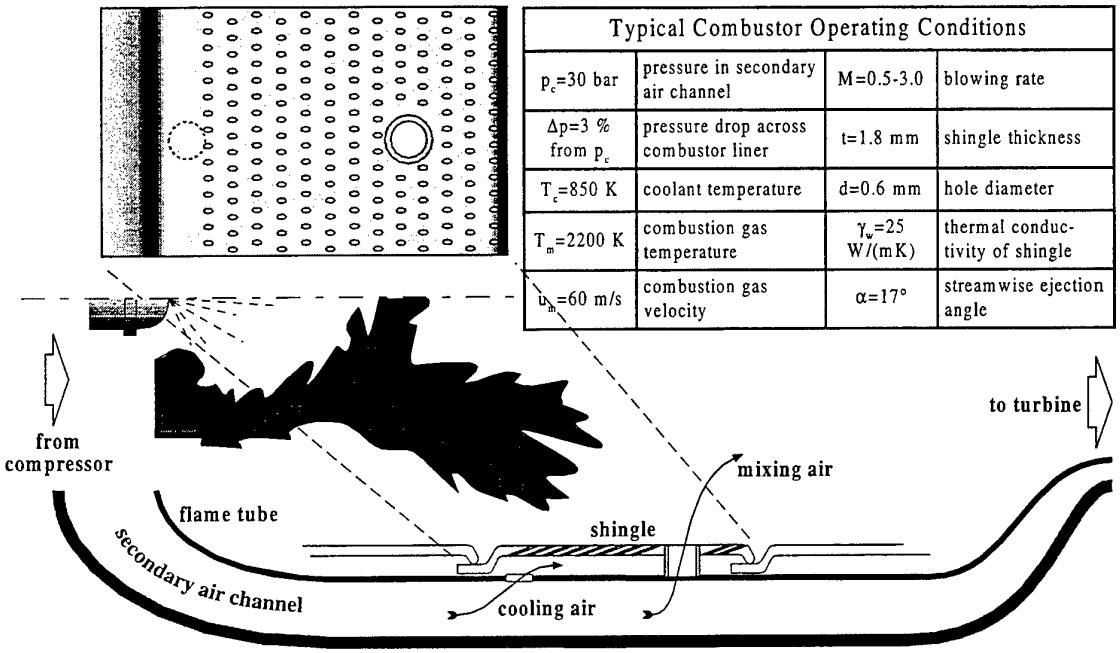

Figure 1. Schematic of a modern effusion cooled combustion chamber

The literature available concerning effusion cooling is by far not as extensive as in the case of pure film cooling. First experimental studies regarding boundary layer development and adiabatic effectiveness at varying blowing angles and hole arrangements were performed by LeBrocq et al. [1]. Utilizing a transient measuring technique Metzger et al. [2] investigated heat transfer and adiabatic effectiveness for inline and staggered hole arrays. The effect of hole density on the heat transfer was subject to the investigations of Mayle et al. [3]. Further fundamental experiments on heat transfer and cooling effectiveness at different ejection angles were performed by Crawford et al. [4]. Kumada et al. [5] applied the heat and mass transfer analogy in their experiments and demonstrated the strong impact of convection on the total cooling effectiveness. All these investigations contribute to a better understanding of the physical phenomena. For the design of effusion cooling, however, the results of these generic experiments have to be transferred to real application conditions. Experimentally demanding but crucial for the transferability is the correct temperature and density ratio between coolant and hot gas. The previously mentioned investigations were all performed at small temperature differences between coolant and hot gas. Ammari et al. [6] studied the influence of densitiy ratio on heat transfer coefficient. Their results show that heat transfer depends on density ratio especially at inclined ejection. The effect of density ratio on adiabatic cooling effectiveness was investigated by Foster et al. [7]. From their results it became obvious that density ratio has a much stronger influence on cooling effectiveness than on heat transfer.

Primary target in applying effusion cooling to combustor walls is the reduction of cooling air since more air is needed for the combustion process itself and for properly cooling turbine vanes, blades, and disks. The pressure drop between outer and inner surface of the flame tube is primarely determined by the kind of flame stabilization and by the combustion itself. Closely related to the pressure drop is the amount of coolant blown through the cooling holes expressed in terms of a dimensionless blowing ratio. Comparatively high blowing ratios are found at combustor liners with accordingly high momentum of the coolant when entering the combustor. As a consequence, the coolant separates from the wall leading to very poor film cooling effectiveness on the hot wall. To prevent cooling jet separation and to increase the operational range of effusion cooling towards higher blowing rates, cooling hole configurations with extremely shallow ejection angles are aimed on. The present study, therefore, concentrates on the investigation of effusion cooling at very shallow ejection angles (17°) under combustor typical conditions. The shallow ejection not only improves the formation of a protective cooling film but also increases the internal convective heat exchange due to an increased hole surface area.

2. EXPERIMENTAL TECHNIQUES

Since investigations of cooling methods in real combustion chambers are extremely expensive and limited in the application of measuring techniques the present study is conducted in a hot wind tunnel at the Institute for Thermal Turbomachinery at the University of Karlsruhe. To guarantee the transferability of the results gained from the experiments to real engine conditions a dimensional analysis has to be performed. Effusion cooling comprises three active areas. On the back surface and on the inner hole surfaces heat is drawn by convection. On the hot gas surface, the thermal load to the combustor liner is drastically reduced by the cooling film. With some conversions 14 dimensionless parameters can be derived from a dimensional analysis. Two major dimensionless parameters the temperature ratio T_m/T_c and the velocity ratio u_c/u_m are expressed in terms of the blowing ratio M and the momentum ratio I, respectively.

$$M = \frac{\rho_c \cdot u_c}{\rho_m \cdot u_m} \qquad I = \frac{\rho_c \cdot u_c^2}{\rho_m \cdot u_m^2}$$

These two quanities are widely used to describe film cooling situations.

Table 1. Characteristic dimensionless parameters

P/d	dimensionless hole pitch	Nu_b	Nusselt number in cooling hole
S/d	dimensionless hole spacing	Nu_c	Nusselt number on cold surface
t/d	ratio of wall thickness and hole diameter	M	blowing ratio
Re_m	main flow Reynolds number	I	momentum ratio
Re_b	cooling hole Reynolds number	Bi_m	Biot number hot gas surface
Re_c	coolant Reynolds number in plenum	Bi_h	Biot number in hole
St	Stanton number on hot gas surface	Bi_c	Biot number on cold surface
Prescribed: α ejection angle in streamwise direction			

Taking now typical operating conditions (see Fig.1) of a real combustion chamber the dimensionless parameters can be determined. The main flow (hot gas flow) Reynolds number turns out to be Re_m=2600, whereas the Reynolds number in the cooling hole and in the plenum varies with blowing rate in a range of Re_b=0...14000 and Re_p=0...240, respectively. The highest values refer to a blowing rate of 3. The Stanton, Nusselt, and Biot numbers can be determined by the known correlations for flat plate flow and pipe flow using the according Reynolds and Prandtl numbers.

As indicated earlier the tests were performed in a hot wind tunnel with special emphasis on a high resolution of local surface temperatures. For this reason a scaling factor of 6.66 was chosen, resulting in an effusion hole diameter of 4 mm and a wall thickness of 12 mm. To get an information on the local relation between heat transfer coefficient and film cooling effectiveness, i.e. dimensionless coolant temperature Θ, at least two tests with identical hot gas temperatures, coolant temperatures and blowing rates but different wall temperatures have to be performed. In the present study two wall materials with different thermal conductivities were used to establish different wall temperatures at otherwise identical conditions. One test case was aimed on adiabatic surface conditions, i.e. a material with very low thermal conductivity at good high temperature capabilities was required. The thermoplast TEKAPEEK met both conditions and was chosen due to its distinguished machinability. The thermal conductivity of this material is 0.3 W/mK and the maximum material temperature is 560 K. Since cooling air temprature is 300 K, the maximum temperature ratio is 1.85. This is somewhat lower than the real temperature ratio of 2.6 (compare Fig.1). Thermal similarity was the target of the other test case. Biot numbers of the real combustor and the test setup, therefore, must be identical. Heat transfer coefficients and wall thickness are given by similarity considerations. The only free variable is the thermal conductivity of the wall. Biot numbers revealed thermal conductivityies in the range of 8 W/mK and 10 W/mK. As a compromise in terms of availability, temperature resistance, and price INCOLOY 800H with a thermal conductivity of 12.2 W/mK was chosen as test plate material.

Two effusion hole configurations were investigated. The hole patterns were drilled into flat plates of the two materials chosen. Figure 2 shows the test section with optical access on either side of the flow channel. On the topwall a traversing mechanism is installed for a total temperature probe. For surface temperature measurements this top wall is equipped with two infrared transmissible windows.

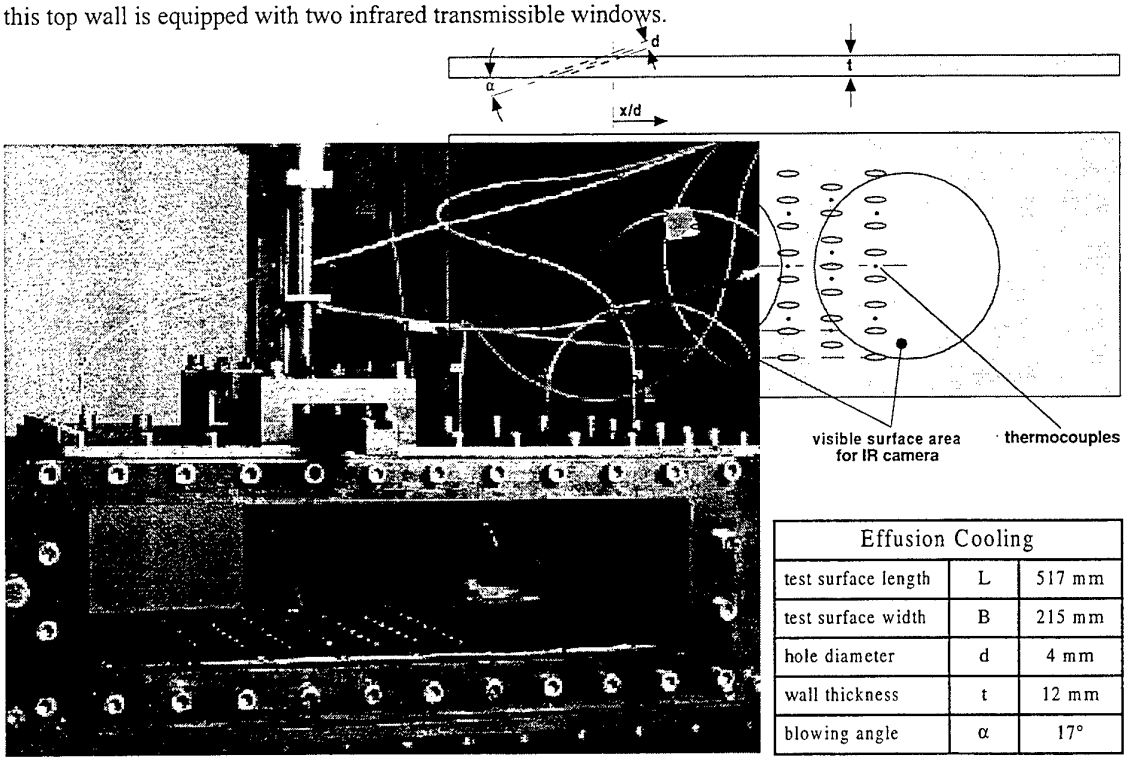

Effusion Cooling		
test surface length	L	517 mm
test surface width	B	215 mm
hole diameter	d	4 mm
wall thickness	t	12 mm
blowing angle	α	17°

Figure 2. Test section with effusion cooled flat wall

The two hole configurations investigated are shown in Figure 3. Both configurations were tested with and without impingement on the cold surface. Diameter and spacing of the impingement holes guarantee a desired distribution of the total pressure drop between impingement and effusion cooling.

The test section is included in a low pressure hot wind tunnel. The air is delivered by a radial blower and then split into main and coolant flow. The main flow is heated up to temperatures of 600 K by an electrical heater. A detailed description of the test facility can be found in Martiny et al. [8]. Surface temperatures of the cooled test plate are measured by an infrared camera. The in-situ calibration of the infrared camera and the correction due to radiating side walls and the non-perfect transmissivity of the window is given by Martiny et al. [9].

3. RESULTS

Near Adiabatic Wall, Hole Configuration A

Figure 4 top demonstrates the surface temperature distributions in terms of cooling effectiveness patterns for three blowing rates. Attached cooling films are formed downstream of every ejection hole for small blowing rates (M=0.5). The coolant streaks superpose and merge with downstream distance. Downstream of the last row of holes cooling effectiveness drops rapidly due to the little amount of coolant introduced into the boundary layer. At a blowing rate of M=1.2 the coolant starts to detach from the wall, resulting in comparatively low effectiveness within the first rows of holes. Further downstream the coolant is brought back to the surface by diffusion. The cooling effectiveness increases considerably. The drop in efficiency downstream of the effusion hole array is not as pronounced as in the low blowing rate case. At the highest blowing rate (M=3.0) the ejection holes act as strong heat sinks. There are steep temperature gradients around the holes and almost no cooling film formation within the first rows of holes. Hot spots detected just downstream of the cooling holes are caused by downwash of hot gas under the detached coolant jet (augmented by a pair of kidney vortices). The formation of a closed cooling film is

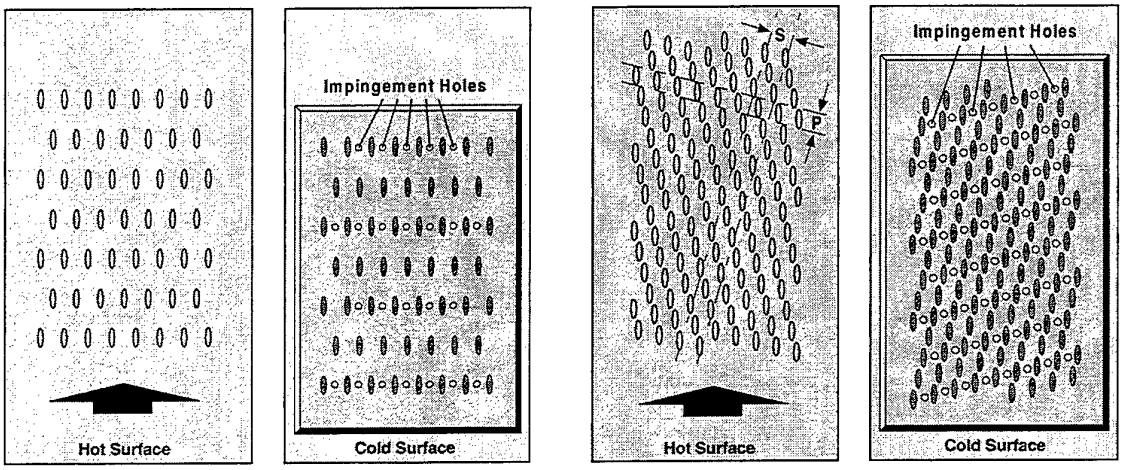

Cooling Hole Configuration A			
		Effusion Cooling	Impingement Cooling
streamwise hole distance	P	30 mm	60 mm
lateral hole distance	S	18 mm	18 mm
hole density	ρ_h	1870 m^{-2}	935 m^{-2}
hole diameter	d	4 mm	4.13 mm

Cooling Hole Configuration B			
		Effusion Cooling	Impingement Cooling
streamwise hole distance	P	13 mm	26 mm
lateral hole distance	S	15 mm	15 mm
hole density	ρ_h	5034 m^{-2}	2515 m^{-2}
hole diameter	d	4 mm	3.1 mm

Figure 3. Hole configurations of effusion test plates

shifted further downstream. Cooling effectiveness stays on a high level even downstream of the hole array due to the high amount of coolant blown into the hot gas.

The formation of cooling effectiveness is shown in the lower part of Figure 4. There are basically two schemes of developing cooling films. At low blowing rates the laterally averaged cooling effectiveness continuously increases with surface length. In contrast to this, at higher blowing rates the formation of a cooling film is shifted downstream since coolant jets penetrate into the main flow without forming a protective film. Dissipation of the jets leads to a thick cold layer in the downstream part of the effusion array with an accordingly high and stable cooling effectiveness. The coolant ejected with low blowing rates is relatively soon mixed up by the hot gases. This is expressed by the pronounced drop in cooling effectiveness in the rear part and downstream of the effusion array.

At this point it can be stated, that low blowing rate ejection performs better within the effusion hole array than high blowing rate ejection. However, this applies for cooling film formation only. Higher blowing rates come along with increased heat transfer on the cold surface and within the cooling holes leading to higher total cooling efficiencies. A good compromise between cooling film development and convective cooling requires a combined treatment of the cooling methods as will be shown in chapter 4.

Diabatic Wall, Hole Configuration A without Impingement

To establish realistic surface temperature distributions, the Biot numbers of the real combustor and the experiment must be identical. This was realized by chosing INCOLOY 800 H as effusion wall material. The surface temperature measurements were performed with and without impingement cooling on the back surface of the test plate. In Figure 5 total cooling effectiveness distributions are given for different blowing rates without impingement cooling. The analysis of the surface temperature distributions on the metal test plate is dominated by the interference of convective and film cooling. In general the hole array acts as heat sink in the midportion of the test surface. As a consequence, heat fluxes from areas without cooling holes upstream and downstream of the effusion array are formed. This becomes obvious by the high blowing ratio dependent level of effectiveness right at the beginning of the effusion hole area. In contrast to the thermoplast material, the effect of single coolant jets is no longer visible due to the high thermal conductivity of the metal plate. The lateral temperature distributions for all blowing rates

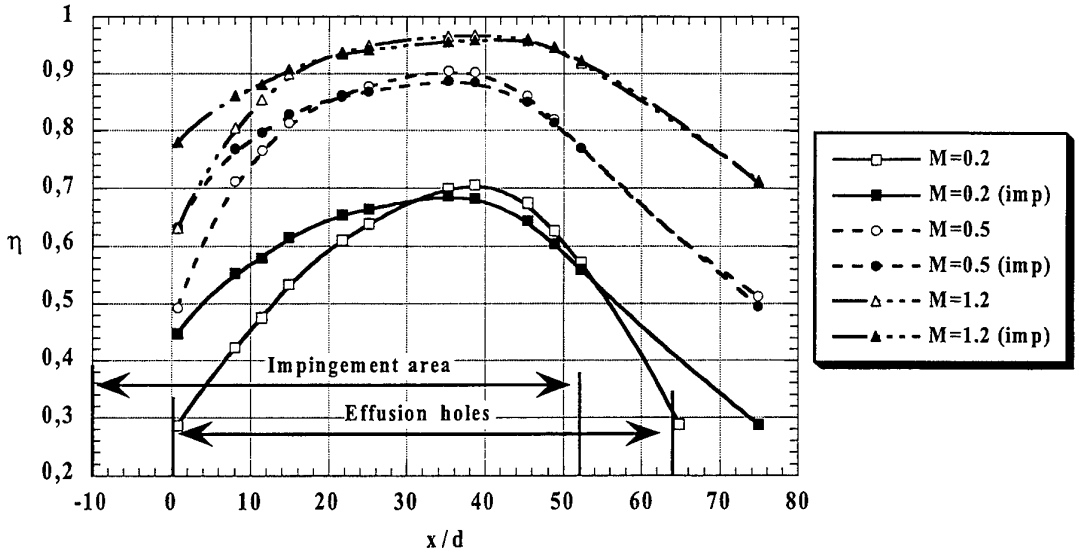

Figure 7. Effect of impingement cooling on laterally averaged cooling effectiveness for different blowing rates (Cooling hole configuration B, INCOLOY 800H)

4. THEORETICAL MODEL

The experimental results revealed, that surface temperatures of effusion cooled combustor liners are determined by a variety of parameters. The interaction of convective cooling within the holes and film cooling on the hot gas surface renders the prediction of surface temperatures rather difficult. For design purposes a theoretical model is needed, that accounts for the different cooling effects simultaneously, i.e. film cooling on the hot gas side, convective cooling in the holes and on the back surface of the tile. In the present model one pitch of an effusion cooled wall is taken as control volume. It is assumed, that upstream and downstream boundary conditions are periodical, i.e. the control volume is at a downstream location, where the cooling scheme is fully developed. The cold gas boundary is far off the cold surface to ensure, that the coolant is unaffected by the hot wall and can be described by its enthalpy H_c.

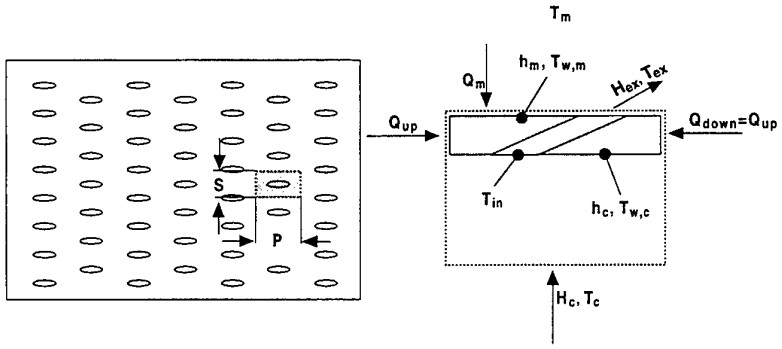

Figure 8. Control volume for the theoretical effusion model

The unknown temperatures T_{wc}, T_{wm}, T_{in} and T_{ex} have to be expressed by a system of four equations. A detailed description of the mathematical model and a comparison between calculated and measured cooling hole exit temperatures as well as a comprehensive parametric study of the theoretical model is given in Martiny et al. [10]. As indicated before, the coupling of the cooling phenomena is very complex, therefore, a multidimensional optimization method based on Microsoft EXCEL was applied. Once the governing equations are introduced into EXCEL, the heat balance can be solved iteratively for almost every combination of geometrical and aero-thermal boundary conditions. In Figure 9 the theoretical model is applied to the two effusion hole configurations investigated experimentally. For reasons of comparison, the coolant mass flux per surface area is the same for both hole configurations, i.e. the blowing ratios differ considerably. The consequences on the other describing parameters can be taken from Table 2.

Table 2. Aerothermal parameters of the effusion cooling model

Cooling hole configuration			A	B
Mass flux per unit surface area	m/A	kg/s•m²	0.707	
Hot gas velocity	u_m	m/s	18	
Blowing ratio	M	-	2.66	1
Air velocity in cooling hole	u_b	m/s	24	9
Film cooling heat transfer coefficient	h_0	W/m²•K	228	163
Adiabatic film cooling effectiveness	η_{aw}	-	0.40	0.49
Heat transfer coefficient on cold surface	h_c	W/m²•K	91	115
Heat transfer coefficient in cooling hole	h_b	W/m²•K	135	42

To get an information on the contributions of the various cooling phenomena, the according heat transfer coefficients and/or the adiabatic effectivenesses can be turned "on and off" in the model. The first column in Figure9 represents pure convection on the back surface of the test plate. There is virtually no ejection through the cooling holes ($h_b \approx 0, \eta_{aw}=0$). Although there is the same amount of coolant in both hole configurations and hence identical coolant velocities on the cold surface, configuration B exhibits a considerably higher effectiveness of 38.9% than configuration A with 26.9%. The difference is primarely caused by a higher heat transfer coefficient due to the higher number of stagnation points with according short running lengths along the back surface in case B. The second column gives the effectiveness for convection within the cooling holes only. There is no convection on the back surface and no protecting film on the hot gas surface ($h_c \approx 0, \eta_{aw}=0$). Here, the effectiveness is governed by the internal heat transfer coefficient (proportional to the coolant velocity) and the heat exchanging surface. In case of hole configuration B the increase of the heat exchanging surface due to the higher hole density dominates the reduced heat transfer coefficient. Combining convection in the cooling hole and on the back surface leads to effectivenesses demonstrated in column 3 of Figure 9 ($\eta_{aw}=0$). The effectiveness of 45.7% of configuration A represents 67% of the maximum achievable total effectiveness of 67.6%. In configuration B, 71% of the maximum effectiveness can be obtained by convective cooling only. Columns 4 and 5 show combinations of now film cooling with either convection on the back surface or convection within the cooling holes. Basically, the effectivenesses reflect the differencies between both hole configurations obtained with pure convection (see column 3). The combination of all cooling phenomena is demonstrated in the last column of Figure 9. Although the adiabatic cooling effectivenesses of both cases differ considerably (see Table 2), the augmentation in total effectiveness from pure convection given in column 3 to the combination of all cooling contributions in column 6 is almost the same.

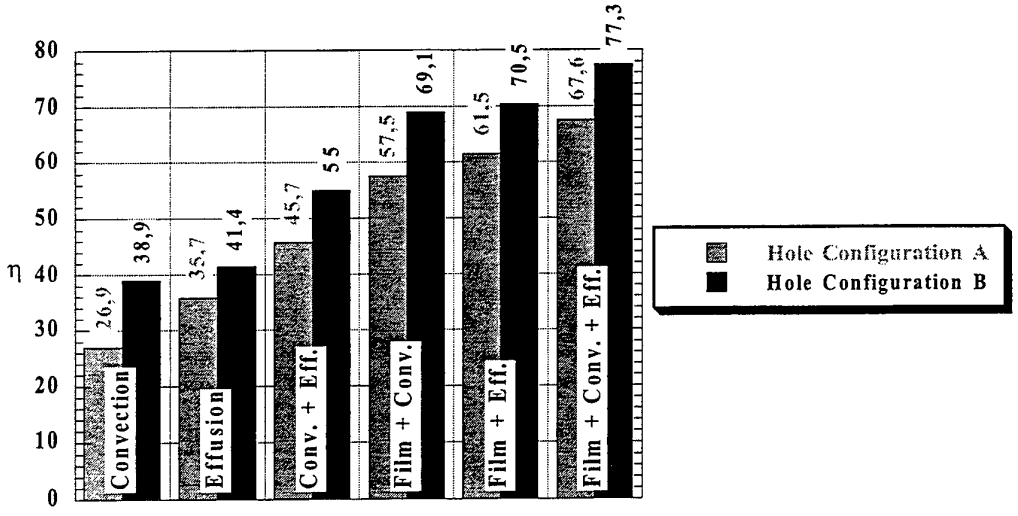

Figure 9. Contribution of the different cooling phenomena on the total cooling effectiveness for two cooling hole configurations

This is caused by the blowing ratio dependent heat transfer coefficient on the hot gas side, which is higher in case of hole configuration A. The calculated total effectivenesses of 67.6% and 77.3% in case A and B, respectively, are somewhat underpredicted, as a comparison with the experimentally determined effectivenesses in Figures 5 and 7 reveals. The major reasons for the underestimation are the correlations used for the film cooling heat transfer coefficient and for the cold surface heat transfer coefficient. However, the method presented, is a very helpful tool for an instantaneous assessment of variations of aero-thermal boundary conditions and of the geometry.

5. CONCLUSIONS

A comprehensive study of the thermal behaviour of an effusion cooled test plate representing a combustor liner was performed. Two effusion hole patterns were investigated with and without impingement cooling on the cold surface of the test plate. The results revealed, that impingement promotes cooling primarely in areas where film cooling effectiveness is poor. The effect of cooling hole arrangement and density was pointed out in analysing two different cooling hole configurations. To get an instant information on the contributions of the various cooling methods a one-dimensional model was developed and applied to cooling hole configurations investigated experimentally. The basic dependencies could be clearly demonstrated. The improvement of the correlations used in the model is subject to further studies.

REFERENCES

1. P.V. LeBrocq, B.E. Launder, C.H. Priddin: „Experiments on Transpiration Cooling: Discrete Hole Injection as a Means of Transpiration Cooling - An Experimental Study", Proc of the IMechE 187, pp. 149-157, 1973
2. D.E. Metzger, D.I. Takeuchi, P.A. Kuenstler: „Effectiveness and Heat Transfer with Full-Coverage Film Cooling", ASME Journal of Engineering for Power, Vol.95, pp. 180-184, 1973
3. R.E. Mayle, F.J. Camarata: „Multihole Cooling Film Effectiveness and Heat Transfer", ASME Journal of Heat Transfer, Vol.97, pp. 534-538, 1975
4. M.E. Crawford, , W.M. Kays, R.J. Moffat: „Full-Coverage Film Cooling Part I: Comparison of Heat Transfer Data for Three Injection Angles", ASME Journal of Engineering for Power, Vol.102, pp. 1000-1005, 1980
5. M. Kumada, M. Hirata, N. Kasagi: „Studies of Full-Coverage Film Cooling Part 2: Measurements of Local Heat Transfer Coefficients", ASME Paper No 81-GT-38, 1981
6. H.D. Ammari, N. Hay, D. Lampard: „The Effect of Density Ratio on the Heat Transfer Coefficient From a Film-Cooled Flat Plate", ASME Journal of Turbomachinery, Vol.112, pp. 444-450, 1990
7. N.W. Foster, D. Lampard: „Effects of Density and Velocity Ratio on Discrete Hole Film Cooling", AIAA Journal 13, pp. 1112-1114, 1975
8. M. Martiny, A. Schulz, S. Wittig: „Full-Coverage Film Cooling Investigations: Adiabatic Wall Temperatures and Flow Visualization", ASME Paper No 95-WA/HT-4, 1995
9. M. Martiny, R. Schiele, M. Gritsch, A. Schulz, S. Wittig: „In-Situ Calibration for Quantitative Infrared Thermograpgy", QIRT 96, Eurotherm Seminar No 5, pp 3-8, 1996
10. M. Martiny, A. Schulz, S. Wittig: „Mathematical Model Describing the Coupled Heat Transfer in Effusion Cooled Combustor Walls", ASME Paper No 97-GT-329, 1997

ACKNOWLEDGEMENT

The study was supported by the German „Arbeitsgemeinschaft Hochtemperaturgasturbine AG TURBO" through grant by the German Ministry of Science, Research and Technology BMBF.

EXPERIMENTAL STUDY OF THE FLOWS WITHIN A LEVITATED SPOT-HEATED DROP

E.H. Trinh, S.K. Chung
Jet Propulsion Laboratory
4800 Oak Grove Drive
Pasadena, CA 91109, USA
Email: Eugene.H.Trinh@jpl.nasa.gov; Fax: (818) 393-5039

S.S Sadhal
Department of Aerospace & Mechanical Engineering
University of Southern California
Los Angeles, CA 90089-1453, USA
Email: sadhal@usc.edu; Fax: (213) 740-8071

Keywords: microgravity, levitation, acoustic, undercooling, thermocapillarity

ABSTRACT. The internal flows within single drops levitated in air have been experimentally examined on Earth and under low-gravity conditions. The motivation for this study is provided by the need to assess the impact of the levitation fields: Can a quiescent undisturbed state be reached when a liquid sample is electrostatically or ultrasonically levitated on Earth? The usefulness of the containerless experimentation methods for free drops and bubbles can only be rigorously established if the potential interfering effects associated with levitation do not significantly alter the characteristics of the phenomena under investigation. For example, in the case of the thermocapillary flows generated within a free drop by laser spot heating, the background flow within the unheated drop in an isothermal environment must be characterized first. Using both ultrasonic and electrostatic levitation techniques, we have developed the ability to stably hold single drops and to observe the internal flows under laser spot-heating. The fluid motion under the action of both natural buoyancy and surface tension gradients are three dimensional and asymmetrical, even though the heating is centered on the equator of the levitated drop. In addition, the asymmetrical heat distribution also induces rotation of the drop, especially when ultrasonic levitation is used. In order to eliminate the buoyant contribution, low-gravity experiments are under consideration. Initial space-based investigations using an ultrasonic device have revealed that any residual interference from acoustically-induced stresses and flows are eliminated when the sound power is reduced to a very low level. These data also show, however, that a 6 mm diameter drop remains very sensitive to aerodynamic drag exerted by even very slow circulation. This drag constitutes an effective torque driving the drop into slow solid-body rotation.

1. INTRODUCTION

Recent microgravity flight experiments using electromagnetically levitated molten metals have demonstrated the feasibility of measuring the thermophysical properties of highly undercooled melts (Robinson [1]). Earth-based investigations in the same area using electrostatically levitated and laser-heated metals and semiconductors have also achieved deep undercooling and shown that measuring the surface tension, viscosity, specific heat, density, and electrical conductivity was also practical (Rhim et al. [2, 3]; Ohsaka, Chung & Rhim [4]; Chung, Thiessen & Rhim [5]; Rulison & Rhim [6]). In both cases, the millimeter-size samples were processed under high vacuum, and were melted and re-solidified in a completely containerless fashion. The level of undercooling achieved in each case was comparable, and did not reveal an obvious microgravity-related advantage in terms of undercooling enhancement. Thus, it appears that the rationale for microgravity-based containerless investigations of the metastable liquid phase should be based on the greater accuracy of thermophysical property measurement, rather than the ability to penetrate deeper into the undercooled region. The argument is that the opportunity to reduce the intensity of the fields (electromagnetic, electrostatic, acoustic) used to position the liquid sample will lead to a minimization of their interfering effects, and consequently will yield more accurate measurements. Examples of these field effects are: the induction of internal fluid circulation, the static deformation of the sample shape, the constraints in the sample motion due to the force fields, and the induced and uncontrolled sample rotation.

The research we describe here relates to the experimental evaluation the effects of levitation fields in the context of the measurement of the surface tension, viscosity, and thermal diffusivity of levitated molten materials. The application of levitation methods under the full effect of gravity allows us to evaluate the interfering action of electric and ultrasonic fields by repeating the same investigation in low gravity. The fundamental motivation is to use recently developed containerless experimentation methods to determine the thermophysical properties of levitated undercooled molten materials for use both at 1-G and in reduced gravity. The microgravity investigation thus allows the validation of the theoretical predictions of the high-intensity field effects by providing an experimental platform where they can be drastically reduced.

Levitation methods have been implemented as an alternative to the free fall in drop tubes approach to study the properties of materials removed from container walls. The purpose of isolating the sample from a container is either contamination avoidance or the minimization of the probability for heterogeneous nucleation. The advantage of a levitated sample is its spatial stabilization for a sufficiently long time to carry out the measurement of its characteristics.

The issue we are particularly concerned with is the question of how accurately we are able to measure the properties of levitated samples and how we deal with highly viscous melts. The theoretical underpinnings of all the non-contacting methods used for specific physical property measurement rely on some specific assumption about the initial and boundary conditions relevant to the samples under study. For example, the accurate determination of the surface tension and viscosity of free liquid drops requires modifications to the earlier treatments of the frequency and damping of spherical drop shape oscillations by Rayleigh [7] and Lamb [8]. These modifications have to account for the non-spherical equilibrium shape of the levitated drops (Shi & Apfel [9]; Suryanarayana & Bayazitoglu [10]), the effects of free electric charges (Feng & Beard [11, 12, 13]; Trinh, Holt & Thiessen [14]; Tsamopoulos, Akylas & Brown [15]; Natarajan & Brown [16]), the effects of internal flows (Mashayek & Ashgriz [17]), the impact of rotation (Annamalai, Trinh & Wang [18]) and nonlinear oscillations (Trinh & Wang [19]), and the influence of the levitation fields on the drop motion (Cummings & Blackburn [20]). All these perturbations arise from the action of high intensity electric, electromagnetic, or acoustic fields used for the levitation of the liquid samples. A detailed investigation of the various side-effects of levitation fields has not yet been carried out, and it appears that only ad-hoc modifications of simple theories have been used to analyze the results of space experiments. Under certain circumstances, some of these perturbations were ignored altogether due to the lack of information on the drop behavior. As a result, the accuracy of the measured material physical parameters could be further improved with a better understanding of these high field effects. We believe that reliable results from careful experimental and theoretical fluid dynamical studies would favorably impact this area of fundamental material science.

Actual conditions encountered at high temperature in electromagnetic and electrostatic levitation devices at 1-G are generally difficult to analyze because the exact behavior of the levitated sample cannot be measured directly. For example, the internal flows in opaque materials can be modeled using simulated conditions, but the resulting predictions cannot be directly validated by carrying out measurements in actual instruments. We believe that a more tractable approach would be to study the same phenomena using model materials that allow quantitative experimental measurements to be used to validate theoretical models. The understanding of the physical mechanisms determining the dynamics of the levitated samples must be acquired first, before their effective application to real systems can be obtained. An understanding of the crucial parameters will allow the selection of an optimal instrument to carry out the required measurements with the best accuracy.

The rationale for low-gravity experiments has been based on the ability to neglect all the perturbing effects as the field intensity is drastically reduced. Recent results of a flight investigation indicate that current actual conditions aboard the Space Shuttle require a minimum level of sample positioning capability that can still interfere with the sample dynamics (Trinh et al. [21]).

2. EXPERIMENTS

Experiments were carried out in 1-G and microgravity with the use of an acoustic levitator shown in Figure 1. Some experiments were carried out using a hybrid acoustic-electrostatic levitator. For ground-based work,

spherical drops with diameter ranging between 2-4 mm and composed of water, water-glycerin mixtures, and silicone oil were levitated in air using combined electrostatic-ultrasonic forces, and spot heated using a focused infrared laser. Nearly spherical drops with a deviation from sphericity of less than 1% could be maintained motionless for extended periods of time using electrostatic levitation alone. Drop rotation was induced, however, as soon as the acoustic field was activated due to the induced steady streaming flows generated within the levitation chamber. The electric field magnitude used ranged between 5 and 10 kV, and the surface charges on the levitated drops was on the order of 5×10^{-11} Coulombs. The ultrasonic frequency used was approximately 22 kHz, and the sound pressure level ranged between 135 and 165 dB (re 0.0002 microbar).

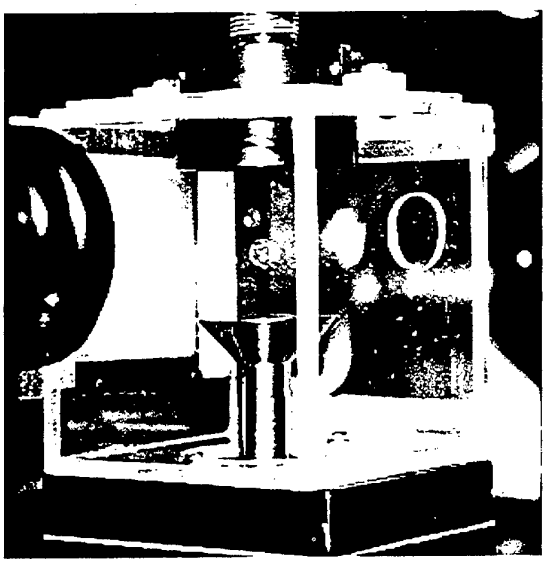

Figure 1: Typical levitation apparatus used for ground-based and microgravity studies.

Three-dimensional thermocapillary flows were detected on spot-heated levitated spherical drop at 1-G for drops with viscosity between 0.05 and 1 Poise. The flows were induced as soon as the heating laser power was turned on, and dissipated as soon as it was turned off, providing a clear experimental correlation between laser heating and internal flow. The visualization of these flows were carried out using two CCD video camera to provide simulated three-dimensional visualization of the suspended tracer particles motion within the drop.

Using uncharged and drastically flattened drops that were levitated by ultrasonic forces alone, we could measure symmetric and regular two-dimensional flows because of the inhibition of major buoynacy-driven flows due to the thinness of the flattened drops. When flattened, the drops had a diameter as large as 1 cm, but their thickness ranged between 100 and 300 microns. The path of the suspended tracer particles was visualized using CCD cameras, and their digitized images were frame-averaged in order to reveal the flow pattern.

The flight investigation using the Middeck Glovebox facility flying aboard the Space Shuttle used only ultrasonic levitators to investigate the internal flow of spherical drops at very low acoustic intensity in order to minimize the rotational motion. Non-uniform heating of the drop surface was provided by a heated miniature thermistor placed in the drop vicinity, or directly contacting it. The acoustic frequency was 21.8 kHz and the acoustic pressure level was as low as 120 dB. The maximum thermistor temperature was 48°C.

Ground-Based Studies of Nearly Two-Dimensional Thermocapillary Flows in Flattened Levitated Drops

Heat input to levitated samples is generally not uniform, and thermal gradients often exist both on the surface as well as in the liquid bulk. On Earth, these result in buoyant flows, and in low gravity thermocapillary convection will be dominant. Under the best circumstances, these thermocapillary flows retain some order and symmetry, but their coupling with the oscillatory dynamics of the levitated drops quickly results into three-dimensional

Figure 2: A disk-shaped ultrasonically levitated drop of glycerol. The aspect ratio can be continuously varied by adjusting the acoustic pressure level. The central portion can be made very thin (< 1 micron) for viscous liquids. The central dimple observed in the photograph is removed for lower acoustic pressure, and the opposed drop surfaces can be made more parallel. The drop side dimension is 4.5 mm.

and disordered motion. Effects of these flows on the dynamics of electrostatically levitated drops have been theoretically addressed recently (Li & Song [22]), but no exhaustive experimental study has been carried out. Our preliminary Earth-based experimental data on the behavior of a spot-heated and electrostatically levitated drop at ambient temperature reveal that modest surface thermal gradients initiate thermocapillary flows that quickly induce three-dimensional fluid motion involving drop rotation. This rotation instability is greatly minimized if spot heating is carried out along the drop vertical symmetry axis at the top or bottom of the drop. Thus, it is very likely that a laser-melted and electrostatically positioned material sample will be characterized by substantial internal flows while rotating in a direction influenced by the heating configuration. In addition to the static distortion introduced by the electric field used for drop positioning, these flows and the uncontrolled rotational drop motion will influence the shape oscillations of lower-viscosity liquids.

Under the restriction of axial symmetry, we had developed a theoretical treatment of the thermocapillary flows within levitated drops using pure heat conduction conditions (Sadhal, Trinh & Wagner [23]). We have attempted to experimentally verify the theoretical predictions both on Earth as well as in microgravity. We have discovered that even in microgravity, rotational drop motion is readily driven by thermocapillary flows, and the condition of axial symmetry could not be experimentally obtained with current levitation techniques. Only by using drastically flattened drops (to a nearly disk-like shape) that were ultrasonically levitated at 1-G and spot heated on one side, could we obtain nearly axially symmetric flow fields reminiscent of the theoretically predicted patterns. Figure 2 shows a photograph of such a flattened drop viewed at a slight angle. The main drop plane is perpendicular to the direction of gravity. By using suspended tracer particles and laser illumination, we have been able to resolve the three-dimensional flows within the disk-shaped drop. The flattening of the drop in a plane perpendicular to gravity minimizes the influence of natural buoyancy, and reveals the essential features of thermocapillary flows in the major plane of the drop.

Using a high-viscosity liquid ($\mu > 10$ poise) and an ultrasonic levitator, a drop can be stably held in a very thin disk-like shape for a substantial time without the onset of shape instability, i.e. the shape will remain stationary for a long time. The central area of the drop can be shaped by the acoustic field into a dimple with the thinnest sheet at the very center (or very nearly flat if so desired). The thickness of this central region can be adjusted through an increase or decrease in the acoustic pressure. At high acoustic pressure, lower viscosity drops would atomize, or would undergo shape instability and breakup.

Drops of 200 cSt silicone oil (Polydimethylsiloxanes) were ultrasonically levitated in ambient air and under atmospheric pressure. The acoustic pressure were adjusted in order to induce a drastic flattening of the drop

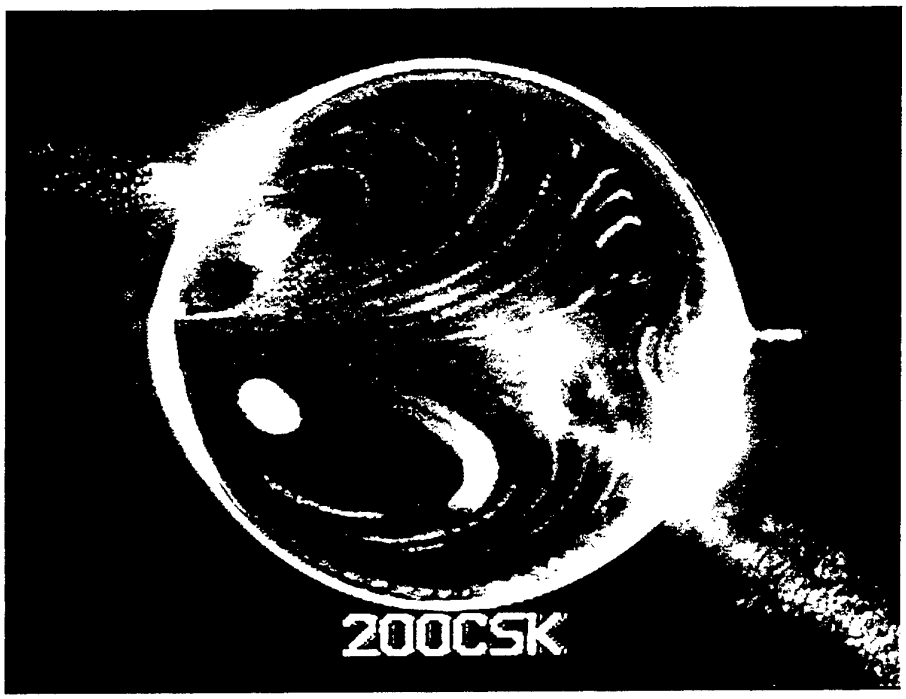

Figure 3: Time-lapse video image of circulatory flow induced in a flattened levitated drop heated with a focused laser on the left side. The 200 cSt silicone oil drop is ultrasonically levitated at 1-G in air at STP, and the flow pattern is made visible by suspended tracer particles illuminated with a laser sheet.

in order to achieve very high diameter-to-thickness ratios (on the order of 20). Under these conditions, the levitated drop assumes the shape of a circular disk with a slightly thicker lip at the outer circumference (see Figure 2). Shape aspect ratios between 1.5 to 50 can easily be achieved using silicone oil at 1-G. A focused CO_2 laser is aligned to heat a small area (on the order of 200 microns diameter) at one side of the drop. Diametrically opposed is a very thin glass fiber contacting the drop surface used to arrest the drop rotation. The drop also contains suspended polymeric tracer particles with a size distribution between 10 and 50 microns. A video camera is placed perpendicular to the drop surface in order to record the tracer particle motion under a He-Ne laser sheet illumination.

Under these circumstances, we believe that we can observe mainly two-dimensional thermocapillary flows driven by the laser spot-heating. Under careful examination, a circulatory motion directed normal to the drop main cross section can be seen at the edge of the drop. This circulatory motion increases in extent towards the drop center for lower viscosity liquids. With 200 cSt silicone oil, this outer circulatory motion is restricted to a region within the first 5% of the drop diameter. We believe that this steady circulation is induced by the acoustic streaming flow induced by the levitation field.

With laser heating raising the local surface temperature in a range between 10 and 100°C, we have been able to record steady thermocapillary-induced motion in the plane of the flattened drop. Figure 3 shows the general flow pattern for a laser spot heated impacting the drop surface at the left edge. Close examination reveals a double set of dipole-like circulation pattern. A higher velocity (1 to 5 cm/s) small vortex is located near the heated spot region, while a larger counter-rotating vortex extends over the majority of the drop cross-section. These measurements were carried out for fairly low values of the Marangoni number (Ma=Re.Pr, where Re and Pr are the Reynolds and Prandtl numbers, respectively) between 100 and 250, and are the results of a feasibility study aiming to demonstrate the extent to which the buoyancy-driven convective flow could be inhibited in

drops characterized by a very high aspect ratio. More detailed measurements will be carried out using digital Particle Image Velocimetry.

Microgravity Glovebox Experiment on Differentially Heated Drops

A compact experimental apparatus including an ultrasonic levitator, electronic control, a sting heater, and laser illumination has been flown aboard the Space Shuttle to demonstrate the feasibility of acoustically positioning a spherical drop in low gravity for the measurement of thermocapillary flows. The ability to drastically reduce the intensity of the ultrasonic positioning field in microgravity has been demonstrated by a first set of light experiments carried out on STS-94. Spherical drops were quiescently positioned in ambient Shuttle environmental conditions and the residual uncontrolled drop rotation was measured to be on the order of 0.1 rps along a fixed axis perpendicular to the levitator symmetry axis. Figure 4 is a video image of a freely positioned drop

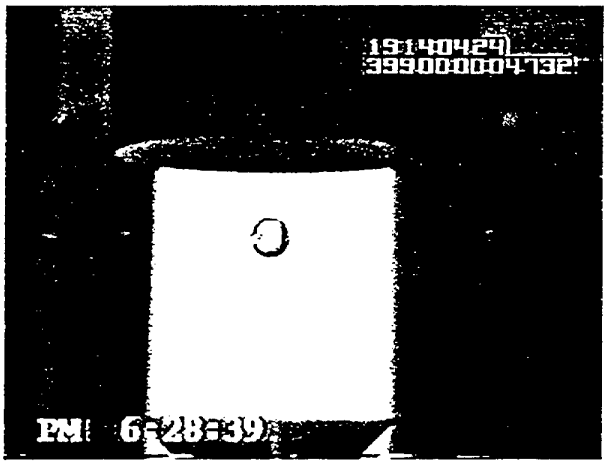

Figure 4: Positioned drop in low gravity using an ultrasonic levitator. In this video frame, the drop is shown between the ultrasonic wave generator at the bottom and the reflector at the top. The drop diameter is 6 mm.

in the IFFD (Internal Flow in Free Drop) apparatus during the STS-95 flight. A drop is shown between the horn of an ultrasonic driver and the reflector required to establish a resonant standing wave. Drops of water, aqueous solutions of glycerol of different viscosity, and silicone oil were used in drops with diameter ranging between 2 and 7 mm. The liquid samples also contained polymeric tracer particles in order to visualize the internal motion and rotational behavior of the drops.

A second flight of the apparatus on STS-95 allowed the investigation of the behavior of a freely positioned drop in the vicinity of a sting heater. In this implementation a 2 mm diameter cylindrical thermistor was used as a local heating source placed within 3 mm of an ultrasonically positioned droplet at ambient Space Shuttle conditions. The heater maximum temperature was limited to 48°C because of safety requirements, and the water-glycerol samples viscosity was 10 cSt. The Marangoni number range investigated was therefore below 200, and the anticipated thermocapillary flow velocity was small. Also carried out were a series of measurement of the drop internal flow with the sting heater contacting the drop at various acoustic power level. Figure 5 shows a slightly flattened drop with the sting heater located at about 3 mm away, and a spherical drop contacting the sting heater. The flattening is due to the acoustic field. The surface of the sting heater was treated with an anti-wetting agent in order to minimize the liquid-heater contact area.

Even with a low background residual drop rotation, the thermocapillary flows could be detected because of the redirection of the motion of the suspended tracer particles. Upon differential heating, the solid-body rotational motion of the drop was altered by the addition of the lateral thermocapillary-induced motion. Velocities varying between 0.1 to 0.5 mm/s were recorded depending upon the heater power setting.

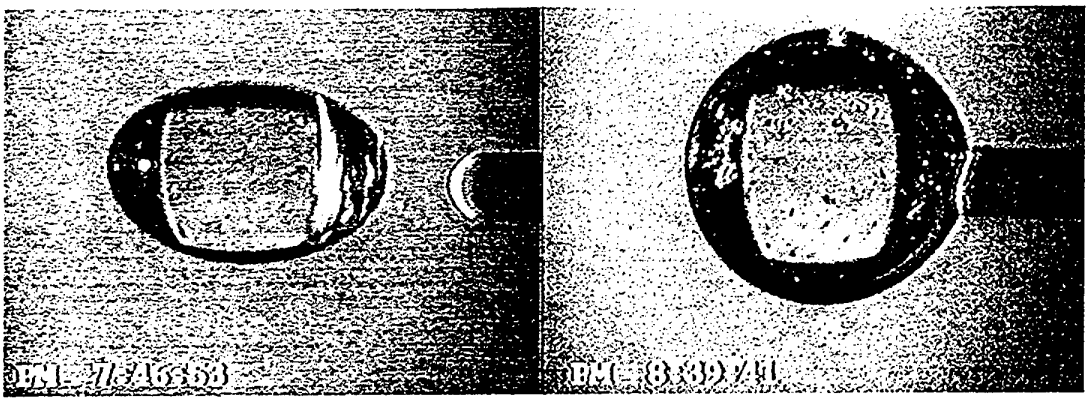

Figure 5: Ultrasonically positioned drop with sting heater placed (a) 3 mm away; and (b) in contact with it. The thermistor was used as a heater by drawing a limited electric current in order to bring the tip to a maximum temperature of 48°C. Very slow thermocapillary flows were observed in both configurations.

3. CONCLUSIONS

The effect of levitation fields on the fluid motion has been experimentally examined for heated drops. The following observations have been made:

1. Modest thermal gradients on Earth-based levitated drops initiate thermocapillary flows that quickly develop three-dimensional fluid motion leading on to drop rotation. The heating configuration probably has a role in the orientation of the rotation.

2. With flattened disk-like drops, spot heating leads two-dimensional thermocapillary flows that can be observed in the plane of the disk. Also, a circulatory motion normal to the main cross section is seen. Drop viscosity is an important parameter that determines the size of this circular-motion region. Lower viscosity causes the region to be larger. It is likely that this steady circulation is induced by the acoustic streaming flow brought about by the levitation field.

3. For a flattened drop, the gravitational potential over the height is considerable reduced owing to the thinness, and contributes to the inhibition of buoyancy-driven flows.

4. Under microgravity conditions, the acoustic field while being of low intensity, still causes some residual drop rotation. Nevertheless, the detection of thermocapillary flows was possible.

ACKNOWLEDGMENTS

The support of this work under the NASA Microgravity Fluid Physics Program is gratefully acknowledged.

REFERENCES

1. M.B. Robinson. Microgravity Science Laboratory (MSL-1) Final Report, Proceedings of the Microgravity Science Laboratory (MSL-1) One-Year Science Review Meeting, Marshall Space Flight Center, Hunstville, AL, Aug. 25-26 (1998).
2. W.K. Rhim, S.K. Chung, E.H. Trinh, and D.D. Elleman. Charged drop dynamics experiment using an electrostatic-acoustic hybrid system. *Mat. Res. Soc. Symp. Proc.*, 87:329–337. 1987.
3. W.K. Rhim and T. Ishikawa. Noncontact electrical resistivity measurement technique for molten metals. *Rev. Sci. Instrum.*, 69:3628–, 1998.
4. K. Ohsaka, S.K. Chung, and W.K. Rhim. Specific volume and viscosities of the Ni-Zr alloys and their correlationwith the glass formability of the alloys. *Acta Mater.*, 46:4535–, 1998.

5. S.K. Chung, D.B. Thiessen, and W.K. Rhim. A noncontact measurement technique for the density and thermal expansion coefficient of solid and liquid materials. *Rev. Sci. Instrum.*, 68:2597–, 1997.

6. A.J. Rulison and W.K. Rhim. Constant-pressure specific heat to hemispherical total emissivity ratio for undercooled liquid nickel, zirconium, and silicon. *Metall. Mater.Trans. B*, 26:503–, 1995.

7. J.W.S. Rayleigh. *Proc. Roy. Soc.*, 29:71–, 1879.

8. H. Lamb. *Hydrodynamics.* Cambridge University Press, 6th edition, 1932. Reprinted, Dover, New York, 1945.

9. T. Shi and R.E. Apfel. Oscillations of a deformed liquid drop in an acoustic field. *Phys. Fluids*, **95**:1545–1552, 1995.

10. P.V.R. Suryanarayana and Y. Bayazitoglu. Effect of static deformation and external forces on the oscillations of levitated drops. *Phys. Fluids A*, 3:967–977, 1991.

11. J.Q. Feng and K.V. Beard. Small amplitude oscillations of electrostatically levitated drops. *Proc. Roy. Soc. Lond. A*, 430:133–150, 1990.

12. J.Q. Feng and K.V. Beard. Resonance of a conducting drop in an alternating electric field. *J. Fluid Mech.*, 222:417–, 1991.

13. J.Q. Feng and K.V. Beard. Three-dimensional oscillation characteristics of electrostatically deformed drops. *J. Fluid Mech.*, 227:429–447, 1991.

14. E.H. Trinh, R.G. Holt, and D.B. Thiessen. The dynamics of levitated drops in an electric field. *Phys. Fluids*, 8:43–, 1996.

15. J.A. Tsamopoulos, T.R. Akylas, and R.A. Brown. Dynamics of charged drop break-up. *Proc. Roy. Soc. Lond. A*, 401:67–88, 1985.

16. R. Natarajan and R.A. Brown. The role of three-dimensional shape in the break-up of charged drops. *Proc. Roy. Soc. Lond. A*, 410:209–227, 1987.

17. F. Mashayek and N. Ashgriz. Nonlinear oscillations of drops with internal circulation. *Phys. Fluids*, 10:1071–, 1998.

18. P. Annamalai, E. Trinh, and T.G. Wang. Experimental study of the oscillations of a rotating drop. *J. Fluid Mech.*, 158:317–327, 1985.

19. E. Trinh and T. G. Wang. Large amplitude free and driven drop-shape oscillations: experimental observations. *J. Fluid Mech.*, **122**:315–338, 1982.

20. D.L. Cummings and D.A. Blackburn. Oscillations of magnetically levitated aspherical droplets. *J. Fluid Mech.*, 224:395–416, 1991.

21. E.H. Trinh, S.S. Sadhal, D.A. Thomas, and R.K. Crouch. Internal flows in free drops. MSL-1 / L+1 Conference, Marshall Space Flight Center, August 1998.

22. B.Q. Li and S.P. Song. Surface oscillations and fluid flow in magnetically-positioned droplets under microgravity conditions. Paper presented at the 1st Pacific Rim Conference on Microgravity Science, Tokyo, June 1998.

23. S.S. Sadhal, E.H. Trinh, and P. Wagner. Unsteady spot heating of a drop in a microgravity environment. *Microgravity Sci. Tech.*, **9**:80–85, 1997.

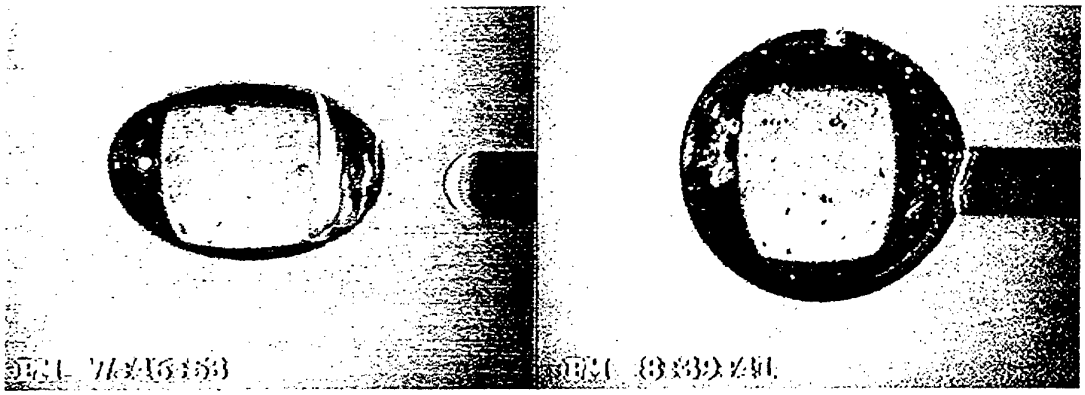

Figure 5: Ultrasonically positioned drop with sting heater placed (a) 3 mm away; and (b) in contact with it. The thermistor was used as a heater by drawing a limited electric current in order to bring the tip to a maximum temperature of 48°C. Very slow thermocapillary flows were observed in both configurations.

3. CONCLUSIONS

The effect of levitation fields on the fluid motion has been experimentally examined for heated drops. The following observations have been made:

1. Modest thermal gradients on Earth-based levitated drops initiate thermocapillary flows that quickly develop three-dimensional fluid motion leading on to drop rotation. The heating configuration probably has a role in the orientation of the rotation.

2. With flattened disk-like drops, spot heating leads two-dimensional thermocapillary flows that can be observed in the plane of the disk. Also, a circulatory motion normal to the main cross section is seen. Drop viscosity is an important parameter that determines the size of this circular-motion region. Lower viscosity causes the region to be larger. It is likely that this steady circulation is induced by the acoustic streaming flow brought about by the levitation field.

3. For a flattened drop, the gravitational potential over the height is considerable reduced owing to the thinness, and contributes to the inhibition of buoyancy-driven flows.

4. Under microgravity conditions, the acoustic field while being of low intensity, still causes some residual drop rotation. Nevertheless, the detection of thermocapillary flows was possible.

ACKNOWLEDGMENTS

The support of this work under the NASA Microgravity Fluid Physics Program is gratefully acknowledged.

REFERENCES

1. M.B. Robinson. Microgravity Science Laboratory (MSL-1) Final Report, Proceedings of the Microgravity Science Laboratory (MSL-1) One-Year Science Review Meeting, Marshall Space Flight Center, Hunstville, AL, Aug. 25-26 (1998).
2. W.K. Rhim, S.K. Chung, E.H. Trinh, and D.D. Elleman. Charged drop dynamics experiment using an electrostatic-acoustic hybrid system. *Mat. Res. Soc. Symp. Proc.*, 87:329–337, 1987.
3. W.K. Rhim and T. Ishikawa. Noncontact electrical resistivity measurement technique for molten metals. *Rev. Sci. Instrum.*, 69:3628–, 1998.
4. K. Ohsaka, S.K. Chung, and W.K. Rhim. Specific volume and viscosities of the Ni-Zr alloys and their correlationwith the glass formability of the alloys. *Acta Mater.*, 46:4535–, 1998.

5. S.K. Chung, D.B. Thiessen, and W.K. Rhim. A noncontact measurement technique for the density and thermal expansion coefficient of solid and liquid materials. *Rev. Sci. Instrum.*, 68:2597–, 1997.
6. A.J. Rulison and W.K. Rhim. Constant-pressure specific heat to hemispherical total emissivity ratio for undercooled liquid nickel, zirconium, and silicon. *Metall. Mater.Trans. B*, 26:503–, 1995.
7. J.W.S. Rayleigh. *Proc. Roy. Soc.*, 29:71–, 1879.
8. H. Lamb. *Hydrodynamics.* Cambridge University Press, 6th edition, 1932. Reprinted, Dover, New York, 1945.
9. T. Shi and R.E. Apfel. Oscillations of a deformed liquid drop in an acoustic field. *Phys. Fluids*, **95**:1545–1552, 1995.
10. P.V.R. Suryanarayana and Y. Bayazitoglu. Effect of static deformation and external forces on the oscillations of levitated drops. *Phys. Fluids A*, 3:967–977, 1991.
11. J.Q. Feng and K.V. Beard. Small amplitude oscillations of electrostatically levitated drops. *Proc. Roy. Soc. Lond. A*, 430:133–150, 1990.
12. J.Q. Feng and K.V. Beard. Resonance of a conducting drop in an alternating electric field. *J. Fluid Mech.*, 222:417–, 1991.
13. J.Q. Feng and K.V. Beard. Three-dimensional oscillation characteristics of electrostatically deformed drops. *J. Fluid Mech.*, 227:429–447, 1991.
14. E.H. Trinh, R.G. Holt, and D.B. Thiessen. The dynamics of levitated drops in an electric field. *Phys. Fluids*, 8:43–, 1996.
15. J.A. Tsamopoulos, T.R. Akylas, and R.A. Brown. Dynamics of charged drop break-up. *Proc. Roy. Soc. Lond. A*, 401:67–88, 1985.
16. R. Natarajan and R.A. Brown. The role of three-dimensional shape in the break-up of charged drops. *Proc. Roy. Soc. Lond. A*, 410:209–227, 1987.
17. F. Mashayek and N. Ashgriz. Nonlinear oscillations of drops with internal circulation. *Phys. Fluids*, 10:1071–, 1998.
18. P. Annamalai, E. Trinh, and T.G. Wang. Experimental study of the oscillations of a rotating drop. *J. Fluid Mech.*, 158:317–327, 1985.
19. E. Trinh and T. G. Wang. Large amplitude free and driven drop-shape oscillations: experimental observations. *J. Fluid Mech.*, **122**:315–338, 1982.
20. D.L. Cummings and D.A. Blackburn. Oscillations of magnetically levitated aspherical droplets. *J. Fluid Mech.*, 224:395–416, 1991.
21. E.H. Trinh, S.S. Sadhal, D.A. Thomas, and R.K. Crouch. Internal flows in free drops. MSL-1 / L+1 Conference, Marshall Space Flight Center, August 1998.
22. B.Q. Li and S.P. Song. Surface oscillations and fluid flow in magnetically-positioned droplets under microgravity conditions. Paper presented at the 1st Pacific Rim Conference on Microgravity Science, Tokyo, June 1998.
23. S.S. Sadhal, E.H. Trinh, and P. Wagner. Unsteady spot heating of a drop in a microgravity environment. *Microgravity Sci. Tech.*, **9**:80–85, 1997.

COOLING OF TWO CYLINDERS IN A ROW BY A SLOT JET OF AIR

F. Gori and L. Bossi
Dipartimento di Ingegneria Meccanica
Università di Roma "Tor Vergata"
Via di Tor Vergata 110 - 00133 Roma
Email: gori@uniroma2.it; Fax: 06-2021351

Keywords: heat transfer, air jet flow, two cylinders

ABSTRACT. The heat transfer on two cylinders in a row by a slot jet flow of air has been investigated experimentally. The slot jet has a height of S=5 mm. The cylinders diameter is D=10 mm. The first cylinder is set at a distance H/S=6 from the slot exit. The second cylinder is set a distance from the first cylinder variable from L/S=4 to L/S=8. The Reynolds number range is Re_D=4000÷20000. The influence of the first cylinder on the second one is to decrease the heat transfer in a jet flow, just opposite to what observed in a uniform flow. Local Nusselt number on the two cylinders has been investigated as a function of Reynolds number, the angle from the impinging point and the different distances between the two cylinders. A closed vortex region between the cylinders appears at a distance L/S=4 and is dependent by the Reynolds number. The best configuration of the two cylinders for obtaining the maximum heat transfer is H/S=6 and L/S=4.

1. INTRODUCTION

Heat transfer between a jet flow and flat surfaces has been the subject of a large number of publications [1] . On the other side, most of the surfaces used in the cooling or heating processes are cylindrical. From few years the cylindrical surfaces have been investigated more intensively, with special attention to a jet flow of water [2,3,4,5] and air [6,7,8,9,10]. Most of the papers on water cooling [2 - 4] have been concerned with the mean heat transfer around the circumpherence of the three cylinders investigated. The local Nusselt results of [5] are relative to the first cylinder only. The results presented in [6,9,10] are relative to the heat transfer on one cylinder only. The present paper, on the other side, is presenting the heat transfer results, local and average, on two cylinders cooled by a slot jet of air.

2. EXPERIMENTAL APPARATUS

The experimental apparatus is schematically shown in Fig. 1 where S is the slot height, H is the distance between the slot and the first cylinder, and L is the distance between the first and the second cylinder. The radial fan has an electric power of 750 W and a maximum mass flow rate of 0.45 kg/s. The settling chamber is made with a rectangular channel of 150 mm of lenght and a square section of 135 by 135 mm. The converging duct

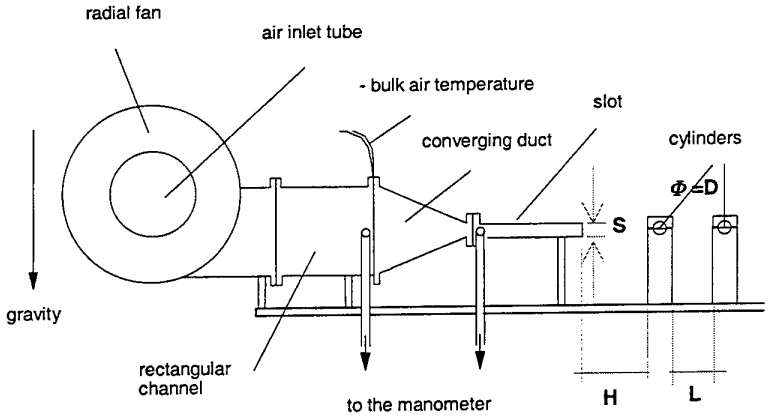

Fig. 1 Experimental apparatus

has a contraction ratio of 13.5:1, an angle of 30° and a rectangular final section of 135 mm by 5 mm. The slot jet is made with a horizontal channel, 135 mm wide, 160 mm long and with the height of 5 mm. The lenght of the slot allows to the flow to be fully developed at the exit. The cylinders are made by an AISI 304L stainless steel tube, with a tickness of 0.2 mm, 10 mm of external diameter and 135 mm long, i.e: as wide as the slot jet. A teflon bar is located inside the tube to press the thermocouples on its internal wall and to reduce the heat transfer. Grooves on the teflon bar allow the thermocouples to be positioned correctly and the decreasing depth of the grooves (as shown in Fig. 2) allow the thermocouples to be in tight contact to the internal side of the wall. On Fig.2 it is also shown the position of each of the five thermocouples along the surface; i.e: at angles of 0°, 90°, 180°, 225° and 315° from the front stagnation point. The steel tubes are heated by eletrical current with a dissipated power of 11 W. The mass flow rate of air is measured through the pressure loss across the converging duct as shown on Fig. 2. The data acquisition system is made of on A/D converter and a multiplexer for the thermocouples readings. The eletric current is measured through the voltage drop on the 0.1 ohm reference shunt of the feeder.

3. EXPERIMENTS

Experimental Analysis

In each experiment the temperatures, the mass flow rate, the electrical resistance of the cylinders and the power dissipated are measured. The power dissipated in the cylinder is related to heat balance equation

$$P=h_iA(T_i-T_a) \tag{1}$$

where P is the electric power, h_i is the local heat transfer coefficient, A is the total surface of the cylinder, T_a is the air temperature and T_i is the average local temperature of the thermocouple.
The local Nusselt number is evaluated by

$$Nu_i=h_iD/k \tag{2}$$

where D is the diameter of the cylinder and k the thermal conductivity of air. The mean Nusselt number is calculated by

$$Nu_m=h_mD/k \tag{3}$$

where h_m is the mean convective heat transfer coefficient defined by

$$P=h_mA(T_m-T_a) \tag{4}$$

and T_m is given by

$$T_m=\Sigma_iT_i/n \tag{5}$$

where n is the number of thermocouples.

Uncertainties

The copper-constantan thermocouples have 0.25 mm diameter wires. Their calibration uncertainty is lower than 0.05°C. The temperature drop across the thin layer of the stainless steel tube has been evaluated as 0.01°C. Uncertainties due to the circumpherential conduction of heat can be considered as given by the maximum value of about 0.15°C. The local temperature registered by each thermocouple is assumed as the average within at least ten minutes where the maximum variations are ±0.15°C. In conclusion, the uncertainty of the temperature is assumed to be ±0.15°C. Details of the uncertainty analysis can be found in [8].

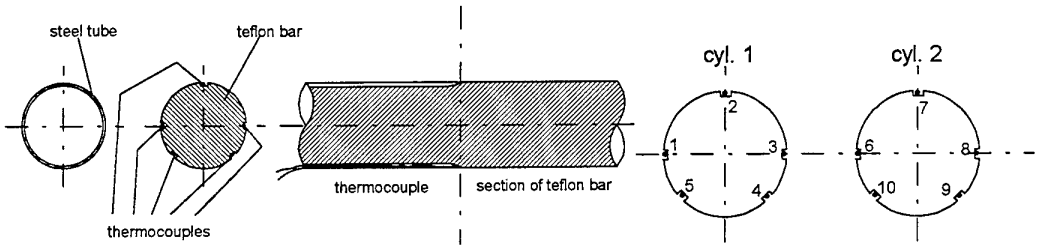

Fig. 2. Cylinders configurations and thermocouples position

The measurements of the electric power dissipated in the tubes gives a maximum uncertainty of 10^{-2} W. The evaluation of the power dissipated in each experiment has been controlled carefully taking into account the influence of: natural convection, thermal radiation, heat conduction at the edge of the cylinder and the boundary condition of the casing. The detailed description of this analysis can be found in [8] and is not reported here. It can be summarized by the uncertainty on the Nusselt number which ranges from 6% at Re=4000 to 3% at Re=20000.

Experimental Results

Mean experimental Nusselt numbers are presented in Fig. 3 versus Reynolds numbers. The data predicted for a uniform flow (u.f.) are also reported as comparison. The lower curve of Nu_m is given by the equation[11]

$$Nu_m = (0.4\ Re^{0.5} + 0.06\ Re^{2/3})\ Pr^{0.4} \tag{6}$$

Where Re and Pr are the Reyynold number and Praudtl number. These predictions correspond to a uniform flow with a zero level of turbulence (Tu=0%). The highest data reported for a uniform flow in Fig.3 are obtained by the equation:

$$Nu_m = (1.07 + 0.015 Tu\ Re^{1/2})\ 0.63\ Re^{1/2} \tag{7}$$

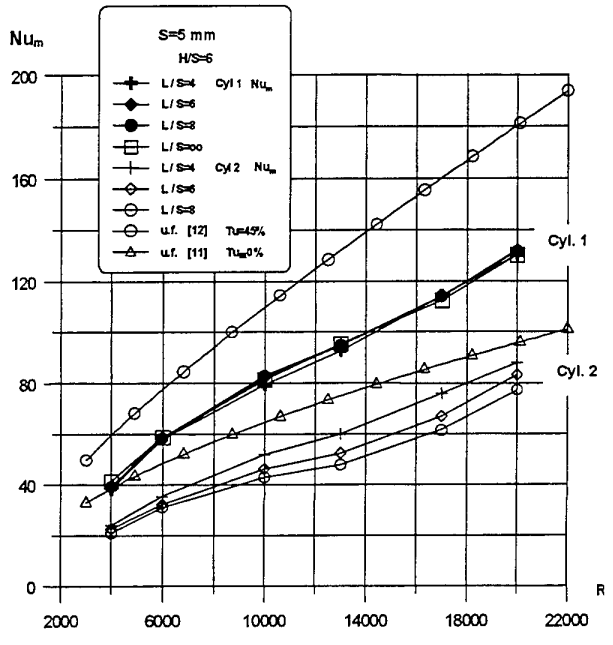

Fig. 3. Average Nusselt on the two cylinders

proposed by Kondjoyan and Alvarez [11] for a uniform flow with a high level of turbulence (Tu≅45%). The experimental results of this work, reported on Fig. 3, are obtained with the first cylinder at a distance from the slot jet of H/S=6 which is considered the distance of the maximum mean Nusselt number. The second cylinder is set at a distance from the first one variabile in the range L/S=4÷8. The mean Nusselt numbers on the first cylinder are pratically not influenced by the presence of the second cylinder and are equal to the values measured with a single cylinder only. The mean Nusselt results on the second cylinder are much lower than those on first one with a reduction of about 100% at Re≅4000 and around 40% at Re≅20000. This result is in agreement to the results obtained in water jet [4] but opposite to what has been observed in a uniform flow by Kostic and Oka [13]. The mean Nusselt

number on the second cylinder is also dependent by the distance between the first and the second cylinder, L. The mean Nusselt number decreases for increasing L/S because of the nature of the jet configuration and the decrease of velocity with the distance from the jet outlet.

Fig. 4 shows the different trend of the mean Nusselt number in a jet flow as compared to a uniform flow [13]. The mean heat transfer coefficient in a jet flow is lower on the second cylinder than on the first one while it is higher in a uniform flow. In fact, in a uniform flow the turbulence induced by the presence of the first cylinder increases the mean Nusselt number. This is the confirmation the first cylinder acts as a promoter of turbulence as compared to the second cylinder. A detailed exam of Fig. 4 shows the Nusselt numbers obtained in [13] on the first cylinder are qualitatively similar to those of Fig. 3, although there are some differences from the quantitative point of view. As a conclusion the mean Nusselt numbers on the first cylinder at low Reynolds are similar between jet an uniform flow up to about Re≅6000. From Re≅6000 to Re≅20000, the mean Nusselt number due to a slot jet flow is higher as compared to a uniform flow confirming the effectiveness of the jet flow in the cooling process. It must be noted that the results of Kostic [13] are somewhat higher than those predicted by equation (6) due to Whitaker [11]. The detailed examination of Fig. 4, as far as the Nusselt number on the second cylinder is concerned, shows the remarkable decrease of the heat transfer coefficient on the second cylinder in a jet flow. On the contrary it is evident in Fig. 4 the consistent increase of the mean Nu on the second cylinder in a uniform flow. Such an increase of Nu brings the data a little aboove the data in a jet flow. In other words the turbulence induced by the first cylinder on the second one is enough to produce higher mean Nusselt than those measured in a jet flow. As a conclusion the heat transfer data on the first cylinder in a jet flow are comparable with those measured on the second cylinder in a uniform flow where the turbulence is increased by the first one. As observed in [9] the turbulence level in the jet flow is capable to produce an increase of the Nusselt number at high Reynolds numbers.

Fig. 5 reports the local heat transfer coefficient, or local Nusselt number on the second cylinder, as a function of the angle from the impingement point at several Reynolds numbers, ranging from Re=4000 to Re=20000. The data of Fig. 5a are obtained by the fixed thermocouples while those of Fig. 5b are got by the rotation of the cylinder along its axis, hence they are measured by the thermocouples rotated around the impinging point. The data measured on the second cylinder have a different qualitative trend with respect to the angle from the impingement point. At low Reynolds number, Re≅4000, the local Nusselt numbers are almost constant along the circumpherence of the cylinder. On the impingement point the Nu is a little higher because of the low Reynolds number of the jet flow and the influence induced by the first cylinder. At higher Reynolds numbers the local Nusselt number on the impinging point (θ=0°) is markely higher than on the rest of the circumpherence. The local Nusselt has the minimum in the range of the angle from θ=135° to θ=180°. It must be noted that the second cylinder is put at the distance L/S=4 or L/D=2 from the first cylinder. This distance is considered as the distance of the second regime of flow by Kostic and Oka [13] and it will be commented later. Indeed the results of Fig. 5a and Fig. 5b are in qualitative good agreement with those of Kostic [13] for L/D=6-9 up to θ=100°. From

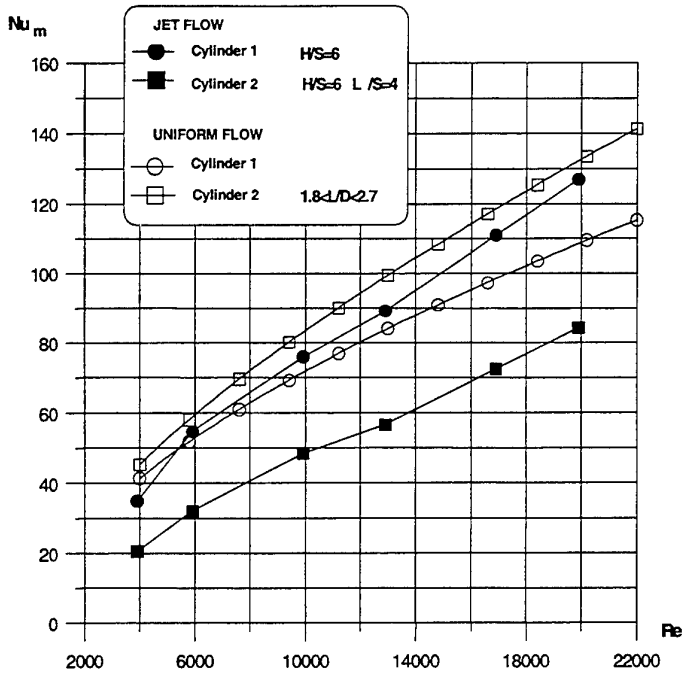

Fig. 4. Comparison between jet and uniform flow

θ=100° to θ=180° a completely different picture can be observed for the data of the local Nusselt numbers. The results of Fig. 5a-5b shows an almost continuous decrease of the local Nusselt with the angle. A different trend is present on the second cylinder of Kostic [13] where, after the absolute minimum at θ=100°, which is the point of transition from laminar flow to boundary layer flow, the Nusselt increases up a second relative minimum, θ=150°, which is the separation point from boundary layer flow to turbulent flow. The present trend of the data on the second cylinder is consistent with the data measured along the first cylinder [10] and they appear to be peculiar (characteristic) of the jet flow in the actual configuration as compared to the uniform flow.

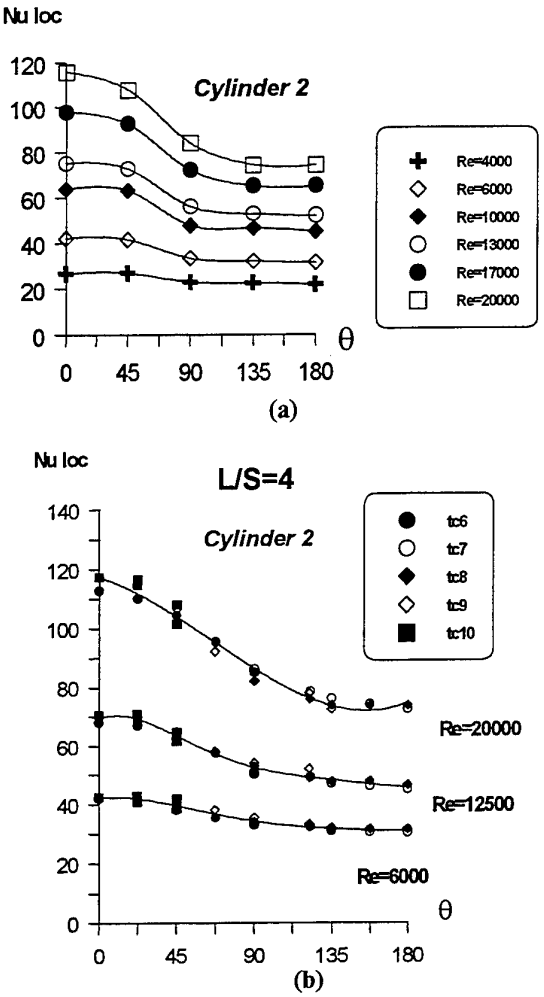

Fig. 5. Local Nusselt number on the second cylinder versus the angle from the impinging point

The characteristics of the local Nusselt number in a jet flow are also clearly evidenced by Fig. 6 where the Nusselt number is presented versus the Reynolds number at several angles from the impinging point. Fig. 6 put in clear evidence that the jet flow on the impinging area θ=0-45° of the second cylinder can be as effective as uniform flow only at high Reynolds numbers. In fact, at low Reynolds numbers, Re<10000, the local Nusselt at θ=0-45° is lower than the mean Nusselt in uniform flow. At medium Reynolds, Re≅10000-14000, the Nusselts are comparable and at high Reynolds, Re≥16000, the local Nusselt on the surface area θ=0-45° is higher than in a uniform flow at Tu=0% [11]. The results of Kostic [13] for a uniform flow have shown that two different characteristic flow patterns have been found on dependence whether the distance between the two cylinders is greater than L≥3.8D. For a distance lower than 3.8D two reattachment points are obtained on the front side of the second cylinder because of the formation of a closed vortex region between the cylinders. The local Nusselt number results for this configuration is different at the impinging point. Indeed, the maximum of the local Nusselt is no more present at θ=0° as it happens for L>3.8D, but the maximum is shifted toward the area θ=50-70°. The experimental results with a jet flow are more complex than in a uniform flow because in the case of two cylinders two distances are to be taken into consideration, i.e. the distance of the first cylinder from the jet exit and the distance of the second cylinder from the first one.

The results of the present work are presented for the fixed distance H/S=6 of the first cylinder from the jet exit, because this is considered the position of the maximum mean heat transfer on the first cylinder. Then, the distance between the two cylinders is the only variable in order to compare the data with those of Kostic [13] and to the goal of finding the best configuration of the two cylinders with respect to the heat transfer. The experimental configuration of the cylinders in the present apparatus does not permit, because of the supports of the cylinders, to put the cylinders at a distance lower than L/S=4 which corresponds to L/D=2. This means the apparatus allows to verify the distance found by Kostic[13], L/D=4, as the critical distance for the appearance of the second regime of flow or the closed vortex region between the cylinders. Fig. 7 presents the local Nusselt results on the first and second cylinder versus the angle from the impinging point at several Reynolds numbers and two distances between the cylinders, i.e. L/S=4 and L/S=8 which correspond to L/D=2 and L/D=4. The influence of the distance L between

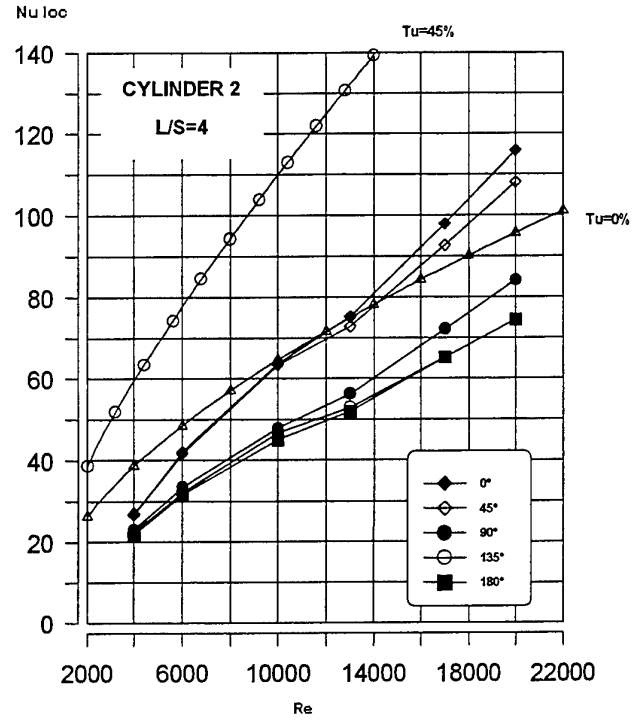

Fig. 7. Local Nusselt number on the second cylinder versus Reynolds number

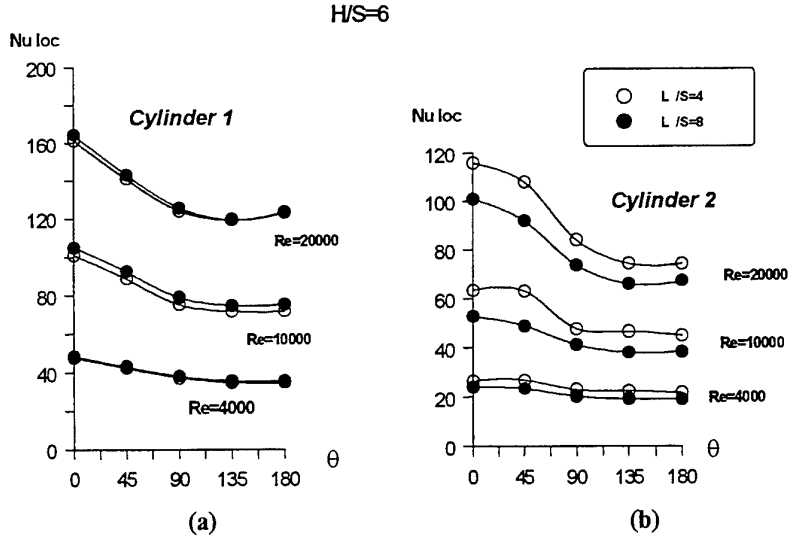

Fig. 6. Local Nusselt number on the two cylinders at two distances, *L/S*, between them

the two cylinders is negligible on the first cylinder (Fig. 7a) because the first one is set at H/S=6 from the jet exit, i.e. it is in the position of the maximum heat transfer.

Fig. 7b, on the contrary, shows the local heat transfer on the second cylinder is sensible to the distance L/S between the cylinders, although in a different manner at the different Reynolds number, with the trend to increase with decreasing the distance L. At low Reynolds, Re≅4000, the increase is low but the trend is clear. At medium Reynolds, Re≅10000, the increase of local Nusselt is consistent, especially in the area θ=0-45° with the trend of Nu to be higher at 45° rather than at 0°. This trend is quite similar for Re≅4000 and Re≅10000 with the conclusion that the closed vortex region can be present at the distance L/S=4 (L/D=2) and low Reynolds number. In conclusion, in a jet flow the closed vortex region needs a lower distance between the cylinders to form as compared to the uniform flow. Indeed at L/D=2 the closed vortex region is beginning while in the uniform flow it is already present at L/D=3.8. This conclusion is also in agreement to the appearance of a reduction of the local Nu at Re≅10000, Fig. 7a, i.e. the closed vortex region is detrimental also for the first cylinder (decrease of local Nu). For high Reynolds number, Re≅20000, the increase of the local Nu is remarkable in the whole range of the circumpherence (θ=0-180). At Re≅20000, the local Nusselt at 45° is lower than at 0° showing the closed vortex region is no more effective. Indeed the decrease of local Nu at Re≅20000 is almost negligible on the first cylinder.

In conclusion, in a jet flow, the presence of the closed vortex region is also dependent by the flow regime i.e. by the Reynolds number. The present apparatus does not allows to

decrease the distance between the cylinders below L/S=4 (L/D=2) but it is interesting to identify the best configuration of the two cylinders. Fig. 8 presents the ratio of h/h_{max} or $Nu_m/Nu_{m\,max}$ versus the distance L/S at several Reynolds number on the two cylinders. $Nu_{m\,max}$ for the first cylinder is obtained at H/S=6 without the second cylinder or with the second cylinder at an infinite distance from the first one. $Nu_{m\,max}$ for the second cylinder is obtained at L/S=4 from the first cylinder.

From Fig.8 it appears the conclusion is different at low Reynolds (Re≤10000) and high Reynolds (Re≥17000). The ratio $Nu_m/Nu_{m\,max}$ on the second cylinder is always increasing with the decreasing distance L while on the first cylinder this trend is different for low or high Reynolds numbers. At low Reynolds the $Nu_m/Nu_{m\,max}$ decreases at L/S=4 and the possible reason is the appearance of the closed vortex region. At high Reynolds this trend is less marked suggesting the closed vortex region is not present. In conclusion, the best configuration of the two cylinders, indipendently by the Reynolds number, from an engineering stand point, is with the second cylinder at a distance L/S=4 from the first one, assumed the first one is at the distance H/S=6 from the jet exit.

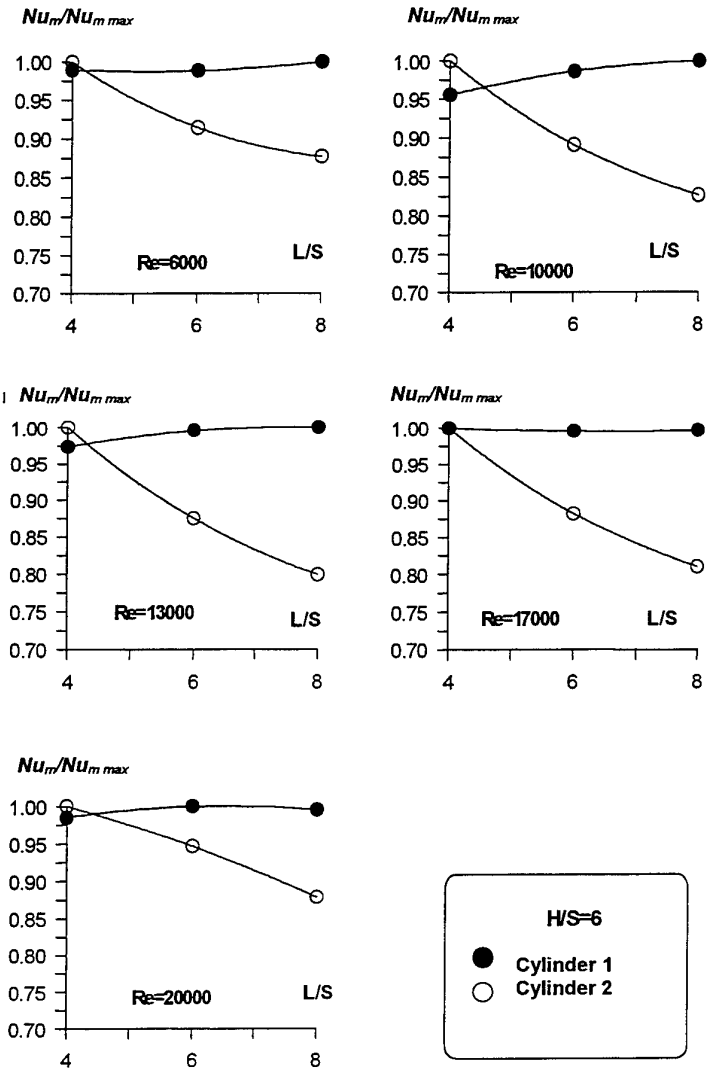

Fig. 8. Ratio of mean Nusselt number to the mean maximum Nusselt number

NOMENCLATURE

Latin

A	cylinder surface, m^2
D	cylinder diameter, m
H	distance between the slot and the first cylinder, m
h	convective heat transfer coefficient, W/ m^{2K}
I	direct electric current, A
k	thermal conductivity of the air, W/mK
L	distance between the first cylinder and the second one, m
n	number of parts of the cylinder surface
Nu	Nusselt number, dimensionless
P	total electric power, W
Pr	$=\mu/\rho\alpha$ Prandtl number, dimensionless
R	electrical resistance, Ω
Re	$=v\rho D/\mu$, Reynolds number, dicensionless
S	slot height, m
T	temperature, K
Tu	$=RMS(v)/u_\infty$ turbulence percentage, dimensionless
v	velocity, m/s

Greek

α	thermal diffusivity, m^2/s
μ	dynamic viscosity, kg/m s
ρ	density, kg/m^3
θ	angle with the impingement point, °

Subscript

a	Relative to the air
I	different part of cylinder surface
loc	local
m	arithmetic mean
s	relative to the slot
∞	mean flow

REFERENCES

1. 1. H. Martin, *Heat and Mass transfer between Impinging Gas Jets and Solid Surfaces,* Advances in Heat Transfer, v.13, 1-60 (1977), Academic Press, New York.
2. 1. C. Bartoli, S. Faggiani, *Impingement Heat Transfer at an Array of Circular Cylinders,* ExHFT4, Brussels, (1997).
3. 1. C. Bartoli, S. Faggiani, D. Rossi, "Optimum Heat Transfer From an Array of Cylinders to a Liquid Submerged Jet", *Proc.of Eurotherm Seminar 55, Heat Transfer in Single Phase Flows 5*, 1997, NTUA, Athens, Greece.
4. 1. C. Bartoli, S. Faggiani S, D. Rossi, "Forced and mixed convection heat transfer from an array of cylinders to a liquid submerged jet", Rev. Gen. De Thermique, 37: 431-439,1998.
5. 1. C. Bartoli, S. Faggiani, "Local Nusselt Number at a Cylinder Cooled by a Slot Jet of Water", International Journal Heat and Technology v. 16, n.2 (1998).
6. 1. F. Gori, P. Coppa, "Circumferential variation of heat transfer on three circular cylinder cooled by a slot jet of air", *Heat Transfer 1998, Proceedings of 11th IHTC, v.5*, Kyongju, Korea (1998).
7. 1. S. Marsili, "Convezione forzata di getti d'aria su una schiera di tre cilindri", Tesi di Laurea, Università di Roma "Tor Vergata" (1996).
8. 1. L. Bossi, "Termofluidodinamica di getti d'aria raffreddanti uno o più cilindri in linea", Tesi di Laurea, Università di Roma "Tor Vergata" (1998).
9. 1. F. Gori, L. Bossi, "Influence of the turbulence level in the jet flow on the heat transfer upon cylinders: preliminary results", *XVII Congresso UIT*, Ferrara , Italy (1999).
10. 1. F. Gori, L. Bossi, "On the cooling effect of an air jet along the surface of a cylinder", submitted for publication (1999).
11. S. Withaker, "Forced convection heat transfer correlations for flow in pipes, past flat plates, single cylinders, single spheres and flow in packed beds and tubes bundles" AICHE J., v.18: 361-371(1972).
11. A. Kondjoian, G. Alvarez, "Etude bibliografique sur les coefficients de transfert de chaleur et de matiere convectifs entre l'air et un ensemble de produits; 1. Du cylindre ou de la sphere isoles à un ensemble de deux à quatre de ces objects", Entropie, n.195 (1996).
12. Kostic and Oka, "Fluid flow and heat transfer with two cylindersin cross-flow", Int. J. Heat Mass Transfer, v. 15: 279-299 (1972).

HEAT TRANSFER ENHANCEMENT FROM CYLINDRICAL HEATERS TO A WATER SLOT JET

Carlo Bartoli, Sergio Faggiani, Marco Lorenzini.
Dipartimento di Energetica, Università degli Studi di Pisa
E-mail: faggiani@ing.unipi.it; c.bartoli@ing.unipi.it; marco.lorenzini@studenti.ing.unipi.it
Fax: +39-050-569666

Keywords: submerged jet, single – and two – phase heat transfer, forced and free convection.

ABSTRACT. Heat transfer from an array of circular cylinders to an impinging slot jet of water is studied both for single – phase and two – phase conditions. Different geometrical configurations were investigated in order to find those maximising the heat transfer coefficient The dependence on such parameters as jet velocity and subcooling is also examined. For the single – phase situation three different configurations are proposed and correlation for both the cylinder closest to the jet outlet and the other two are given, the latter taking the contribution of free convection into account. For two-phase conditions, one configuration is given, with the same type of correlation for all cases. Increasing the jet subcooling allows higher heat fluxes – up to and exceeding 3 MW/m^2 – to be dissipated, but the heat transfer mode worsens.

1. INTRODUCTION

Cooling by means of cylindrical or slot jets has been intensively investigated since the 70s. Nowadays this refrigeration technique is largely employed in electronics to increase the heat transfer coefficient (as the big number of circuits per chip and the big power per circuit imposes) and in metallurgical processes [1,2]. In comparison with uniform flow, impingement jet cooling allows the dissipation of higher heat fluxes and a reduction both in the electrical power required to circulate the fluid and in its flow rate. The authors have investigated over the last six years the case of electrically heated circular cylinders impinged by a submerged jet of distilled water. The aim of this experimental research is to suggest configurations that maximise the heat transfer coefficient and to analyse the enhancement both in single – phase and two – phase conditions. In the former case an array of three cylinders was studied, whereas for the two – phase situation the analysis has been limited to two cylinders, as a third would scantly benefit from the jet. Very simple correlations, based on easily measurable quantities, are given for the best configurations.

2. EXPERIMENTAL SET – UP AND PROCEDURE

The apparatus (Fig.1) consists of a test section of AISI107 stainless steel. The vessel, 5, has four circular windows for experiment visualisation. A thermostatic water tank, 1, a pump, 2, a regulating valve, 3, a turbine flowmeter, 4, and a long rectangular duct for flow stabilisation complete the set – up. The jet pours into the test section, impinges onto the first of a number of hollow stainless steel cylinders (Fig. 2) supplied with DC current and the spent fluid finally flows into the tank through a hole in the top lid. The inner temperature of each cylinder is measured by a 0.5 mm – diameter T – type thermocouple. The external temperature is calculated through the Fourier equation as a function of the dissipated electric power per unit volume and of the hollow cylinder radii:

$$T = T_i + \frac{\dot{q}^*}{4 \cdot k} R_i^2 \cdot \left[1 + 2 \cdot \ln\left(\frac{R_e}{R_i}\right) - \left(\frac{R_e}{R_i}\right)^2 \right] \cdot \qquad (1)$$

Radial conduction is assumed as being dominant. Indeed, investigations performed with a sliding thermocouple showed that the temperature variation along the test length of the cylinder didn't exceed the value of measurement uncertainties. Angular dependence, although already investigated in previous papers [3,4], was not considered here, as an average value was sought. A thermocouple at the jet outlet measured the water temperature at the exit of the rectangular duct.

Two 0.2 mm – diameter platinum sensing leads were used to measure voltage drop, while I was imposed.

Finally, $\dot{q}$ was calculated as

$$\dot{q} = \frac{V \cdot I}{f\hat{I}\pi \cdot D_c \cdot l}. \qquad (2)$$

The following parameters were set prior to each test run:

- velocity of the jet at slot outlet, v;
- jet temperature, T_s;
- distance between the heaters, L_1, L_2, for single – phase conditions, L for two – phase conditions;
- distance between heater and slot, Z.

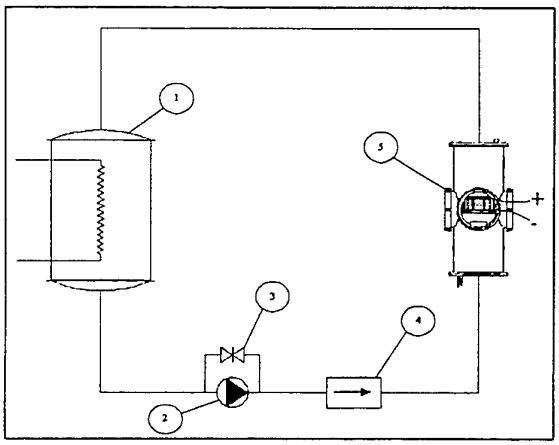

Fig. 1 - Experimental set – up.

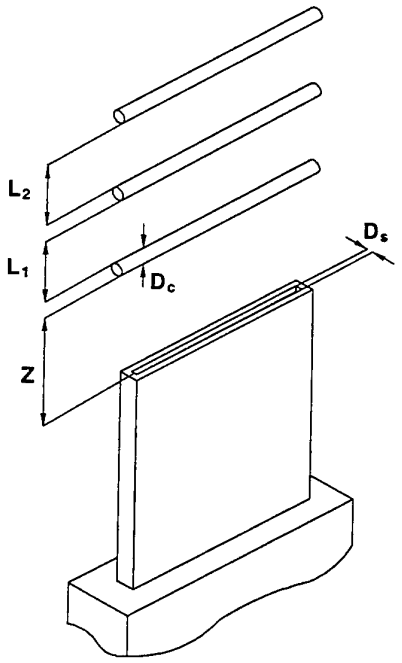

Fig. 2. Detail of the slot and cylinders

The distilled water was degassed by letting it boil for two hours, then electrical power was supplied stepwise to the heaters. In single – phase conditions this was accomplished by a single source, while in two – phase conditions two sources were employed in order to allow higher heat fluxes to be dissipated on the cylinder closer to the slot exit. Measurements were made at intervals of at least 150 seconds, and tests were repeated at least two times for the same conditions. Uncertainty analysis has been carried out according to [5]. Uncertainty sources are reported in Table 1, while calculated values for $\dot{q}$ and ΔT are 2% and ±0.5 K respectively.

Table 1. Uncertainty Sources

Measured Quantity	Reference Value	Overall Uncertainty
Cylinder temperature	$T\text{-}T_+$=5 K	0.5 K
Water bulk temperature	323.15 K	0.5 K
Flow rate	1 kg/s	3%
Current	100 A	0.3%
Voltage	0.5 V	0.2%
Cylinder thickness	$0.5 \cdot 10^{-3}$ m	2%
Heater area	$1 \cdot 10^{-3}$ m^2	1%

3. EXPERIMENTAL RESULTS

Single – Phase Conditions

The test runs have been performed within the following limits of variability of the parameters:

$1.5 \cdot 10^3 \leq Re \leq 3 \cdot 10^4 \quad 2.7 \leq Pr \leq 7 \quad 2 \cdot 10^4 \leq \dot{q} \leq 6 \cdot 10^5 \quad 1 \leq L_1/D_s \leq 6 \quad 1 \leq L_2/D_s \leq 6$

According to the previous results [6], the maximum Nu for all the cylinders occurs in the range $3 \leq Z/D_s \leq 7$, mostly at $Z/D_s \cong 5.5$; a similar conclusion have recently been obtained with air jets by Gori and Coppa [7,8] therefore all the experiments described in the present paper have been performed at $Z/D_s \cong 5.5$ The trend of Nu as a function of Re is quite complex because of the occurrence of some irregularities in form of sudden rises or sharp pits (Fig. 3).

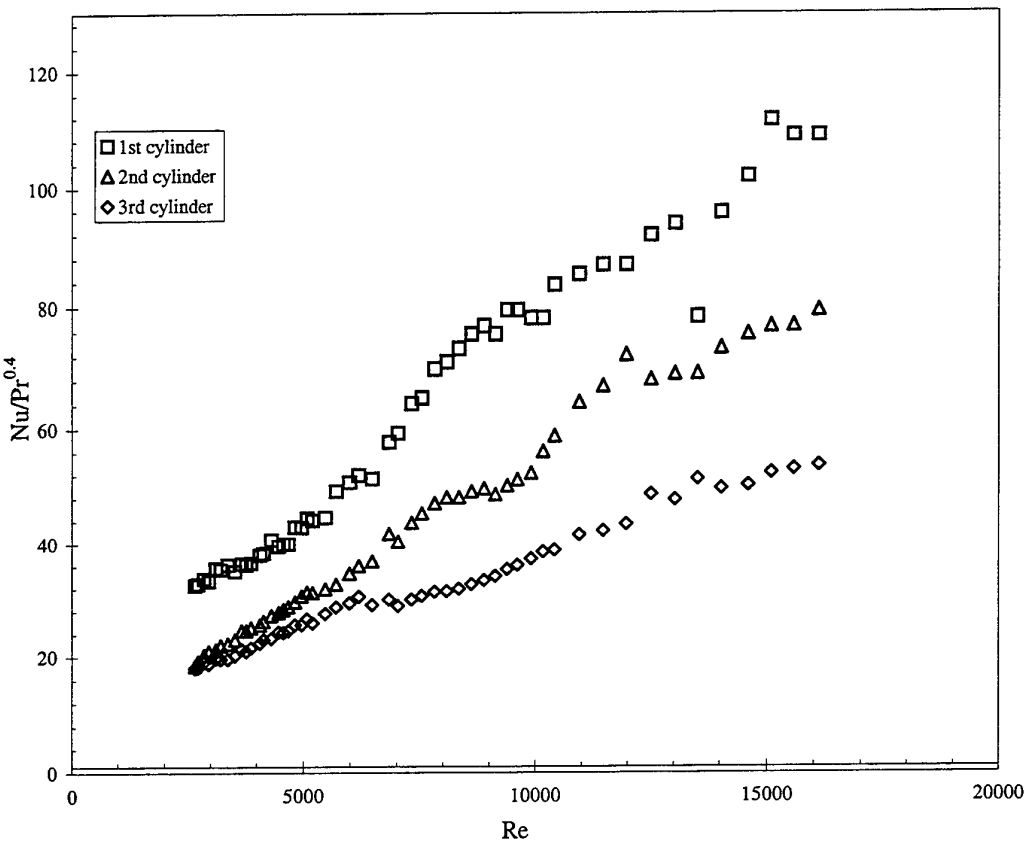

Fig. 3. Trends of $Nu/Pr^{0.4}$ for three cylinders.

However, within limits of error which are usually accepted for practical purposes, the Nu can be considered as regularly increasing with increasing Re for all the cylinders. For a single cylinder or the first of an array the average trend can be predicted within ± 12% by means of the previously proposed correlation [3]:

$$\frac{Nu}{Pr^{0.4}} = 0.040\left(\frac{D_c}{D_s}\right)^{-0.85} Re^n \tag{3}$$

$$n=0.82\left(\frac{D_c}{D_s}\right)^{0.09} \tag{4}$$

Here the properties of the fluid are evaluated at the slot exit temperature and Nu is based on D_s.

For the second and third cylinder Nu depends on Z/D_s, L_1/D_s L_2/D_s and $\dot{q}$. Consequently, suitable experiments have been performed varying the parameters L_1/D_s and L_2/D_s between 1 and 6: the configuration, which allows the maximum Nu, resulted

$L_1/D_s = 1.2, \qquad L_2/D_s = 3.2.$

This configuration is markedly asymmetric. Such a characteristic can be unfit from the practical point of view, thus symmetric configurations have been sought: Nu slightly lower than the former ones (the third Nu is about 10 % lower, the other are unchanged) can be obtained with

$L_1/D_s = L_2/D_s = 1.2.$

According to the above observations, correlations have to take into account the influence of the parameters Z/D_s, D_c/D_s, L_1/D_s and L_2/D_s. Concerning the first two parameters, the neighbourhood of the maximum heat transfer and the previously determined dependence, i. e. $\frac{Z}{D_s} \cong 5.5$ and $\left(\frac{D_c}{D_s}\right)^{0.15}$, are chosen for the correlation which follows. When the thermal flux, $\dot{q}$, increases beyond $6 \cdot 10^4$ W/m^2 the contribution of natural convection must be taken into account up to Re=1.5-2·10^4 for the second and the third heaters, but for the first cylinder it can be neglected in the whole range of the Reynolds number.

The proposed correlating equation is:

$$\frac{Nu}{Pr^{0,4}} = C_1 \cdot Gr^{0.33} + C_2 \cdot \left(\frac{D_c}{D_s}\right)^{0.15} Re^n \qquad (5)$$

with Nu based on D_c. The value of C_1, d C_2 and n obtained by means of a least squares fit, are reported in Table 2 for the best studied configurations. The maximum error corresponding to each case is reported too.

Equation (5) holds up to $\dot{q} = 6 \cdot 10^5$ W/m^2; it is based on the average film temperature and takes into account the contribution of the forced and free convection. All the experimental data are correlated by this equation with an average uncertainty of $\pm$ 10% and a maximum uncertainty of 13%. It is worth noting that this maximum belongs to the Nusselt number of the third cylinder. The contribution of the free convection is taken into account by means of $Gr^{1/3}$, the recommended exponent for fully turbulent conditions. Most of the results reported and discussed in the present paper have been obtained with circular cylinders of 3mm o.d. However some test runs have been performed with slightly smaller or larger heaters, namely with cylinders of 2 and 6 mm o.d. The results of these test runs are completely in agreement with those of accuracy these experimental results too.

Table 2. Values of C_1, C_2 and n for Equation (5).

Configuration	Cylinder	C_1	C_2	n	Max error [%]
L_1/D_s=1.2	2nd	0.83	0.034	0.80	10
L_2/D_s=1.2	3rd	0.53	0.14	0.62	13
L_1/d_s=1.2	2nd	0.81	0.033	0.81	8
L_2/D_s=1.2	3rd	0.43	0.083	0.69	13
L_1/d_s=3.2	2nd	0.56	0.031	0.80	9
L_2/D_s=3.2	3rd	0.39	0.10	0.63	13

Two – Phase Conditions

In the two – phase case configurations with one and two cylinders (with 3 mm o.d.) were studied, the slot width being 2 and 3 mm. The results for a single cylinder are thoroughly reported in [9]. Tests were conducted for both saturated (T_s = 373.15 K) and subcooled conditions (($\Delta T)_{sub}$=10, 20 and 30 K respectively). Geometrical parameters varied as follows:

$$2.5 \le \frac{Z}{D_s} \le 7.5 \qquad 2.5 \le \frac{L}{D_s} \le 5 .$$

The trends of $\dot{q}$ as a function of ΔT are reported at set geometrical and dynamical conditions on a Log-log graph (Figs. 4, 5).

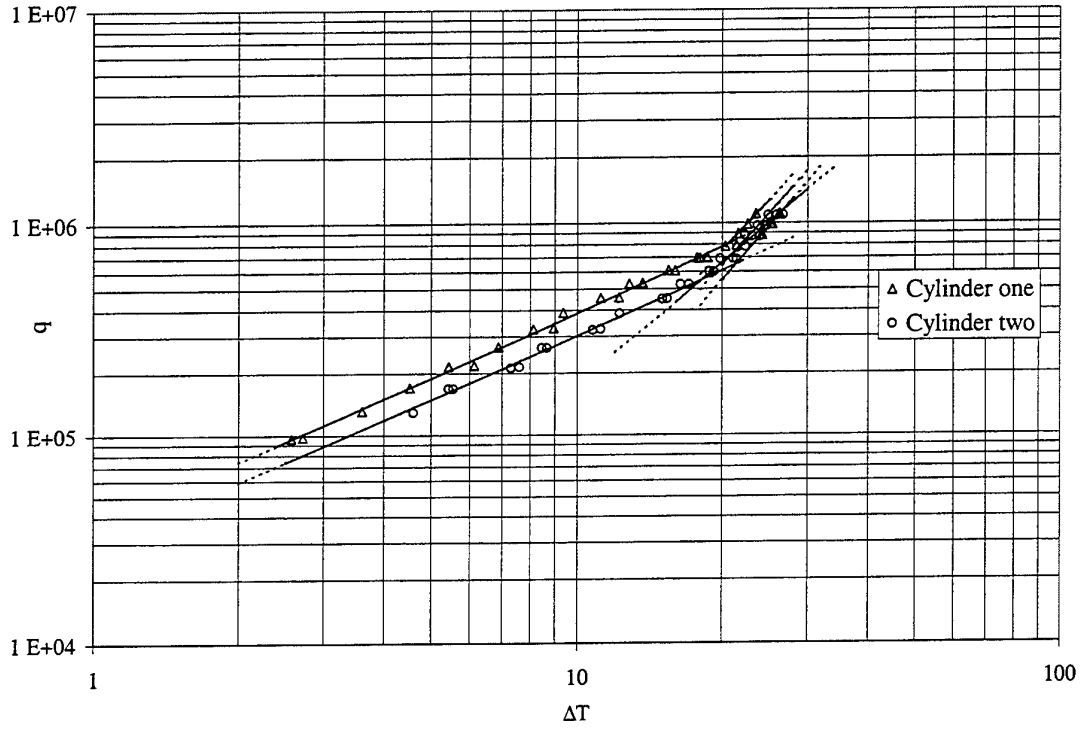

Fig. 4. Trend of $\dot{q}$ versus ΔT for saturated boiling and interpolating curves

First, the influence of jet velocity on heat transfer was assessed. Geometrical parameters were set at Z/D_s = 5 and L/D_s = 5, Ts = 373.13 K. It was found that increasing velocity increases both the $\dot{q}$ for a set ΔT and the maximum $\dot{q}$ which can be dissipated without reaching burnout conditions: these benefits display an asymptotical behaviour as velocity is increased. Thus, a jet velocity of v = 2.5 m/s is chosen to run the most of the tests, this value giving higher heat transfer while still being technically feasible.

Jet outlet temperature T_s was then set and runs conducted to analyse the influence of the geometrical configuration on heat transfer. Tests were then made for Z/D_s and L/D_s in the above ranges In the case of saturated boiling the cylinder farther from the slot, henceforth referred to as cylinder two, didn't show any marked differences in the value of $\dot{q}$ as Z/D_s was varied. On the other hand, the cylinder closer to the jet, henceforth referred to as cylinder one, showed a sharp decrease for $Z/D_s < 3.5$ and a smooth maximum around Z/D_s = 5 A selection of values for $\dot{q}$ as a function of Z/D_s at set ΔT are reported in Table 4. It is interesting to note that for Z/D_s =3.3 cylinder 2 dissipates more than cylinder one. This situation, however is very peculiar.

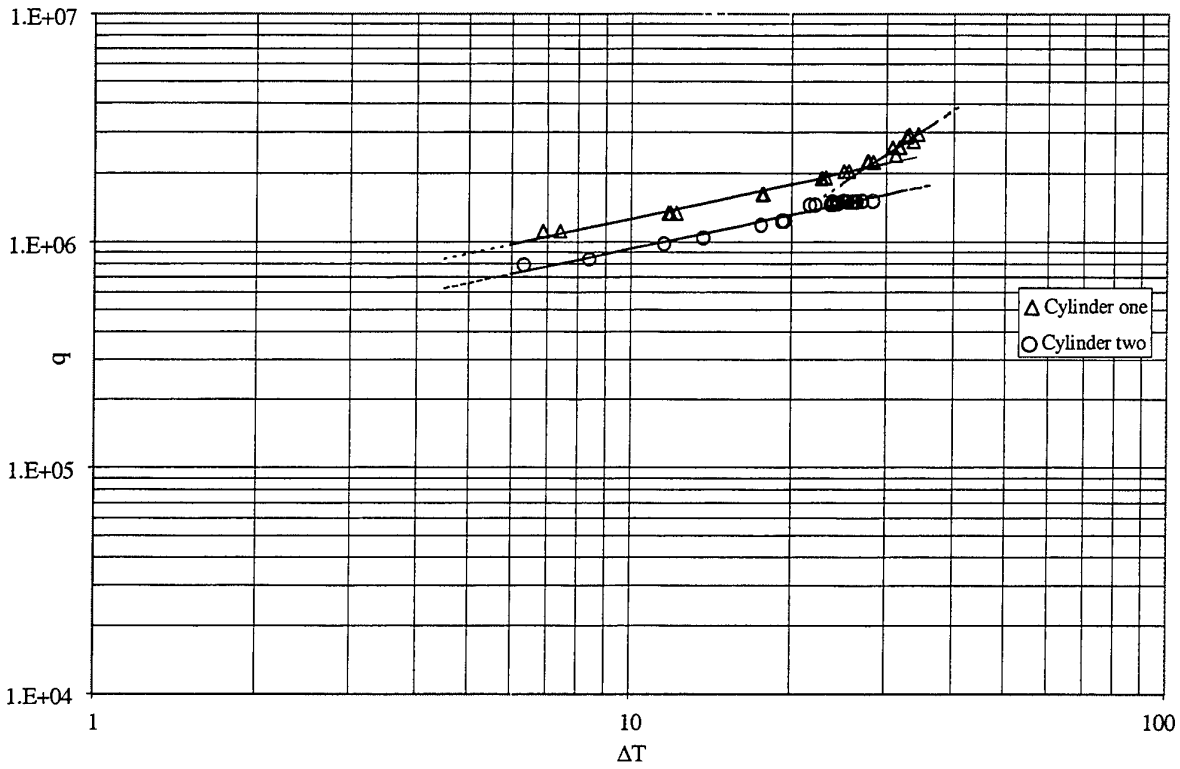

Figure 5. Trend of $\dot{q}$ versus ΔT for subcooled boiling ($(\Delta T)_{sub}$ = 20 K) and interpolating curves

Further tests were made with varying L/D_s, while keeping Z/D_s constant at 5. No tests with L/D_s >5 were made: in this case the jet would have had very little influence on cylinder two, resulting in conditions very close to pool boiling. Experimental evidence showed that $\dot{q}$ for a set ΔT didn't exhibit variations of note as L/D_s varied. Nonetheless, L/D_s = 5 allowed the dissipation of higher heat fluxes. Once the most favourable values for Z/D_s and L/D_s had been determined, correlations linking $\dot{q}$ with ΔT were given using a least-square method for the fit in the form:

$$\dot{q} = c \cdot \Delta T^m \tag{6}$$

The coefficients c and m for the studied configurations are reported in Table 3, complete with average and maximum error for each case. The value of ΔT at which the slope changes is also reported, this corresponding to a transition from incipient to fully nucleate boiling. Film boiling conditions were not investigated. It is important to remark that for high subcoolings no change in the slope for cylinder two occurs, even though visual observation would testify the occurrence of fully nucleate boiling.

For fully nucleate boiling, cylinder one showed shifts for data obtained from different tests, as already reported in [9], while cylinder two displayed no such behaviour. The former case corresponds to some instability in the boiling process. Yet, this is of no great consequence for practical applications since the variations in ΔT are rather small this is also why only one average value of c and m for both shifts is given.

Also for the other three values of T_s the best geometrical configuration turned out to be Z/D_s = 5 and L/D_s = 5 D_s. Values for c and m for these cases are similarly reported in Table 3. For high subcoolings ($(\Delta T)_{sub}$=20 K and $(\Delta T)_{sub}$ =20 K) the maximum heat fluxes increase markedly, but heat transfer coefficients decrease, this meaning a worsening in the process.

Table 3. Selected Values of $\dot{q}$ as a Function of Z/D_s for the Case T_s=373,15 K, $\Delta T \cong 22$ K.

Z/D_s	$\dot{q}\left[\frac{MW}{m^2}\right]$	
	Cylinder 1	**Cylinder 2**
3.3	0.78	0.87
5.0	0.98	0.88
6.6	0.98	0.87

Table 4. Values of c and m for the Best Configurations.

T_s	Cylinder 1					Cylinder 2				
	ΔT^*		c	m	Error [%] Avg\max	ΔT^*		c	m	Error [%] Avg\max
100	22	$\Delta T^* < 22$	4.5	1.0	3\8	19	$\Delta T^* < 19$	4.5	1.0	4\7
		$\Delta T^* \geq 22$	2.6	2.4	6\14		$\Delta T^* \geq 19$	3.4	1.9	5\10
90	27	$\Delta T^* < 27$	5.3	0.65	3\10	24	$\Delta T^* < 24$	5.2	0.58	3\5
		$\Delta T^* \geq 27$	3.9	1.64	2\10		$\Delta T^* \geq 24$	4.4	1.22	1\3
80	27.5	$\Delta T^* < 27.5$	5.6	0.48	3\7	-	-	5.5	0.50	3\7
		$\Delta T^* \geq 27.5$	4.1	1.55	3\7					
70	28	$\Delta T^* < 28$	6.0	0.27	3\7	-	-	5.8	0.30	2\6
		$\Delta T^* \geq 28$	4.5	1.36	5\8					

4. CONCLUSIONS

1. For single – and two – phase conditions $Z/D_s \cong 5.5$ was found to be the best value for heat transfer purposes. This corresponds in both cases to a distance Z roughly equal to the length of the potential core.
2. For single – phase conditions L_1/D_s =1.2, L_2/D_s =3.2 give the best values of Nu, but this configuration is asymmetrical, which might make it unfit for practical applications . To make up for this values of L_1/D_s = L_2/D_s =1.2 may be chosen, since the Nu is only slightly lower. Should the spacing between the cylinders be too narrow another solution may be to use $L_1/D_s = L_2/D_s$ =3.2. In the latter case, for Re = 15000 and Pr = 4.85 the values of Nu for the first, second and third cylinder were Nu = 62.5, Nu =38.3 and Nu = 25.5 respectively.
3. In two – phase conditions, the best configuration was found to be $Z/D_s = L/D_s$= 5, the former parameter having a more marked influence on heat transfer. The influence of L/D_s was limited to the maximum heat flux which may be dissipated, and can be varied if needed. No dependence on the level of subcooling was found, this influencing only the maximum value of $\dot{q}$ which can be dissipated albeit at the expenses of a worsening of the heat transfer mechanism. Accordingly the choice of $(\Delta T)_{sub}$ is dictated by the project needs.
4. It is important to mark the fact that the heat fluxes dissipated by the two cylinder may differ greatly, that by cylinder one being the bigger. This is by no means an hindrance as the electrical components often work at different powers [10].

NOMENCLATURE

Symbol	Description	Units
D_c	Cylinder outer diameter	[m]
D_s	Slot width	[m]
Gr	Grashof number	[-]
I	Current	[A]
k	Thermal conductivity	[W/m K]
l	Distance between the sensing leads	[m]
L	Distance between the two cylinders	[m]

L_1	Distance between cylinders one and two	[m]
L_2	Distance between cylinders two and three	[m]
Nu	Nusselt number	[-]
Pr	Prandtl number	[-]
$\dot{q}$	Specific heat flux per unit area	[W/m^2]
$\dot{q}$ *	Specific heat flux per unit volume	[W/m^3]
Ra	Rayleigh number	[-]
Re	Reynolds number	[-]
T	Calculated temperature at cylinder outer surface	[°C]
T_s	Jet temperature at outlet	[°C]
T_r	Reference temperature	[°C]
T*	Temperature at which change in boiling regime occurs	[°C]
ΔT	$T-T_r$	[K]
$(\Delta T)_{sub}$	Value of subcooling	[K]
ΔT^*	T-T*	[K]
v	Jet velocity at outlet	[m/s]
V	Voltage drop	[V]
Z	Distance between cylinder 1 and slot	[m]

REFERENCES

1. F. P. Incropera "Liquid Cooling of Multi-Chip Modules" *Proceedings of the IX National Heat Transfer Conference pp. 3-22* edited by P. Di Marco, Pisa Italy (1991).
2. E. M. Sparrow, A. Alhomoud, Impingement heat transfer at a circular cylinder to an offset or non-offset slot jet, Int J. Heat Mass Trans., v. 27 pp. 2297-2306 (1984).
3. C. Bartoli, S. Faggiani, "Local Nusselt Number at a Cylinder Cooled by a Slot Jet of Water", Heat and Technology, v. 16, n. 2, pp. 33-37 (1998).
4. S. H Lee., E. S Lee," Effect of Wall Heat Conduction on Convection Heat Transfer from a Circular Tube in Crossflow", *Proceedings of the 2nd International Symposium on Two – phase Flow Modelling and Experimentation,v.1, pp.481 – 487,* Edited by G. P. Celata, P. Di Marco and R. K. Shah, Pisa, Italy (1999).
5. R. J. Moffat, "Describing Uncertainties in Experimental Results", Experimental Thermal and Fluid Science, v. 1, pp 3-17 (1988).
6. C. Bartoli, S. Faggiani, D. Rossi, "Forced and Mixed Convection Heat Transfer from an Array of Cylinders to a Liquid Submerged Jet", Revue General de Thermique, v. 37, pp.431-439 (1998).
7. F. Gori, P. Coppa, "Circumferential Variation of Heat Transfer on Three Circular Cylinders Cooled by a Slot Jet of air", *Proceedings of the 11th IHTC, v.5, pp.477-483,* edited by J. S. Lee, Kyongju, Korea (1998).
8. F. Gori, P. Coppa, "Circumferential Variation of Heat Transfer on Three Circular Cylinders Cooled by a Slot Jet of air" Heat and Technology, v.16, n.2, pp.63-69 (1998).
9. C. Bartoli, P. Di Marco, S. Faggiani, "Heat Transfer and Flow Pattern at a Cylinder Impinged by a Slot Jet During Incipient and Nucleate Boiling", Experimental Thermal and Fluid Science, v. 15, pp.101-108 (1997).
10. W. Nakayama, M. Behnia, H. Mishima, "Impinging Jet Boiling of a Fluorinert Liquid on a Foil Heater Array", *Proceedings of the 11th IHTC, v.2, pp.319-324,* edited by J. S. Lee, Kyongju, Korea (1998).

THE INFLUENCE OF PRANDTL NUMBER ON HEAT TRANSFER EFFECTS AROUND A SPHERE PLACED IN A TURBULENT BOUNDARY LAYER

C.-F. Li, G. Hetsroni, A. Mosyak
Faculty of Mechanical Engineering
Technion - Israel Institute of Technology
Haifa 32000, Israel
Email: hetsroni@tx.technion.ac.il; Fax: (972)-4-8324533

Keywords: DNS, solid particles, near-wall turbulence, heat transfer, thermal pattern

ABSTRACT. Direct numerical simulation (DNS) is performed to solve the governing equations for fluid flow and heat transfer around a sphere which is placed on the bottom wall of a flume. Two way coupling is used to account for the effect of the sphere on the structure of the near-wall turbulence and on the main stream. The calculation of the thermal field is done with the same grid system used for the velocity field. Water and transformer oil were used as test fluids, with the Prandtl numbers Pr = 5.4 and Pr = 55, respectively. The heat transfer calculations were carried out at the constant mean heat flux along the bottom. For both Prandtl numbers the DNS results indicate enhancement of heat transfer coefficient associated with a flow motion toward the wall. The thermal pattern around the sphere is obtained and the effect of Prandtl number is discussed.

1. INTRODUCTION

The scalar transport on a small particle stationary or in motion on the bottom wall of a flume is not only interesting from a pure heat-mass transfer point of view but also has many applications. Prediction of flow and heat transfer around bodies mounted on a surface is very important in relation to many types of heat exchangers, and numerical investigations were performed in the past [1-3]. Numerous experimental and numerical investigations have been reported on local heat-mass transfer distributions around an obstacle at Prandtl number Pr = 1 [4-6]. It is clarified that heat transfer strongly depends on the boundary layer characteristics. Studies of heat (or mass) transfer for a flow around submerged objects are limited, particularly for cylinders, cubes and parallelepipeds resting on a surface. On the other hand, there has been no specific effort to predict heat or mass transfer patterns that result from flow around submerged spherical particle, perhaps because that flow and temperature fields are complex.

The purpose of the present study is to predict details of heat transfer around a sphere submerged in a flume by direct numerical simulation (DNS). We aim to calculate the temperature distribution in a turbulent boundary layer at Pr = 5.4 and Pr = 55, and to get the influence of Prandtl number on heat transfer enhancement near the sphere.

2. MATHEMATICAL DESCRIPTION

Flow Field

We examine in some details the two-way coupling and interaction between large particles ($Re_p > 1$) and the turbulence in the near wall region of an open channel turbulent flow. The time-dependent, three-dimensional Navier-Stokes and continuity equations are solved in a rectangular domain. The flow geometry and coordinate system are shown in Fig. 1. The streamwise direction is denoted by x_1, the spanwise direction by x_2, and the wall-normal direction by x_3, while the velocity components are u_1, u_2, u_3, correspondingly. The flow is driven by a constant streamwise pressure gradient. The governing equations for the flow field are

$$\frac{\partial u_i^+}{\partial x_i^*} = 0 \tag{1}$$

$$\frac{\partial u_i^+}{\partial t^*} = u_j^+ \frac{\partial u_i^+}{\partial x_j^*} = -\frac{\partial p^+}{\partial x_i^*} + \frac{1}{Re_\tau} \frac{\partial^2 u_i^+}{\partial x_j^* \partial x_j^*} \tag{2}$$

The equations have been made dimensionless with the channel half depth H and the friction velocity u_τ ($u_i^+ = u_i/u_\tau$; $x_i^* = x_i/H$; time $t^* = t/(H/u_\tau)$; and pressure $p^+ = p/\rho u_\tau^2$). The Reynolds number Re_τ is defined as $Re_\tau = u_\tau H/\nu$, with ν the kinematic viscosity. The boundary conditions are $u_1^+ = u_2^+ = u_3^+ = 0$ (no-slip) on the bottom wall, and $\frac{\partial u_1^+}{\partial x_3^*} = \frac{\partial u_1^+}{\partial x_3^*} = 0$, $u_3^+ = 0$ at the free surface. Periodic boundary conditions are imposed in streamwise (x_1) and spanwise (x_2) directions. The initial conditions are the mean profiles for the velocity superimposed with sinusoidal perturbations.

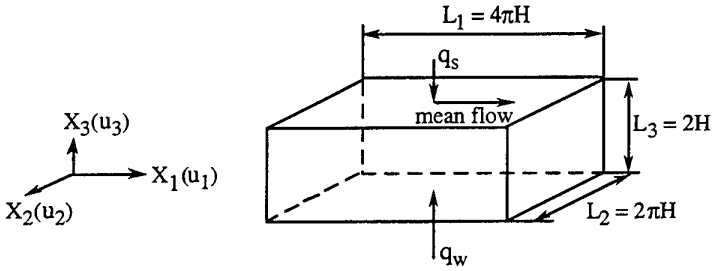

Fig. 1. Computational domain and coordinate system

A pseudo-spectral method is employed to solve the governing equations. In the homogeneous (x_1 and x_2) directions, all the quantities are expressed by Fourier expansions. In the x_3-direction which is nonhomogeneous, they are represented by Chebyshev polynomials. A full description of the numerical scheme can be found in [7]. In the present study the turbulent channel flow of Reynolds number $Re_\tau = 85.4$ is simulated. The bulk Reynolds number $Re = 2H\, u_B/\nu$ is about 2600, where 2H is the flow depth, 2H = 37 mm, and u_B is the bulk streamwise velocity. The calculations were carried out in a computational domain of $L_1^+ \times L_2^+ \times L_3^+ = 1074 \times 537 \times 171$ wall units in the x_1 , x_2 and x_3 directions with a resolution of $128 \times 128 \times 65$. A nonuniform distribution of collocation points is used in the x_3-direction due to the nature of the Chebyshev polynomials, and the first collocation point away from the wall is at $x_3^+ = 0.1$.

After the flow field is brought to a stationary state, the sphere of diameter $d^+ = 17$ is introduced into the flow, where $d^+ = d\, u_\tau / \nu$, d is the sphere diameter. In the present study we only simulate the cases of a single sphere stationary on the bottom, and a single sphere touching the bottom and moving in the flow direction at a velocity $v^+ = v/u_\tau = 5$, or counter the flow direction at a velocity $v^+ = -5$. Two-way coupling of sphere effect on the flow field is introduced as follows. All the velocities in the collocation points occupied by the sphere were made to be zero in the case of stationary sphere or equal to the uniform velocity of the moving sphere and Eq. (2) was solved with an additional source term S_{pi} :

$$\frac{\partial u_i^+}{\partial t^*} = u_j^+ \frac{\partial u_i^+}{\partial x_j^*} = -\frac{\partial p^+}{\partial x_i^*} + \frac{1}{Re_\tau}\frac{\partial^2 u_i^+}{\partial x_j^* \partial x_j^*} + S_{pi} \tag{3}$$

A full description of iterative solution of Eq. (3) can be found in [8].

Temperature Field

The thermal problem to be considered is the same as that of the experiment [9]. The bottom wall of a flume is heated at a constant heat flux q_w = constant, and the free surface is regarded as an adiabatic surface $q_s = 0$. The governing equation for the thermal field is given as follows [10,11]:

$$\frac{\partial \theta^+}{\partial t^*} + u_j^+ \frac{\partial \theta^+}{\partial x_j^*} - \frac{u_1^+}{2u_B^+} = \frac{1}{Re_\tau Pr}\frac{\partial^2 \theta^+}{\partial x_j^* \partial x_j^*} \tag{4}$$

Where θ is the local temperature difference $\theta = \langle Tw,x_1\rangle - T(x_1, x_2, x_3,t)$, and $\langle Tw,x_1\rangle$ is ensemble temperature along the x_2-direction on the bottom wall and time at x_1 position, T is the fluid temperature. The dimensionless

variables are defined as: $\theta^+ = \theta / \theta_\tau$, $\theta_\tau = q_w/\rho c_p u_\tau$ is the friction temperature; $u_B^+ = u_B/u_\tau$; $Pr = \nu/\alpha$ is Prandtl number. The last term on the left side of Eq. (4) corresponds to that an averaged temperature which increases linearly in the x_1-direction with isoflux boundary condition. In the x_3-direction, the boundary condition is $\frac{\partial \theta^+}{\partial x_3^*} = Re_\tau Pr$ on the bottom wall, and $\frac{\partial \theta^+}{\partial x_3^*} = 0$ at the free surface.

Any buoyancy effect was neglected, and hence the temperature was considered as a passive scalar. As the initial condition a uniform distributed temperature field was projected on the velocity field. The heat transfer simulation was started after the velocity field had reached a steady state. Then once the velocity field was calculated at each time step, the temperature field was obtained by integrating the energy equation. This calculation was done by the fully implicit method in time advancement and power-law scheme for the convection and diffusion terms [12], with the same grid system used for the velocity field. We assume that all material and fluid properties are constant, so that the hydrodynamic results obtained earlier may be employed directly in the heat transfer analysis.

3. RESULTS AND DISCUSSION

Heat Transfer Quantities Near The Motionless Sphere On The Bottom

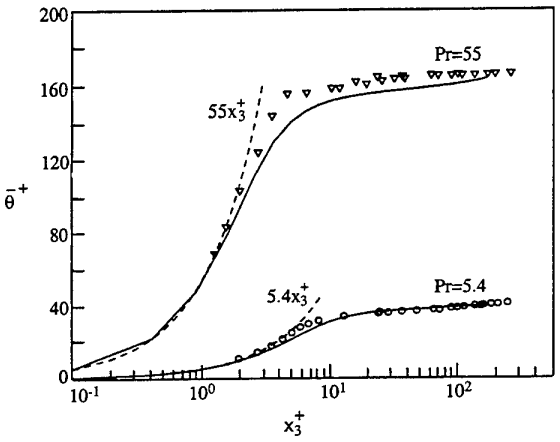

Fig. 2. Nondimensional mean temperature profiles uctuations present DNS, Experimental data [13]: O - water, Pr=5.4, ∇ -Oil, Pr = 55

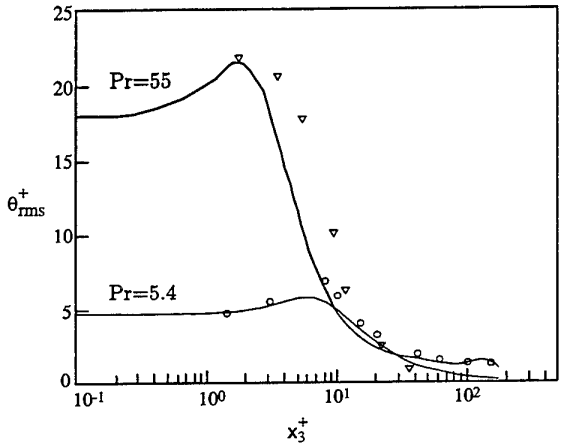

Fig. 3. Intensity of temperature present DNS; Experimental data [13]: O- water, Pr = 5.4; ∇ - Oil, Pr = 55

Statistical quantities for initial temperature field. Fig. 2 shows the distribution of the mean temperature $\bar{\theta}^+$ vs x_3^+ in the situation without particles. The present results are compared with experimental data reported in [13] for water (Pr = 5.4) and transformer oil (Pr = 55) channel flow. For water flow (Pr = 5.4) the agreement is good as for the conductive sublayer ($\theta^+ = Pr\ x_3^+$) as for the logarithmic region. For oil flow (Pr = 55) the agreement between the DNS and the experimental data is also good but the present DNS result gives slightly lower values of the nondimensional mean temperature. This may be due to a change of oil physical properties near the wall in the experiments of [13]. The root- mean-square temperature fluctuations normalized by the friction temperature are compared with pervious

The flow pattern around the sphere. The spherical particle of the diameter $d^+ = 17$ is located at the position x_1^+=507.1, x_2^+=253.5, x_3^+= 0. Typical instantaneous flow around the sphere in the $x_1^+ - x_3^+$ plane is shown in Fig. 4. The vector velocities show that the sphere affects only the region close to the surface of the sphere. At the present Reynolds number, the recirculating flow is fairly weak. For a free stream relative to a front of the sphere two areas may be defined: the flow along the sphere surface in the positive x_3^+ direction

(measured from the front stagnation point) and the flow in the negative x_3^+ direction. The flow in the positive x_3^+ direction accelerates from the front stagnation point and reaches a maximum velocity at x_3^+ about 3. The flow in the negative direction decelerates from the stagnation point and reaches a zero velocity at the bottom.

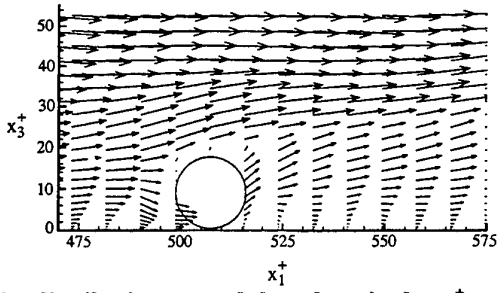

Fig. 4. Velocity distribution around the sphere in the x_1^+ - x_3^+ plane (x_2^+=253.5)

Comparison of heat transfer coefficients. Normalized heat transfer coefficients was calculated for each of the cross sections shown in Fig. 5a. The normalization was performed with the time and space averaged heat transfer coefficient, h, which was derived from the average heat flux and bottom temperature without the sphere. In Fig. 5 the DNS made at Pr = 5.4 are compared with experimental results of [9]. The present calculation agrees well with the experiments. The front and side flow regions causes intense heat removal which resulted in a rise of the heat transfer in the region of about $-2 < x_{1c}^+/d^+ < -0.5$ (x_{1c}^+ is the streamwise distance from where the sphere touches the wall). In the region of $-0.5<x_{1c}^+/d^+<2$ the flow in the near bottom region, despite recirculations, prevented intense heat removal which resulted in a local decrease of the heat transfer coefficient.

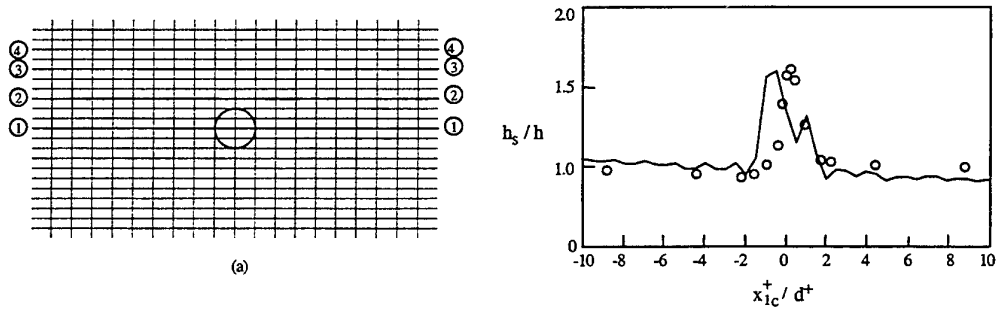

Fig. 5. Comparison between numerical and experimental results of normalized heat transfer coefficient
(a) Positions along each of the cross sections identified by a number in the circle
(b) Comparison with the experiment [9] along cross section 1-1, water flow, Pr = 5.4

Heat transfer coefficients along different cross sections. Fig. 6a,b shows the variations of normalized heat transfer coefficient along each cross section depicted in Fig. 5a. The results are shown in Fig. 6a and Fig. 6b for Prandtl number Pr = 5.4 and Pr = 55, repectively. Although the distribution for both cases is qualitatively similar, the quantitative comparison shows marked differences. Because the temperature boundary layer is much smaller in the case of Pr = 55 compared to the case of Pr = 5.4, the corresponding peak of heat transfer coefficient is higher for Pr = 55. The largest heat transfer enhancement appears along the axis of the sphere symmetry (Line 1-1), where the normalized heat transfer coefficient reaches the value of about 1.55 for Pr = 5.4 and of 2.5 for Pr = 55. For both cases the maximum peak location is about 0.5 – 1 particle diameter before the center of the sphere. Between the first and second peak the minimum of heat transfer coefficient was observed. This minimum corresponds a small hot temperature area after the sphere. For Pr = 55, the second peak is also more pronounced than that for Pr = 5.4. For both Prandtl numbers studied the value of h_S/h is about 1.4 - 1.5 at $x_{1c}^+/d^+ = 0$, i.e. the cooling is enlarged.

Along the cross section, which is of 0.75 sphere diameter spanwise away from the center of sphere (Line 2-2), value of enhancement heat transfer decreases, but still remains higher for Prandtl number Pr = 55 than that for

Pr = 5.4. The location of the first peak shifts downstream, and the very small second peak is observed only for Pr = 55. Along the cross section of 1.5 sphere diameters away from the center of sphere (Line 3-3), the influences become smaller. Further far away, along the cross section of 2 sphere diameters away from the center of sphere (Line 4-4), it could be observed no influence any more. So the particle affected area is limited about 2 sphere diameters in the spanwise direction near the sphere.

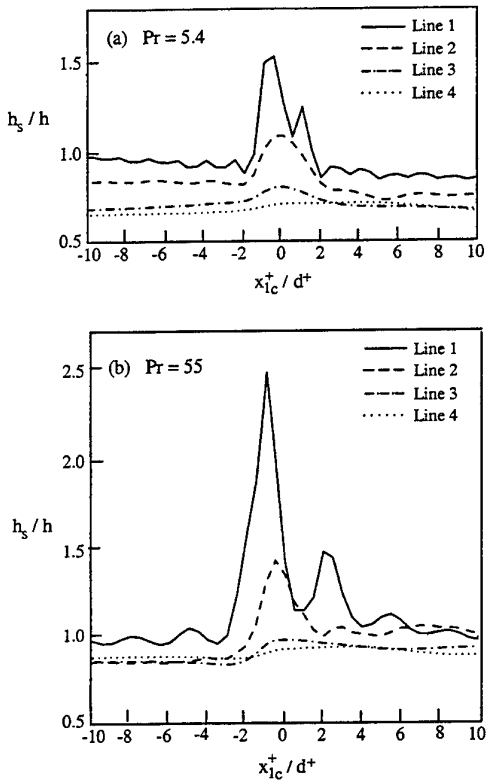

Fig. 6. Values of normalized heat transfer coefficient along lines indicated in Fig. 5a, DNS results (a) Pr = 5.4; (b) Pr = 55

Heat Transfer Quantities Near the Moving Sphere

Fig. 7a,b shows the streamwise velocity vectors for the case of a moving sphere which touches the bottom and moves at the constant velocity in the flow direction ($v^+ = 5$) and countercurrent to the fluid ($v^+ = -5$), respectively. For the sphere movement in the flow direction (Fig. 7a), the flow covered front of the sphere entirely and shear layer reattachment occurred at a location on the sphere surface at the angle of about 90° measured from the front stagnation point. For the case of the sphere moving in the countercurrent direction relative to a steady free stream, the shear layer reattached at the front of the sphere (Fig. 7b). Fig. 7a,b shows that for the sphere moving in the steady flow, the location of the flow separation on the sphere surface moves toward to the rear stagnation point with the reduction of the particle Reynolds number.

The comparison of normalized heat transfer coefficient along the axis of the sphere symmetry is shown in Fig. 8a, b for the moving sphere in both water and oil flow. It can be seen that sphere movement in the flow direction (Fig. 8a) affects normalized heat transfer coefficient more for oil flow than that for water flow. This effect increases when the sphere moves countercurrent to the flow direction (Fig. 8b). Especially for the sphere moving countercurrent to the flow direction, normalized heat transfer coefficient increases more near the sphere, and for both Prandtl number studied three maximum points can be clearly marked.

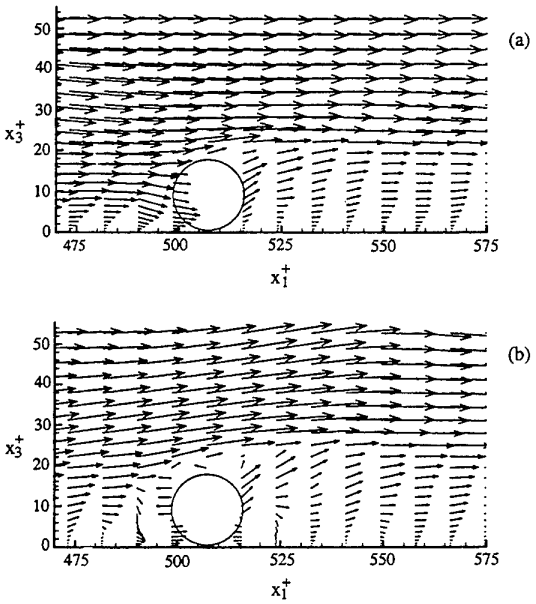

Fig. 7. Velocity vectors around the sphere in the x_1^+ - x_3^+ plane (x_2^+=253.5) (a) The sphere moves downstream, v^+= 5; (b) The sphere moves upstream, v^+= -5

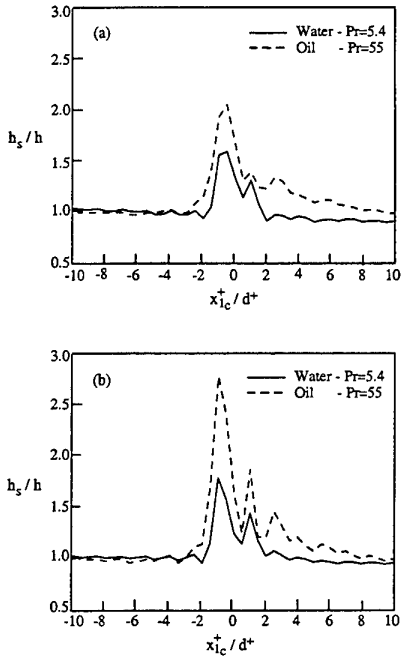

Fig. 8. Comparison of normalized heat transfer coefficient along cross section 1-1 (a)The sphere moves downstream, v^+= 5; (b) The sphere moves upstream, v^+= -5

4. CONCLUSIONS

The DNS study of the flow characteristics around a single sphere submerged in turbulent flow in a flume was performed. Two way coupling is used to account for the effect of the sphere on the structure of the near-wall turbulence and main stream. Water and transformer oil were studied as the test fluids with the Prandtl number Pr = 5.4 and Pr = 55, respectively. The calculation of heat transfer was performed for the single sphere attached to the bottom of the flume and for the sphere that touched the bottom and moves on it. The DNS were carried out at the constant mean heat flux along the bottom of the flume.

For the sphere attached the bottom of the flume the calculation shows a cooler area in the front of the sphere and a cooler tail in the wake, which increases with increasing Prandtl number. Variation of heat transfer coefficient for water flow agrees well with experimental results presented in the literature. For both Prandtl numbers the DNS results indicate the essential enhancement of heat transfer coefficient due to the presence of the sphere. This effect is more pronounced in the region within about two particle diameters from the center of the sphere. The heat transfer augmentation for Pr = 55 is higher than that for Pr = 5.4. For the sphere that moved in the streamwise direction, the region of lower temperature is greater than that for a sphere in countercurrent motion. It was shown that a decrease of bottom temperature is associated with a flow toward the wall, whereas an increase of it is associated with motion away from the wall.

ACKNOWLEDGEMENTS

This research was supported by the Basic Research Foundation administered by the Israel Academy of Sciences and Humanities and by Ministry of Science, State of Israel. The Research was also supported by the Fund of the Promotion of Research at the Technion.

REFERENCES

1. R.J. Goldstein, J. Karni, "The Effect of a Wall Boundary Layer on Local Mass From a Cylinder in Crossflow", Trans. ASME, J. Heat Transfer, vol.106, pp.260-267 (1984).
2. E.M. Fisher, P.A. Eibeck, "The Influence of a Horseshoe vortex on Local Convective Heat Transfer", Trans. ASME, J. Heat Transfer, vol.112, pp.329-335 (1990).
3. M.K. Chyu, V. Natarajan, "Local Heat/Mass Transfer Distributions on the Surface of a Wall-Mounted Cube", Trans. ASME, J. Heat Transfer, vol. 113, pp.851-857 (1991).
4. T. Igarashi, H. Yamasaki, "Fluid Flow and Heat Transfer of a Rectangular Cylinder in the Turbulent Boundary Layer on a Plate", Trans. JSME, vol.55B, pp.3157-3165 (1989).
5. G.K. Morris, S.V. Garimella, "Thermal Wake Downstream of a Three-Dimensional Obstacle", Exp. Thermal and Fluid Science, vol. 12, pp.65-74 (1996).
6. M. Nakajima, T. Ota, "Numerical Simulation of Three Dimensional Unsteady Flow and Heat Transfer Around a Surface-Mounted Hexahedron in a Channel", *Proceedings of 11th IHTC*, vol. 3, pp.133-138, Kyongiu, Korea (1998).
7. K.L. Lam, "Numerical Investigation of Turbulent Flow Bounded by a Wall and a Free-Slip Surface", Ph.D. Thesis, Univ. Calif. Santa Barbara (1989).
8. C. Li, A. Mosyak, G. Hetsroni, "Direct Numerical Simulation of Particle Turbulence Interaction", Int. J. Multiphase Flow, vol. 25, pp.187-200 (1999).
9. G. Hetsroni, R. Rozenblit, D.M. Lu, "Heat Transfer Enhancement by a Particle on the Bottom of a Flume", Int. J. of Multiphase Flow, vol.21, pp.963-984 (1995).
10. N. Kasagi, Y. Tomita, A. Kuroda, "Direct Numerical Simulation of the Passive Scalar Field in a Turbulent Channel Flow", Trans. ASME, J. of Heat Transfer, vol.114, pp.598-606 (1992).
11. H. Kawamura, K. Ohsaka, K. Yamamoto, "DNS of Turbulent Heat Transfer in Channel Flow with Low to Medium High Prandtl Number Fluid", Int. J. Heat Fluid Flow, vol.19, pp.482-491 (1998).
12. S.V. Patanker, *Numerical Heat Transfer and Fluid Flow*, Hemisphere, Washington, D.C. (1980).
13. A. Zukauskas, A. Slanciauskas, *Heat Transfer in Turbulent Fluid Flows*, (Edited by J. Karni), Springer-Verlag, Berlin, New York, Paris (1987).

HEAT TRANSFER IN THE WAKE BEHIND A LONGITUDINAL VORTEX GENERATOR IMMERSED IN DRAG-REDUCING CHANNEL FLOWS

Jens F. Eschenbacher*, Mizuho Joko, Kazuyoshi Nakabe and Kenjiro Suzuki
Department of Mechanical Engineering
Kyoto University
E-mail: jens@htrans.mech.kyoto-u.ac.jp ; Fax: +81-75-753-5851

Keywords: drag-reducing flow, vortex generator, heat transfer, wake flow, longitudinal vortex

ABSTRACT. An experimental study of wall heat transfer in the wake behind a single wing-type vortex generator (WVG) was made in drag-reducing flows with three different surfactant solutions, Cetyl-trimethyl-ammonium-chloride(CTAC) with same amounts of sodium salicylate (NaSal) dissolved in water. The additive concentration was varied between 0ppm (C0), 30ppm (C30) and 200ppm (C200). The WVG was mounted on the heat transfer target surface of the bottom wall in the test section. The Reynolds number, based on the main flow velocity and the channel height was set in the range from 7.3×10^3 up to 4.4×10^4 under considerations of the temperature dependence of the non-Newtonian surfactant fluid. It was found, that small amounts of CTAC/NaSal added in water reduce the heat transfer coefficients drastically, and that this reduction could be locally recovered in the wake behind the WVG. The longitudinal vortex generated behind the WVG was found to play an important role for heat transfer enhancements of drag-reducing flows. Comparison with the case of pure water, C0, reveals that the heat transfer coefficients of the surfactant solutions can recover to the ones of Case C0 locally in the wake behind the WVG. The heat transfer recovery regions correspond to the location of the longitudinal vortice which were observed narrower but longer in the surfactant solutions than in the pure water. Depending on the surfactant concentration, fluid temperature and flow velocity, the generated longitudinal vortex was locally able to recover the reduced wall heat transfer coefficient of the surfactant solution completely up to the value of water.

1. INTRODUCTION

Global warming and limited fossil energy resources are key factors why in the recent years, the issue to use energy more effectively became one of the top topics in the energy policy of leading industrial countries. As the demand of heating energy in industrial and residential areas increases steadily, there exists a serious environmental problem with a temperature rise in rivers and seas because of "waste heat". The waste heat originates in mostly water lower than 120°C, which cannot be used for industrial applications anymore but may still used in residential heating devices. In regions where a huge part of the primary energy is generated by fossil fuels, it is significant to manage and use the heat energy more rationally. Far district heating or cooling transport system are one of the most economical solutions to simultaneously decrease both, the waste heat from industrial plants and heating energy from residential houses. The system, however, is unfortunately still limited through the distance between the industrial fields and the residential areas. In other words, after a certain distance, the consumption of pumping energy will exceed the saving in heat energy.

In the case where small amounts of polymers or surfactants were added to water, it was found that the coefficients of both, wall friction and heat transfer in turbulent flows were reduced up to 80 percent [1, 2]. This remarkable drag-reducing characteristic, which depends on additive concentration, solution temperature and flow conditions, is assumed to originate in damped turbulence through an unique internal alignment of the additives in the solution [2]. In other words, the addition of surfactant constrains the fluid to change from Newtonian to non-Newtonian manner. Whereas polymers get weaken in their drag-reducing performance due to mechanical degradation of the molecules, the surfactant solutions exhibit high performance to recover and keep their structure over a long period. Up to now, it is known that the phenomena of "Drag-Reducing" could appear when turbulence motions normal to the main flow direction are suppressed mainly through small addition of soluble high polymers or surfactants into turbulent flow [1]. The reduction of irreversible dissipation energy lead, for example in pipe flows, to a reduced pressure drop or to an increased flow rate with a given pressure gradient. In flows with coexistence of temperature and concentration gradients the convective heat or mass transfer appear also decreased due to the damped momentum exchange. Exceeding a certain wall shear stress over a critical value, τ_c, the suppressed coefficients of drag and heat transfer recover up to the values of the pure solvent. Lowering the shear stress below the critical value leads again to drag-reducing flow conditions. This

special feature of drag-reducing surfactant solutions and the apparent flow laminarization seems to be very attractive for engineering applications like far district heating/cooling systems or other long piping systems to reduce pumping energy and pipe heat loss. The reduction of wall heat transfer through drag-reducing flow, however, does not always take an advantage, if one considers more efforts in heat exchanger performance. It is, therefore, of practical worth to develop an effective method to locally enhance the heat transfer with a minimum corresponding increase of pressure loss over a wide area.

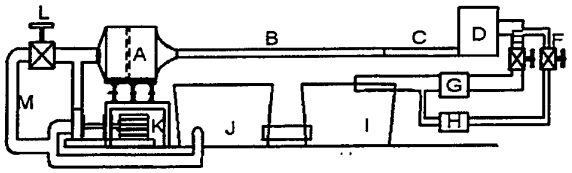

A: Settling Chamber
B: Developing Zone
C: Test Section
D: Outlet of the water channel
E: Valve for Main flow
F: Valve for Side flow
G: Orifice
H: Magnetic Flowmeter
I: Tank I
G:Tank II
K: Pump
M: Bypass
L: Bypass valve

Fig. 1. Experimental apparatus.

2. EXPERIMENTAL SETUP AND PROCEDURE

The drag-reducing fluids were prepared using equal amounts of Cetyl-trimethyl-ammonium-chloride $C_{16}H_{33}N(CH_3)_3^+Cl^-$ (CTAC) and sodium salicylate (NaSal) dissolved in water. The concentrations of the fluids were varied in three steps, C0, C30 and C200 corresponding, respectively, to 0 (water), 30 and 200ppm. The experiments were carried out in a closed loop rectangular duct as shown in Fig. 1. The working fluid was reserved in two tanks ($1m^3$ each) connected by pipes. The fluid was sucked by a centrifugal pump and driven through a settling chamber into the test section of the duct (W = 500mm in width and H = 25 mm in height). The duct itself consists of an entrance region, 205H long, and the following test section, 40H long, made of acrylic plates to have an optical access all through the duct wall. The mass flow rate was adjusted by main and bypass valves and monitored by two parallel flow meters installed downstream of the test section. The main flow temperature was precisely controlled within its fluctuation of 0.1K via a temperature regulator installed in the downstream tank.

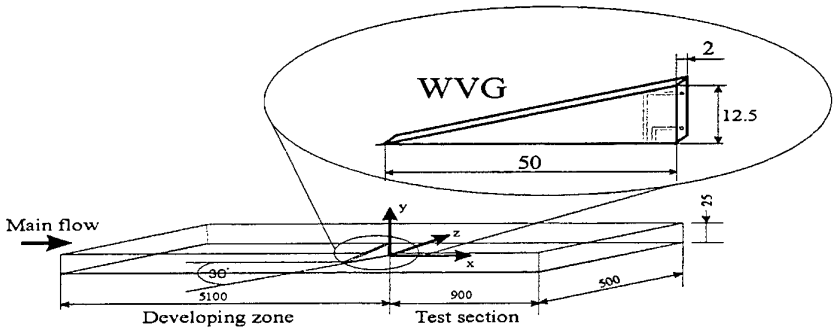

Fig. 2. Dimensions of the test section

Fig. 2 shows the test section and a delta-shaped winglet vortex generator, WVG, together with the coordinate system. The WVG was made of brass and attached to the bottom surface of the test section. Its angle of attack against the main flow was fixed at 30 degrees. The height of the trailing edge was 0.5H and the base length was

set equal to 2H, according to Ref. [3]. To conduct flow visualization and improve PIV measurements, the trailing surface was equipped with two holes for dye or tracer injection.

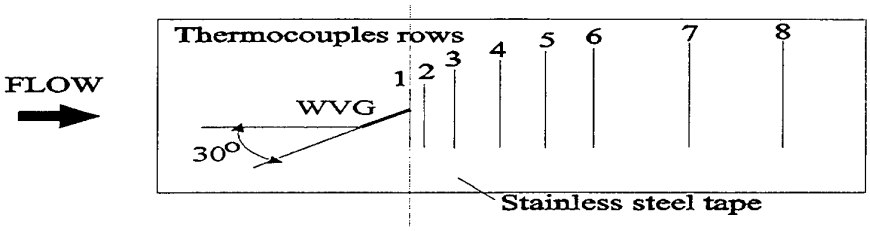

Fig. 3. Heat transfer target plate with the Vortex generator and the thermocouple locations.

To perform heat transfer measurements, the bottom surface of the test section was adhered with electrically heated stainless steel sheets, 0.02mm in thickness, and the local wall temperatures were monitored with 220 pairs of K-type thermocouples. The locations of the thermocouples were plotted in Fig. 3, which are aligned in 8 rows at x/H = 0, 1.0, 2.5, 5.0, 7.5, 10, 15 and 20 downstream of the vortex generator. The local Nusselt numbers were derived from $Nu = h \cdot H / \lambda_w$ where λ_w denotes the thermal conductivity of water and h the heat transfer coefficient defined as follows: $h = q_w / (T_w - T_b)$, where q_w indicates the local wall heat flux estimated by current and voltage measurements. T_w stands for the local wall temperature, and T_b the bulk temperature at an arbitrary streamwise location, defined as follows:

$$T_b = T_i + \frac{1}{\rho \cdot C_p \cdot U_m \cdot H} \int_0^x q_w \cdot dx$$

where T_i represents the inlet fluid temperature before approaching the heated bottom wall, and U_m the cross-sectional averaged velocity of the main flow directly calculated with the measured flow rate. ρ and C_p, respectively, represent the density and specific heat capacity of water. The Reynolds number based on the duct height is defined as follows: $Re = \rho \cdot u \cdot H / \eta$, where η represents the dynamic viscosity of the solvent.

In order to investigate the mechanism of heat transfer recovery, the flow velocities were also measured using particle image velocimetry (PIV). For this measurement, the cross-section perpendicular to the main flow direction was illuminated by double sheets of two Nd:YAG pulse lasers and its images were recorded in frame grabber memories through a cross-correlation CCD camera. The velocity vectors in the cross-sections were estimated by cross-correlation coefficients calculated with a pair of video images captured by the camera. The velocity vector distributions shown in the following chapters were arithmetically averaged over 4 individual velocity vector frames, each of which was calculated with two sequential image frames of 1.0 ms.

3. RESULTS AND DISCUSSIONS

Figure 4 shows the spanwise Nusselt number distributions developing in the wake of the WVG for three different concentration, C0, C30 and C200. The origin of the coordinate, (x/H, z/H) = (0,0), in the figure was located at the trailing edge of the WVG. The Reynolds number was fixed at Re = 1.1 x 10^4 and the temperature of the fluid was set to 25°C. Cross-sectional images of the flow visualized with fluorescent dyes previously in Ref. [4] clearly revealed that the longitudinal vortex was situated along the streamwise direction in the central region of the duct width. Heat transfer enhancement regions observed in the present experiment were found to apparently correspond to the locations of the vortex. For the surfactant cases of both C30 and C200, it can be seen that the heat transfer coefficients are decreased to one third of the pure water case, C0, in the outer regions around z/H < -1.5 and 0.5 < z/H. In these regions, the value of the heat transfer coefficient does not vary with the surfactant concentration in the present flow condition. The results obtained here coincide with the ones by Cho and Hartnett [5] reporting that the maximum heat transfer reduction depends on neither the type nor the concentration of additives.

It was found in comparison of the central region around, $-1.5 < z/H < 0.5$, with the outer region that the central portion of Nusselt number distributions, in particular at $x/H = 1$ and 2.5, recovered well up to the ones of the water, depending on the surfactant concentration. In the C30 case, the peak Nusselt number exceeds five times the one in the outer region and reaches the value of the water case, whereas in the C200 case, the maximum value is only about two times larger than the one in the outer region. These jumps in heat transfer performance could be explained by the dependence of critical shear stress on the surfactant concentration. Near-wall shear stress caused by high rotational velocity of the longitudinal vortex in the range of $-1.5 < z/H < 0.5$ may exceed the critical shear stress and then change local fluid properties into the ones similar to water. In the C200 case, on the other hand, the critical shear stress is relatively higher than the one in the C30 case under the present Reynolds number, and the local shear stresses do not reach the critical one yet, retaining the drag-reducing fluid character. Thus, the C200 case shows a moderate increase of Nusselt number in the above spanwise range, compared with the C0 and C30 cases. Detained observation reveals that there exists a valley in the Nusselt number distributions, a minimum in the heat transfer, in the C0 and C30 cases. One more observed fact is that the location of the peak Nusselt number in the C200 case is different from the other two cases. This shift towards positive z direction may be linked directly with the size of longitudinal vortex, and will be discussed later.

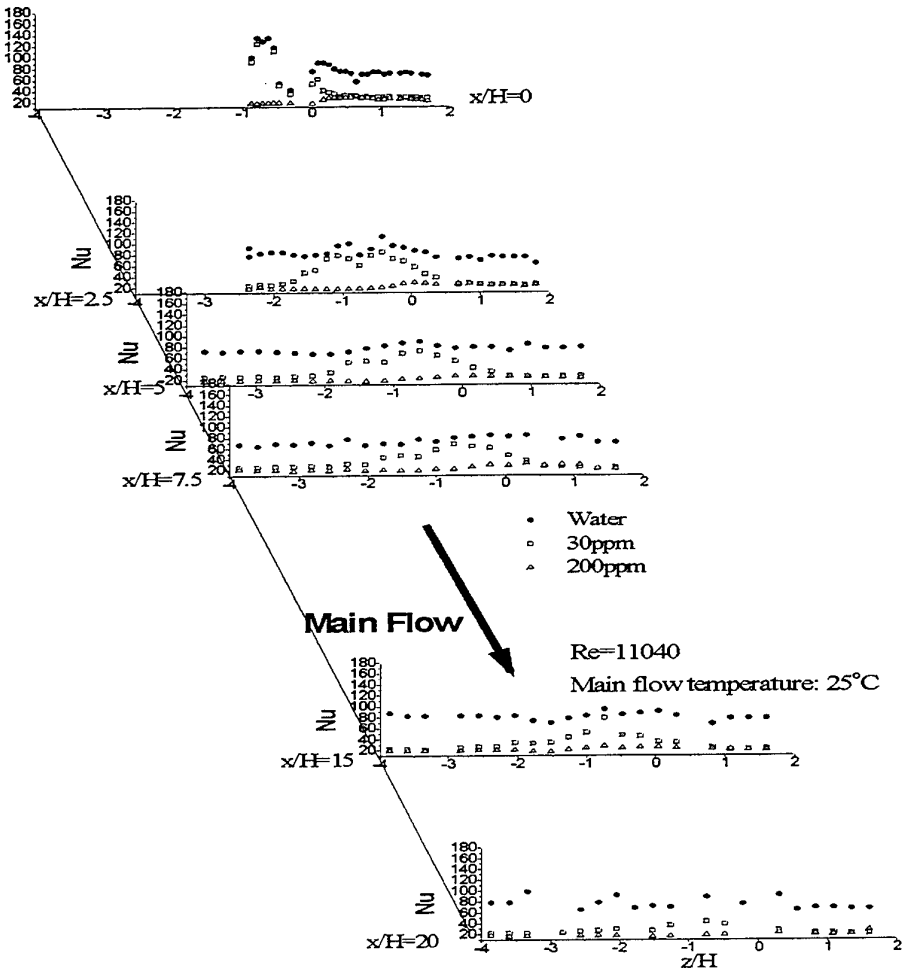

Fig. 4. Spanwise distributions of Nusselt number over the test section (Re = 11,040 and T = 25 °C).

Concentrating the point of view more down stream of the origin, it is obvious that on one side the C200 local maximum in Nusselt number is rapidly diminishing after x/H=2.5 and on the other hand, the heat transfer enhancement region in the case of C30, remains down to x/H = 15. This contrast is considered to depend on the fluid properties changing tremendously if local shear stresses are exceeding a critical value. In the C200 case, where the critical shear stress is relatively high and the drag-reducing effect exists over the entire cross-section, the longitudinal vortex generated in the wake of the WVG is considerably small in diameter and stabilized in wake core. In the C30 case, rotating motions of the longitudinal vortex limited by the top and bottom walls could exchange its momentum with the surrounding main flow when the local shear stresses exceed the critical value. This leads to downwash motions with the entrainment of the main cool fluid, which enhances the local heat transfer at the corresponding location of the vortex. The main reason the heat transfer enhancement region remains down to x/H = 15 may found in the drag-reducing property of the outer regions, although the enhanced region disappears after x/H = 5 in the C0 case of water. The outer region where the shear stress is below the critical value dampens the momentum exchange between vortex core and its vicinity. This provokes a lag in vortex growth and higher vortex stability, compared with the water case. At x/H = 20, far downstream, the Nusselt numbers of all concentration conditions almost fall back to the value in the region with no influence of the vortex.

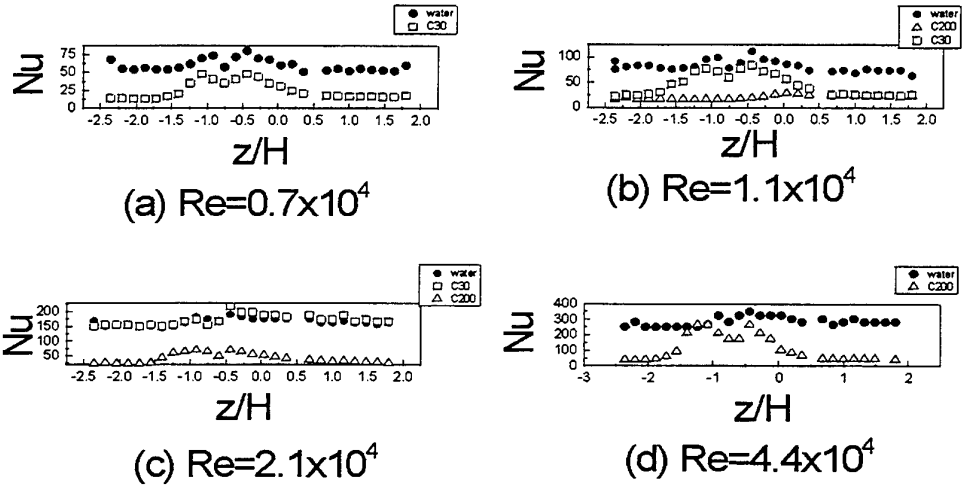

Fig. 5. Spanwise distributions of Nusselt number under different Re number conditions (T = 25 °C and x/H =2.5).

Fig. 5 shows the cross-sectional local Nusselt number distributions for three concentrations, C0, C30 and C200, under four different Reynolds number conditions, (a) ~ (d). The streamwise position was at x/H = 2.5, and the fluid temperature was fixed at constant, 25 °C. In Fig. 5(a) Re = 0.7 x 10^4, the results of the C30 case show 60% reduced wall heat transfer in the outer region and a remarkable increase up to 2/3 times the value of water, C0, in the vortex region, $-1.5 < z/H < 0.5$. No plots of the C200 case were drawn in the figure, since no remarkable enhanced region was observed under this Reynolds number condition. In higher Reynolds number case, (b) Re = 1.1 x 10^4, the C30 case shows that the Nusselt number distribution in the vortex area has an even steeper gradient and approaches the distribution of the C0 case. Beside this, the C0 case shows a moderate heat transfer and the C200 case almost retains its reduced heat transfer feature over the spanwise cross-section. In much higher Reynolds number case, (c) Re = 2.1 x 10^4, the patterns of Nusselt number distributions changed significantly. The surfactant solution of the C30 case acts like the water case, C0, over the whole cross-section. The Nusselt number distribution of the C200 case, in contrary, shows a relatively small peak corresponding to the vortex behaviors. In the highest Reynolds number case, (d) Re = 4.4 x 10^4, it can be seen that the Nusselt number in the C200 case was increased remarkably due to the increase of the main flow velocity. This feature observed here is similar to the C30 case under lower Reynolds number flow condition, and is caused by the shear stress which is locally enhanced by the generated vortex and exceeds the critical shear stress depending on

the solution concentration [6]. It is conjectured from the results of Fig. 5 that the internal flow alignment of the surfactant solution is broken through an increase of flow velocity, and then local shear stress and heat transfer coefficient are increased eventually over the whole spanswise locations.

To see the reason why the heat transfer enhancement area of C200 is significantly smaller than the one of the other two cases, the apparent length-scales of the vortex were compared among the three cases. Figure 6 shows cross-sectional velocity vector maps at x/H = 2.5 under the Reynolds number Re = 2.1 x 10^4 in three different surfactant solutions; (a) the pure water, C0, (b) C30 and (c) C200. The direction of the main flow comes out of the figure, viewing upstream against the flow.

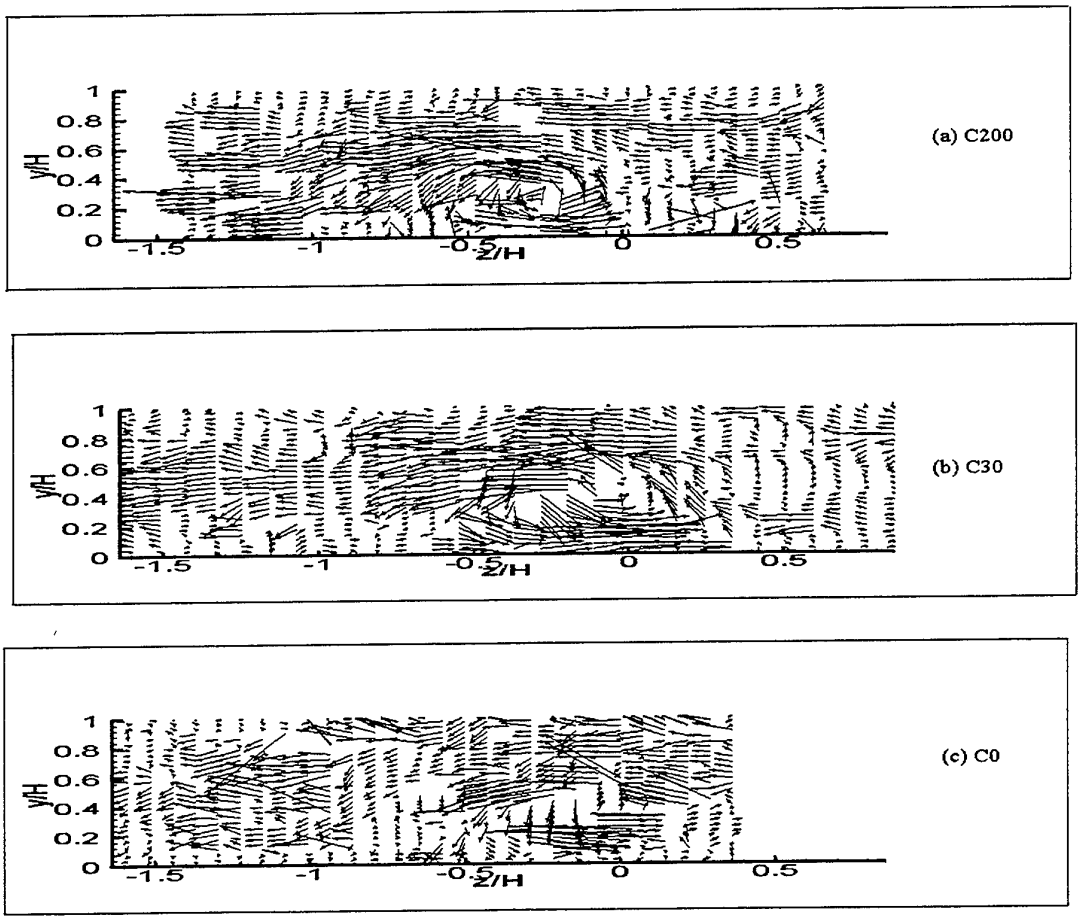

Fig. 6. Velocity vector distributions in cross-sections under different concentration conditions (Re = 11,040, T = 25 °C and x/H = 2.5)

It is obviously observed in each plot that a large-scale longitudinal vortex is generated downstream of the VGW, and that the scale and intensity of the vortex strongly depend on the surfactant concentration. The generated vortex in the case of C200 did not dissipate over the whole channel height, whereas the vortices in the C0 and C30 cases grew their scales and exchanged their momenta with the main flow. Thus, the C200 surfactant flow is concluded to still have the drag-reducing effect.

Higher momentum exchange of the non drag-reducing flows relative to the drag-reducing flow causes quick decay of the vortex and large peak of local Nusselt number shown in Fig. 4 downstream of x/H = 1.0 for both C0 and C30. The comparison between the results shown in Figs. 5 and 6 conspicuously reveals that the peak Nusselt numbers of C0 and C30 are located around z/H = -0.5, where the flow changed into non drag-reducing

flow instead of low spanwise sweeping velocity near the bottom wall. In the case of C200 solution, as mentioned above, the vortex remains far downstream and did not dissipate and thus the heat transfer performance was remarkably lower than the other cases, C0 and C30.

To examine the enhancement mechanism of the wall heat transfer in detail, a map of the cross-sectional velocity vector distribution is shown in Fig. 7, C30 under Re = 1.1 x 10^4. The orthogonal projection of the WVG onto the y-z plane is also shown in this figure. One of the highlighted locations could be around z/H = -0.6, in particular, since there it will be the condition where the drag-reducing effect exists in the main flow and the micelle structure seems to be locally broken through the longitudinal vortex. At this point, the recirculating flow of the vortex reattached to the bottom surface and the local heat transfer obtained could be the maximum as shown in Fig 4. The similarity between the high velocity gradient and high heat transfer rate indicates that the micelle alignment must be broken there and thus the heat transfer performance of water could be recovered. In addition, it can be observed that after the reattachment, the recirculating flow of the vortex breaks and separates towards the negative z direction.

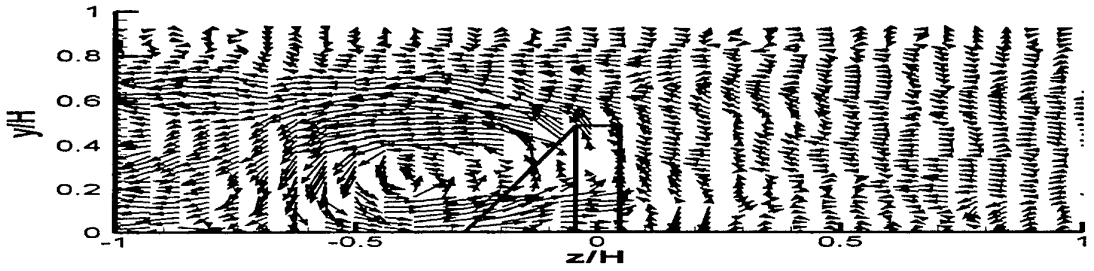

Fig. 7. Velocity vector distribution in cross-section (Re = 11,040, T = 25 °C, C30 and x/H = 5).

Figure 8 shows the spanwise Nusselt number distributions at several streamwise locations in six different temperatures from 25 °C to 48 °C under Re = 1.1 x 10^4. At any streamwise location, the local Nusselt number distribution throughout the whole spanwise region is drastically increased at temperatures higher than 40°C. This jump at a certain temperature and the stable peak of the heat transfer far downstream of the WVG below this temperature could correspond to a breakdown in the micelle alignment caused by the solution temperature similar to the break down by shear stress observed in Fig. 6. In other words, an increase in the main flow temperature shrinks the ordering forces of the micelle alignment, diminishes the critical shear stress and recovers the reducing in heat transfer performance of the drag-reducing flow over the whole cross section.

CONCLUSIONS

The wall heat transfer measurements have shown that the added surfactants reduce the wall heat transfer performance of water up to 70%. However, when a wing-type vortex generator was immersed in drag-reduced flow, the produced longitudinal vortex was locally able to break the orderly flow structure of surfactant solution and thus recover the heat transfer reduction up to the maximum value of water. This enhancement of the wall heat transfer coefficient mainly depends on the flow and temperature conditions of the solution whereas in water case the longitudinal vortex causes only a moderate increase of local Nusselt numbers. The surfactant flow of C30, in particular, shows that an increase in velocity or temperature of the main flow above a certain level causes a drastically change in the wall heat transfer performance towards similarity of pure water. It is also shown that the longitudinal vortex remains far downstream of the vortex generator due the dumped momentum exchange in drag reducing flow and thus enhances the heat transfer in the wake of the vortex generator up to x/H = 15. The growth of the vortex diameter with increasing down stream location was for the same reason detected to be dependent on the internal flow alignment of the surfactants in the flow field. Although it could be seen that C200 solution shows an higher internal structure stability as C30 and so the set in of heat transfer enhancement caused by the longitudinal vortex was shifted to wards larger Reynolds number which is equal to higher wall shear stresses. Generally, the vortex generator caused enhancement in wall heat transfer for drag-reducing flow was found to be larger than for water flow.

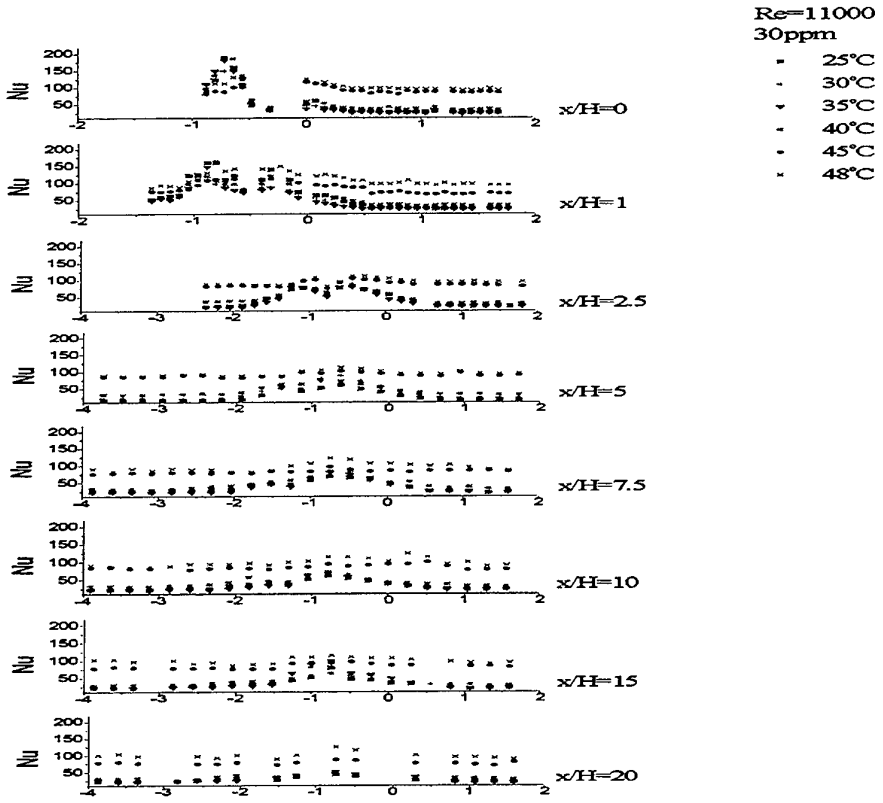

Fig. 8. Temperature dependence of Nusselt number distributions (Re = 11,040 and C30).

ACKNOWLEDGEMENTS

The authors are thankful to the "Deutscher Akademischer Austauschdienst (DAAD)" for its financial support in form of a scholarship to enable to perform the present study.

REFERENCES

1. Y. Kawaguchi, H. Daisaka, A. Yabe, K. Hishida and M. Maeda, "Turbulent Characteristics in Transition Region of Dilute Surfactant Drag Reducing Flows", Proceedings of the 11th Symposium on Turbulent Shear Flows, v. 1, pp. P1-49 - P1-54, Grenoble, (1997).
2. G. Wellinghoff, "Zum Einflu von Reibungsminderern auf den Druckverlust und den Warmeubergang in Fernwarmeleitungen", Forschungsbericht T86-058 Technologische Forschung und Entwicklung-Nichtnukleare Energietechnik, pp.30-31 (1986).
3. St. Tiggelbeck, N. K. Mitra and M. Fiebig , 1993:"Experimental investigations of heat transfer enhancement and flow losses in a channel with double rows of longitudinal vortex generators"Int. J. Heat and Mass Transfer, Vol 26, No.9, pp2327-2337, 1993
4. J. Eschenbacher, M. Joko, K. Nakabe and K. Suzuki, "Visualization of the Drag Reduced Flow Disturbed by a Vortex Generator", Proceedings of 36th National Heat Transfer Symposium of Japan, v. III, pp. 549-550, Kumamoto, (1999).
5. Y.I. Cho and J.P. Hartnett, "Non-Newtonian Fluids in Circular Pipe Flow", Advances in Heat Transfer, v. 15, pp. 59 (1982).

A. Gyr and H.W. Bewersdorff, "Drag Reduction of Turbulent Flows by Additives", pp.5-6, Kluwer Academic Publisher, Dodtrecht, Netherlands (1995).

HEAT TRANSFER AND FLUID FLOW FOR A THERMAL PLASMA JET IMPINGING NORMALLY ON A FLAT PLATE

Xi Chen, Peng Han, Heping Li and Xiaohu Ye
Department of Engineering Mechanics, Tsinghua University, Beijing 100084, China
Email: cx-dem@mail.tsinghua.edu.cn; Fax: (8610)-6278-5569

Keywords: thermal plasma, impinging jet, modeling, measurements

ABSTRACT. Modeling and experimental results are presented concerning the heat transfer and fluid flow for an argon d. c. arc plasma jet impinging normally upon a flat plate. Both laminar and turbulent flow regimes are involved in the study. Temperature- and concentration-dependent gas properties are used, and the mixing between the argon plasma jet and the ambient air is modeled by using the combined-diffusion-coefficient approach. For the case of turbulent flow, the $K-\varepsilon$ two-equation turbulence model is employed in the modeling. The modeling results show an appreciable difference in the mixing processes for the laminar and turbulent regimes. A transient method is employed to measure the local heat flux distribution along the surface of flat plate impinged by the argon plasma jet, whereas the pressure distribution along the plate surface and the electron temperatures near the plate surface are measured by using a stationary water-cooled probe. Different gas flowrates, arc currents and plate-standoff-distances are covered in the measurements. The predicted and measured heat flux and pressure distributions can be well approximated by the Gaussian distributions. The measured electron temperatures near the cold plate are shown to be much higher than the plate temperature, implying that the near-wall boundary is in a state of highly thermodynamic non-equilibrium.

1. INTRODUCTION

As a partially ionized, chemically reactive and high energy-density source, the thermal plasma has found extensive application in industries and laboratories. Practical examples include the thermal plasma spraying for producing thermal-protection or anti-wear coating, the preparation of diamond or high-tech ceramic films by using a thermal plasma CVD (Chemical Vapor Deposition) method, the preparation of ultrafine powders with sizes of submicrons or nanometers, the thermal plasma destruction of wastes, and so on. As a requirement raised in the development of thermal plasma science and technology, it is desirable to study in some detail the plasma flow and heat transfer for a thermal plasma jet impinging normally upon a flat plate. As well known, the adhesive strength, residual stresses and other characteristics of a coating, or the uniformity and morphology of a diamond film, are often dependent on the temperature or the history of the temperature variation of the workpiece or substrate. The control of substrate or workpiece temperature in those processes requires the knowledge of heat transfer and fluid flow. The plasma in the vicinity of a cold wall (workpiece or substrate) is often in a non- LTE (Local Thermodynamic Equilibrium) state. In addition, when the plate or workpiece is located in ambient air, the entrainment of the ambient air into the plasma jet will also affect the flow and heat transfer.

Although the fluid flow and heat transfer for a non-ionized gas jet impinging upon a flat plate have been widely studied, our knowledge about their counterparts under thermal plasma conditions is still incomplete due to the difficulty encountered in the experimental or modeling studies for the plasma case. Refs. [1-9] reported some experimental results obtained by using a steady or transient calorimetric probe. Modeling study has not been well conducted, especially for the case that a thermal plasma (e.g. argon plasma jet) impinges normally upon a flat plate located in an air surroundings.

This paper presents some modeling and experimental results obtained recently in our Lab concerning the heat transfer and fluid flow for an argon d. c. arc plasma jet impinging normally upon a flat plate located in ambient air. Both laminar and turbulent flow regimes are involved in the study. Temperature- and concentration-dependent gas properties are considered in the modeling. The mixing between the argon plasma jet and the ambient air is modeled by using the so-called combined-diffusion-coefficient approach [10-12]. For the case of turbulent flow, the standard $K-\varepsilon$ two-equation turbulence model is employed in the modeling. A transient method is employed to measure the local heat flux distribution along the plate surface, whereas the pressure

distribution along the plate surface and the electron temperatures near the water-cooled plate are measured by using a stationary water-cooled probe. Different gas flowrates, arc currents and plate-standoff-distances are covered in the modeling and in the measurements.

2. MODELING

Different from the case of an ordinary-temperature gas jet impinging upon a flat plate, the modeling for the present case is complicated due to the following new special features: (1) All the thermophysical properties of argon and air (and thus their mixture) are temperature-dependent, and (2) The gas mixture contains many different species, such as electrons, argon atoms, argon ions, oxygen molecules, oxygen atoms, oxygen ions, nitrogen molecules, nitrogen atoms, nitrogen ions, etc. In the present modeling, temperature-dependent properties of the gas mixture are calculated by using the property database of pure argon, 75% (mole fraction) argon - 25% air, 50% argon - 50% air, 25% argon - 75% air, and pure air at different temperatures. Linear interpolation is used to calculate the gas properties for any fixed temperature and mole ratio. The existence of so many different species in the gas mixture makes it very difficult to solve accurately the species conservation equations. In order to simplify the computation, the simplified approach called the combined-diffusion-coefficient method [10-12] is employed here. Namely, due to the smallness of electron mass, mass flux of electrons transported in the diffusion processes can be completely neglected in comparison with that of heavy particles. As a result, one can divide the gas species into two groups (A and B). The first group (group A) includes all the particles from argon (argon atoms, argon ions and electrons), while the second group (group B) includes all the particles from air (oxygen molecules, oxygen atoms, oxygen ions, nitrogen molecules, nitrogen atoms, nitrogen ions and electrons). After introducing the combined ordinary diffusion coefficient ($\overline{D}^{x}_{AB}$) and the combined thermal diffusion coefficient ($\overline{D}^{T}_{AB}$), only the diffusion of the A particles (or B particles) in the gas mixture needs to be considered in the computation of species concentration, and the mass diffusion flux of A particles ($\vec{J}_A$) can be expressed as [10,11]

$$\vec{J}_A = -\left(n^2/\rho\right)\overline{m}_A\overline{m}_B\overline{D}^{x}_{AB}\nabla\overline{X}_A - \overline{D}^{T}_{AB}\nabla \ln T \tag{1}$$

where n is the number density of all the gas particles, ρ the gas density, T the gas temperature, X_A the mole fraction of A particles in A+B mixture, and $\overline{m}_A$ and $\overline{m}_B$ are the mean mass of heavy particles in group A and in group B, respectively. Since the mass fraction of A particles in the gas mixture (f_A) can be calculated by

$$f_A = \overline{M}_A X_A /(X_A\overline{M}_A + X_B\overline{M}_B) = \overline{M}_A X_A / \overline{M} \tag{2}$$

Eq. (1) can be rewritten in the form expressed by the gradient of the mass fraction of A particles and the temperature gradient [12], and this form will also be used in this study. $\overline{M}$ and $\overline{M}_A$ (or $\overline{M}_B$) in Eq. (2) are the mean mass of all the gas particles (including electrons) and that of group A (or group B).

In this study, the following assumptions are employed: (1) Steady and axisymmetrical flow; (2) Optically thin plasma; (3) The gas is in the local LTE and LCE (Local Chemical Equilibrium) state. The governing equations used in the present modeling for the laminar flow can thus be written as follows:

Continuity equation

$$\frac{\partial(\rho u)}{\partial x} + \frac{1}{r}\frac{\partial(r\rho v)}{\partial r} = 0 \tag{3}$$

Momentum equations (axial, radial and tangential)

$$\rho u\frac{\partial u}{\partial x} + \rho v\frac{\partial u}{\partial r} = -\frac{\partial P}{\partial x} + 2\frac{\partial}{\partial x}\left(\mu\frac{\partial u}{\partial x}\right) + \frac{1}{r}\frac{\partial}{\partial r}\left[r\mu\left(\frac{\partial u}{\partial r} + \frac{\partial v}{\partial x}\right)\right] \tag{4}$$

$$\rho u\frac{\partial v}{\partial x}+\rho v\frac{\partial v}{\partial r}=-\frac{\partial P}{\partial r}+\frac{\partial}{\partial x}\left[\mu\left(\frac{\partial v}{\partial x}+\frac{\partial u}{\partial r}\right)\right]+\frac{2}{r}\frac{\partial}{\partial r}\left[r\mu\left(\frac{\partial v}{\partial r}\right)\right]-\mu\frac{2v}{r^2}+\rho\frac{w^2}{r} \tag{5}$$

$$\rho u\frac{\partial(wr)}{\partial x}+\rho v\frac{\partial(rw)}{\partial r}=\frac{\partial}{\partial x}\left[\mu\frac{\partial(rw)}{\partial x}\right]+\frac{1}{r}\frac{\partial}{\partial r}\left[r\mu\frac{\partial(rw)}{\partial r}\right]-\frac{2}{r}\frac{\partial(\mu rw)}{\partial r} \tag{6}$$

Energy equation

$$\rho C_P u\frac{\partial T}{\partial x}+\rho C_P v\frac{\partial T}{\partial r}=\frac{\partial}{\partial x}\left[\kappa\frac{\partial T}{\partial x}\right]+\frac{1}{r}\frac{\partial}{\partial r}\left[r\kappa\frac{\partial T}{\partial r}\right]-U_r-\frac{\partial}{\partial x}[(h_A-h_B)J_x]$$

$$-\frac{1}{r}\frac{\partial}{\partial r}[r(h_A-h_B)J_r]-\frac{\partial}{\partial x}\left[\frac{\kappa}{C_P}(h_A-h_B)\frac{\partial f_A}{\partial x}\right]-\frac{1}{r}\frac{\partial}{\partial r}\left[r\frac{\kappa}{C_P}(h_A-h_B)\frac{\partial f_A}{\partial r}\right] \tag{7}$$

Species conservation equation

$$\rho u\frac{\partial f_A}{\partial x}+\rho v\frac{\partial f_A}{\partial r}=\frac{\partial}{\partial x}\left[\Gamma_f\frac{\partial f_A}{\partial x}\right]+\frac{1}{r}\frac{\partial}{\partial r}\left[r\Gamma_f\frac{\partial f_A}{\partial r}\right]+S_f \tag{8}$$

in which

$$S_f=\frac{\partial}{\partial x}\left(\Gamma_f\frac{f_A}{\overline{\overline{M}}}\frac{\partial\overline{M}}{\partial x}\right)-\frac{\partial}{\partial x}\left(\Gamma_f\frac{f_A}{\overline{\overline{M}}_A}\frac{\partial\overline{M}_A}{\partial x}\right)+\frac{1}{r}\frac{\partial}{\partial r}\left(r\Gamma_f\frac{f_A}{\overline{\overline{M}}}\frac{\partial\overline{M}}{\partial r}\right)$$

$$-\frac{1}{r}\frac{\partial}{\partial r}\left(r\Gamma_f\frac{f_A}{\overline{\overline{M}}_A}\frac{\partial\overline{M}_A}{\partial r}\right)+\frac{\partial}{\partial x}\left(\overline{D}_{AB}^T\frac{\partial\ln T}{\partial x}\right)+\frac{1}{r}\frac{\partial}{\partial r}\left(r\overline{D}_{AB}^T\frac{\partial\ln T}{\partial r}\right) \tag{9}$$

In the foregoing equations, u, v and w denote the axial (x-), radial (r-) and tangent ($\theta-$) components of gas velocity, P is the gas pressure, whereas ρ, μ, κ, C_p and h are the temperature- and concentration-dependent gas density, viscosity, thermal conductivity, specific heat at constant pressure and enthalpy, respectively. U_r is the radiation power per unit volume of the plasma. Γ_f in Eq. (8) is the effective coefficient defined as [12]

$$\Gamma_f=\frac{\rho}{\overline{\overline{MM}}_A}\overline{m}_A\overline{m}_B\overline{D}_{AB}^x \tag{10}$$

whereas J_x and J_r are the axial and radial components of the diffusion flux vector ($\vec{J}_A$) of argon in the gas mixture.

For the case of turbulent flow, Eqs. (3)—(8) are still be employed, but ρ, u, v, w, T and f_A are all their time-averaged values, and the transport coefficients μ, κ and Γ_f are substituted by those representing laminar plus turbulent values. In addition, the following equations concerning the turbulent kinetic energy (K) and its dissipation rate (ε) are used.

$$\rho u\frac{\partial K}{\partial x}+\rho v\frac{\partial K}{\partial r}=\frac{\partial}{\partial x}\left(\Gamma_K\frac{\partial K}{\partial x}\right)+\frac{1}{r}\frac{\partial}{\partial r}\left[r\Gamma_K\left(\frac{\partial K}{\partial r}\right)\right]+G-\rho\varepsilon \tag{9}$$

$$\rho u\frac{\partial \varepsilon}{\partial x}+\rho v\frac{\partial \varepsilon}{\partial r}=\frac{\partial}{\partial x}\left(\Gamma_{\varepsilon}\frac{\partial \varepsilon}{\partial x}\right)+\frac{1}{r}\frac{\partial}{\partial r}\left[r\Gamma_{\varepsilon}\left(\frac{\partial \varepsilon}{\partial r}\right)\right]+\frac{\varepsilon}{K}(c_1 G-\rho\varepsilon c_2) \tag{10}$$

where the generation term is

$$G=\mu_t\left[2\left(\frac{\partial v}{\partial r}\right)^2+2\left(\frac{\partial u}{\partial x}\right)^2+2\left(\frac{v}{r}\right)^2+\left(\frac{\partial w}{\partial x}\right)^2+\left(\frac{\partial w}{\partial r}-\frac{w}{r}\right)^2+\left(\frac{\partial u}{\partial r}+\frac{\partial v}{\partial x}\right)^2\right] \tag{11}$$

As in the standard two-equation turbulence model used for ordinary-temperature flows, the turbulent viscosity (μ_t) is calculated by $\mu_t = 0.07\rho K^2/\varepsilon$, $C_1 = 1.44$, $C_2 = 1.92$, and the turbulent Prandtl numbers are taken to be 0.9, 1.0 and 1.3, respectively, for energy, turbulent kinetic-energy and dissipation-rate transport. Gas density fluctuation is ignored in the present modeling, since a recent study based on the 3-equation turbulence model [13,14] shows that including the density fluctuation does not affect appreciably the computed temperature and flow fields.

The computational domain used in this study is shown in Fig. 1. The boundary conditions for the case of laminar flow are as follows: At torch exit (A—B), $v = 0$, $f_A = 1$, u and T profiles are given as the power-law forms, and $w = 0.1u$ (or using the computed profiles from the d. c. arc torch modeling); axial symmetrical conditions are used along the axis (*A—F*); non-slip velocity boundary conditions, fixed temperatures and zero argon diffusion fluxes at the solid walls (*B—C* and *E—F*); zero temperatures and air concentration gradient are used at the free boundaries (*C—D* and *D—E*). On the other hand, for the case of turbulent flow, the boundary conditions along the solid wall are substituted by those given from the wall function methods.

SIMPLEC algorithm and 62 x 40 grid points are employed in the computation. Typical computed results are shown in Figs. 2—4 for laminar flow regime (argon flowrate 0.53 STP m3/hr, arc current 221 A), while Figs. 5 and 6 plot the computed isotherms and argon mass fraction contours for turbulent flow regime (argon flowrate 2.1 m3/hr, arc current 221A). Comparison of the results in Figs. 2 and 4 to those in Figs. 5 and 6 reveals that since the transport coefficients for the turbulent regime are significantly greater than their counterparts for the laminar case, the gas temperature and argon mass fraction along the jet axis decrease more rapidly for the turbulent case than for the laminar case. Near the flat plate, which is located at the distance 50 mm from the nozzle exit (orifice radius 4 mm) of the argon plasma jet, gas temperature is about 7000 K and argon mass fraction is as great as 0.8 (or 80 %) for the laminar regime. On the other hand, corresponding temperature and argon mass fraction are approximately 3200 K and 0.15 (15 %). The difference between the modeling results for laminar and turbulent regimes is expectable because turbulent diffusion will significantly enhance the entrainment of the cold ambient air into the argon plasma jet.

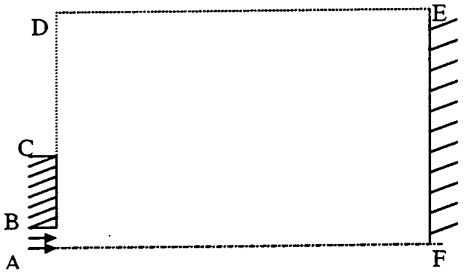

Fig. 1 Computational domain

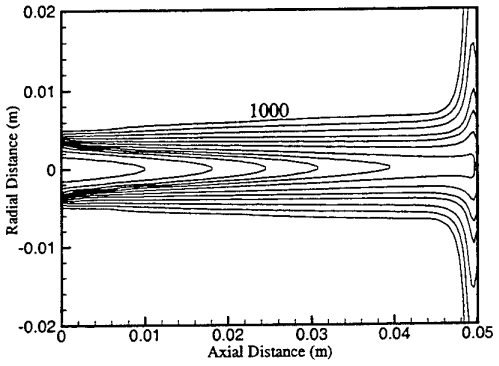

Fig. 2 Computed isotherms (outer line: 1000K, temperature space: 1000K; laminar flow

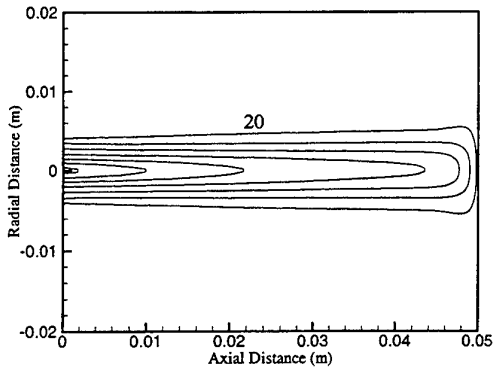

Fig. 3 Computed axial velocity contours (outer line 20 m/s, velocity space 40m/s; aminar flow)

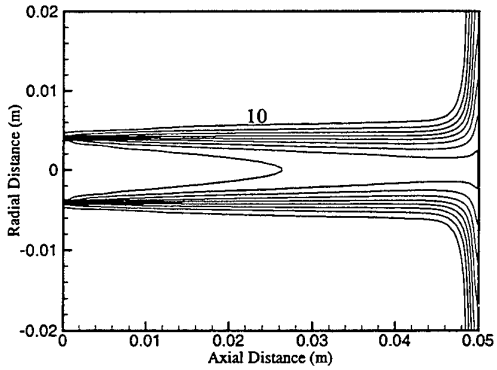

Fig. 4 Computed f_A contours (outer line 10 % argon, mass concentration space 10 %; laminar flow)

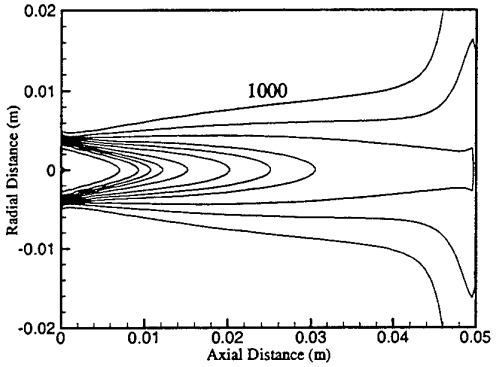

Fig. 5 Computed isotherms (outer line: 1000K, temperature space: 1000K; turbulent flow regime)

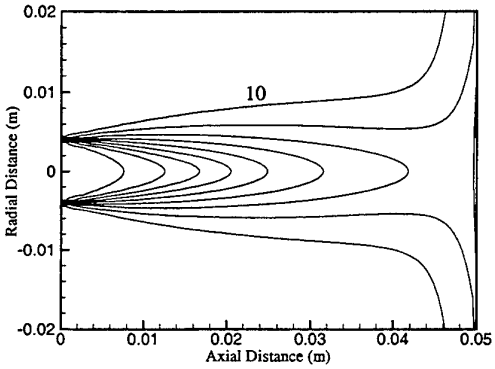

Fig. 6 Computed f_A contours (outer line 10 % argon, mass concentration space 10 %; turbulent flow regime)

3. EXPERIMENTS

The transient heat-flux probe shown in Fig. 7 is employed to measure the local heat flux distribution along the surface of the flat plate impinged by the argon plasma jet. A small copper cylinder (0.5 *mm* radius and 1 *mm* length) embedded at the center of a large flat plate and carrying with a pair of thermocouple (0.2 *mm* diameter) at the rear surface of the cylinder is used as the sensitive element of the plate-type heat flux probe. The frontal surface of the cylindrical sensor is flushed with that of the plate and the sensor is insulated from the plate by ZrO_2 powders. By sweeping the copper plate across the plasma jet with a speed of about 0.1 *m/s*, the sensor is rapidly heated and the temperature response signals of the thermocouple can be obtained. The output information of the thermocouple is put into an amplifier and then transferred to a personal computer, where the A/D conversion and data processing are performed. Figure 8 shows a typical recorded temperature-rising curve. One can clearly observe that the sensor temperature increases rapidly when the sensor is immersed into the plasma jet. In order to reduce the superimposed noise signal in the actual response curve (curve A in Fig. 8), fast Fourier transformation (FFT) is performed and thus a smoothed curve (curve B in Fig. 8) is obtained. Differentiating the temperature rising curve B with respect to time and using the heat flux expression $q = \delta\rho_s C_{Ps} dT/d\tau$ (where δ, ρ_s and C_{Ps} are sensor thickness, density and specific heat), we can get the local heat flux distribution along the plate surface. Here we have assumed the sensor temperature is everywhere uniform due to the smallness of the Biot number involved in this experiment. An error analysis shows that the probe can well follow the changing of the input heat flux, and the conduction heat loss through the ZrO_2 layer or

along the thermocouple wires and the radiative loss from the front face of the sensor are negligibly small.

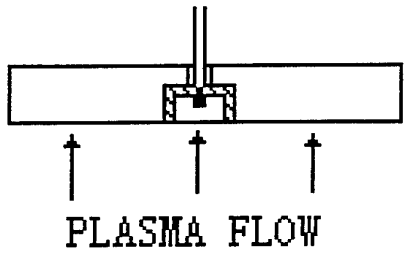

Fig. 7 The configuration of the heat flux probe

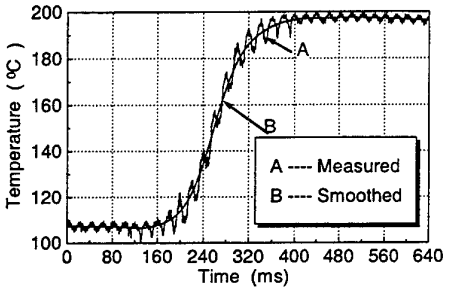

Fig 8. A typical recorded temperature-rise curve and its smoothed counterpart

A stationary water-cooled plate-type probe with a central hole is used for measuring the impact pressure, and the pressure distribution along the plate surface is obtained by moving the plate probe laterally. On the other hand, the electron temperature is measured by using the stationary water-cooled probe similar to that used for the pressure measurements but with a tungsten wire in the central hole of the plate center (Fig. 9) and run as an electrostatic probe or the Langmuir probe [15-17]. The tip of the tungsten-wire is flushed with the frontal surface of the plate. The electron temperature (T_e) near the cold plate surface is deduced from the measured V-I characteristics of the electrostatic probe in the electron-retarded region [15] by using the relation

$$T_e = \frac{k}{e} \times \frac{1}{\partial \ln(I + |I_{is}|) / \partial V_p} \tag{12}$$

where k and e are the Boltzmann constant and the elementary charge, I and $|I_{is}|$ are the probe current and the absolute value of the ion saturation current, whereas V_p is the voltage applied between the tungsten wire and the anode of the arc plasma torch.

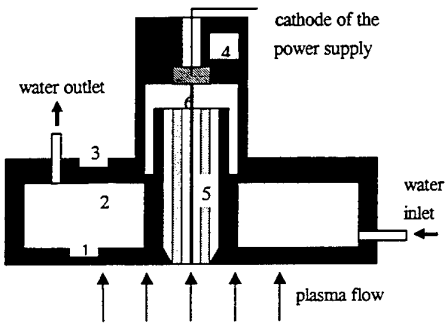

Fig. 9 Schematic of the water-cooled plate-electrostatic probe assembly.
1--water-cooled flat plate; 2--rubber washer; 3--brass cover board; 4--polythene sleeve; 5--ceramic sleeve; 6--probe (tungsten wire)

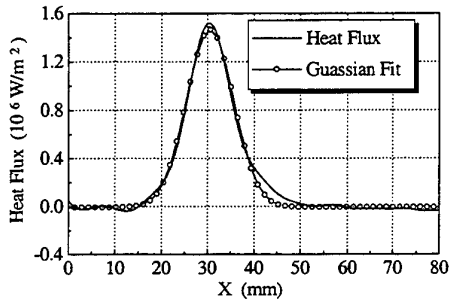

Fig. 10 A typical result of measured heat flux density distribution (continuous line) in comparison with a fitted Gaussian curve

Different gas flowrates (involving both laminar and turbulent regimes), arc currents and plate-standoff-distances are covered in the measurements. The measured data of the local heat flux and impact pressures show good reproducibility and fairly good axisymmetry except for a few cases where arc root may change its location abruptly. The measured heat flux distribution can be well approximated by the Gaussian distribution as follows:

$$q(r) = q_c \exp\left[-(r/R_g)^2\right] \tag{13}$$

Fig. 10 shows a typical result. r in Eq. (13) is the radial distance from the jet axis, while q_c and R_g are the central (maximum) heat flux and the Gaussian radius. Fig. 11 shows that the maximum heat-flux density decreases, while the Gaussian radius increases with the increase of the dimensionless standoff distance $Z^* = L/d_o$ (L is the distance between the flat plate and the torch exit, and d_o is the orifice diameter of torch exit). The central heat flux increases with increasing arc current (Fig. 12) or argon flowrate (not shown here). It is also found that when the probe has passed through the plasma jet, the measured heat fluxes are even less than zero, corresponding to the total heat loss from the hot sensor to its surroundings. From Fig. 10 we can estimate this heat loss and obtain $|q_{loss}|_{max}/q_c < 2.5\%$. This fact demonstrates that the heat loss from the sensor is indeed negligibly small, in good agreement with our error analysis.

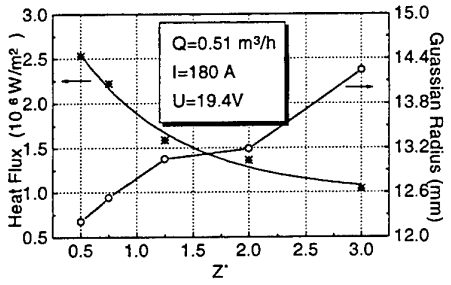

Fig. 11 Variation of the central heat flux and the Gaussian radius with the dimensionless standoff distance $Z^* = L/d_o$

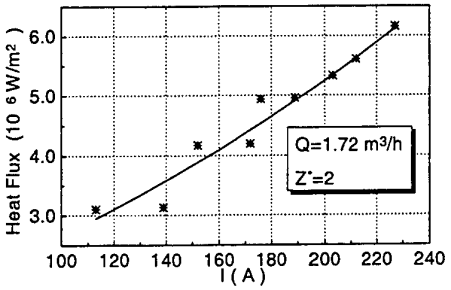

Fig. 12 Variation of the measured central heat flux with the arc current (turbulent flow regime)

The pressure distribution on the plate surface also assumes a Gauss-type distribution, showing its maximum value at the axis of the plasma jet and a rapid decrease in the radial direction, as shown in Fig. 13. Fig. 14 demonstrates that a linear relationship between the logarithm of the probe current and the probe voltage does indeed exist, and thus the electron temperature can be deduced by using Eq. (12). The electron temperatures measured in the near-wall region of the plate are shown to be around 10000 K, and thus to be always much higher than the plate temperature (or the heavy-particle temperature near the cold plate). Namely, the near-wall boundary layer is shown to be in the state of highly thermodynamic non-equilibrium. Due to the problem that the tungsten wire is oxidized in the air-containing gas, the reproducibility of the electron-temperature measurements is not good. Such a problem of the tungsten-probe contamination in an oxidizing atmosphere was also encountered by the authors of Ref. [16], although some others did not mention it [17].

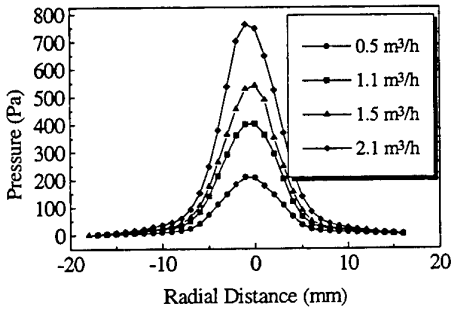

Fig. 13 Radial distributions of the impact pressure along the flat plate (Z^*=2; I=160 A)

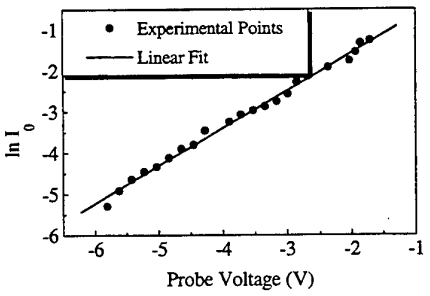

Fig. 14 Logarithm of the probe current *versus* the probe voltage

4. DISCUSSION

In the experiments it is found that the heat flux or the pressure distribution on the plate surface can be represented well by a Gauss-type distribution, i.e. the heat flux or the pressure distribution can be described with two parameters, i.e., its maximum value at the jet axis and corresponding Gaussian radius. This finding is also supported by the modeling work. Fig. 15 and Fig. 16 show a few typical modeling results concerning the local heat flux distributions and the pressure distributions along the plate surface for 4 different cases with arc currents and voltages being 229 A, 21.4 V (curve 1), 189 A, 19.0 V (curve 2), 142 A, 19.3 V (curve 3) and 107 A, 20.1 V (curve 4). The argon flowrate is fixed to be 1.72 STP m^3/hr, whereas the dimensionless standoff-distance Z^*=4. As seen, the computed heat flux and pressure distributions in Figs. 15 and 16 show good similarity with those obtained in the experiments.

The present modeling can predict reasonable temperature, concentration and flow fields. In addition, it can also predict the correct orders of magnitude of the surface heat fluxes and the surface pressures. However, at present, quantitative agreement between the modeling and experimental results cannot be achieved. It is believed that this situation is due to the following two reasons. The first is that the upstream boundary conditions (especially those at A-B in Fig. 1) cannot be given accurately. In addition to the power-law profiles, we also tried to use the predicted velocity and temperature profiles at the torch exit obtained from the modeling for an axi-symmetrical

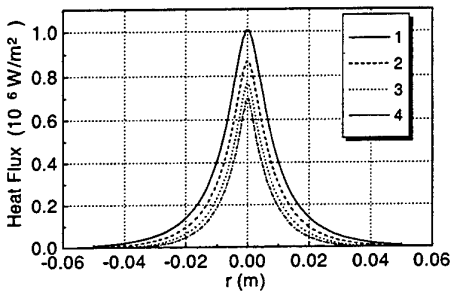

Fig. 15 Computed heat flux distributions along the plate surface for 4 different arc currents

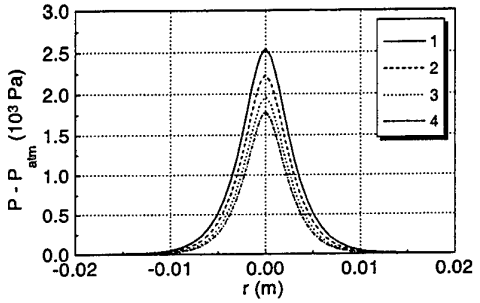

Fig. 16 Computed pressure distributions along the plate surface for 4 different currents

d. c. arc plasma torch as the inlet conditions, but the profiles are also not too accurate due to the existence of the three-dimensional effects. The second is that in the present modeling work, LTE assumption has been employed. However, as the experiment indicated, the boundary layer near the flat plate is in a highly non-equilibrium state. One should try to use a two-temperature plasma model to replace the present LTE model. Obviously, further more research efforts are required.

ACKNOWLEDGMENT

This work was supported by the National Natural Science Foundation of China through grants No. 59676011 and No. 59836220. The authors would like to thank Dr. A. B. Murphy for his providing the property data of the argon-air mixture.

REFERENCES

1. J. M. Badie, B. Granier and B. Bonduelle, J. De Physique, 51, pp. 273-279 (1990).
2. P. Pavlovic, P. Stefanovic and V. Vujovic, *Proceedings of the International Symposium on Heat and Mass Transfer under Plasma Conditions*, pp. 315-322, Cesme, Turkey (1994).
3. G. Chambon, P. Lucchese and P. Fauchais, *Proceedings of the International Symposium on Heat & Mass Transfer Under Plasma Conditions*, pp. 323-333, Cesme, Turkey (1994).
4. T. Kishigami, J. V. Heberlein and E. Pfender, *Proceedings of the 10th International Symposium on Plasma Chemistry*, v. 1, Paper No. 1.3-11, Bochun, Germany (1991).

5. K. E. Starner, ISA Trans., 7, pp. 181-186 (1968).
6. D. R. Burnett, Transactions of the ASME, J. Heat Transfer, 83, pp. 505-506 (1961).
7. Flamant G. , Philippot E. , Granier B., Peroy J. Y. and Vilcocq B., *Proceedings of the International Symposium on Heat and Mass Transfer under Plasma Conditions*, pp. 335-342, Cesme, Turkey (1994).
8. J. K. Kilham and M. R. I. Purvis, Comb. Sci. & Tech., 18, pp. 81-90 (1978).
9. G. Venuti and P. Valentin, High Temp. High Pressure, 11, pp. 301-310 (1979).
10. A.B. Murphy, Plasma Chemistry and Plasma Processing, v.15, pp. 279-307 (1995).
11. A.B. Murphy, Journal of Physics D: Applied Physics, v. 29, pp. 1922-1932 (1996).
12. Xi Chen, M. Sugasawa and N. Kikukawa, Journal of Physics D: Applied Physics, v. 31, pp. 1187-1196 (1998).
13. Xi Chen, A. Merkhouf and M. I. Boulos, *Proceedings of the 3rd Asia-Pacific Conference on Plasma Science and Technology*, v. 1, pp. 71-76, ed. by A. Kanzawa, Tokyo, Japan (1996).
14. Rubin Ye, P. Proulx and M. I. Boulos, Int. J. Heat Mass Transfer, v. 42, pp. 1585-1595 (1999).
15. E. Leveroni and E. Pfender, Rev. Sci. Instrum. v. 60, pp. 3744-3749 (1989).
16. H. A. Habiger and M. Auweter-Kurtz, Journal of Thermophysics and Heat Transfer, 12, pp. 198-205 (1998).
17. E. P. Szuszczewicz and J. C. Holmes, J. Appl. Phys., v. 46, pp. 5134-5139 (1975).
18. P Han, L Yu and X Chen, *Proceedings of the 13th International Symposium on Plasma Chemistry*, v. 1, pp. 338-343, ed. by C. K. Wu, Peking University Press, Beijing, China (1997).

STUDY ON CHARACTERISTICS OF AIR DUCT OF SMALL-SCALE REFRIGERATION INSTALLATION WITH AIR FORCED CONVECTION COOLING

Wei Hu, Hemin Shao
Researching & Development Center
Shanghai Delphi Automotive Air-Conditioning Systems, Co., Ltd., Shanghai, 201204, China
Email: saac@public1.sat.net.cn; Fax: (86 21)-5891-2279

Xiongcai Que
Institute of Refrigeration and Cryogenics Engineering,
Shanghai Jiao Tong University, Shanghai, 200030, China

Keywords: indirect cooling, refrigeration installation, air duct, characteristics, numerical method

ABSTRACT. This paper is concerned with characteristics of air duct of small-scale refrigeration installation with air forced convection cooling. The subject of this thesis is a domestic indirect cooling electrical freezer-refrigerator. A model and corresponding computer code of three-dimensional air flow in it are developed with Finite Volume Method and SIMPLEST algorithm in original variable form at general curvilinear coordinate. Distribution characteristics of the flow field and pressure loss are analyzed. Experiments are performed and have confirmed the numerical results. A model of the fan for performance prediction is proposed. At the same time, the authors have carried out the experiment of the factual product, the result of test has shown the validation of the model. As we know, the fan is always operating with the air duct. So analyses are made on the coupled relationship between the fan and the air duct. On the basis of them, the authors have been studied the changing parameters of the operating point. The optimal design of the air duct is also discussed. At last, the authors propose a practicable method of electing and designing the fan.

1. INTRODUCTION

The refrigeration installation with air forced convection cooling (i.e. Indirect Cooling Refrigeration Installation, ICRI) has been widely used in many fields of national economy that are closely related to people's life. There is a difference between ICRI and DCRI (Direct Cooling Refrigeration Installation), i.e. the former has the Air Cycling Cooling System (ACCS) while the latter has not. The ACCS, generally also including the evaporator and the electrical fan, effects the performance of refrigeration appliance greatly for its function of transporting the cooled air and distributing the cooling capacity. Recently, modern design methods based on system dynamic simulation have been developed rapidly, but most of researches focus on the four main components of the refrigeration system. The design of the ACCS is still on the basis of experiences, which has been a barrier of design-computerization. Therefore, it is an urgent task to effectively design the ACCS to meet the needs for high performances of the whole equipment and to match the refrigeration system well. With respect to the present conditions and questions in the field of the ACCS, the paper is focused on the characteristics of it.

Due to the vast number of the ICRI types available, it has not been possible to examine each of them. Instead, this paper concentrates on one common group of the ICRI, i.e. the domestic indirect cooling electrical freezer-refrigerator, whose simple geometrical structure is shown in Fig.1. The up-box is refrigerator, while the down-box is freezer. The evaporator is horizontally placed between the refrigerator and the freezer in vertical direction. The blower transports the cooled air from the evaporator to the refrigerator and the freezer. The authors study the flow resistance of the air duct of the ICRI and the flow field in it. Codes for the numerical simulation of air flow are developed with Finite Volume Method and SIMPLEST algorithm in original variable form at general curvilinear coordinate. Using CFD as a design tool, the designers can obtain a visual presentation of what is happening inside the components of interest. CFD can also predict the performance of the air duct during the design stage (i.e. prior to its manufacture) to assist the optimal designs [1-3].

The electrical fan, as the power source of the ACCS, plays a critical role on the performance of the whole equipment and contributes significantly to the overall power consumption. Though the power consumption of the

fan itself is low, the performance of the appliance will decrease sharply if the flow rate and (or) total pressure supplied by it do not satisfy the needs of the system. A model for performance prediction of the fan has been developed by the authors. The calculation result of the factual product has shown the validation of the model.

As we know, the ACCS is an organic system, the fan always operates with the air duct. The coupled relationship between the fan and the air duct is significant to the whole system. So analyses are made on it. On the basis of them, the authors have been studied and analyzed the ACCS. At the same time, the authors propose a new method of electing and (or) designing the fan based on the former results.

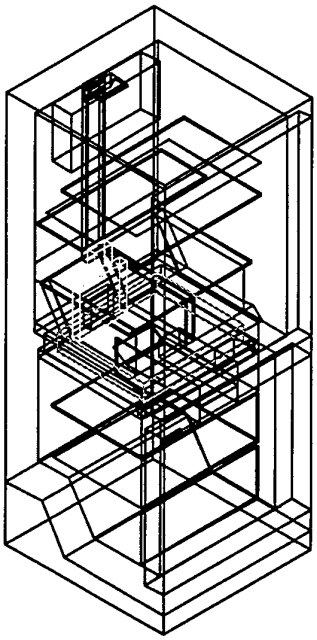

Fig. 1. The simple geometrical structure of refrigerator-freezer

2. STUDY OF AIR DUCT

Mathematical Formulation And Numerical Procedure

The mathematical formulation of the air duct is based on the following assumptions:

(1) the flow is steady
(2) as the flow is predominantly of low Mach number, the fluid can be treated as incompressible
(3) no heat transfer is considered, i.e. the flow is isothermal
(4) for the existence of the blower, the buoyancy effects are not considered
(5) the temperature and humidity in the air are determined by the experiment.

Governing equations and solution algorithm. Fig. 1 describes the freezer-refrigerator modeling in this study. Most parts of the air duct involve curved or angled surfaces and using a conventional Cartesian grid would mean that the surfaces were approximated by a series of short zigzagging straight lines. As the pressure loss in the ducts is dependent on the surface roughness, such an approximation could produce large prediction errors. So a three-dimensional non-orthogonal curvilinear coordinate (i.e. Body-fitted) grid system is used to ensure that the curved walls of the ducts are accurately modeled.

The equations governing the motion of air inside the refrigerator-freezer are the time-averaged Navier-Stokes equations and the mass continuity equation, which can be found in many textbooks and articles [4,5]. Because of the limited space, the equations are presented here. A number of turbulence models have been developed over the years by various investigators. The two-equation k-ε model, which is of moderate complexity, has been

extensively tested and proved to be adequate over a wide range of engineering applications. As a result, the two-equation k-ε model is adopted in the present work. In the region of low Reynolds number close to the walls, the wall function is used instead [5].

Boundary conditions. The flow simulation results are evidently depending on the assumption of appropriate boundary conditions. The boundary conditions for the problem can be classified into three main categories.

1. *Inlet boundary.* At an inlet, all variables, except pressure, are prescribed. As regards the pressure boundary, it can be either be prescribed if known or expressed in terms of a mass flow rate. At present, the latter is chosen.
2. *Outlet boundary.* At an outlet, the pressure boundary is applied. The velocities are determined in such a way that the mass conservation should be satisfied.
3. *Wall boundary.* In a turbulent flow, the steepest velocity gradients occur in the region closest to the wall. This renders the imposition of the usual non-slip condition impractical unless a very fine grid distribution is used near the wall. Moreover, it is physically meaningless to integrate the k-ε model equations up to the wall because it is not valid in the vicinity of the wall. As the wall approaches, the flow regime changes to laminar flow. One solution is the use of the wall function method which is already mentioned above. The authors have just used it.

Evaporator model. The modeling of the evaporator shown in Fig. 2 runs into special problems because of the complex structure of finned-tube heat exchangers and available capacities of the computer. Moreover, when the outside air temperature of the evaporator is below dew point and zero simultaneously, frost will deposit on the surface of the finned-tube. As a detailed modeling of the evaporator is not possible, a simplified description has to be found. At present, we propose the following two procedures:

1. Due to the fact that the distribution of flow in the evaporator is almost uniform, it is reasonable to abstract a representative element as the object of studying, as shown in Fig. 2; and
2. Take account of the pressure drop in the flow direction for the existence of the frost, treat frost thickness uniform on all surfaces.

On the basis of the two procedures above, we can obtain the real flow information, which can aid us to design the evaporator better.

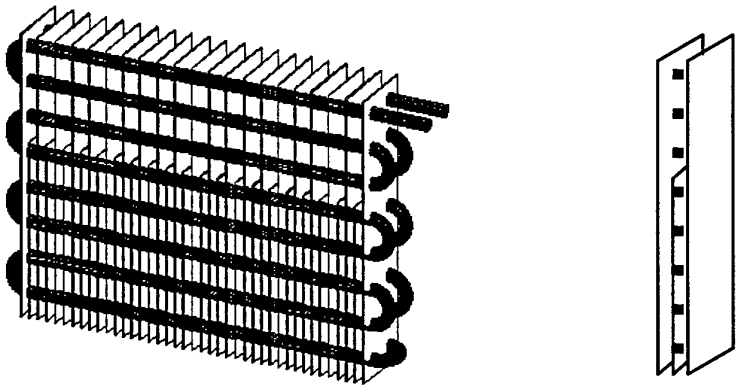

Fig. 2. The evaporator and its representative element

Numerical calculation. Based on the analyses above, the computer codes for the simulation of air flow in the refrigerator-freezer are developed by the authors. Some results are shown in Fig. 3, Fig. 4 and Fig. 5. The least square regression method is used to fit the data points, which is also used below. Though the frost thickness is related to time, the air flow is treated as steady under every frost thickness. The discussion of results will be offered below.

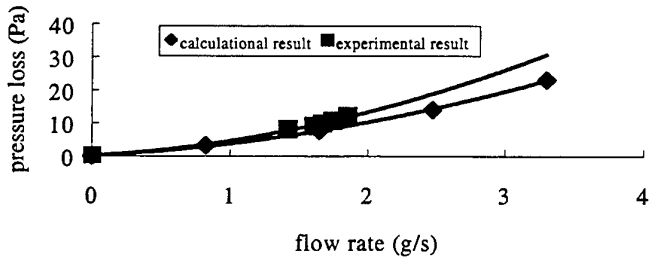

Fig. 3. The calculation and experiment results of the refrigerator

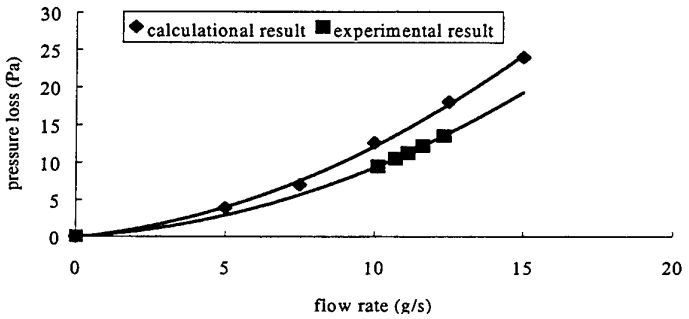

Fig. 4. The calculation and experiment results of the freezer

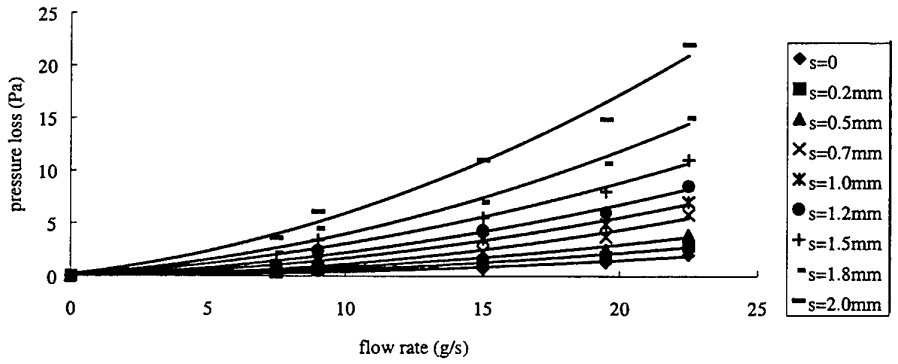

Fig. 5. The calculation results of evaporator at different frost thickness (s refers to frost thickness)

Experimental Investigation

The test bench for the flow rate and pressure drop characteristics of the air duct has been designed and set up [6]. The air flow rates and the pressure drop of the freezer and the refrigerator are of major concerns. In order to obtain the curves of pressure drops *vers.* flow rate, the authors designed an inverter to change speeds of the fan, i.e. the flow rates. The temperature and the moisture of air in the ducts are measured using a HMP35 type moisture

transducer with a platinum-resistance temperature transducer of the VAISALA Company, whose precision for moisture is ±2%. The pressure drops are measured using differential pressure transducers of the SETRA Corporation with the uncertainty of ±0.11%. The pitot tubes in conjunction with the SETRA pressure transducers are used to measure the air velocities. The flow rate is obtained by multiplying the air velocity by the corresponding cross-sectional area. All data signals are collected and converted by the HP3054A data acquisition system [6,7,8]. The test data of the temperature and the humidity if the air are shown in Fig. 6.

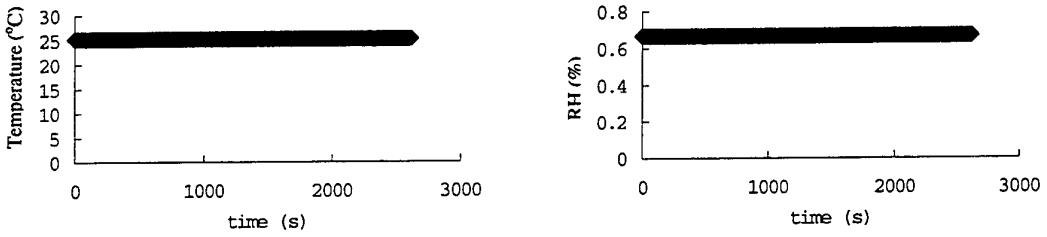

Fig. 6. The test temperature and humidity of air

On account of frosting on outside surface of the evaporator, the authors design an experimental rig to verify the exactitude of model of finned-tube evaporator dynamic frosting and heat transfer [7,8]. The rig can record the dynamic data of temperature, humidity and pressure drop. Experimental study has been carried out. Parts of experimental results are shown in Fig. 7, which indicates the calculation and experiment results of pressure drop of the evaporator.

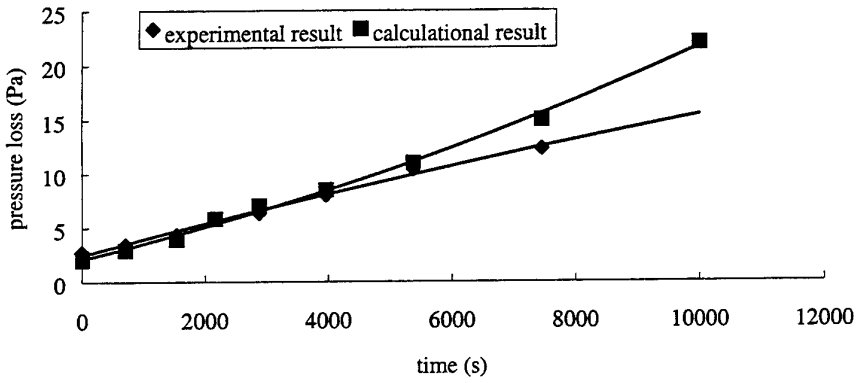

Fig. 7. The calculation and experiment results of pressure loss of the evaporator

3. ANALYSES OF ACCS

Computation Of Fan

As mentioned above, the fan is the power source of the ACCS, and has an important effect on the performance of the whole appliance. The factual product used here is a centrifugal fan. The authors propose a model for performance prediction based on the former researches [9]. Using this model, performance parameters including efficiency can be calculated from the geometrical dimensions of the fan and some experiential formulae. At the same time, the authors have carried out an experiment on a standard test rig [7]. Some results of computation and experiment are shown in Fig. 8 and Fig. 9.

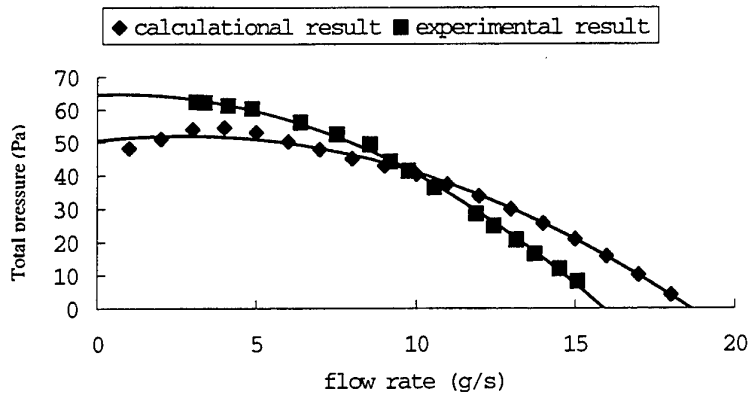

Fig. 8. The calculation and experiment results of total pressure of the fan

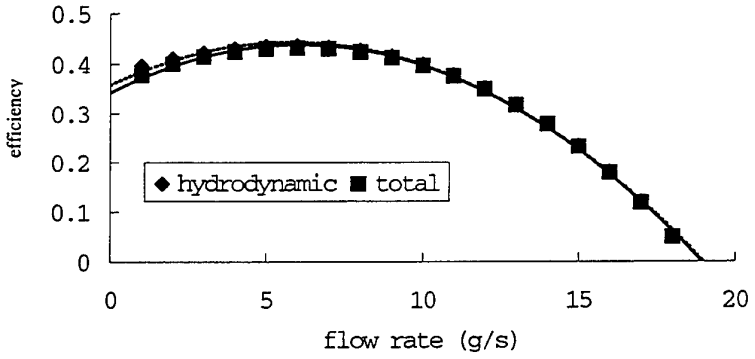

Fig. 9. The calculation efficiency of the fan

Characteristics Of ACCS

It is well known that the ACCS is a system, in which the fan operates with the air duct. The section point of performance curves of the fan and the air duct is called operating point of the whole system. With the change of either the performance curve of the fan or that of the air duct, the operating point will change, as shown in Fig. 10. The total performance curve of the air duct is changing because the thickness of frost on surfaces of the evaporator is changing with time. Therefore, the operating point is also changing simultaneously. The parameters of operating point can be obtained by solving the performance curve of the air duct compared with that of the fan by way of iteration method. The results are shown in Table 1. and Fig. 10.

Table 1. The Change of Parameters of the Operating Point

Time(s)	0	703	1548	2162	2878	3964	5370	7464	10000
flow rate(g/s)	15.361	15.285	15.22	15.12	15.005	14.895	14.715	14.485	14.07
Pressure(Pa)	19.035	19.423	19.758	20.244	20.853	21.405	22.299	23.422	25.393

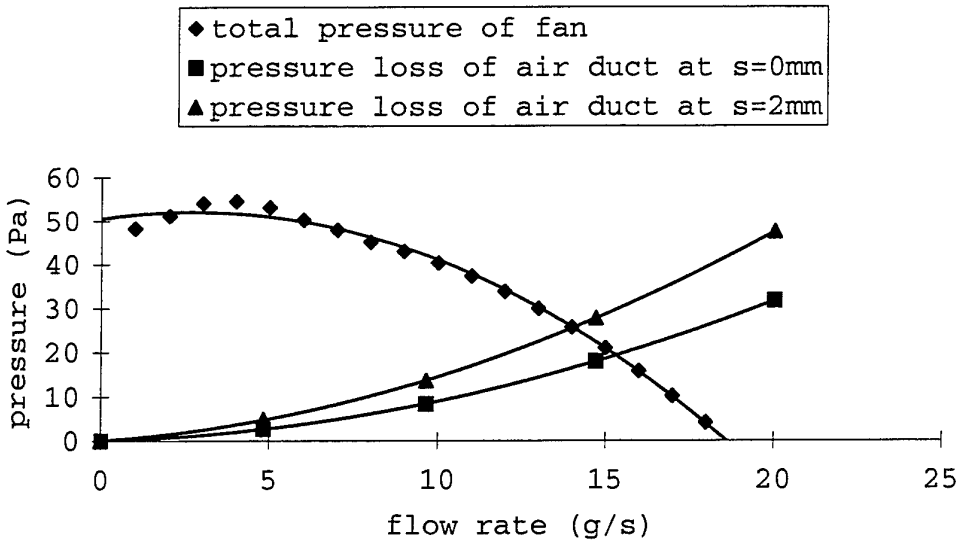

Fig. 10. The change of the operating point

4. RESULTS AND DISCUSSION

Computational And Experimental Results

A comparison of pressure losses at different flow rates is made between experimental techniques and CFD predictions. From results of computation and experiment, we can see that the numerical results are confirmed acceptable. On the whole, the consistency of computational and experimental results is good. In other words, the computer codes for the air duct and the model for the fan are valid and conceivable. Fig. 11 shows the predicted flow distribution of the air duct at the middle section at a flow rate of 20×10^{-3} g/s^{-1}. We can see the flow patterns from it, which will be useful in the later discussion.

Design And Optimization

CFD can provide exact predictions of flow field, which is useful for the optimal design. It is seen from Fig. 11 that a strong vortex can be identified in area (A), which leads to a considerable increase of the turbulence level and pressure loss. It is also seen that the flow field in the adjustable damper area (B) is very disorderly, which means that the pressure drop of the area is high. At the same time, we can see that an inhomogeneous flow at the return area (C) occurs, which leads to an increase of pressure loss and a non-uniform inflow to the evaporator. With those information, the optimization of the critical areas can proceed.

Election Of Fan

Though the power consumption of the fan itself is low, generally less than 10w, the performance of the appliance will decrease sharply if the flow rate and (or) total pressure supplied by it do not satisfy the needs of the system.

At present, the authors propose a practicable method of electing the fan. First, compute the pressure losses of the whole air duct at different flow rates, then regress a pressure loss *vers.* flow rate curve. Second, determine the total pressure of the fan through the regression curve according to the needed air flow rate that obtained from simulations and computations of the evaporator and refrigeration system. Third, design or elect the fan in accordance with the determined total pressure and the flow quantity. If the fan is offered, the operating point can be obtained from the pressure loss *vers.* flow rate curves of the fan and the air duct, then designers may determine whether the fan offered meets the needs. Considering the limited space of the factual fan volute, it is valid to increase the number of vanes of the impeller if the total pressure and (or) flow rate is less than the quantity needed.

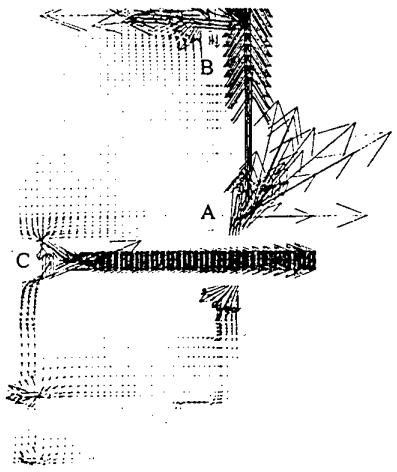

Fig. 11. The computed flow field of middle section in width direction

5. CONCLUSIONS AND PROSPECTS

The present study has shown how CFD can be applied for the design and optimization of the air duct of indirect cooling refrigeration appliances. The computational results are able to give a detailed insight into the complex flow field in the air duct and by this means increase the understanding of the flow physics. The numerical method has proved to be a power tool for a systematic comparison of different design plans and moreover, it allows a sophisticated optimization of them with regard to the flow field and pressure losses in the air duct. At the same time, a model for the performance prediction of the fan has been developed. The result comparison of the factual product between calculation and experiment has shown the validation of the model.

A practicable method of designing and (or) electing the fan is proposed. Experimental results and discussion have proved it to be a power method during the process of designing and (or) electing the fan. An optimal use of the method is believed to be in an early stage of the development process, where no prototypes are available. Thus, the number of experimental tests as well as time and costs during the development process of new products could be greatly reduced.

To some extent, theoretical and experimental studies of this paper build the base of dynamic simulation, optimal matching between the refrigeration system and the ACCS with enclosure structure, and design modernization of ICRI.

REFERENCES

1. B. Youn, et al, J. Fluids Engineering v.116, pp.488-493 (1996)
2. K. Cheong,, et al, "A New Method for Determination of Velocity Pressure Loss-Factors for HVAC System Components", *Proceedings of 13th AIVC Conference*, France (1992)
3. E. Dekam and J. Calvert, Int. J. Heat & Fluid Flow, v.9, pp.2-7 (1988)
4. D. Damin, et al, ASHRAE Trans, v.95, pp.23-29 (1989)
5. W. Q. Tao, *Numerical Heat transfer*, Xi'an Jiao Tong University Publishing House (1988)
6. W. Hu, Study on Characteristics of Air Duct of Small-Scale Refrigeration Installation with Air Forced Convection Cooling, Dissertation of Shanghai Jiao Tong Univ. (1998)
7. B. Yu, Researches on Characteristics of Small-Scale Refrigeration Installation with Air Forced Convection Cooling, Ph.D Dissertation of Shanghai Jiao Tong Univ. (1996)
8. L. Z. Jiang, Dynamic Simulation and Experimental Study of Finned-Tube Evaporator under Dry, Wet and Frost Condition, Dissertation of Shanghai Jiao Tong Univ. (1996)
9. B. Eck, *Fans*, 1st English edition (1973)

C. Natural Convection

NUMERICAL COMPUTATION OF OSCILLATORY RAYLEIGH-BENARD NATURAL CONVECTION OF GALLIUM IN A RECTANGULAR REGION WITH ASPECT RATIOS EQUAL TO FIVE

Mitsuyuki Hatanaka, Toshio Tagawa and Hiroyuki Ozoe
Institute of Advanced Material Study
Kyushu University, Kasuga Koen 6-1
Kasuga 816-8580, Japan
Tel: 81-92-583-7834, Fax: 81-92-583-7838
E-mail: ozoe@cm.kyushu-u.ac.jp

Keywords: Rayleigh-Benard convection, gallium, low-Prandtl number, computation

ABSTRACT. Present paper considers unsteady fully three-dimensional natural convection of the low-Prandtl number fluid in a shallow rectangular region with an aspect ratio(width/depth) of five heated from below and cooled from above. Four vertical boundaries were assumed to be dragless and thermally insulated to simulate the convection in an infinite wide shallow fluid layer heated from below. The model equations consist of equation of continuity, three-directional momentum equations and energy equation. These simultaneous nonlinear partial differential equations were approximated with HSMAC finite difference scheme with second order central difference for the inertial terms. Numerical grids of 41×41×16 were employed after several tests on the grid size effects. Sample computations were carried out for Pr = 0.023 and Ra = 2100, 2200, 2500 and 3000. Oscillatory responses were successfully obtained for all cases studied.

1. INTRODUCTION

Rayleigh-Benard natural convection has been studied extensively after the pioneering work of Benard [1] and Rayleigh [2]. However, the most of the work has been limited to high Prandtl number fluid. Recent development in industries increases the usage of liquid metal such as molten steel, molten semi-conducting material and/or various alkali-metals for nuclear reactor. Then, its oscillatory characteristics in the heat and flow appear to have affected the final products. This again calls up the necessity to study the oscillatory natural convection of the low-Prandtl number fluid. Nakano et al.[3] made a fairly detailed literature survey on this subject which is not repeated herein. Nakano et al. carried out transient three-dimensional numerical calculation on this aspect and reported oscillatory transient convection characteristics. However, their computation was limited to only Ra = 2000 due to the limitation in the computational facilities. This report considers the wider range for the Rayleigh number Ra = 2100 to 3000 at Pr = 0.023.

2. MODEL SYSTEMS AND COMPUTATIONAL SCHEME

The system considered in the present work is shown in Fig. 1. It consists of a square rectangular region with five times longer in the X- and Y-coordinate directions than the fluid depth in the gravitational Z-direction. Figure 2 shows boundary conditions of the present system. Top plate is cooled at an isothermal temperature and the bottom plate at a larger isotherm. The vertical side boundaries are thermally adiabatic and normal gradients of the tangential velocity components are zero to simulate the infinitely wide fluid layer both in the X- and Y-coordinates. The gravity is parallel to the Z-coordinate. The model equation for the natural convection in the above region can be represented by the following conservation equations in a Cartesian coordinate with dimensionless variables. The continuity equation, the momentum equation and the energy equation are given by

$$\nabla \cdot U = 0 \tag{1}$$

$$DU/D\tau = -\nabla P + Pr\nabla^2 U + (0,\ 0,\ PrRa(\theta + 0.5 - Z))T \tag{2}$$

$$D\theta/D\tau = \nabla^2\theta + W \tag{3}$$

The deviation of temperature from a conduction state was employed as a more sensitive variable for this low Prandtl number fluid.

$$\theta = (T - T_0) / (T_h - T_c) - (0.5 - Z) \quad (4)$$

The dimensionless variables were defined as follows.

$X = x/x_0$, $Y = y/x_0$, $Z = z/x_0$, $U = u/u_0$, $V = v/u_0$, $W = w/u_0$, $\tau = t/t_0$, $P = p/p_0$,
$\Phi = (T - T_0)/(T_h - T_c)$, $x_0 = H$, $u_0 = \alpha/H$, $t_0 = H^2/\alpha$, $p_0 = \rho\alpha^2/H^2$, $T_0 = (T_h + T_c)/2$,
$Pr = \nu/\alpha$, $Ra = g\beta(T_h - T_c)H^3/(\alpha\nu)$.

Average Nusselt number was defined as follows,

$$Nu = q / q_{cond}. \quad (5)$$

$$q = \iint \left[-k\partial T / \partial z + \rho C_p (T - T_0) w\right] dxdy \quad (6)$$

$$q_{cond} = \iint \left[-k\partial T / \partial z\right]_{z=0} dxdy \quad (7)$$

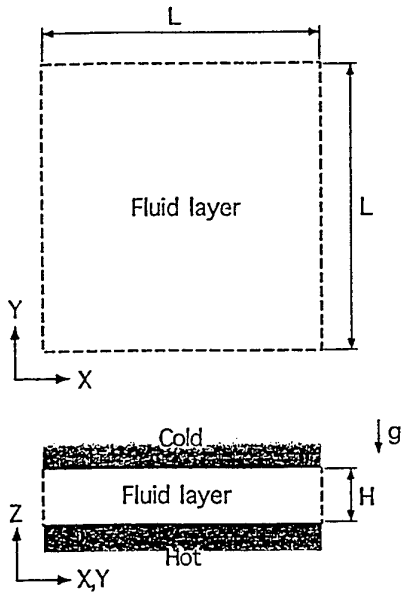

Fig. 1 Schematics of the system

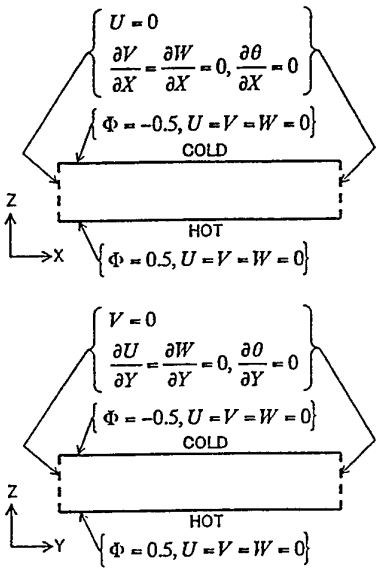

Fig. 2 Boundary conditions

Initial conditions are as follows.

$U = V = W = \theta = 0$

To start the convection, random values to satisfy the next condition were assigned at Z = 0 plane,

$$|\theta| \leq \pm 10^{-5}$$

Boundary conditions corresponding to Fig. 2 are as follows.

$U = V = W = \theta = 0$ at $Z = 0, 1$

$U = \partial V/\partial X = \partial W/\partial X = \partial\ \theta/\partial X = 0$ at $X = 0, L$

$U = \partial U/\partial Y = \partial W/\partial Y = \partial\ \theta/\partial X = 0$ at $Y = 0, L$

The above partial differential equations were approximated with finite difference equations for the system divided by staggered meshes with uniform grids. HSMAC [4] computational scheme was employed with second order central difference for inertial terms. The continuity condition is kept to satisfy less than 10-6.

3. COMPUTED RESULTS

At the beginning, the effect of computational grid size was tested. Figure 3 shows computed transient responses of the average Nusselt number at Ra = 1800 and Pr = 0.01 with four different grid numbers in equal grid divisions for each case. Thin rigid line represents that with 41×41×8 in the X-, Y- and Z-directional grid numbers for the system with 5×5×1 lengths. It gives a constant value in the average Nusselt number at 1.00068. Thin dotted line for 51×51×11 gives large amplitude oscillation. Bold rigid line for 41×41×13 gives also oscillation which agrees with the bold dot line of 61×61×13. These suggest that the grid number in the horizontal direction affects less the result but the one in the vertical direction affects more. Figure 4 shows also preliminary computations with 41×41×13 for Pr = 0.01 and Ra = 1800, 1850 or 1900. As the Rayleigh number increases, the oscillatory characteristics increase. Following computations were carried out with 41×41×16 with the above preliminary test computations. Figure 5 shows transient responses of the velocity components for Pr = 0.023 and Ra = 2100, 2200, 2500 and 3000. With the increase in the Rayleigh number, the oscillation becomes more random. The responses in the average Nusselt number become also more oscillatory. The average and high and low limits in the average Nusselt number are shown in Fig. 6. The average Nusselt number oscillates fairly in the wide range but the time-averaged values of the black square symbols agree with those obtained by Rossby [5] for Pr = 0.025 in a much shallow circular layer. Therefore the present simulation appears to be supported by the classical experimental data.

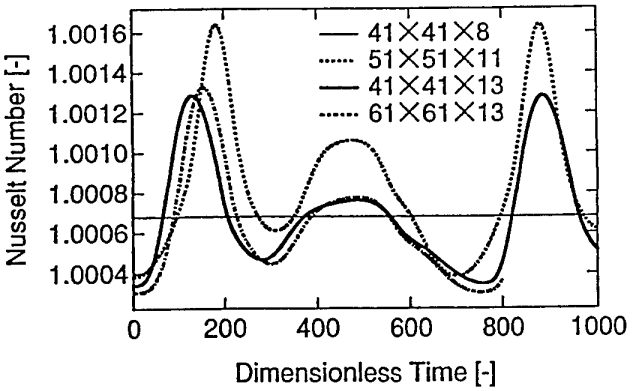

Fig. 3 Effect of the grid numbers. Pr=0.01, Ra=1800

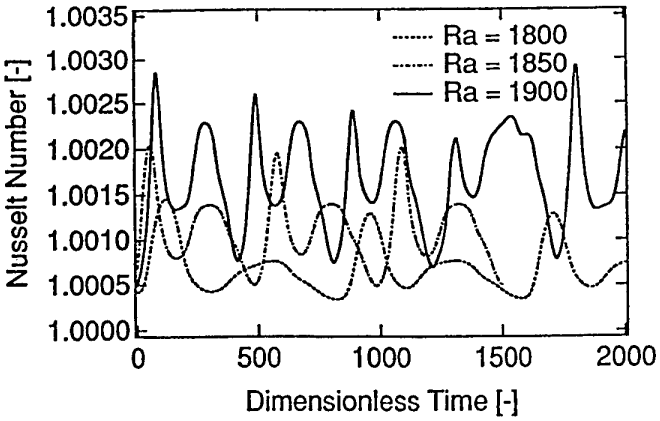

Fig. 4. Preliminary results on the effect of the Rayleigh number with grids 41 x 41 x 13 at Pr = 0.01

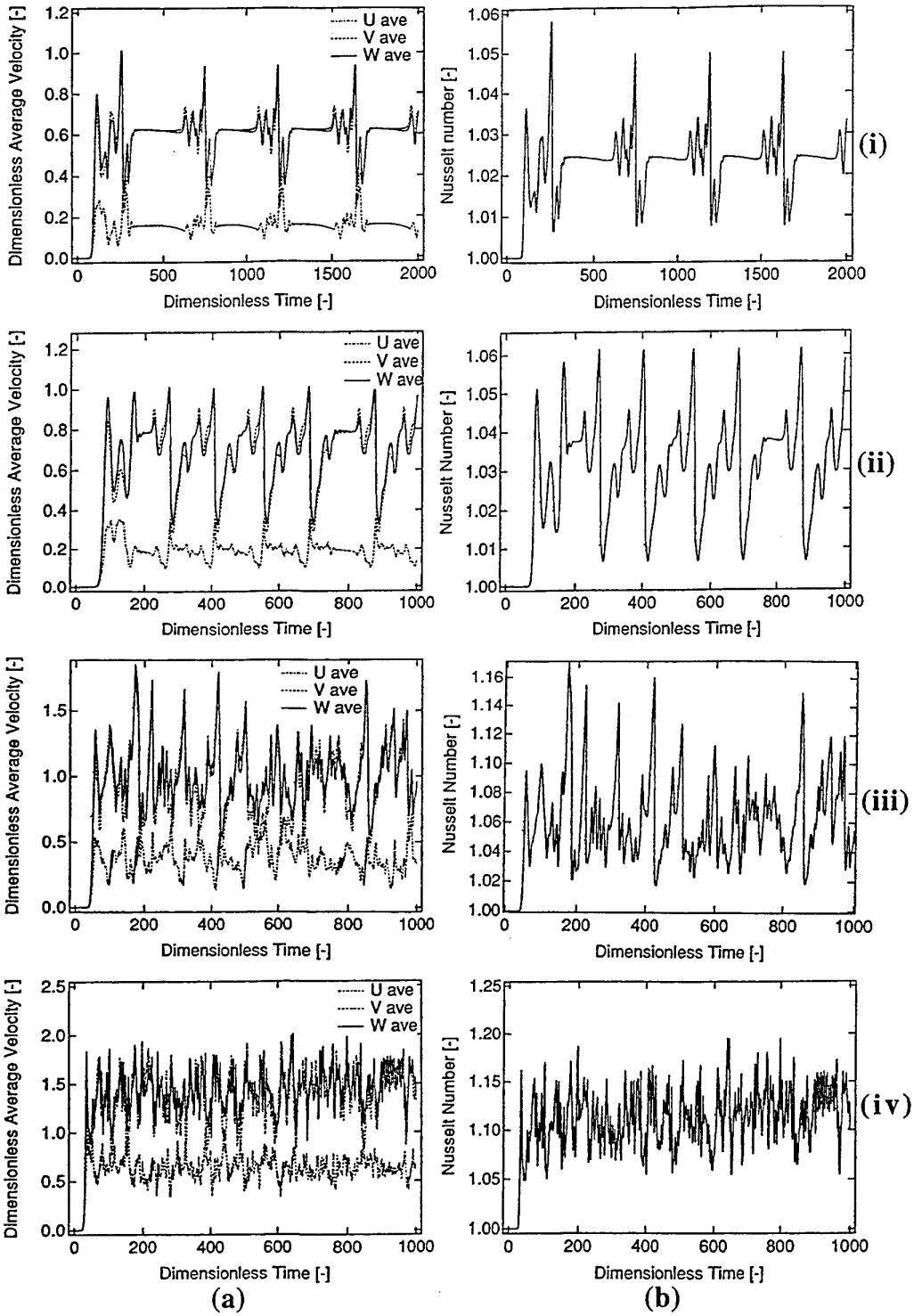

Fig. 5 **Transient responses in the velocity components (a) and the average Nusselt numbers (b) at Pr = 0.023 and Ra = (I) 2100, (ii) 2200, (iii) 2500 and (iv) 3000**

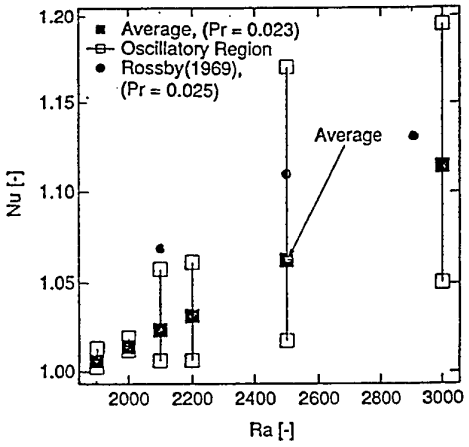

Fig. 6 Summary of the computed average Nusselt number at Pr = 0.023

More detailed transient characteristics may be seen as a series picture of the instantaneous velocity vectors and isothermal contours. Figure 7 (a) shows a response curve of the temperature deviation θ from the conduction

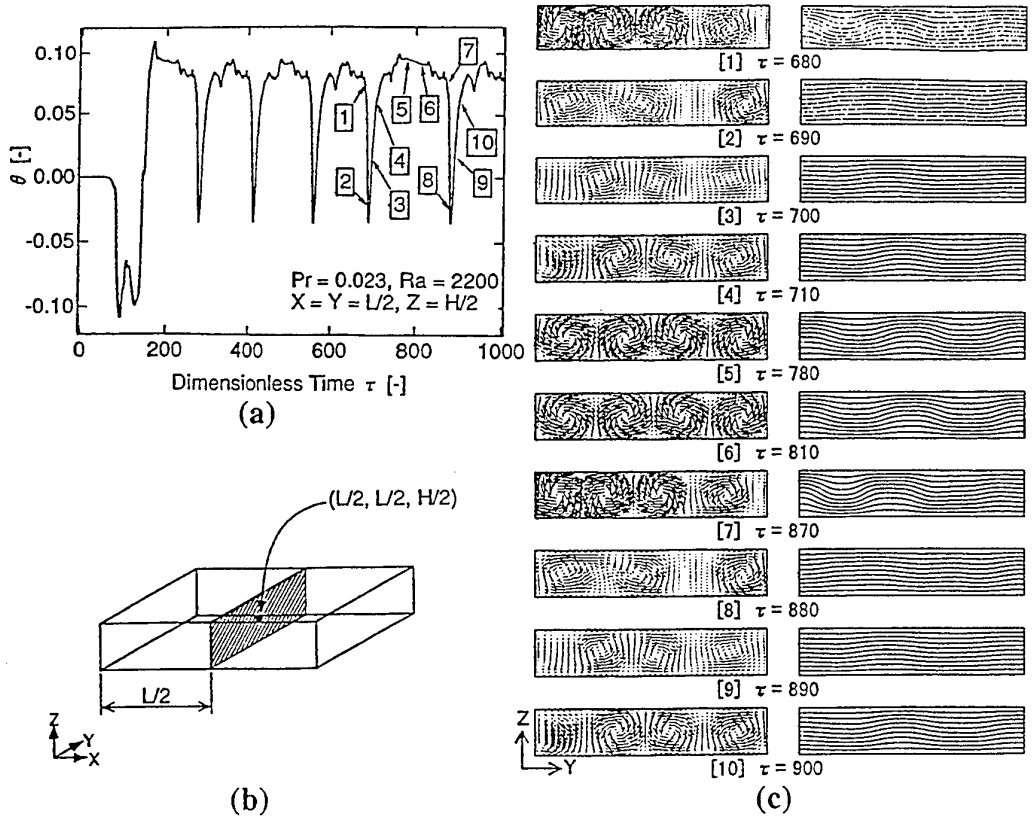

Fig. 7 Transient responses of the velocity vectors and temperature deviation θ from a conduction state at the center of the region. Pr = 0.023, Ra = 2200. (a) transient responses of θ (b) schematic view of the region (c) Instantaneous graphs at 10 instants

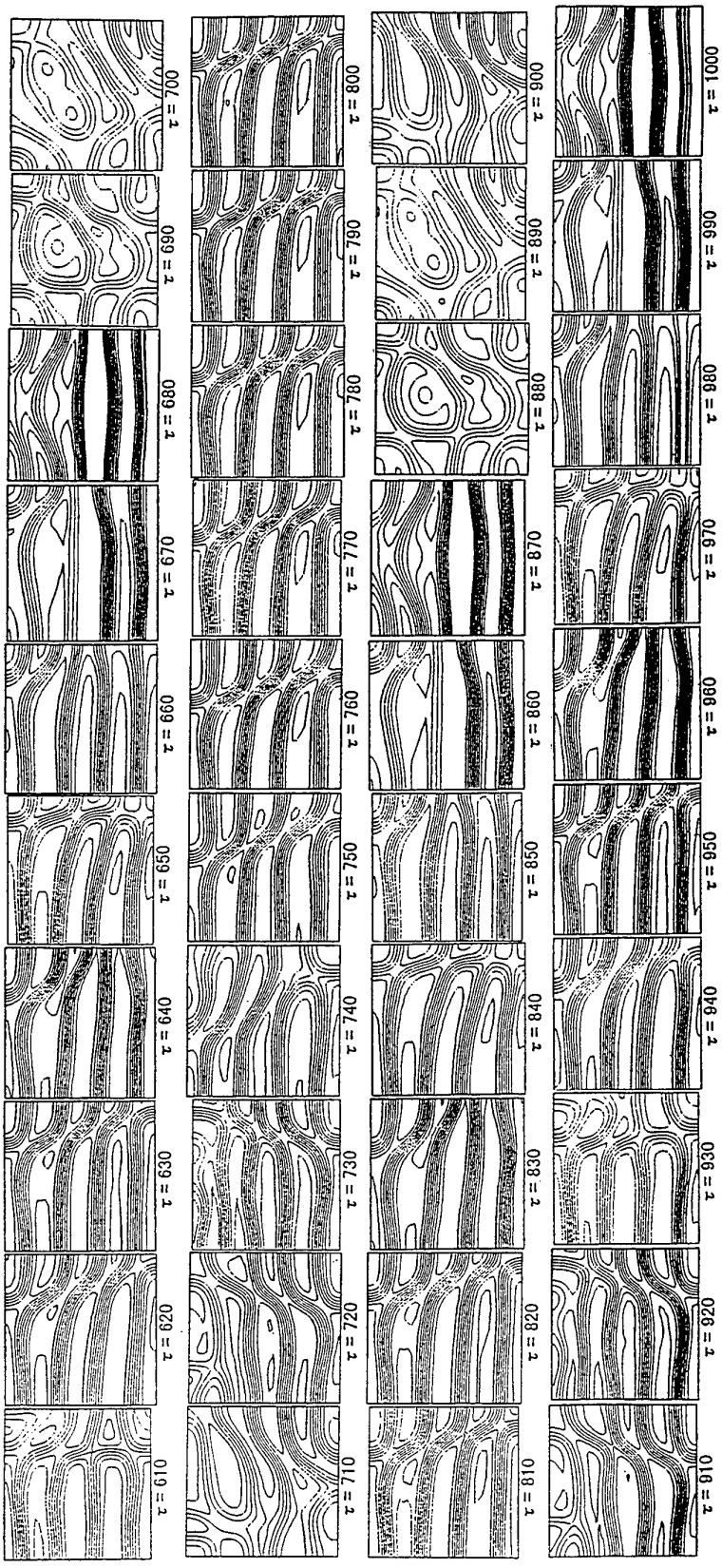

Fig. 8 A series of isothermal contours at Z = 0.5 and Pr = 0.023 and Ra = 2200 for τ = 610~1000.

temperature profile at the center of the computational domain (X, Y, Z) = (L/2, L/2, 1/2) as shown in Fig.7 (b). Between τ= 680 to 900, 10 points are indicated for which instantaneous vertical side views of the velocity vectors and isotherms are shown in Fig.7 (c). Depending on the instants, four to three roll cells appear with various strengths in the velocity vectors. For example, at points 2 and 8, θ decreases sharply and becomes negative. In picture (c), the velocity vectors are downward with three weak roll cells and the isotherms incline downward in the center of the domain. Points 1 and 7 give the similar shape in the velocity vectors and points 4 and 10 also resemble.

Figure 8 shows more detailed series pictures of isotherms at a middle height at 40 instants from τ= 610 to 1000. This series pictures represent rather regular oscillatory characteristics since similar contours can be seen periodically. This agrees with periodical responses as seen in Fig. 7(a).

REFERENCES

1. H. Benard, Les Tourbillous cellulaires das une nappe liquide, Revue generale des Sciences pures et Appliquees, 11, p1261 and p1309, 1900.
2. Lord Rayleigh, On convective currents in a horizontal layer of fluid when the higher temperature is on the under side, Philos. Mag. 32, pp.529-546, 1916.
3. A. Nakano, H. Ozoe and S. W. Churchill, Numerical computation of natural convection for a low-Prandtl-number fluid in a shallow rectangular region heated from below, The Chemical Engineering Journal, 71, pp.175-182, 1998.
4. C.W. Hirt, B.D. Nichols, and N.C. Romero, Los Alamos Scientific Laboratory, LA-5852, 1975.
5. H. T. Rossby, A study of Benard convection with and without rotation, J. Fluid Mech., Ser. A 2 (3), pp.334-339, 1990.

NOMENCLATURE

C_p	specific heat of fluid [J/(kg·K)]
g	acceleration due to gravity [m/s2]
H	height of a layer [m]
k	thermal conductivity [W/(m·k)]
l	width in the x- and y-coordinate [m]
L	= l/H
Nu	average Nusselt number = q / qcond
p	pressure [Pa]
P	= p / p_0 [Pa]
Pr	Prandtl number = ν/α
q	total heat transfer rate [W]
q_{cond}	conductive transfer rate [W]
Ra	Rayleigh number = $g\beta(T_h-T_c)H^3/(\alpha\nu)$
t_0	= H^2/α [s]
t	= time [s]
T	temperature [K]
T_0	= $(T_h + T_c)/2$ [K]
T_c	cold wall temperature [K]
T_h	hot wall temperature [K]
u	velocity component in the x-coordinate [m]
u_0	= α/H [m/s]
U	= u/u_0
v	velocity component in the y-coordinate [m/s]
V	= v/u_0
w	velocity component in the z-coordinate [m/s]
W	= w/u_0
x_0	= H [m]
x	horizontal coordinate [m]
X	= x/x_0
y	horizontal coordinate [m]
Y	= y/x_0
z	vertical coordinate [m]
Z	= z/x_0

GREEK LETTERS

α	thermal diffusivity [m^2/s]
β	volumetric coefficient of expansion [1/K]
ν	kinematic viscosity [m^2/s]
τ	= t/t_0
θ	= $(T-T_0)(T_h-T_c) -(0.5-Z)$ [K]

NATURAL CONVECTIVE HEAT TRANSFER IN A COMPOSED THERMAL DIODE

Youn J. Kim*, I.- J. Hwang
School of Mechanical Engineering, Sungkyunkwan University
E-mail: yjkim1@yurim.skku.ac.kr or ijhwang@kict.re.kr

U.-C. Jeong
Dept. of Building Science & Utility Services
Kyungmin Junior College
E-mail: ucjeong@netsgo.com

Keywords: natural convection, thermal diode, dimensionless channel depth, guide vane

ABSTRACT. The steady natural convection heat transfer in an air filled enclosure, which is composed of the rectangular and parallelogrammic portions, has been studied numerically and experimentally. The air-filled enclosure consists of vertical heat source and sink walls, and adiabatic plates at the top and bottom walls. With the constant geometrical aspect ratios, the effects of guide vane installed in a composed enclosure having the various dimensionless channel depths, d^*, are studied to find the enhancement of heat transfer of inner diode to a certain extent. The governing equations for two dimensional, laminar, natural convection process in an enclosure are discretized by the control volume approach which insures the conservative characteristics to be satisfied in the calculation domain, and solved by a modified SIMPLE algorithm. Computations are carried out for Prandtl number Pr=1, and the constant modified Grashof number $Gr^* = 1.4 \times 10^{10}$ and $\varphi = 45^\circ$. In order to compare the numerical results with experimental one, experimental apparatus are composed. To get the greater understanding of the flow and heat transfer behaviors, flow patterns with streamlines and isotherms at different dimensionless channel depths are shown. Experimental results showed that for given modified Grashof number the increasing size of a guide vane in the composed enclosure enhances the heat transfer rate.

1. INTRODUCTION

In the heat transfer literatures there exist lots of work on the subject of natural convection in differentially heated air-filled vertical enclosures. Natural convective heat transfer occurs in a wide variety engineering flow applications and systems; for example, reduction of heat losses in solar collectors, building insulation, nuclear reactor safety, the containment of heat generating radioactive wastes, and cooling of heat generating components in power plant, etc. (see also Gebhart et al. (1988) for a review). A number of investigators, also, studied the dynamic behavior of thermal diode for space heating of passive solar buildings (MacGregor and Emery 1969, Jasinsky and Buckley 1977, Seki et al. 1983, Emara and Kulacki 1980, Jones 1986, Chen 1988).

Nakamura and Asako (1980) investigated both analytically and experimentally free convective heat transfer in a parallelogrammic enclosure filled with air for the case of one vertical side uniformly cooled and the opposing vertical side uniformly heated. Bergholz (1980) investigated the thermal convection of a heat generating fluid in a rectangular enclosure, cooled at the side walls, in the boundary layer regime at large internal Rayleigh numbers, using a modified Oseen linearization method.

Recently, Jones and Cai (1993) studied numerically transient natural convection in a rectangular open thermosyphon having asymmetric thermal boundary conditions. One vertical wall of the thermosyphon is either heated by constant heat flux or cooled by convection to the surrounding. They demonstrated that stratification is the key to good performance of the thermal diode. Here, the thermal diode represents a kind of heat exchanger that transports heat preferentially in one direction, and blocks heat flow in the opposite direction.

From the foregoing literature survey, it appears that there may be a great lack of information on the heat transfer characteristics of the composed geometry of rectangular and parallelogrammic portions. The objective of this paper, therefore, is to elucidate the effects of inclination angles and geometrical channel depths on the characteristic steady free convective heat transfer in an air-filled enclosure that is composed of the rectangular and parallelogrammic portions. This has one vertical inlet wall constantly heated as the heat flux q'', the

opposing vertical wall isothermally cooled T_c, the parallel adiabatic top and bottom walls inclined, and equipped with a guide vane. Due to the temperature difference between the vertical heat source and sink walls, the fluid in the upper and lower regions will circulate inside the loop automatically under the influences of the buoyancy effect. These features of the study make it very attractive for the improvement of energy efficiency of building envelopes and solar energy utilization.

2. NUMERICAL SIMULATION

2.1 Formulation of Problems

The air-filled rectangular-parallelogrammic thermal diode consists of vertical heat source and sink walls, a guide vane, and adiabatic plates at the upper and lower walls as shown in Fig. 1. In this study, two geometrical aspect ratios are introduced; one for a parallelogrammic portion of enclosure as *W/H*, the other for a rectangular portion as *L/H*. Here *W* and *L* are denoted as the width of the parallelogrammic and rectangular portions of enclosure, respectively. And *H* is denoted as the height of composed enclosure.

The governing equations for the natural convection process in the composed enclosure are the conservation equations of mass, momentum and energy. In this study, the flow is assumed to be steady and laminar, and the transport properties are uniform except for density. The working fluid is newtonian and incompressible, and viscous dissipation is neglected in the energy equation. It is assumed that the variation of density with temperature is calculated using the Boussinesq approximation.

For the sake of convenience, the following dimensionless variables are introduced:

$$x = X/\ell,\ y = Y/\ell,\ u = u'\ell/\eta,\ v = v'\ell/\eta,\ p = \rho v^2 p'/\ell^2,\ \Theta = (T - T_c)/(T_h - T_c) \tag{1}$$

where primes represent dimensional variables, and ℓ denotes the characteristic length which equals to *W+L*.

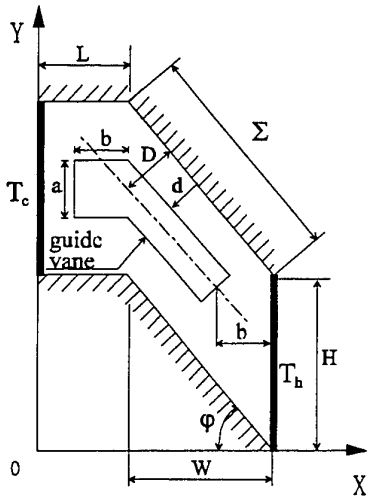

Fig. 1. Schematic diagram of the modeled enclosure

With the help of these variables, the dimensionless governing equations can be written under steady-state conditions, as follows:

Continuity:
$$\frac{\partial u}{\partial x} + \frac{\partial v}{\partial y} = 0 \tag{2}$$

Momentum:

x-direction
$$u\frac{\partial u}{\partial x} + v\frac{\partial u}{\partial y} = -\frac{\partial p}{\partial x} + \frac{\partial^2 u}{\partial x^2} + \frac{\partial^2 u}{\partial y^2} - \frac{Ra}{\ell^3 \mathrm{Pr}}\Theta \tag{3}$$

y-direction
$$u\frac{\partial v}{\partial x} + v\frac{\partial v}{\partial y} = -\frac{\partial p}{\partial y} + \frac{\partial^2 v}{\partial x^2} + \frac{\partial^2 v}{\partial y^2} - \frac{Ra}{\ell^3 \mathrm{Pr}}\Theta \tag{4}$$

Energy:
$$u\frac{\partial \Theta}{\partial x} + v\frac{\partial \Theta}{\partial y} = \frac{1}{\mathrm{Pr}}\left\{\frac{\partial^2 \Theta}{\partial x^2} + \frac{\partial^2 \Theta}{\partial y^2}\right\} \tag{5}$$

where *u* and *v* are the velocities in the *x*- and *y*-directionsrespectively, *p* is the pressure and Θ is the dimensionless temperature. The dimensionless parameters that govern the flow are the inclination angle φ, the Rayleigh number, *Ra*, and the Prandtl number, *Pr*, and be conventionally defined as follows:

$$Ra = \frac{g\beta\Delta T\ell^3}{\alpha\eta},\ \mathrm{Pr} = \frac{\mu C_p}{\kappa} = \frac{\eta}{\alpha} \tag{6}$$

where β is the coefficient of volumetric expansion of the working fluid, η is the kinematic viscosity, κ is the thermal conductivity, α is the thermal duffusivity, C_p is the specific heat at constant pressure, and ΔT is the

temperature difference between the heated and cooled walls.

The solution to the foregoing set of equations must satisfy the following boundary conditions:

$$\begin{aligned} &u = v = 0 \text{ at the solid boundaries (no-slip condition)} \\ &\Theta = 0 \quad \text{for } X = 0,\ H \le Y \le \Sigma \cdot sin\varphi + H \\ &\Theta = 1 \quad \text{for } X = L + W,\qquad 0 \le Y \le H \\ &\frac{\partial \Theta}{\partial n} = 0 \quad \text{on adiabatic walls and a guide vane} \end{aligned} \tag{7}$$

where n denotes normal direction from the walls.

For future reference, we also define the following local Nusselt number, Grashof number, and modified Grashof number:

$$Nu = \frac{q''}{\Delta T}\frac{\ell}{\kappa},\quad Gr = \frac{g\beta\Delta T\ell^3}{\eta^2},\quad Gr^* = Gr \cdot Nu = \frac{g\beta q''\ell^4}{\kappa\eta^4} \tag{8}$$

where q'' is the heat flux from the heated wall.

2.2 Methods for Solution

The governing equations (2)-(5) subject to the above boundary conditions were solved numerically by the finite volume method, using the calculation procedure described by Karki and Patankar (1988). Because of no-slip boundary conditions, steep velocity gradients exist adjacent to the walls. Therefore, variable size grids shall be used to resolve the flow fields adequately in the viscous sub-layer adjacent to the walls. A coordinate transformation is necessary which maps the irregularly-shaped physical domain of the composed enclosure into a computational domain with a regular shape, where well-established finite-volume approaches can be employed to solve the problem. Fig. 2 shows grid systems adopted in this study.

To simplify the analysis, we choose the constant geometrical aspect ratio, H/W=4/3. For the case of a single guide vane installed, the geometry of thermal diode consists of a/H=0.15, and b/L=0.5. Also, in order to find the characteristics of flow fields in the channel with the installed guide vane, the dimensionless channel depth has been defined as follows and varied from 0.3 to 1 (see Fig. 1).

$$d^* = d/D \tag{8}$$

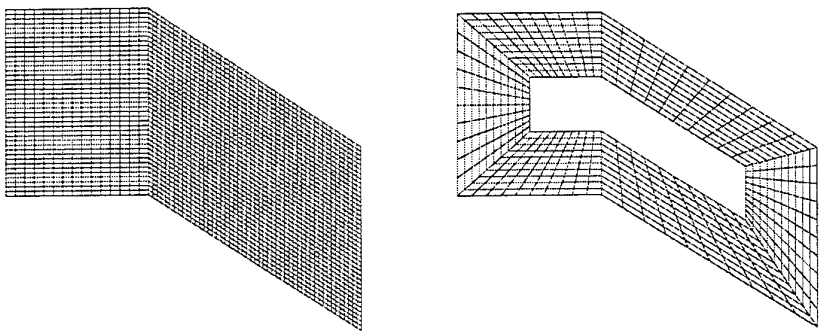

a) no guide vane b) with a guide vane

Fig. 2. Grid system of the modeled thermal diode

3. EXPERIMENTAL APPARATUS AND PROCEDURE

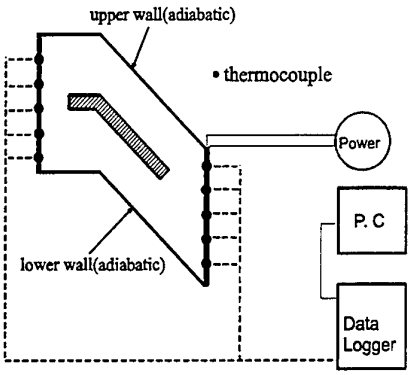

Fig. 3. Schematic diagram of the experimental apparatus

A schematic diagram of air-filled rectangular-parallelogrammic thermal diode is shown in Fig. 1. It mainly consists of two vertical copper plate, each 400mm long and 800mm wide, enclosed with two acryl plates that wrapped with 10mm glass wool layer and 50mm styrofoam inclined from the horizontal. Heat sink wall is made of 2mm thick copper plate. The other opposing vertical wall is made of 5mm thick copper plate heated by main heater. Guard heaters are mounted on the backside of the main heater to minimize heat loss to surrounding, and covered with 15mm thick asbestos layer.

Also, asbestos sheeting is used as a gasket between the copper and main heater to reduce the thermal conduction between two.

All the heat generated by the main heater then flows inwards to the enclosure. To find the surface temperature on the heat sink and source walls, measurements are obtained from 9 copper-constantan T-type thermocouples of 0.32mm in diameter penetrating each plate. All the thermocouples are calibrated up to 120°C. The outputs of these thermocouples are continuously recorded on data acquisition system (YOKOKAWA, DL5180). The required electric power was taken the A.C. mains via a stabilizer. The main heater input was measured in the usual way by a wattmeter accurate to ±0.5%.

In order to compare the numerical results, the experiments were carried out with heat flux values which ranged from 110 to 140W/m^2 giving modified Grashof number (Gr*) in the range of 1.11×10^{10}~1.40×10^{10} for an aspect ratio, H/W=4/3. For the case of a guide vane installed, furthermore, the geometry of thermal diode consists of a/H=0.15, and b/L=0.5. The modified Grashof number controlled with ±2% error limit. Also, steady state values from the measured heat flux and local temperatures are used for processing of experimental data.

4. RESULTS AND DISCUSSION

Qualitative visual numerical results were obtained to study the effect of dimensionless channel depth of the composed enclosure with installed guide vane on the flow patterns and temperature distributions. Fig. 4 shows the characteristics of streamlines and temperature fields for the various dimensionless channel depths in the composed enclosure with the constant modified Grashof number, $Gr^* = 1.4\times10^{10}$ and $\varphi = 45°$.

Numerical results show that there exist a steeper gradient of streamlines and temperature in the near region of heat sink and source walls as the dimensionless channel depth decreases. Regardless of the installed guide vane size, the local cell is eventually decreased. And a global convective cell enhancing a main flow pattern of air is formed clearly because a driving force is increased by buoyant force from the heat source of lower vertical plate to the heat sink of upper vertical plate as the dimensionless channel depth decreases. Preferably, in the case of the installed a larger size of guide vane, lots of the local cells are created, and the patterns of global convective cells are complex. In the side view of energy transfer, however, the energy density moving to the heat sink of the upper region is high, which is understood that the global convective cell forms densely and the local cell disappears as increasing the dimensionless channel depth.

With the existence of a guide vane in the enclosure, typically, hot air is stagnated in the lower region of the heat source because of the flow obstacle. But, the energy density transferred to the upper region of the heat sink increases highly since the driving force due to hot air flow is improved by decreasing the cross-sectional area of flow passage due to the installation of the guide vane as well as the temperature gradient increases.

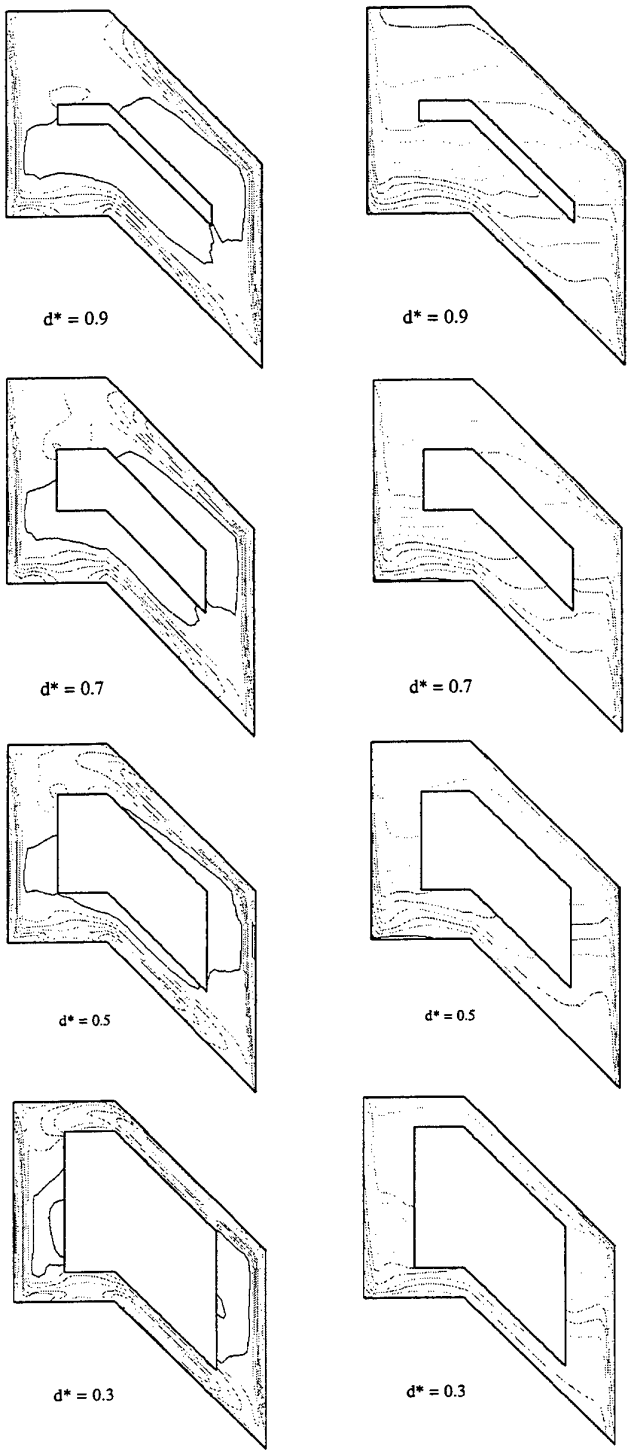

Fig. 4. Contour plots for streamlines and iso-thermal lines with dimensionless channel depth with the constant modified Grashof number $Gr^* = 1.4\times10^{10}$ and $\varphi = 45^\circ$.

As shown in Fig. 4(a) the heat transfer performance may be markedly disturbed by the complex mechanism of the flow patterns followed with the retarded velocity in the enclosure. It is also seen that there is a general trend toward larger temperature differences adjacent to the hot and cold walls.

Experimental results are obtained to study the effect of inclination angle of the composed enclosure and the thickness of installed guide vanes on the flow patterns and temperature distributions. With the help of the measured temperature and heat flux in steady state and the characteristics from T_{ref}, Nusselt number and the modified Grashof number are calculated using the foregoing fomulas.

The effects of the variation of dimensionless channel depth with inclination angles on the heat transfer are shown in Figs. 5~8 for the three different modified Grashof numbers, i.e, $Gr_1^* = 1.11\times10^{10}$, $Gr_2^* = 1.27\times10^{10}$, and $Gr_3^* = 1.40\times10^{10}$. In the case of non-existence of a guide vane ($d^* = 1$), the heat transfer rates are little affected by the inclination angle. When the inclination angles are greater than 30° and dimensionless channel depth are less than 0.5, however, Nusselt number are increased considerably as the dimensionless channel depth decreases. The below experimental results can be easily explained with the foregoing numerical results for the same geometrical configuration of enclosure shown in Fig. 1.

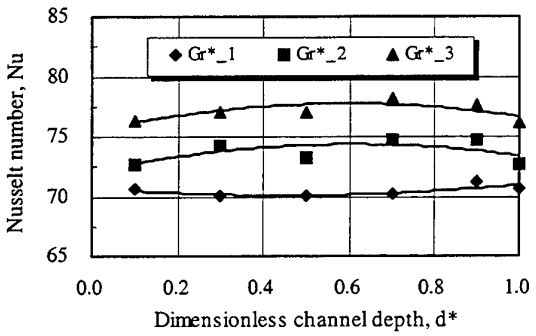

Fig. 5. Effects of dimensionless channel depth on heat transfer ($\varphi = 15^\circ$)

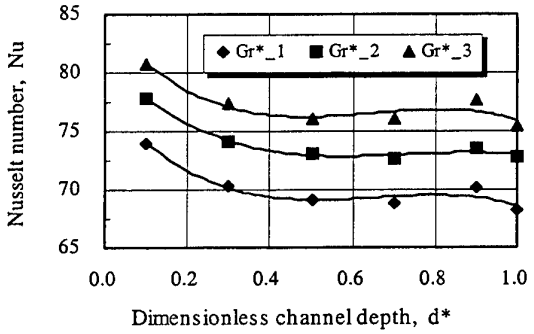

Fig. 6. Effects of dimensionless channel depth on heat transfer ($\varphi = 30^\circ$)

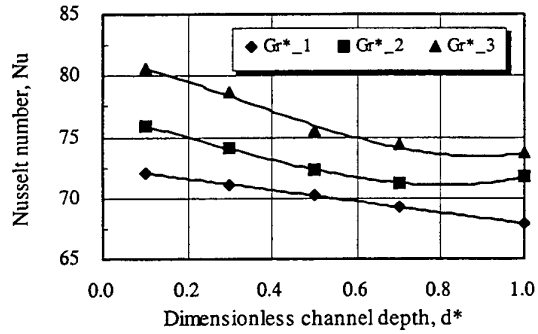

Fig. 7. Effects of dimensionless channel depth on heat transfer ($\varphi = 45^\circ$)

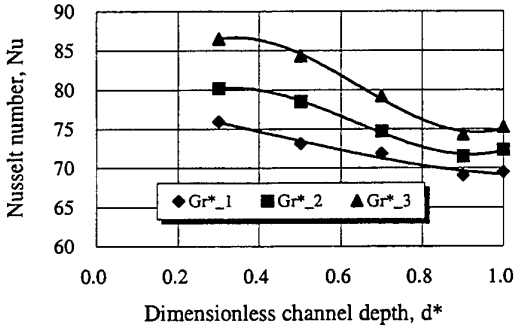

Fig. 8. Effects of dimensionless channel depth on heat transfer ($\varphi = 60^\circ$)

5. CONCLUSIONS

This paper describes the results of numerical and experimental investigation into the natural convective thermal behavior of an air-filled composed enclosure that has the rectangular and parallelogrammic portions. The major objective of this study is to determine the heat transfer characteristics of the composed thermal diode with a guide vane installed having different dimensionless channel depth.

Numerical results show that for the constant inclination angle $\varphi = 45°$, the existence of installed guide vanes in the composed enclosure shows large enhancement of the heat transfer rate that is increased as the dimensionless channel depth (d^*) increases. Experimental results show that for given modified Grashof number the increasing size of a guide vane in the composed enclosure enhances the heat transfer rate. Especially, the installation of guide vane increases the energy moving density. Thereafter, it needs the further study for a wide range of Grashof numbers and the geometrical shapes of the guide vane to get the correlative expressions of the heat transfer rates.

REFERENCES

1. B. Gebhart, Y. Jaluria, R.L. Mahajan, and B. Sammakia, *Buoyancy-Induced Flows and Transport*, Hemisphere, Cambridge (1988).
2. R.K. MacGregor, and A.F. Emery, "Free convection through vertical plane layers – Moderate and high Prandtl number fluids," ASME J. of Heat Transfer, Vol. 91, pp. 391-403 (1969).
3. T. Jasinsky, and S. Buckley, "Thermosyphon analysis of a thermic diode solar heating system," ASME Paper No. 77-WA/Sol-9 (1977).
4. N. Seki, S. Fukusako, and A. Yamaguchi, "An experimental study of free convective heat transfer in a parallelogrammic enclosure," ASME J. Heat Transfer, Vol. 105, pp. 433-439 (1983).
5. A.A. Emara, and F.A. Kulacki, "A numerical investigation of thermal convection in a heat—generating fluid layer," ASME J. Heat Transfer, Vol. 102, pp. 531-537 (1980).
6. H. Nakamura, and Y. Asako, "Heat transfer in a parallelogrammic enclosure (1st Report, Heat transfer by free convection)," Transactions JSME, Vol. 46, pp. 471-481 (1980).
7. R.F. Bergholz, "Natural convection of a heat generating fluid in a closed cavity," ASME J. Heat Transfer, Vol. 102, pp. 242-247 (1980).
8. K. Chen, "Design of a plane-type bidirectional thermal diode," ASME J. Solar Energy Engineering, Vol. 110, pp. 299-305 (1988).
9. G. F. Jones, "Heat transfer in a liquid convective diode," ASME J. Solar Energy Engineering, Vol. 108, pp. 163-171 (1986).
10. K.C. Karki, and S.V. Patankar, "Calculation procedure for viscous incompressible flows in complex geometries," Numerical Heat Transfer, Vol. 14, pp. 295-308 (1988).
11. G.F. Jones, and J. Cai, "Analysis of a transient asymmetrically heated/cooled open thermosyphon," ASME J. of Heat Transfer, Vol. 115, pp. 621-630 (1993).

NATURAL CONVECTION OF LIQUID METAL WITH AND WITHOUT SEEBECK EFFECT

Masayuki Kaneda, Toshio Tagawa, Hiroyuki Ozoe and Koichi Kakimoto
Institute of Advanced Material Study,
Kyushu University, Kasuga Koen 6-1, Kasuga 816-8580, Japan
E-mail: ozoe@cm.kyushu-u.ac.jp ; Tel.: 81-92-583-7834; Fax: 81-92-583-7838

Yukou Inatomi
The Institute of Space and Astronautical Science, 3-1-1,
Yoshinodai, Sagamihara, Kanagawa 229-8510, Japan

Keywords: seebeck effect, liquid metal, natural convection, magnetic field

ABSTRACT. Natural convection of liquid metal in a cubic enclosure heated from one vertical wall and cooled from an opposing vertical wall is studied under a horizontal lateral magnetic field parallel to the heated and cooled walls. The Seebeck effect is further considered for the present system. The Seebeck effect means the electric current induced having temperature difference in the two metals between two points. This effect may be induced for the liquid and solid boundaries of metals. This system was modeled and numerically computed. When the Seebeck effect is not considered, the Lorentz force increases with the Hartmann number, Ha, to decrease the average Nusselt number. When the Seebeck effect was considered, the average Nusselt number at Ha = 200 decreased. However at Ha = 400, the average Nusselt number increased with the Seebeck effect. This peculiar characteristic is due to the complicated convection of the Seebeck effect on the heat transfer surface.

1. INTRODUCTION

Natural convection of liquid metal has been studied extensively due to the safety of nuclear reactor so far. Liquid metal such as molten metal or molten semi conducting material has also been used for the high quality recent industrial products such as steel or silicon crystal rod. Such high quality products require strict control for the convection of molten material for which well understanding is required for the heat and fluid flow. Liquid metal usually conducts electricity and the Lorentz force is induced with an application of the magnetic field, which can be employed to control the convection. In these industrial processes, the manufacturing processes are operated at high temperature. The high temperature differences may induce another effect such as the thermoelectric voltage known as Seebeck effect. Seebeck effect has been directly employed for a thermocouple. The electric voltage is generated between two junctions consisting of two different metals kept at different temperatures. This effect also may occur between liquid and solid of metal if the Seebeck coefficients are different. Seebeck coefficients and theoretical approach for convection was reported by Shercliff [1]. Application for crystal growth was studied by Zheng and Larsen [2] recently. However, there appears to be very few works on its general characteristics, various effects of many parameters with combination of gravity force. There are also many variations under the effects of the magnetic field.

In the present paper, the effect of Seebeck current was considered in addition to the usual electro magnetic current for the convection of liquid metal.

2. MATHEMATICAL MODEL

The model system is shown in Fig. 1. The liquid metal is placed in a cubic enclosure whose one vertical wall is heated isothermally and an opposing vertical wall is cooled with four other walls thermally insulated. The natural convection of liquid metal in a cubic enclosure with the effect of Lorentz and gravity forces can be modeled by the following equations. Seebeck effect can be considered in Ohm's law due to the temperature gradients. The temperature deviation from a conduction state Φ was employed as a variable. The model equations become as follows in dimensionless variables.

$$\nabla \cdot \mathbf{U} = 0 \tag{1}$$

$$D\mathbf{U}/D\tau = -\nabla P + Pr\nabla^2 \mathbf{U} + Ha^2 Pr\, Ra^{-2/3} (\mathbf{J}\times\mathbf{B}) + (0,\ 0,\ Pr(\Phi+0.5-X/L))^T \tag{2}$$

$$D\Phi/D\tau = \nabla^2 \Phi + U/L \tag{3}$$

$$\mathbf{J} = (-\nabla\Psi_e + \mathbf{U}\times\mathbf{B} - S_f\nabla\Phi) + \{S_f/L,\ 0,\ 0\}^T \tag{4}$$

$$\mathbf{J}_{wall} = -C_m\nabla\Psi_e \tag{5}$$

$$\nabla\cdot\mathbf{J} = 0 \tag{6}$$

Boundary conditions are as follows.

$U = V = W = 0$	at $X = 0, L,\ Y = 0, L$ and $Z = 0, L$
$\Phi = T-0.5+X/L = 0$	at $X = 0, L$
$\partial\Phi/\partial Y = 0$	at $Y = 0, L$
$\partial\Phi/\partial Z = 0$	at $Z = 0, L$

The electric current is conserved in the liquid metal and wall. Then we can get following equation where C_m is electric conductivity of the wall divided by that of fluid.

$$J_x^{|}\ \text{interface} = 2C_m\,[-(\partial\Psi_e/\partial X)-(S_f/2)\{(\partial\Phi/\partial X)-1/L\}]\ /\ (1+C_m)$$

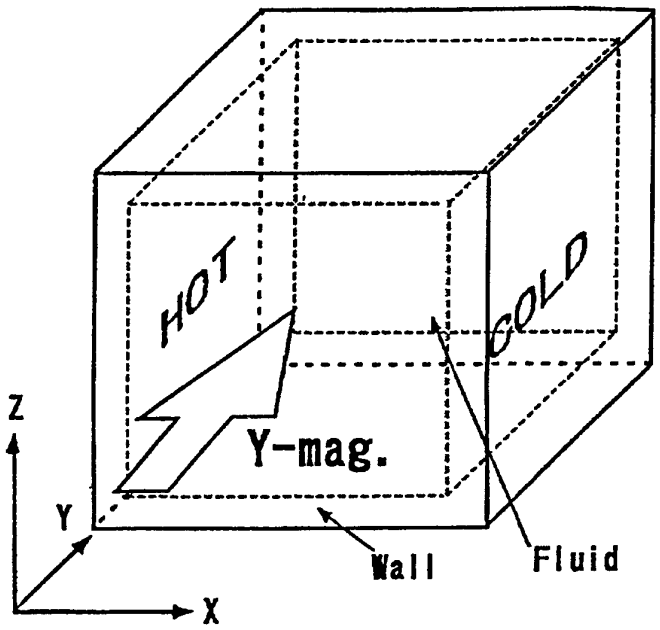

Fig. 1 Schematics of the system. A white arrow means the direction of the magnetic field

Initial cond

$U = V = W$
$J_x = J_y = J_z = \Psi_e = 0.$

The above partial differential equations were approximated by finite difference equations with staggered meshes of 45×45×45 in which 10×10×10 were for a wall region, about 7% of the inner length of a cubic enclosure. The mesh widths were denser near the wall boundaries. The inertial terms in the momentum equation were approximated with third order upwind scheme and whole equations were numerically integrated with HSMAC scheme.

3. COMPUTED RESULTS

3.1 Average Nusselt Number

The common parameters studied in this work are Pr = 0.025, Ra = 10^5 and Cm = 1 under the Y-directional magnetic field. Transient numerical computations converged successfully. The computed cases and the computed average Nusselt numbers on the hot wall (almost equal to that of the cold wall) are listed in Table 1. The results are complicated. For usual natural convection in a cubic enclosure, at Ha = 0, the convection becomes rather oscillatory and the average Nusselt number slightly oscillates between 3.126 and 3.185. For the system without considering the Seebeck effect (S_f = 0), Nu decreases to 1.498 and 1.061 for Ha = 200 and 400, respectively. This can be understood as the usual effect of the Lorentz force by the application of a static magnetic field. For the system with considering the Seebeck effect (S_f = -30), Nu decreases to 1.363 and 1.251 for Ha = 200 and 400, respectively.

Table 1 Computed Cases and Results. Common Conditions are Pr = 0.025, Ra = 10^5, Cm = 1 with Y-Directional Magnetic Field.

S_f	Ha	$Nu_{hot\ wall}$
0	0	3.126~3.185
0	200	1.498
	400	1.061
-30	200	1.363
	400	1.251

The amount of decrease is more extensive in comparison to that without Seebeck effect. However, at Ha = 400, Nu is equal to 1.251 which is larger than Nu = 1.061 without Seebeck effect. This means the Nusselt number increases if the Seebeck effect is considered at Ha = 400. This suggests that Seebeck effect is not simple and the reasoning can not be obtained only from these numerical values of the average Nusselt number. Followings are more detailed representation of the computed results for these cases.

3.2 Computed Velocity Vectors and Isotherms

The velocity vectors and isotherms are then shown in Fig. 2. At Ha = 0, the usual natural convection of liquid metal at Pr = 0.025 represents oscillatory and non-uniform velocity profiles. Near the top and bottom walls the velocity vectors are something like longitudinal convection pattern. The isotherms on the left hand side are also like vortex streets.

When the magnetic field in the Y-direction is applied without considering the Seebeck effect, the magnitude of velocity vectors decrease extensively due to the flow suppressing effect of the Lorentz force at Ha = 200. The non-uniform velocity vectors are now aligned and the isotherms become simplified. At Ha = 400, this becomes more pronounced and the isotherms become almost parallel to suggest the conduction like situation.

When the Seebeck effect is considered, as shown in the right-hand side at Ha = 200, the velocity vectors at Z = 0.5L are surprisingly upward along both the heated and cooled walls. However, the magnitude of the upward velocity is larger on the heated wall. The isotherms become also severely twisted in the bottom center to suggest a strong concentration of downward current. At Ha = 400, the upward flow along the heated and cooled walls are further pronounced and the resulted downward flow occurs near the top wall from the location at about 30% shifted to the cold wall. Near the bottom wall the separated flow can be seen at the mid distance between hot and cold walls. The isotherms become more complicated to reflect these peculiar convection modes. These can be understood more easily by the following graphs.

Figure 3 shows the velocity vectors and isotherms at a vertical cross section at Y = 0.5L. At Ha = 0, the almost symmetric velocity vectors and isotherms are apparent in terms of a center point (X = Z = 0.5L). Without considering the Seebeck effect, at Ha = 200, the convection becomes weak in general and isotherms are parallel and vertical. At Ha = 400, this becomes more pronounced.

When the Seebeck effect is considered, the upward flow along the heated wall on the left hand side reaches the

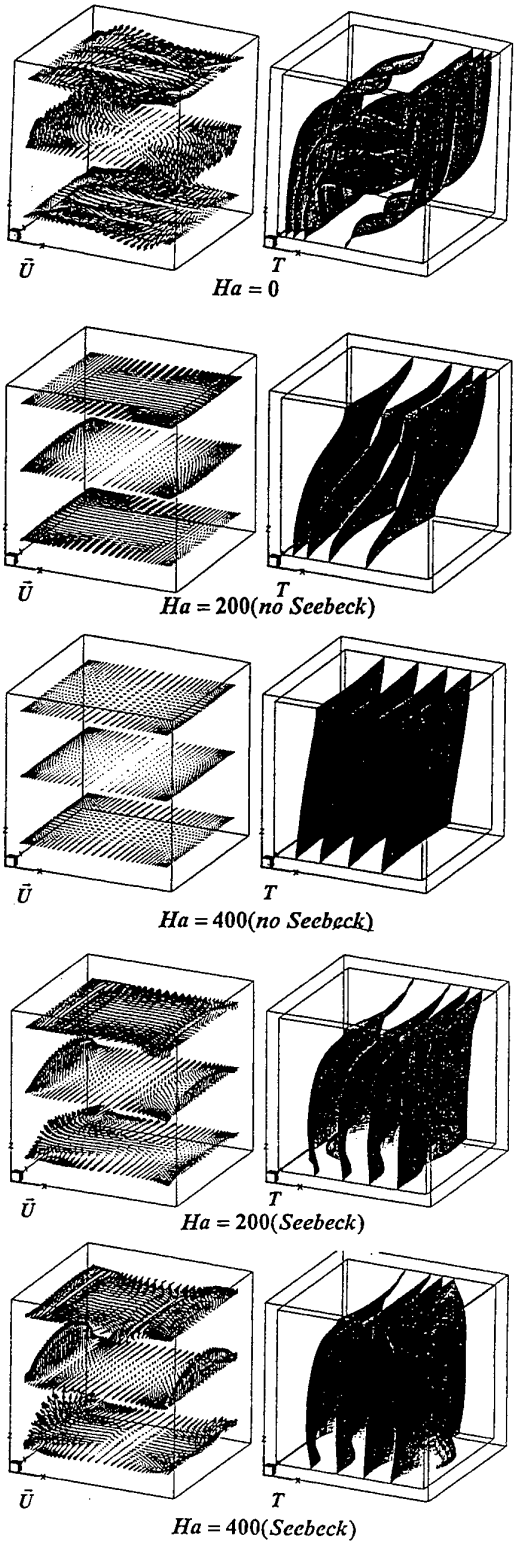

Fig. 2 Computed velocity vectors and isothermal planes

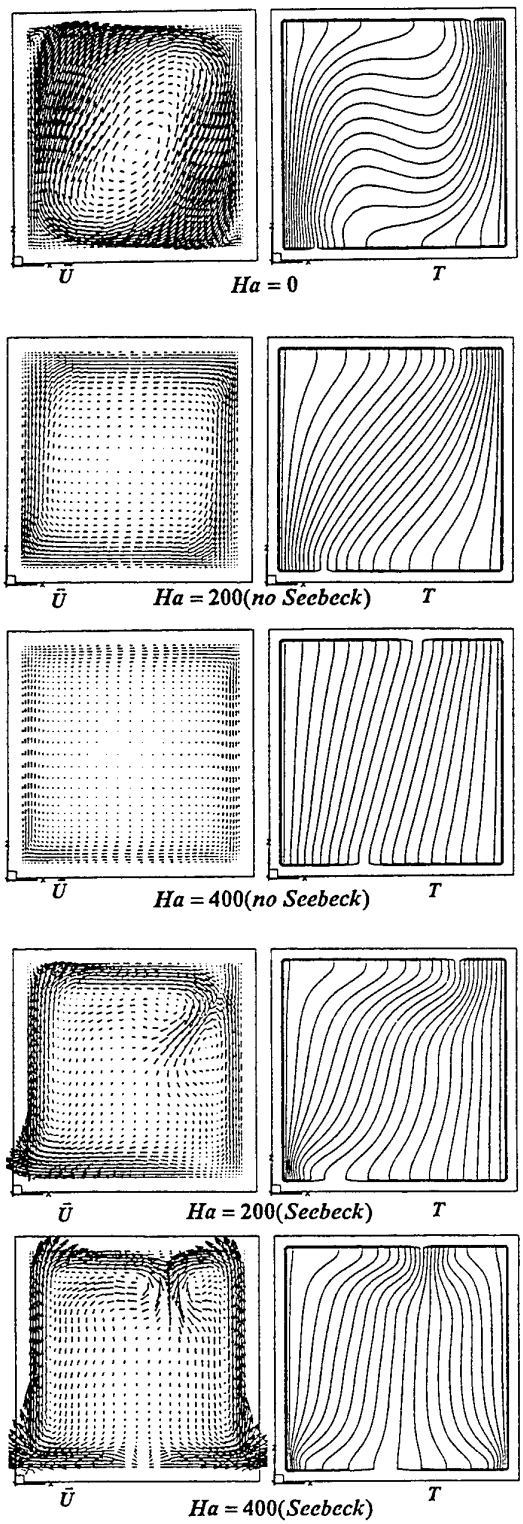

Fig. 3 Vertical side view of the velocity vectors and isotherms

top of the cold wall and meets the upward flow along the cold wall and turns to the core region. This current finally arrives at the bottom of the heated wall with fluctuating flow. At Ha = 400, the upward flows along the heated and cooled walls meet at the top wall at about 30% shifted to the cold wall and descends downward. The downward flow are rather aligned in the core region and separated at the bottom center.

3.3 Local Nusselt Number

Figure 4 shows distribution of the local Nusselt number on the hot wall for all cases studied. The average Nusselt numbers corresponding to these distributions are summarized in Table 1. At Ha = 0, the convection is time-dependent and vortex streets appear to give four small rolls near the bottom of the hot wall. This is due to characteristics of the natural convection of low Prandtl number fluid. When the Seebeck effect is not considered, the local Nusselt number becomes almost uniform. Under the Seebeck effect a large spot of the local Nusselt number near the bottom of the hot wall appear at Ha = 200 and 400 due to the cold current of the flow along the bottom wall as seen in Figs. 2 and 3.

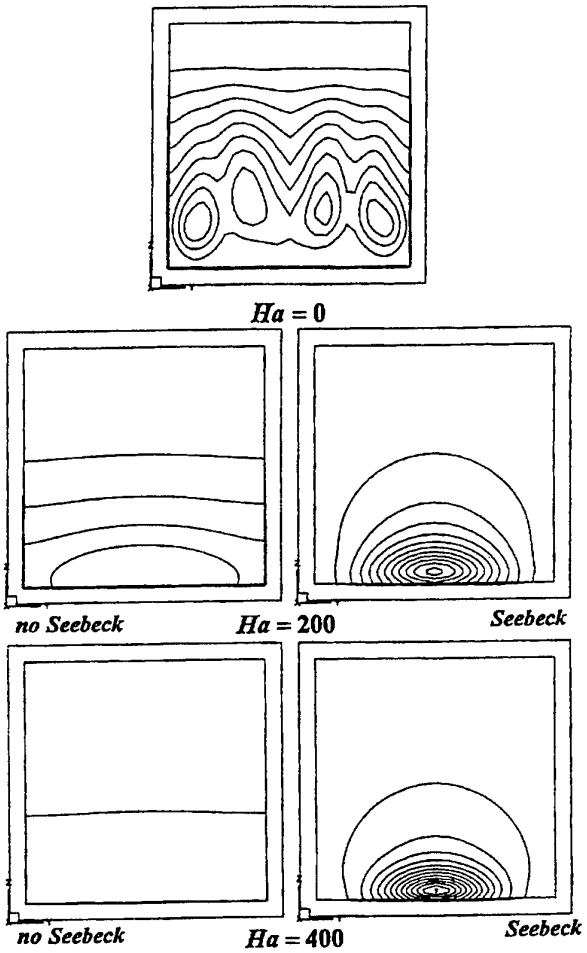

Fig. 4 Contour maps of the local Nusselt number over a hot wall

3.4 Long Term Streak Lines

The convection can be sometimes better demonstrated by the long term streak lines and presented in Fig. 5. At Ha = 0, the streak lines are alternately dense and sparse in the Y-direction which corresponds to that of Fig. 2. When the Seebeck effect is not considered, streak lines are almost equivalent to that of the two-dimensional flow both at Ha = 200 and 400. When the Seebeck effect is considered, the streak lines are complicated and separated to those on the side of hot wall and the cold wall. Depending on the initial point, strong three-dimensional movement of the streak lines in the Y-directional coordinate is apparent.

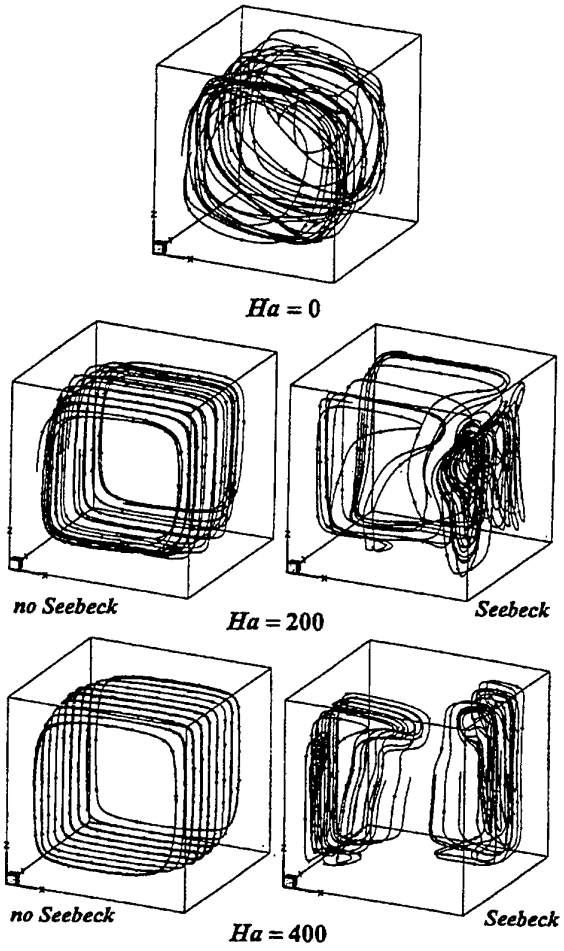

Fig. 5 Long term streak lines for each case studied

4. CONCLUSIONS

Mathematical model for the Seebeck convection was derived and numerically computed for the convection of liquid metal with and without the Seebeck effect under the magnetic field. The convections are quite different from that without a magnetic field. Seebeck effect is quite complicated to introduce the upward flow both along the hot and cold walls, and the average Nusselt number differs depending on the Hartmann number.

REFERENCES

1. J. A. Shercliff, Thermoelectric magnetohydrodynamics, J. Fluid Mech., vol. 91, pp.231-251, (1979).
2. L. L. Zheng and D. J. Larsen, Jr., Thermoelectric effects on interface demarcation and directional solidification of bismuth, J. Crystal Growth, vol.180, pp. 293-304, (1997).

NOMENCLATURE

b	magnetic induction	$[T = kg/(s^2 \cdot A)]$	**B**	$= b/b_0$	[-]
b_0	uniform magnetic induction in the y-direction	$[T = kg/(s^2 \cdot A)]$	C_m	$= \sigma_w / \sigma_f$	[-]
			C_p	specific heat of fluid	$[J/(kg \cdot K)]$

e	electric field intensity	[V/m = m·kg/(s^3·A)]
e_0	$= u_0 b_0$	[V/m = m·kg/(s^3·A)]
E	$= e/e_0$	[-]
g	acceleration due to gravity	[m/s^2]
Ha	$= (\sigma_f/\mu)^{1/2}\, b_0 l$	[-]
J	$= j/j_0$	[-]
j	electric current density	[A/m^2]
j_0	$= \sigma_f u_0 b_0$	[A/m^2]
L	$= l/x_0$	[-]
l	internal length of a cubic enclosure	[m]
Pr	$= \nu/\alpha$	[-]
p	pressure	[Pa]
p_0	$= \rho\alpha^2/x_0^2$	[Pa]
Ra	$= g\beta(\theta_h-\theta_c)l^3/(\alpha\nu)$	[-]
S_f	$= s_f\,(\theta_h-\theta_c)/(\alpha b_0)$	[-]
s_f	Seebeck coefficient of fluid	[V/K]
s_w	Seebeck coefficient of wall	[V/K]
T	$= (\theta-\theta_0)/(\theta_h-\theta_c)$	[K]
t	= time	[s]
t_0	$= x_0^2/\alpha$	[s]
U	$= u/u_0$	[-]
u	x-directional velocity component	[m/s]
u_0	$= \alpha/x_0$	[m/s]
V	$= v/u_0$	[-]
v	y-directional velocity component	[m/s]
W	$= w/u_0$	[-]
w	z-directional velocity component	[m/s]
X	$= x/x_0$	[-]
x	coordinate	[m]
x_0	$= Ra^{-1/3}\, l$	[m]
Y	$= y/x_0$	[-]
y	coordinate	[m]
Z	$= z/x_0$	[-]
z	coordinate	[m]

GREEK LETTERS

α	thermal diffusivity	[m^2/s]
β	volumetric coefficient of expansion	[1/K]
θ	temperature	[K]
θ_0	$= (\theta_h+\theta_c)/2$	[K]
θ_h	hot wall temperature	[K]
θ_c	cold wall temperature	[K]
ν	kinematic viscosity	[m^2/s]
ρ	density of fluid	[kg/m^3]
σ_f	electric conductivity of fluid	[1/(Ω·m)]
σ_w	electric conductivity of wall	[1/(Ω·m)]
τ	$= t/t_0$	[-]
Φ	$= T - 0.5 + X/L$	[-]
Ψ_e	$= \psi_e/\psi_{e0}$	[-]
ψ_e	electric scalar potential	[V]
ψ_{e0}	$= \alpha b_0$	[V]

IMPROVEMENT OF THE BASIC CORRELATING EQUATIONS AND TRANSITION CRITERIA OF NATURAL CONVECTION HEAT TRANSFER

Shi-Ming Yang
Institute of Engineering Thermophysics and Energy
Shanghai Jiaotong University
Fax: (0086-21)-6282-0892

Keywords: natural convection, heat transfer, correlating equations, transition criterion

ABSTRACT. In this paper, improvements in the basic physical laws of natural convection heat transfer were implemented in two major respects through incorporating recent research findings in this field. A preferred transition criterion was adopted to correlate all the experimental data in this paper. Since the transition of correlation are primarily flow stability problems, the Grashof number, instead of the Rayleigh number, was found to be the preferred criterion. Furthermore, in the case of natural convection heat transfer from horizontal cylinder, a series of experimental data in the high Rayleigh number regions were available recently. These data made it possible to establish new reliable correlation and also to test the validity of previous correlation. It is concluded that the previous correlation for horizontal cylinder in high Rayleigh number regions was based on unreliable experimental results. The transition of laminar correlation for horizontal cylinder occurred at much higher values of Rayleigh number than the previous recommendation. In the case of natural convection teat transfer from vertical plate, more accurate property values for air under pressurized conditions are now available. This made it possible to re-plot the reliable data of Saunders. From this result and experimental result of Warner and Arpaci, a new set of basic correlation in natural convection heat transfer for laminar, transitional and turbulent regimes are recommended. These recommendations reflect a better understanding of the basic physical laws in the field of heat convection.

1.INTRODUCTION

In the literature, the recommended laminar-turbulent transition criterion was Ra $=10^7$ for air for horizontal cylinder, and Ra $=10^9$ for vertical plate for all fluids. Experimental evidences, however, disagree with these recommendations. For vertical surface, the laminar-turbulent transition was found at Ra $=4\times10^{10}$ for ethylene glycol [1]. For the horizontal cylinder, laminar-turbulent criteria of Ra $=4.0\times10^8$ for air and Ra $=3.3\times10^9$ for water were reported [4]. Bejan and Lage [2] after re-examining a number of previous works on this issue claim that Gr number is a better predictive parameter of transition than the previously used Ra number. For the vertical plate, they concluded that the transition for local Nu number occur at an approximately constant local Grashof number Gr_x of 10^9 irrespective of the fluid. It is proper to point out that transition phenomena primarily are flow stability problems. These problems are controlled by the Navier-Stokes equation of the fluid flow. Dimensional analysis of the Navier-Stokes equation for natural convection yields the Grashof number as the relevant dimensionless number for flow stability: Similar to the role of Re number as the stability criteria in forced convection heat transfer, the Gr number is the proper stability criterion in natural convection heat transfer from the theoretical grounds. The adoption of Gr number as the transition criteria throughout this paper results a substantial improvement of our understanding on the basic laws of natural convection heat transfer. To meet the needs of engineering predictions, revision of the previous transition criteria and correlation equations for both vertical plate and horizontal cylinder are necessary. It is the object of this paper to formulate more reasonable scheme of he recommendations of the transition criteria and correlating equations based on the recent progress on this issue.

2. HORIZONTAL CYLINDER

In the range of Ra $=10^4$ -10^7. the recommended correlating equation of Morgan [3];

$$Nu=0.48Ra^{1/4} \tag{1}$$

remains to be the best correlation for air in this range. To accommodate liquids and oils, a physical property correction term is required. Various forms of correction terms have been found to be effective [7]: $(Pr_f/Pr_w)^{0.11}$,

$Pr^{0.047}$and $(Pr_f/Pr_w)^{1/4}$. The following correlation is recommended for all media:

$$Nu=0.48Ra^{1/4}(Pr_F/Pr_W)^{0.11} \quad (2)$$

Morgan's recommendation for the transition for the laminar regime at Ra $=10^7$ and the turbulent correlation beyond this transition, however, are questionable. The data bases of Morgan;s recommendation for $Ra>10^7$ are put into close scrutiny. No air data with $Ra>1.1\times10^7$ and water data with $Ra>10^9$ were included in the data bases. In addition to the criticism that Morgan had included liquid data without taking into account the physical property correction term, the inclusion of Ackermann's data with effect of boiling over predicts the Nu values. Only part of the Ackermann's data belongs to the natural convection category [5]. It may be pointed out for instance that for the case with heating power of 1199 kw, among the 7 data points reported, only 2 points belong to the natural convection category. The rest 5 points with wall temperature of 102.0-106.0^{0}C, all above the boiling point, exhibit the effect of boiling on a α -- Δt plot [8]. It has been shown in [7], excluding all data with the effect of boiling, the Ackermann's data follow the laminar correlation nicely. Overlooking of this necessary discrimination was the cause to obtain an erroneous early criterion of transition.

In order to establish the correct criteria of transitions, extension of experimental ranges to higher Ra number regions are required. The author of this paper and his colleagues conducted in recent years a series of experimental researches in the high Ra number regions [4-7]. Physical details of these experiments are given in Table 1. D and L denotes diameter and length of cylinder, D_c denotes the clearance distance above the cylinder in test. It may be pointed out that the recent summary of experimental research literature survey by Morgan [9] will be more comprehensive if these high Ra number literatures are incorporated in it. The results of these experimental studies can be summarized as follows:

Table 1. Physical Details of Experiments

Reference	Pressure (atm)	D(mm)	L/D	D_c/D
Yang [4]	1	210	7	28,3.8
Yang [5]	1	280, 500	7, 2	17, 12

Laminar-Transitional Criterion for Air

It is well known that no physical property correction factors are involved in air correlation. To take advantage of the simplicity of the air correlation, a series of experimental investigations in air with large diameter cylinders (D=210,280,and 500mm) were conducted. An extension of Ra number more than an order of magnitude was achieved and the highest Ra number attained was 6.0×10^8 . In Fig.1, the air data is shown in open circles. The

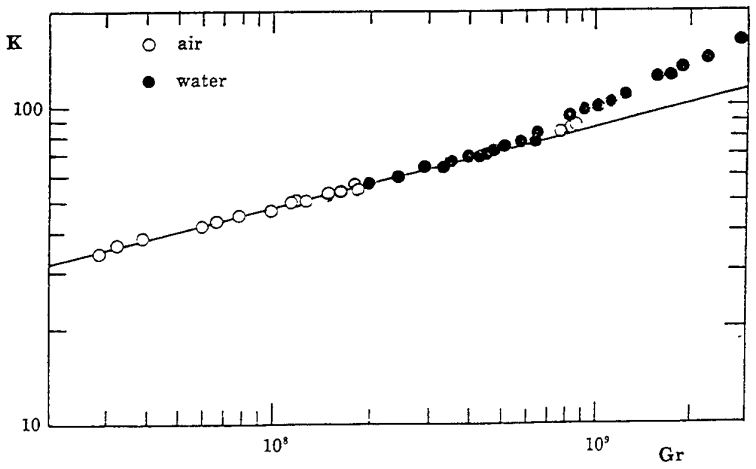

Fig. 1 K verses Gr plot

ordinate K denotes $NuPr^{-0.25}$ $(Pr_f/Pr_w)^{-0.11}$. The lower line denotes the laminar correlation of equation (2). A

distinct feature of the average heat transfer correlation for horizontal cylinder is that every data point on the Nu-Ra graph represents the average heat transfer of the whole circumference of the cylinder. Therefore, the change of slope at the critical points will be gradual and can be determined easily from either deviating or approaching the laminar or the turbulent correlation. The last few data points for air on Fig.1 were located in the early stage of transition. This facilitates the determination of the transition Gr number. A laminar-transitional criterion was in this way established at $Gr=5.76\times10^8$.

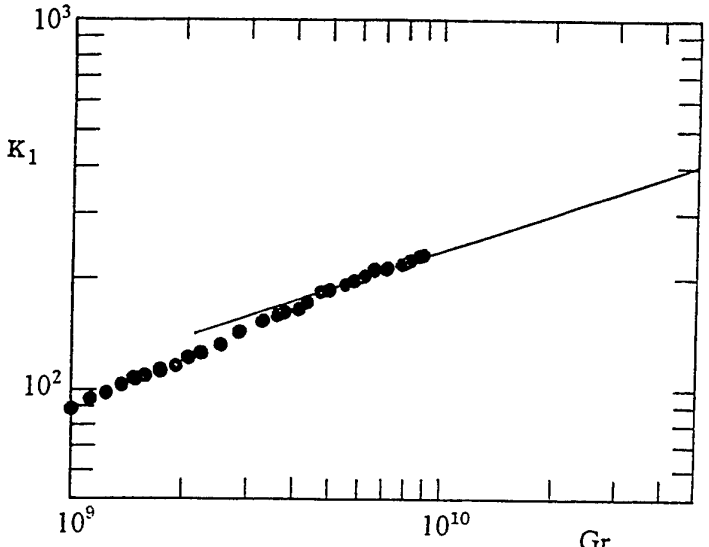

Fig. 2 K_1 versus Gr plot

Laminar-Transitional Criterion for Different Media

To test the applicability of the laminar-transitional criterion for liquids as well as to establish the transitional-turbulent criterion, experimental investigations in water with large diameter cylinders (D=210mm) were conducted. The maximum Ra number attained was 2.84×10^{10} . An extension of Ra number more than three orders of magnitude above 10^7 was achieved. To the knowledge of the author, this is the first set of data covering the whole transitional regime for the horizontal cylinder. The solid dots in Fig.1 and Fig.2 denote the water data. The ordinate of Fig.2 is K_1, which denotes $NuPr^{-1/3}(Pr_f/Pr_w)^{-0.11}$. As can be seen from the figure, the end of the laminar correlation for water has the same criterion in terms of Gr number ,$Gr=5.76\times10^8$. The general applicability of both the air and water data of the same laminar-transitional criterion demonstrates the universal role of the Gr number in the transition phenomena. Experimental results fail to support the Morgan's recommendation of transition at $Ra=10^7$ for air or the McAdams' assertion that laminar-turbulent transition at $Ra=10^9$ for all media. Direct experimental confirmation of transition criterion for oil is welcome. At present, this paper tentatively recommends the new laminar-transitional criterion to be applicable to different media.

Transitional-Turbulent Criterion

As is well known, Nu number in the turbulent correlation of heat transfer is proportional to the one third power of Ra number. The entrance into the one third power of the Ra number regime will be taken a the transitional-turbulent criterion. In this way , the transitional-turbulent criterion was determined from Fif.2 as $Gr=4.65\times10^9$. Although experimental data for other media are welcome, this value will be tentatively recommended as the transitional-turbulent transition criterion for all media. The turbulent correlation shown as the line in Fig.2 has the following form:

$$Nu=0.11Ra^{1/3}(Pr_f/Pr_w)^{0.11} \qquad (3)$$

This is an improvement of a previous plot in [4] with the property variation parameter incorporated in the abscissa. This correlation is in agreement with the re-plotted turbulent correlation on heat transfer for vertical plate, as will be seen in the next section of this paper.

Transitional Region

There is always a transitional region in between the end of laminar correlation and the beginning of the turbulent correlation. The slop of correlation in transitional region is larger than 1/3. Neglect of this region will over-simplify the actual situation and lead to a so-called laminar-turbulent criterion. The following tentative heat transfer correlation was recommended for this region:

$$Nu=0.0165Ra^{0.42}(Pr_f/Pr_w)^{0.11} \quad (4)$$

In addition, the recommended new C and n values in the typical correlating equation for air:

$$Nu=CRa^n \quad (5)$$

are listed in Table 2.

Table 2. Recommended C And N Values In Equation (5)

Geometry	Gr range	C	n
Horizontal Cylinder	1.43×10^4--5.76×10^8	0.48	1/4
	5.76×10^8--4.65×10^9	0.0165	0.42
	$>4.65\times10^9$	0.11	1/3
Vertical Plate	1.43×10^4--3×10^9	0.59	1/4
	3×10^9--2×10^{10}	0.0292	0.39
	$>2\times10^{10}$	0.11	1/3

3. VERTICAL PLATE

Similar analysis for the vertical plate case will be considered in the present section. To take advantage of the simplicity of the air correlation, average heat transfer data for air will be first considered. It is fortunate that there are two sets of good average heat transfer data in high Ra number regions, they are the data of Saunders [11] and the data of Warner and Arpaci [12]. The physical property values used by Saunders, however, need to be revised. For instance, the heat conductivity at 43^0C under atmospheric pressure, 0.0239W/m ^{0}C was used, which is 13% lower than the more reliable new values in [13]. A re-plot of Saunders' data using new physical property values giver in [13] was conducted in [6]. The new plot is shown in Fig.3. As can be seen from the figure, the laminar region follows the McAdams correlation:

$$Nu=0.59Ra^{1/4} \quad (6)$$

nicely. In the turbulent region, the new correlation is:

$$Nu=0.11Ra^{1/3} \quad (7)$$

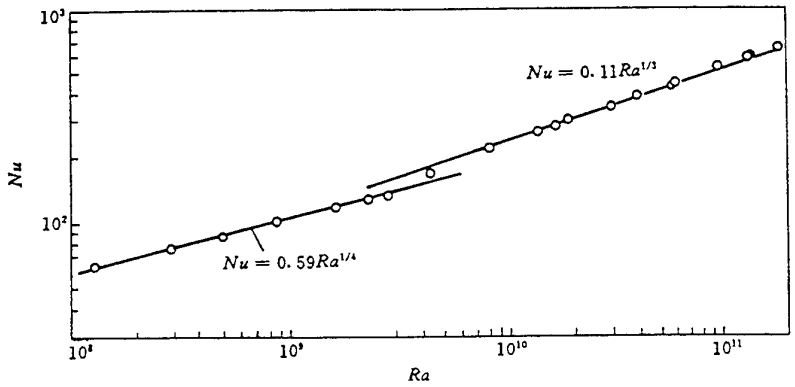

Fig. 3. A re-plot of Saunders' air data

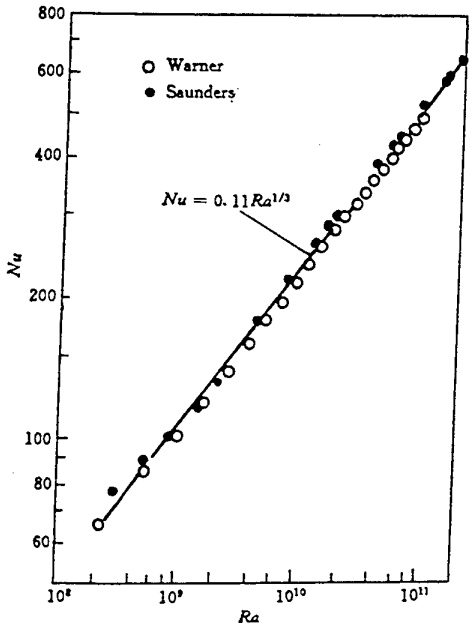

Fig. 4 Correlation of data from different sources in the turbulent region

The constant is 10 percent larger than the previous turbulent correlation. The experimental results of Siebers also support Equation (7) in the turbulent region [14]. Siebers' data extends to a Ra number as high as 1.4×10^{12} . Fig.3 and Fig.4 provide also the basis for the determination of the transition criteria. In terms of the preferred Gr number, the laminar-transitional criterion is3×10^{9}. This value is in general agreement of the recommendation of Saunders. It is also consistent with the findings on the criterion on local Gr number by Cheesewright [15] Pirovano [16] for air and Min [17] for water. This criterion is also in consistent with the experimental findings of Farmer and McKie on oil with Pr number of 200 [10]. They found that at Ra $=6\times10^{10}$, which corresponds to Gr$=3\times10^{8}$, oil data remain following the laminar correlation . Siebers [14] identified the laminar-transitional criterion for local Nusselt number Nu at Ra$=5\times10^{8}$. Since sufficient allowances are needed for the average Nusselt number to reflect the effect of local disturbances, the difference between the local and the average criteria seems to be reasonable. The transition-turbulent criterion is identified at Gr$=2\times10^{10}$. This value is also in consistent with the findings of Cheesewright [15] and Min [17] on the criteria for local Gr numbers. Experimental data in the transitional region are in fair agreement with the connecting line between the laminar-transitional criterion and the transitional-turbulent criterion. The following tentative correlation for the transitional region is recommended:

$$Nu=0.0292Ra^{0.39} \tag{8}$$

A summary of the recommended correlation and criteria of transitions for air is also shown in Table2. Incorporating proper physical property correction factors, Eq . 6-8 can be extended to cover all media.

4.CONCLUDING REMARKS

Progress in recent years in the following three respects provided the basis to improve the basic correlating equations and transition criteria for natural convection heat transfer. Much needed experimental data in high Ra number regions had been reported. Gr number had been identified as the preferred transition criterion. More accurate property values are available. A more reasonable new scheme of correlating equations and transition criteria are recommended in this paper to supersede the previous recommendations.

REFERENCES

1. Y. S. Touloukian,, G. A. Hawkins and M. Jakob, Heat Transfer by Free Convection from Heated Surfaces to

Liquids, Trans ASME,v. 70, p.13 , (1948).
2. A. Bejan and J. L. Lage, The Pr Number Effect on the Transition in Natural Convection along a Vertical Surface, J. Heat Transfer.v .112, pp.787-790, (1990).
3 V. T. Morgan, The Overall Convection Heat Transfer from Smooth Circular Cylinders, in *Advances in Heat Transfer*, v. 11. Eds.J. P. Hartnett and T. F. Irvine, Jr, Academic press, New York, pp. 199-264,(1975).
4. S. M. Yang and Z. Z. Zhang, An Experimental Study of Natural Convection Heat Transfer from a Horizontal Cylinder in High Rayleigh Number laminar and Turbulent Regions, *Proceedings of the 10th. Intern.Heat Transfer Conf,*v 7,pp.185-190.(1994).
5. S. M . Yang and C. J. Jiang, Criterion of Transition to Transitional Correlation of Natural Convection. Heat Transfer from Horizontal Cylinder in Air, *Heat Transfer Science and Technology.* Ed. B X. Wang, Higher Education Press, Beijing, pp.181-186, (1996).
6. S. M. Yang, A Review of Progress on the Fundamental Physical Laws for Natural Convection ,*Heat Transfer Research and Progress*, Eds. W. Q. Tao et al , Higher Education Press, Beijing, pp.17-26, (1995)
7. Z. Z. Zhang and S. M. Yang, Experimental Study of High Rayleigh Number Natural Convection Heat Transfer from a Horizontal Cylinder, J. Engineering Thermophysics, v.16, pp.444-449,(1995)
8. G.Ackermann, Z. Forsch. Gebiete Ingenieurw, v .3 pp.42-50,(1932)
9. V. T .Morgan, Heat Transfer by Natural Convection from a Horizontal Isothermal Circular Cylinder in Air, Heat Transfer Engineering, v .18, pp25-33,(1997)
10. W. P. Farmer and W. T. Mckie, Natural Convection from a Vertical Isothermal Surface in Oil, ASME Paper No.64-WA/HT-12, (1964)
11. O. A. Saunders, The Effect of Pressure upon Natural Convection in Air, Proceedings Royal Society (London), Series A, v. 157, pp.287-291,(1936).
12 C.Y. Warner and V. S. Arpaci, An Experimental Investigation of Turbulent Natural Convection in Air at Low Pressure along a Vertical Heated Flat Plate, Intern.J. .Heat mass Transfer, v11.,pp.397—406, (1968)
13. N. B .Vargaftik, *Tables on the Thermophysical Properties of liquids and Gases* ,2nd Ed, Wiley, New York (1975).
14. D.L.Siebers, R. F. Moffatt and R. G.Schwind, Experimental Variable Properties Natural Convection from a Large Vertical Flat Surface, J. Heat Transfer,v.107,pp.124-132,(1985)
15. R. Cheesewright, Turbulent Natural Convection from a Vertical Plane Surface, J. Heat Transfer,v.90, pp. 1-8,(1968)
16. A. Pirovano, S. Viannay, and M. Jannot, Convection Naturelle En Regime Turbulent LeLong D"Une Plaque Verticale, *Proceedings 4th Intern. Heat transfer Conf, Paris -Versaillem* France, v. 4th, Paper NC1.8, (1970)..
17. G.Y .Min, Research on the Process of Natural Convection Heat Transfer in Open Space for Different Fluids, Chinese Journal of Mechanical Engineering,v12, No 2, pp.85-96, (1964).

HEAT TRANSFER ENHANCEMENT OF HORIZONTAL CYLINDER BY ULTRASOUND

Ning ZHU
Department of Mechanical Engineering
Shizuoka Institute of Science & Technology
Email:zhuning@me.sist.ac.jp; Fax:(81)-538-450120

Keywords: heat transfer enhancement, ultrasonic, cavitation

ABSTRACT. Heat transfer enhancement by using ultrasound is treated as a potentially useful technology because it can be electrically controlled and realized with nondestructive method. The purpose of the present paper is to make clear the enhancement mechanism of natural convective heat transfer in the ultrasonic field in terms of cavitation. An experimental system set-up was established to fulfil this purpose. It is found that with the irradiation of the ultrasound, the heat transfer coefficient is increased to some different extent. The maxim increase ratio reaches 3 times at the loop point of the standing wave where cavitation bubbles are easily generated.

INTRODUCTION

Heat transfer enhancement by using ultrasound is treated as a potentially useful technology because it can be electrically controlled and realized with nondestructive method. Some papers[1,2] have been published to explain the reasons of ultrasound wave's influence on heat transfer process. Generally speaking, the reasons that lead to heat transfer enhancement by ultrasound lie in (1) cavitation; (2) acoustic streaming. Either cavitation or acoustic streaming can stir the flow field near the heat transfer surface and make the temperature boundary become thin. Since cavitation comes from the decreasing sound pressure amplitude inside the sound field and is easily appeared at the loop point of the standing wave[3], so at the present paper, the influence of the cavitation on the heat transfer enhancement is focused on and experimentally investigated. Measured local temperature profile and heat transfer coefficient profile along the peripheral direction for a heated horizontal cylinder were compared. Besides, an ultrasonic sensor was used to visualize the experimental sound field. It is found that for the heated horizontal cylinder under our experimental condition, a uniform heat transfer coefficient profile can be obtained because the local heat transfer coefficients are increased to different extent according to their geometric locations in the sound field.

EXPERIMENTAL SYSTEM AND METHOD

The experimental system set-up for enhancing heat transfer by using ultrasound shown in Fig.1 is consisted of an

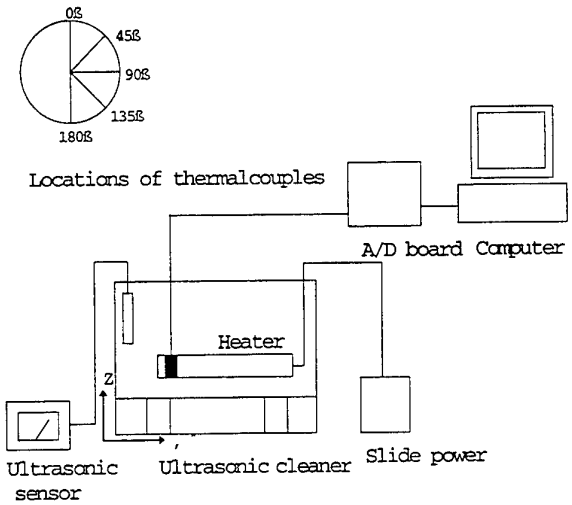

Fig.1 Experimental system for heat transfer enhancement by using ultrasound

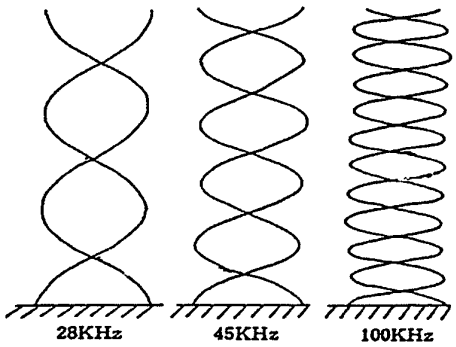

Fig.2 Typical standing waves inside sound field of ultrasound cleaner

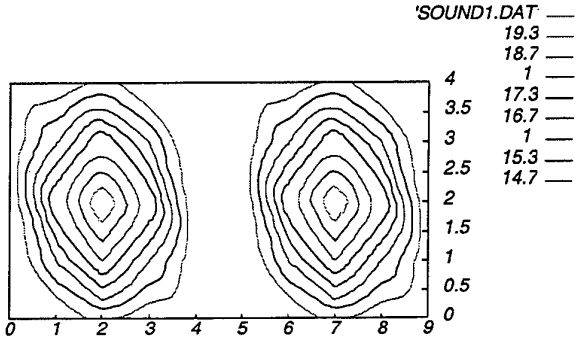

Fig.3 Visualization of sound field of ultrasound cleaner (f=28kHz)

Ultrasound cleaner(resonant frequencies are 28kHz, 45kHz and 100kHz) with 2 vibrators equipped, a ceramic cylinder heater (D=12.3 mm, L=170mm, P=200W), a slide power source, an ultrasonic sensor, a piece of A/D board and a computer.

As for sound visualization experiment, the ultrasonic sensor is inserted into the sound field to measure the sound pressure of the sound field. The vertical sound pressure change inside the ultrasonic cleaner is also measured to confirm the existence of the standing wave and the position of the loop point and node point. In order to check the happening of cavitation inside the ultrasound cleaner, the thin film of aluminum is employed. The aluminum film is immersed inside the cleaner, then with the irradiation of the ultrasound; part of the film are eroded where the cavitation occurs.

As for heat transfer enhancement experiment, a ceramic horizontal heater is immersed inside the ultrasonic cleaner. As the wave length for the present experiment is 53.7mm(f=28kH), the heater is immersed inside the sound field with its bottom side being at the position of the 1/4 wave length where the node point is located.

5 pairs of thermocouples are placed along the peripheral direction of the heater and their locations are shown in Fig.1. Heat transfer enhancement experiment is conducted when the ultrasound (f=28kHz) is employed. Temperature signals from thermocouples are transferred to the computer through the A/D board. Heat transfer coefficient is calculated on the condition of equal heat flux.

RESULTS AND DISCUSSIONS

Fig2 shows the typical standing waves under the frequencies of 28kHz, 45kHz and 100kHz. With the decreased frequency, the wavelength increases accordingly. The visualization result of the sound field with the irradiation of ultrasound of 28kHz is shown in Fig.3. From Fig.3, it is clear that the positions of the maximum sound pressure are consistent with the positions of the 2 vibrator.

Fig.4 depicts the vertical sound pressure change inside the sound field near the position of the vibrator. As the loop points and node points appear periodically, thus the existence of the standing wave is confirmed.

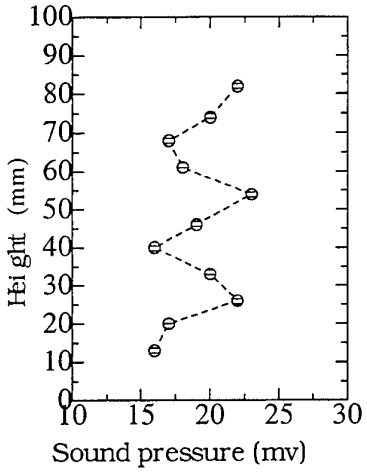

Fig.4 Vertical sound pressure profile at x=105 mm

Figs 5,6,7 are the results of the confirmation of cavitation. It is clear that the cavitation obviously occurred when resonant frequency is 28kHz, and at the frequency of 100kHz, the cavitation virtually could not be confirmed. Based on these facts, the following heat transfer experiment is conducted on the condition of 28kHz.

Fig5. Confirmation of cavitation at frequency of 28kHz

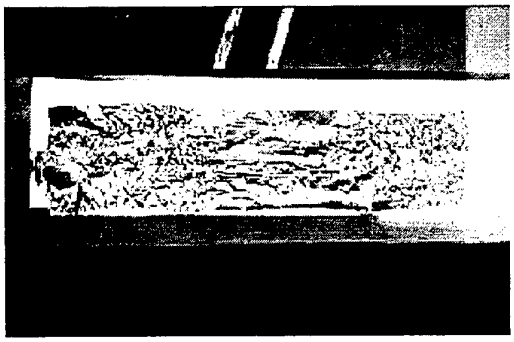

Fig6. Confirmation of cavitation at frequency of 45kHz

Fig7. Confirmation of cavitation at frequency of 100kHz

Figs.8 and 9 show the comparison results of the local temperature profile and heat transfer coefficient profiles with/without the ultrasound irradiation. The results that without ultrasound irradiation, the measured temperature profile and heat transfer coefficients profile along the peripheral direction of the horizontal cylinder agrees with the theoretical values have been confirmed from Figs.8 and 9. Further, it is known that the temperature value at $\theta=0^0$

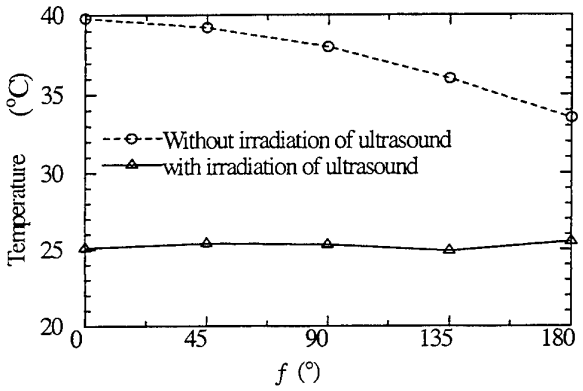

Fig.8 Comparison of local temperature profiles along peripheral direction

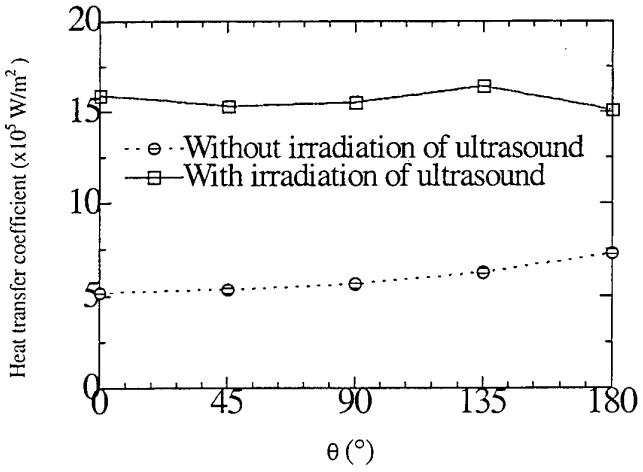

Fig.9 Comparison of local heat transfer coefficient profiles along peripheral direction

decreases most drastically due to its location at the loop of the standing wave where cavitation can most easily happen and the maximum heat transfer enhancement ratio reaches 3 times. On the other hand, the temperature value at $\theta=180^0$ decreases slightly because of its location at the node of the standing wave of the ultrasound.

CONCLUTIONS

The following condusions can be drawn:

(1) The ultrasound field is visualized by using the ultrasonic sensor.

(2) The existence of the standing wave is confirmed.

(3) With the irradiation of the ultrasound, the heat transfer coefficients along the peripheral direction of the horizontal cylinder are increased to some different extent according to the location inside the sound field. The maxim increase ratio reaches 3 times at the loop point of the standing wave.

(4) With the proper control of the sound field or the geometric position of the heat transfer surface inside the sound field, the heat transfer enhancement can be intellectually controlled.

ACKNOWLEDGMENTS

This work was performed with the financial support from the foundation of Shizuoka Institute of Science & Technology, for which the authors are very grateful. The authors also express sincere thanks to undergraduate students N. NAGOJI and T. SUGIMOTO for their efforts in doing this experiment.

REFERENCE

1. S.NOMURA, et al, Proc. of 33rd National Heat Transfer Symposium of Japan, pp.383-384 (1996).
2. Y.IDA, et al., Proc. of 30th National Heat Transfer Symposium of Japan, pp. 754 (1993).
3. T.Mitui, Acoustics Engineering, Syoukoudou, (1988).

A THERMAL DESIGN APPROACH FOR NATURAL AIR COOLED ELECTRONICS EQUIPMENT CASINGS

Masaru Ishizuka
Mechanical Systems Laboratory
Research and Development Center
Toshiba Corporation.
Email:masaru.ishiduka@toshiba.co.jp ,Fax:81-(44)-520-2057

Keywords: thermal design, natural convection, electronic equipment, air-cooled casing, and chimney effect, flow resistance coefficient

ABSTRACT. This paper describes a practical thermal design approach to natural air-cooled electronic equipment casings. A set of simplified equations for the thermal design of natural air-cooled electronic equipment casings has been proposed. The proposed set of the equations satisfied the demand of practical air cooling systems, since it takes account of the factors such as stack effect, air flow resistance, heat transfer due to natural convection and so on. The effects of the outlet area and the location of the main power dissipation unit on the natural cooling capability of electronic equipment casings were studied using a set of equations. The results have shown that a uniform temperature distribution could be achieved in the case of placing the main power dissipation unit at the bottom of the casing. It has also been suggested that the outlet vent area should be limited within some threshold value so that the value of heat removed from the casing surface would be higher than that from the outlet vent.

1. INTRODUCTION

In recent years, the increasing demand of compactness and high-speed performance of electronic equipment had led to an increasing trend of power dissipation density. Therefore, suitable cooling techniques to the thermal designing of electronic equipment need to be developed. Several research reports on electronic equipment cooling are available in the literature sources [1-5]. In these studies it can be observed that air-cooling is getting one of the important cooling techniques, since most of the electronic equipment are cooled by air convection. Although fan cooling is most widely used in the air cooling techniques, the noise generated by the fan is publicly criticized. As a result, cooling on the basis of natural convection is one of the attractive approaches. However, only limited data on natural convection, which can be used in the practical design of electronic equipment. Noronha[6] studied the effect of the component locations in cabinets to achieve maximum natural cooling efficiency. Guglielmini et al[7] have reported on the natural air cooling of electronic cards in ventilated enclosures. Ishizuka et al.[8] proposed an approach using a simplified set of equations which represent the cooling capability through a natural air-cooled electronic equipment casings. However, detailed discussions on derivation of the set of equations were not made in that paper. Therefore, in the present work, an attempt has been made to study the effects of the outlet vent area and power dissipation unit location on the natural air-cooled electronic equipment casings.

2. SET OF EQUATIONS

Ishizuka et al. [8]has proposed the following set of equations for practical applications to the thermal designing of electronic equipment.

$$Q=Q_1+Q_2 =1.78S_{eq}\cdot \Delta T_m^{1.25}+300Ao(h/K)^{0.5}\Delta T_o^{1.5} \quad (1)$$

$$K=2.5(1-\beta)/\beta^2 \quad (2)$$

$$\Delta T_0=1.3\Delta T_m \quad (3)$$

$$S_{eq}= S_{top}+ S_{side}+ 1/2S_{bottom} \quad (4)$$

where, h denotes the weighted mean distance from the heater position to the outlet and K is the flow resistance

coefficient resulted from the air passage obstruction at the outlet. Strictly speaking, the flow resistance coefficient is a function of the Reynolds number and porosity coefficient. However, since the effect of the Reynolds number on K is weaker than that of the porosity coefficient β, K can be approximated as a function of the porosity coefficient. Eq. (2) was obtained by Ishizuka at al.[9]. Therefore, Eq.(2) can be considered to be reasonable for practical applications.

3. APPLICATIONS OF THE EQUATIONS

Equations (1),(2) and (3) were applied to practical equipment casings[8]. The results are shown below. The three casings in Table 1 were used as application examples. Casing C1 and C2 include a power unit at the bottom and three-stage(C1) or two -stage(C2) longitudinal PCBs (printed circuit boards) above the power unit. In either case, air-flow paths are provided between the PCBs. casing C1, Casing C2 and casing C3 are shown in Fig.1, 2 and 3, respectively. Other specifications for these three casings are shown in Table 1.

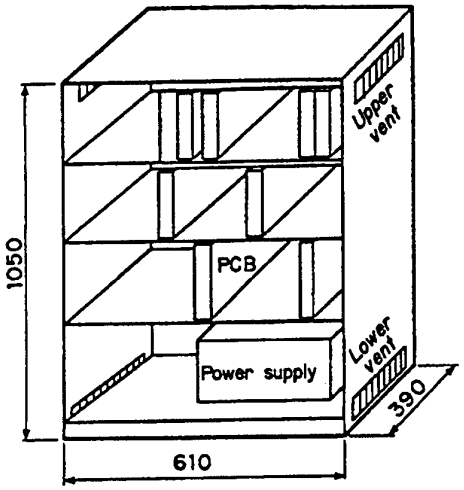

Fig. 1Casing C1

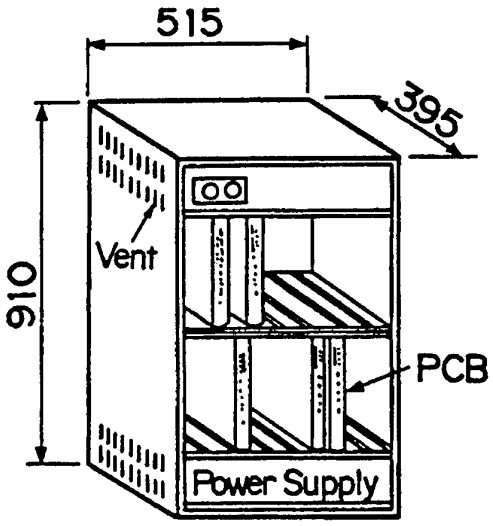

Fig.2 Casing C2

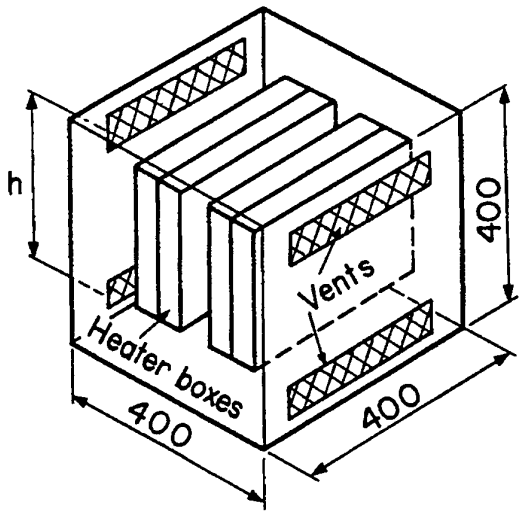

Fig. 3 Casing C3

Table 1 The size of the casings

Casting	Length (m)	Width (m)	Height (m)
C1	0.635	0.37	1.143
C2	0.514	0.395	0.910
C3	0.4	0.4	0.4

Note that the vent area A_o for casing C1 was adjusted by using a vinyl tape and that three vent area sizes were tested, A_o = 0.03, 0.02, and 0.012,m2 .The inlet vent areas were larger than the outlet areas for all of the three casings. As the chimney height, which is difficult to strictly define in practice, is defined as the distance from the upper surface of the power unit to the outlet (in casings C1 and C2) or the distance from the inlet to the outlet (in casing C3). Figure 4 shows a comparison between the predicted values and measured values. The measured value was obtained by averaging measurements at five points for each vent. The vertical axis (y-axis) shows the difference between the predicted value and the measured value, normalized by the measured value, while the horizontal axis (X-axis) represents power dissipation Q inside the casing. Varying their load conditions changed the power dissipation values of casings C1 and C2. In addition, it is seen that the individual supplied power values account for approximately 80 % when the load is small. The result in Fig.4 shows a good agreement between predictions and measurements (within 10 %). It is especially worth noting that Eq. (1) yields a considerably good approximate value, although the value K should be greatly affected by the casing structure. It is generally believed that a certain correction must be made to the chimney height in each application according to pertinent heater locations. In order to examine the inner temperature distribution, the temperature rise inside casing C2 is shown in Fig.5, as an example. It is observed in this figure that air heated by the power supply unit goes upward, promoting heat exchange with the casing surface, and is ejected to the outside stagnation at the upper inside space of the casing. The temperature distribution is well unified because of good inside ventilation. C= 1.2 is obtained from the measured temperature and Eq.(1), which confirms that the value evaluated by Eq.(3) is reasonable. It should be noted, however, that the set of Eqs.(1)-(4) is not for predicting the temperature rise inside the current electronic equipment but should be used for designing electronic equipment casings, which requires proper vent designing. This is emphasized because, In most vent designs, the conditions assumed in the introduction should be taken into consideration. In this regard, Eq.(1) is considered reasonable as a simple

equation for use in casing thermal design, since the chimney effect, flow resistance, and surface area effect are included in it.

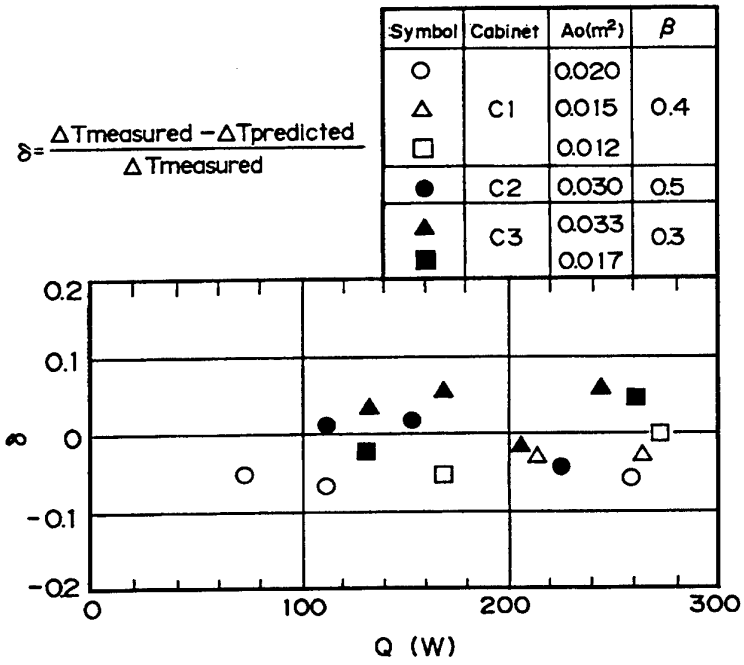

Fig. 4 Comparison between predicted and measured temperature rise values (The uncertainty for δ was estimated less than 1.5%)

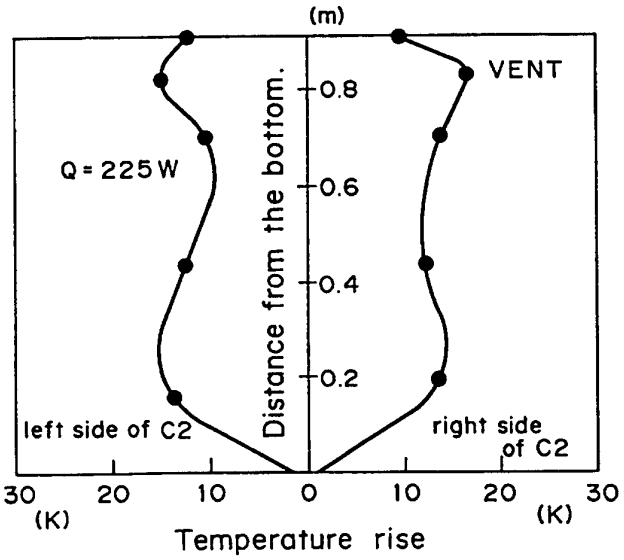

Fig. 5 Temperature rise distribution inside casing C2

4. EFFECT OF THE SUPPLY UNIT LOCATION ON THE TEMPERATURE DISTRIBUTION IN THE CASING

Figure 7 shows the temperature rise trends in casing C1 when the power dissipation unit was placed at the top or the bottom of the casing, as indicated in Fig.6. When placing the power dissipation unit at an upper position in the casing, the temperature distribution was found to be non-uniform. Also, a hot spot area can be seen near the dissipation unit. On the other hand, when the power unit is kept at the bottom of the casing, a rather uniform temperature distribution was observed, and no hot spot area near the power unit could be found. It can also be observed from this figure that, in the latter case, the air heated by the power supply unit moves upward while promoting heat exchange with the casing surface, and finally comes out of the casing after undergoing a slight air stagnation effect near the upper portion of the casing due to the resistance to flow resulted from the vent.

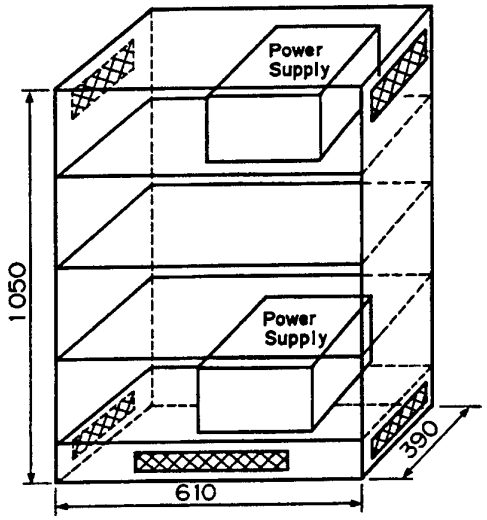

Fig. 6 Power dissipation unit location

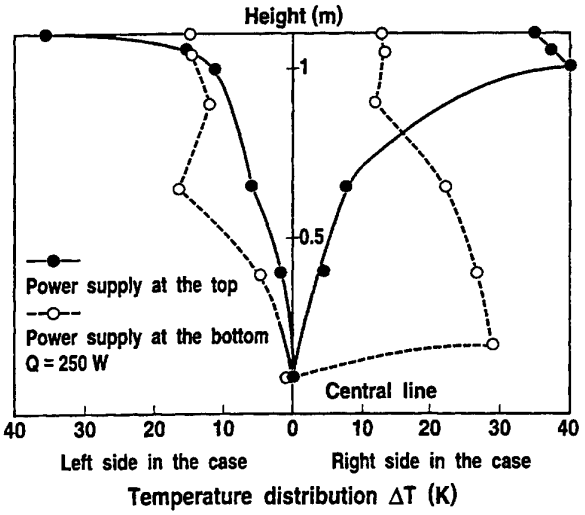

Fig.7 The temperature rise trends in casing C1 when power supply unit was placed at top or bottom of the casing

5. EFFECT OF THE OUTLET VENT AREA ON COOLING EFFECTIVENESS

The set of equations shows that the amount of heat removed from the vent increases without any limit, as the vent area Ao increases. This is not plausible in reality. Since the chimney, flow resistance and surface area effects are all included in Eq.(1), it is important to develop a criterion regarding the outlet vent area value A_o of the casing for thermal design. Figure 8 shows the relationship between the outlet vent area A_o and the outlet air temperature rise $\bullet T_o$. In Fig.8, $A_o=0$ represents the condition when the casing is sealed, and the line represents the values predicted by Eq.(1). The figure shows that, for an Ao value below 0.02 m^2, the predicted temperature decreases with an increase in Ao. However, when the Ao value goes beyond 0.02 m^2, the measured temperature does not decrease any more. This can be explained by the fact that, when A_o gets smaller than 0.02 m^2, the flow resistance source of the main flow in the casing comes from the vent area. On the contrary, for Ao having a value 0.02 m^2, the flow resistance to the main flows in the casing is expected to resulted from other sources, such as frictional resistance due to the printed circuit boards. The driving force of the flow in the casing is forced to be matched with these resistance values. Therefore, one serious problem is to determine the threshold value for A_o. However, it is not an easy task to fix the threshold value, since the parameters associated with problems in the casing are quite numerous. Also, the flow inside the casing is complicated. Therefore, under such a condition, the results of an attempt made to determine the threshold value for A_o are shown in Fig.9. Figure 9 shows the variation in the ratio Q_1/Q_2 in regard to the amount of heat removed from the casing surface versus that from the outlet vent with an equivalent surface area, where only limited values of A_o for the three previously mentioned casings are considered. It can be seen from this figure that the ratio between Q_1 and Q_2 for a limited A_o value was found to be approximately one. However, since this A_o value is determined on the basis of only a limited number of experimental data, there still remains some doubt in regard to its generality and reasonableness. Nevertheless, the value of A_o can be considered as apertinent suggestion with regard to thermal designing. This indicates that it may be more important to consider the heat removal from the casing surface than to consider the heat removal from the outlet vent in thermal designing of natural air cooled equipment casings, that is,

$$Q_1/Q_2 > 1 \qquad (5)$$

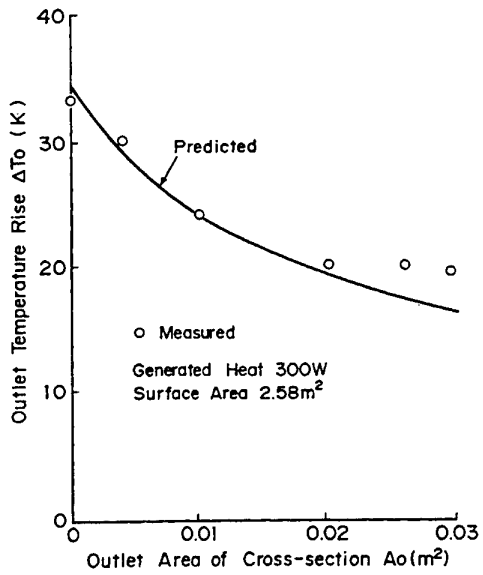

Fig. 8 Relationship between outlet vent area A_o and outlet air temperature rise $\bullet T_o$

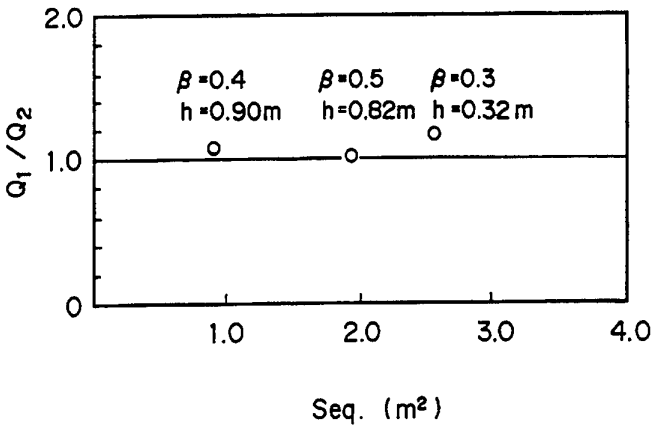

Fig.9 Variation in the ratio Q_1/Q_2

6. CONCLUSIONS

A practical thermal design approach for natural air-cooled electronic equipment casings has been presented. A set of simplified equations for the thermal design of natural air cooled electronic equipment casings have been proposed and the effects of the power dissipation unit location and the outlet vent area on the natural air cooling capability of electronic equipment casings have been studied using those simplified equations. The results have shown that a uniform temperature distribution could be achieved when the main power dissipation unit is placed at the bottom of the casing. It has also been suggested that the outlet vent area should be limited within some threshold value so that the value of heat removed from the casing surface would be higher than that from the outlet vent.

REFERENCES

1. W. Aung, Cooling Technology for Electronic Equipment, Hemisphere, New York,(1988).
2. A.E. Bergles, Heat Transfer in Electronic and Microelectronic Equipment, Hemisphere New York(1990).
3. G.J. Hwang, Transport Phenomena in Thermal Control, Hemisphere, New York(1989).
4. W. Nakayama, Thermal Management of Electronic Equipment: A review of technology and research topics, Applied Mechanics Reviews, vol.39, no.12, pp.1847-1868(1986).
5. H. Xie, and Y.C. Lee, Study of an Air Cooling Scheme for 3-D Packaging, Journal of Electronic Packaging, Transactions of the ASME,Vol.116, , pp.30-36(1994).
6. R.I. Noronha, Free Convective Cooling of Cabinets Containing Heat Dissipating Components, Proc. Instn. Mech. Engrs., Vol.179, Pt.1, No.13, pp.439-450(1964).
7. D. Guglielmini, G. Milano, and Misale M., Natural Air Cooling of Electronic Cards in Ventilated Enclosures, Second UK National Conference on Heat Transfer, Vol. I, pp.199-210(1988).
8. M. Ishizuka, Y. Miyazaki, and Sasaki, T., On the Cooling of Natural Air Cooled Electronic Equipment Casing, Bulletin of JSME, Vol.29, No.247, pp.119-123(1986).
9. M. Ishizuka ,Y. Miyazaki and T. Sasaki, Air Resistance for Perforated Plates in Free Convection, Transactions of the ASME, Journal of Heat Transfer, Vol.109,pp.540-543(1987).
10. A.D. Kraus, and A. Bar-Cohen, Thermal Analysis and Control of Electronic Equipment, McGraw-Hill Book Company, pp.142-143(1983).

NATURAL CONVECTION OF COLD WATER IN A RECTANGLE

Evgueny V. Kalabin, Pavel T. Zubkov
Mathematical Simulation Laboratory
Surgut State University
Email: zpt@surgu.wsnet.ru; Tel/Fax: +7(3462)-283-687

Keywords: steady, unsteady flows; square cavity

ABSTRACT. The steady and unsteady solutions in the problem of the natural convection of water near its density maximum (about 4 °C) in a rectangle cavity are considered. We use the square with the side length H as one of the kinds of rectangles. The vertical walls of cavity are adiabatic and horizontal walls have an isothermal segment from 0.25H to 0.75H and other adiabatic segments. The temperature on top T_u is less than the temperature on bottom T_d, and they are symmetrical relatively to the temperature of density maximum T_{inv}. The control volume method with SIMPLER algorithm is used in numerical calculations. The steady unsymmetrical, two symmetrical and one unsteady oscillatory water flows may be obtained for fixed Grashof number. In this paper all the solutions are studied in detail. The oscillations of the average Nusselt numbers on top and bottom of the square and the average kinetic energy of water flow are shown for the unsteady solution. The Fourier analysis of oscillatory characteristics is made. The isotherms, streamlines and the distribution of kinetic energy in cavity are shown for all kinds of solutions.

1. INTRODUCTION

The natural convection of cold water complicates by nonlinear density-temperature relation. The cold water has a maximum of its density about 4 °C. Many various kinds of water flow exist as a result of this phenomenon. For example, numerous experimental works [1] show that the thermal expansion anomaly leads to the change of convection motion. The existence of more than one convective flows is a well known fact. In [2] two steady solutions of water convection near density inversion point have been obtained in a square cavity with isothermal top and bottom sides and vertical walls with temperature linear depending on the height. The point of existence of several steady flows of cold water in the square cell with different initial conditions were also numerically investigated in [3]. The existence of solution and its stability at various Grashof numbers has been regarded also in [3]. The transition of one kind of solution at given Grashof number to another one has been investigated.

In the present paper we study the convective flow of cold water in a square cavity with the specific boundary conditions, the different initial conditions and with the fixed Grashof number.

2. FORMULATION OF THE PROBLEM

The natural convection of the water near its density maximum in a square cavity (Fig.1) is considered. The height and width of cavity are equal to H. We have the following boundary conditions: the horizontal walls have an isothermal segments Γ_d, Γ_u and the other parts of bound are adiabatic.

The natural convection of incompressible fluid is described by the following system of equations in Boussinesq approach:

$$\rho_m \frac{\partial \vec{v}}{\partial t} + \rho_m(\vec{v}\cdot\nabla)\vec{v} = -\nabla p + \rho_m \nu \Delta \vec{v} + \vec{g}\rho(T)$$
$$\frac{\partial T}{\partial t} + (\vec{v}\cdot\nabla)T = \chi \Delta T, \qquad \nabla \vec{v} = 0 \tag{1}$$

Here $\vec{v} = (u,v)$ is the fluid velocity; T is the temperature; p is the pressure; $\vec{g} = (0,-g)$ is the gravity acceleration; ν is the kinematic viscosity; χ is the thermal diffusivity; ρ_m is the maximum value of water density.

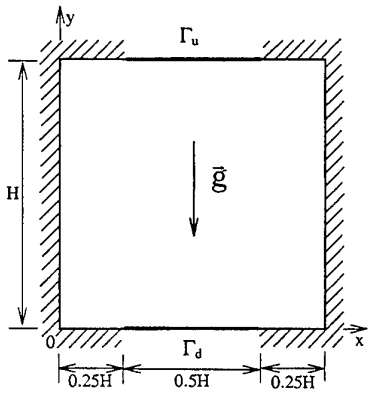

Fig. 1

The boundary conditions are:

$$\vec{v}\big|_{\Gamma} = 0, \qquad \left.\frac{\partial \dot{O}}{\partial n}\right|_{\Gamma/(\Gamma_u \cup \Gamma_d)} = 0$$

$$T\big|_{\Gamma_u} = T_u, \qquad T\big|_{\Gamma_d} = T_d \tag{2}$$

Here Γ is all the bound and Γ_u, Γ_d are isothermal segments. The temperatures T_d and T_u are symmetrical relatively to the temperature of density maximum T_{inv}.

In that case the thermophysical properties are independent on temperature, except for the density in the buoyancy force. We use the approximation of nonlinear density-temperature relation of water suggested by Gebhard and Mollendorf [4]:

$$\rho = \rho_m\left(1 - \beta\left|T - T_{inv}\right|^{\gamma}\right) \tag{3}$$

Therefore in equation system (1) we have $\rho(T) = -\rho_m\beta\left|T - T_{inv}\right|^{\gamma}$. Here $\rho_m = 999.972\ kg/m^3$ is the maximum of density; $T_{inv} = 4.029325^{\circ}C$ is the temperature of density extremum; $\beta = 9.297173\cdot 10^{-6}(^{\circ}C)^{-\gamma}$ and $\gamma = 1.894816$.

The dimensionless variables are taken as:

$$X = \frac{x}{H}, \quad Y = \frac{y}{H}, \quad U = \frac{uH}{\nu}, \quad V = \frac{vH}{\nu},$$

$$\tau = \frac{t\nu}{H^2}, \quad \Theta = \frac{T - T_{inv}}{T_d - T_u}, \quad P = \frac{pH^2}{\nu^2\rho_m} \tag{4}$$

After substitution (4) into (1) we have the following dimensionless system of equations:

$$\frac{\partial \vec{V}}{\partial \tau} + (\vec{V}\cdot\nabla)\vec{V} = -\nabla P + \Delta\vec{V} + Gr\left|\Theta\right|^{\gamma}\vec{e}_y$$

$$\frac{\partial \Theta}{\partial \tau} + (\vec{V}\cdot\nabla)\Theta = \frac{1}{Pr}\Delta\Theta, \quad \nabla\vec{V} = 0 \tag{5}$$

Here $Gr = g\beta\left|T_d - T_u\right| H^3/\nu^2$ is the Grashof number and $Pr = \nu/\chi$ is the Prandtl number. In the considered temperature range for water, $Pr \approx 11.59$. We use the fixed Grashof number $Gr = 2\cdot 10^5$.

The dimensionless boundary conditions are:

$$\vec{V}\big|_{\Gamma} = 0, \qquad \left.\frac{\partial\Theta}{\partial n}\right|_{\Gamma/(\Gamma_u \cup \Gamma_d)} = 0 \tag{6}$$

$$\Theta\big|_{\Gamma_u} = -0.5, \qquad \Theta\big|_{\Gamma_d} = 0.5 \tag{7}$$

It is easy to see that the equation system (5) accepts inversion: if $\vec{V}, \Theta$ are the solution under boundary condition (6) and (7) then $\vec{V}, -\Theta$ will be solutions of (5) under boundary conditions (6) and

$$\Theta\big|_{\Gamma_u} = 0.5, \qquad \Theta\big|_{\Gamma_d} = -0.5 \tag{7'}$$

The following dimensionless characteristics of water flow are used:

$$E = \frac{1}{S}\iint_S \frac{\bar{V}^2}{2} dXdY \tag{8}$$

$$Nu_d = -\left.\frac{\partial\Theta}{\partial Y}\right|_{Y=0}, \qquad Nu_u = \left.\frac{\partial\Theta}{\partial Y}\right|_{Y=0} \tag{9}$$

$$\overline{Nu}_d = \frac{1}{0.5}\int_{0.25}^{0.75} Nu_d dX, \quad \overline{Nu}_u = \frac{1}{0.5}\int_{0.25}^{0.75} Nu_u dX \tag{10}$$

Here E is the average kinetic energy; Nu_u and Nu_d are the dimensionless local heat fluxes on top and bottom, $\overline{Nu}_u$ and $\overline{Nu}_d$ are the dimensionless average heat fluxes (or Nusselt numbers) on upper and lower sides of square respectively.

The control volume method with SIMPLER algorithm [5] is used in numerical calculations. All the results were obtained on uniform grid with 80x80 control volumes.

3. RESULTS AND DISSCUSSIONS

Steady Solutions

With the fixed Grashof number $Gr = 2 \cdot 10^5$ the three different kinds of steady solutions have been obtained: two are symmetrical relatively to the vertical line passing through the center of square and one is unsymmetrical. The structure of fluid flow can be defined by description of temperature and stream function (F) in cavity. The distribution of local kinetic energy of water flow in square is also investigated. The heat transfer on the top and bottom of cavity is estimated by the local Nusselt numbers.

It is easy to see that the cavity has a symmetry relatively to the vertical line X=0.5. Let us name the solution in Fig.2 as «the first symmetrical solution» and the solution in Fig.3 as «the second symmetrical solution».

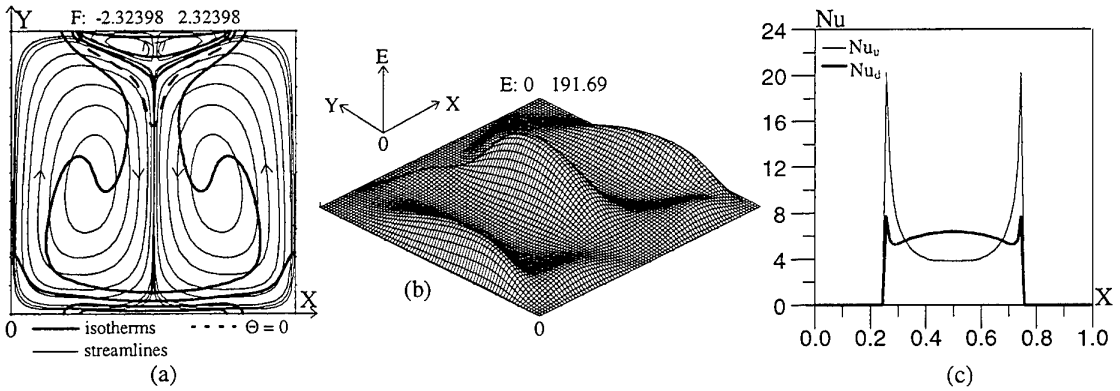

Fig. 2. The first symmetrical steady solution

The first symmetrical solution has been obtained by solving (5)-(6) with the initial condition $\bar{V} = 0$, $\Theta = 0.5$. In Fig.2 the streamlines, isotherms, distribution of local kinetic energy and local Nusselt numbers on top and bottom of cavity are shown. The flow consist of two main vortexes which occupy almost the whole cavity and two secondary vortexes near upper isothermal bound segment (Fig.2(a)). In the middle of square water is moving down. The maximum of flow kinetic energy (Fig.2(b)) is in the center of the square (because in there we have the maximum of flow intensity). The average kinetic energy is equal to 36.23. In Fig.2(c) it is seen that the maximum values of local heat fluxes on top and bottom are in points of boundary conditions breaks. The average Nusselt numbers on top and bottom are equal to 6.03.

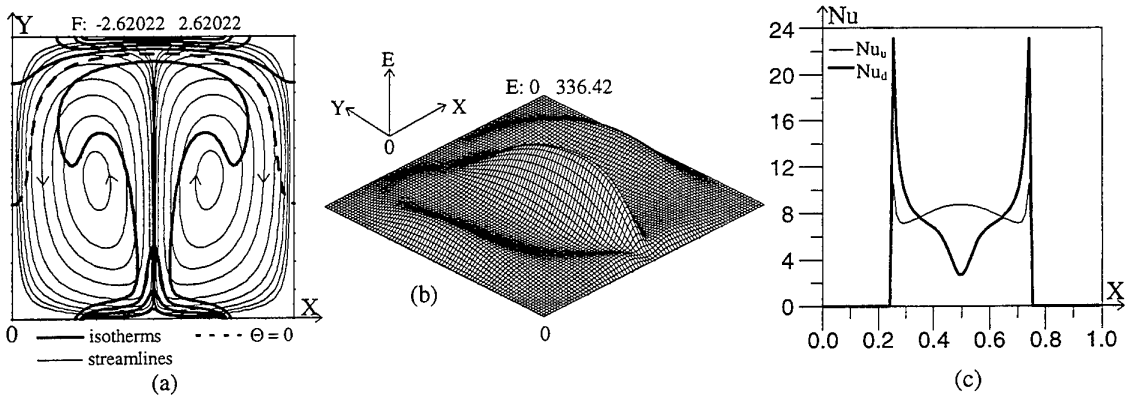

Fig. 3. The second symmetrical steady solution

The second symmetrical steady solution has also been obtained by solving (5)-(6) but with the initial conditions $\bar{V} = 0$ and $\Theta = -0.5$. Fig.3(a) shows that flow consists of two main vortexes only. In the middle of the cavity the water is moving up. The maximum of local kinetic energy is also in the center of the square (Fig.3(b)), but the value of this maximum is much bigger in comparison with local energy maximum in the first solution. The average kinetic energy is equal to 49.43. The flow intensity is much bigger in the center of square than near the walls in comparison with the first solution. This fact can also be seen in Fig.3(c): the peaks of local heat flux on top and bottom are bigger and the distribution of local Nusselt number on bottom has a different form. The average heat flux on top and bottom are equal to 8.14.

Some additional manipulations must be made to get the unsymmetrical solution. The initial conditions $\bar{V} = 0$, $\Theta = 0.5 - X$ and $Gr = 10^5$ are taken. The steady unsymmetrical solution is obtained with these values of parameters. This solution is used as the initial condition with increasing Gr. Then the steady solution is obtained with these parameters, Gr is changing again and so on. Gr is increasing step by step up to $Gr = 2 \cdot 10^5$ and thus the needed steady unsymmetrical solution is obtained.

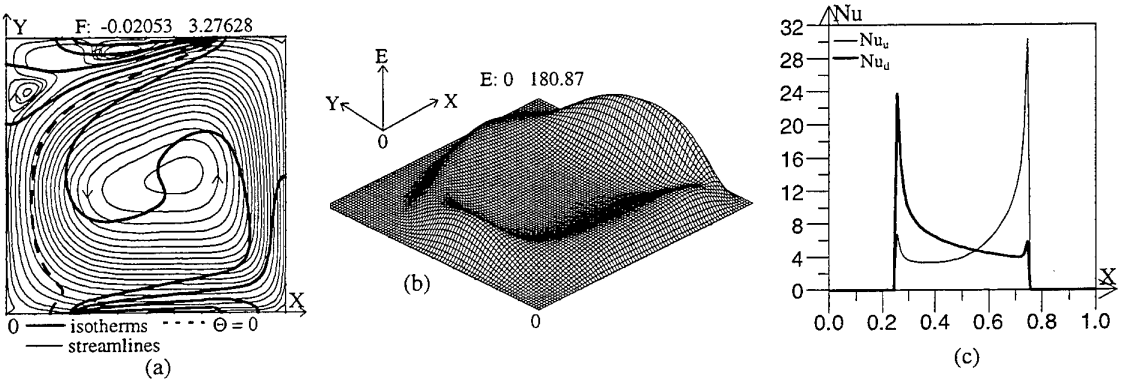

Fig. 4. The unsymmetrical steady solution

The flow of unsymmetrical solution in Fig.4(a) consists of one big vortex, two secondary vortexes are near one of the upper corners and three very little vortexes are in other corners. The distribution of local kinetic energy in Fig.4(b) has a maximum near the right wall of cavity and it is less than the same characteristic of other steady solutions. In Fig.4(c) the peaks are at the points of breaks of boundary condition again. The values of local flux at those points are much bigger in comparison with the same above. The average Nusselt numbers on top and bottom are equal to 6.43.

If the manipulations which must be made to get the unsymmetrical solution above are made by using the initial conditions $\bar{V}=0,\ \Theta=-0.5+X$, one more steady flow may be obtained. This flow looks like the unsymmetrical solution above but water in the main vortex is moving clockwise and secondary vortexes are in the other upper corner. This solution is not studied in detail since it has the same values of characteristics as the unsymmetrical solution above.

Unsteady Solution

The unsteady unsymmetrical solution has been obtained under the initial values in the interior of square taken as $\bar{V}=0,\ \Theta=0.5-X$. The flows at different times of oscillation period are shown in Fig.5. it can be seen that the flow has the following oscillations: the little vortex periodically appears near the lower and right point of boundary condition break; this vortex is getting bigger and moving to the right wall of cavity and disappears in the corner. The existence of this vortex leads to changing of flow intensity in main vortex and because of that the flow oscillations take place in upper left corners too. The secondary vortexes are increasing and decreasing in there. Fig.6(a) shows that the oscillations of average kinetic energy and heat fluxes on top and bottom are periodical. Also this fact can be seen in Fig.6(b), the oscillations with using E and Nu_d as the coordinates are shown there. The Fourier spectrum of obtained oscillations is shown in Fig.6(c) (as example the spectrum for Nu_d oscillations is shown). The average value of kinetic energy is equal to 42.87 and the average value of heat fluxes is equal to 6.60.

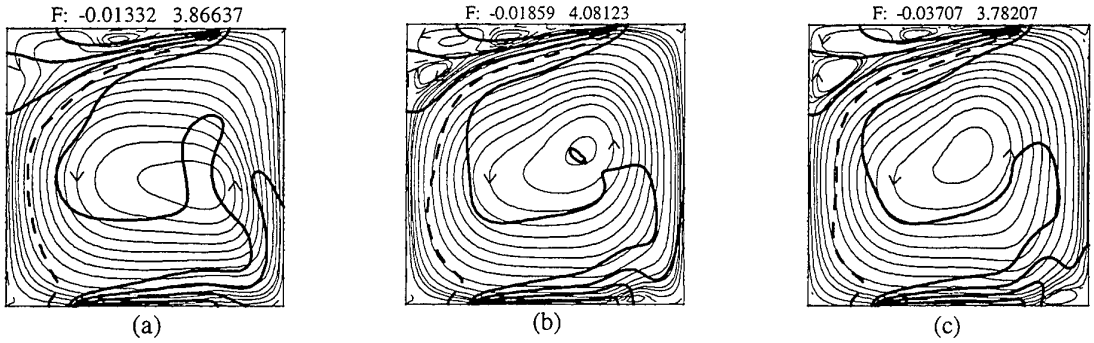

Fig. 5. The oscillations of water flow of unsteady solution

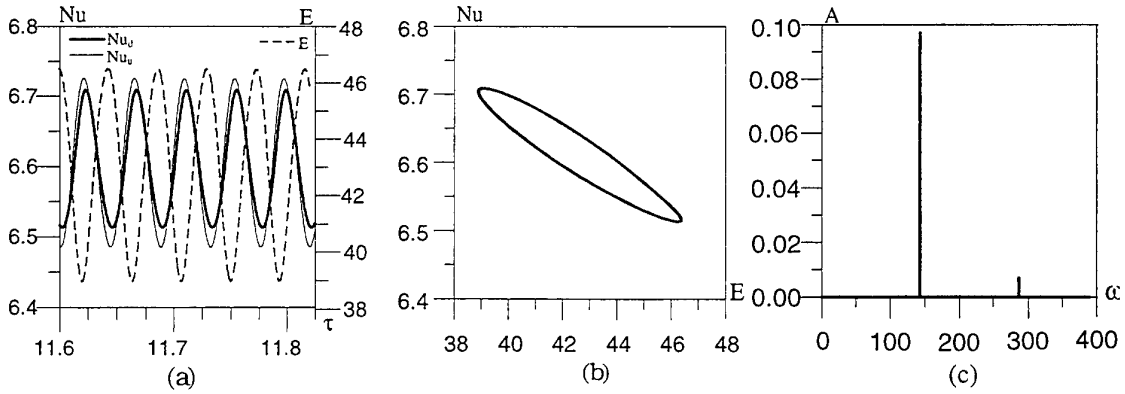

Fig. 6. Some characteristics of unsteady solutions

The one more unsteady unsymmetrical solution has been obtained under the initial values in the interior of the square taken as $\bar{V}=0,\ \Theta=-0.5+X$. This solution is symmetrical to unsteady solution above relatively to the

vertical line X=0.5. Therefore it has the same oscillations of characteristics as the solution above and it is not studied in details.

4. CONCLUSIONS

The problem of natural convection of cold water in cavity with broken boundary conditions is very interesting to investigate because the diversified kinds of solutions may be obtained. In this paper, several different steady and one unsteady solution has been obtained with the fixed Grashof number. Numerical results of stream function, isotherm lines, distribution of flow kinetic energy and average energy, local and average Nusselt numbers are represented. The second symmetrical steady solutions has a maximum average heat flux and a maximum average kinetic energy in comparison with the other solutions. The first symmetrical steady solution has a minimum heat flux through the cavity and the unsteady solution has a minimum average kinetic energy. The unsteady oscillatory solution has been obtained by using some disturbances.

5. REFERENCES

1. S.L. Braga, R. Viskanta, Int. J. Heat Mass Transfer, v.35, pp.861-875, 1992.
2. A.S. Blohin, N.S. Blohina, DAN AN USSR, ser. Geophys.,v.193,• 4,pp.805-807,1970.
3. A.V. Gorelikov, V.G. Klimin, P.T. Zubkov, «Natural convection of water near to density inversion point», *Proceedings of the International Conference on Fluid Engineering, v.3, pp.1617-1621*, Tokyo, Japan (1997).
4. B. Gebhart, J. Mollendorf, Deep Sea Res. v.24, pp.831-848 (1977)
5. S.V. Patankar, *Numerical Heat Transfer and Fluid Flow,* McGraw-Hill, New York (1980).

D. Boiling and Condensation

CRITICAL HEAT FLUX IN SUBCOOLED POOL BOILING

Li Jin, Sadao Yokoya, Makoto Watanabe and Masahiro Shoji
Department of Mechanical Engineering
The University of Tokyo
7-3-1 Hongo, Bunkyo-ku, Tokyo 113-8656, Japan
Email: shoji@photon.t.u-tokyo.ac.jp; Fax: +81-3-5800-6987

Keywords: pool boiling, subcooled boiling, critical heat flux, macrolayer model

ABSTRACT: To understand the mechanism of subcooled CHF(Critical Heat Flux), the experiment of pool boiling of water was conducted on a cooper heated surface at subcooled conditions under atmospheric pressure. CHF increases with subcooling and agree well with available empirical correlations of Zuber et al., Kutateladze, and Ivey and Morris. At low subcooling less than 55 K, a vapor mass was formed to cover the heated surface and the critical condition is understood basing on the macrolayer consumption model of Katto and his co-workers by employing newly defined time period for macrolayer consumption and by assuming that the initial dry area fraction of the heated surface depends on CHF. At high subcooling more than 55K, it was found that a vapor mass hardly cover the heated surface, so the macrolayer model is difficult to apply from its physical basis. The mechanism of CHF remains unknown in the present study.

1. INTRODUCTION

The mechanism of CHF(Critical Heat Flux) at subcooled conditions is not fully made clear although useful empirical correlations [1, 2, 3] are available. The hydrodynamic model of Zuber [4] and the macrolayer consumption model of Katto and his co-workers [5, 6] are well applied to saturated CHF but the former model of Zuber is difficult to apply to the subcooled condition because of its physical basis. In contrast, Katto's model may apply to the subcooled condition but the applicability has not sufficiently been studied in the past.

According to the model of Katto and Yokoya [5], the critical condition arises when the consuming time of macrolayer is equal to the hovering period of a vapor mass on a heated surface. The condition can be described as follows from the energy balance:

$$q_c \tau_d = \rho_L \delta h_{fg} \left(1 - \frac{A_v}{A_w}\right) \tag{1}$$

where q_c is the critical heat flux, ρ_L the liquid density, h_{fg} the latent heat of evaporation, τ_d the hovering period of a vapor mass on a heated surface, δ the macrolayer initial thickness, and A_v/A_w the initial dry area fraction of the heated boiling surface. As is clear in Equation (1), the main parameters of the model are τ_d, δ and A_v/A_w. Considering the buoyancy and the inertia force acting on a vapor mass, Katto and Yokoya [5] derived the following expression for the vapor mass departure period from the heated surface:

$$\tau_d = \left(\frac{3}{4\pi}\right)^{1/5} \left[\frac{4(\xi\rho_L + \rho_v)}{(\rho_L - \rho_v)g}\right]^{3/5} \left(\frac{qA_w}{\rho_v h_{fg}}\right)^{1/5} \tag{2}$$

On the other hand, Haramura and Katto [6] proposed the following expression of macrolayer initial thickness, basing on the Helmholtz instability:

$$\delta = 0.5\pi\sigma \frac{\rho_v + \rho_L}{\rho_v \rho_L} \left(\rho_v h_{fg}\right)^2 \left(\frac{A_v}{A_w}\right)^2 \frac{1}{q_c^2} \tag{3}$$

No theoretical expression has been given for A_v/A_w in the pastbut, but Harmura and Katto[6] derived the following relation by their expression for CHF to Zuber's [4]:

$$\frac{A_v}{A_w} = 0.0584\left(\frac{\rho_v}{\rho_L}\right)^{0.2} \quad (4)$$

It is known that the macrolayer model of Katto and his coworkers applies well to CHF at saturated conditions, however it is not fully confirmed if the model applies also to the subcooled condition. At high subcooling, a vapor mass is hardly formed and difficult to departure from the heated surface because of the strong condensation effects whereas the critical condition exists even at such high subcooling. The present study aims to experimentally investigate whether or not the macrolayer model applies to subcooled conditions. It should be mentioned here for the formation mechanism of macrolayer that not a few hypotheses have been proposed against Equation (3). It should also be pointed out that Equation (4) has not yet been verified by any experiment. These are the problems to discuss and consider in the present study.

2. EXPERIMENT

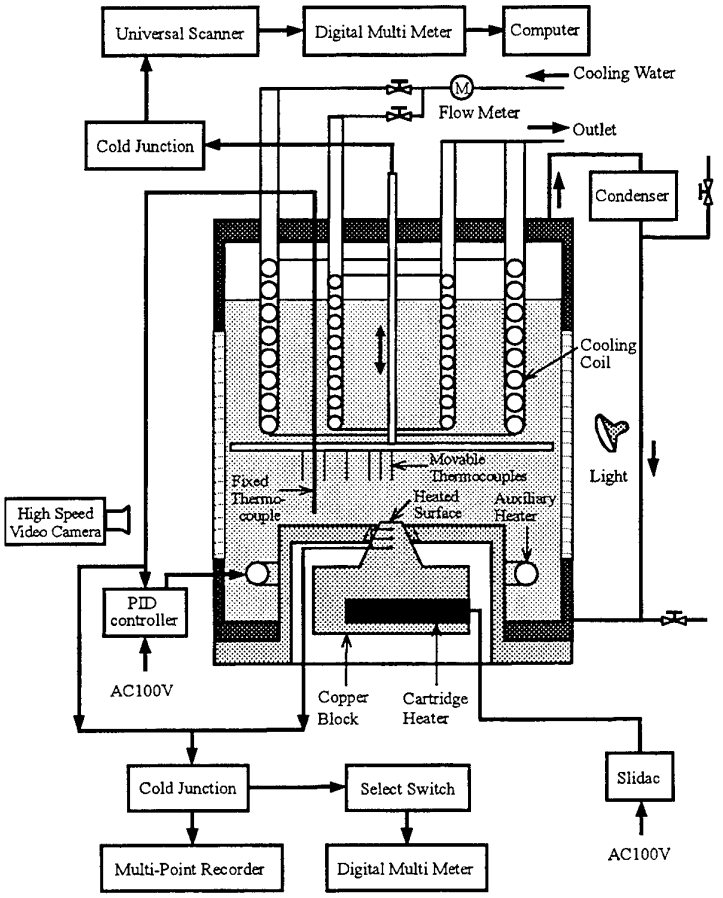

Figure 1. Experimental apparatus

Figure 1 is the schema of the experimental apparatus employed in the present study. The vessel for boiling test is made of brass with a size of 150mm x 150mm x 170mm. The vessel has windows to observe the boiling aspects on a heated surface. The boiling surface is the end of a heated copper block, the diameter of which is 10 mm. The surface was finished using 4/0 sand paper. Three sheathed K-type thermocouples are embedded in the heated block at 4mm, 8mm and 12mm from the boiling surface to measure the heat flux and the surface temperature. At the lower part of the copper block, a heater of 2.5 kW is embedded. The temperature of test water was controlled by the auxiliary heater and the cooler in the test vessel. In the cooler, low temperature

water was circulated using a pump. The temperature of water was kept constant by employing PID controller. The spatial distribution of water temperature in the vessel above the heated surface was measured in detail in the preliminary tests. Typical results of the measurement are shown in Figure 2. From the result, the temperature of water at 5 mm high from the boiling surface and 35mm apart from the center of the boiling surface in the horizontal direction is employed as the representative temperature of subcooled water.

The experiment was performed under atmospheric pressure by changing subcooling of water from 0 to 73K. The aspect of boiling, that is, the process of bubble growth and departure, was observed using high-speed VTR(648 frames/speed, shutter speed:10ms). The water was degassed by boiling for 30 minutes before each test. The dada were automatically recorded using a data acquisition system.

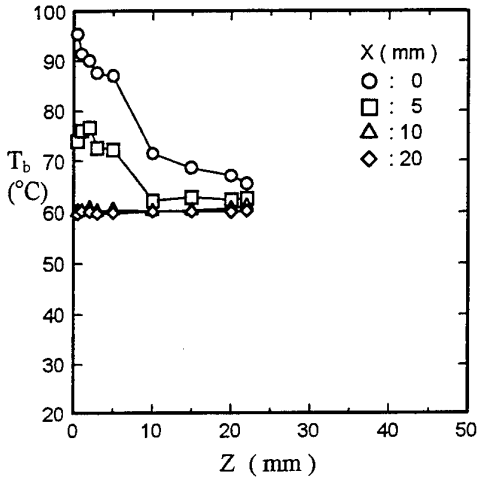

Fig. 2. (a) Water temperature distribution in vertical direction

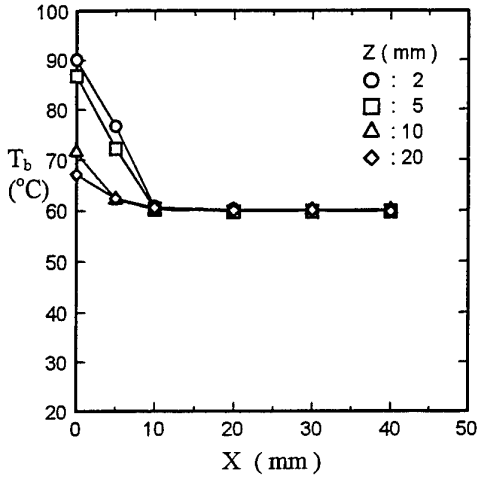

Fig. 2. (b) Water temperature distribution in horizontal direction

3. EXPERIMENTAL RESULTS

Boiling Curve

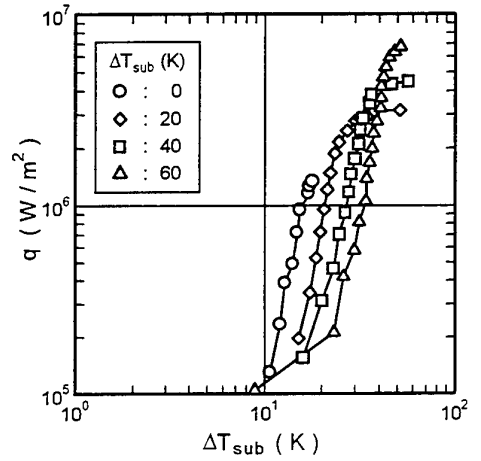

Fig. 3. Boiling curve

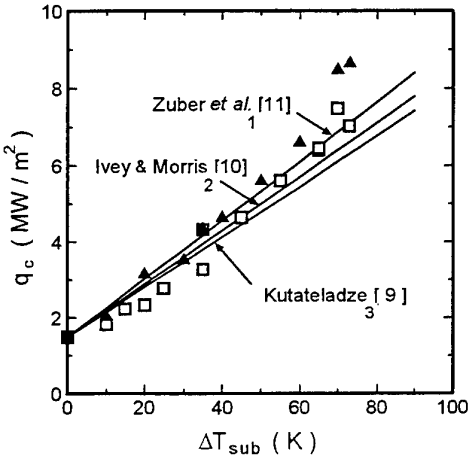

Fig. 4. Data of subcooled CHF

Figure 3 shows the boiling curves which depend on water subcooling. CHF increases with the increase of subcooling. As the subcooling increases, the boiling curve shifts to the direction of higher wall superheat, which may partly due to the method of the tests repeated from lower to higher subcooling.

Subcooled CHF

Figure 4 shows the data of CHF at subcooled conditions. As is expected, CHF increases with water subcooling, and the data at low subcoolings less than 55K are well correlated by every equation of Zuber et al. [1], Ivey and Morris [2] and Kutateladze [3]. The data at high subcooling (ΔT_{sub}>55K) seem to deviate from the correlations.

Boiling Aspects

The aspect of boiling, especially the process of formation, growth and departure of a vapor mass, was observed using high speed VTR. From the observation, it is found that the aspect can be classified into three types depending on the subcooling as follows:

Regime-I: low subcooling of ΔT_{sub}=0-15K, Fig. 5(a). The behavior of a vapor mass is fundamentally the same to that of saturated condition. As was reported by Katto and Yokoya [5], three types of vapor mass (Type-A ,Type-a and Type-B) appears which have different shapes, sizes and departure frequencies. Type-A vapor mass has little effects of the preceding vapor mass. The vapor mass of Type-a is formed immediately after the departure of Type-A vapor mass. The Type-B vapor mass is affected by the preceding Type-A or Type-a vapor mass. Three types of vapor mass repeatedly appear at low subcoolings but only Types of A and B appear at moderate subcoolings.

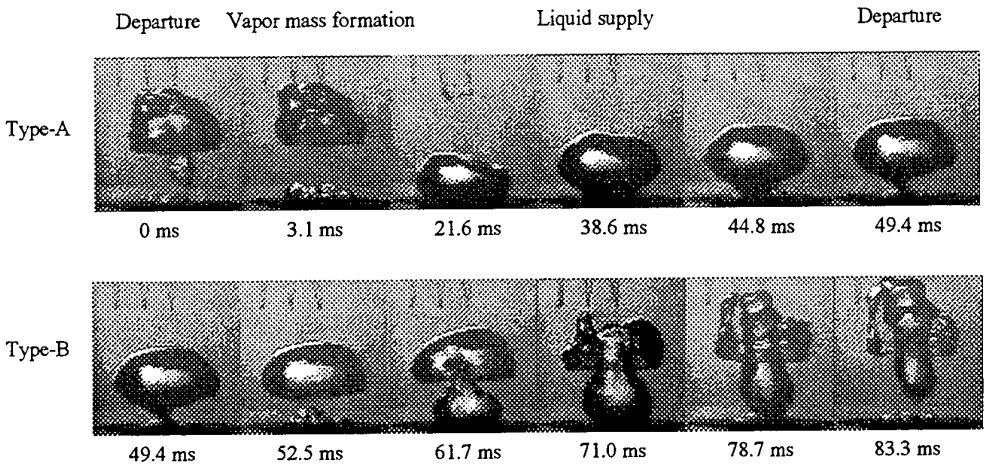

Fig. 5(a). Successive stages of growth and departure of a vapor mass at ΔT_{sub}=15K.

Regime-II: moderate subcooling of ΔT_{sub}=15-55K, Fig. 5(b). A vapor mass has a unique shape and uniform departure period since the condensation effect is strong and the effect of the preceding bubble is not so strong. Thus only the vapor mass of Type-A appears without accompanying the vapor mass of Type-a or Type-B. In this regime, many tiny isolated bubbles appear first on the heated surface, and then grow and coalesce to form a vapor mass which covers the heated surface. This feature is different from that at the saturated condition.

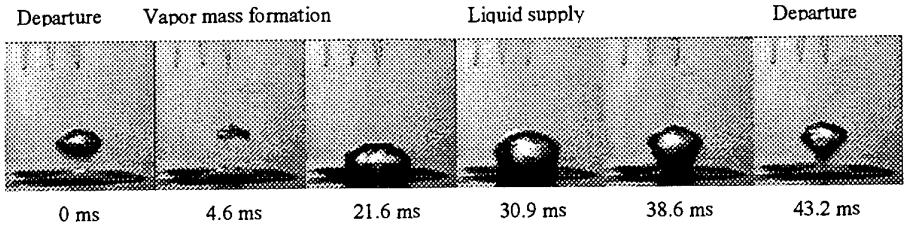

Fig. 5(b). Successive stages of growth and departure of a vapor mass at ΔT_{sub}=45K.

Regime-III: high subcooling of ΔT_{sub}>55K, Fig. 5(c). Small bubbles appear irregularly in time and space, and no vapor mass which covers the heated surface is formed any more. In other words, the departure of a vapor

mass from the heated surface never takes place at high subcooling.

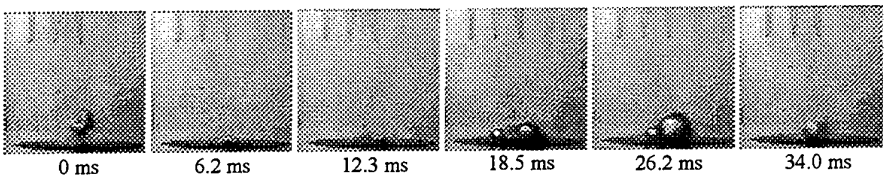

Fig. 5(c). Successive stage of growth and departure of a vapor mass at ΔT_{sub}=65K.

Growth and Departure of a Vapor Mass

In the hypothesis of Katto and Yokoya [5], it is assumed that the macrolayer is formed at the base of a vapor mass, and the vapor mass hovers on a heated surface for a certain time. So the model can apply only in the regimes of I and II mention above where a vapor mass is actually formed and departs from the heated surface. Among the three types of a vapor mass, the frequency of the Type-A vapor mass is longest, so it may relate most closely to critical condition. Thus the behavior of a vapor mass of Type-A was observed in detail using high-speed VTR. Figure 6(a) shows the process of vapor mass formation, growth and departure together with the definition of time periods. The time period of each process actually changes with subcooling as shown in Fig. 6(b). The time period τ_d in Equation (1) may correspond to the time period t_2 in Figure 6(a) which is the interval from the state-3 (formation of macrolayer) to the state 5(liquid starts to be supplied to the heated surface). This time period is different from the vapor mass departure period, t_0 in Fig. 6(a), which was employed in the hypothesis of Katto and Yokoya [5] at the saturated condition, because it requires the time for the tiny bubbles to coalesce and to form a vapor mass at the subcooling conditions. It may be reasonable to assume that the heated surface would not reach the critical condition if the surface is not over-heated at the instant of the state-5 in Fig. 6(a) since the liquid starts to be supplied to cool the surface at this state.

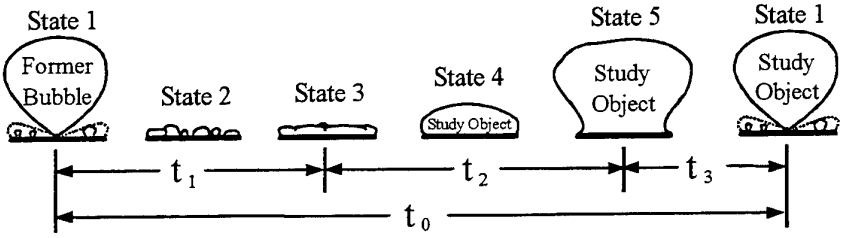

Fig. 6(a). Schema of time interval between stages of growth and departure of a vapor mass

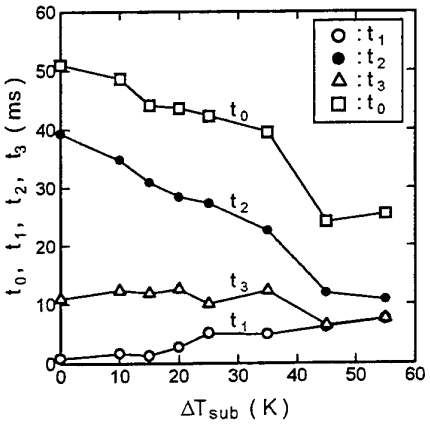

Fig. 6(b). Variation of time periods with subcooling

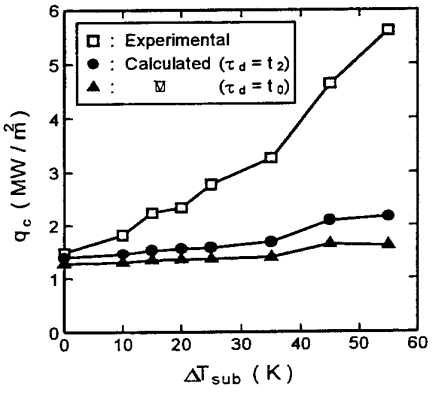

Fig. 7. Prediction for subcooled CHF

4. DISCUSSIONS

Macrolayer Model

Equation (2) for the vapor mass departure period can not applied to the subcooling case. If we substitute Equation (3) and Equation (4) into Equation (1), we can obtain the following equation:

$$q_C = \left\{0.00171\pi\sigma h_{fg}\left(1+\frac{\rho_v}{\rho_L}\right)(\rho_v h_{fg})^2\left[1-0.0584\left(\frac{\rho_v}{\rho_L}\right)^{0.2}\right]\left(\frac{\rho_v}{\rho_L}\right)^{0.4}\right\}^{1/3} \tau_d^{1/3} \quad (5)$$

The critical heat flux can be calculated from this Equation (5) once τ_d is given. Figure 7 shows the calculated CHF compared with experimental data when measured t_2 is employed as τ_d in Equation (1). In Fig. 7, also the estimated values of CHF are shown for comparison when t_0 is employed as τ_d just as at the saturated condition. As seen in Fig.7, both results of calculation do not explain the experimental results. This may indicate that the hypothesis of Katto and his co-workers can not directly apply to the subcooling case.

In general, it is known that Equation (4) yields too small value of A_v/A_w. Expression (1) suggests that A_v/A_w is a function of only system pressure, that is, of thermophysical properties but this has not yet been verified experimentally. So when we employ the equation of Haramura and Katto [6] for the macrolayer thickness, substitution of Equation (3) into Equation (1) yields

$$\left(\frac{A_v}{A_w}\right)^2\left(1-\frac{A_v}{A_w}\right) = \frac{2\tau_d q_C^3}{\pi\sigma h_{fg}\left(1+\frac{\rho_v}{\rho_L}\right)(\rho_v h_{fg})} \quad (6)$$

Equation (6) gives us the value of A_v/A_w if we use the measured CHF as q_c and the measured t_2 as τ_d. Figure 8 shows the results, which clearly indicate that A_v/A_w changes depending on CHF.

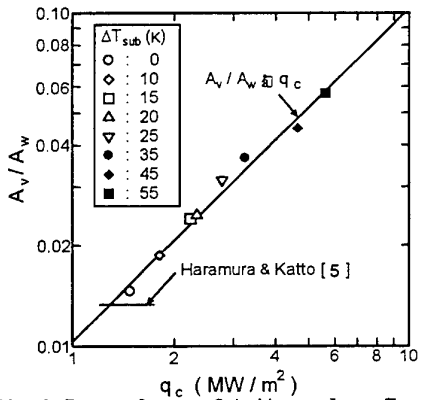

Fig. 8. Dependence of A_v/A_w on heat flux

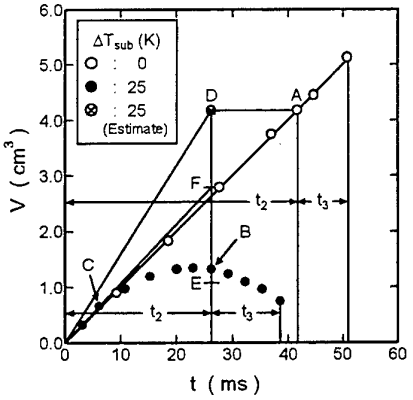

Fig. 9. Time variation of volume of a vapor mass

Dependence of Macrolayer Thickness on Heat Flux

Figure 8 indicates that A_v/A_w is proportional to CHF. In this case, Haramura and Katto's correlation, Equation (3), suggests that the macrolayer thickness is constant independent of heat flux. This may be easily understood if we consider in the model of Haramura and Katto that the number of nucleation site increases in proportion to heat flux. According to many available experiments, however, it is also well known that the macrolayer thickness in nucleate boiling decreases with increasing heat flux. Namely, we are facing the problem of inconsistency. The answer to this problem is not obtained in the present study, however, fortunately the macrolayer thickness relates directly to the volume of a vapor mass, so we can discuss this problem from the data of volume of a vapor mass.

At saturated condition, the volume of a vapor mass is directly proportional to CHF because the macrolayer would be perfectly consumed at the critical condition. Namely,

$$V_c = V_{t=t_2} \propto \delta \tag{7}$$

Figure 9 shows the variation of the vapor mass volume at two conditions of saturated and subcooling of 25K. The point A in Fig.9 indicates the volume of a vapor mass at the saturated critical condition. If the macrolayer thickness decreases by inversely proportional to the square of heat flux as suggested by Haramura and Katto [6], the thickness at the subcooling of 25 K should be 1/3.5 of the value at point A because the values of CHF at conditions of saturated and subcooling of 25K were 1.48 MW/m^2 and 2.77 MW/m^2, respectively. If the macrolayer of this thickness is consumed in time of t_2 at the subcooling of 25 K without condensation, the volume of a vapor mass would be the value at the point E in Fig. 9. The actual volume of a vapor mass is the one at the point B in Fig. 9. The volume at the point B (with condensation) is larger than the volume at the point E (without condensation). This suggests that the thickness of macrolayer does not depend on heat flux so strongly as the model of Haramura and Kattos insists.

If we assume here that the initial thickness of macrolayer is independent of CHF and that there is no effects of condensation, the volume of a vapor mass at the subcooling of 25 K would be the value at the point D in Fig. 9. Actually, condensation is strong so that the vapor mass volume may decrease from point D to point B. The slope OD represents the rate of evaporation, dV/dt, due to macrolayer consumption in case of no condensation. Namely, it relates to heat flux as

$$q_C = \rho_v h_{fg} A_w \left(\frac{dV}{dt}\right) \tag{8}$$

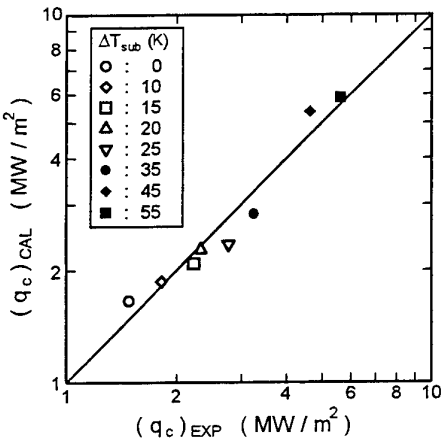

Fig. 10. Estimated and measured CHF

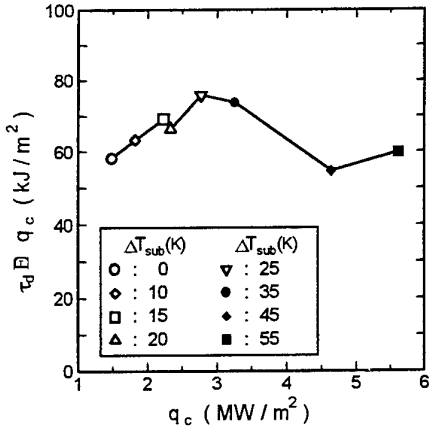

Fig. 11. Values of measured $q_C \tau_d$

From the measured value of t_2, it is possible to estimate CHF at every subcooling condition from Equation (8). The results are shown in Fig.10, which agree well with experimental data. Summarizing the discussion in this section, we may say, from the measurement of the vapor mass volume, that the macrolayer thickness does not change so much with heat flux.

When A_v/A_w is proportional to heat flux, the macrolayer thickness would be constant at a fixed system pressure, depending only on the thermophysical properties. Since A_v/A_w is very small in general when compared with unity, Equation (1) yields

$$q_C \tau_d = q_C t_2 = \text{const.} \tag{9}$$

Figure 11 show how the relation of Equation (9) holds in the present experimental. It may be said that Equation (9) hold well in Fig.11. This result agrees well with recent experimental results of Brusstar et al. [7][8] at

reduced gravity and at subcooling conditions.

5. CONCLUSIONS

The experiment of boiling of water was conducted at subcooling conditions in order to investigate whether or not the CHF phenomenon is explained by the macrolayer consumption hypothesis of Katto and his co-workers. As the results of the experimental study, the following conclusions are obtained:

(1) CHF at low and moderate subcoolings less than 55K can be explain using macrolayer model if we assume that 1)the initial dry area fraction of a heated surface changes with heat flux, and 2)the time period which should relate to macrolayer consumption time is the period between the time at which the macrolayer is formed and the time at which the liquid starts to be supplied to the heated surface (at the instant when the shape of a vapor mass starts to deform with a nest).

(2) No vapor mass is formed at high subcooling more than 55K. The mechanism of CHF under this condition remains unknown in the present study. It would be necessary to consider the evaporation heat transfer at the triple line of a single as well as a coalescence bubble.

NOMENCLATURE

A:	Area
g:	Acceleration of gravity
h_{fg}:	Latent heat of evaporation
q:	Heat flux
t_0,t_1,t_2,t_3:	Time interval, Fig. 6(a)
V:	Volume of a vapor mass

Greeks

δ:	Macrolayer initial thickness
ρ:	Density
σ:	Surface tension
τ_d :	Vapor mass hovering time (Time interval corresponding to macrolayer consumption)

Subscripts

C:	Critical heat flux
L:	Liquid (water)
V:	Vapor, or Dry area of a heated surface
W:	Wall

REFERENCES

1. N. Zuber et al., Int. Develop. Heat Transfer, ASME, pp. 230-236 (1961).
2. H.J. Ivey and D.J. Morris, UKAEA Report No. AEEW-R 137 (1962).
3. S.S. Kutateladze, Zh. Tekh. Fiz., v. 20, pp. 1389-1392 (1950).
4. N. Zuber, USAEC REPROT AECU-4439 (1959).
5. Y. Katto and S. Yokoya, Int. J. Heat Mass Transfer, v. 11, No. 6, pp. 993-1002 (1968).
6. Y. Haramura and Y. Katto, Int. J. Heat Mass Transfer, v. 26, No. 3, pp. 389-399 (1983).
7. M.J. Brusstar et al., Int. J. Heat Mass Transfer, v. 40, No. 17, pp. 4007-4019 (1997).
8. M.J. Brusstar and Jr. H. Merte, Int. J. Heat Mass Transfer, v. 40, No. 17, pp. 4021-4030 (1997).

NUCLEATION SITE INTERACTION AND ITS EFFECTS ON NUCLEATE BOILING HEAT TRANSFER

X. F. Peng, L. H. Chai, and B. X. Wang
Thermal Engineering Department, Tsinghua University, Beijing 100084, China
Email: pxf-dte@mail.tsinghua.edu.cn ; Fax: (8610)6277-0209

Key words: boiling heat transfer, bubble, nucleation, thermal interaction

ABSTRACT. Nucleation site interaction during boiling process was investigated to demonstrate its effects on active site density and associated boiling heat transfer. Considering that nucleation site interaction is induced by non-uniform temperature distribution depending mainly on boiling wall properties and thickness, boiling experiments on the surface of different material plate walls with different thickness were conducted to reveal the nucleation site interaction. Plate material and thickness were found to have significant influence on the nucleate boiling heat transfer caused by the thermal interaction in the plate. This is quite distinct from the effect of single bubble-waiting period and growing period commonly expected.

1. INTRODUCTION

Boiling nucleation and bubble dynamics have been one of critical topics in boiling heat transfer research field. Boiling is an extremely complex and illusive process and research must place great emphasis on fundamental understanding of the process [1]. Liquid nucleate boiling is a process of site activating to form an embryo and bubble growing. In classical theories, heat transfer predictions still remain principally an empirical art, and traditional modeling efforts typically use a linearized approach. For example, the physical phenomena are analyzed on the basis of a single site or vapor bubble, and the heat transfer rate is obtained for a given active site density distribution by assuming uniform thermal boundary conditions. The analysis always assumes that the bubbles have no effect on the formation of adjacent bubbles. Consequently, possibly important interactions between active sites are ignored or partially included in empirical coefficients. So far, only a few studies have focused on the physical nature of boiling processes and have limited success regarding the mechanistic modeling of boiling. Some recent investigations [2] show that boiling is one example of nonlinear spatio-temporal systems where even very small systems exhibit very complex behavior. They suggested that such nonlinear behavior is one of the reasons that mechanistic predictive capability for the boiling process has remained elusive. Actually, the traditional linear approach conflicts with experimental observations of physical phenomena, such as boiling hysteresis, intermittent activity, deactivation of sites with increasing heat flux, and interactions among nucleation sites [2, 3]. These imply that more experimental and theoretical investigations are highly needed to understand some new and/or unordinary aspects. Boiling process may also occur under the unusual condition such boiling in microchannels/microstructures, and under microgravity [4, 5], which requires an avenue of thought and research to modify the available heat transfer mechanisms. It is obvious that detailed and precise experimental information, especially correct thermal boundary conditions including temporal and spatial information, is necessary to simulate/model boiling process. Shoji [2] summarized recent development of researches dealing with nonlinear behaviors of boiling, and Gorenflo et al. [3] mainly reviewed and discussed the interactions between the heat transfer and bubble formation in nucleate boiling. However, nonlinear research on boiling is still very limited, and little information is currently available for understanding and/or describing the phenomena.

An investigation was conducted to experimentally provide some evidences of nonlinear characteristics of pool boiling, and exhibit the heat transfer aspects. Four flat heating plates, two made of aluminum having thickness of 6 mm and 11 mm, two made of stainless steel having thickness of 6 mm and 11 mm, were tested. The temporal and spatial temperature dynamic variation was measured. The experimental results indicate that the thermophysical properties and thickness of the heating plate result in quite different spatio-temporal temperature distribution on the surface of heating plate while boiling nucleation is occurring. From the observation and experimental measurement, the nucleation site interaction was analyzed. The interaction plays critical role and results in great consequence on the boiling heat transfer [6, 7].

2. EXPERIMENTAL DESCRIPTION

Experimental Apparatus

The pool nucleate boiling experiments on the surfaces of different material metal plate with different thickness were conducted to investigate the nucleation site interaction. The schematic of the experimental set-up is shown in Fig. 1(a), which mainly consists of test section, liquid tank, power supply and measurement system, and cooling loop.

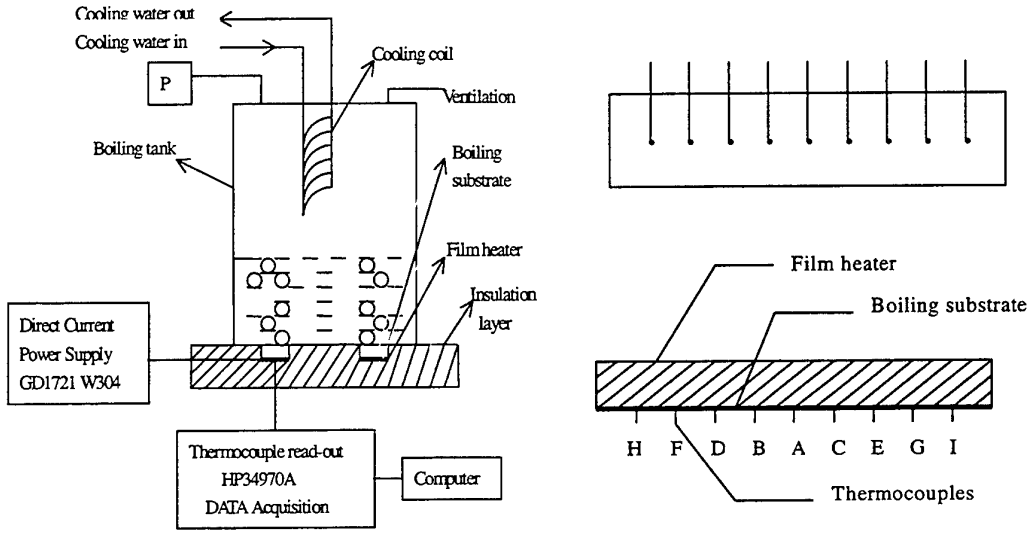

(a) Schematic of test apparatus

(b) Boiling surface (20 mm×60 mm, Thermocouples were installed uniformly)

Fig.1 Experimental apparatus

The liquid tank was made of a circular Pyrex vessel having height of 120 mm and inside diameter of 110 mm. The bottom of the tank was made of insulation material plate into which two 20×60 mm rectangular metal plates having variable thickness were symmetrically mounted. These two metal plates were placed into the channels as boiling substrates and sealed with 704-silicone rubber. Nine copper-constantan (T-type) thermocouples were uniformly embedded into the bottom of the metal plates to measure the boiling surface temperature. The film heaters were coated onto the bottom side of the metal plates. The heaters have electric resistor of 9.00 ohm, 9.04 ohm, 9.04 ohm and 8.95 ohm, respectively. There are four kinds of test sections were used in this experimental investigation. Two were made of aluminum plates having thickness of 6 mm and 11 mm. Another two were made of 0.13C-12.95Cr-0.14Ni stainless steel plates having thickness of 6 mm and 11 mm. Liquid methanol, ethanol and n-pentane were used as working fluids. The detailed test section is shown in Fig. 1(b).

A GD1721 direct current power supply was connected in series with a standard resistor and film heater. The resistor was used to measure the system electric current. This power supply can provide desired heat flux by adjusting the voltage input.

The date acquisition system includes one 16-channel input modules (with 14 for thermocouple and 2 for voltage and electric current) whose uncertainty is 0.1% provided by the manufactures, and a RS232 interface connected to a personal computer.

A water-cooled coil was used to condense the vapor generated and minimize the loss of the test liquid and stabilize the system pressure. Atmospheric pressure was maintained by venting the test vessel to ambient. The U-typed pipe is used to monitor the pressure in the vessel. The whole test section was placed into the insulation house to minimize the loss of heat flux.

Experimental Procedure and Data Reduction

The parameters required to measure in this experiments are the boiling wall temperature, the voltage drop U across the film heater and current I. The heat flux can be calculated by the measured voltage , U, across the film heater and the current, I, as

$$q'' = UI / A \tag{1}$$

Time-area averaged temperature is defined as

$$\overline{T} = \frac{1}{At}\int_A \int_t T dA dt \tag{2}$$

The bottom time-area averaged temperature of the boiling substrates can be obtained by data acquisition system, and then the boiling wall surface time-area averaged temperature can be corrected by one-dimensional heat conduction model at each applied heat flux as

$$\overline{T}_w = \overline{T} - q'' b / \lambda \tag{3}$$

And wall superheat is obtained as

$$\Delta\overline{T}_{sup} = \overline{T}_w - T_s \tag{4}$$

In the experiment, the experimental system is first started up with no power input. Then it is necessary to heat the test liquid at small power until it reaches the saturation temperature of working liquid. Increasing the voltage input of DC power to obtain desired heat flux. A comparison was then made between two average temperatures for each thermocouple after each heat flux increment. The procedure was repeated until the temperature difference for all thermocouples was less than 0.2 K. The test section is considered to be at steady conditions. Usually, it takes about 2 minutes to reach the steady conditions after each heat flux increment. The temperatures of all measured points were recorded and the voltage and current were measured as the steady state was reached.

The heat losses from substrate were estimated to be less than 6%. The uncertainty estimates in temperature are about 5%. Repeated experiments show that the reproduction was satisfactory.

3. RESULTS AND DISCUSSIONS

The temperature histories are obtained by data acquisition systems to investigate the temperature wavy characteristics and thermal interactions. Figure 2 shows the situation before the occurrence of boiling. Very clearly, the wall temperatures are quite uniform and stable for single-phase convection. The non-uniform appears when the nucleate boiling occurs. Figure 3 shows the situations of the wall temperature as a function of time at different measured locations. The performance of the wall temperatures for different positions is very similar, but not in same chronology. The wavy change of wall temperature with significant amplitude and irregular period/frequency can be attributed to the thermal interactions. Nucleation or bubble generation on the wall surface results in the temperature variation both at the corresponding site and at/in adjacent site/area. In other word, either nucleation or bubble departure at same point or those at adjacent sites may induce the temperature variation at any other points. When very careful comparison is made for Fig. 3 and other associated results, it is easy to find that the wall temperatures usually decrease at adjacent points while the wall temperature becomes higher at a measured point. This does demonstrate the interaction between nucleation sites. The wavy characteristics become more evident with the increasing applied heat flux. Therefore, the nonlinear thermal interactions will become more evident with the increasing applied heat flux.

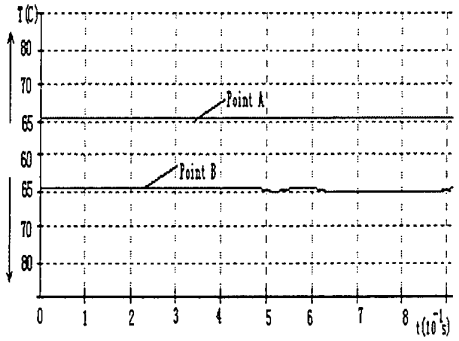

Fig. 2 Wall temperature history before boiling ($q=16.75kW/m^2$)

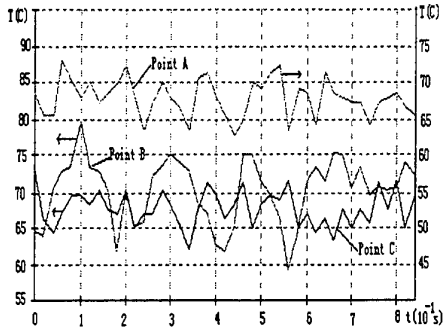

Fig.3 Wall temperature history for nucleate boiling

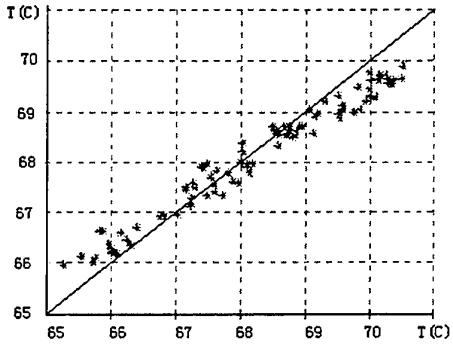

Fig. 4 The temperature relation at two adjacent points (Points B and C) (Aluminum, b=11mm)

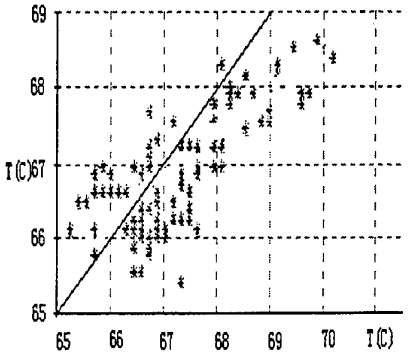

Fig. 5 The temperature relation at two adjacent (Points B and C) (Aluminum, b=6mm)

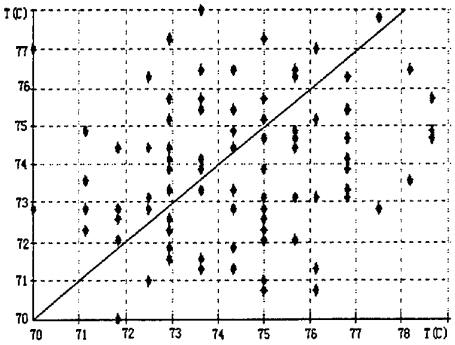

Fig. 6 The temperature relation at two adjacent Points (Points B and C) (Stainless steel, B=6mm)

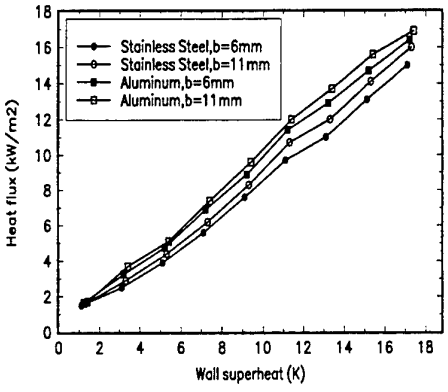

Fig. 7 Experimental data of pool nucleate boiling (test liquid: methanol)

The thermal interactions are significantly influenced by the properties and thickness of test plate. Boiling experiments on aluminum wall with thickness of 6 mm and 11 mm, and 0.13C-12.95Cr-0.14Ni stainless steel plates with thickness of 6 mm and 11 mm were conducted to reveal this thermal interaction characteristics. To explore the temperature interrelationship of two adjacent positions, the temperatures at two adjacent points are obtained by data acquisition system, represented by x-axis and y-axis, respectively. The results for different plates are illustrated in Figs. 4~6. Figure 4 presents the results for aluminum having thickness of 11 mm, figure 5 for aluminum having thickness of 6 mm, and figure 6 for stainless steel having thickness of 6 mm. The deviation from the diagonal in figures indicates the degree of the thermal interaction. Very apparently, for about same applied heat fluxes the scatter is quite different for the tested plates with different thickness, as shown in Fig. 4-6. This implies that the wall properties and thickness greatly affect the thermal interactions. The thinner the plate and the smaller the thermal conductivity, the strong the thermal interactions will be. From the comparison, the thermal conductivity plays a more critical role for the thermal interaction.

The thermal interactions influence the temperature distribution or superheat degree of boiling surface, and furthermore, change actual active site density and associated nucleate boiling heat transfer. The results of boiling experiments of liquid methanol, ethanol and n-pentane are illustrated in Figs. 7-9. Apparently, the wall thermal conductivity greatly affects nucleate boiling heat transfer. At same superheat, the heat flux for plate having larger thermal conductivity is higher than that for the plate having smaller thermal conductivity. Simultaneously, the wall plate thickness also affects nucleate boiling heat transfer. At same superheat, the heat flux for thicker plate is higher than that for thinner one. This is because the conductivity and plate thickness cause thermal interactions different. In reality, the thermal interaction for the plates with higher values of thermal conductivity and thickness will become weaker and have less influence in decreasing the heat transfer.

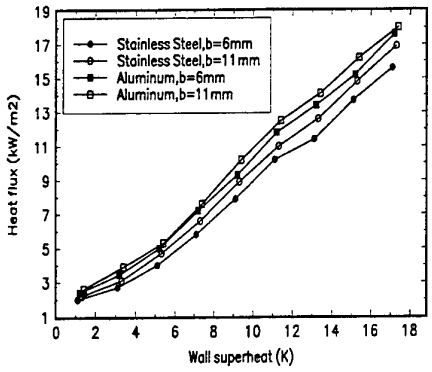

Fig. 8 Experimental data of pool nucleate boiling (test liquid: ethanol)

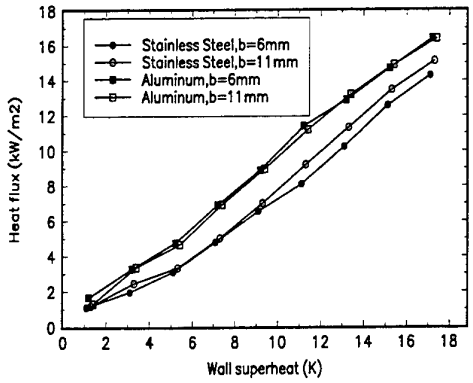

Fig. 9 Experimental data of pool nucleate boiling (test liquid: n-pentane)

So far, not much attention has been paid to the wall effects on nucleate boiling heat transfer for a long time. In available investigations, the researches are only focused on the wall surface characteristics, such as micro-geometry, roughness and wet-ability. The scatter in experimental data for nucleate boiling used to be attributed these surface characteristics. However, some experiments evidenced that the thermophysical properties or material of boiling surfaces and thickness of boiling substrates results in significant impact on boiling nucleation and the heat transfer. The scatter and deviation in experimental data is not just caused by surface characteristics and measurement certainty, but also by the thickness and thermophysical properties of boiling substrates. Apparently, both surface characteristics (roughness, aging, wet-ability) and bulk characteristics (substrate properties, thickness) are critical aspects necessary to be included in the research of nucleate boiling heat transfer. For surface characteristic effects often mask the bulk effects, it is worthy to distinguish the surface effect from bulk effects. In present experiments, some special care was made to guarantee that four

plates made from different materials with different thickness have similar surface characteristics. Therefore, the differences in boiling heat transfer for four plates are mainly caused by the bulk effects.

The bulk effects on boiling heat transfer will arise in two different ways. First, the decrease of wall temperature with the bubble forming and growing affects its waiting time period and growing period, and associated heat transfer. This kind of phenomenon is reflected in penetration distance induced by growing bubble. The penetration distance has an order of 1.5 mm for aluminum and 0.4 mm for stainless steel, respectively. It is expected that the boiling heat transfer coefficient will be independent of plate thickness if the thickness exceeds the penetration distance. Secondly, the decrease of wall temperature with the bubble forming and growing, affects adjacent bubble formation and growth, and thus changes the whole nucleate boiling performance and associated heat transfer. This kind of phenomenon is called thermal interactions. In present experiments, the plate, 6mm and 11mm in thickness, respectively, is much larger than penetration distance. Obviously, the differences in boiling heat transfer for four plates are mainly caused by the thermal interactions.

4. CONCLUSIONS

Nucleation site interaction during boiling process greatly affects active site density and associated boiling heat transfer. The nucleation site thermal interaction is realized by non-uniform temperature distribution. The temperature distribution is highly dependent upon boiling wall properties and thickness. The experiments on metal plate substrates machined from different material with different thickness were conducted to investigate the nucleation site interaction. It was revealed that boiling wall properties and thickness have a significant influence on nucleate boiling heat transfer. It seems surprising that boiling wall properties and thickness influence nucleate boiling heat transfer through the thermal interaction, not through depressing the single bubble waiting period and growing period as commonly expected.

ACKNOWLEDGMENT

The project was supported by the National Natural Science Foundation of China through contract #59625612.

REFERENCES

1. V. K Dhir,. "Nucleate and transition boiling heat transfer under poor and external flow conditions", *Proc. 9th Int. Heat Transfer Conf.*, Hemis. Publ. Corp., New York, *V.*1, *pp.*129-155. (1990)
2. D.Gorenflo, A. Luke and E. Danger, "Interactions between heat transfer and bubble formation in nucleate boiling", *Proceeding of International Heat Transfer Conference*, *v.*1, *pp.149-174,* edited by J. S. Lee, Kyongju, Korea (1998).
3. Shoji M. "Boiling chaos and modeling. *Proceeding of International Heat Transfer Conference*, *v.*1, *pp.3-21,* edited by J. S. Lee, Kyongju, Korea (1998).
4. X. F. Peng and B. X. Wang, "Forced-convection and boiling characteristics in microchannels", *Proceeding of International Heat Transfer Conference*, *v.*1, *pp.371-390,* edited by J. S. Lee, Kyongju, Korea (1998).
5. L. H. Chai, X. F. Peng, B. X. Wang and J. M. Ochterbeck, Int. J. Heat Mass Transfer, v. 41, pp. 3529-3535 (1998).
6. L. H. Chai, X. F. Peng and B. X. Wang, J. of Engineering Thermophysics, v. 20, pp. 332-336 (1998).
7. L. H. Chai and X. F. Peng, Natural Journal, v. 20, pp. 243-244 (1998).

NOMENCLATURE

A	surface area	b	plate thickness
I	electric current	q	heat flux
t	time	T	temperature
U	voltage		

Greek symbols

λ	thermal conductivity

Subscripts

sup	superheat	w	wall

EFFECTS OF PARALLEL ELECTRODES ON ELECTRO-HYDRO-DYNAMICALLY (EHD) ENHANCED BOILING HEAT TRANSFER

Jafar Madadnia, Victor Ramsden, & Thai H. Nguyen
Faculty of Engineering, University of Technology, Sydney, NSW 2007, Australia
Email: : j.madadnia@uts.edu.au, vicr@eng.uts.edu.au, tnguyen@ipe.com.auFax: (61-2) 9514 2655

Keywords: boiling heat transfer, electrohydrodynamic, parallel electrodes, refrigerant R11, enhanced convection

ABSTRACT. Prediction and modelling of Electro-Hydro-Dynamic (EHD) effects in boiling is the key to improving the determination of enhanced convection heat transfer in heat exchangers. The experimental investigation presents the qualitative, and the quantitative analysis. Theoretical models were developed and validated by the experimental data from the EHD effects with parallel electrodes, on the enhancement of pool boiling heat transfer of R11 in both free convection, and nucleate regions. The qualitative analysis showed that EHD effects could locally reduce the heat transfer rates through holding bubbles and hence blanket partially the heating surfaces. The quantitative analysis indicated that the EHD effects varied with the electrode-voltages, electrode orientation, and the boiling regions. Application of EHD increased the maximum heat transfer capacity of the boiling surface.

NOMENCLATURES

a & b	coefficients of linear models	q"	heat flux (W/m^2)
h	heat transfer coefficient (W/m^2K)	ΔT_e	wall super heat = $T_s - T_{sat}$ (K)
h_n	heat transfer coefficient (with electrode-voltage of n kV)	$V_{electrode}$	electrode-voltage (2, 4, 6, 8, and 10kV)
p	pressure (Pa)		

1. INTRODUCTION

Boiling and condensation are characterised with a very high and efficient convection heat transfer making boilers and condensers to occupy relatively smaller spaces. In recent years the dramatic growth of solid state technology has brought a challenging prospect of thermal design and management for heat exchanger designers. The successful operation of modern electronic devices; ranging from microelectronic devices to large power tubes, is critically dependent on efficient and reliable heat removal.

Application of electric fields can enhance convection heat transfer by inducing the EHD induced fluid motion in boiling regions. This phenomenon was recognised over a century ago. However, it is only during the last three decades that some efforts have been made to investigate the phenomenon in fluids at moderate temperatures (1-12). The need for improved electronic cooling technologies and enhanced heat removal methods have attracted the attention of a large number of investigators. The rising levels of overall power dissipation and chip-level heat-flux have renewed interest in phase-change heat removal techniques. Rapid development of circuit integration currently underway is requiring a fresh look at the need to enhance heat transfer using different electronic designs and electrohydrodynamic (EHD) effects in boiling and condensation. Intensity of cooling requirements in the some of electronic, computing and space applications, have rationalised EHD research in boiling and condensation. Isothermal cooling, phase change and high density differences, are some of the attracting features of the combined applications.

2. EXPERIMENTAL APPARATUS

The experimental apparatus, as shown in Figure 1, consists of three main components namely; a multi-phase heat transfer unit, electrodes, and a DC-power supply unit. The test rig to provide a pool boiling of R11 affected by EHD. The saturation pressure and temperature are controlled by a flow of cooling water through the condenser coil. Two thermocouples (T-type and K-type with different sensitivity) were soldered on the heater to record the temperature of heater's surface. The heater of a 12 mm copper tube with a uniform surface

temperature is used to heat R11. The boiling regions on the heater are observed through a clear cylindrical glass tube.

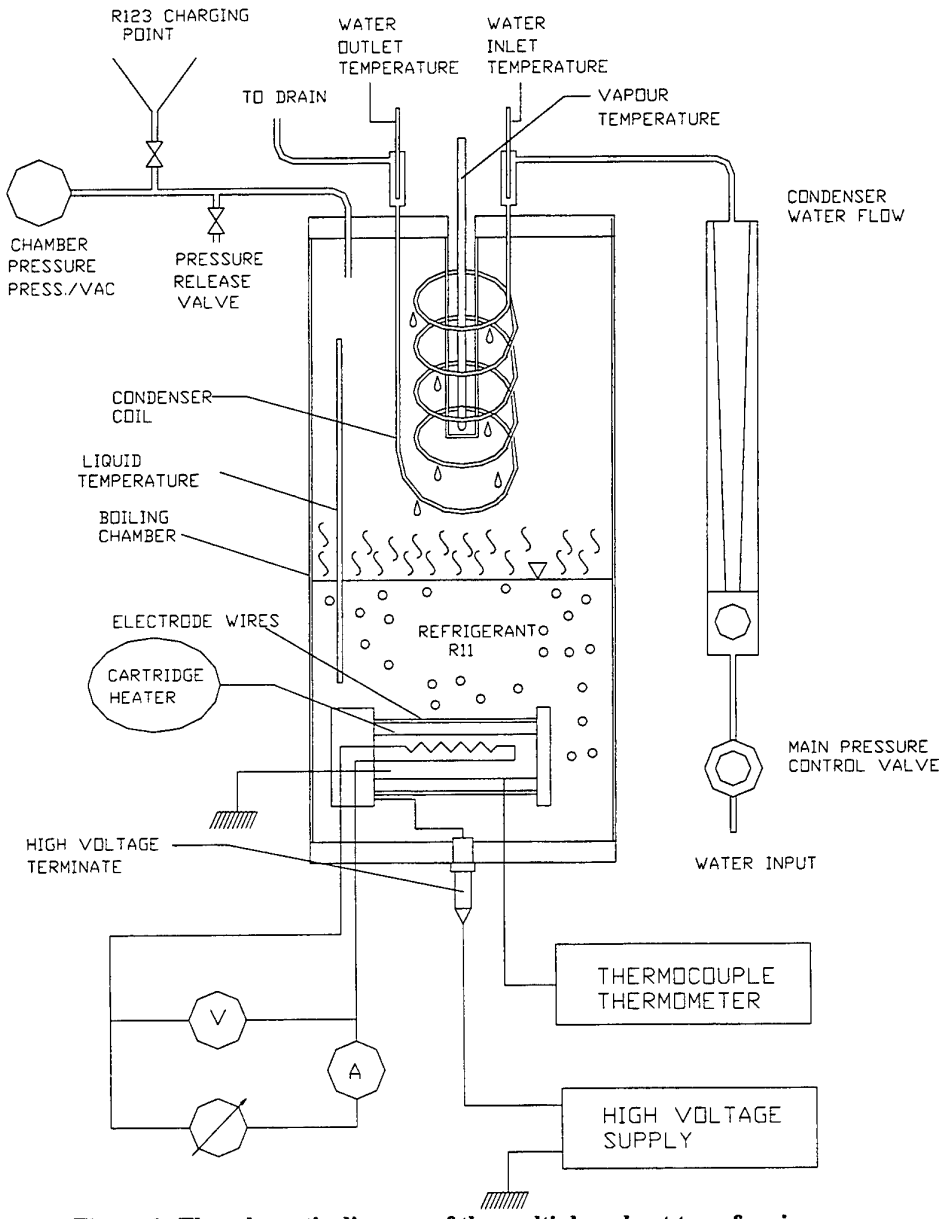

Figure 1: The schematic diagram of the multiphase heat transfer rig

2.1 High Voltage Power Supply

A variable voltage 10kV-5mA power supply supplied the electrodes voltages. Car battery cables were used to connect the power supply to the test section. These high tension cables can withstand the input voltage about 20kVAC while the maximum output voltage is about 15kVAC. A variable transformer converts the 240V alternative currents (AC) into a direct current (DC) with the maximum output voltage 15 kVDC.

2.2 Refrigerant R11

R11 was selected as the di-electric fluid as its saturation temperature is around 23^0C at the ambient pressure and can be stored in a low pressure container.

2.3 Electrode-Design

There are several different electrode designs. However, only electrodes with straight wires as shown in Figure 2b, were used at this work. A support mechanism was designed to hold the electrodes at their positions around the heater. The design consisted of 8 straight copper wires of 1.5mm in diameter, positioned parallel to the heater tube. The distance of electrodes from the heater surface was 2mm.

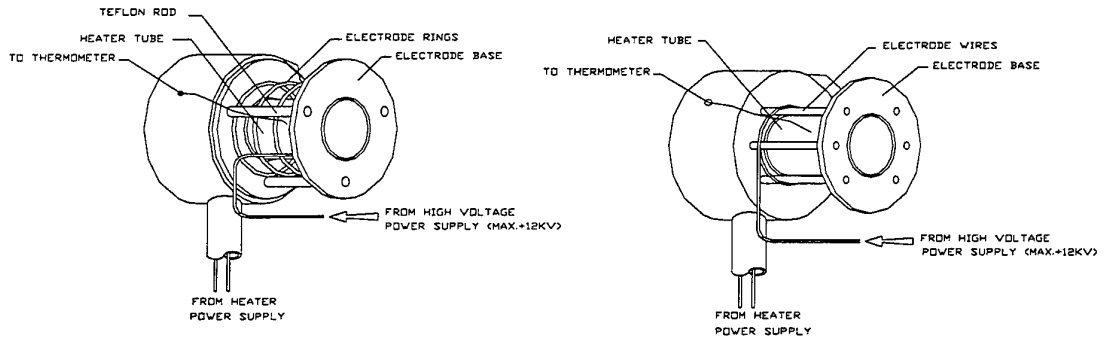

a) Electrode with helical coiled wires **b) Electrode with straight wires**

Figure 2. Schematic diagram of electrode designs

3. EXPERIMENTAL PROCEDURES

In the present study, a direct-current electric force was applied on a pool boiling of R-11. Heat transfer data were taken in the natural convection, and the nucleate boiling regimes. Prior to each test, the heater surface was cleaned and polished with a fine sand paper (a high grade finish surface is needed).

The heating tube was electrically earthed and the electrodes were connected to the positive life voltage. During the experiment, the pressure and the saturation temperature are kept constant. The experiments were made at a constant pressure of 20 kPa (g). The steady state temperatures of the pool and the heater tube are recorded each time when the power to the heater was increased. Data were also taken during unsteady periods of heating up and cooling down. Before every experiment the base boiling conditions with zero EHD were observed. Then the data were collected when the electrode voltages of 2, 4, 6, 8 and 10 kV were applied.

4. RESULTS AND DISCUSSIONS

4.1 Qualitative Analysis

It was noticed that in the natural convection regime, prior to the nucleate boiling, EHD acts on the liquid and separates the hot liquids from the heating surface, so this so called the *electroconvection effect,* facilitates the movement of colder fluid to the heating region.

In the nucleate boiling regime, EHD forces push the bubbles and locally blanket to the heating surface. In general, EHD also affects on the inception of nucleation, locations of nucleate points, the dynamics of bubbles, the change of nature of heat transfer at different locations.

Figure 3a shows eight electrodes were positioned in 45 degree from each other, and the bottom two electrode wires were placed symmetrically in 22.5 degree respective to the vertical line. It was noticed that bubbles were hold between the two bottom electrodes at EHD voltages exceeding 10 kV, and consequently heat transfer coefficients were adversely affected due to the bubbles blanketing the heating surface. As the upper half of heater was not affected by the orientation of the electrodes, a non-uniform distributions of heat transfer rate and temperature were developed on the heater surface. The electrodes were rotated 22.5 degrees and positioned at zero degree relative to the vertical line (see Figure 3b). At this orientation of electrodes, EHD could not hold the bubbles on the surface and bubbles raised to the free surface as soon as nucleated. This showed that the orientation of electrodes could alter EHD affects.

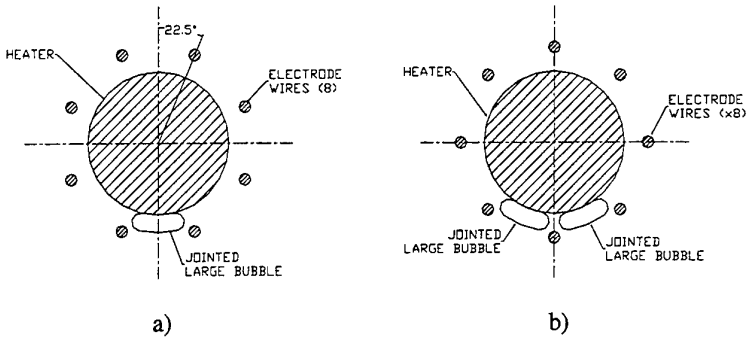

Figure 3: Orientation of electrodes in respect to vertical line

4.2 Quantitative Analysis (EHD Modelling)

The reference conditions for pool boiling were set when zero voltage applied to the electrodes (zero EHD). The heat flux to the heater was varied while maintaining the saturation pressure and temperature. Experimental data from the different regions in the boiling curve, such as, free convection, nucleate, transition, and film boiling regions were collected and (h_0) the convection heat transfer coefficient at zero EHD was determined for each data point.

These experiments were repeated when 2kV, 4kV, 6kV, 8kV, and 10kV were applied to the electrodes ($V_{electrode}$). Corresponding convection heat transfer coefficients (h_2 , h_4 ,h_6 , h_8 , and h_{10}) were then determined. The ratio of these convection heat transfer coefficients to the corresponding reference convection heat transfer coefficient (h_0), at both the free convection, and the nucleate regions, were plotted respectively against, the electrode-voltages ($V_{electrode}$) in Figures 4a & 4b, and the heat transfer flux (q" w/m^2) in Figures 5a & 5b.

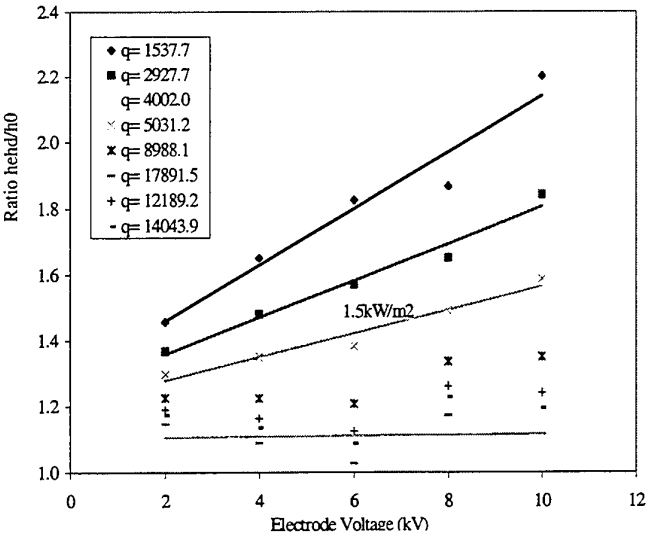

Figure 4a. Effects of electro voltage on convection transfer in free convection region

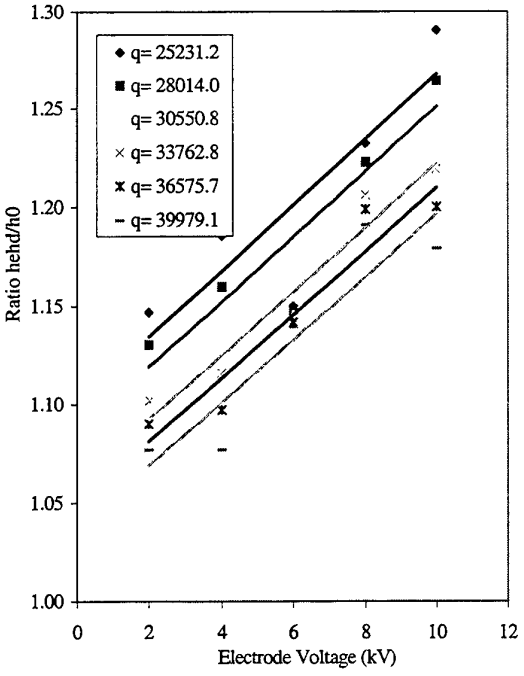

Figure 4b. Effect of electro voltage on convection heat tranfer in nucleate

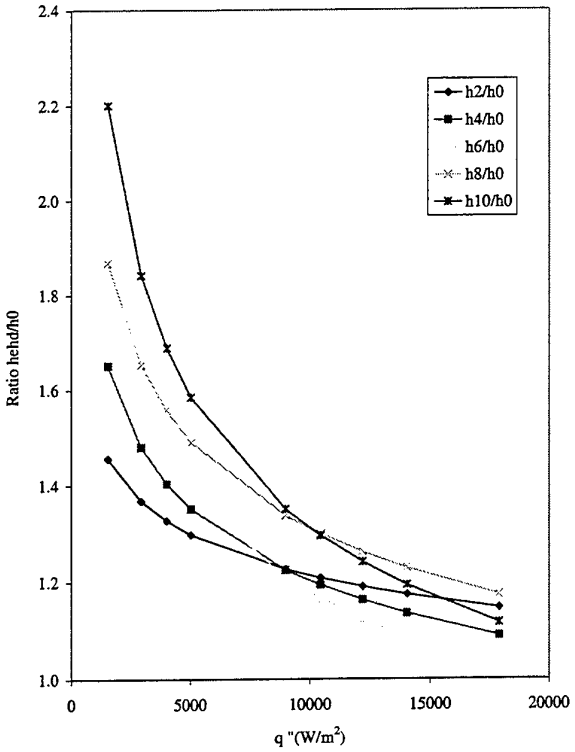

Figure 5a. EHD effect on convection heat transfer free convection boiling

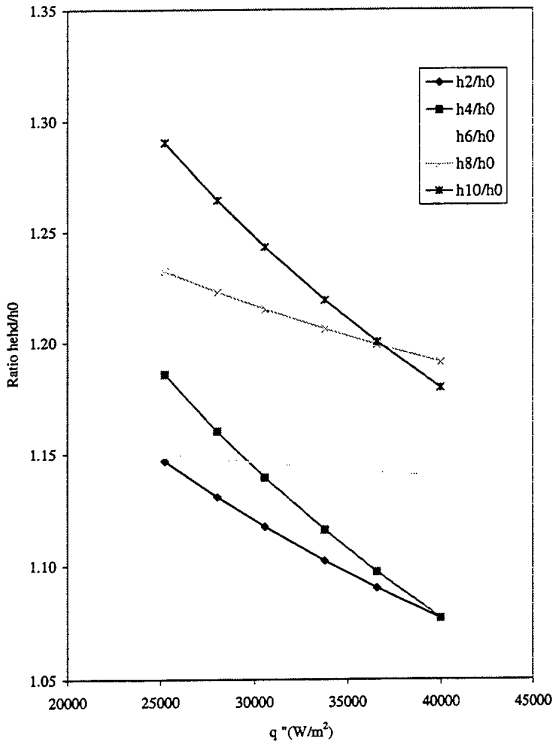

Figure 5b. EHD effect on convection heat transfer in nucleate

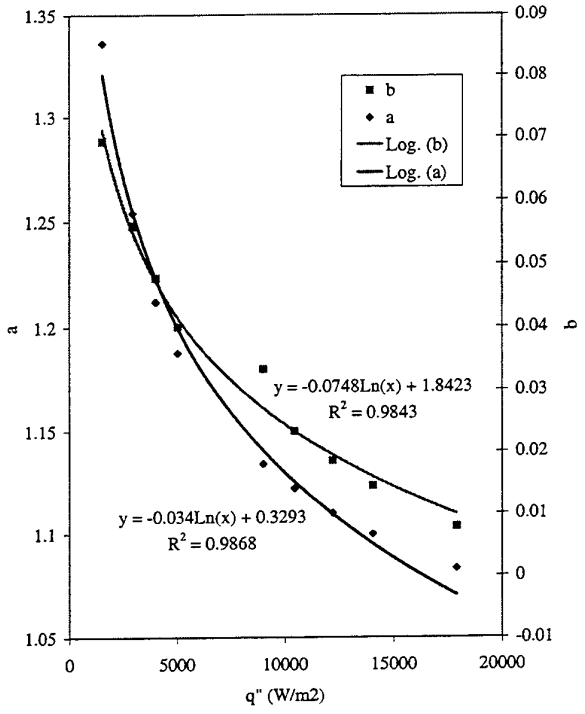

Figure 6a. Coefficient of modelling for free convection region

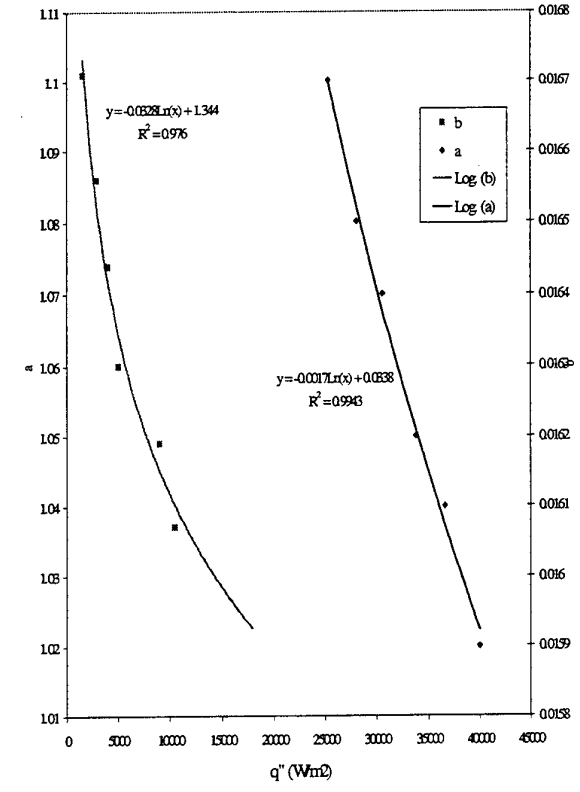

Figure 6b. Coefficient of modelling for free nucleate region

The best curve-fits to the Figures 4a & 4b suggest linear models for both the free convection, and the nucleate regions with the following format:

$$(h_{EHD})/(h_0) = a \,.\, (V_{electrode}) + b$$

Figures 6a & 6b present values of "a" & "b" at different heat fluxes for both the free convection, and the nucleate regions respectively. The slops ("a") and the constant values ("b") decrease with increase of the heat flux. The following logarithmic distributions were obtained for "a" and "b" as a function of the heat flux (q").

a = -0.034 ln (q") + 0.3293,	b= -0.0748 ln (q") + 1.8423	(for the free convection boiling region)
a= -0.0017 ln (q") + 0.0338,	b = -0.0328 ln (q") + 1.344,	(for the nucleate boiling region).

It is anticipated to predict the EHD-enhanced convection heat transfer coefficients (h_{ehd}), with the known values of h_0 and $V_{electrode}$, for boiling in both free convection, and the nucleate regions.

The qualitative analysis showed that EHD could locally reduce heat transfer rate by blanketing the heating surfaces and restricting bubble dynamics. The quantitative analysis suggested a correlation for the determination of the convection heat transfer rate.

REFERENCES

1. H.D. Young, (1992) *Physics, extended version with modern physics*, 8th ed., Addison Westley, Inc.
2. P.M. Gerhart, R.G. Gross, and J. Hochstein, (1992), *Fundamentals of Fluid Mechanics*, 2nd ed., Addison Westley, Inc.
3. G.V. Wylen, R. Sonntag, and C. Borgnakke, (1994) – *Fundamentals of Classical Thermodynamics*, 4th ed., John Wiley & Sons, Inc.
4. F.P. Incropera, and D.P. Dewitt, (1996) – *Fundamentals of Heat and Mass Transfer*, 4th ed., John Wiley & Sons, Inc.
5. J. Dally, W. Riley, and K. McConnel, (1993) – *Instrumentation for Engineering Measurement*, 2nd ed., John Wiley & Sons, Inc.
6. J.S. Yagoobi, C.A. Geppert, and L.M. Geppert, (1995) – *Electrohydrodynamically Enhanced Heat Transfer in Pool Boiling*. Dept. of Mechanical Engineering, Texas A&M University, College station, USA.
7. J. Madadnia, (1998) - *Electrohydrodynamically Enhanced Multi-phase Heat Transfer*, Faculty of Engineering, Mechanical Engineering, University of Technology, Sydney, Australia.
8. J.S. Yagoobi, E. Bryan, and J.A. Castaneda, (1995) – *Theoretical Analysis of Ion-Drag Pumping*. Dept. of Mechanical Engineering, Texas A&M University, USA.
9. T. Yajima, and A. Yabe, (1998) – *Time Variation of the Film Thickness under the Boiling Bubbles in Saturated Pool Boiling Heat Transfer*, Institute of Engineering Mechanics, University of Tsukuba Japan & Mechanical Engineering Laboratory Fluid Division MITI/AIST Japan.
10. A. Yabe, Y. Mori, and K. Hijikata, (1996) - *Active Heat Transfer Enhancement by Utilizing Electric Fields,* Annual Review of Heat Transfer, Vol.7.
11. F.M. Verplaetsen, and J.A. Berghmans, (1998) – *Film Boiling of an Electrically Insulating Fluid in the Present of an Electric Field*, Department of Mech. Eng., Katholieke Universiteit Leuven Belgium.
12. M. Ohadi, and S.V. Dessiatoun, (1998)– *Liquid-Vapor Seperation and Thermal Management in an Electrohydrodynamically-Enhanced Capillary Pumped Loop*, Department of Mechanical Engineering University of Maryland USA.

EHD ENHANCEMENT OF BOILING HEAT TRANSFER IN VERTICAL TUBE

Enke An, Ruiyang Li, Hongling Yu, Zhihang Chen, Xuan Huang and Xuelai Zhang
College of Power Engineering
University of Shanghai for Science and Technology
Email: lizhendk@online.sh.cn; Fax: (21)-65682258

Key Words: Boiling Heat Transfer, EHD, Heat Transfer Enhancement

ABSTRACT. The applicability of electrohydrodynamics (EHD) technique for in-tube boiling heat transfer enhancement of R11 in vertical tube was investigated experimentally. The test rig was similar to a separated heat pipe which consisted of a tube-in-tube heat exchanger with hot water or cold water flowing in the outer tube and refrigerant flowing through the inner tube. A coaxial stainless steel cylindrical electrode with an outer diameter (OD) of 2.5mm and a length of 800mm was inserted through the test section, which was a smooth stainless steel pipe with an inner diameter of 25mm. The experiments was conducted under different values of heat flux, electric high voltage, and superheat. It was found that R11 exhibits an evident response to the EHD effect. An increase in the heat transfer coefficient of as high as 300% was obtained compared to the base case (absence of EHD effect). The electrical power consumption was found to be less than 0.3% of the corresponding heat transfer rate.

1. INTRODUCTION

The electrohydrodynamics (EHD) enhancement of heat transfer refers to the coupling of an electric field with the fluid field in a dielectric fluid medium. The net effect is the production of secondary motions which cause better mixing of the flow and increased activity near the heat transfer surface, leading to heat transfer coefficients which are in most cases an order of magnitude higher than those achievable by conventional enhancement techniques.[1]

The driving force electrically inducing secondary motions responsible for the EHD heat transfer enhancement is an electric (or EHD) body force. For a dielectric fluid of permittivity ε, density ρ, and temperature T under applied electric field strength of E, this body force can be expressed as[2~3]

$$f_E = q\bar{E} - \frac{1}{2}E^2\nabla\varepsilon + \frac{1}{2}\left[E^2\rho\left(\frac{\partial\varepsilon}{\partial\rho}\right)_T\right] \tag{1}$$

where q is the electric field space charge density in the fluid. The first component on the right-hand side of Eq. 1, called electrophoretic force, results from the net free charge within the fluid. For the two-phase processes, the EHD current discharge is insignificant, thus the first term dose not contribute strongly to the EHD body force. However, the second term called the dielectrophoretic, and the third term, called the electrostrictive force, contributes substantially to the EHD body force in a phase-change process. The dielectrophoretic force is produced by the spatial change of the dielectric constant (ε), and the electrostrictive force is produced by the inhomogeneity of the electric field distribution. Also, both terms depend on E^2; thus, the magnitude of E plays an important role in phase-change processes.

Several studies have demonstrated the applicability of the EHD technique to the boiling heat transfer enhancement of out-tube boiling of refrigerants. Increases of the boiling heat transfer coefficient up to seven-and-half fold by EHD technique have been reported in many studies. However, a comprehensive literature search failed to identify any previous work on EHD-enhanced in-tube boiling heat transfer in vertical tube[4~7]. The objective of the present study was to quantify the applicability of the EHD technique in an in-tube boiling heat transfer enhancement of R11. The experiments included the study of the EHD-enhanced boiling heat transfer coefficients and heat flux as a function of superheat and a given applied electric field potential.

2. EXPERIMENTAL APPARATUS

A schematic of the test facility is shown in Figure 1. The setup consisted of four distinct flow loops: a refrigerant flow loop similar to a separated gravity heat pipe, a hot-water loop providing heating energy to the test section, a cold-water loop providing cooling energy to another test section, and a refrigeration loop condensing and subcooling cold-water entering the test section in tube-in-tube.

The hot-water heating loop includes hot water tank, a pipe pump, a precision mass flow meter, an electric preheater, and inlet and outlet thermopiles. The cold-water cooling loop includes a cold water tank, a pipe pump, a precision mass flow meter, and inlet and outlet thermopiles. The test section is a separated gravity heat pipe. The boiling section is a vertical mounted tube-in-tube heat exchanger in which hot water flows in the outer tube. The condensation section is a horizontally mounted tube-in-tube heat exchanger in which cold water flows in the outer tube, and the test refrigerant circulated in the inner tube depending on gravity. The inner diameters of the inner and the outer tube were 25mm and 60mm, respectively. The length of test section is 800mm with a wall thickness of 3 mm. The tube fitting are used on both ends of the test section to facilitate quick and easy replacement of the electrodes and the test section.

Figure 2 shows the locations of thermocouples in the test section. The inner tube consisted of two tightly fitting tubes. Wall temperature in the test section is measured using insulated armory thermocouples (type E) welded directly between the two tubes of the tube-in-tube. Temperatures are measured at four axial locations at equal intervals of 200mm. At each axial location, the thermocouple is placed at four positions at intervals of 90° from another point of the tube. The thermopiles (each end has 8 junctures) are placed at inlet and outlet of the water to measure the temperature drop of hot water/cold water through heat exchanger. Two measuring points for work refrigerant temperature are placed in the thermally insulated end of the test section. Before installation, the thermocouples are selected from the spool where differences in the readings are found to be within 0.3°C in a temperature range of 0°C to 100°C.

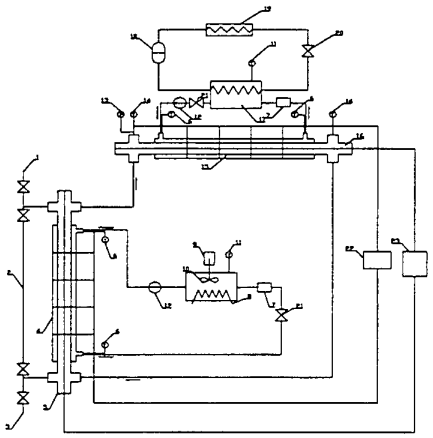

Figure 1 Schematic diagram of experimental apparatus

1. Charge inlet	2. Liquid level indicator	3. Discharge outlet
4. Hot water	5. Boiling section	6. Thermppiles
7. Flow meter	8. Electric heater	9. Motor
10.Treater	11.Thermocouple	12.Pipe pump
13.Barometer	14.Satuation temperature	15.Cooling water
16.Condensing section	17. Evaparator	18. Compressor
19. Condenser	20. Choke instrument	21. Valve
22. Data-acquisition system	23. High voltage instrument	

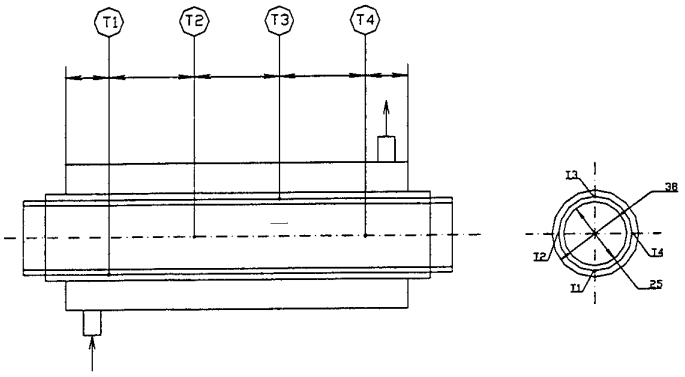

Fig. 2 Wall temperature arrangement

The electrode used in the experiments is a simple coaxial cylindrical rod with a diameter of 2.5mm. Positive potential was applied to the electrode through DC high voltage supplier, whereas the tube is grounded.

Heating energy to the test section is supplied by hot water. Condensing energy to another test section carried away by cold water. The whole test rig is thermally insulated. Heat flux on test tube surface is controlled by regulating the temperatures of hot and cold water and their mass flow rates.

The data-acquisition system consisted of a personal computer, a analog-to-digital (a/d) card with multiplexes of 16 channels. The data-acquisition source code provides monitoring of 14 thermocouples and 2 thermopiles. The readings from two mass flow meters are the parameter that had to be entered manually. Data reduction calculations pertaining to the heat transfer coefficient and heat flux are also performed on the computer.

3. DATA PROCESSING

The heat transfer coefficient could be determined using the defining equation

$$h = \frac{Q}{A(T_W - T_S)} \tag{2}$$

where Q is the energy transferred on the test surface, Tw is the average tube wall temperature of the inner test section, and Ts is the saturation temperature of refrigerant.

The inside tube-wall temperature is calculated by presuming that heat is conducted only radial from the outside to the inside of the test-section tube, so

$$T_{wi} = T_{wo} - \frac{Q\ell n(R_2/R_1)}{2\pi KL} \tag{3}$$

Where T_{w0} is the average value of the four pairs of thermocouples on wall at an axial position, k is the thermal conductivity of the tube material, and L is the length of the test section tube.

Under the assumption of a constant thermal conductivity, the heat transfer ratio with and without the EHD field could reduce to the ratio of Nussult numbers:

$$\frac{Nu}{Nu_0} = \frac{h}{h_0} \tag{4}$$

where h is heat transfer coefficient under the effect of electric field, and Nu_0 and h_0 represent the heat transfer coefficients and the Nusselt number for the base case (absence of electric field) respectively.

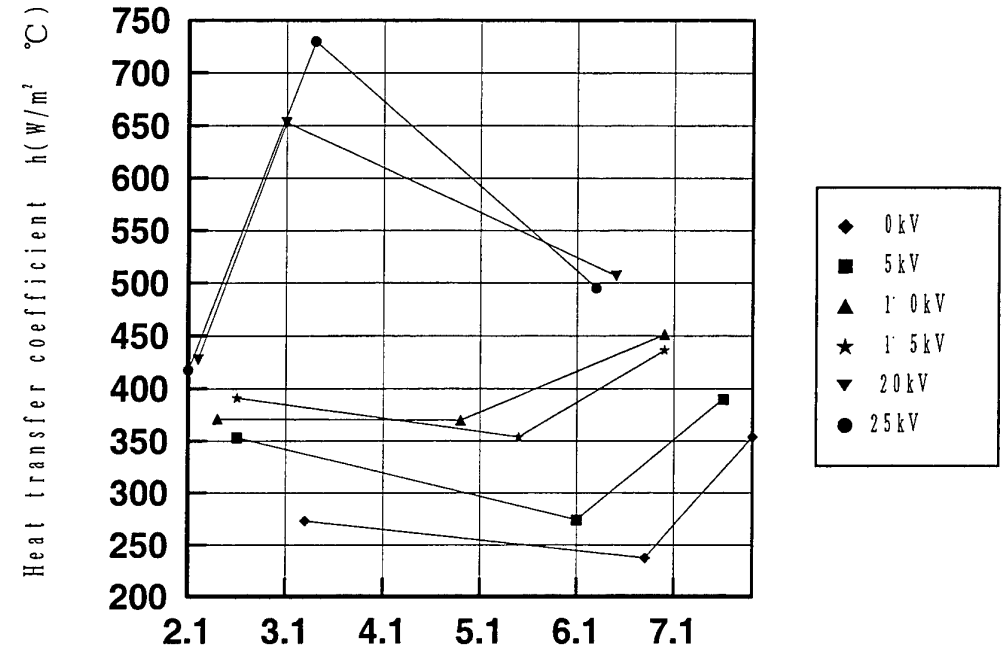

Fig 3 Relation between heat transfer coefficient and superheat

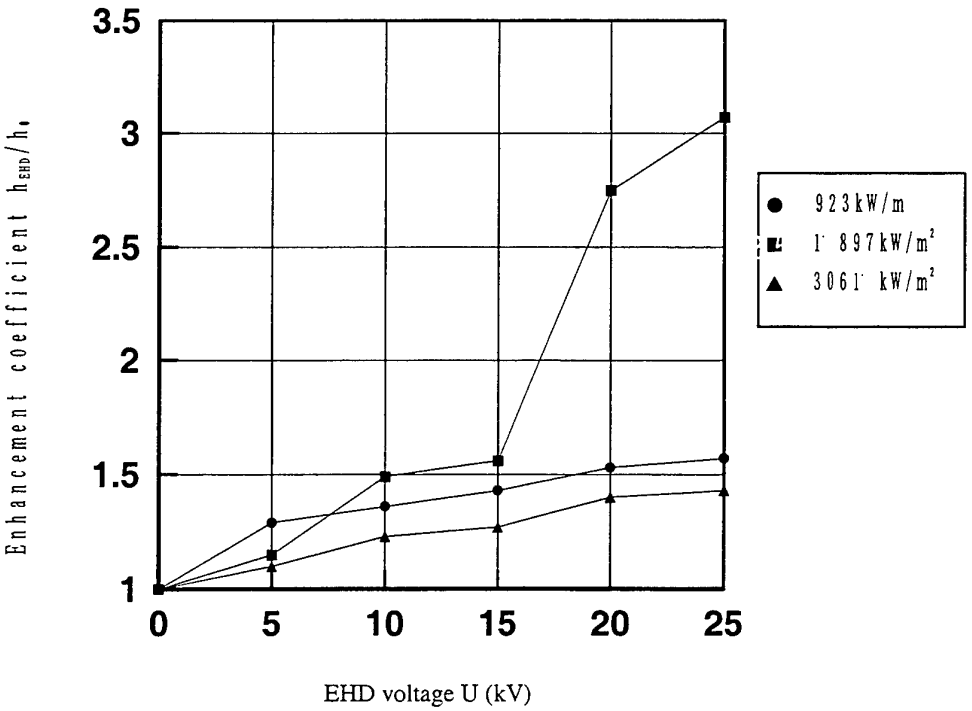

Fig. 4 Relation between EHD enhancement coefficient and electric voltage

4. RESULTS AND DISCUSSION

The experiment was conducted under a pressure of 83kpa, which corresponded to a saturation temperature of 18.5°C. Distribution of the average heat transfer coefficient as a function of superheat is shown in Figure 3. The values of heat transfer coefficients are recorded and plotted for the applied electric voltage of 0, 5, 10, 15, 20, 25kV respectively. It could be seen that an increase in electric field strength results in an increase of heat transfer coefficients. Application of high-voltage field increases significantly the heat transfer coefficients due to the EHD –induced secondary motion effects.

Figure 4 shows an EHD enhancement coefficient (h/h_0) as a function of the heat flux at various high voltage levels. It's seen that the EHD enhancement coefficient is larger than 140%. The maximum reaches to 300% and takes place at the heat flux of 2500w/m^2 and the electric high voltage of 20kv.

The EHD current is near zero, and the maximum EHD power consumption is less than one watt and occurred at highest voltage (25kV). The maximum EHD power consumption was less than 0.3% of the heat transfer capacity.

5. CONCLUSIONS

Results of an experimental investigation on the effect of high voltage on boiling heat transfer in a vertical tube using R11 as working fluid are reported in this paper. For this experiment, a smooth stainless steel test section tube and a simple coaxial cylindrical electrode are utilized to apply the EHD field. It is demonstrated that R11 responds well to the EHD effect. An enhancement of about 130~300% in the test condition is obtained. The EHD power consumption is less than 0.3% of the corresponding heat transfer capacity. Higher enhancements could be expected if the EHD field is applied over the enhanced tubes for an optimized electrode geometry. Experiments are in progress, which may quantify the effect of such optimization.

REFERANCES

1. Abtar Singh, Michael M.Ohadi, and Serguei Dessiatoun. ASHRAE Transactions,1997-10-3
2. Thomas F.Irvine, Jr. And Jamwes P.Hartnett. Heat Transfer, Academic Press, New York,1978
3. A.Yabe. Proceeding of ASME/JSME Thermal Engineering Conf.,v.3,1991
4. L.W.Chubb. UK Patent,No.100796,1916
5. P.H.G.Allen and P.Cooper. Proceedings of 3 Int. Symp. on the Large Scale Application of Heat Pumps,1987
6. P. Cooper, C.P.Eng. ASHRAE Transactions:Symposia,1992-5-3
7. Abtar Singh, Michael M.Ohadi,Serguei Dessiatoun, and William Chu. ASHRAE Transactions: Symposia, 1994-10-3

BUBBLE STRUCTURE OF HIGH HEAT-FLUX BOILING IN TWO-DIMENSIONAL SPACE

Shigefumi Nishio
Institute of Industrial Science
University of Tokyo
Email:nishios@cc.iis.u-tokyo.ac.jp, Fax:+81-3-5411-0694

Hiroaki Tanaka
Graduate School, University of Tokyo
Email:hiroaki@cc.iis.u-tokyo.ac.jp, Fax:+81-3-3401-6575

Keywords: boiling heat transfer, subcooling, bubble structure, critical heat flux

ABSTRACT. The present study is an attempt to attain a good understanding of the effects of liquid's wetting ability and subcooling on bubble behavior of high heat-flux boiling. This was accomplished by observing bubble behavior for boiling of water, ethanol, and R141b in a quasi-two-dimensional space. It was found that, even in the quasi-two-dimensional space employed in the present study, CHF increases for increasing liquid subcooling in a range of low subcooling and the dependence of CHF on subcooling in this range is in reasonable agreement with the correlating equation by Ivey and Morris. If subcooling is increased further, CHF approaches a unique value as Elkassabgi and Lienhard reported. For bubble behavior in saturated boiling, large coalesced bubbles like filmwise bubbles were observed at high heat fluxes even for R141b which is a highly wetting liquid. As for the effect of subcooling on bubble behavior of high heat-flux boiling, the time and spatial mean structure changes from filmwise to discrete bubbles for increasing subcooling. Even at highly subcooled boiling, however, a large coalesced bubble appears intermittently and it triggers CHF. This result indicates that, even in subcooled boiling, the appearance of large coalesced bubble is the key condition for CHF.

1. INTRODUCTION

Boiling phenomena are very important in the energy equipment utilizing vapor such as power plants and also in the cooling control systems utilizing high heat-transfer rates of boiling such as cooling of steel plates and electronic chips. These applications have promoted understanding of the structural and heat transfer aspects of boiling phenomena.

For steady-state nucleate boiling of saturated liquid at high heat fluxes, Gaertner [1] reported the following triple-layer structure based on still photographs and high-speed motion pictures of boiling. The first layer is the liquid layer including numerous columnar stems of vapor attached to the boiling surface. This layer has been called as the "macrolayer". The second layer includes large mushroom bubbles formed by coalescence of the vapor stems. Gigantic vapor slugs exist in the third layer and they result from coalescence of the mushroom bubbles rising up from the second layer. In this paper, this model is called as the triple-layer model of bubble structure.

It is very important to examine the validity of the triple-layer model because the model has given the typical image of high heat-flux boiling of saturated liquid including transition boiling. For example, based on this model, Haramura and Katto [2] proposed the so-called "macrolayer dryout model" for CHF of saturated liquid. In the model, focusing on coalescence of vapor stems, the initial thickness of macrolayer just after the departure of a coalesced bubble was modeled from the viewpoint of the Kelvin-Helmholtz instability. Then, the occurrence of CHF was explained as the competing process of coalesced bubble departure and macrolayer dryout. Dhir and Liaw [3] proposed the so-called "unified model" for saturated pool boiling based on the triple-layer model.

Katto and Yokoya [4] observed behavior of the liquid film under a coalesced bubble for pool boiling of saturated water by setting optical equipment very close to the surface. They confirmed the existence of a liquid film, and they reported that CHF in saturated pool boiling related closely to the dryout of the liquid film (macrolayer) and

the periodic departure of coalesced bubbles. The macrolayer dryout model can explain the effects of several parameters on CHF, but there are also the following experimental results.

(1) The macrolayer dryout model assumes the stationary vapor stems of small diameters attached to the boiling surface, but this situation is very different from the results of observation reported by Nishio et al. [5] and Oka et al. [6]. Nishio et al. conducted a pool boiling experiment of saturated R113 on a plate of single crystal sapphire, and they observed dynamic behavior of liquid-solid contact from below the transparent boiling surface. The results indicate that, at CHF, dry areas become closely packed and the wetted area exists only like a network of wriggling continuous canals of liquid (they named this situation of liquid-solid contact as the liquid-solid contact of network pattern). As the result, the fraction of liquid-solid contact at CHF is decreased below 50%. The liquid-solid contact of network pattern was observed also by Oka et al., and it is much different from the triple-layer model in which isolated vapor stems of small diameters are attached to the boiling surface. In addition, Nishio et al. defined the contact-line-length density, Γ, as the total length of the triple-phase contact line existing on unit area of the boiling surface and they showed that Γ reaches the maximum at a heat flux very near CHF. This result indicates that the contact-line-length density must be one of the important quantities representing the boiling structure.

(2) Nishio et al. [5] conducted also a pool boiling experiment for saturated ethanol in a quasi-two-dimensional space. In their experiment, a horizontal ribbon heater of small width was sandwiched by two vertical glass plates to realize a quasi-two-dimensional boiling space. The results indicate that, at CHF, bubbles of very large mass, which can be called as the filmwise bubbles, are formed and a liquid film attached to the boiling surface does exist under the filmwise bubble. In addition, vigorous generation of promary bubbles does occur in the liquid film and they grow to semi-spherical bubbles like vapor domes. This result gives an image of the boiling structure different from the triple-layer model, but it is similar to the result obtained by Galloway and Mudawar [7] for forced convection boiling in a narrow channel.

(3) Based on the experiments by Tong et al. [8], and Carvalho and Bergles [9], Sadasivan et al. [10] described as follows; "With a highly wetting liquid, the discrete bubble region of nucleate boiling extends very close to CHF. Lateral coalescence of these discrete bubbles is just beginning to occur at heat fluxes just below CHF so that some coalesced bubbles as well as discrete bubbles appear on the heater. The importance of the macrolayer as it relates to nucleate boiling and CHF is currently unclear for these fluids."

(4) As coalescence of bubbles is suppressed in subcooled boiling, the heat flux, at which coalescence of bubbles begins to occur, tends to be higher for increasing liquid subcooling. For example, Elkassabgi and Lienhard [11] reported experimental results for CHF of subcooled liquids around horizontal cylinders. The photographs in their report show clearly that, at CHF, coalesced bubbles tend to be replaced by discrete bubbles for increasing liquid subcooling. The present authors believe that CHF models for saturated boiling should include a potential to be extended to CHF of subcooled boiling, but there is no clear way for the macrolayer dryout model to be extended to CHF of highly subcooled liquids.

Based on understanding mentioned above, in the present study, it was attempted to attain a good understanding of the effects of wetting ability and subcooling of liquid on the bubble structure. This was accomplished by observing the bubble behavior in the quasi-two-dimensional space mentioned above.

2. EXPERIMENTAL APPARATUS

One of the difficulties in observation of the real bubble behavior in boiling on a horizontal flat plate is that the three-dimensional and dynamic motion of bubbles obstructs our view of the real bubble behavior on/near the boiling surface. In the present experiments, thus, it was attempted to observe clearly sectional views of bubble behavior by using a quasi-two-dimensional boiling system as shown in Fig.1. The test liquids used in the experiments were water, ethanol, and R141b. The wetting ability of R141b is highest among these liquids.

The boiling surface was an epoxy resin plate with a copper film of 30μm thickness on one side. The total thickness of the plate was 1.6mm. The length of the test section of the copper film (60mm) was larger than the

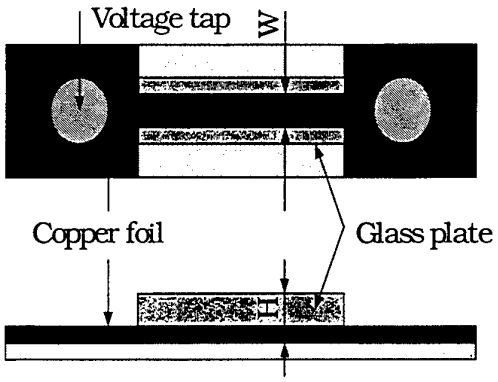

Fig.1 Schematic diagram of boiling surface

most dangerous wavelength of the Rayleigh-Taylor instability for water (27mm). As shown in Fig.1, the boiling surface was sandwiched by two vertical glass plates to realize a quasi-two-dimensional boiling space. The width of the boiling surface or the gap between the vertical glass plates was set to W=1.0mm which is much smaller than the most dangerous wavelength for water. Following our previous report [5], the height of the glass plates was set to H=1.7mm because the experimental values of CHF of saturated ethanol for H=0.5-15.0mm were in good agreement with the prediction from the following Zuber's equation,

$$q_{CHF}[\Delta T_{sub}=0]=0.131 h_{LV}\rho_V\left(\frac{\sigma g(\rho_L-\rho_V)}{\rho_V^2}\right)^{1/4} \tag{1}$$

where, h_{LV} is the latent heat of vaporization, ρ_V is the density of saturated vapor, ρ_L is the density of saturated liquid, σ is the surface tension, and g is the gravitational acceleration. The boiling surface was heated directly with a DC current flowing in the copper film. To calculate the temperature of the copper film from its electric resistance, the DC current flowing in the film and the voltage between the voltage taps shown in Fig.1 were measured. The measurement was repeated by increasing the electric current step by step, and it was continued until burnout of the copper film occurred. Calibration of the electric resistance to temperature was conducted for each boiling surface. To make uniform the experimental condition, the surface of the copper film was polished with an emery paper of #3000.

In the present experimental system (quasi-two-dimensional system), liquid subcooling, ΔT_{sub}, was defined as the value measured at the top of the glass plates. This value of liquid subcooling is much smaller than that for bulk liquid. Boiling behavior between the glass plates were observed through the glass plates with a high-speed video system (500 and 1000 frames/sec).

3. EXPERIMENTAL RESULTS

Effect of Subcooling on CHF

Figs.2 to 4 show the experimental results of CHF obtained for water, ethanol, and R141b respectively. Elkassabgi and Lienhard [11] identified the ranges of low, moderate, and high subcooling for the effect of subcooling on CHF. In the range of low subcooling, CHF increases the following equation..

$$q_{CHF}[\Delta T_{sub}]=q_{CHF}[\Delta T_{sub}=0]\left(1+0.102\left(\frac{\rho_V}{\rho_L}\right)^{1/4}Ja\right),\quad Ja\equiv\frac{\rho_L c_{pL}\Delta T_{sub}}{\rho_V h_{LV}} \tag{2}$$

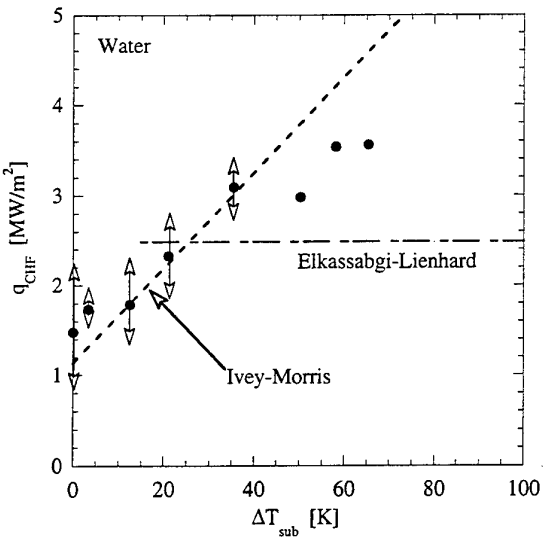

Fig.2 Effect of subcooling on CHF (water)

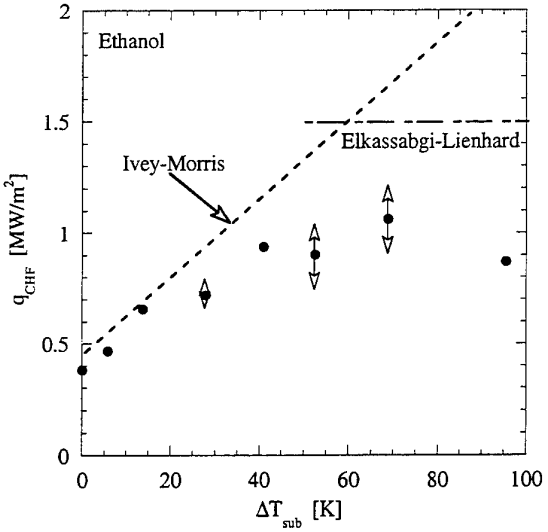

Fig.3 Effect of subcooling on CHF (ethanol)

In the range of high subcooling, however, CHF becomes independent of liquid subcooling. They proposed the following equation for this range.

$$q_{CHF}[\Delta T_{sub}] = \left(0.01 + 0.0047\exp\left[-1.11\times10^{-6}\chi\right]\right)\rho_V h_{LV}\sqrt{\frac{RT_{sat}}{2\pi}}, \quad \chi \equiv \frac{L}{\kappa_L}\sqrt{RT_{sat}} \tag{3}$$

This correlating equation was proposed by Ivey and Morris [12], and L is the representative length of the heater, R is the gas constant, κ_L is the thermal diffusivity of liquid. In the present case, L was set equal to W. Equations (2) and (3) are shown in each figure together with the experimental data.

The following results are obtained from Figs.2 to 4. First, for three liquids tested in the present experiments, the experimental data of CHF in a range of small subcooling, are in reasonable agreement with the predictions of equation (2). This result indicates that, at least in the range of small subcooling, the definition of ΔT_{sub} in the present study is reasonable and boiling phenomena in the quasi-two-dimensional space are not so far from those in a usual three-dimensional space.

Next, as Elkasabgi and Lienhard reported for cylindrical heaters, it is found from Figs.2 and 3 that CHF approaches a unique value for increasing liquid subcooling. As seen from Figs.2 and 3, however, the experimental data in the range of high subcooling are higher for water and lower for ethanol than the prediction from equation (3). This may result from the assumption of L=W.

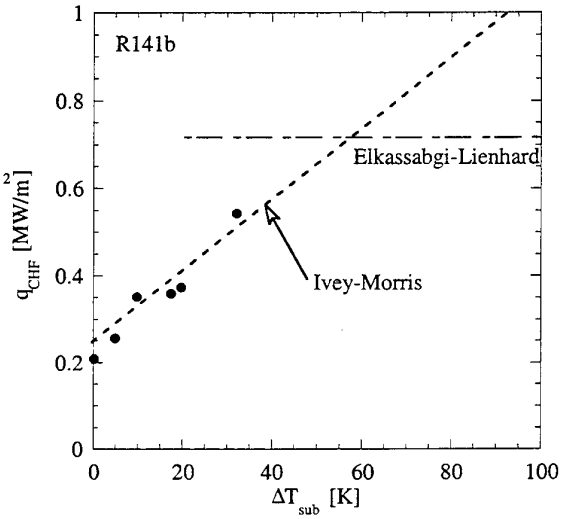

Fig. 4 Effect of subcooling on CHF (R141b)

Bubble Behavior at Saturated Boiling

Figs.5 to 7 show the typical pictures of bubble behavior obtained at non-dimensional heat-flux levels of q/q_{CHF}=0.25, 0.40, 0.50, 0.75, 1.0 for water, ethanol, and R141b respectively. The picture shown at the top for each subcooling shows the situation just before the occurrence of CHF.

Comparing the pictures for saturated boiling at a fixed non-dimensional heat-flux level, it is found that interaction or coalescence between discrete bubbles becomes weak in the order of water, ethanol, and R141b. This result indicates that, as Sadasivan et al. [10] stated, the discrete bubble region of nucleate boiling extends to high heat fluxes for highly wetting liquids.

Even in the case of saturated boiling of R141b, however, very large coalesced bubbles like filmwise bubbles are observed at CHF as well as water and ethanol. It can be thus concluded that, for saturated boiling, appearance of large coalesced bubbles prepares the occurrence of CHF.

As mentioned already, Nishio et al. [5] conducted boiling experiments for saturated ethanol in the quasi-two-dimensional space, and they reported that vigorous generation of primary bubbles occurred in a liquid film intervening between the filmwise bubble and the boiling surface and they grow to semi-spherical bubbles like vapor dome. Such vigorous generation of primary bubbles like vapor domes was observed also for all the liquids used in the present experiments. This result indicates that the vigorous generation of primary bubbles under the filmwise bubble is the universal structure at high heat-flux nucleate boiling of saturated liquids.

Bubble Behavior at Subcooled Boiling

Comparing the pictures at a fixed non-dimensional heat-flux level (for example, q/q_{CHF}=0.75 for ethanol), it is found that coalescence of bubbles becomes to be suppressed for increasing liquid subcooling. To show clearly this tendency, the bubble size was measured at 0.5mm above the boiling surface with the video pictures. The results for the averaged size were plotted to liquid subcooling together with the critical wavelength of the Rayleigh-Taylor instability, λ_{cr} as a reference value. The critical wavelength is given by

$$\lambda_{cr} = 2\pi\sqrt{\frac{\sigma}{g(\rho_L - \rho_V)}} \tag{4}$$

It is found clearly from this figure that the bubble size decreases rapidly for increasing liquid subcooling. Especially in the case of ethanol at ΔT_{sub}=70K, which corresponds to the range of high subcooling, the discrete bubble region of nucleate boiling extends up to CHF as shown in Fig.6.

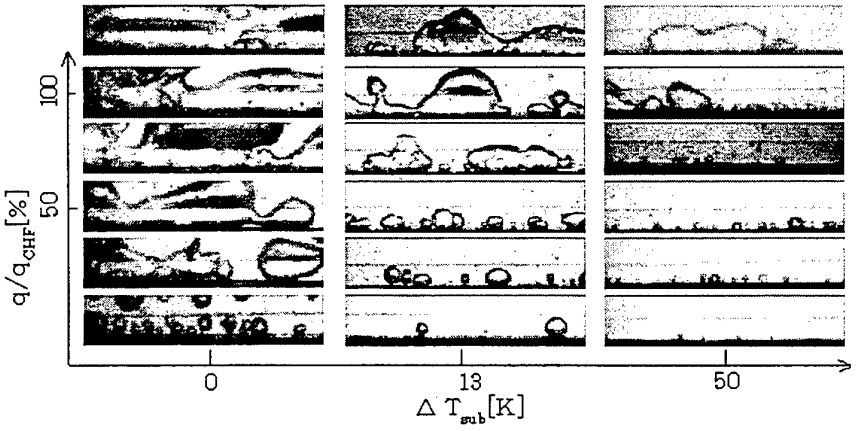

Fig.5 Effect of liquid subcooling on bubble behavior (water)

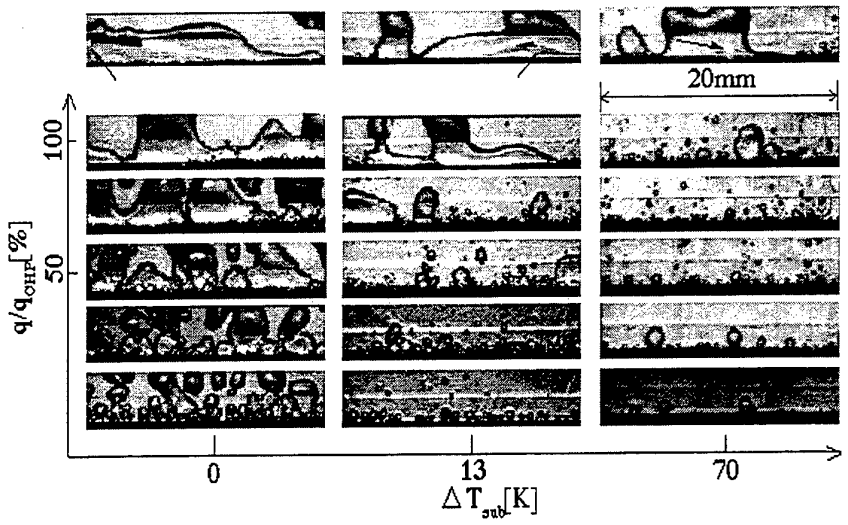

Fig. 6 Effects of liquid subcooling on bubble behavior (ethanol)

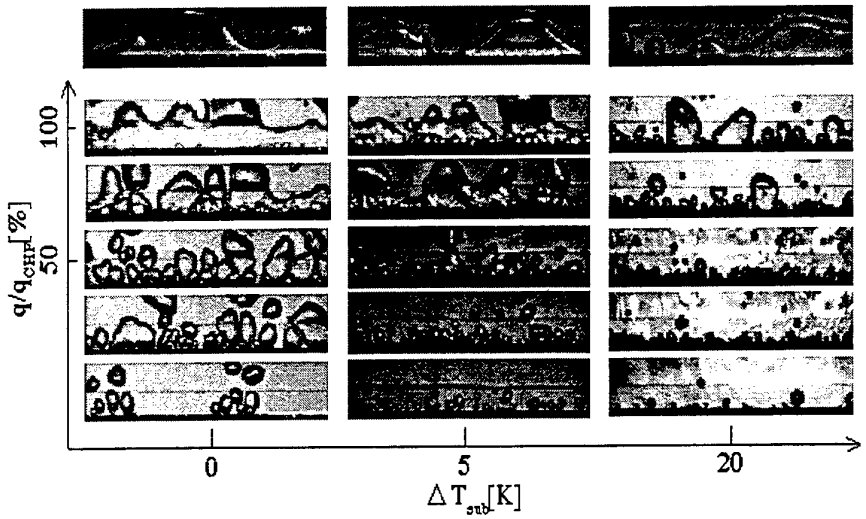

Fig. 7 Effects of liquid subcooling on bubble behavior (R141b)

Triggering Mechanism of CHF at High Subcooling

The averaged behavior of bubbles changes from the filmwise bubbles to discrete bubbles for increasing liquid subcooling in this way, but the video pictures suggests that a coalesced bubble appear intermittently at CHF even for the case of highly subcooled liquid. The pictures shown at the top in each figure are the situation just before the occurrence of CHF. The arrow on each top picture in Fig.6 denotes the location where the physical burnout occurred. It is found from these top figures that the occurrence of CHF is triggered by appearance of large coalesced bubble(s) even in highly subcooled boiling.

In summary, CHF relates closely to appearance of large coalesced bubble(s) irrespective of wetting ability and subcooling of liquid.

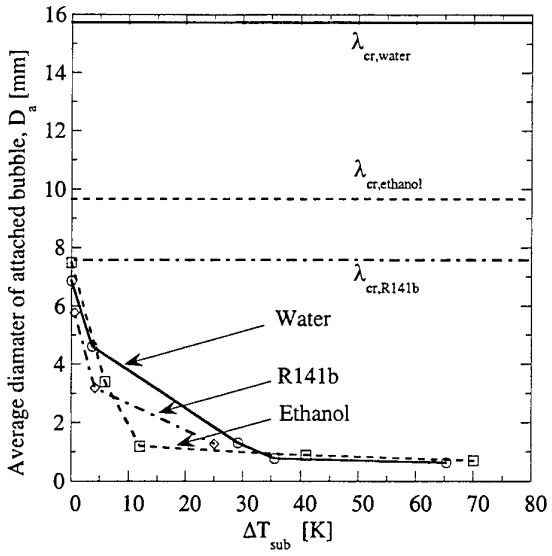

Fig.8 Effect of liquid subcooling on averaged sizeof bubbles

4. CONCLUSION

In the present study, to attain a good understanding of the effects of wetting ability and subcooling of liquid on bubble behavior, it was attempted to observe the bubble behavior in a quasi-two-dimensional space. The results obtained can be drawn as follows.

(1) CHF approaches a unique value for increasing liquid subcooling.
(2) In saturated boiling of highly wetting liquids, while the discrete bubble region of nucleate boiling extends to high heat fluxes, very large coalesced bubbles like filmwise bubbles are observed at CHF even for such highly wetting liquids.
(3) While coalescence of bubbles becomes to be suppressed for increasing liquid subcooling, a large coalesced bubble appears intermittently and it triggers CHF.
(4) CHF relates closely to appearance of large coalesced bubble(s) irrespective of wetting ability and subcooling of liquid.
(5) Vigorous generation of primary bubbles under the filmwise bubble is observed universally at least for high heat-flux nucleate boiling of saturated liquid.

REFERENCES

1. J.A.Gaertner, ASME J.Heat Transfer v.87, pp.17-29(1965).
2. Y.Haramura and Y.Katto, Int. J. Heat Mass Transfer v.26, pp.389-399(1983).
3. V.K.Dhir and P.Liaw, ASME J.Heat Transfer v.111, pp.739-746(1987).
4. Y.Katto and S.Yokoya, Int. J. Heat Mass Transfer v.41, pp.3191-3201(1998).
5. S.Nishio, N.Nagai, and T.Gotoh, Int. J. Heat Mass Transfer v.11, pp.993-1002(1968).
6. T.Oka, Y.Abe, Y.H.Mori and A.Nagashima, ASME J. Heat Transfer v.117, pp.406-417(1995).
7. J.E.Galloway and I.Mudawar, Int. J. Heat Mass Transfer v.30, pp.2511-2526(1993).
8. W.Tong, A.Bar-Cohen, T.W.Simon, Proc. 4th ASME/JSME Thermal Engineering Joint Conference v.2, pp.433-439(1991).
9. R.D.M.Carvallo and A.E.Bergles, Proc. 10th Int.Heat Transfer Conference v.5, pp.25-30(1994).
10. P.Sadasivan, C.Unal and R.Nelson, ASME J,Heat Transfer v.117, pp.558-567(1995).
11. Y.Elkassabgi and J.H.Lienhard, ASME J,Heat Transfer v.110, pp.479-486(1988).
12. H.J.Ivey and D.J.Moriis, Proc. 3rd Int.Heat Transfer Conference v.III, pp.129-142(1966).

EXPERIMENTAL STUDIES FOR EHD BOILING HEAT TRANSFER ENHANCEMENT OUTSIDE A TUBE

Huang Xuan, Li Ruiyang, Yu Hongling, An Enke and Chen Zhihang
College of Power Engineering, University of Shanghai for Science and Technology
Email: lizhendk@online.sh.cn; Fax: (21)-65682258

Keywords: heat transfer enhancement, boiling heat transfer, electrohydrodynamics (EHD)

ABSTRACT. The application of electrohydrodynamic (EHD) technique on boiling heat transfer enhancement outside a tube was investigated experimentally. R11and R123 were used as working fluids .The experimental rig is a smoothly copper tube of 25mm OD and 400mm long. Six copper wires, each with a diameter of 2mm and located 5mm away from the heat transfer surface served as the high-voltage electrodes. The electrodes were oriented at 60° intervals. Comparison between the EHD enhancement factors of R11 and R123 at different heat flux and different voltages was conducted. The results show that R123 has a much better response to the EHD effect than R11, the EHD enhancement factor decreased with the heat flux, and the power consumption by EHD high voltage supplier is different for R11 and R123.

1. INTRODUCTION

The electrichydrodynamic (EHD) enhancement of heat transfer refers to the coupling of an electric field with the fluid field in a dielectric fluid medium. Heat transfer enhancement techniques can be divided into two types: passive and active. The EHD enhancement of heat transfer is a new and promising active technique. In fact, the phenomenon of enhancement on heat transfer of EHD has been known for almost 80 years[1], but people did not pay much attention to it. In 1960 Bochirol reported the first quantitative studies in this field[2]. Recently, reducing the temperature differentials at heat exchangers becomes particularly important in the developments of ocean thermal energy conversion (OTEC) plants, geothermal energy plants, solar pond generation plants and similar plants utilizing the organic Rankine cycle (ORC). EHD technique can promote efficiency of heat transfer greatly, so it has attracted much attention gradually. In this research, an experiment on EHD enhancement of boiling heat transfer on a tube was conducted using R11 and R123 as working fluids respectively. Some comparisons on the results such as heat transfer coefficient, power consumption by supplied high voltage were carried out in this paper.

2. EXPERIMENTAL FACILITY

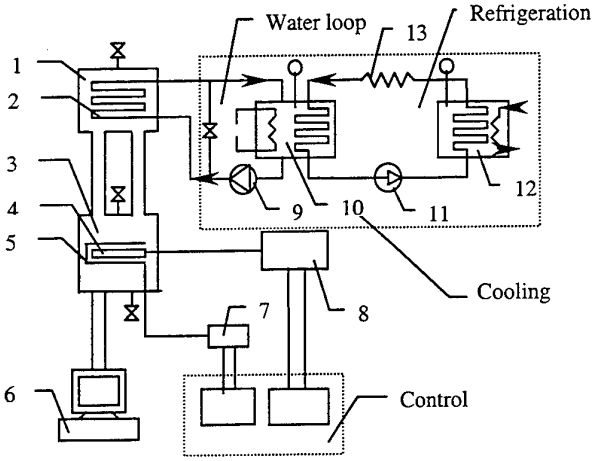

1-Cooling chamber	2-Condensing tubes	3-Boiling chamber	4-Test tube
5-Electrodes	6-Computer	7-High-voltage supply	8-Variable transformer
9-Water pump	10-Heat exchanger	11- Compressor	12-Condenser 13-Capillary

Fig.1 Schematic of experimental system for EHD enhancement of boiling heat transfer

A schematic of the experimental system is depicted in Fig.1. The setup consists of six major components: a boiling chamber, a condensation chamber, a cooling system, a high-voltage power supply system, a control system and a measuring system. Both of the boiling and the condensation chambers have the same size of 250mm×250mm×400mm. A test section which consists of test tube and electrodes is installed in the boiling chamber and a condensing coil in the condensation chamber. The cooling system consists of a cycling water loop and a refrigeration loop. A water-cooled refrigeration unit is used for cooling the water in the cycling water loop. The flow rate and temperature of the cooling water are adjusted though the condensing tubes to maintain the system pressure at the set value and keep stability.

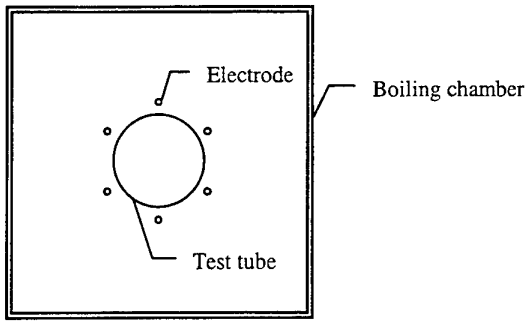

Fig.2 Cross-sectional view of the test section apparatus

The test section is shown in Fig 2. A smooth copper tube of 25mm O.D, 22mmI.D and 400mm long is heated in it. Six copper wires, each with a diameter of 2mm and located 5mm away from the heat transfer surface were served as the high voltage electrodes.

As shown in Fig 3, an electrical cartridge heater is inserted inside the test tube to provide the heating energy. The heater has an outside diameter of 16mm and a heating length of 400mm. A copper filler tube of 22mm O.D, 16mm I.D and 400mm long was placed and soldered in between the electric heater and the test tube to provide a uniform conduction. Wall temperature in the test is measured by three pairs of type E thermocouples welded directly onto the outside of the filler tube. The thermocouples were placed circumferential positions at intervals of 90^0 from the top point to the bottom of the filler tube. A 0 to 50kV and 0 to 2mA power supplier is used as high voltage source for the experiments.

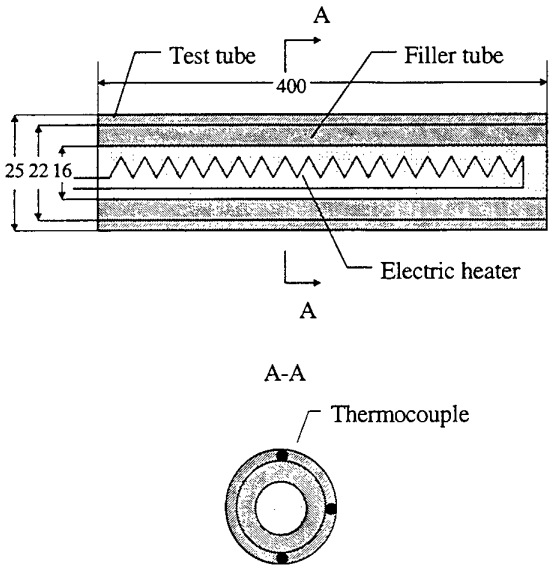

Fig.3 Configuration of test tube and locations of thermocouples

3. DADA PROCESSING

The heat transfer coefficient α was calculated as

$$\alpha = \frac{Q}{A(T_w - T_l)} \tag{1}$$

where Q is heat transfer rate determined by the heater current and voltage readings to the test section, T_w and T_l are the heat transfer surface and liquid temperatures, respectively. The enhancement factor f is defined as

$$f = \frac{Nu_{EHD}}{Nu_0} = \frac{\alpha_{EHD}}{\alpha_0} \tag{2}$$

where Nu_{EHD} and Nu_0 represent the Nusselt numbers with or without the electric field, respectively. The enhancement factor f represents the efficiency of EHD augmentation of heat transfer directly.

Finally, the power consumption by the high voltage is calculated as

$$Q_{EHD} = \phi \cdot i \tag{3}$$

where ϕ and i are the applied high-voltage potential and current, respectively.

4. EXPERIMENTAL RESULTS AND DISCUSSION

All of the experiments were conducted close to atmospheric pressure which corresponded to a saturation temperatures of 27.7°C and 23.7°C for R123 and R11 respectively. In the actual experimental procedure, there was a little fluctuation in the system pressure. The saturation temperatures ranged from 27.6°C to 29.0°C for R123 and 23.7°C to 24.3°C for R11, respectively. The heat flux values were 2, 4 and 6kW/m^2. The voltage was raised from 0 to 20 kV. Fig.4 and 5 show the boiling heat transfer coefficients versus applied voltage at different heat flux levels for R123 and R11, respectively.

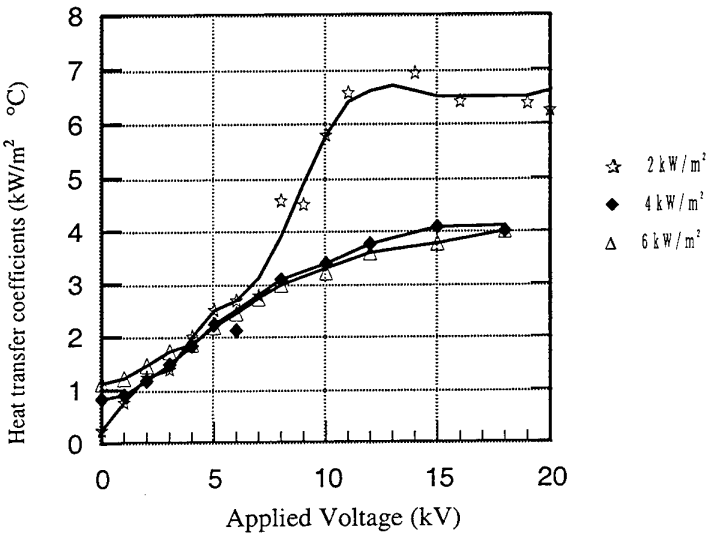

Fig.4 Heat transfer coefficients for R123

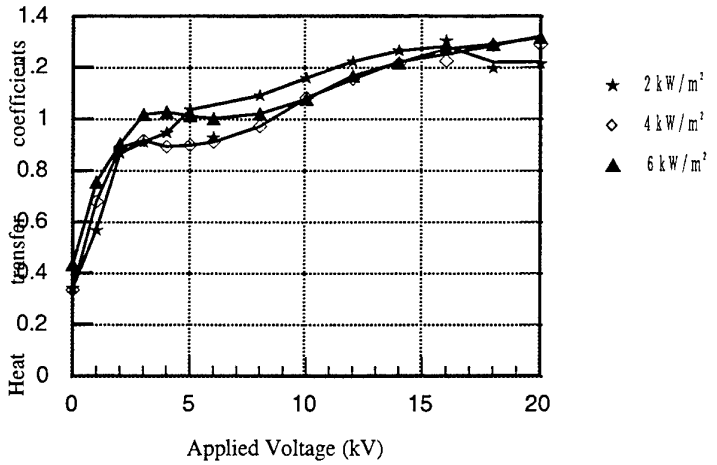

Fig.5 Heat transfer coefficients for R11

As seen in Fig.4, R123 exhibits a much better EHD-enhanced heat transfer performance. At the heat flux $q=2kW/m^2$, the heat transfer coefficient increases rapidly with applied voltage until 11kV, when applied voltage is higher than 11kV, the heat transfer coefficient does not increase evidently. For heat fluxes of 4 and 6 kW/m^2, the heat transfer coefficients increase almost on an exponential curve with the applied voltage. As shown in Fig.5, the heat transfer coefficient increases quickly as the electric voltage is applied, then increases slowly with the increase of applied voltage for R11.

Fig.6 is a plot of enhancement factor for R123 and R11 versus applied voltage at heat flux $q=2kW/m^2$. Fig.7 shows enhancement factor for R123 and R11 versus applied voltage at heat fluxes of 4 and 6 kW/m^2. As seen in Fig.6, R123 has a much better response to EHD effect than R11, the enhancement factor were about 24.5 and 3.4 for R123 and R11 at 10kV, respectively. As shown in Fig.7, at higher heat fluxes, difference between the enhancement factors of R123 and R11 decreased.

From Fig.4 to Fig.7, we can see that the enhancement magnitude decreases with increasing heat flux. This could be attributed to the increase in the buoyancy-driven forces and their dominance over EHD forces at high fluxes. It is due to the attenuation of the effective local field strength caused by the number increase of departed bubbles as the heat flux increases. The reason of a better enhancement of heat transfer coefficient with R123 may be the more favorable electrical parameters such as electric conductivity.

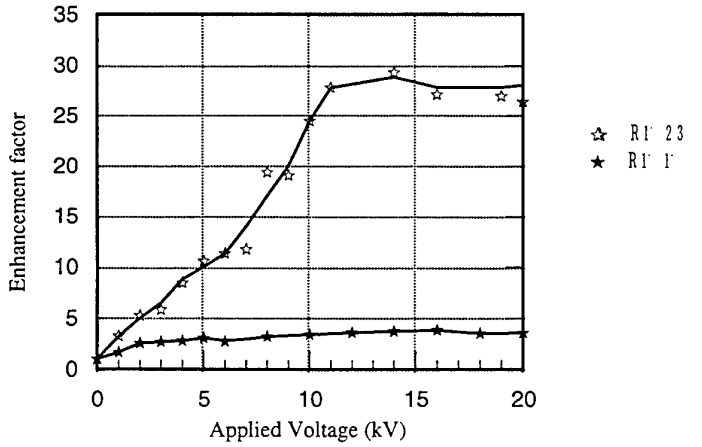

Fig.6 Enhancement factor for R123 and R11 at heat flux of $2kW/m^2$

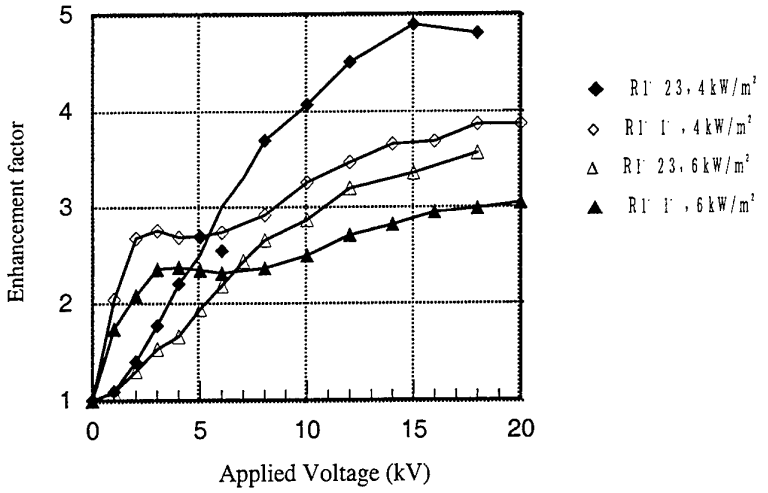

Fig.7 Enhancement factor for R123 and R11 at heat fluxes of 4.6kW/m^2

Power consumption results

Fig.8 shows the variation of the EHD power consumption with applied voltage for R123 and R11 at a heat flux of 6kW/m^2. When DC voltage is applied in R123, a relatively large amount of electric current flows instantaneously in proportion to the electrostatic capacity, and soon after the start of the process the current begins to decrease as a equilibrium state is approached. A similar phenomenon was also reported by Ogata in 1992[3]. We used the maximum electric current to calculate the power consumption by the applied high voltage for R123. During the experiment it was found that the power consumption increase a little with the increase of heat flux. The maximum EHD power consumption for R123 is much greater than for R11, it reaches to 20 watt, but the later only 2 watt at a heat flux of 6kW/m^2 (188W of energy transferred by heat). In other words, maximum EHD power consumption for R123 is about 10.6% and only 0.27% for R11 related to the energy transferred by heat.

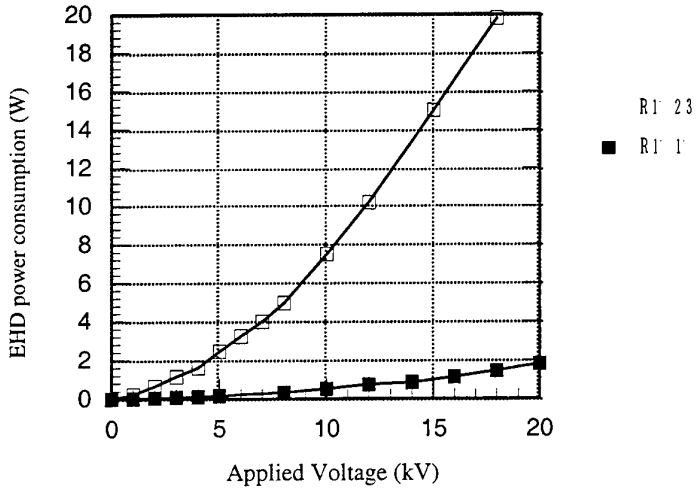

Fig.8 EHD power consumption for R123 and R11 at heat flux of 6kW/m^2

4. CONCLUSIONS

From the experimental studies of EHD enhancement of boiling heat transfer outside a tube for R123 and R11, the following conclusions could be obtained:

1) EHD technique can greatly enhance boiling heat transfer. For the experimental condition of this research, an enhancement factor up to 29.3 was obtained for R123 and an enhancement factor of 3.7 was obtained for R11.
2) R123 has a much better response to the EHD effect than R11.
3) The EHD enhancement factor decreases with heat flux.
4) Compared with the quantity of heat transfer, the power consumption by EHD high-voltage supplier is very small and can be negligible for the working fluid of R11, but the power consumption is much higher for R123.

NOMENCLATURE

A	heat transfer area
f	enhancement factor
Q	heat transfer rate
Q_{EHD}	EHD power consumption
ϕ	applied high-voltage potential
i	applied high-voltage current
Nu	Nusselt number
T	temperature

Subscripts

0	Zero electric field case
EHD	electric field case
w	wall
l	liquid

REFERENCES

1. L.W. Chubb. UK Patent, 100796(1916).
2. L. Bochirol, E. Bonjour, L. Weil C R Hebd Seances Acad Sci(Pari), v.250, pp.76~78(in French)(1960).
3. J. Ogata, Y. Iwafuji, Y. Shimada and T. Yamazaki ASHRAE Trans,v.98, pp.435~444(1992).
4. R.Y. Li, L.B. Chen, Z.H. Chen and Y.C. Yuan, J East China University of Technology, v.18, pp.5~12 (in Chinese)(1996).
5. J. Ogata, Y. Iwafuji, Y. Shimada and T. Yamazaki. ASHRAE Trans, v.98, pp.435~444(1992).
6. P. Cooper ASME J Heat Transfer, v.112, pp.458~464(1990).
7. M.M. Ohadi, R.A. Papar, T.L. Ng, M,A. Faani and R. Radermacher, ASHRAE Trans, v.98, pp.427~434(1992).
8. A. Yabe, T. Taketani, H. Maki, K. Takahashi, Y. Nakadai, ASHRAE Trans, v.98, pp.455~461 (1992).
9. C. Damidis, T.G. Karayiannis, R.K. AI-Dadah, R.W. James, M.W. Collins, P.H.G. Allen, ASHRAE Trans, v.98, pp.462~472(1992).
10. J. Ogata, A. Yabe. Int J Heat Mass Transfer, v.36, pp.775~782(1993).
11. J. Ogata. Int J Heat Mass Transfer, v.36, pp.783~791(1993).
12. T.G. Karayiannis. Applied Thermal Engineering, v.18, pp.809~817(1998).

SUPERHEAT LIMIT OF LIQUID MIXTURES

Chao Liu, Danling Zeng and Keqiang Xing
College of Thermal Engineering
Chongqing University
Chongqing 400044, China

Keywords: homogenous nucleation, superheat limit, metastable state

ABSTRACT. The superheat limit of liquid mixtures is determined on the basis of fluctuation theory of statistical thermodynamics. Analytical results for superheat limits about 28 kinds of different mixtures have been compared to published experimental data for hydrocarbon and non-hydrocarbon mixtures by the help of Peng-Robinson equation. The comparison shows a good agreement. The expressions given in the paper are universal and applicable for any mixtures of liquids to predict their superheat limit so that neither additional experimental factors nor partial constraints need to be added on them.

NOMENCLATURE

a Peng-Robinson constant
A constant defined in Peng-Robinson equation
b Peng-Robinson constant
B constant defined in Peng-Robinson equation
c_v specific heat at constant volume
C_v heat capacity of the system at constant volume
f fugacity of component
k Boltzmann constant
P pressure
P^l liquid phase pressure
P_c parachor
r radius of a buble
R_m general gas constant
s modified factor
T temperature
v molar volume
w work
x liquid phase mole fraction
y vapor phase mole fraction
z compressibility factor

Greek symbols

ρ density
σ surface tension
φ fugacity coefficient

Superscipts and subscripts

I component
m modified liquid properties in neighborhood of nucleus
l liquid
v vapor
1 the first listed substance
cal calculation value
exp experimental value

1. INTRODUCTION

Homogenous nucleation, the spontaneous formation of vapor within a metastable liquid, plays a fundamental role in the physics of phase transition. According to classical thermodynamics, a liquid will boil under a given pressure when its temperature reaches the saturation temperature. However, under particular conditions when perturbation is carefully eliminated, the liquid can be heated to a much higher temperature. For example, liquids held at 1 atm. can be superheated to temperature which is about 80-90% of their critical temperature [1]. The direct mixing of a cold volatile liquid with a hot nonvolatile liquid can often lead to significant superheating of the volatile liquid which is so high that they boil with explosive violence, when nucleation occurs. This limit of superheat is therefore readily attained and represents quite a significant hazard to industry. For example, such explosive boiling has been observed in liquid natural gases spilling in water, the reaction between water and liquid metals and the burning of water-in-oil emulsions [2]. In these situations the homogeneous nucleation of bubbles either within the volatile liquid or at the interface between the volatile and nonvolatile liquid is responsible for the explosive boiling effect. Because of the hazards and possible benefits, the importance of understanding on the superheat phenomenon and an accurate prediction of the limit of superheat are too obvious to need proof. Superheat limit, or the limit of homogeneous nucleation, represents the deepest possible penetration of a liquid in the domain of metastable states in phase transition. At constant pressure and composition, it is the highest temperature below the critical point a liquid can sustain without undergoing a phase transition; whereas at constant temperature, it represents the lowest pressure.

Usually, there exists difference between the homogeneous nucleation of pure and mixtures of liquid. When nucleation occurs in liquid mixtures there are two different effects which are not present in pure liquids. Both effects are resulted from different volatility of different liquids. Firstly, the composition in vapor nucleus is a mixture whose composition different from the liquid surrounding it. Therefore, the condition of phase equilibrium must be extended to contain each component. Secondly, the formation of vapor nucleus may change the composition of the liquid in its adjoining field. This occurs because volatile components are preferentially vaporized, and because the ability of diffuse of molecules in the liquid phase is limited.

The purpose of the present paper is to extend the thermodynamic fluctuation theory to include the two effects stated above and to testify the correctness of the assumption, proposed by the authors [3] to be applied to liquid mixtures. In the present paper the attention is focused on the determination of the theoretical superheat limit in homogeneous nucleate boiling. Differing from previous works, the paper considered the superheat limit of liquid mixtures by applying the fluctuation theory of statistical thermodynamics. The formulae for calculating the superheat limit are derived from Gibbs canonical ensemble and expressed in general forms without particular constraint attached to them.

2. REVIEW OF LITERATURES

Ward, et al [4] considered nucleation in liquids containing dissolved gases. They thought that diffusion in the liquid is so low that the gas could hardly enter into nucleus at all and so neglected the effect of local liquid phase composition changes near the nucleus. Forest and Ward [5-6] and Mori, et al. [7] have presented theoretical and experimental studies regarding liquids with dissolved gases. Later, Hijikata, et al. [8] which verified experimentally that in some cases the rate of diffusion of gas molecules governs the vapor nucleation process. Blander, Katz et al. [9-12] considered the limiting case when only one component is volatile in a binary mixture. They assumed the growth of such a nucleus was governed by diffusion of the volatile constituent into the nucleus. Pinnes and Muller [13] considered the two features of vapor nucleation in multicomponent liquids and calculated superheat limits of some binary hydrocarbon mixtures by using W-B-R equation of state extrapolated into the metastable region. Avedisian[14-15] studied widely the superheat limit of liquids from both experimental and theoretical way and gained rich results.

3. THE DETERMINATION OF SUPERHEAT LIMIT USING FLUCTUATION THEORY

3.1. A Hypothesis

It is a widely accepted that spontaneous nucleation in a metastable liquid can be induced by the fluctuation of parameters in a liquid system. So we should relate the superheat limit quantitatively to the strength of fluctuation appearing in a system. Let us imagine that the liquid is subdivided into small subsystems, each has a volume equaling to that of a critical bubble. If in the subsystems the energy fluctuation is strong enough to reach the necessary work needed to create a cavity with the same volume, the phase transition would be induced spontaneously. The higher the temperature of the metastable liquid mixtures, the stronger the energy fluctuation in the system, until the temperature approaches its upper limit the liquid can sustain without undergoing a phase transition.

Based on above analysis, we proposes a hypothesis as followings: The spontaneous nucleation will occur in a metastable liquid mixture system under a certain temperature at which the energy fluctuation in its subsystems with the size of a critical bubble is strong enough to reach the work needed for forming a cavity with the same size. The superheat of the liquid mixture corresponding to such a case is defined as the theoretical limit of superheat of a liquid mixture in homogeneous nucleate boiling.

3.2. The Superheat Limit Of Liquid Mixtures

The thermodynamic criteria of equilibrium for a critical vapor bubble are written as:

$$T^V=T^L \tag{1}$$

$$P^V=P^L+2\sigma/r_c \tag{2}$$

$$f_i^V(T^V,P^V,y_i)=f_{im}^L(T^L,P^L,x_{im}),\ (i=1,2,3,...n) \tag{3}$$

$$x_{im}=x_i+s(x_i-y_i),\ (i=1,2,3,...n) \tag{4}$$

Here T^v , P^v are temperature and pressure of vapor phase respectively ; T^L , P^L are temperature and pressure of liquid phase respectively; f_i is the fugacity of ith component in vapor and liquid phase of mixtures. The fugacity of ith liquid: $f_i^L=\phi_i^L.x_i.P^L$; and of ith vapor: $f_i^V=\phi_i^V.y_i.P^V$. Parameter ϕ_i is coefficient of fugacity of ith component, which is evaluated from the given equation of state. S is modified factor [13].
By using the above symboles, Equation (3) is written by

$$P^v=(\sum\frac{\phi_i^L}{\phi_i^v}x_{im})\cdot P^L \tag{5}$$

Combining Equations (2) and (5), critical radium is obtained:

$$r_c=\frac{2\sigma}{P^v-P^L}=\frac{2\sigma}{1-\sum(\phi_i^L/\phi_i^v)x_{im}}\cdot\frac{1}{P^L} \tag{6}$$

It is seen that Equation (6) only gives a relation between temperature T of the superheat liquid mixtures and the critical radius r_c of the bubble. In order to determine T, an additional equation relating both T and r_c must be provided. The following is an approach to provide such an additional relation on the basis of the thermodynamic fluctuation theory.

3.3 Energy Fluctuation in Canonical Ensemble

From statistical thermodynamics it is convenient to demonstrate that the energy fluctuation in a Gibbs canonical ensemble can be expressed by

$$\sigma(E)=\sqrt{kT^2C_v} \tag{7}$$

Here k is Biltzmann's constant, T and C_v stands for the temperature and the heat capacity of the system. When the specific heat c_v at constant volume of liquid is used the above equation can be transformed into the following form

$$\sigma(E)=\sqrt{4kT^2\pi r_c^3\rho^\ell c_v/3} \tag{8}$$

3.4 The Critical Radius of Bubbles

The necessary work to form a cavity with the size r_c of bubble in superheated liquid can be written in

$$W_{cr}=\sigma A+P^L\Delta V=4\pi r_c^2\sigma+4\pi r_c^3\left(1-\rho^v/\rho^\ell\right)P^L/3 \tag{9}$$

Here σ is surface tension. The first and second terms in the expression stand for surface work and volumetric work to form critical vapor bubble respectively.

An expression for the critical radius of bubbles is obtained in accordance with above-mentioned hypothesis under the condition that the energy fluctuation is of the same order of magnitude as the least work, i.e.

$$\sigma(E)=W_{cr} \tag{10}$$

By combining Equations (9) and (10), we have

$$\left(4\pi\rho^\ell c_v kT^2/3\right)^{1/2}r_c^{-1/2}=4\pi\sigma+4\pi r_c\left(1-\rho^v/\rho^\ell\right)P^L/3 \tag{11}$$

This relation is the additional equation that we need for solving the equation for superheat limit of liquid mixtures.

4. DISCUSSIONS

4.1 Equation of State

The fugacities of each component in mixtures were evaluated by using the relative equation of state. Although Pinnes and Muller [13] applied W-B-R equation of state to get the fugacity for the components ,we found difficulties to obtain the results. Thus Peng-Robinson equation of state

$$p = \frac{R_m T}{v-b} - \frac{a(T)}{v(v+b)+b(v-b)} \tag{12}$$

was used in our study.

The fugacities was evaluated by Equation (12):

$$\mathrm{Ln}\phi_i = \frac{b_i}{b}(Z-1) - \mathrm{Ln}(Z-B) - \frac{A}{2\sqrt{2}B}\left(\frac{2\sum_j x_j a_{ij}}{a} - \frac{b_i}{b}\right)\cdot \mathrm{Ln}\frac{Z+2.414B}{Z-0.414B} \tag{13}$$

where for a binary mixture, we have

$$a=\sum\sum x_i x_j a_{ij} \;;\; b=\sum b_i x_i \;;\; a_{ij}=(a_i a_j)^{1/2}(1-k_{ij}).$$

For a ternary mixture, $a=\sum\sum\sum x_i x_j x_k a_{ijk}$; $b=\sum b_i x_i$; $a_{ijk}=(a_{ji}a_{jk}a_{ik})$; $a_{ij}=(a_i a_j)^{1/2}(1-k_{ij})$; $a_{jk}=(a_j a_k)^{1/2}(1-k_{jk})$; $a_{ik}=(a_i a_k)^{1/2}(1-k_{ik})$.

Here $A=\dfrac{aP}{R_m^2 T^2}$, $B=\dfrac{bP}{R_m T}$, $Z=\dfrac{PV}{R_m T}$,

The parameters a and b were obtained from the pure component data and kij is an empirical by determined interaction parameter. For hydrocarbon mixture Peng and Robinson had found that $k_{ij}=0$. The equations were solved numerically and the results were compared with some binary mixture data available in the literature.
Usually equation of state, for example, Peng-Robinson equation and W-R-B equation, were obtained by the semi-empirical and semi-theoretical ways, strictly speaking they held only for the stable states. But in our study, we need to evaluate the metastable properties, because the superheat limit occurrs in the metastable area. So we have to extrapolate the equation of state into metastable field. The extrapolation of the properties may cause error in the results (in fact, it is almost unavoidable so far in any study if one wants to know the properties of a metastable liquid). Skripov[16] had verified that such a way to extrapolate the equation of state does not result in abrupt change of the P-V-T data.

4.2 The Surface Tension

To apply the hypothesis to the real liquid mixtures, it is necessary to be able to evaluate thermodynamic properties of both liquid phase and vapor phase. The Peng-Robinson equation of state is used for this purpose. It provides algebraic relations for pressure and fugacity of both phases. The empirical coefficients for each component were obtained from reference [17].

An algebraic expression is also needed for the surface tension at the interface between a multicomponent liquid and its vapor. The method of basing the surface tension for the mixture on the surface tension for each pure constituent is not applicable, because there exist a possibility of a mixture whose temperature exceeds the critical point of one constituent. The parachor equation does not have this drawback. The equation, originally developed by Bachinskil and Madeod and later extended to mixture by Weinaug and Katz[18] related the surface tension directly to the density and composition of the adjacent liquid and vapor phases by using the

parachor, Pc;

$$\sigma^{1/4} = \frac{\rho^L}{M^L}\sum_i([P_c]_i x_i) - \frac{\rho^v}{M^v}\sum_i([P_c]_i y_i) \qquad (14)$$

4.3 Results

Data for 90 pure substances and 28 mixtures have been compiled by Avedisian[1] over a rang of pressures, nucleation rates and compositions. The data were mainly obtained by the help of following experimental methods, for example, pulse heating method, isobaric heating and isothermal decompression of capillary tube method, and floating droplets method. A compilation of the data was extracted from a great number of related papers, so that it included most of the results published. Therefore, we firmly believe that a comparison with experimental data compiled by Avedisian would be a best test to our results. Table 1 and Table 2 give out the comparison between calculating and experimental results of superheat limits of some ternary mixtures and binary mixtures respectively.

Table 1: Limits of Superheat of Ternary Mixtures(P=0.101Mpa)

Ethane/N-Propane/N-Butane ($C_2H_6/C_3H_8/C_4H_{10}$)

$X(C_2)$	$X(C_3)$	$Y(C_2)$	$Y(C_3)$	T_{cal}(k)	T_{exp}(k)[1]
0.806	0.073	0.948	0.032	284.44	280.8-283.4
0.092	0.811	0.215	0.750	317.76	324.0-329.8
0.100	0.771	0.238	0.714	316.12	326.0-331.0
0.235	0.433	0.538	0.361	308.80	324.8-344.2
0.113	0.652	0.293	0.623	310.65	329.4-334.8
0.160	0.299	0.463	0.320	314.72	337.8-354.4
0.135	0.160	0.429	0.205	331.77	344.6-355.8

Table 2: Limits of Superheat of Binary Mixtures

(1) Carbon dioxide (Gas) / R22 (CO_2/$ClCHF_2$)

P(MPa)	x_1	Y_1	T_{cal}(k)	T_{exp}(k)
0.095	0.180	0.383	313.02	309.0
0.350	0.180	0.376	315.01	311.7
0.510	0.180	0.372	316.26	312.9
0.610	0.180	0.370	317.04	313.6
0.710	0.180	0.367	317.82	314.1
0.810	0.180	0.365	318.60	315.0
0.910	0.180	0.362	319.38	315.5
1.020	0.180	0.359	320.56	316.2
0.110	0.130	0.291	316.78	314.3
0.250	0.130	0.288	317.88	315.2
0.350	0.130	0.286	318.67	316.6
0.460	0.130	0.284	319.54	317.1
0.530	0.130	0.282	320.09	317.5
0.650	0.130	0.280	321.04	318.2
0.770	0.130	0.277	321.98	319.1
0.850	0.130	0.275	322.62	319.4
0.910	0.130	0.274	323.09	319.7
0.990	0.130	0.272	324.07	320.1
0.095	0.090	0.211	319.54	319.0
0.193	0.090	0.209	320.31	319.8
0.460	0.090	0.204	322.44	321.2
0.490	0.090	0.204	322.68	321.8
0.610	0.090	0.202	323.63	322.5
0.740	0.090	0.200	324.67	323.5
0.810	0.090	0.199	325.23	324.1
0.850	0.090	0.198	325.55	324.5
0.910	0.090	0.197	326.03	324.7
0.960	0.090	0.196	326.81	325.4
1.010	0.090	0.195	327.21	326.0
0.095	0.030	0.075	323.76	323.5
0.148	0.030	0.075	324.19	323.9
0.182	0.030	0.074	324.47	324.4
0.230	0.030	0.074	324.86	324.9
0.280	0.030	0.074	325.26	325.2
0.370	0.030	0.073	325.99	325.6
0.400	0.030	0.073	326.23	325.9
0.560	0.030	0.072	327.53	327.4
0.740	0.030	0.070	329.00	329.2
0.810	0.030	0.070	329.57	329.5
0.910	0.030	0.069	330.38	330.1
1.010	0.030	0.069	331.65	330.8

(8) Benzene/Cyclo-hexane (C_6H_6/C_6H_{12})

P(MPa)	x_1	Y_1	T_{cal}(k)	T_{exp}(k)
0.310	0.955	0.957	491.47	498.4
0.310	0.890	0.894	490.90	497.4
0.101	0.800	0.808	486.79	493.1
0.310	0.774	0.782	489.96	495.8
0.310	0.660	0.671	489.11	493.7
0.101	0.600	0.613	485.21	490.4
0.310	0.511	0.525	488.12	493.6
0.101	0.400	0.414	483.85	489.8
0.310	0.392	0.406	487.40	492.5
0.310	0.235	0.246	486.58	492.1
0.101	0.200	0.210	482.70	489.7

5. CONCLUSIONS

Two features distinguishing vapor nucleation in multicomponent liquids from the single component case are pointed out in the paper, which affect the state of nucleus. Both phenomena have been incorporated into the thermodynamic fluctuation theory of nucleation. Analytical results for superheat limits have been predicted and compared with published experimental data for hydrocarbon and non-hydrocarbon mixtures. The comparison shows a good agreement as seen from the tables. These expressions given in the paper are universal and applicable for any mixtures of liquids to predict their superheat limit so that neither additional experimental factors nor particular constraints need to be added on them.

REFERENCES

1. M. Blander and J.L. Katz, AIChE Journal, V. 21, No. 5, pp. 833-848 (1975).
2. C.T. Avedisian, J. Phys. Chem. Ref. Date, V. 14, No. 3, pp. 695-727 (1985).
3. D.L. Zeng, Science in China (Series A), V. 39, No. 3, pp. 301-308 (1996).
4. C.A. Ward, A. Balakrishnan, and F.C. Hooper, J. Basic Eng., 92D. pp. 695-704 (1970).
5. T.W. Forest and C.A. Ward, Journal of chemical Physics, V. 66, No. 6, pp. 2322-2330 (1977).
6. T.W. Forest and C.A. Ward, Journal of chemical Physics, V. 69, No. 5, pp. 2221-2230 (1978).
7. Y. Mori, K. Hijikata and T. Nagatani, Int. J. Heat Mass Transfer, V. 19, pp. 1153-1159 (1976).
8. K. Hijikata, Y. Mori and T. Nagatani, ASME Journal of Heat Transfer, V. 100, pp. 460-465 (1978).
9. W. Porteous and M. Blander, AIChE Journal, V. 21, No. 3, pp. 560-566 (1975).
10. B.S. Holden and J.L. Katz, AIChE Journal, V. 24, No. 2, pp. 260-267 (1978).
11. J.G. Eberhart, W. Kremsner and M. Blander, Journal of Colloid and Interface Science, V. 50, No. 2, pp. 369-378 (1975).
12. T.A. Renner, G.H. Kucera and M. Blander, Journal of Colloid and Interface Science, Vol. 52, No. 2, pp. 391-396 (1975).
13. E. L. Pinnes and W.K. Mueller, ASME Journal of Heat Transfer, V. 101, pp. 617-621 (1979).
14. C.T. Avedisian and I. Glassman, Int. J. Heat Mass Transfer, V. 24 ,pp. 695-706 (1981).
15. C.T. Avedisian and I. Glassman, ASME Journal of Heat Transfer , V. 103, pp. 272-280 (1981).
16. V.P. Skripov, *Metastable Liquids*, John Wiley & Sons (1974).
17. R.C. Reid, J.M. Prausnitz and T.K. Sherwood, *The Properties of Gases and Liquids*, Third Edition, McGraw-Hill Inc (1977).
18. C.F. Weinaug and D.L. Katz, Industrial and Engineering chemistry, V. 35, No. 2, pp. 239-246 (1943).

EXPERIMENT OF BOILING HEAT TRANSFER IN A NEW TYPE OF HORIZONTAL THREE DIMENSIONAL MICROFIN TUBE FOR R134A *

Jie Zhou, Qinghua Chen, Mingdao Xin, Gang Zhang, and Wenzhi Cui
Institute of Engineering Thermophysics
Chongqing University, Chongqing 400044, China
Email: qhchen@cqu.edu.cn

Keywords: boiling, 3-D inner microfin tube, heat transfer enhancement

ABSTRACT. In-tube boiling experiment for R134a is performed in a new type of horizontal three-dimensional (3-D) microfin tube. The effects of mass flux, vapor quality, heat flux and boiling pressure on the heat transfer coefficient are reported. Compared with the data of the smooth tube, the average enhancement ratio is between 2.1 to 2.7. The heat transfer coefficients are higher 30%~40% than the data in the paper [3]. Based on the experimental data, an empirical correlation is obtained and the maximum deviation is within ±25%.

1. INTRODUCTION

It has been the common knowledge that the most effective approach in enhancing in-tube boiling and condensation is to use microfin tubes. The reason is the larger heat transfer enhancement relative to the slightly increased pressure drop. Therefore, micro-fin tubes have been widely applied to air-conditioning and refrigeration industries. However, these microfin tubes are almost single helix (2-D) microfin tubes. In resent years, a 3-D microfin tube, which has higher performance than 2-D microfin tube, has been developed. However, there are only several papers on the in-tube boiling heat transfer of 3-D microfin tube published.

Chamra, Webb et al[1] tested the in-tube boiling performances of 3-D micro-fin tube with 14.88-mm I.D. Their 3-D microfin tubes were manufactured from a flat strip. The desired microfin geometry was embossed on the flat strip by passing though a special roller. Then the strip was rolled into a circular shape and the axial seam was weld by high frequency method. As compared with smooth tube, the enhancement ratios of 1.9~4.5 were attained in their experiment of R22. They concluded that the higher performance of 3-D microfin tube occurs because the tube has more fins, higher fin height, and lower fin included angle. Another experimental findings on R22 boiling heat transfer performance in a 3-D micro-fin tube with 8.92-mm I.D. are presented by Kuo et al[2] and the average enhancement ratio is approximately equal to 2.2.

In reference [3] we have conducted the investigation of the boiling heat transfer performance in a 3-D microfin tube with 12-mm I.D. for R134a [3]. The average enhancement ratio is 1.5~2.1 as compared with the data of the smooth, which are calculated by Wattelet's correlation. In the present paper the experiments of a new type of 3-D microfin tube are performed. One of the purposes is to examine the influence of microfin numbers on the performance of boiling heat transfer. The differences between the two kinds of microfin tubes in paper [3] and in present paper are microfin numbers and inside diameter. In reference [3] the microfin numbers are 90-fin/cm^2 and inside diameter is 12 mm, while in this paper the microfin numbers reach 235-fin/cm^2 and inside diameter is changed into 14 mm. In addition, the investigations of R134a boiling heat transfer performance in 3-D microfin tubes are scarce. Extensive studies are needed for this new alternative refrigerant. Therefore, this paper investigates the boiling heat transfer of R134a in the new type of 3-D micro-fin tube. The experimental results are compared with the data from the paper [3] and from Wattelet's correlation [4] for smooth tubes.

2. TEST APPARATUS

The 3-D micro-fin tube has 16-mm O.D. and 14-mm I.D. (measured from fin root). The 3-D microfin geometry is formed by machining two sets of grooves on the inside surface. The grooves of one set is parallel to the center line and the helix angles (measured from center line) of another sets of grooves is 89°. The fin height h is 0.2-mm., and the fin pitch p in the axis and helix grooves directions is 0.65-mm. Moreover, the fin apex angles (β_1, β_2) of each micro-fin is 45°. The micro-fin numbers per unit area is 237 fins/cm^2.

* Supported by the National Natural Science Foundation of China

The experimental apparatus is the same as described in the paper [3]. The horizontal test section is a double-pipe heat exchanger with 4.0-m effective length. It is divided into ten subsections. In each subsection, the inner tube is the 3-D microfin copper tube, which is 0.4-m in length. The subsections are connected by eleven 6.0-cm long pressure-proof quartz glass tubes for flow pattern observing. The glass tubes have identical inside diameter to the test tubes. The heating water is a counter flow in the test section annulus, while R-134a is boiling inside the test tubes. All temperatures are measured by using 0.2-mm copper-constantan thermocouples in the experiment The uncertainty in temperature measurements is ±0.15°C. The inlet and exit temperatures of refrigerant and heating water for each subsection are measured. The wall temperatures of subsections are measured using thermocouples attached on the outside of the test tubes. For each subsection, the thermocouples are arranged at three axial locations, and there are three, three, three circumferencial points at the three locations, respectively . In addition, two precise pressure gauges (Uncertainty :±2.0 KPa) measure the test section inlet and exit pressure. Both flow meters of refrigerant and water were calibrated using a dead-weight balance and a stopwatch. The flow rate was checked by recording the quantity of refrigerant and water received in respective measuring tanks over a fixed time. A moderately long time was chosen to reduce the error. The refrigeration flow meter has ±2.0 kg/h uncertainty and the water flow meter has ±1.5 kg/h uncertainty.

3. DATA REDUCTION

The heat transfer rate in each subsection is determined from the energy balance:

$$Q_i = m_c Cp_c (T_{i,in} - T_{i,out}) \tag{1}$$

where $T_{i,in}$ and $T_{i,out}$ are the heating water temperatures at the inlet and outlet of each subsection, and Cp_c is the isobaric specific heat of water, which is calculated according to the average temperature $(T_{c,in}+T_{c,out})/2$. For the microfin tubes, the heat flux in each subsection can be calculated as:

$$q_i = Q_i / A_{in} \tag{2}$$

where A_{in} is nominal area of inside surface of the tube.
The local heat transfer coefficient for the microfin tube is defined as:

$$a_i = q_i / (T_{w,in} - T_{sat}) \tag{3}$$

The quality change in each test section is given by the energy balance:

$$\Delta X_i = Q_i / (m_R (h'' - h')) \tag{4}$$

The average quality in each test section is given by:

$$x_i = x_{i,in} + \Delta x_i / 2 \tag{5}$$

4. EXPERIMENTAL RESULTS AND DISCUSSIONS

Fig.1 is the boiling heat transfer coefficients against vapor quality for mass fluxes from 70 to 210 kg/m^2·s. The saturated pressure is 0.57 MPa. The heat flux is 10 Kw/m^2. The heat transfer coefficients increase as the mass flux increases. The mass flux has a strong effect on the heat transfer coefficients. However, the trends of the heat transfer coefficient curves are different. At the mass flux of 70 kg/m^2·s, The heat transfer coefficients indistinctively change with the vapor quality. From flow pattern observation, the stratified flow is the dominant flow pattern and the nucleate boiling is superior in the heat transfer at this mass flux. At the mass flux of 210 kg/m^2·s, the annular flow is dominant flow pattern, Therefore, higher heat transfer coefficients are obtained. Along with the increase of vapor quality, the coefficients increase first, and then they decrease. The reason can be explained that the upper part of the inside surface in the tube begins to become part dry-out when vapor quality is at a certain value. Although the heat transfer coefficients decrease, they still keep larger values. This results from that phenomena, which the flow liquid droplets in the center part of the tube continuously hit on the wall and flow liquid film on the wall exists until very high vapor quality through the visual observation. Chamra et al [1] also obtained the similar experimental results, but they do not explain the reason.

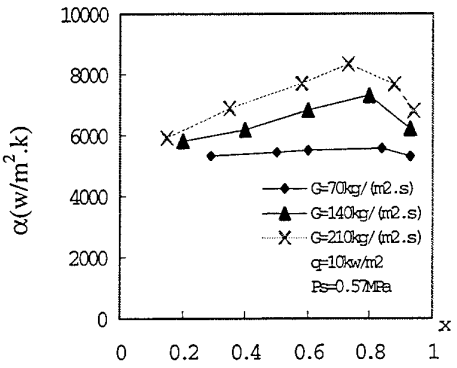

Fig.1. Boiling heat transfer coefficient vs. vapor quality at different mass flux

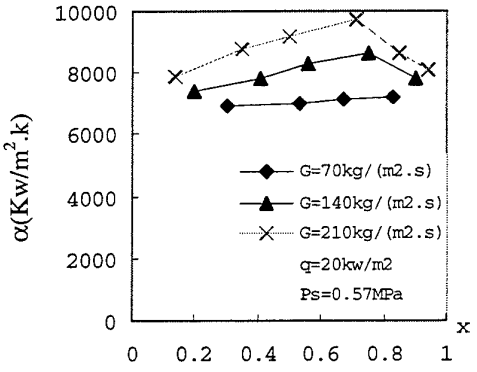

Fig.2. Boiling heat transfer coefficient vs. vapor quality at different mass flux

Fig.2 shows the boiling transfer coefficients against vapor quality for mass fluxes as the heat flux increases to 20 Kw/m^2. The saturation pressure is equal to that of Fig.1. The trends and the results from Fig.1 can be also attained from Fig.2. As compared Fig.2 with Fig.1, the boiling heat transfer coefficients rise when the heat flux increases at a fixed mass flux.

The effect of saturation pressure on the boiling heat transfer coefficient is illustrated in Fig.3. As shown, the boiling heat coefficients increase with the saturation pressure. Then the effect of pressure is not very significant., because the variation of saturation pressure is small.

Fig.4 and Fig.5 demonstrate the variation of the average heat transfer coefficient vs. mass flux. In Fig.4, the heat flux is 10kw/m^2. While in Fig.5, the heat flux is 20kw/m^2. For comparison, the data of the paper [3] and the smooth tube are also shown in Fig.4 and Fig.5. The data of the smooth tube are calculated by Wattelet's correlation [4]. Fig.4 and Fig.5 show the average heat

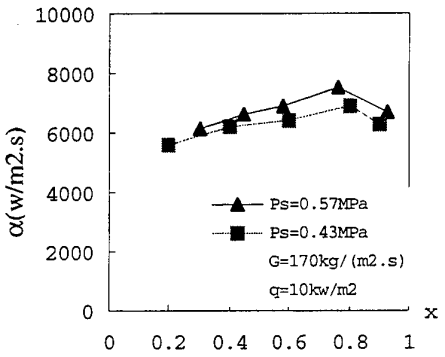

Fig.3. Effect of saturation pressure on the heat transfer coefficient

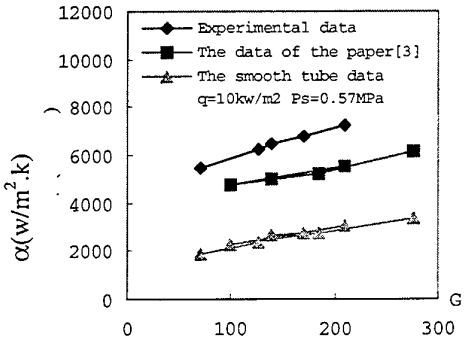

Fig.4. Experimental data compared with the Data of the paper [3] and the smooth tube (q=10kw/m^2)

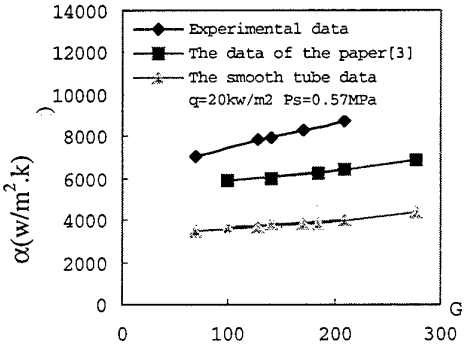

Fig.4. Experimental data compared with the Data of the paper [3] and the smooth tube (q=20kw/m^2)

transfer coefficients are significantly superior to those of the smooth tube. The average enhancement ratio slightly increases as the mass flux decreases (from 2.4 to 2.7) in Fig.4, but the average enhancement ratio hardly vary with the mass flux (approximately equal to 2.1) in Fig. 5. Apparently, the average enhancement ratio increases as the heat flux decreases. The average enhancement ratio is 2.1~2.7 as described above. Furthermore, Fig.4 and Fig.5 show that the average heat transfer coefficients are higher than those of the paper [3]. Compared with the paper [3], the average heat transfer coefficients promote 30%~40%. Therefore, the more the microfin numbers the higher the heat transfer coefficients.

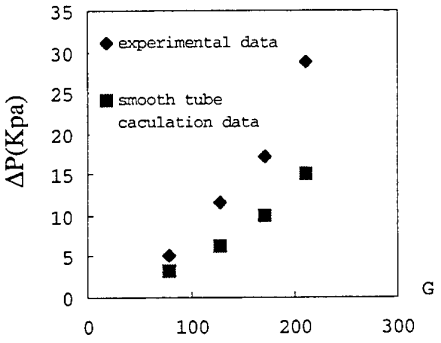

Fig.6. The pressure drop compared with the data of the smooth tube

The effect of the mass flux on the pressure drop is plotted in Fig.6. The tests are performed in 4.66m long test section (include eleven 6.0cm visual subsection). The entering and leaving vapor qualities are 0 and 0.9, respectively. As shown, the pressure drop greatly increases as the mass flux increases. The pressure drop of the smooth tube, calculated by Friedel correlation[5], is also shown in Fig.6. As compared to the data of the smooth tube, the pressure drop increase 55%~91%.

According to 178 experimental data, the empirical correlation is obtained, and is expressed by:

$$\alpha/\alpha_l=335Bo^{0.3}Xtt^{-0.57}(P/Pc)^{0.38} \tag{6}$$

Where the boiling number $Bo=q/(Gh_{fg})$; the Martinelli parameter $Xtt=(\mu_l/\mu_v)^{0.1}(\rho_v/\rho_l)^{0.5}[(1-x)/x]^{0.9}$; and the Dittus-Boelter equation is used to calculate α_l, and is written as $\alpha_l=0.023[Re(1-x)]^{0.8}Pr^{0.4}\lambda_l/D$. Fig.7 shows the predicted heat transfer coefficients agree with the experimental data within ±25%.

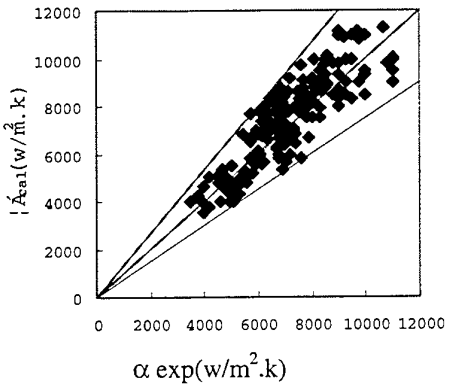

Fig.7. The comparison of the predicted data with the experimental data

5. CONCLUSIONS

1. This paper reports the boiling heat transfer performance of the new 3-D micro-fin tube is significantly superior to the smooth tube. The boiling heat transfer coefficients compared with the data from Wattelet's correlation[4] for smooth tubes, the average enhancement ratio is 2.1~2.7 under the test condition. The

pressure drop compared to the data of smooth tube, calculated by Friedel correlation, the pressure drop increase 55%~91%.

2. The heat transfer coefficient increases with mass flux, heat flux and saturation pressure.
3. The boiling heat transfer coefficients are higher 30%~40% than those of the paper [3], because the new 3-D microfin tube has more fins.
4. The empirical correlation offers a reference for the design of the evaporator for the new 3-D microfin tube.

NOMENCLATURE

A_{in} the nominal inside area of the tube, m^2
d_{in} the diameter to the fin base, mm
G refrigerant mass flux, $kg/m^2 \cdot s$
h enthalpy of the saturated refrigerant liquid, kJ/kg
ΔL_i the length of one subsection, m
m_R refrigerant mass flow rate, kg/s
q heat flux, Kw/m^2
T_i heating water temperatures, °C
T_w average surface temperature of the test tube, °C
Pc critical pressure, MPa
Δx change in vapor quality
β apex angle of the fin
Bo the boiling number
Cp_c the isobaric specific heat of water, $Kw/(m^2 \cdot k)$
d_{out} the outer diameter of the tube, mm
h fin height, mm
h″ enthalpy of the saturated refrigerant vapor, kJ/kg
m_c heating water mass flow rate, kg/s
p fin pitch, mm
Q_i heat transfer rate at each subsection, Kw
T_{sat} saturated temperature, °C
P saturated temperature, MPa
x_I local vapor quality
α local heat transfer coefficient, $Kw/m^2 \cdot$ °C
λ_w the thermal conductivity of the tube, $w/(m \cdot k)$
Xtt the Martinelli parameter

SUBSCRIPTS
i designates subsection of test tube

REFERENCES

1. L.M.Chamra, R.L.Webb et al., Advanced micro-fin tubes for evaporation. Int. J. Heat and Mass Transfer. Vol. 39. No. 9, PP. 1827-1838, 1996.
2. C. S. Kuo and C .C. Wang, In-tube evaporation of HFC-22 in a 9.52*mm* micro-fin /smooth tube. Int. J. Heat and Mass Transfer. Vol. 39. No. 12, PP. 2559-2569,1996.
3. J.Zhou, M.D.Xin et al., Boiling in a horizontal three dimensional microfin tube for R134a. Multiphase Flow and Heat Transfer Proc. of the Fourth International Symposium, Xi'an China, 1999.
4. J. P. Wattelet et al., A correlation for forced convective boiling heat transfer of pure refrigerants in a horizontal smooth tube. Int. J. Heat Mass and Transfer, Vol. 36, No. 13, PP. 3351~3360,1993.
5. L.Friedel, Improvered friction pressure drop correlations for horizontal and vertical two phase pipe flow. European Two Phase Flow Group Meet, Ispra, Italy, Paper E2, 1979.

EXPERIMENTAL STUDY ON PHASE DISTRIBUTION IN INCLINED SUBCOOLED BOILING ANNULUS

T.H. Lee, M.O. Kim, H.K. Cho and G.C. Park
Department of Nuclear Engineering, Seoul National University,
San 56-1 Shinlim-dong, Gwanak-gu, Seoul 151-742, Korea
E-mail: thlee@plaza.snu.ac.kr; Fax:+82-2-889-2688

Keywords: inclined, subcooled boiling, two-conductivity probe, void fraction, interfacial area concentration

ABSTRACT. The profiles of local vapor phase parameters over the cross section were measured in the inclined subcooled boiling in a concentric annulus with a uniformly heated inner tube. Two-conductivity probe technique was applied to measure the local values of interfacial parameters such as void fraction and interfacial area concentration. Experiments were conducted for five angles of inclination (0° (vertical), 15°, 30°, 45°, 60°) and flow conditions were controlled by mass flux, heat flux and inlet subcooling for each inclination. Based on the measurements, the influences of channel inclination and flow conditions on the profiles were investigated for understanding those effects on the internal phase distribution of inclined boiling flow.

1. INTRODUCTION

The detailed knowledge of internal structure in the dispersed two-phase flow is important in the optimum design and safety analysis of various equipment in the nuclear, refrigeration, chemical and petroleum industries. The void fraction and the interfacial area concentration (IAC) are fundamental parameters describing local internal structure for the dispersed two-phase flow. The local void fraction represents the local phase distribution and the IAC describes the available interfacial area for the interfacial transport of mass, momentum and energy. For the purpose of providing basic information on the internal structure, a lot of experimental studies have been carried. However, most of the study have been concentrated on the adiabatic two-phase flow with air-water in vertical or horizontal conduit. Also, two-phase flow in inclined conduit has been mostly investigated based on the global measurements [1-4]. So, works on the local measurements of two-phase flow parameters in inclined flow are limited so far. Spindler [5] measured the local void fraction and bubble frequency in inclined pipe. As the inclination was changed from vertical to horizontal, the bubbly flow pattern disappeared because of high local concentration of voids at upper pipe crown, and flow pattern transition was also observed with changing equivalent bubble diameters. Those observations explicitly indicate that two-phase flow structure is strongly influenced by the angle of inclination. However, that work was limited to adiabatic air-water two-phase flow. For inclined boiling flow where the phase change continuously takes place, the works on the local measurements of two-phase flow parameters are very scarce. In inclined boiling system, the heat transfer depends on the orientation of channel as reported by Fedorov and Klimenko [6]. In their experimental work, the heat transfer coefficient in the upper circumference of the channel showed somewhat weaker dependency on the heat flux than in the lower circumference. This effect is obviously connected to non-uniform temperature distribution due to the asymmetry of the two-phase flow structure. The mechanism of boiling heat transfer in inclined flow is closely related to the phase distribution as well as the flow pattern. Therefore, for comprehensive understanding of heat transfer phenomena in the inclinable systems such as ship reactor and absorber tube of a concentrating parabolic through collector with direct steam generation, it is necessary to know the flow structure from the local measurements at different angles of inclination. In this study, The internal phase distributions of subcooled boiling in vertical and inclined annuli have been experimentally investigated. Using a two-conductivity probe technique, the profiles of local interfacial parameters such as void fraction and IAC were measured at different levels of mass flux, heat flux, inlet subcooling and inclination. Based on the profile measurements, the influences of flow conditions and channel inclination on the internal flow structure were investigated.

2. EXPERIMENTAL FACILITY AND PROCEDURE

A schematics of the test loop is described in Fig. 1. The test loop basically consists of a test channel, a water storage tank, a pump, a preheater and a water purification unit. The test channel is the vertical concentric annulus of 2.37 m long with a heated inner tube, and the angle of inclination can be adjusted between vertical and horizontal. The inner tube of 19 mm outer diameter is composed of a heated section and copper electrodes silver

soldered to both ends of the heated section. The heated section is a 1.67 m long Inconel 625 tube with 1.5 mm wall thickness and is filled with magnesium oxide powder insulation. The tube is uniformly heated by a 54 kW DC power supply. The outer tube is comprised of two stainless steel tubes with 37.5 mm inner diameter, which are connected by a transparent glass tube so that visual observation and taking photograph are possible. The transparent glass tube is 50 mm long and is installed just below the measuring section. The measuring section is located at 1.61 m downstream of the beginning of the heated section. To measure the distributions of two-phase flow parameters over the cross section, the outer tube of measuring section is designed to be rotated by 360°. Traversing units with 0.01 mm spatial resolution are used to position the local probes in a direction perpendicular to the axis of the test channel.

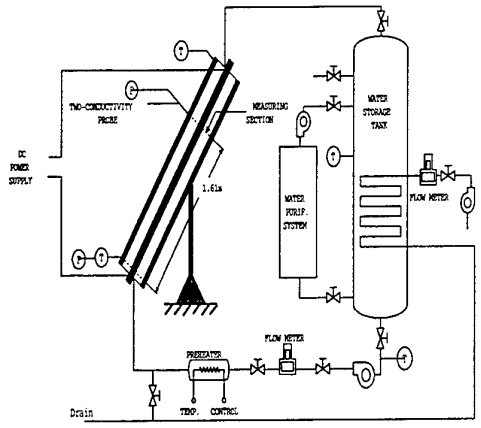

Fig. 1. Schematics of experimental facility

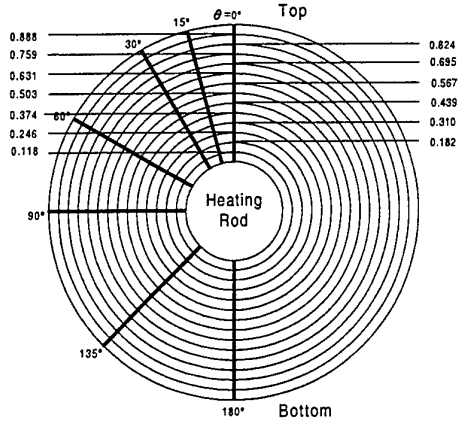

Fig. 2. Probe positions in inclined channel

Demineralized water was used as a working fluid, and its flow rate entering the test channel was measured by turbine flow meter. The test channel inlet and exit temperatures were measured using the calibrated platinum resistance temperature detectors with the estimated error of ±0.2 °C. The absolute pressures at inlet and measuring section were measured within the uncertainties of ±0.001 Mpa. Experiments were carried out at different levels of mass flux, heat flux, inlet subcooling and channel inclination. Five angles of inclination (0°(vertical), 15°, 30°, 45°, 60°) were selected. Mass flux, heat flux and inlet subcooling were adjusted at $714 < G < 1061$ kg/m^{2}s, $120 < q'' < 307$ kW/m^2 and $10 < \Delta T_{sub} < 22$ °C, respectively. The uncertainties in the mass flux, heat flux and inlet subcooling measurements were estimated to be ±1% of the rated mass flux, ±1% of the rated heat flux and ±0.3 °C, respectively. The system pressure was maintained at 1 to 2 bar, and it was not controlled but determined by net volume expansion balanced by the bubble generation rate in the test channel and the ventilation rate in the storage tank. For vertical channel, 13 measuring positions have been chosen along the radial direction, assuming the symmetry of flow. For inclined channels, the probe was traced at 91 selected points as illustrated in Fig. 2. Additionally, the fundamental photography using the high speed digital video camera (SPEED CAM512) was performed to visualize the overall flow structure.

3. MEASURING METHOD

Local vapor phase parameters such as void fraction, bubble frequency, vapor bubble velocity and IAC were measured by the two-conductivity probe method which has a merit in the local measurements for a wide range of void fraction. Especially, in view of local measurement in inclined subcooled boiling with local void fractions ranging from 0% to 70%, the probe method is considered to be the good choice. The two-conductivity probe identifies each phase of the two-phase mixture by using the difference of electrical resistance between the vapor and liquid phases. The two-conductivity probe in this study consisted of two-sensors which were made of teflon-coated stainless steel wire with a diameter of 0.076 mm. The two sensors were adjusted for a distance of 1.5 mm in the length-wise direction and were aligned in the axial direction. Instantaneous change in local resistivity sensed by the probe was converted into a voltage drop between a probe tip and the ground by an A. C. rectifier circuit. Ideally, the voltage signals is the two-state square-wave. However, the signals generally deviate from the

ideal signal form due to the finite size of the sensor and the possible deformation of the vapor bubble interface before the sensor enters into one phase from the other. Thus, it is necessary to determine the proper threshold above which the signal can be considered a vapor bubble. In this study, the threshold was calculated based on the signal height and slope criterion for individual bubble. The threshold for each bubble was assumed to be proportional to its signal height. Thus, the threshold, T was calculated by a product of a proportional constant, S and signal height, $(H_g - H_l)$ for each bubble as follows;

$$T = S\,(H_g - H_l) + H_l \tag{1}$$

Even though a signal above the threshold of Eq. (1) corresponds to a bubble, multi-peaked signals above the threshold can exist, which can be caused by the avalanche of bubbles or wetting of the probe tips. These bubbles are discriminated as the separate bubbles by the slope criterion. The main advantage of the present algorithm is that the threshold for each bubble is varied in accordance with the signal drift induced by probe fouling, change of flow condition and water conductivity. The proportional constant was determined by calibrating the two-conductivity probe to the global void fraction by the quick closing valve technique in air-water flow. From the calibration, the proportional constant of 0.35 was found to be reasonable for channel inclination of 0°~60°. A more information concerning the determination of probe distance and proportional constant are presented in Lee et al.[7]. The local void fraction was simply determined by dividing the accumulated time which the sensor was exposed to the vapor phase by the total sampling time. The local vapor bubble velocity in the axial direction was calculated by taking into account the distance between the tips of the upstream and downstream sensor and the time difference between the upstream and downstream signal. The local IAC was estimated using the methodology suggested by Kataoka et al. [8]. Based on the assumptions that the bubbles are spherical and every part of the bubbles has the same probability being intersected by the probe, they derived the following expression for local IAC, $a_i(r)$.

$$a_i(r) = \frac{4N_t \left\{ \sum_j \frac{1}{|v_{szj}|} / (\sum_j) \right\}}{1 - \cot\frac{\alpha_o}{2} \ln(\cos\frac{\alpha_o}{2}) - \tan\frac{\alpha_o}{2} \ln(\sin\frac{\alpha_o}{2})} \tag{2}$$

where

$$\frac{\sin 2\alpha_o}{2\alpha_o} = \frac{1 - (\sigma_z^2 / \overline{|\vec{v}_{sz}|^2})}{1 + 3\,(\sigma_z^2 / \overline{|\vec{v}_{sz}|^2})} \tag{3}$$

$$\sigma_z = (\sum_j N_{szj}\,(v_{szj} - v_{sz})^2 / \sum_j N_{szj})^{1/2} \tag{4}$$

In Eqs. (2)-(4), v_{szj}, v_{sz}, N_{szj} and N_t denote the interfacial velocity, arithmetic mean of v_{szj}, number of bubbles having v_{szj} and bubble frequency, respectively. In the present study, the local IAC was calculated from the equations by using the measured vapor velocity spectrum and bubble frequency at each measuring point.

4. EXPERIMENTAL RESULTS AND DISCUSSION

Local Void Fraction

The void fraction is one of fundamental parameters which characterize the structure of flow boiling because it reflects the energy of fluid and influences the distributions of other local parameters. The typical radial profiles of local void fraction are represented in Fig. 3 for five angles of inclination. For inclined flow, radial profiles at θ=0° and 90° are presented. Also, the effects of mass flux and inlet subcooling on the void fraction profiles are

described in Figs. 4 and 5, respectively where the profiles at $\theta=0^{\circ}$ are shown for inclined flow. In those figures, $(r-R_i)/(R_o-R_i)=1$ indicates the inner surface of outer tube and $(r-R_i)/(R_o-R_i)=0$ means the heated surface. In the present experiment, the void fraction at the position less than 0.11 of $(r-R_i)/(R_o-R_i)$ were not measured due to the probe geometry. One of the unique characteristics of the subcooled boiling is the existence of two distinguishable flow regions in the flow channel made by the thermal non-equilibrium of two phases. One of the regions is the bubble boundary layer as the two-phase region and the other is the subcooled liquid core. The thickness of bubble boundary layer is affected by inlet subcooling, mass flux and wall heat flux [9,10] and mainly dependent on the bubble size [9] which is determined by a balance of bubble coalescence and condensation rates. Also, the channel inclination causes non-uniform bubble boundary layer thickness since the increase of bubble size due to bubble coalescence is expected as moving upper part of the cross section.

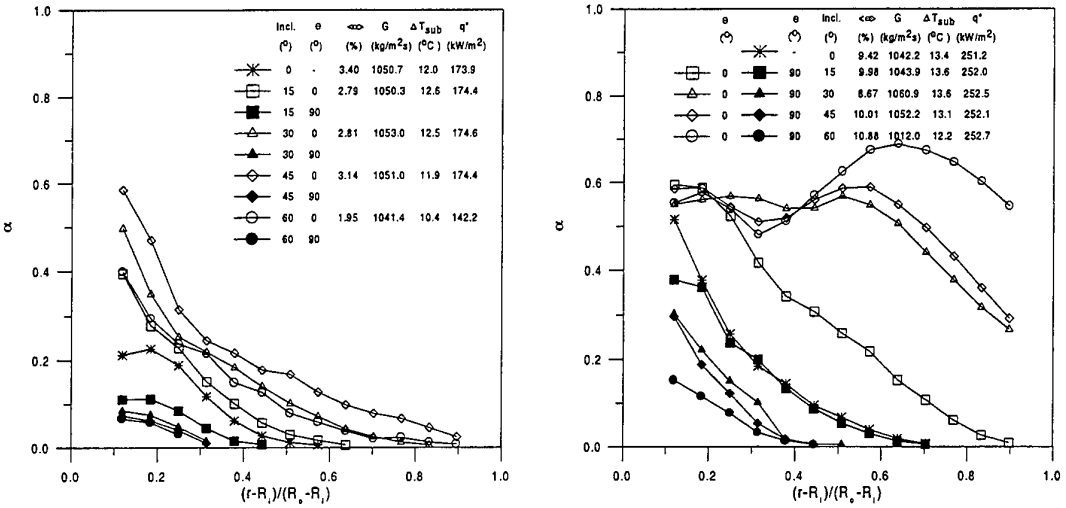

Fig. 3. Void fraction distributions for five inclinations

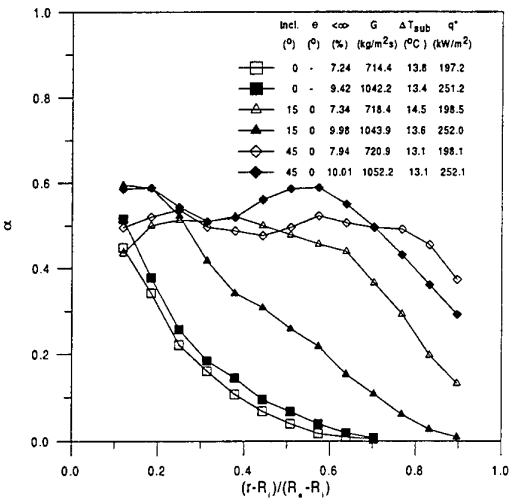

Fig. 4. Mass flux effect on void fraction frofile

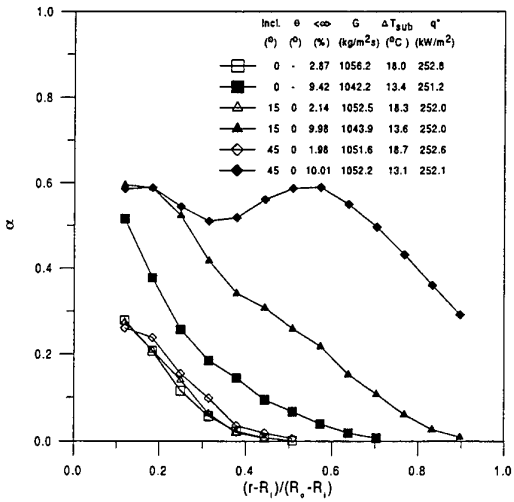

Fig. 5. Inlet subcooling effect on void fraction profile

For vertical flow, the local void fraction decreases from the heated surface to the subcooled liquid core. The peak local void fraction is always observed near the heated surface. The peak value of the void fraction near the heated surface is quite different from the wall void peaking phenomena in the air-water bubbly flow, which is due to the migration of bubbles toward the wall. In subcooled boiling, the high local void fraction near the

heated surface is explicitly due to the large number of bubbles generated from the boiling sites on the heated surface. Many bubbles with small sizes generated on the boiling sites are detached from the heated surface when their sizes exceed a certain critical size. The detached bubbles will then migrate laterally toward the subcooled liquid core under competing processes of bubble coalescence and condensation because the local pressure around the heated surface is higher than that in the subcooled liquid core due to the volume expansion induced by bubble generation. And thus, the direction of the bubble movement is opposite to the case of wall peaking in the air-water flow. Bubbles migrating to the subcooled liquid core is condensed by the subcooled water, and thus the local void fraction decreases as moving toward the subcooled liquid core. The effects of heat flux, mass flux and inlet subcooling on the profile of local void fraction can be found from Figs 3, 4 and 5. Considering the boundary between bubble layer and subcooled liquid core to be the intersection of abscissa and zero value of void fraction, the figures show that the thickness of bubble layer increases with wall heat flux, and decreases with mass flux and inlet subcooling.

For inclined flow, the migration of bubbles toward the upper part of the cross section can be seen irrespective of flow conditions. Thus, the bubble layer increases as moving to upper part of the cross section as shown in Fig. 3. As the channel inclination increases, the bubble layer grows in the upper part and diminishes in the lower part. For area-averaged void fraction of about 10% at 60° inclination, the bubble layer bridging the channel gap extended to θ=60° (In most experimental conditions, the bubble layer filling the channel gap was limited to θ=30°.). However, at $135° \leq \theta \leq 180°$, the bubbles were detected in the thin layer near the heated surface ($(r-R_i)/(R_o-R_i) < 0.3$). This observation explicitly indicates that the increase of channel inclination intensifies the asymmetry of the two-phase flow structure. As shown in Fig. 3, the void fraction profiles in the lower part show the same trend as those in vertical flow where the local void fraction is a maximum near the heated surface. On the other hand, the void fraction profiles in the upper part is influenced by the channel inclination and area-averaged void fraction in different ways. For low area-averaged void fraction, the maximum void fraction is observed near the heated surface at θ=0°, irrespective of channel inclination. However, for high area-averaged void fraction, the location of maximum void fraction moves toward the outer wall at θ=0° as the channel inclination increases. For area-average void fraction of about 10% and channel inclination above 30°, the local void fraction is a maximum between the center of channel gap and the outer wall at θ=0° and more shift of maximum void fraction location to outer wall is found with the channel inclination. The non-uniformity of phase distribution by inclination is influenced by mass flux and inlet subcooling. As shown in Figs. 4 and 5, the inclination effect on the profiles of void fraction is reduced as mass flux and inlet subcooling increases.

The local void fraction is governed by bubble size and bubble frequency. With the assumption that bubbles are spherically shaped, the equivalent bubble diameter (Sauter mean diameter, D_s) can be estimated from the simple geometrical relation between the void fraction, α, and IAC as follows;

$$D_s = 6\,\alpha / IAC \tag{5}$$

Typical bubble frequency and Sauter mean diameter profiles are presented in Fig. 6 and 7, respectively, for the corresponding flow conditions of Fig. 3. For vertical flow, the profiles of local void fraction and local bubble frequency are very similar, and the local Sauter mean diameter distribution is nearly uniform. This means that the increase of local void fraction is not due to the increase of bubble size but mainly due to the increase of vapor bubble frequency for a given flow condition. For inclined flow, the bubble frequency and Sauter mean diameter increase as moving to the upper part of the cross section. These profiles explicitly indicate that a number of vapor bubbles migrate toward the upper part by buoyancy, and bubble size increases by the bubble coalescence due to the high vapor bubble population. As shown in Figs. 3 and 6, the void fraction profile at θ=0° is similar to the bubble frequency profile for low area-averaged void fraction, but the former considerably deviates from the latter for high area-averaged void fraction. The high local void fraction in the small bubble frequency region can be accounted by bubble size. Thus, the bubble size plays a important role in void fraction profile in inclined flow, and its effect becomes stronger with the channel inclination. It is interesting to note that the Sauter mean diameter is larger than the channel gap size for the channel inclination of 30°~60°. This observation implies that the flow pattern changes to slug flow in the upper part of cross section. The fundamental photographic studies regarding overall phase distribution in the measuring section indicated that bubbles with the lateral sizes comparable to channel gap existed depending on channel inclination and flow conditions.

Local Interfacial Area Concentration

The IAC is also important to determine the thermohydrodynamic behavior of two-phase flow. In particular, it is indispensable in two-fluid formulation where the interfacial transfer terms are expressed by the product of IAC and driving force. The radial profiles of local IAC are illustrated in Fig. 8.

For vertical flow, the distributions of local IAC have the same trend as those of local void fraction and local bubble frequency as shown in Figs. 3, 6 and 8. From Eq. (5), it is obvious that besides the void fraction, the bubble size also has a important effect in determining the IAC since the surface-to-volume ratio of a small bubble is larger than that of a larger bubble. However, the Sauter mean bubble size profiles are fairly uniform as illustrated in Fig. 7 and the increase of local void fraction depends on the local bubble frequency. Thus, the observed similarity in profiles of the void fraction, bubble frequency and IAC is not surprising.

For inclined flow, the IAC increase as moving to upper part of cross section for all flow conditions. For low area-averaged void fraction where the Sauter mean bubble size is fairly uniform at all θ as shown in Fig. 7, the profiles of local void fraction, bubble frequency and IAC show similar trend as described in Figs. 3, 6 and 8. However, for high area-averaged void fraction, the IAC profile very closely follows the bubble frequency profile

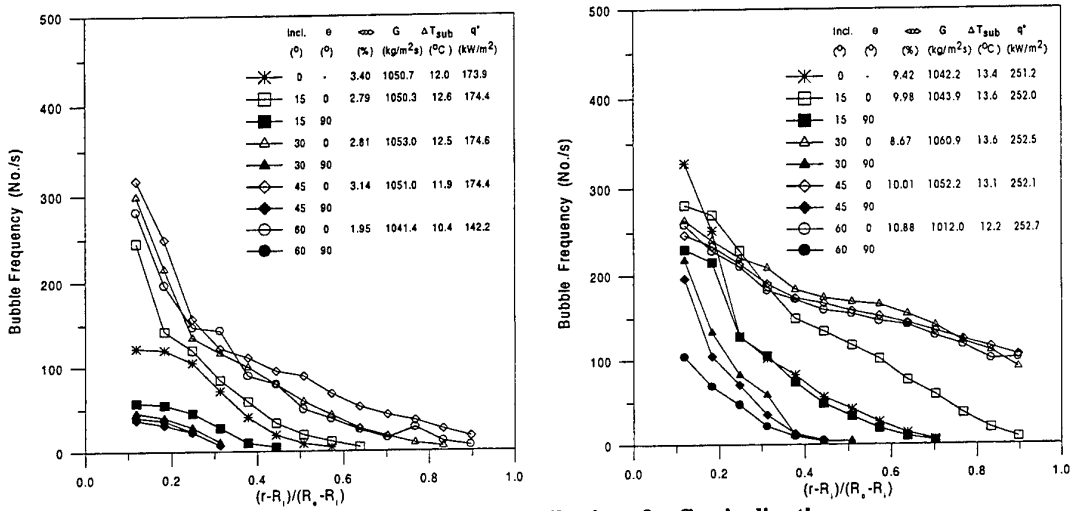

Fig. 6. Bubble frequency distributions for five inclinations

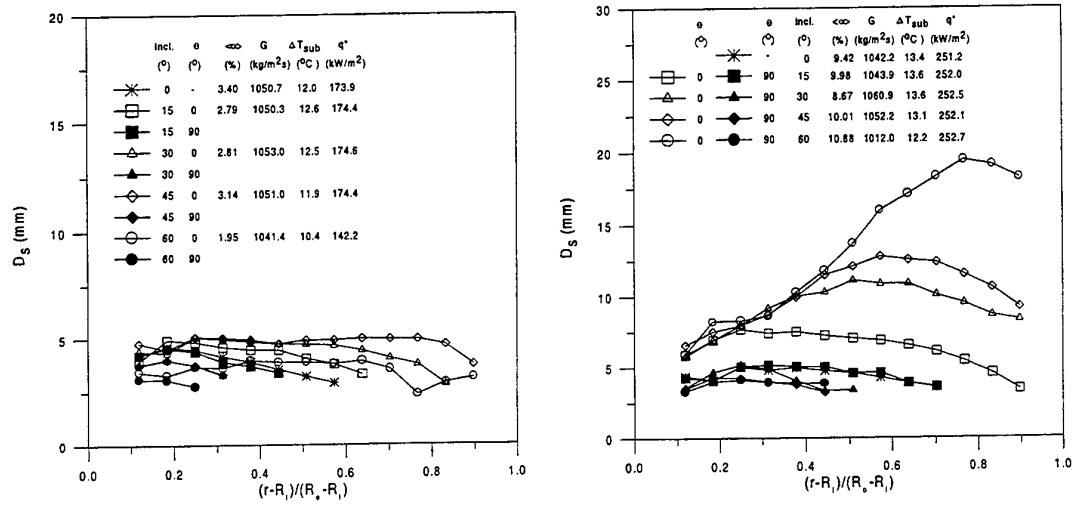

Fig. 7. Sauter mean diameter distributions for five inclinations

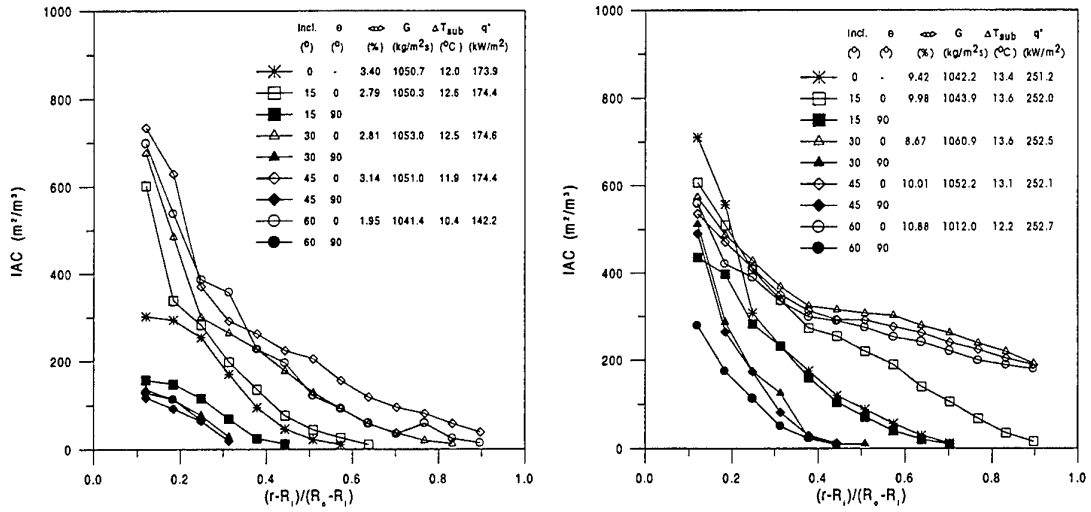

Fig. 8. IAC distributions for five inclinations

but that in the upper part is quite different from the void fraction profile. For the channel inclination of 30°~60°, the local IAC around the maximum void fraction point is much lower that that near the heated surface. The small IAC around the maximum void fraction point can be easily noted since the local bubble frequency is small compared with that near the heated surface as shown in Fig. 6. Although the local bubble size is also important in determining the IAC because the local IAC can be expressed as the product of bubble surface area and bubble number density, the effect of bubble frequency on the IAC is found to be much more dominant than the bubble size effect in the present experiment. However, the growth of bubble size due to bubble coalescence causes the reduction of local bubble number density at a point. Thus, the local IAC is also influenced by local bubble size in inclined flow. As shown in Fig. 8, the local IAC near the heated surface at $\theta=0^\circ$ in low area-averaged void fraction is larger than that in high area-averaged void fraction in spite of local void fraction in low area-averaged void fraction being small compared with that in high area-averaged void fraction. This is due to the fact that the IAC is inversely proportional to the local bubble size for a fixed local void fraction as indicated in Eq. (5). From the data near the heated surface with similar local void fraction in Fig. 3 and corresponding local Sauter mean diameter and IAC in Figs. 7 and 8, it can be noted that the Sauter mean diameter is smaller in low area-averaged void fraction and thus the IAC is larger. As the channel inclination increases, the IAC increases due to the increase in bubble frequency for low area-averaged void fraction. However, for high area-averaged void fraction, the local IAC at $\theta=0^\circ$ decreases as the channel inclination increases from 30° to 60°. The decrease of local IAC is attributed to more reduction of local bubble frequency due to larger bubbles in higher inclination as shown in Fig. 6. As shown in Figs. 3 and 8, the observed local void fraction can reach 0.7, whereas the peak IAC can go up to 750 m^2/m^3. Since the local transports of mass, momentum and energy are directly proportional to IAC, the figures point out the existence of a highly non-symmetric interfacial transport in inclined boiling flow.

The effect of mass flux on the local IAC is illustrated in Fig. 9. Also, the corresponding effect on the local Sauter mean bubble diameter is shown in Fig. 10. For vertical flow, the present data show that the local IAC decreases with the mass flux for the same local void fraction. For the area-averaged void fraction above about 7%, the change of bubble boundary layer thickness with mass flux is small. Thus, the bubble number density in the bubble layer increases with mass flux. Since the bubble coalescence rate will be enhanced due to random collision and turbulent wake of bubbles in high mass flux condition, the bubble size increases. So, the local IAC decreases with mass flux for the same local void fraction. The increase of local bubble size with mass flux can be seen in Fig. 10. Although the turbulent eddies which have equivalent size with the bubble size can break up the bubble as reported by Wu et al.[11], the bubble break up rate by the liquid turbulence is found to be negligible compared with the bubble coalescence rate in the subcooled boiling flow. The effect of mass flux on the local IAC for inclined flow is observed to be the same as that for vertical flow as shown in Fig. 9. Also, as the channel inclination increases, the IAC decreases since the bubble size increases with the inclination for the same local void fraction.

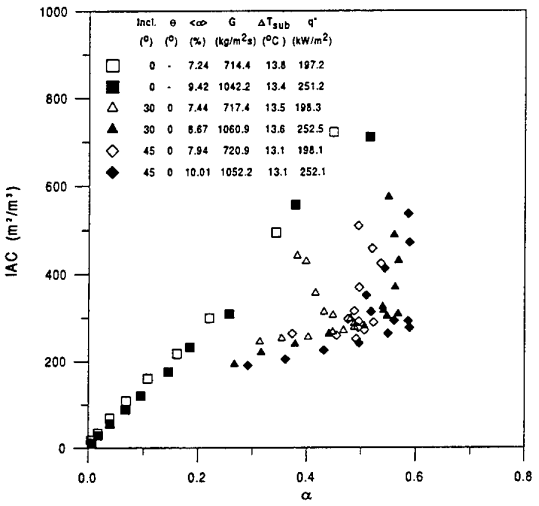

Fig. 9. Effect of mass flux on IAC

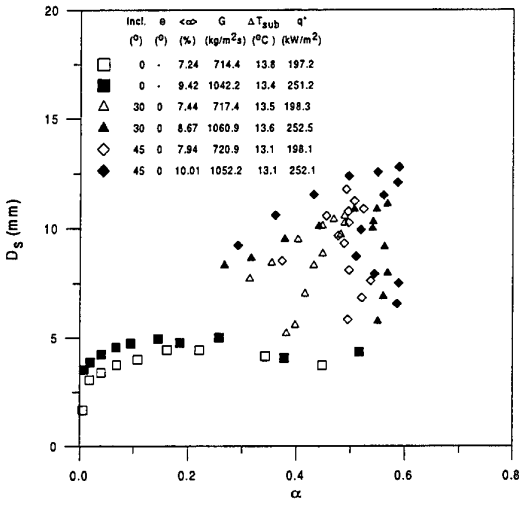

Fig. 10. Effect of mass flux on sauter diameter

Fig. 11. shows the effect of inlet subcooling on the local IAC for the similar area-averaged void fraction and mass flux. For the channel inclination of 60°, the slug flow was observed in the upper part of cross section for the high area-average void fraction and low subcooling from the fundamental photography. Thus, data sets for the area-average void fraction where the bubbly flow is sustained in all channel inclination are shown in the figure. For all channel inclination, the local IAC decrease as the inlet subcooling increases. In order to gain the same area-average void fraction for same mass flux condition, a larger heat flux is required for a higher inlet subcooling. Since the bubble departure diameter increases with heat flux as reported by Unal[12], it can be expected that the bubble sizes in bubble layer are larger at higher subcooling. Thus, the local IAC at high inlet subcooling is considered to be smaller than that at low subcooling due to the increase of bubble size with inlet subcooling.

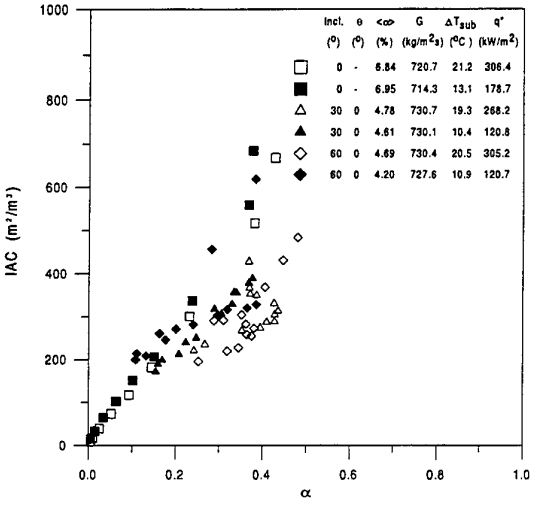

Fig. 11. Effect of inlet subcooling on IAC

5. SUMMARY AND CONCLUSIONS

The internal phase distribution of subcooled boiling in vertical and inclined annuli was experimentally investigated by using a two-conductivity probe technique. The local values of the interfacial parameters such as void fraction and IAC were measured. For vertical flow, the maximum void fraction is always observed near the heated surface. Also, The bubble boundary layer increases with heat flux, and decreases with inlet subcooling and mass flux. For inclined flow, the point of maximum void fraction is influenced by area-averaged void fraction and channel inclination. For low area-averaged void fraction, the local void fraction has a maximum near the heated surface at $\theta=0^{\circ}$. However, for high area-averaged void fraction about 10%, the location of maximum void fraction moves toward the outer wall at $\theta=0^{\circ}$ and more shift to outer wall was observed with the channel inclination. The maximum void fraction is attributed to large bubble size created by bubble coalescence, and flow pattern transition to slug flow was also observed in the upper part. The non-uniformity of phase distribution by inclination is reduced as mass flux and inlet subcooling increase. The bubble size distribution is nearly uniform in vertical flow. Thus, the profiles of local void fraction, bubble frequency and IAC show very similar trend. However, for inclined flow, the IAC profile is closely follow the bubble frequency but is quite

different from the void fraction profile in high area-averaged void fraction. Although the bubble size have a crucial effect to the void fraction profile, its effect on the IAC profile was found to be negligible compared with the bubble frequency effect. Also, the local IAC was observed to decrease with mass flux and inlet subcooling.

REFERENCES

1. P.L. Spedding, J.J.J. Chen and V.T. Nguyen, Int. J. Multiphase Flow, Vol. 8, No. 4, pp. 407-431 (1982).
2. J.F. Stanislav, S. Kokal and M.K. Nicholson, Int. J. Multiphase Flow, Vol. 12, No. 3, pp. 325-335 (1986).
3. D. Barnea, O. Shoham, Y. Taitel, and A.E. Dukler, Chemical Eng. Sci., Vol. 40, pp 131-136 (1985).
4. A.R. Hasan and C.S. Kabir, Int. J. Multiphase Flow, Vol. 18, No.2, pp. 279-293 (1992).
5. K. Spindler, "Void Fraction Distribution in Two Phase Gas Liquid Flow in Inclined Pipes", *Proceedings of the 10th International Heat Transfer Conference, Vol. 6, pp. 265-270,* Brighton, UK (1994).
6. M.V. Fedorov and V.V. Klimenko, Thermal Engineering, Vol. 35, pp. 347-349 (1988).
7. T.H. Lee, M.O. Kim, H.K. Cho and G.C. Park, "An Experimental Study of Forced Convective Subcooled Boiling in Vertical and Inclined Annuli", *Proceedings of 2nd international Symposium on Two-Phase Modelling and Experimentation, Vol. 1, pp. 225-232,* Pisa, Italy (1999).
8. I. Kataoka, M. Ishii and A. Serizawa, Int. J. Multiphase Flow, Vol. 12, No. 4, pp. 505-529 (1986).
9. L.M. Jiji and J.A. Clark, ASME J. of Heat Transfer, Vol. 86 pp. 50-58 (1964).
10. R.P. Roy, V. Velidandla, S. P. Kalra and P. Peturaud, ASME J. of Heat Transfer, Vol. 116, pp. 660-669 (1994).
11. Q. Wu and M. Ishii, "One-Dimensional Model for Sauter Mean Diameter Development in Vertical Air-Water Bubbly Flow", *Proceeding of 8th International Topical Meeting on Nuclear Reactor Thermal-Hydraulics, pp. 101-108,* Kyoto, Japan (1997).
12. H.C. Unal, Int. J. Heat Mass Transfer, Vol.19, pp.643-649 (1976).

BOILING HEAT TRANSFER AND FRICTIONAL PRESSURE DROP IN INTERNALLY REBBED TUBES AT HIGH PRESSURES

Tingkuan Chen Yushan Luo Jianxue Zheng Qincheng Bi
National Laboratory of Multiphase Flow in Power Engineering
Xi'an Jiaotong University, Xi'an, Shaanxi, 710049, CHINA
E-mail: chentk@xjtu.edu.cn; Fax: 0086-29-2668789

Keywords: boiling, pressure drop, internally ribbed tube, steam boiler

ABSTRACT. This paper describes the experimental results on boiling heat transfer and frictional pressure drop of high pressure steam-water two-phase flow in internally ribbed tubes used in once-through boilers of large thermal power plants. The test tubes are 4 thread internally ribbed tubes with diameter of 28x6mm and 22x5mm. The experimental parameters are: pressure p=13~27Mpa; mass velocity G=400~1800 kg/m^2.s; and steam quality x=0~1. The boiling heat transfer is measured in heated vertical upward tubes and the frictional pressure drop is measured in adiabatic horizontal tubes. Based on the tests, the wall temperature profiles of internally ribbed tubes are obtained; the critical heat flux, critical steam quality and critical mass velocity at the beginning of boiling heat transfer deterioration are given; the correlation of boiling heat transfer coefficient, post dryout heat transfer coefficient and two-phase frictional pressure drop are established. The results may be recommended to be used for the design of large steam boiler.

1. INTRODUCTION

In modern large capacity thermal power plants, the boiling heat transfer deterioration may occur in the furnace water wall tubes of boilers, even leading to failure of the tubes. Swenson et al.[1] reported that nucleate boiling may be maintained by use of certain configurations of internally ribbed surfaces in evaporating tubes at much lower mass velocity and higher steam quality than those in smooth tubes. After this, the internally ribbed tubes have been widely used as the measure to prevent the boiling heat transfer deterioration in large capacity power boilers and a lot of studies on the boiling heat transfer characteristics for various internally ribbed tubes were carried out. Watson et al.[2] studied the critical heat flux of a ribbed tube with 10 threads at the pressure of 18.6MPa. Nishikawa et al.[3] investigated the boiling heat transfer characteristics for three types of ribbed tube with different internal configurations at pressures from 16.7 to 20.6MPa. Recently, in order to develop the supercritical sliding pressure operation power boilers, Iwabuchi et al.[4] investigated the heat transfer performances of an internally ribbed tube with 4 threads in the near critical pressure region from 19.6 to 22.6MPa. Köhler et al.[5] experimentally studied the heat transfer and pressure drop in a ribbed tube with 4 threads in a wide pressure range from 5.0 to 22.0MPa. In order to determine the effectiveness for eliminating boiling heat transfer deterioration and frictional pressure drop of the internally ribbed tubes used for the 300MW and 600MW once-through power boilers and to provide the reliable data for the design and operation of the boilers, this research project was conducted.

2. EXPERIMENTAL APPARATUS

The experiments were carried out in the electrically heated high pressure steam-water loop of Xi'an Jiaotong University. The test tubes were 4 threads internally ribbed tubes with diameter of 28x6mm and 22x5mm, which are used for water wall tubes of 600MW and 300MW once-through boilers, respectively. The 28x6mm tube is made of 12Cr1MoV steel. Its configuration parameters are: equivalent I.D. 15.24mm, minimal I.D. 14.38mm, maximal I.D. 16mm, rib hight 0.81mm, groove width 9mm, pitch 21mm; helix angle 61.15°. The 22x5mm tube is made of 20g carbon steel. Its parameters are: equivalent I.D. 11.69mm, minimal I.D. 11mm, maximal I.D. 12mm, rib hight 0.5mm, groove width 5.38mm, pitch 10.04mm; helix angle 49.3°.The boiling heat transfer was measured in uniformly heated vertical upward tubes and the frictional pressure drop was measured in adiabatic horizontal tubes. The test pressure p were from 13 to 27MPa, mass velocities G were from 400~1800 kg/m^2.s, inside wall heat flux q based on equivalent I.D. were 200~800 kW/m^2. For making comparison, the boiling heat transfer and frictional pressure drop in smooth tubes with same I.D. were also studied under the similar conditions as above.

The experiments were carried out at conditions of a fixed pressure, mass velocity and heat flux in the test tubes,

by increasing gradually the power of the preheater of the test loop and measuring the outside wall temperature profiles and pressure drop along the test tubes in an enough wide range of steam quality, the boiling heat transfer and frictional pressure drop characteristics were obtained at various experimental parameters.

3. BOILING HEAT TRANSFER CHARACTERISTICS

3.1 Wall Temperature Profiles

The outside wall temperature profiles for the 22x5mm ribbed tube and the smooth tube at pressures of 19.5MPa and 21MPa are shown in Figure 1 and Figure 2, respectively. Because of the swirling and disturbance of internal grooves in ribbed tube, the liquid film flow rate on the tube wall increases, so the tube wall can be cooled quite well, the heat transfer deterioration can be restrained effectively. It is seen from the Figure 1 that, along with the increase of steam quality, the wall temperature of the ribbed tube is continuously on a level slightly higher than the saturated temperature of the fluid. Up to the quality increased to near unity, the tube wall temperature rises due to the dryout of the liquid film on the inside wall. Whereas in the smooth tube, the wall temperature begins to rise at quite lower steam quality. According to the tests, the ribbed tube can prevent the heat transfer to deteriorate effectively, up to the pressure rises to 20.5 MPa.

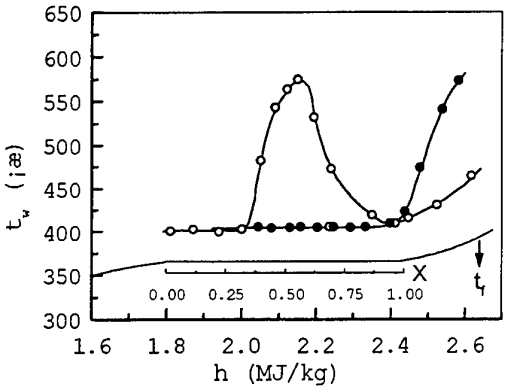

- Smooth tube:G=1200 kg/m^2.s,q=500 kw/m^2
- Ribbed tube: G= 800 kg/m^2.s,q=500 kw/m^2

Fig.1. Comparison of wall temperature profiles at 19.5MPa between the ribbed tube and the smooth tube

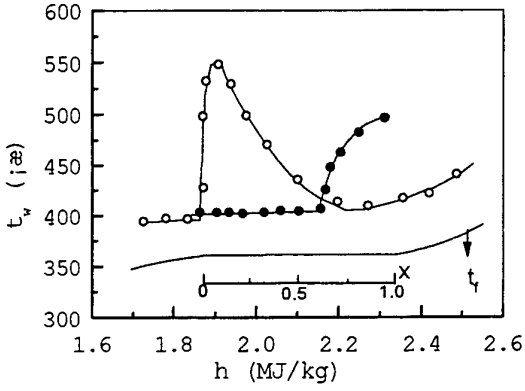

- Smooth tube:G=1200 kg/m^2.s,q=400 kw/m^2
- Ribbed tube: G= 800 kg/m^2.s,q=500 kw/m^2

Fig.2. Comparison of wall temperature profiles at 21MPa between the ribbed tube and the smooth tube

At the near critical pressures from 20.5MPa to 22MPa, the ribbed tube still has the advantage of preventing the boiling heat transfer from deterioration comparing with the smooth tube as shown in Figure 2 at pressure of 21MPa. But in this region, the boiling heat transfer deterioration in the ribbed tube occurs at lower qualities, so the effectiveness of preventing the heat transfer deterioration has somewhat decrease, for this great attention should be paid in design and operation. When the pressure reaches and exceeds the critical pressure, the wall temperature profile of the ribbed tube is similar to that of the smooth tube and there are better heat transfer characteristics for both tubes. When the enthalpy of the fluid increases to near the phase change point, the wall temperature begins to rise steadily.

3.2 Critical Conditions

The main factors affecting the boiling heat transfer characteristics in vertical upward tubes are pressure, heat flux, steam quality and mass velocity. There are two kinds of boiling heat transfer deterioration in boiling systems. The first kind is the Departure from Nucleate Boiling (DNB) occurring in low qualities and subcooling region, the second is the Dryout occurring in high qualities region. The minimal heat flux causing the heat transfer deterioration is referred to critical heat flux at a certain pressure, mass velocity and quality. In general, it is used for DNB. The steam quality at which the heat transfer deterioration begins to occur is referred to critical steam quality at a certain pressure, heat flux and mass velocity. In general, it is used for Dryout.

The critical heat flux at pressure of 16MPa and 21MPa for 28x6 ribbed tube are shown in Figure 3 and Figure 4, respectively. From Figure 3 it is seen that at subcritical pressures, the critical heat flux is complicated with steam quality. It has a minimal value between the quality of 0.3 and 0.4 and has a maximal value between 0.6 and 0.7. At near critical pressures from Figure 4, the critical heat flux decreases with increasing quality. The critical heat flux increases with increasing mass velocity and decreases with increasing pressure.

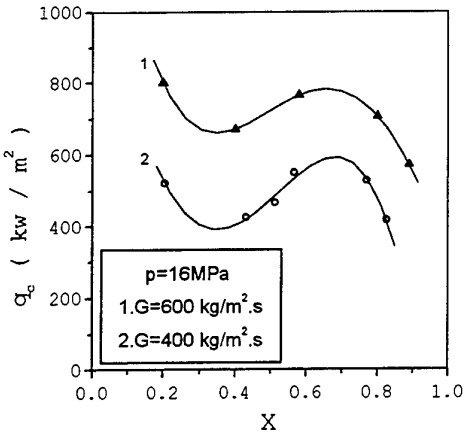

Fig. 3. The critical heat flux at p=16Mpa

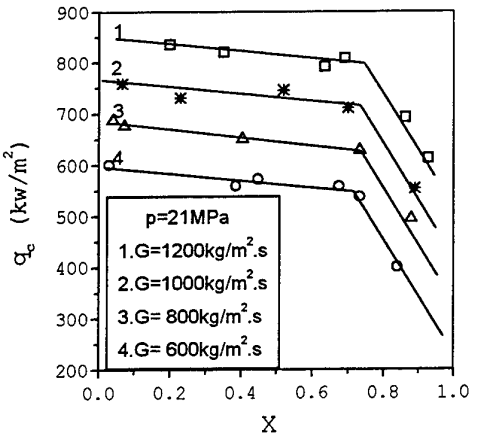

Fig. 4. The critical heat flux at p=19MPa

In steam boiler, in general, the kind of boiling heat transfer deterioration is Dryout. When the pressure is less than 20.5MPa, the critical steam quality x_c is very high, about more than 0.8. In the near critical pressure region, the critical quality decreases. For example, at p=21MPa, q=400~600 kW/m^2, G=600~800 kg/m^2.s, the x_c is about 0.6~0.65.

In boiler design, the critical mass velocity Gc is used frequently. If the mass velocity in ribbed tube decreases to less than the critical value, the critical quality would reduce to very low value, it would lead to the DNB heat transfer deterioration to occur and the wall temperature to rise rapidly. Based on the tests, the critical mass velocity increases with increasing the pressure and heat flux. For example, at p=16MPa, q=400~600 kW/m^2, the G_c is about 400~500 kg/m^2.s; at p=19MPa, q=400~600 kW/m^2, the G_c is about 500~600 kg/m^2.s; at p=21MPa, q=400~600 kW/m^2, the G_c is about 600~700 kg/m^2.s. In boiler design, the mass velocity in ribbed tubes must be higher than the critical mass velocity.

3.3 Heat Transfer Coefficients

In experimental tests, the outside wall temperature of the tube is measured by thermocouples, the following equation is used to calculate the inside wall temperature:

$$\frac{d^2t}{dr^2}+\frac{1}{r}\frac{dt}{dr}+\frac{1}{k}\frac{dk}{dt}\left(\frac{dt}{dr}\right)^2+\frac{W\eta}{FLk}=0 \qquad (1)$$

Where, W is heating power, kW; η is heating efficiency; F is cross sectional area of tube wall, m^2; L is heating length, m; k is heat conductivity, W/m°C; t is temperature, °C; r is radius, m.

Thus, the heat transfer coefficients at different conditions can be obtained.

3.3.1 Single phase heat transfer. Based on the tests. The heat transfer of single phase water in ribbed tubes may be correlated as following relationship at pressures from 13MPa to 22MPa:

$$Nu = 0.053\,Re^{0.74}\,Pr^{0.4} \qquad (2)$$

It is higher than that in smooth tubes about 4-20%. The relative errors between the predicted values and the

experimental results are less than 10%.

In supercritical pressure region, the heat transfer characteristics in ribbed tubes may be correlated as following relationship at pressures from 23MPa to 27MPa.

When the fluid enthalpy is lower than the phase change point:

$$Nu = 1.277Re^{0.416}\left[\left(\frac{h_w - h_f}{t_w - t_f}\right)\frac{\mu_w}{k_w}\right]^{1.114}\left(\frac{\nu_f}{\nu_w}\right)^{0.458} \tag{3}$$

When the fluid enthalpy is higher than the phase change point:

$$Nu = 66.68Re^{0.178}\left[\left(\frac{h_w - h_f}{t_w - t_f}\right)\frac{\mu_w}{k_w}\right]^{1.191}\left(\frac{\nu_f}{\nu_w}\right)^{1.706} \tag{4}$$

The physical properties of the fluid in Nu and Re are determined by the wall temperature. In the equations; The h is enthalpy; μ is viscosity; ν is specific volume; the subscripts w express on basis of wall temperature; f express on basis of fluid temperature. The relative mean error of Eq.(3) is 15.3%. The relative mean error of Eq.(4) is 20.7%.

3.3.2 Two phase convective heat transfer. In internally ribbed tubes the main mechanism of boiling heat transfer is forced convection. We use the following relationship to correlate the experimental data:

$$\frac{\alpha_{tp}}{\alpha_l} = C\left(\frac{1}{X_{tt}}\right)^{C_1}\left(\frac{p}{p_{cr}}\right)^{C_2}\left(\frac{G}{G_{max}}\right)^{C_3} \tag{5}$$

Where: α_{tp} is the two phase convective heat transfer coefficient; α_l is the singlephase liquid heat transfer coefficient, it may be determined by Eq.(2); p_{cr} is critical pressure, p_{cr}=22.115MPa; G_{max} is maximal mass velocity in test, G_{max}=2000 kg/m2.s; X_{tt} is the Martinelli parameter for turbulent-turbulent flow as follows:

$$X_{tt} = \left(\frac{\Delta p_l}{\Delta p_g}\right)^{1/2} = \left(\frac{1-x}{x}\right)^{0.9}\left(\frac{\rho_g}{\rho_l}\right)^{0.5}\left(\frac{\mu_l}{\mu_g}\right)^{0.1} \tag{6}$$

Where the subscripts 1 is liquid phase; g is gas phase. Based on the tests, the following relationships are obtained:

at pressures from 13MPa to 20.5MPa:

$$\frac{\alpha_{tp}}{\alpha_l} = 0.89\left(\frac{1}{X_{tt}}\right)^{0.26}\left(\frac{p}{p_{cr}}\right)^{-1.38}\left(\frac{G}{G_{max}}\right)^{-0.67} \tag{7}$$

at pressures from 20.5MPa to 22MPa:

$$\frac{\alpha_{tp}}{\alpha_l} = 0.58\left(\frac{1}{X_{tt}}\right)^{0.82}\left(\frac{p}{p_{cr}}\right)^{-11.58}\left(\frac{G}{G_{max}}\right)^{-0.26} \tag{8}$$

The relative mean error of Eq.(7) is 12.6%, Eq.(8) is 10.3%.

3.3.3 Post dryout heat transfer. In post dryout region of the tube, the vapour becomes superheated, heat being transferred from the vapour to the residual liquid droplets which evaporate gradually along the tube. So the physical properties of the fluid are determined on basis of gas phase. Based on the tests, the following relationship is obtained to predict the post dryout heat transfer coefficients for internally ribbed tubes at pressures from 13MPa to 22MPa:

$$Nu_g = 0.012\left\{Re_g\left[x+\frac{\rho_g}{\rho_l}(1-x)\right]\right\}^{0.85} Pr_{gw}^{2.1} q^{0.95}\left(\frac{k_g}{k_{cr}}\right)^{-1.3} \tag{9}$$

The RMS error of Eq.(9) is 18.7%.

4. FRICTIONAL PRESSURE DROP

The frictional pressure drop of single phase water can be determined by following equation:

$$\Delta p_l = \lambda_l \frac{1}{d}\frac{\rho w^2}{2} \tag{10}$$

Where λ_l is the frictional factor of single phase water. Based on the tests, theλ_l is in the range of 0.035 to 0.042 for both internally ribbed tubes with diameter of 28x6mm and 22x5mm at Re more than 10^5, which is greater than that in smooth tubes about 50~60%.

The frictional pressure drop of two-phase flow can be expressed by following relationship:

$$\Delta p_{tp} = \Phi_{LO}^2 \Delta p_{LO} \tag{11}$$

Where Δp_{LO} is single phase water pressure drop based on the total flow; ϕ^2_{LO} is referred to the two phase frictional multiplier which is determined by experimental tests.

The chisholm's B coefficient method[6] is used to correlate the experimental data on the frictional pressure drop of steam water two phase flow in the ribbed tubes, which may be expressed as follows:

$$\Phi_{LO}^2 = 1+\left[\left(\frac{\rho_l}{\rho_g}\right)-1\right]\left[Bx(1-x)+x^2\right] \tag{12}$$

Based on the tests, the coefficient B is in the range of 1.2 to 2.0, we may take the average value, B=1.6. Thus, the Eq.(12) may convert to following from:

$$\Phi_{LO}^2 = 1+\left[\left(\frac{\rho_l}{\rho_g}\right)-1\right]\left[1.6x-0.6x^2\right] \tag{13}$$

5. CONCLUSIONS

1. When the pressure is lower than 20.5MPa, the ribbed tubes can eliminate the boiling heat transfer deterioration effectively. In near critical pressure region from 20.5MPa to 22MPa, the effectiveness of ribbed tubes has somewhat decrease. When the pressure reaches and exceeds the critical pressure, the heat transfer characteristics of ribbed tubes are similar to those of smooth tubes, and both of them have a good heat transfer performance.
2. Based on the tests, the relationships of heat transfer and frictional pressure drop for ribbed tubes at various conditions are given. Which may be recommended to use for boiler design.

ACKNOWLEDGEMENTS

This project was supported by the National Natural Science foundation of China and cooperated with Shanghai Boiler Work and Harbin Boiler Work.

REFERENCES

1. H.S. Swenson, et al., Trans. ASME Ser. A V.84, pp.365-371 (1962).
2. G.B. Watson, et al., "Critical Heat Flux in Inclined and Vertical Smooth and Ribbed Tubes", *Proceedings of the 5th Int. Heat Transfer Conference, V.4, pp.275-279,* Tokyo (1974).
3. K. Nishikawa, et al., "Flow Boiling Crisis in Grooved Boiler Tubes", *Proceedings of the 5th Int. Heat Transfer Conference, V.4, pp.270-274,* Tokyo (1974).
4. M. Iwabuchi, et al., "Heat Transfer Characteristics of Rifled Tubes in the Near-Critical Pressure Region", *Proceedings of the 7th Int. Heat Transfer Conference, v.5, pp.313-318,* Munich (1982).
5. W. Köhler, et al., "Heat Transfer and Pressure Loss in Ribbed Tubes", *Proceedings of the 8th Int. Heat Transfer Conference, V.6, pp.2861-2865,* San Francisco (1986).
6. D. Chisholm, *Two-Phase Flow in Pipelines and Heat Exchangers,* George Godwin, London (1983).

TRANSIENT BOILING HEAT TRANSFER ON SMALL FINNED SURFACES

Satoshi Kumagai and Jun Fushimi
Department of Machine Intelligence and Systems Engineering
Tohoku University
Email: kumagai@verdure.mech.tohoku.ac.jp; Fax: +81-(22)-217-6932

Masaaki Izumi
Department of Applied Chemistry and Molecular Science
Iwate University
Email: izumi@iwate-u.ac.jp; Fax: +81-(19)-621-6338

Keywords: boiling heat transfer, finned surface, transient performance

ABSTRACT. Many types of structured surface have been studied on their boiling heat transfer performance because of their high potential in removing generated heat. Most of them, however, concerned with only a steady state. But a rapid change in heat generation frequently occurs in many practical cases. In this study, transient pool boiling heat transfer from surfaces with stud fins or groove fins was investigated under atmospheric pressure. Tested surfaces were 0.5 - 1.5 mm in the fin thickness, 0.5 - 3.0 mm in the spacing and 0.5 - 2.0 mm in the height. Stepwise heat input that exceeds CHF of all surfaces was supplied by a steam impingement (158 °C, 0.6 MPa) to the opposite end surface of a small copper finned column and the time constant of heating was about 1.5 sec, that should be a rather slow change as a transient phenomenon. Those surface can achieve high heat transfer performance in a steady state. Comparisons of transient and steady state boiling characteristics are presented for those surfaces, showing not a small effect of fin configuration on the transient boiling performance. The CHF in transient heating was almost the same value as that in steady state for groove finned surfaces. On the other hand, the CHF of stud finned surfaces was mostly smaller in transient heating than in steady state. The nucleate boiling period that was defined as the duration from the moment when a temperature rise was recorded at the base surface to the moment of CHF, was longer in the groove finned surfaces than the stud ones.

1. INTRODUCTION

Though boiling has fairly good performance of heat transfer by nature, still more advance has been desired intending to get higher efficiency apparatus of heat transfer. Especially CHF is one of the most serious issue in its application to industrial practice. Transient performance of boiling heat transfer under sudden increase of power input has also been studied so as to remove accidentally generated high heat flux safely. As to CHF, Rosenthal [1] and Tachibana et al. [2] experimented on transient pool boiling of water on a thin metallic ribbon or a wire heated by exponentially increased DC power input, to get a result that CHF increases with increase of the heating rate. On the contrary, Kozawa et al. [3] showed considerably lower CHF under stepwise increase of heat input than under steady state in a similar experiment using R-113. They attributed this to the fact that the initial active nucleation site intensity is quite sparse in highly wettable liquid and the bubble generation after the beginning of heating delays much.

On the other hand, it is well known that a finned surface has good performance in heat removal as well as in stabilizing high heat flux boiling [4,5,6]. This finned surface should also be considered effective in removing high heat flux from a high temperature high heat generating object with steep variation of heat generation rate [7], by delaying the transition from nucleate boiling to film boiling to maintain stable boiling for a long term. Though many investigation has reported about boiling fins, most of them treated under steady state condition.

In this experiment transient pool boiling heat transfer performance was examined after stepwise heat input was supplied to the backside of a finned substrate from pressurized steam. The boiling liquid was highly wetting R-113, whose transient CHF was reported to be lower than steady CHF [3]. The effect of fin configuration on transient CHF and removable heat up to sudden jump-up of the surface temperature was tested for stud and groove fins comparing with a unfinned plane surface.

2. EXPERIMENTAL APPARATUS AND PROCEDURE

Figure 1 shows the schematic diagram of the apparatus. The heat transfer surface /1/ was attached in the bottom wall of the boiling vessel /9/ through the insulating Bakelite plate /3/. Heat was supplied from impinging steam jet to the back surface of a copper circular column whose front surface was the finned heat transfer surface. Steam was generated in a boiler and introduced to the steam chamber /5/ to blow stepwisely from a nozzle by opening the 3-way cock /7/ suddenly. The pressure of the steam in the chamber was kept at 0.6 MPa and its temperature was 158 °C. The inside of the boiling vessel was maintained at the atmospheric pressure and its saturation temperature, and the depth of the boiling liquid was kept constant using the condenser /9/ and auxiliary heater /10/.

Figure 2 shows the details of the tested finned surfaces. Thee types of fin configuration i.e. simple fin, groove fin and stud fin were examined. A plane surface was also prepared for comparison. The height and the spacing of the fin was taken as the parameter. Four K-type sheathed thermocouples of 0.5 mm dia. were inserted into the heat conducting copper column up to the center line at prescribed distance from the base heat transfer surface. The output of them was recorded almost simultaneously by a data logger at every 0.1 second through amplifiers.

3. DATA ESTIMATION PROCEDURE

In this experiment the copper column conducts heat one dimensionally in the axial direction. The heat flux and the surface temperature were calculated using the measured temperatures at the four positions. They were evaluated at a virtual flat surface on the fin base. The procedure to determine them was as follows. The axial temperature distribution at every instance was supposed to be expressed with the equation (1) where the constants C_1, C_2 and A were determined by the measured temperatures so as to minimize the difference between the measured and the approximated temperatures. The form of this equation was employed considering the fact that the solution of the one-dimensional heat conduction equation for semi-infinite body is given with a error function.

$$T = C_1 + C_2 \int_0^{x/A} \exp\left(-\eta^2\right) d\eta \qquad (1)$$

In addition, inverse heat conduction problem was solved [8] to get the instantaneous surface condition using the transient temperature information inside the column. The ob-

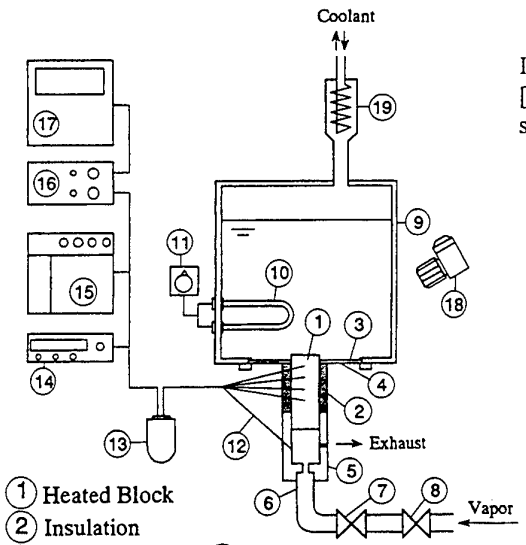

Fig. 1. Experimental apparatus

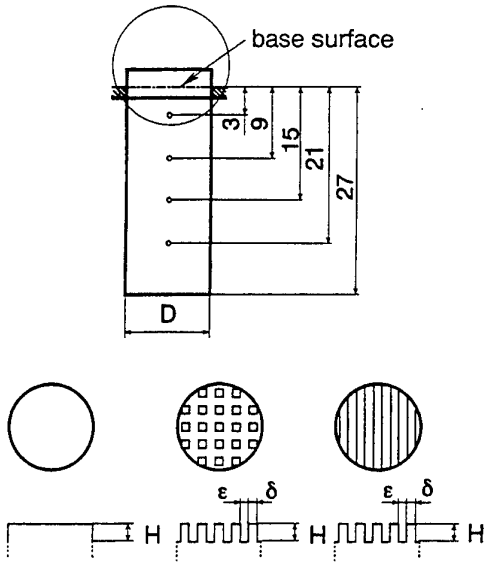

Fig. 2. Tested finned surface and heat conducting column

tained data of heat flux and surface superheat for several conditions of the fin configuration were in good agreement among the two methods. Therefore, equation (1) was adopted in the following.

In this experiment heat was supplied to the back face of the heat conducting column. Therefore, some delay was involved in recognizing the increase of the heat flux from the beginning of heating. Here, the moment was adopted as the origin of time when any change was recorded at the base surface. And a step function was applied to the correlation of the obtained surface heat flux vs. time as follows.

$$q = q_0\left(1 - e^{-t/t_0}\right) \tag{2}$$

The time constant of heating was defined as the value of t_0 in this equation. The result for the plane surface is shown in Fig. 3. From this figure t_0 was about 1.5 sec. The time constant in the experiment by Kozawa et al. [3] evaluated with the same function was in the order of 0.001 sec. Present experiment was done under fairly slow heating rate as a transient boiling experiment.

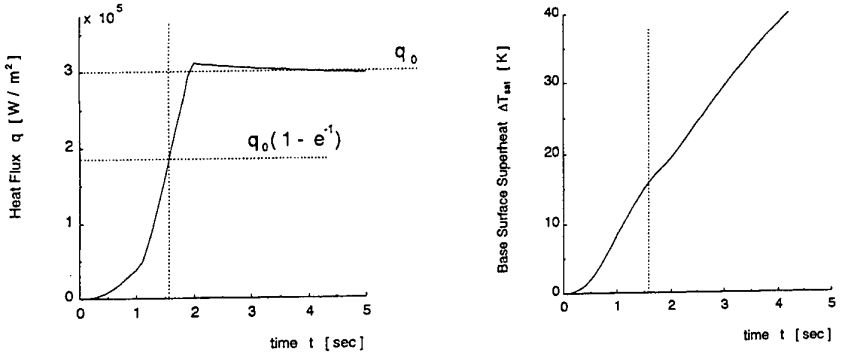

(a) heat flux (b) surface superheat

Fig. 3. Time sequence of the heat flux and the surface superheat of the plane surface

4. RESULT AND DISCUSSION

Heat Transfer and Aspect of Transient Boiling

Boiling curve. An example of the obtained boiling curves is shown in Fig. 4 for the case of a groove finned surface (2.0 mm in the height, H, 1.0 mm both in the thickness, δ, and the spacing, ε), where the transient boiling is compared with the steady state one. In the non-boiling region, transient heat flux is much higher than steady state one. As the heat is transferred in accordance with the temperature gradient in the liquid, such a fact should be reasonable in the early stage of heating where the thermal boundary layer with convection is not developed yet. The same result was reported by Sakurai et al. [9] for water, showing higher heat transfer enhancement in higher heating rate. In the present experiment, however, the heat conducting column was relatively large. Moreover, the heat flux transferred to the liquid was evaluated from the temperature distribution based on the data measured at the inside of the column. Therefore it was difficult to estimate accurate heat flux in the very early stage of heating because of the effect of heat absorption by the upper part of the column. The heat flux shown in this figure at low wall superheat in non-boiling region should be fairly over estimated.

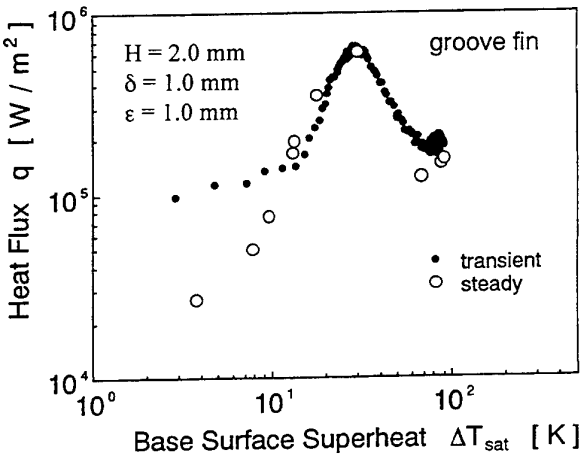

Fig. 4. An example of boiling curves

On the contrary, the difference in the boiling curves disappears between transient and steady state in the nucleate boiling regime. Nucleate boiling continued for several seconds depending on the fin configuration. After reaching CHF which is almost equal to or less than that in steady state, the boiling regime turned to film boiling. This decreasing tendency of CHF in transient boiling is the same as the result of Kozawa et al. [3] for R-113.

Boiling aspects. Transient boiling aspects are shown in Fig. 5 along with the time. The superheated liquid layer begins to form just after the beginning of heating. Then, boiling starts with appearance of small bubbles in the case of the plane surface, as shown in the picture a-1. Adding to the growth and spread of the initially generated bubbles, newly generated bubbles cover the surface to develop nucleate boiling on the whole surface (picture a-2). As the boiling regime approaches CHF, the bubbles form 3 or 4 large coalescent bubbles of about 10 mm in diameter periodically just above the surface (pictures a-3, 4). Then whole surface is covered with vapor, to go to film boiling (picture a-5, 6, 7). The size of the ejected bubbles in film boiling was about 8 mm which corresponds to the critical wave length, and the period of ejection settles in about 60 ms.

Boiling aspects on the finned surfaces are shown in Figs. 5b and 5c for a stud and a groove finned surface, respectively. At the incipience of boiling, bubbles generate simultaneously at many sites to form large coalescent bubbles

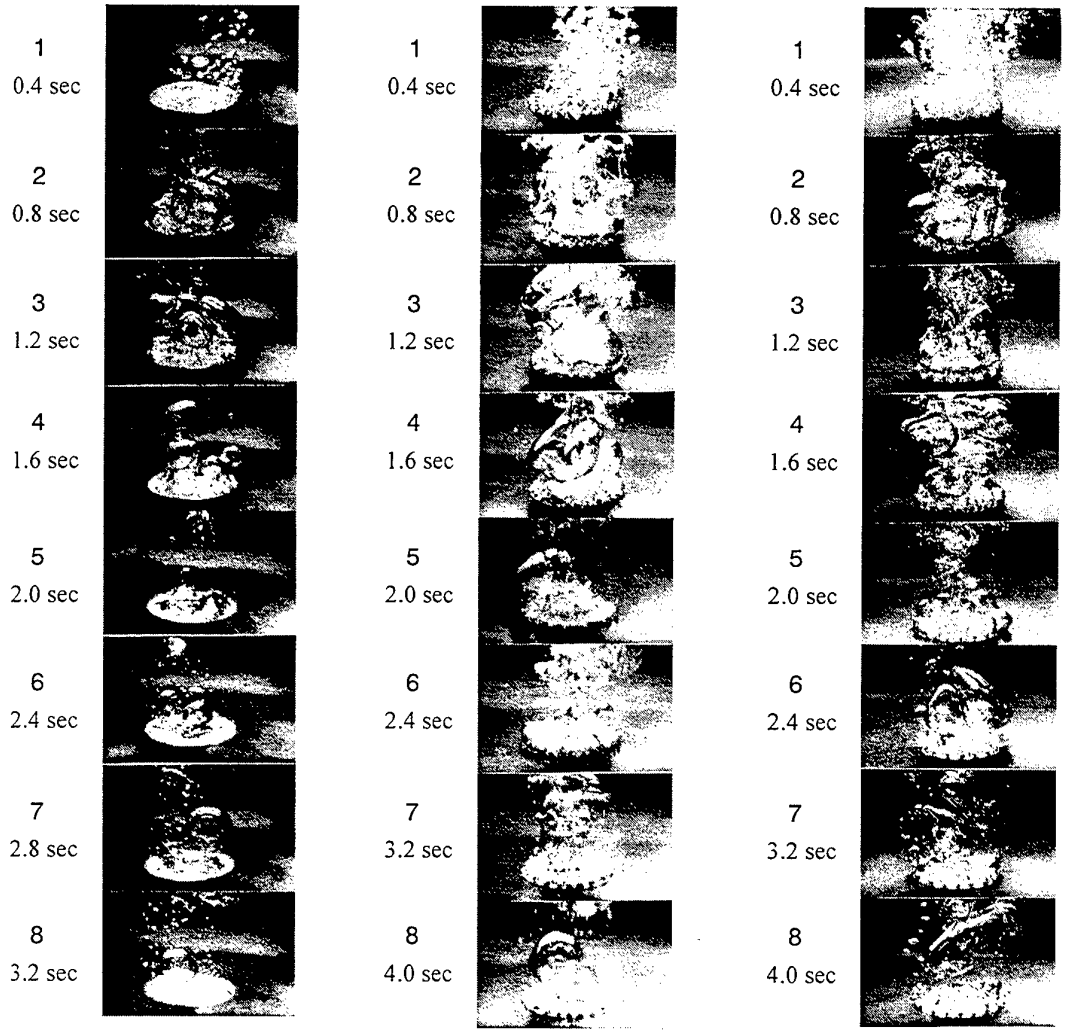

(a) plane surface (b) stud finned surface (H=1.0mm, δ=1.0 mm, ε=1.0 mm) (c) groove finned surface (H=1.0mm, δ=0.5 mm, ε=2.0 mm)

Fig. 5. Boiling aspects on the surfaces of different configuration

above the surface. But nucleate boiling continues for a while and the delay time up to the transition to film boiling takes longer in the finned surfaces than in the plane surface.

Effect of the Fin Configuration on the Heat Transfer Performance

Figure 6 shows time sequence of the base surface heat flux and the superheat under transient heating condition for both a stud and a groove finned surfaces which have the same height, thickness, spacing, and also nearly the same heat transfer performance under steady state, together with the steady CHF. Though the steady CHFs are nearly the same between the two surfaces, the transient CHF of the stud fin is less than the steady CHF unlike the groove fin whose transient CHF is almost equal to the steady CHF. The bubbles generated on the stud finned surface immediately coalesce with each other and spread over the whole surface shortly to fill up the fin spacing. Moreover, the departure of those coalescent bubbles delays on a finned surface. Therefore, a smooth liquid-vapor reciprocation is failed on the surface, resulting in degraded heat transfer performance under transient condition. The nucleate boiling period, τ_b of the groove finned surface is longer than that of the stud finned surface. Here, τ_b is defined as the time duration from the moment when a temperature rise is recorded at the base surface to the moment of CHF. Especially, the term in which the high heat flux around the CHF is maintained is fairly longer in the groove fin as shown in Fig. 5-c, and stable periodical departure of coalescent bubbles continues for a while.

The reason should be as follows. Bubbles first generate at the high temperature fin base. In the case of groove fins, a bubble which generated at some location hardly extend to distant places with one rush, because the neighboring fin gaps are completely separated with each other. Therefore, the bubble generating points spread gradually. In the case of stud fins, on the contrary, all the fin gaps are connected into one unit like a lattice. So, bubbles spread over the whole surface immediately after a bubble appeared at a spot. Those were confirmed by observations with VTR and stills.

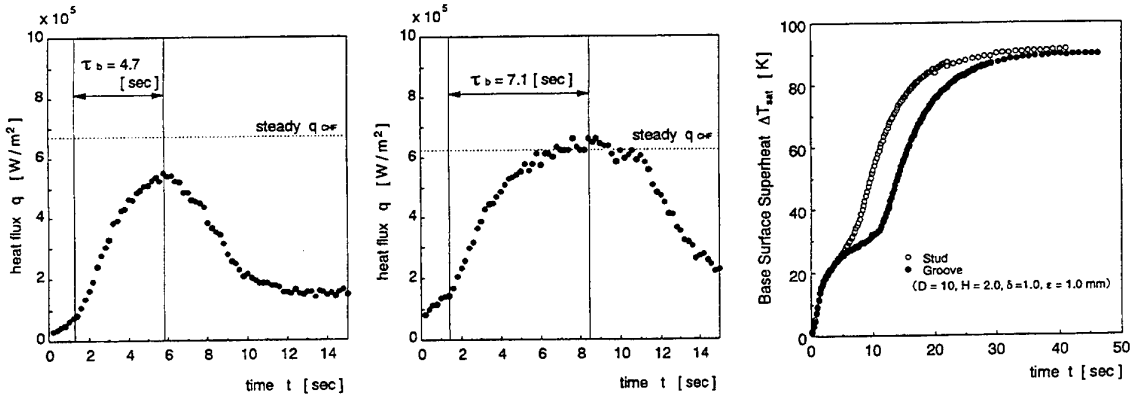

(a) stud fin (b) groove fin (c) surface superheat

Fig. 6. Time sequence of the heat flux and the superheat at the fin base

Effect of the Fin Height

Figure 7 shows the steady and transient CHF data of the stud finned surfaces against the fin height for two different fin spacings. The fin height of 0 mm corresponds to a plane surface. The transient CHF (solid symbols) as well as the steady CHF (open symbols) increases with increasing of the fin height. But the transient CHF is lower than the steady one, and the difference between those CHFs expands with the fin height. Under a condition of sudden increase in heat input like this experiment, the departure of bubbles is more prevented with increasing of the fin height. Therefore, when we use a stud finned surface we may not expect as much heat transfer enhancement in transient boiling according to an increase of the fin height as in steady state.

Figure 8 shows the transient CHF of the groove finned surfaces comparing with the steady CHF. Unlike the stud finned surfaces, no clear difference can be seen among both CHF data for H = 1 mm and 2 mm. As for H = 0.5 mm, the transient CHF is less than the steady one, which is the same as in the plane surface (H = 0 mm), indicating that the fin of such a low height does not perform enough the fin effect.

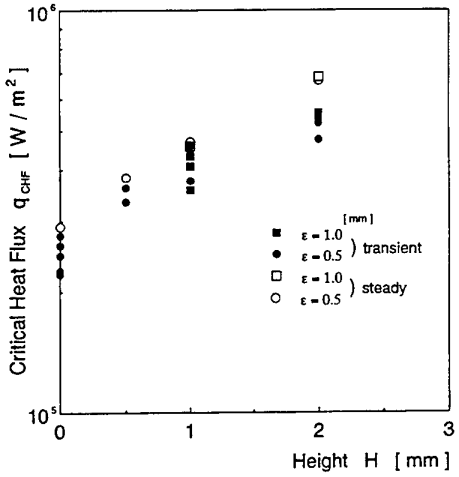

Fig. 7. CHF vs. fin Height (stud fin)

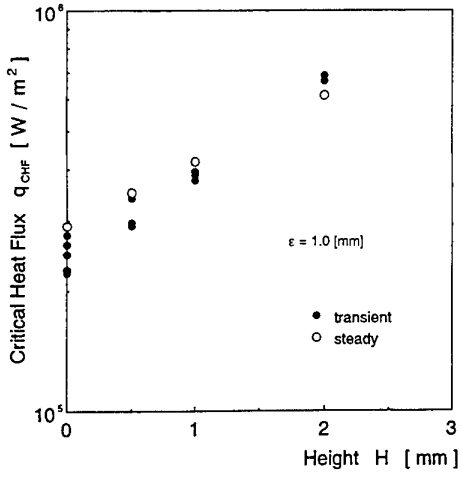

Fig. 8. CHF vs. fin height (groove fin)

Figures 9 and 10 show the nucleate boiling period, τ_b and the effective heat removal, Q_b, respectively. The latter is defined as the integration of the heat flux with time from the beginning of heating to CHF. Both increase with increasing of the fin height. In the case of the stud fin, the CHF of high finned surfaces in transient boiling is less than that in steady state, as shown in Fig. 7. But the transient CHF itself does not decrease with increasing of the fin height. Therefore, the increase of τ_b directly resulted in the increase of Q_b. In the case of the groove fin, both the CHF and the nucleate boiling period increase with increasing of the fin height. Therefore the increasing rate of Q_b for H is larger in the groove finned surfaces than in the stud ones.

Consequently, to increase the height of groove fins under transient boiling is as effective as under steady state in realizing stable high performance heat removal by delaying the transition of boiling regime to film boiling. As for stud fins, to increase the fin height is effective also in transient boiling, though the effect is smaller than in steady state.

Effect of Fin Spacing

Stud finned surface. Figure 11 shows the effect of the fin spacing on the transient CHF of two different height stud finned surfaces comparing with the steady CHF. In this figure, $\varepsilon = 0$ mm means a simple cylinder fin of the

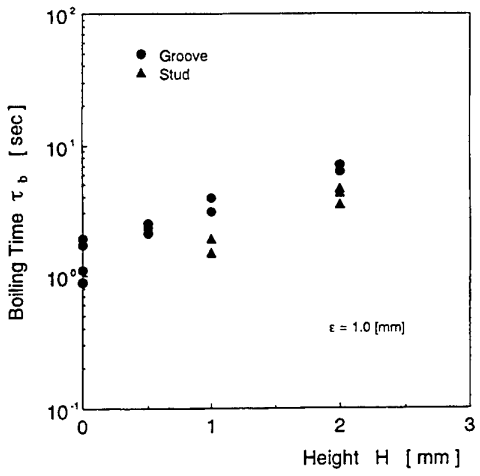

Fig. 9. Nucleate boiling period vs. fin height

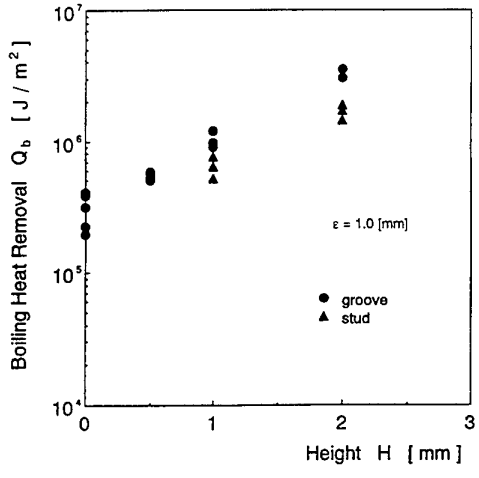

Fig. 10. Effective heat removal vs. fin height

same height with no base area, and $\varepsilon = \infty$ corresponds to the plane surface. Though the trend of the transient CHF against ε is the same as that of the steady one, showing high performance at $\varepsilon = 0.5$ mm and 1.0 mm, the CHF value is much smaller in transient boiling than in steady boiling at every fin spacing. The effect of the fin spacing on the nucleate boiling period and the effective heat removal are shown in Figs. 12 and 13, respectively. In the case of 2.0 mm in the fin height, H, both increase with decreasing of the fin spacing. But the difference is not clear in H = 1 mm. Therefore, narrowing the stud fin spacing to increase the number of fins in transient boiling is effective in some degree for high finned surfaces by inhibiting transition of boiling regime. Fins, however, prevent smooth liquid-vapor reciprocation, resulting in degraded CHF in transient boiling.

Groove finned surface. Figures 14, 15 and 16 show the transient CHF, the nucleate boiling period and the effective heat removal of the groove finned surfaces against the fin spacing, respectively. The transient CHF is almost as high as the steady one, different from the stud finned surfaces. The boiling period, and so the effective heat removal increase with decreasing of the fin spacing. Consequently, narrowing the fin spacing is very effective for groove finned surfaces within the range of the present experiment.

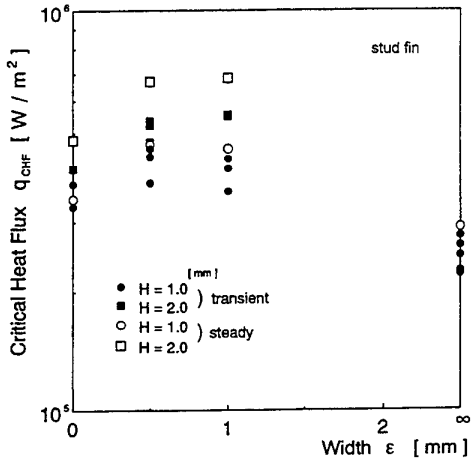

Fig. 11. Effect of fin spacing on CHF in stud fin

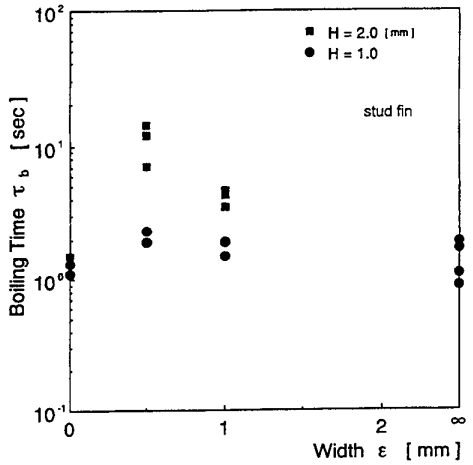

Fig. 12. Effect of fin spacing on nucleate boiling period in groove fin

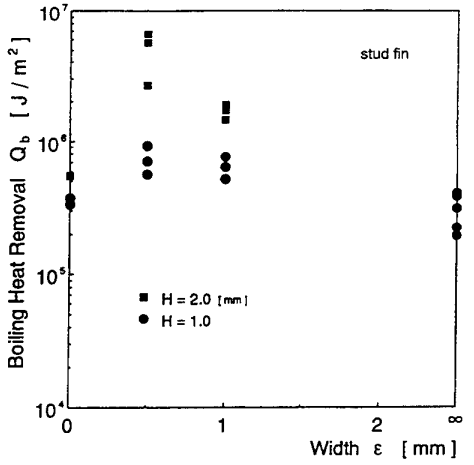

Fig. 13. Effect of fin spacing on effective heat removal in stud fin

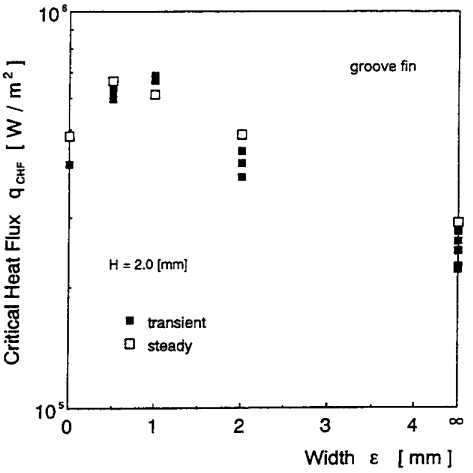

Fig. 14. Effect of fin spacing on CHF in groove fin

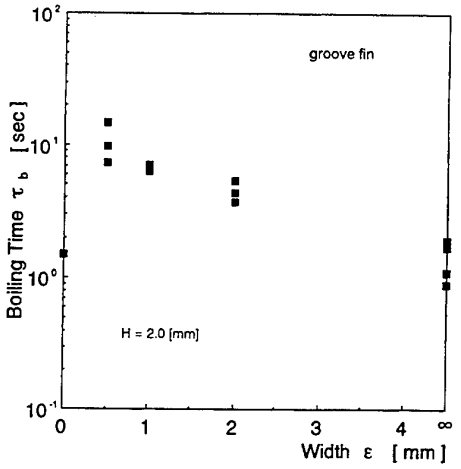

Fig. 15. Effect of fin spacing on nucleate boiling period in groove fin

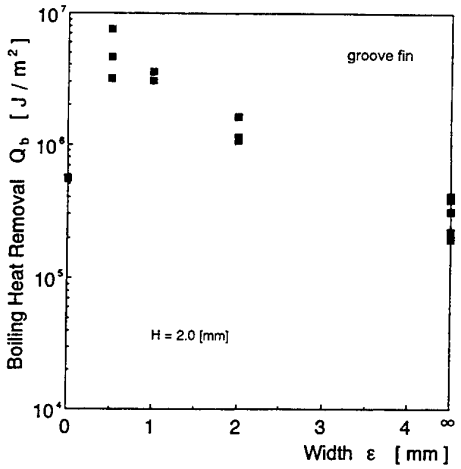

Fig. 16. Effect of fin spacing on effective heat removal in groove fin

5. CONCLUSIONS

Comparisons of transient and steady state boiling characteristics are presented experimentally for stud and groove finned surfaces, showing that there exists a suitable fin configuration and arrangement for high performance of heat removal. CHF in transient boiling is almost as high as in steady state in groove finned surfaces, but is degraded in stud finned surfaces. Nucleate boiling period is elongated even with a low finned surface like H = 1 mm comparing with a plane surface. Effective heat removal increases with increasing of the fin height and decreasing of the fin spacing within the range of this experiment.

REFERENCES

1. M. W. Rosenthal, Nucl. Sci. Eng., 2-5, pp.640-656 (1957).
2. F. Tachibana, M. Akiyama and H. Kawashima, J. Nucl. Sci. Tech., 5-3, pp.133-135 (1968).
3. Y. Kozawa, T. Inoue, and K. Okuyama, " Enhancement of Bubble Formation and Heat Removal in Transient Boiling", *Proc. 22nd National Heat Transfer Conf. Japan*, pp.10-12 (1985) (in Japanese).
4. C.-C. Shih and J.W. Westwater, Int. J. Heat Mass Transfer, 17-1, pp.125-133 (1974).
5. S. Kumagai, S.-G. Jho, Y. Hirono, R. Shimada and T. Takeyama, Heat Transfer Japanese Research, 16-2, pp.69-81 (1987).
6. A. E. Bergles, G. Guglielmini, M. Misale and C. Schenone, "Pool Boiling from Multiple Square-Shaped Spines in a Highly-Wetting Fluid", *EUROTHERM Seminar No 48: Pool Boiling 2, pp.149-155*, edited by D.Gorenflo et al., Paderbom, Germany (1996).
7. S. Kumagai, S. Matsui, R. Shimada, T. Haraguchi, M. Ohuchi and T. Takeyama, "On the Characteristics of Transitional Phenomena in Heat Transfer from Extended Surfaces to Boiling Liquid", *Proc. 9th Int. Heat Transfer Conf.*, v.4, pp.87-92, edited by G. Hetsroni, Jerusalem, Israel (1990).
8. M. Shoji, Trans. Japan Soc. Mech. Engrs., 44-381, pp.1633-1643 (1978) (in Japanese).
9. A. Sakurai and M. Shiotsu, Trans. ASME J. Heat Transfer, 99-4, pp.554-560 (1977).

Ahmad, G.E. 751
Ahn, J. 212
Ahn, Y. 557
Akisawa, A. 759
Akisawa, A. 1145
Allcock, H.R. 1483
Altraide, A. 191
Amazouz, M. 917
Amazouz, M. 1084
An, E. 355
An, E. 367
Anderson, R. 1033
Ando, D. 1226
Antohi, C. 866
Aoki, H. 748
Aoyama, S. 843
Aoyama, S. 852
Arlabosse, P. 923
Asano, H. 1122
Asano, H. 1438
Assassa, G.M.R. 766
Baba, A. 1710
Bae, S.C. 1153
Bai, Q. 521
Bai, W.D. 1703
Bartoli, C. 247
Behnia, M. 873
Benali, M. 917
Benali, M. 1412
Benning, L. 1483
Bhattacharyya, S. 1353
Bi, Q.C. 393
Bi, Q.C. 438
Bingue, J.P. 1266
Bockhorn, H. 1573
Boral, A.A. 888
Borisov, I. 422
Borzenko, V.I. 512
Bossi, L. 239
Buchner, H. 1573
Bull, S.R. 18
Cai, J.Y. 416
Cai, S. 1651
Cannon, A.M. 1483
Cao, X.Y. 1281
Cao, X.Y. 1603
Cao, Z.H. 1651
Carrere-Gee, C. 923
Casey, R.T. 1524
Cen, K.F. 1281
Cen, K.F. 1333
Cen, K.F. 1566
Cen, K.F. 1586
Cen, K.F. 1603
Chai, L.H. 343
Chan, A.M.C. 408
Chan, C.K. 1508
Chan, C.K. 1515
Chandratilleke, T.T. 191
Chang, L.J. 1002
Chazly, N.E. 826
Chen, C.T. 636
Chen, D.Z. 1595
Chen, G.H. 910
Chen, G.H. 1048
Chen, G.J. 588
Chen, G.Y. 1553
Chen, H.P. 1496
Chen, J. 1397
Chen, M.J. 1581
Chen, Q.H. 379
Chen, T.K. 393
Chen, T.K. 416
Chen, X. 270
Chen, Y. 1427
Chen, Y. 1433
Chen, Y. 1632
Chen, Z.H. 355
Chen, Z.H. 367
Chen, Z.H. 598
Chen, Z.Q. 505
Chen, Z.Q. 529
Cheng, K. 1212
Cheng, P. 505
Cheng, P. 529
Cheng, P. 1192
Cheng, X.H. 1728
Cheng, Y.C. 1476
Cheung, C.S. 1397
Cheung, F.B. 888
Cheung, F.B. 1289
Chi, Y. 1333
Chi, Z.H. 1586
Chiu, H.H. 1640
Cho, H.K. 384
Choi, M. 1532
Chou, C.S. 474
Chou, T.C. 1257
Chow, A. 680
Chua, H.T. 1145
Chung, B.T.F. 581
Chung, J.D. 1532
Chung, K.C. 636
Chung, S.K. 229

Ciocan, V. 866
Cote, R. 1084
Cui, W.Z. 379
Cui, Y.B. 1662
Cunnington, G.R. 613
Da Veiga, V.R. 1114
Dai, X.W. 1632
Davis, S.B. 1686
Deeb, S.E. 826
Deng, P.G. 1217
Deng, X.H. 1217
Denner, H.D. 1212
Diaz, G. 940
Ding, L.S. 650
Dong, Y.X. 980
Druck, H. 740
Du, D.X. 658
Du, D.X. 665
Du, J.H. 490
Dubble, E.H. 1007
Duluc, M.C. 127
Eder, A. 1273
Eder, A. 1296
Eisen, S. 1366
El-Kotb, M. 826
Elphick, I.G. 408
Eschenbacher, J.F. 262
Fagguani, S. 247
Fan, M.X. 1566
Fan, W.C. 1340
Fedkin, M.V. 1483
Fei, Q. 1002
Feng, B. 1560
Feng, Y. 1208
Feng, Z. 643
Feng, Z.X. 1646
Fiebig, M. 598
Francois, M.X. 127
Francois, M.X. 1164
Fridman, A. A. 96
Fridman, A.A. 1266
Fu, H.L. 497
Fu, X.Y. 1033
Fudym, O. 923
Fujii, I. 1540
Fujii, T. 1122
Fujii, T. 1438
Fujioka, K. 628
Fujita, Y. 521
Fujiyoshi, M. 1404
Fushimi, J. 399
Gale, T.K. 1686
Ganzha, V.L. 688
Gao, X. 1566
Garner, S.D. 1007
Gavotti, N. 539
Gerlach, C. 1273
Gerlach, C. 1296
Goldstein, R.J. 206
Gong, L.H. 1198
Gopinath, A. 1170
Gori, F. 239
Grandum, S. 860
Groll, M. 708
Groll, M. 957
Groll, M. 1130
Gu, F. 1305
Gu, Z.Z. 1651
Guo, F.Z. 1203
Guo, F.Z. 1208
Guo, T.M. 588
Guo, X.F. 1433
Guo, X.Q. 588
Guo, X.S. 1566
Guo, Y.C. 1508
Guo, Y.C. 1515
Guo, Z. 658
Guo, Z.Y. 118
Guy, C. 1412
Hahne, E. 740
Hamada, K. 843
Han, B. 206
Han, P. 270
Han, X. 1603
Hara, T. 1178
Haruki, N. 695
Haruki, N. 723
Haruki, N. 852
Haruki, N. 1138
Hatabaka, M. 288
Hawlader, M.N.A. 451
He, K.X. 680
Hein, D. 1347
Hetsroni, G. 72
Hetsroni, G. 255
Hiller, G. 1677
Hirashima, M. 564
Hirata, M 57
Hirata, Y. 628
Hisazumi, Y. 1122
Ho, C.J. 881
Hoffmann, S. 1573
Hofmann, M.A. 1483
Holden, C. 680
Honda, T. 1546
Horibe, A. 695
Horibe, A. 723
Horibe, A. 852

Horibe, A. 1138
Hosatte, S. 1084
Hoshi, A. 796
Hsiau, S.S. 474
Hsieh, S.S. 1015
Hsu, C.T. 505
Hsu, C.T. 731
Hu, G. 1333
Hu, W. 279
Huang, J. 1002
Huang, S.H. 821
Huang, X. 355
Huang, X. 367
Huang, X.Y. 497
Hugron, I. 1412
Hui, C.K.P. 1090
Hussien, H.M.S. 751
Hwang, I.J. 295
Hwang, Y.W. 965
Hyuga, T. 521
Ichimiya, K. 184
Inaba, H. 695
Inaba, H. 723
Inaba, H. 852
Inaba, H. 1138
Inada, T. 860
Inatomi, Y. 302
Ipek, O. 778
Ishizuka, M. 321
Iwai, H. 161
Izumi, M 399
Jang, K.J. 1015
Jebali, F. 127
Jegla, Z. 1624
Jeong, U.C. 295
Jerbi, F.J. 1164
Jiang, X.J. 1586
Jiang, Y. 788
Jiang, Y. 804
Jiang, Y. 1059
Jiang, Y. 1066
Joko, M. 262
Jones, J.C. 1313
Jordan, M. 1273
Jung, I.S. 212
Kage, H. 932
Kakimoto, K. 302
Kalabin, E.V. 328
Kameda, K. 1138
Kaneda, M. 302
Kang, Y.B. 788
Kang, Y.B. 804
Kang, Y.M. 430
Kasagi, N. 972
Kashiwagi, T. 759
Kashiwagi, T. 1145
Kato, Y. 1546
Katsuta, M. 1153
Kaviany, M 32
Kawaguchi, Y. 716
Kellam, E.C. 1483
Kennedy, L.A. 96
Kennedy, L.A. 1266
Khalatov, A. 422
Khattab, N. 826
Kida, T. 1138
Kim, M. 557
Kim, M.O. 384
Kim, M.S. 965
Kim, Y.J. 295
Kimura, M. 843
Kimura, T. 1540
Klein, H.P. 1130
Komiya, A. 873
Koo, J.H. 1289
Koyama, S. 445
Kudra, T. 917
Kuge, K. 1546
Kumagai, S. 399
Kuo, J.T. 474
Kurosaki, Y 84
Kuwahara, K. 149
Kuwahara, K. 445
Kuznetsov, A.V. 896
Kwan, M.K. 731
Kwanka, K. 1347
Ladevie, B. 482
Ladevie, B. 923
Lam, W.C. 1404
Lazarescu, C.D. 866
Lecomte, D. 923
Lee, B.D. 650
Lee, J.S. 212
Lee, L. 1098
Lee, S.C. 613
Lee, T.H. 384
Lee, T.S. 1581
Lee, T.S. 1640
Leong, K.C. 497
Leung, D.Y.C. 1427
Leung, D.Y.C. 1553
Leutz, A. 759
Li, B.Q. 1433
Li, B.Q. 1722
Li, C.F. 255
Li, G.H. 1615
Li, H.B. 1433
Li, H.P. 270

Li, J. 335
Li, M. 1728
Li, P.W. 716
Li, Q. 1203
Li, Q. 1208
Li, Q.Y. 1615
Li, R. 355
Li, R.Y. 367
Li, X.Z. 1212
Li, Y.D. 1420
Li, Z. 658
Li, Z.W. 1388
Li, Z.Y. 177
Li, Z.Z. 1603
Li, Z.Z. 1646
Liang, J.T. 1184
Liao, G.X. 1340
Liao, H.Q. 1722
Lin, F. 1388
Lin, G.T. 821
Lin, H.H. 821
Lin, J.Y. 1041
Lin, R. 1360
Lin, W.Y. 1508
Linak, W.P. 1686
Ling, S.C. 1446
Liu, B.M. 451
Liu, C. 373
Liu, C.Y. 497
Liu, D.C. 1496
Liu, H. 1420
Liu, H.C. 1640
Liu, H.T. 1468
Liu, X.G. 1651
Liu, Y. 1305
Liu, Y. 1615
Liu, Y.F. 1591
Liu, Y.P. 1595
Liu, Y.W. 1212
Liu, Z.L. 1360
Liu, Z.T. 1397
Liu, Z.Y. 1054
Lloyd, A.C. 138
Lorenzine, M. 247
Lou, H. 1241
Lu, G.Q. 1192
Lu, S.S. 860
Lu, Y.Z. 1054
Lubiez, J.V. 1164
Luo, W.H. 1566
Luo, Y. 416
Luo, Y.H. 393
Luo, Z.Y. 1566
Lvov, S.N. 1483
Ma, W.M. 1305
Ma, Z. 581
Ma, Z.Y. 1333
Machida, K. 843
Madadnia, J. 349
Makino, T. 604
Malyshenko, S.P. 512
Mandel, H. 740
Martiny, M. 221
Maruyama, S. 873
Matsuno, Y. 932
Matsushita, M. 843
Mayinger, F. 1273
Mayinger, F. 1296
Mayinger, F. 1366
Mayinger, F. 1379
Mbarawa, M. 1524
McClain, R.L. 940
Mei, Y.G. 980
Meng, X.Z. 459
Meng, X.Z. 1159
Mertz, R. 708
Mertz, R. 957
Mettawee, E.S. 766
Meyer, J.P. 1076
Meyer, J.P. 1105
Meyer, J.P. 1114
Mi, J. 1609
Miller, A. 1033
Milton, B.E. 1524
Mo, J. 680
Mohamad, M.A. 751
Morford, R.V. 1483
Morin, M. 1412
Mosyak, A 72
Mosyak, A 255
Mujumdar, A.S. 910
Mujumdar, A.S. 932
Murayama, Y. 1546
Mutaf-Yardimci, O. 96
Nagayama, G. 672
Nakabe, K. 262
Nakamura, S. 1715
Nakata, T. 695
Nathan, G.J. 1609
Negishi, K. 564
Neo, E.C. 161
Ng, K.C. 1145
Ng, M.L. 1476
Nguyen, T.H. 349
Nguyen, T.V. 1453
Nie, J.H. 177
Nigmatulin, R 110
Nishio, S. 360

Nobuchika, K. 695
North, M.T. 573
Novellani, M. 466
Nursubyakto 191
Ofner, B. 1366
Ogura, H. 932
Oido, K. 628
Oka, M. 813
Okada, S.Y. 604
Olaru, I. 866
Oliveira, A.A.M. 32
Ooyatsu, N. 1710
Osa, N. 445
Ota, T. 199
Ozoe, H. 288
Ozoe, H. 302
Pacheco-Vega, A. 940
Paitoonsurikarn, S. 972
Pan, Y.K. 910
Pao, H.P. 1446
Park, G. 557
Park, G.C. 384
Park, G.C. 430
Park, K.S. 1532
Peng, X.F. 343
Petit, P.J. 1076
Polasek, F. 539
Poslushny, G. 1500
Prechtl, P. 1379
Qiu, J.R. 1560
Qiu, Y. 980
Que, X.C. 279
Quitard, M. 482
Raghavan, G.S.V. 1090
Ramsden, V. 349
Ren, B.Z. 1002
Ro, S.T. 965
Rong, S.X. 588
Rozenblit, R. 72
Sadhal, S.S. 229
Saenger, M. 1677
Saha, B.B. 1145
Saito, T. 84
Saitoh, T.S. 796
Saitoh, T.S. 1226
Saitoh, T.S. 1233
Sanchez, J.G. 1098
Santini, R. 466
Sato, K. 695
Sato, M. 748
Satoh, I. 84
Saveliev, A.V. 96
Saveliev, A.V. 1266
Saxena, S.C. 688
Schmidt, B. 708
Scholz, K.H. 1500
Schulz, A. 221
Seames, W.S. 1686
Sen, M. 940
Serizawa, A. 643
Shao, H. 279
Sharkawy, A.E. 826
Sheen, P.J. 949
Shen, B.X. 1496
Sheng, X.L. 650
Shevtsov, S. 422
Shi, M.H. 905
Shiah, S.W. 888
Shih, Y.C. 1289
Shimogori, M. 1710
Shoji, M. 335
Shu, Z.D. 1703
Smid, J. 474
So, R.M. 169
Soudarev, A. 1500
Stehlik, P. 1624
Stubington, J.F. 1662
Stubington, J.F. 1669
Sugimto, K. 1438
Sugiyama, T. 1024
Sumathy, K. 774
Sun, C.C. 1257
Sun, C.Y. 588
Sun, G.J. 1586
Sun, H. 650
Sun, J.Y. 1041
Sun, L.S. 1728
Sun, S.J. 1404
Sun, X.X. 1728
Suzuki, A. 759
Suzuki, H. 1024
Suzuki, K. 161
Suzuki, K. 262
Suzuki, Y. 972
Swanepoel, W. 1105
Swift, G.W. 2
Syred, N. 422
Tadrist, L. 466
Tagawa, T. 288
Tagawa, T. 302
Tagishi, A. 1715
Takahashi, K. 873
Takarayama, N. 1710
Takeguchi, S. 1153
Tan, G.H. 881
Tanaka, H. 360
Tao, W.Q. 177
Tian, F.J. 1433

Tomiyama, S. 695
Toriyama, K. 184
Trinh, E.H. 229
Tsai, H.H. 474
Tsai, Y.C. 1015
Tsuchimoto, N. 1438
Tsuruta, T. 672
Vanhorn, S.R. 1321
Vesely, S. 1500
Vigneault, C. 1090
Vinogradov, E. 1500
Vitali, J.A. 1321
Wakabayashi, H. 604
Wako, Y. 748
Wang, A.L.T. 1669
Wang, B.X. 343
Wang, B.X. 490
Wang, B.X. 665
Wang, C.Y. 1460
Wang, D.Q. 459
Wang, F. 1333
Wang, J. 598
Wang, J.C. 680
Wang, J.F. 1048
Wang, L.B. 980
Wang, N.N. 1250
Wang, Q.H. 1560
Wang, Q.W. 177
Wang, S. 118
Wang, S.P. 835
Wang, X. 905
Wang, X. 1122
Wang, X. 1489
Wang, X.S. 1340
Wang, Y. 1646
Wang, Z.G. 459
Wang, Z.G. 1159
Wang, Z.N. 701
Watanabe, C. 445
Watanabe, M. 335
Wei, C.Y. 1333
Wei, Q.D. 1651
Wei, X.J. 1483
Wendt, J.O.L. 1686
Weng, L.C. 1640
Werther, J. 1677
Whitaker, S. 482
Willers, E. 1130
Wittig, S. 221
Wong, H. 621
Wu, C.Z. 1427
Wu, C.Z. 1632
Wu, F. 1217
Wu, G.T. 1002
Wu, J. 1560
Wu, X.P. 1340
Wu, Y.Z. 1212
Wyczalek, F.A. 1327
Xiang, J. 1728
Xiao, L.Q. 835
Xin, M.D. 379
Xing, K.Q. 373
Xiong, F. 701
Xiong, Z.H. 1632
Xu, B.Y. 1427
Xu, S.S. 1657
Xu, X.D. 1198
Xu, X.F. 1566
Xu, X.Y. 1433
Xu, Y.Q. 1305
Yabe, A 716
Yabe, A 860
Yabe, T. 1153
Yamada, N. 1233
Yamagishi, F. 695
Yamanaka, T. 1024
Yamashita, T. 1438
Yan, J.H. 1333
Yan, W.M. 949
Yan, W.P. 1591
Yan, Z.D. 1397
Yang, B.C. 821
Yang, B.C. 1289
Yang, D. 1566
Yang, H. 1212
Yang, H.M. 1305
Yang, K. 199
Yang, K.T. 940
Yang, L.W. 1184
Yang, S.M. 310
Yang, X.L. 1433
Yao, B. 1340
Yao, Q. 1281
Ye, X.H. 270
Yeh, C.L. 1640
Yin, X.L. 1427
Yokota, K. 1546
Yokota, M. 852
Yokoya, S. 335
Yong, Y.P. 1651
Yoshikawa, H. 199
Yoshino, H. 1241
Yoshizawa, Y. 1546
You, L.X. 1468
Yu, B.F. 459
Yu, B.F. 1159
Yu, C.J. 1566
Yu, H.L. 355

Yu, H.L. 367
Yu, J. 445
Yu, S.M. 1250
Yu, W.P. 905
Yu, X.L. 1397
Yue, D.T. 1002
Yun, Y. 1703
Zakharov, Y. 1500
Zeng, D.L. 373
Zhang, G. 379
Zhang, H. 621
Zhang, H. 701
Zhang, H.S. 1595
Zhang, H.X. 1048
Zhang, J.W. 1603
Zhang, L. 1198
Zhang, L. Winston 989
Zhang, L.Z. 1066
Zhang, L.Z. 1560
Zhang, S.H. 1489
Zhang, S.Z. 1048
Zhang, W. 1203
Zhang, X. 860
Zhang, X.L. 355
Zhang, X.S. 997
Zhang, Y. 910
Zhang, Y. 1646
Zhang, Y.H. 980
Zhang, Y.P. 788
Zhang, Y.P. 804
Zhang, Y.P. 1059
Zhang, Y.P. 1066
Zhang, Z.J. 490
Zhao, C.Y. 169
Zhao, L.F. 1489
Zhao, L.J. 910
Zhao, T.S. 438
Zhao, T.S. 529
Zhao, Z.L. 1427
Zheng, J.X. 393
Zheng, L. 1360
Zheng, Q.G. 1703
Zhou, H. 1586
Zhou, J. 379
Zhou, J. 1694
Zhou, J.H. 1281
Zhou, J.M. 1615
Zhou, J.S. 1566
Zhou, L.P. 997
Zhou, Q.T. 701
Zhou, T.H. 1468
Zhou, X.Y. 1483
Zhou, Y. 1184
Zhou, Z.J. 1281
Zhu, N. 316
Zhu, W.X. 1184
Zhu, Y.Q. 804
Zhu, Y.X. 788
Zhu, Y.X. 1059
Zou, Z.Q. 1728
Zubkov, P.T. 328
Zuo, Z.J. 573
Zuo, Z.J. 1007